Periodically driven many-body quantum systems

Quantum Ratchets, Topological States and the Floquet-Boltzmann Equation

I n a u g u r a l - D i s s e r t a t i o n

zur

Erlangung des Doktorgrades

der Mathematisch-Naturwissenschaftlichen Fakultät

der Universität zu Köln

vorgelegt von

Maximilian Genske

aus

Bremen

Köln 2017

Berichterstatter:	Prof. Dr. Achim Rosch
(Gutachter)	Prof. Dr. Sebastian Diehl

Tag der mündlichen Prüfung: 07. Juli 2017

Abstract

Controlling and manipulating complex many-body quantum systems will be a key ingredient for the development of next-generation technologies. While the realisation of a universal quantum machine is still out of reach, in recent years experimental systems of ultracold atoms have already evolved into a vivid field of research for quantum simulation. Crucially, such systems even allow for the successful *quantum engineering* of targeted many-body systems by means of coherent *periodic driving*. The essential properties of these *Floquet* systems encompass two main aspects: fast driving facilitates the simulation of effective static systems, and interactions lead to unique heating effects as energy is only conserved modulo the driving frequency. Within this thesis we theoretically study both of these aspects in respective model systems.

In part I of this thesis, we investigate the dynamics of excitations of a bosonic Mott insulator in a designed one-dimensional Floquet system. Here, periodic driving in combination with breaking all mirror symmetries of the system can induce directed motion of particles. In the limit of small excitation densities, the effectively non-interacting quantum ratchet determines the motion of holes and doublons in the Mott insulator and can in fact be used to manipulate the dynamics of such. This little quantum machine can also be used to drive particles against an external force, where transport is possible but requires the fulfilment of a commensurability condition for long times.

In part II, we discuss the role of interactions for periodically driven systems by means of a Floquet version of the Boltzmann equation. Starting from the Keldysh approach, we develop this semiclassical formalism based on a clear separation of time scales. The result is a description of the dynamics and the scattering of Floquet quasiparticles in such systems. Here, the property of discrete energy violation is naturally encoded in our formalism predicting the heating of interacting Floquet systems to infinite temperatures in the long-time limit. As a first application of this approach, we investigate a cold atom setup realising the Haldane model by means of periodic shaking. While homogeneous systems heat up globally, a confining potential evokes thermoelectric transport effects resulting from spatially dependent heating characteristics. Moreover, we show that the interplay of intrinsic heating, macroscopic diffusion and non-trivial topological properties of the Haldane model lead to an anomalous Floquet-Nernst effect, which describes anomalous particle transport as the result of developing temperature gradients.

In part III, we elaborate on the quantum simulator aspect of ultracold atoms by providing a theoretical framework for a possible simulation of a topological edge state in a one-dimensional optical lattice. In this case, the one-dimensional Dirac equation with spatially varying mass is important, which captures the topological properties of a corresponding system of the BDI symmetry class. We analytically discuss such system and investigate the role of mean-field interaction effects. We also identify the emergence of dynamical instabilities in a realisation with bosonic atoms.

Kurzzusammenfassung

Die Steuerung und Manipulation komplexer Quanten-Vielteilchensysteme wird ein wichtiger Bestandteil für die Entwicklung von Technologien der nächsten Generation sein. Während die Umsetzung einer universellen Quantenmaschine allerdings noch nicht erreichbar ist, haben sich in den letzten Jahren bereits experimentelle Systeme bestehend aus ultrakalten Atomen zu einem lebendigen Forschungsgebiet für die Quantensimulation entwickelt. Solche Systeme erlauben sogar das erfolgreiche '*quantum engineering*' von gezielten Vielteilchensystemen durch kohärentes *periodisches Antreiben*. Die wesentlichen Eigenschaften dieser *Floquet*-Systeme umfassen zwei Hauptaspekte: zum einen ermöglicht schnelles Treiben die Simulation effektiver statischer Systeme, zum anderen führen Wechselwirkungen zu einzigartigen Heizeffekten, da die Energie nur modulo der Antriebsfrequenz erhalten ist. Im Rahmen dieser Arbeit untersuchen wir theoretisch beide Aspekte in jeweiligen Modellsystemen.

In Teil I dieser Arbeit untersuchen wir die Dynamik der Anregungen eines bosonischen Mott-Isolators in einem speziell entworfenen eindimensionalen Floquet-System. Hierbei kann das periodische Antreiben in Kombination mit dem Brechen aller Spiegelsymmetrien des Systems eine gerichtete Bewegung von Teilchen induzieren. Im Limes kleiner Anregungsdichten beschreibt die effektiv nicht-wechselwirkende Quanten-Ratsche die Bewegung von Löchern und Dublonen im Mott-Isolator und kann in der Tat dazu verwendet werden, die Dynamik solcher zu manipulieren. Diese kleine Quantenmaschine kann auch benutzt werden, um Teilchen entgegen eine äußere Kraft zu treiben. Hierbei ist Transport der Teilchen möglich, aber gleichzeitig ist die Erfüllung einer Kommensurabilitätsbedinung für lange Zeiten erforderlich.

In Teil II diskutieren wir die Rolle von Wechselwirkungen für periodisch getriebene Systeme mittels einer Floquet-Version der Boltzmann-Gleichung. Ausgehend von der Keldysh-Methode entwickeln wir diesen semiklassischen Formalismus auf der Grundlage einer klaren Trennung von Zeitskalen. Das Ergebnis ist eine Beschreibung der Dynamik und der Streuung von Floquet-Quasiteilchen in solchen Systemen. Die Eigenschaft der diskreten Energieverletzung ist hierbei auf natürliche Art und Weise in unserem Formalismus codiert, welche das Aufheizen des wechselwirkenden Floquet-Systems auf unendliche Temperaturen im Limes langer Zeiten vorhersagt. Als erste Anwendung dieser Beschreibung untersuchen wir ein System aus kalten Atomen, welches das Haldane-Modell durch periodisches Schütteln realisiert. Während sich homogene Systeme global erwärmen, ruft ein Einschließungspotential thermoelektrische Transporteffekte hervor, die sich aus räumlich abhängenden Heizcharakteristiken ergeben. Darüber hinaus zeigen wir, dass das Zusammenspiel von intrinsischen Heizeffekten, makroskopischer Diffusion und nichttrivialen topologischen Eigenschaften des Haldane-Modells zu einem anomalen Floquet-Nernst-Effekt führt, der anomalen Teilchentransport als Ergebnis der Ausprägung von Temperaturgradienten beschreibt.

In Teil III gehen wir näher auf den Quanten-Simulator Aspekt von Systemen aus ultrakalten Atomen ein, indem wir einen theoretischen Rahmen für eine mögliche Simulation eines topologischen Randzustands in einem eindimensionalen optischen Gitter liefern. Hierbei ist die eindimensionale Dirac-Gleichung mit räumlich variierender Masse von Bedeutung, welche die topologischen Eigenschaften eines entsprechenden Systems der BDI-

Symmetrieklasse erfasst. Wir diskutieren ein solches System analytisch und untersuchen die Rolle der 'Mean Field' - Interaktionseffekte. Zusätzlich identifizieren wir die Entstehung von dynamischen Instabilitäten in einer entsprechenden Realisierung mit bosonischen Atomen.

Contents

1. General Introduction

Ever since the dawn of quantum mechanics more than 100 years ago, this intriguing theory of physics has revolutionized our understanding of the world and yet surprises us by its predictions up until today. Based on the quantum mechanical description of the microscopic world of atoms, molecules and condensed matter, important technological achievements were accomplished which have had an immeasurable impact on science just much as they had on society. In particular, we remark the early developments of semiconductor transistors as well as lasers in the middle of the last century. However, the way we approach the laws of quantum mechanics has fundamentally changed over the course of time: predominantly driven by technological advances, humans do no longer have to be mere observers of nature, but are moving more and more into a position where the control over the quantum world can be facilitated and utilized. This transition from being passive observers to becoming active doers is known as the *second quantum revolution* [1].

At the very end of this technological revolution stands the ultimate goal of developing and building a macroscopic quantum machine, such as a universal quantum computer [2]. To this day, however, the realisation of such devices is unfortunately still out of reach. Yet, first crucial steps have been taken in this direction, allowing to hope for the realisability of quantum technology for everyday purposes in the near future. One of these steps was the implementation and development of *quantum simulators*. Due to natural limitations of classical computing machines in combination with an exponentially growing Hilbert space of a many-particle system, it becomes very often impossible to predict and understand the behaviour of complex quantum systems at macro- and mesoscopic sizes. Here, it is not the property of the single quantum particle that determines the physics, but rather the collective interplay of a large number of such particles. For instance, some exciting phenomena emerging from this interplay, which are yet to be (fully) understood owing to their complexity, are quantum magnetism and high-temperature superconductivity [3]. As was originally pointed out by Feynman [4], a general strategy to yet obtain information may be the quantum simulation of such systems: a complex many-particle quantum system is substituted by a different, more controllable one mimicking the physics of the target system. Insights obtained on the second system can then be directly used to interpret the original one. Nevertheless, despite the tremendous technological advancing we have seen until today, the creation, control and manipulation of such auxiliary many-particle quantum system is still a very demanding task.

One of the most versatile tools in the context of realisable quantum simulators are systems made of *ultracold atoms* in optical lattices [5]. These systems are composed of gases of neutral atoms that are cooled to incredibly small temperatures (as low as $\sim 10^{-10}\,\mathrm{K}$) and captured in the interference pattern of overlapping laser beams. The regular spatial structure of the optical standing waves hereby resemble the periodic potential caused by positively charged nuclei fixed to lattice positions in a conventional solid. Since interactions between the trapped atoms can additionally be imposed and varied by means of external magnetic fields, these systems can be used to simulate the general setting of a typical condensed matter system. Due to the absence of lattice vibrations and defects, cold atoms in optical lattices are particularly well suited to analyse the physics of microscopic model systems, such as Hubbard-type models. Here, the implementation of the optical lattice is

not restricted by geometry or dimension [6]. At the same time, experimental methods have advanced into a state where atoms can be controlled, manipulated and detected on the level of a single lattice site both for bosonic [7,8] and fermionic [9,10] systems. Moreover, time scales of cold atom systems are one of their crucial advantages: atoms in optical lattices tunnel within milliseconds, while the dynamics of electrons in ordinary matter takes place on time scales of femtoseconds. Thus, cold atom systems cannot only be spatially resolved, but also dynamical aspects of respective model systems can be easily detected by modern day technology. First hallmark achievements of ultracold atomic systems encompass the modelling of equilibrium phases of matter, such as superfluid, metallic and Mott-insulating states [11, 12]. In addition, also dynamical studies have drawn much attention, such as studying the coherent time-evolution after a quantum quench [13, 14], the expansion of a cold atomic cloud in a Hubbard model [14], or monitoring the equilibration of an isolated quantum system [15]. Particularly the last example highlights the success of quantum simulators by explicitly outperforming calculating abilities of state-of-the-art supercomputers.

Building on the tremendous success of quantum simulators, most recently, the *engineering* and designing of targeted quantum systems and even novel types of matter was proposed by relatively simple means: coherent *periodic driving*. In fact, time-periodic coherent manipulation of small quantum systems such as single atoms has been a long established tool. In the context of complex many-body systems, however, such manipulation schemes have become available only most recently due to technological advances. Interestingly, periodically driven quantum many-body systems can exhibit rich dynamics and also show exotic phases which are absent in associated undriven versions [16]. Connecting to the discussion of building quantum machines and having this extended 'quantum toolbox' at hand, one might hope to build such a machine not just from assembling individually controllable constituents, but rather from an already existing, possibly complex many-particle quantum system dressed with periodic driving as an additional ingredient. In the field of ultracold atoms in optical lattices, the idea of coherently manipulating many-body states and their dynamics by means of periodic driving has therefore swiftly evolved into a vivid field of research on its own [17]. First remarkable achievements of such Floquet systems were the implementation of quantised particle pumps [18,19], the generation of effective magnetic fields to study quantum spin systems [20] and the proposal for a Floquet topological insulator [21]. Indeed, a large fraction of last-generation realisations particularly aim at the quantum simulation of *topological states of matter* [22]. The most prominent example in this context is the realisation of the Haldane model [23] by means of lattice shaking.

Nevertheless, while quantum simulator realisations with cold atoms are implemented for varying interaction strengths, so far most Floquet engineered systems are built on non-interacting systems. One of the reasons is that interacting Floquet systems naturally connect to the unique behaviour of cold atom systems regarding *non-equilibrium* situations. In general, ultracold gases are very well isolated quantum systems, as they do not couple to a bath. This is in strong contrast to conventional condensed matter systems, where lattice vibration excitations, i.e., phonons, provide a natural thermal bath for the electronic system. So systems of ultracold atoms are not only predestined to work as quantum simulators, but also appear as ideal testbeds to study non-equilibrium dynamics of quantum many-body systems [24,25]. For instance, interacting cold atoms have been used to study coherent non-equilibrium dynamics [26] as well as the corresponding relaxation of such systems [15,27,28]. But also the absence of thermalization in integrable models [29] or in terms of many-body localisation [30] can be investigated in these systems. A Floquet

system is inherently out-of-equilibrium due to the external periodic drive and therefore challenges the thermalization and dynamical aspects of static cold atom systems. The key feature here is the fact that interacting Floquet systems do not preserve energy and are therefore expected to render unique properties in terms of thermalisation and equilibration. In fact, it was only recently shown that a generic interacting isolated Floquet system cannot equilibrate in a conventional sense and must instead approach an infinite temperature state in the long-time limit [31, 32].

Periodically driven systems hold tremendous potential as a tool for engineering exciting quantum systems and creating novel states of matter. *Interacting Floquet systems* exhibit unique non-equilibrium physics. Eventually, all experimental system are (at least weakly) interacting. Hence, in order to be able to describe Floquet engineered systems in all relevant aspects, it is inevitable to also include interaction effects in respective studies. This will not only help to understand such designed quantum systems in more details, but might also lead to emerging new qualitative aspects within this vibrant field of research. Technically, however, dealing with such interacting Floquet systems is far from trivial, as, e.g., standard linear response theory treatments for periodically perturbed ordinary matter fail for arbitrary strong and fast external driving. Therefore, it comes at no surprise that there are still many open questions regarding interacting Floquet systems. One particular interesting and also experimentally highly relevant question is *how* Floquet systems are affected by interactions as a function of time. It is the central question of this thesis to give an answer to this question for the specific case of considering weakly interacting systems.

In general, the content of this thesis can be viewed as residing at the interface of the three main fields of research discussed above: quantum simulation with ultracold atoms, Floquet engineering by periodic driving and non-equilibrium dynamics in interacting many-particle systems. The precise outline of our purely theoretical work is as follows:

In part I of this thesis we consider effectively non-interacting periodically driven systems, thereby focussing on the engineering potential of such. In chapter 2 we first briefly sketch aspects of the creation of ultracold atoms in optical lattices and their associated characteristics. We then give an introduction to concepts and notations of non-interacting Floquet theory. We also aim at providing a list of main recent achievements of non-interacting Floquet systems, thereby stressing the position of such systems at the forefront of research. A concrete Floquet engineered system is presented in chapter 3, where we consider the dynamics of excitations of a bosonic Mott insulator in the presence of a periodic drive. By simultaneously breaking the mirror symmetries of the system, a quantum ratchet is established allowing to control the dynamics of such particles. We find that this little quantum machine can be utilized to, e.g., drive the excitations against an additional external constant force. Furthermore, we discuss possible topological stabilization mechanisms for such ratchets, which, however, appear to be not realisable.

In part II we then consider interactions in Floquet systems. Here, we also give a more in-depth introduction to general interacting Floquet systems, including an overview on recent accomplishments on this matter. Among different interacting Floquet settings, we choose to investigate weakly interacting periodically driven systems by means of a kinetic equation approach. Since the external drive is fast and coherent, the form of such an equation is *a priori* not entirely obvious. To this end, we present a detailed derivation based on a clear separation of time scales starting from a full quantum field theoretical approach. In this context, we first introduce basic notations and re-derive the conventional Boltzmann equation in chapter 4. Subsequently, we adjust the setting to derive a Floquet-Boltzmann equation in chapter 5 which describes the scattering of associated Floquet quasiparticles and allows for scattering processes that violate energy

conservation modulo the external driving frequency. In order to show the working principle we apply this formalism to an interacting version of the recently realised Haldane model [23]. We apply the Floquet-Boltzmann equation to a homogeneous system in chapter 6 and to an inhomogeneous version in chapter 7, thereby calculating the heating behaviour of the respective system. Interestingly, we find for the inhomogeneous case that the presence of a non-trivial topological structure of the underlying lattice model gives rise to anomalous particle currents as a consequence of temperature gradients. We predict this anomalous Floquet-Nernst effect by a hydrodynamic description of the system.

In part III we slightly change gears and solely focus on the quantum simulator aspect of cold atom systems. Here, we present results of a joint collaboration with the experimental group of M. Weitz from Bonn on the simulation of a topological edge state in an optical lattice. In chapter 8, we first discuss the topological properties of a standard BDI-symmetry class model and show how the essential properties can be captured by a massive 1D Dirac equation. By using an adjusted mean-field description of the problem we crucially show that interaction effects are negligible and that therefore experimental results can be safely interpreted in terms of the 1D target system. A quantitative comparison between experimental data and numerical results then indeed suggests the successful simulation of a topological edge state. In chapter 9, we discuss peculiar interaction effects of the bosonic Dirac system. A study of the fluctuation spectrum reveals the emergence of dynamical instabilities, which yields the possibility to study interaction effects in topological matter in the future.

Part I.

Non-interacting Floquet systems

2. Periodic driving as a tool for quantum engineering

A main goal for utilizing the laws of quantum mechanics for everyday life applications is to build a macroscopic *quantum machine*. Such a device can be the analogue to a classical mechanical machine [33] or a universal quantum computer [2, 4, 34, 35], for example. In general, scientists hope that such machines can be more efficient and powerful than conventional, classical devices. Nevertheless, despite the fact that in 1996 Lloyd indeed confirmed [36] Feynman's original conjecture [4] that any (local) quantum system can be simulated by a quantum computer (or likewise by another quantum system), the realisation of a universal quantum computer or machine still faces huge challenges. One of the main issues being the lack of scalability due to decoherence [35]. Having said this, there do exist candidates for quantum computing that are believed to be notably robust against decoherence, such as topological quantum computing by anyons [37, 38]. Leading researchers have therefore only recently expressed their optimism for commercial progress of quantum computers in the near future [39].

In the meantime, however, the idea of Feynman and Lloyd to simulate a quantum system by another one has evolved into a vivid field of research on its own. The general goal of a *quantum simulator* is to mimic the behaviour of a system of interest using a second, more accessible and well-controlled quantum system. This allows to study the physics (and potentially beyond) of complex quantum systems that would be otherwise intractable by classical means, e.g., by conventional computers. Typical quantum simulators that have emerged over the last decades are, among others, neutral atoms (in optical lattices) [6, 11, 40], trapped ions [41, 42], superconducting circuits [43, 44], photonic systems [45] and nuclear spins [46]. The list of possible fields of applications of such quantum simulators is broad and ranges from high-energy physics over cosmology to open systems. In order to obtain an in-depth report about the vast areas of applicability and the tremendous potential of quantum simulators we refer the reader to recent reviews in this topic, such as Ref. [47] and references therein.

The perhaps most important field in the context of quantum simulation is the one of condensed matter physics. Here, particularly systems made of ultracold atoms (bosonic and fermionic) in optical standing waves have developed into a very versatile tool. The reason being that this setup has the potential to mimic the behaviour of electrons experiencing the periodic potential in a solid state system. Important hallmarks in this context were, e.g., the realisation of the Bose-Hubbard model and the successive study of the superfluid to Mott-insulator transition [11] as well as the quantum simulation of ultracold Fermi gases investigating the so called BEC-BCS crossover [48]. Moreover, scientists were able to simulate the effect of electromagnetic fields on charged particles using artificial gauge fields [49–51]. The latter paved the way to studying quantum Hall physics in the context of cold atoms. More recently, researchers have even advanced to simulating relativistic equations [52] and topological states of matter [22]. In fact, chapter 8 of this thesis is dedicated to a recent simulation of a 'massive' Dirac equation using ultracold rubidium atoms, verifying a one-dimensional topological edge state [53].

Despite the huge progress quantum simulators have had so far, they mainly aim at

analysing and simulating already known models and materials. In recent years, however, research has also progressed into a direction where one not merely simulates known materials, but rather manages to realise completely new states of matter. A main player of such *quantum engineering* in the context of ultracold atoms has become the method of periodic driving. Such periodically driven systems at arbitrary frequency and strength are also called *Floquet systems* [54]. These systems give rise to exciting phenomena such as dynamic localization [55], frustrated magnetism [56], the Floquet analogoue of a topological insulator [21] or the realisation of the Haldane model [23]. Moreover, Floquet systems offer also the chance of building little quantum machines as discussed at length in chapter 3 of this thesis. While nowadays periodically driven systems are a major tool for the field of ultracold atoms [17], there are still many aspects to be understood. The latter mainly concerns the effect of interactions in these Floquet system, which is the central topic of this thesis. Nevertheless, understanding the basic, non-interacting principles of these periodically driven systems builds the fundament to the success of Floquet engineering as well as to our work in the following.

To this end, we will introduce important aspects of Floquet engineering in this chapter. First, we will shed light on the topic of ultracold atoms in optical lattices and will briefly elaborate on details that will be important for the remainder of this thesis. Second, we will introduce the *Floquet formalism* which is the natrual language describing those respective systems. Third and last, we will aim at yielding a small overview on recent developments in the context of Floquet engineering - including both experimental advances as well as theoretical ideas.

2.1. Ultracold atoms in optical lattices

Ultracold atoms in optical lattices are engineered closed quantum many-body systems that are highly controllable and therefore offer a unique setting for the quantum simulation of condensed matter systems and for the creation of novel states of matter [6]. In contrast to conventional solid state systems, the microscopic physics of cold neutral atom systems is precisely known owing to their cleanliness and isolation. This allows for a very controlled way of studying also macroscopic phenomena and interpret them faithfully in terms of microscopic constituents and details.

Cold atoms in optical lattices rely on the coherent collective interaction of matter with light, thereby mimicking the physics of a crystalline solid where the ultracold quantum gas resembles electrons. Such systems have not only driven the development of new types of experimental realisations, but also boosted theoretical ideas and tools in the realm of condensed matter physics. This rapidly growing field of research provides an enormous list of remarkable contributions ranging from the detection of the superfluid to Mott insulator transition [11] over the general realisation of topological quantum matter [22] such as the Haldane model [23] to first direct observations of antiferromagnetic correlations in such systems [57]. Technical aspects, experimental details and theoretical visions have been summarised in numerous works. In particular, we like to highlight the reviews by Bloch, Dalibard and Zwerger [5] and by Bloch, Dalibard and Nascimbène [6] as well as recent proceedings on 'quantum matter at ultralow temperatures' [51]. Note that large parts of this section are built on these reviews and that a more in-depth view on the general capabilities of ultracold atoms can be found therein.

In the following, we roughly elaborate on different general aspects of ultracold gases before explaining how they can be trapped by means of laser-light fields. We then demonstrate how these peculiar traps give rise to periodic structures putting the emphasis on

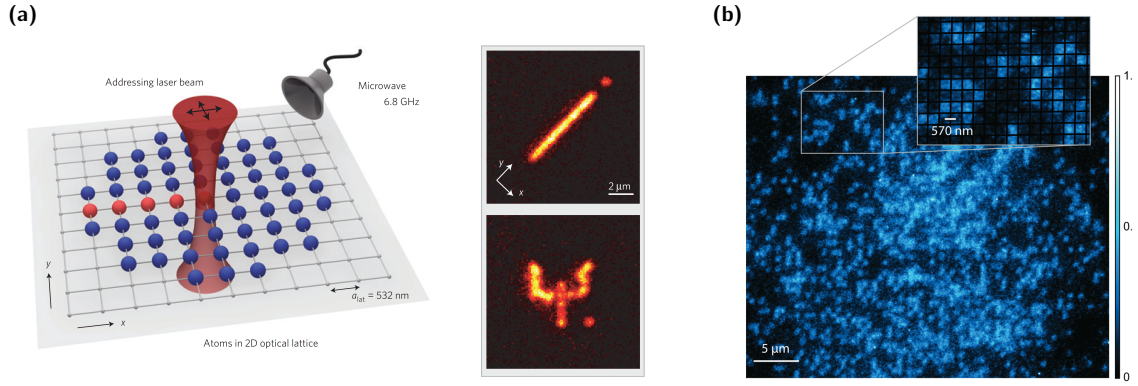

Figure 2.1.: Visualization of state-of-the-art control, manipulation and detection capabilities for systems of ultracold atoms in optical lattices: images of (a) bosonic and (b) fermionic atoms in an optical lattice taken by a quantum gas microscope. The initial state preparation as well as the single-site resolution becomes clearly visible. Figures are taken from Refs. (a) [6] and (b) [10], respectively.

the realisation of Hubbard type models. Due to the high level of controllability such systems can be easily extended to more sophisticated versions. One powerful extension is the implementation of periodic driving leading to the realisation of Floquet systems. The capabilities of such systems will then be exposed in the following sections.

2.1.1. Ultracold quantum gases

Over the last half a century or so, the production of coherent light sources, i.e., *lasers*, have seen a tremendous progress. This resulted not only in a remarkable progress of investigating microscopic details of single atomic or molecular species using, e.g., spectroscopy, but also opened up the possibility to create and study coherent light-matter mixtures.

The first milestones along these lines was reached by producing a Bose-Einstein condensation (BEC) from an atomic vapour in the mid 90's [58,59]. Since densities of such gases are extremely low (up to 10^{-7} smaller than air at room temperature [5]), temperatures ought to be reduced to extremely low values, as well. For this purpose, sophisticated trapping and cooling mechanisms have been developed [60,61]. In particular, these techniques benefit immensely from a simple electronic structure of the used atomic species. Hence, ultracold gases are typically created from *alkali* atoms which possess only a single valence electron. Degenerate quantum gases have been achieved for many atom species such as ^{7}Li,^{23}Na,^{87}Rb which are all of bosonic type [51] and also for fermions such as ^{6}Li, ^{40}K [62]. More recently, degenerate quantum gases of alkaline-earth(-like) species such as ytterbium or strontium became available [63]. Present-day temperatures in such setups are decreased to values as low as $10^{-10}\,\mathrm{K}$ for bosons [64] and $10^{-6}\,\mathrm{K}$ for fermions[1] [62]. Remarkably, these ultracold quantum gases therefore describe the coldest place in the universe.

Those very low temperatures in the respective many-body quantum systems also have a significant impact on the role of interactions [5]. Generally, the interaction between two neutral atoms can be modelled by a van der Waals potential $V_{\mathrm{vdW}}(\mathbf{r}) = -C_6/r^6$, which is cut off at some short distance $|\mathbf{r}| = r_c$ corresponding to the extension of the atom in space

[1] Note that the significant difference between bosons and fermions can be traced back to the statistical properties of fermions. In fact, standard cooling techniques applicable to bosons fail for fermions and a sufficient cooling of the latter is a much harder experimental task. A comprehensive review of ultracold fermi gases can be found in Ref. [62].

and C_6 is the atom dependent van der Waals coefficient. Alkali atoms, for instance, are associated with relatively large C_6-coeffiecients, since they are strongly polarizable. The low-energy scattering properties are also determined by this quantity. In general, two-body scattering events involving a finite relative angular momentum quantum number $l \neq 0$ are allowed. These processes are characterised by a centrifugal energy barrier of height $\propto l/(C_6)^{1/2}$. However, for $l = 1$ these energies correspond to temperatures of $\sim$ 1mK for typical atomic masses. So as soon as atoms - irrespective of their species - are cooled substantially below this threshold, only lowest angular-momentum scattering events are supported by the gas. For bosons this corresponds to *s-wave* collisions. Fermions, on the other hand, undergo s-wave scattering processes only in the presence of a spin-mixture due to the Pauli principle. Assuming that we only need to consider s-wave scattering in the low energy limit, the scattering amplitude as a function of momentum k is approximated as $f(k) \approx -a_s/(1+ika_s)$. This scattering amplitude is the result (irrespective of the value of k) for the pseudopotential [5]

$$V(\mathbf{r}) = \frac{4\pi\hbar^2 a_s}{m}\,\delta(\mathbf{r})\,, \tag{2.1}$$

with m being the atom's mass and, most crucially, a_s describes the *scattering length* which fully specifies the interaction strength of the quantum gas. So while the pseudopotential (2.1) captures all scattering properties in the low energy regime, the characteristics of the degenerate quantum gas depends qualitatively as well as quantitatively on the scattering length a_s. For example, a repulsively, $a_s > 0$, yet weakly interacting bosonic ultracold gas still forms a Bose-Einstein condensate that is well described by a *Gross-Pitaevskii equation* (GPE). This is in fact the natural experimental situation. For a discussion of the GPE we refer the reader to Ch. 8 of this thesis. In contrast, if the interactions are made attractive, $a_s < 0$, the bosonic gas is unstable against a collapse. For fermions, a transition from $a_s < 0$ to $a_s > 0$ is expected to trigger the infamous BCS-BEC crossover [6, 62, 65], where particles form weakly bound Cooper pairs for attractive interactions and are grouped into strongly bound bosonic molecules for repulsive interactions.

At first sight, this tuning of the scattering length seems like a purely academic problem. However, there is indeed a relatively simple way of varying a_s also in experimental circumstances using so called *Feshbach resonances* [66]. The essence of this mechanism is the usage of bound states offered by the atomic gas that are not captured by the simple interaction mechanism of Eq. (2.1). To be more precise, Feshbach resonances emerge in situations when an energy state in an open channel is resonantly coupled to a bound state in a closed channel. In this resonant process, the initially free, scattered particles get temporarily captured in a quasibound state giving rise to a resonance in the scattering cross-section. In the case of ultracold atoms, for instance, such channels may correspond to different spin configurations. This is particularly useful as it allows the tuning of the associated resonances, and therefore of the scattering length by means of magnetic fields. Phenomenologically, this allows to redefine the scattering length as

$$a_s(B) = a_{\mathrm{bg}}\left[1 - \frac{\Delta B_r}{B - B_r}\right], \tag{2.2}$$

where B descibes the magnetic field strength, B_r and ΔB_r mark the position and width of the corresponding Feshbach resonance and a_{bg} is the off-resonant background scattering length. Note that such Feshbach resonances are much better applicable to fermions than to bosons due to a huge lifetime difference resulting from three-body collisions. Interestingly, these Feshbach resonances even allow for studying the limit $a_s \to \infty$ [67]. Here, a fermonic

system becomes scale invariant and the knowledge about the physics of such a *unitary fermi gas* can be applied to other scenarios happening at much larger scales, such as the physics of neutron stars [6].

Hence, ultracold quantum gases are already by themselves very fascinating systems. Using additional trapping techniques their complexity and capability, e.g., in terms of representing quantum simulators for conventional condensed matter systems, can be even enhanced. This additional trapping can conveniently be obtained by means of optical devices and is discussed next. Note that while neutral atoms can also be trapped by magnetic fields (cf. Ch. 8), particularly in fermionic systems the 'magnetic degree of freedom' is often reserved for controlling the interactions as outlined above.

2.1.2. From optical trapping to optical lattices

Optical potentials created by laser light are a powerful tool to confine neutral atoms to setups of reduced dimensionality or even geometry in cases of periodic lattices. The basic concept of such potentials relies on the interaction of the atoms with *far-detuned* (laser) light. This light-matter interaction is most intuitively understood in a (semi)classical setting. Here, the mathematical framework is developed for a classical electromagnetic field interacting with an atom described by a many-level quantum system, where the atom is typically considered as an effective two-level system with ground $|g\rangle$ and excited state $|e\rangle$ separated by an energy difference of ω_0.

Placing an atom into a monochromatic laser-light field of frequency ω_L described by $\mathbf{E}(\mathbf{r},t) = \hat{\mathbf{e}}E_0(\mathbf{r})e^{-i\omega_L t} + c.c.$, with $\hat{\mathbf{e}}$ being the polarization vector, induces an atomic dipole moment $\mathbf{p}$ with amplitude $p_0 = \alpha(\omega_L)E_0$. Here, α denotes the polarizability, where its real part is responsible for the dispersive properties of the light-matter interaction and the imaginary part describes absorption. In cases where the size of the *detuning*, $\Delta = \omega_L - \omega_0$, is small compared to the transition frequency itself, i.e., $|\Delta|/\omega_0 \ll 1$, the rotating-wave approximation is applicable, and the real part of the polarization can be approximated by $\mathrm{Re}(\alpha(\omega_L)) \approx |\langle e|d_{\mathbf{E}}|g\rangle|^2/\hbar(\omega_0 - \omega_L)$, where $d_{\mathbf{E}}$ is the dipole operator in the direction of the field [5]. The induced dipole moment gives rise to an effective light-matter interaction potential for the atom - the *dipole potential* - of the form [61]

$$V_{\mathrm{dip}}(\mathbf{r}) = -\frac{1}{2}\left\langle \mathbf{p}(\mathbf{r})\cdot\mathbf{E}(\mathbf{r})\right\rangle_t \simeq \frac{3\pi c^2}{2\omega_0^3}\frac{\Gamma}{\Delta}I(\mathbf{r})\,, \tag{2.3}$$

where $\langle . \rangle_t$ denotes a time average, we introduced the decay rate $\Gamma = \frac{\omega_0^3}{3\pi\hbar\epsilon_0 c^3}|\langle e|d_{\mathbf{E}}|g\rangle|^2$ and $I = \epsilon_0 c\left\langle \mathbf{E}^2\right\rangle_t = 2\epsilon_0 c|E_0|^2$ is the light-field intensity, with ϵ_0 being the vacuum permittivity and c is the speed of light. The form of the dipole potential (2.3) is equivalent to the energy shift obtained from a second order perturbation theory in a full two-level quantum mechanical treatment. This shift is commonly known as 'AC-Stark' shift. Note that the reason for the dipole potential being proportional to the intensity of the laser can be traced back to the fact that the center-of-mass motion of atoms is much slower that $1/\omega_L$.

A spatially varying density profile $I(\mathbf{r})$ therefore creates a trapping potential for neutral atoms, with associated trapping force $\mathbf{F}_{\mathrm{dip}} = -\nabla_{\mathbf{r}}V_{\mathrm{dip}} \propto \nabla_{\mathbf{r}}I$. Here, the spatial dependence can either result from a focussed laser beam, as used in conventional dipole traps, or from an interference of beams, as exploited in order to establish effective optical lattice structures for neutral atoms, see below. Most importantly, the trapping potential can either be attractive or repulsive depending on the sign of the detuning Δ. For $\Delta < 0$, the laser beam is said to be 'red-detuned' and atoms are attracted to regions of large

light intensities. In contrast, a blue detuned laser, $\Delta > 0$, repels atoms from high to low intensities.

However, it is crucial to note that the dipole potential of Eq. (2.3) is *not* conservative due to spontaneous absorption and emission processes captured by $\mathrm{Im}(\alpha)$. The contribution of the absorption is given by [61]

$$\hbar\Gamma_{\mathrm{sc}} = \frac{\Gamma}{\Delta} V_{\mathrm{dip}} \qquad \text{with} \qquad \Gamma_{\mathrm{sc}}(\mathbf{r}) = \frac{3\pi c^2}{2\hbar\omega_0^3}\left(\frac{\Gamma}{\Delta}\right)^2 I(\mathbf{r}) \tag{2.4}$$

being the scattering rate determined within the same two-level approximation as above. In order to obtain maximally controllable traps, one desires to minimize scattering events while keeping the dipole depth fixed. This is indeed possible by tuning the laser intensity against the detuning: while the dipole potential scales as I/Δ, the scattering rate follows I/Δ^2. Thus, one usually employs large detunings and high intensities which allows for a sufficient suppression of spontaneous scattering events.

The perhaps easiest way to implement a dipole potential is the use of a focussed laser beam that has a spatial profile of $I(r,z) = I_0(z)\exp(-2r^2/w^2(z))$, where r denotes the radial coordinate with respect to the direction of propagation of the laser, z, and $w(z)$ is the $1/e^2$ radius. Around the intensity maximum at $r, z = 0$ the dipole trap is approximately harmonic. More interestingly, however, periodic potentials can be generated by overlapping counterpropagating laser beams. In the simplest case, where two laser beams of the same wavelength λ interfere, an optical standing wave with a regular lattice spacing of $\lambda/2$ forms. The resulting trapping potential of a red-detuned laser is then given by [5]

$$V(r,z) \simeq -V_0 \, \exp\left[-2r^2/w^2(z)\right] \, \sin^2(k_0 z)\,, \tag{2.5}$$

where $k_0 = 2\pi/\lambda$ is the wave vector of the laser and V_0 describes the maximum depth of the potential. By adding additional counterpropagating lasers along perpendicular directions periodic potentials in two- and three dimensions can be formed, respectively. For example, a setup in which the total optical potential is simply the sum of three independent standing waves allows for an approximate description near the center of the trap of [5]

$$V(x,y,z) \simeq V_0 \left(\sin^2(k_0 x) + \sin^2(k_0 y) + \sin^2(k_0 z)\right). \tag{2.6}$$

Note, however, that an additional external harmonic confinement due to the Gaussian profile of the laser beams is still present in most cases. While experiments originally focussed on realising cubic 3D optical lattices [11], by superimposing laser beams of different wavelengths at various angles any lattice geometry that can be conceived by Fourier synthesis can thereby be realised in experiments [6]. Thus, also triangular [56], honeycomb [68] (see also Ch. 6) and Kagomé [69] lattices have among others been achieved experimentally. In addition, more sophisticated dipole trapping schemes allow for, e.g., additional spatial dependences of the lattice. A corresponding example is presented in detail in chapter 8 of this thesis.

A natural energy scale for atoms in optical lattices is the associated *recoil energy*

$$E_r = \frac{\hbar^2 k_0^2}{2m}\,, \tag{2.7}$$

where m describes the mass of the respective atom species used in the experiment. For instance, bosonic rubidium atoms of type ^{87}Rb in a lattice with $\lambda \approx 1\mu$m have a recoil energy of about $E_r \approx 2$kHz. In practise, lattice depths can generally be made deep with relatively little effort in the sense that $V_0/E_r \gg 1$ with $V_0 \sim \mathcal{O}(10\mathrm{kHz} - 100\mathrm{kHz})$. This limit allows for a strong confinement of the atoms in the intensity maxima (minima) of a red (blue) detuned optical lattice. The natural description of such situations at low energies is in terms of Wannier functions and, eventually, of a tight-binding picture.

2.1.3. Band theory and Hubbard models

To model the situation of trapping an ultracold quantum gas in a periodic optical potential we assume that the lattice is homogeneous, e.g., described by Eq. (2.6) for a cubic geometry, and neglect all effects stemming from the Gaussian beam profile discussed above. We also assume that no further trapping mechanism, e.g., in form of a magnetic field, is present. One of the central concepts to model conventional condensed matter systems is the *Bloch theorem* [70]: the eigenstates of the single-particle Hamiltonian $H_0 = -\hbar^2\nabla^2/2m + V_{\text{lat}}$ capturing the dynamics of electrons in the presence of a periodic lattice potential, $V_{\text{lat}}(\mathbf{r}) = V_{\text{lat}}(\mathbf{r} + \mathbf{R}_i)$, where $\mathbf{R}_i$ is a vector connecting two (Bravais) lattice sites, can be chosen to be a Bloch function

$$\psi_{n,k}(\mathbf{r}) = e^{i\mathbf{kr}}\, u_{n,k}(\mathbf{r})\,, \tag{2.8}$$

with $u_{n,k}(\mathbf{r}) = u_{n,k}(\mathbf{r} + \mathbf{R}_i)$. Here, $\mathbf{k}$ denotes a quasimomentum within the first Brillouin zone of the reciprocal lattice, and n encodes all other quantum numbers, such as band index and spin. An alternative complete basis, which becomes particularly useful in the limit of deep lattices, is provided by *Wannier functions*, $w_{n,i}(\mathbf{r})$. These Wannier functions are connected to Bloch functions via Fourier transformation [70], i.e.,

$$w_{n,i}(\mathbf{r}) = \frac{1}{V_{\text{BZ}}} \int_{\text{BZ}} d\mathbf{k}\; e^{-i\mathbf{kR}_i}\, \psi_{n,k}(\mathbf{r})\,, \tag{2.9}$$

where V_{BZ} denotes the volume of the Brillouin zone.

While for arbitrary lattice depths the benefit of Wannier functions is not apparent, they will eventually pave the way to the successful description of discrete lattice models. To this end, we switch to a second quantization picture: the operator that creates a particle at a given point in space $\mathbf{r}$ can be expanded as [5]

$$\hat{\psi}^\dagger(\mathbf{r}) = \sum_{i,n} w_{n,i}(\mathbf{r})\, c^\dagger_{n,i}\,, \tag{2.10}$$

where $c^\dagger_n(\mathbf{r})$ creates a particle in the corresponding Wannier state $w_{n,i}$. The Hamiltonian is then expressed in second quantization form as

$$H_0 = -\sum_{ij,n} J_{n,ij}\, c^\dagger_{n,i} c_{n,j}\,, \tag{2.11}$$

where the hopping strengths $J_{n,ij}$ are matrix elements for transitions between different Wannier states and read as

$$J_{n,ij} = -\int d\mathbf{r}\; w^*_{n,i}(\mathbf{r}) \left(-\frac{\hbar^2}{2m}\nabla^2 + V_{\text{lat}}(\mathbf{r}) \right) w_{n,j}(\mathbf{r})\,. \tag{2.12}$$

In general, these matrix elements connect lattice sites at arbitrary distances. Moreover, they can be understand as the Fourier transformed Bloch energy bands given by [5]

$$\varepsilon_n(\mathbf{k}) = \sum_i J_{n,i}\, e^{i\mathbf{kR}_i}\,. \tag{2.13}$$

In the following, we will consider the interesting regime of having a deep lattice, i.e., $V_0 \gg E_r$. In such situations two properties emerge: first, the deeper the optical potential, the larger becomes the energy gap between the lowest and excited bands. Assuming that thermal energies of the atoms are low compared to this gap, the description can be

effectively reduced to the lowest Bloch band only, $n = 0$. Second, the Wannier functions become exponentially confined in space in the same limit, which strongly suppresses the hopping of particles to non-nearest neighbour sites. This allows to write Eq. (2.11) in its associated *tight-binding* form

$$H_0 = -\sum_{\langle i,j\rangle} J_{ij}\, c_i^\dagger c_j\,, \tag{2.14}$$

where $J_{ij} \equiv J_{0,ij}$ and $\langle i,j\rangle$ indicates summation over nearest-neighbour indices only.

While Eq. (2.14) is equally valid for bosons and fermions, the form of the particle species does matter when incorporating *interactions*. Nonetheless, assuming that a pseudo-potential given by Eq. (2.1) describes the scattering well for both species, one straightforwardly finds the *Bose-Hubbard* model for bosons

$$H_{\mathrm{BH}} = -\sum_{\langle i,j\rangle} J_{ij}\, a_i^\dagger a_j + \frac{U}{2}\sum_i n_i(n_i-1) + \sum_i \varepsilon_i\, n_i\,, \tag{2.15}$$

and the original *Hubbard* model for fermions

$$H_{\mathrm{FH}} = -\sum_{\langle i,j\rangle,\sigma} J_{ij}\, c_{i,\sigma}^\dagger c_{j,\sigma} + U\sum_i n_{i,\uparrow} n_{i,\downarrow} + \sum_{i,\sigma} \varepsilon_i\, n_{i,\sigma}\,, \tag{2.16}$$

where $n_i = a_i^\dagger a_i$ ($n_{i,\sigma} = c_{i,\sigma}^\dagger c_{i,\sigma}$) is the bosonic (fermionic) number operator. Also, the on-site interaction strength U is given as [5]

$$U = \frac{4\pi\hbar^2 a_s}{m}\int d\mathbf{r}\, w(\mathbf{r})^4\,. \tag{2.17}$$

Note that keeping track of the spin index in the fermionic Hubbard model is crucial, since on-site scattering is prohibited for identical particles due to the Pauli exclusion principle. In both cases, we also added an extra on-site energy shift that may be caused by an additional external potential, cf. Chs. 3 and 7.

The Bose-Hubbard model has two quantum phases: the Mott-insulating phase ($U \gg J$ for $\langle n\rangle \in \mathbb{N}$) and the superfluid phase ($J \gg U$). The experimental verification of these two phases [11] as a function of the ratio U/J denotes *the* hallmark in the field of ultracold quantum gases in optical lattices. At the same time, this model strongly demonstrates the potential of ultracold atom systems as quantum simulators: despite its simple structure, solving the bosonic Hubbard model is in fact far from trivial (particularly near the phase transition) and demands advanced numerical techniques [5, 71].

The fermionic Hubbard model - also seemingly simple - has an even richer phase diagram than its bosonic counterpart (with $\langle n\rangle = 1$) [72]. For instance, for large interaction strengths, $U \gg J$, a fermionic Mott insulator forms [12]. Moreover, in this strongly interacting regime superexchange processes provide the basic mechanism for an antiferromagnetic coupling between spins on neighbouring lattice sites [6]. Nonetheless, no direct observation of such a quantum antiferromagnet has been observed until today. Recently, only associated correlations could be measured [57, 73]; at temperatures, however, larger than the antiferromagnetic transition temperature. This reflects one of the main issue of systems with ultracold atoms in optical lattices prohibiting the simulation of arbitrary phases of matter: so far, entropies per particle cannot be lowered to sufficiently small values in the preparation process (cf. discussion of Ch. 6).

Hubbard models of different geometry, interaction type and hopping mechanism build the foundation of the field of ultracold atoms in optical lattices. Variants of these models will be encountered by the reader throughout this thesis. Importantly, periodic driving is

easily encoded in these Hubbard systems by, e.g., lattice shaking, see Sec. 2.3. In order to understand the motivation behind dressing static systems with an additional periodic drive from a quantum engineering perspective, we first introduce the Floquet theory in the following section.

2.2. Floquet theory

The natural language to deal with periodically driven systems - the Floquet formalism - dates back to the original work by Floquet himself in 1883 [54]. Later, this formalism was also introduced in the context of physics when Shirley considered a solution to the Schrödinger equation with a the time-periodic Hamiltonian [74]. In 1973, Sambe developed the formalism even further by adding some mathematical rigor to it [75]. Being then mostly ignored for a couple of decades, the Floquet formalism re-emerged as the natural language in describing the coherent manipulation of atomic systems, which became more and more experimentally realisable due to the technical developments of lasers [76, 77]. Nowadays, researchers are able to coherently manipulate even many-particle systems made of ultracold atoms, see above, by means of (strong) periodic driving. A direct consequence has been the utilization of this driving mechanism to create novel systems and types of matter. The role of the Floquet languge in this context has been summarized recently in a number of works [17, 77–80]. Within this section we will elaborate on the key features of the non-interacting Floquet formalism that are relevant for the course of this thesis. Note that the following parts of the section are strongly inspired by the reviews by Hänggi [77] and Eckardt [17]. Later in chapter 5, we will investigate how this basic notion of describing periodically driven system is extended to capture the presence of interactions.

2.2.1. The Floquet theorem

Throughout the main part of this thesis we are interested in driven quantum systems. In the context of cold atoms as well as other solid state systems, this drive is typically implemented by electro-magnetic fields. It is known that for intense fields, i.e., when fluctuations in the photon number can be ignored, both theories describing the light classically and fully quantum mechanically give the same result [74]. Assuming this situation to hold, a quantization of the drive itself is therefore not necessary. Hence, the system of interest might simply be described by a time periodic Hamiltonian

$$H(t) = H(t+T)\,, \tag{2.18}$$

with T being the period of the drive, and associated driving frequency $\Omega = 2\pi/T$. The discrete time translation symmetry of the system, $t \to t+T$, allows us to apply the Floquet formalism [54], which is the main working horse for *strongly driven* quantum systems.

To elaborate on this Floquet formalism lets start by looking at the Schrödinger equation, which is given by

$$i\hbar\frac{\partial}{\partial t}\left|\psi(t)\right\rangle = H(t)\left|\psi(t)\right\rangle\,. \tag{2.19}$$

Note that from now onwards we set $\hbar = 1$, and we will follow this convention unless stated otherwise. The solution to this equation can formally be given as $\left|\psi(t)\right\rangle = U(t,t_0)\left|\psi(t_0)\right\rangle$ with the help of the evolution operator

$$U(t,t_0) = \mathcal{T}_t \exp\left[-i\int_{t_0}^{t} dt' H(t')\right]\,, \tag{2.20}$$

where $\mathcal{T}_t$ denotes the time-ordering operator. Generically, it is hard - and often even impossible - to evaluate Eq. (2.20). Here, however, the temporal periodicity of H will significantly simplify the problem. To this end, we introduce the *Floquet Hamiltonian*[2]

$$H^F(t) \equiv H(t) - i\frac{\partial}{\partial t}\,. \tag{2.21}$$

Note that the Floquet Hamiltonian is still a Hermitian operator.

One can easily show that H^F is also periodic in time, i.e., $H^F(t) = H^F(t+T)$. It can, thus, be proven that the Floquet Hamiltonian commutes with the evolution operator over one single period, $U(t+T,t) \equiv U^F(t)$,

$$U^F(t)H^F(t) = U^F(t)H^F(t)\left[U^F(t)\right]^{-1}U^F(t) = H^F(t+T)U^F(t) = H^F(t)U^F(t)\,. \tag{2.22}$$

The operator U^F is often called *Floquet operator* in the literature. Owing to their commuting property, H^F and U^F share a common set of eigenstates $\{|\psi_\nu(t)\rangle\}$. Here, the index ν encodes the usual quantum number (e.g., spin, band index, momentum). Since the time-evolution operator must be unitary, the eigenvalue equation for U^F reads[3]

$$U^F(t)\,|\psi_\nu(t)\rangle = e^{i\theta_\nu(T)}\,|\psi_\nu(t)\rangle\ . \tag{2.23}$$

In order to find the relation between the phase θ and the period T we look at the time-evolution over n periods (without loss of generality we assume $t_0 = 0$)

$$U(nT,0) = \mathcal{T}_t\,\exp\left[-i\int_0^{nT} dt'\,H(t')\right] = \mathcal{T}_t\,\exp\left[-i\sum_{k=1}^{n}\int_{(k-1)T}^{kT} dt'\,H(t')\right]. \tag{2.24}$$

Using the temporal periodicity of the original Hamiltonian, $H(t) = H(t+T)$, one obtains

$$U(nT,0) = \mathcal{T}_t\prod_{k=1}^{n}\exp\left[-i\int_0^{T} dt'\,H(t')\right] = \prod_{k=1}^{n}\mathcal{T}_t\,\exp\left[-i\int_0^{T} dt'\,H(t')\right]. \tag{2.25}$$

Here, the fact that equal terms commute has been used in order to move the time-ordering operator in front of the exponential. It finally follows that

$$U(nT,0) = \left[U^F(0)\right]^n. \tag{2.26}$$

Combining this result with Eq. 2.23 then yields $e^{i\theta_\nu(nT)} = e^{in\theta_\nu(T)}$, requiring that θ_ν is directly proportional to T. Introducing a proportionality constant we write $\theta_\nu = -\varepsilon_\nu T$, where $\varepsilon_\nu \in \mathbb{R}$ describes the Floquet exponent or *quasienergy*. The quasienergy is a real parameter and unique up to multiples of $\Omega = 2\pi/T$. The eigenstates $|\psi_\nu(t)\rangle$ thus acquire a phase according to ε_ν when evolved over a single period T. So if the Floquet operator could be (numerically) determined, one would, in principle, be able to solve the eigenvalue equation (2.23). By doing so one would obtain all information about the system in form of the eigenstates and quasienergies. In practice, however, this is often not very appealing due to the time-ordering operator appearing in the expression for U^F.

[2] Note that there is a slight confusion in the literature regarding this nomenclature: sometimes the operator in (2.21) is also called *quasienergy operator*, and the term 'Floquet Hamiltonian' is reserved for an effective time-independent Hamiltonian describing the stroboscopic dynamics of the system (see Sec. 2.2.3).

[3] Note that the eigenvalues $\lambda = e^{i\theta}$ do not depend on t, since $U(t'+T,t+T)U^F(t)\,|\psi_\nu(t)\rangle = U^F(t')\,|\psi_\nu(t')\rangle = \lambda_\nu(t)U(t',t)\,|\psi_\nu(t)\rangle = \lambda_\nu(t)\,|\psi_\nu(t')\rangle$, i.e., $\lambda_\nu(t) = \lambda_\nu(t') = e^{i\theta}$. Here, it was used that $U(t'+T,t+T) = U(t',t)$.

Moreover, it turns out to be convenient to rewrite the eigenstate in the following form

$$|\psi_\nu(t)\rangle = e^{-i\varepsilon_\nu(t-t_0)}\,|\phi_\nu(t)\rangle\ . \tag{2.27}$$

One can now straightforwardly show that the state $|\phi_\nu(t)\rangle$ inherits the time periodicity of the original Hamiltonian (again set $t_0 = 0$ for simplicity):

$$|\phi_\nu(t+T)\rangle = e^{i\varepsilon_\nu(t+T)}\,|\psi_\nu(t+T)\rangle = e^{i\varepsilon_\nu(t+T)}U^F(t)\,|\psi_\nu(t)\rangle = e^{i\varepsilon_\nu t}\,|\psi_\nu(t)\rangle = |\phi_\nu(t)\rangle\ . \tag{2.28}$$

This time-periodic state $|\phi_\nu(t)\rangle$ is also called *Floquet state*. Consequently, the solutions to the time-dependent Schrödinger equation with a time-periodic Hamiltonian can be written as a product of a plane wave characterised by the quasienergy and a time-periodic Floquet state. This is the celebrated *Floquet theorem* [54]. Note that this theorem is in its spirit very much related to the Bloch's theorem for spatially periodic systems [70], see also Eq. (2.8). There are crucial differences, however, and some of the consequences will be discussed in the following. Lastly, we note that any general quantum state $|\Psi(t)\rangle$ can be written as a coherent superposition of eigenstates of Eq. (2.27), i.e.,

$$|\Psi(t)\rangle = \sum_\nu c_\nu\, e^{-i\varepsilon_\nu t}\,|\phi_\nu(t)\rangle\ , \tag{2.29}$$

where $c_\nu = e^{i\varepsilon_\nu t_0}\,\langle\phi_\nu(t_0)|\Psi(t_0)\rangle$.

2.2.2. The extended Hilbert space

In order to gain more insight into the structure of the quasienergies and Floquet states, respectively, we substitute the so called Floquet-state solution (2.27) into the Schrödinger equation (2.19). One obtains

$$H^F(t)\,|\phi_\nu(t)\rangle = \varepsilon_\nu\,|\phi_\nu(t)\rangle\ . \tag{2.30}$$

This equation makes one major strength of the Floquet theory immediately apparent: despite having a time-dependent problem, it is sufficient to solve a *time-independent* eigenvalue problem in order to acquire all information about the system. The drawback is obviously that the Floquet state still depends on time, and, hence, the eigenvalue problem (2.30) would need to be solved for all $t \in [0, T)$. Nonetheless, we will show later why this is often unproblematic in practice.

When looking at the eigenvalue problem (2.30) a bit closer, one realises that there is a certain redundancy in the occurrence of Floquet states. For a given $|\phi_\nu\rangle$ and quasienergy ε_ν one can find a new Floquet state

$$|\phi_{\nu'}(t)\rangle = e^{-in\Omega t}\,|\phi_\nu(t)\rangle \equiv |\phi_{\nu n}(t)\rangle\ , \tag{2.31}$$

with $n \in \mathbb{Z}$, which produces the same physical eigenstate $|\psi_\nu(t)\rangle$ under a simultaneous shift of the quasienergy of the form

$$\varepsilon_{\nu'} = \varepsilon_\nu - n\Omega \equiv \varepsilon_{\nu n}\,. \tag{2.32}$$

Thus, every unique physical eigenstate labeled by ν defines an entire class of solutions (ν, n) with an infinite number of replicas of Floqut states indexed by n. Furthermore, the quasienergy spectrum is periodic with a periodicity of Ω (for a pictorial representation of this periodicity see Fig. 3.3 in Sec. 3.2.1, where eigenvalues take on the form of bands.). Owing to this redundancy, one has the freedom to formulate the problem in such a way

that the unique quasienergies $\varepsilon_\nu = \varepsilon_{\nu 0}$ always lie in a certain energy window of width Ω, e.g.,

$$-\frac{\Omega}{2} \leq \varepsilon_\nu < \frac{\Omega}{2}\,. \tag{2.33}$$

In analogy to the Brillouin zones of spatially periodic systems, we call this window the *first Floquet zone* (1FZ). Throughout this thesis we will follow the convention that Floquet states $|\phi_{\nu,n=0}(t)\rangle$ correspond to quasienergies that lie in the 1FZ. Also, we always refer to these particular Floquet states if no information about the replica index is given. We want to remark, though, that while the quasienergy window (2.33) corresponding to the 1BZ can indeed be chosen arbitrarily for non-interacting systems, more care about this choice needs to be taken for interacting systems. We will elaborate more on this matter in Ch. 5.

Moreover, due to the fact that the Floquet states are time-periodic one can write them in terms of a discrete Fourier transformation, i.e.,

$$|\phi_\nu(t)\rangle = \sum_n e^{-in\Omega t}\,|\phi_\nu^n\rangle\ , \tag{2.34}$$

with $|\phi_\nu^n\rangle$ being a Fourier mode of the respective Floquet state. The time dependence of every Floquet state is hence solely encoded in the Fourier functions $e^{-in\Omega t}$. These functions form a complete orthonormal set in the vector space $\mathcal{T}$ of T-periodic functions. The basis $\{|n\rangle\}$ spans this vector space $\mathcal{T}$, where we define $\langle t|n\rangle = e^{-in\Omega t}$. It is now convenient to view the Floquet Hamiltonian H^F as an operator acting on the composite Hilbert space $\mathcal{F} = \mathcal{H} \otimes \mathcal{T}$, with $\mathcal{H}$ being the physical Hilbert space spaned by some basis $\{|\alpha\rangle\}$. In the literature $\mathcal{F}$ is also known as the *extended Hilbert space* or *Floquet space* [75]. In the following, an operator that is explicitly promoted to act on $\mathcal{F}$ shall be denoted by an overbar, e.g., $H^F(t) \to \bar{H}^F$. The scalar product in $\mathcal{F}$ is defined as

$$\langle\!\langle \psi|\phi\rangle\!\rangle = \frac{1}{T}\int_0^T dt\ \langle\psi(t)|\phi(t)\rangle\ , \tag{2.35}$$

i.e., it is a combination of the typical scalar product in $\mathcal{H}$ and a time averaging over a single driving period T. Here, the 'double ket' notation $|\phi\rangle\!\rangle$ is used to represent elements of $\mathcal{F}$, which can be viewed as vectors of the form (see also Fig. 2.2(a))

$$|\phi_\nu\rangle\!\rangle = \left(\ldots, |\phi_\nu^{-1}\rangle, |\phi_\nu^0\rangle, |\phi_\nu^1\rangle, \ldots\right)^T. \tag{2.36}$$

Note that $|\phi\rangle\!\rangle$ does not depend on time. All temporal dependencies have been absorbed into the structure of the Hilbert space itself. The corresponding state at time t in the physical Hilbert space $\mathcal{H}$ is given by $|\phi(t)\rangle$ according to Eq. (2.34).

One can now reconsider the eigenvalue equation (2.30). Formulated in the extended Hilbert space the expression reads as

$$\bar{H}^F\,|\phi_{\nu n}\rangle\!\rangle = \varepsilon_{\nu n}\,|\phi_{\nu n}\rangle\!\rangle\,. \tag{2.37}$$

Clearly, the eigenstates of $\bar{H}^F$ fulfil the orthonormality condition in the composite Hilbert space $\mathcal{F}$, i.e.,

$$\langle\!\langle \phi_{\nu n}|\phi_{\mu m}\rangle\!\rangle = \frac{1}{T}\int_0^T dt\ \langle\phi_{\nu n}(t)|\phi_{\mu m}(t)\rangle = \delta_{\nu\mu}\delta_{nm}\,. \tag{2.38}$$

The Floquet states also form a complete set in $\mathcal{F}$, i.e., [77]

$$\sum_{\nu,n}\langle\phi_{\nu n}(t)|\phi_{\nu n}(t')\rangle = \delta(t-t')\,. \tag{2.39}$$

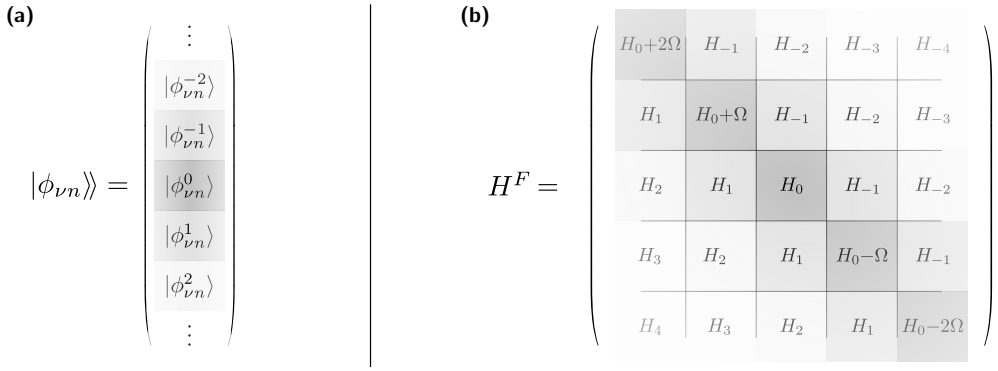

Figure 2.2.: Pictorial representation of objects in the extended Hilbert space $\mathcal{F}$: (a) a Floquet state, see Eq. (2.36), and (b) the Floquet matrix given by Eq. (2.40). Both objects have an infinite extension with respect to the Floquet index. For a monochromatic drive the Floquet Hamiltonian H^F is tridiagonal.

It is useful to stress that while Floquet states of the same class produce the same physical state, they are independent orthogonal solutions in the extended space. As a consequence, the sum in Eq. (2.39) indeed needs to run over *all* replica states in order to guarantee completeness. Note, however, that for fixed times $t = t'$ already the Floquet states of the first Floquet zone only $|\phi_{\nu 0}(t)\rangle$ form an orthonormal set in $\mathcal{H}$.

For practical purposes the *Floquet matrix*, i.e., the matrix representation of $\bar{H}^F$ is needed. By using the basis of Fourier functions $\{e^{-in\Omega t}\}$ the matrix elements of the Floquet matrix are straightforwardly found to be

$$\begin{aligned} H^F_{nm} &= \frac{1}{T}\int_0^T dt\; e^{in\Omega t}\, H^F(t)\, e^{-im\Omega t} \\ &\overset{(2.21)}{=} H_{n-m} - m\Omega\,\delta_{nm}\mathbb{1}\,, \end{aligned} \tag{2.40}$$

with

$$H_n = \frac{1}{T}\int_0^T dt\; e^{in\Omega t} H(t) = H^\dagger_{-n} \tag{2.41}$$

being the Fourier components of the original Hamiltonian. A pictorial representation of the Floquet matrix is given in Fig. 2.2, where every block represents an operator acting on the Hilbert space $\mathcal{H}$. The structure shows two main characteristics with respect to the Floquet indices, n, m. First, the time-independent part of the original Hamiltonian is repeatedly placed on the diagonal, but shifted in energy by Ω from entry to entry. Second, the Fourier components of the drive couple different 'Floquet sectors', meaning that they provide an effective hopping in Floquet space. If the driving part of the Hamiltonian is monochromatic (as it is the case for all 'Floquet problems' in this thesis), the Floquet matrix becomes block tridiagonal. As initially described, this picture resembles the coupling of a quantum system to a classical photon bath. The Floquet index n takes the notion of a relative photon number in this picture. Similiarly, the action of H_n can be viewed as an 'n'-photon process. Alternatively, one could see the Floquet matrix as a representation of quantum particles hopping on a 1D lattice (in energy space). This picture might be helpful to understand transport processes (see Sec. 3.3) or could even be used to engineer novel topological systems [81].

From a practical point of view it still remains unclear, though, how the knowledge about the Floquet matrix simplifies the calculation of Floquet eigenstates and associated quasienergies. A diagonalisation of this matrix is seemingly problematic, because it is

infinite in size. Here, however, one can exploit the redundancy of Floquet states. Because the number of physical solutions is only given by $\dim(\mathcal{H})$, one can safely truncate the Floquet matrix. So in a numerical diagonalisation procedure the Floquet indices of the Floquet matrix are restricted and only run from $-N_f$ to N_f. The first term in Eq. (2.40) linear in Ω ensures that modes with large $|n|$ are suppressed. In order to obtain numerically exact results it is required that $\Omega N_f \gg E_{\max}$, where $E_{\max}$ is the maximal energy scale set by the original Hamiltonian H. One should construct the Floquet matrix in such a way that the first Floquet zone lies in the middle on the quasienergy spectrum. If this is the case, the corresponding Floquet states and quasienergies are least affected by the truncation. Once all ε_ν and $|\phi_\nu\rangle\!\rangle$ associated with the 1FZ are numerically found, all other states as well as the full quasienergy spectrum can be constructed from Eqs. (2.31) and (2.32). Note that typical driving frequencies in this thesis (and also in many relevant experiments, see, e.g., Ch. 6) already fulfil the condition $\Omega \gtrsim E_{\max}$. Therefore, it is often sufficient to truncate the Floquet matrix quite rigorously with $N_f \sim \mathcal{O}(1) - \mathcal{O}(10)$. A concrete example of a readily diagonalisable Floquet Hamiltonian is given in Sec. 3.2.1, where the quasienergies yield (Floquet) bands because of an underlying spatially periodic lattice system.

We conclude this section by looking once again at the redundancy of the Floquet structure and its origins: in the case of spatially periodic systems, using Bloch's theorem enforces a nominally infinite number of (electronic) bands. In the Floquet case, in contrast, the resulting infinite bands are not unique, but rather replicas of each other. This can be traced back to the very different role taken by space and time in single-particle quantum mechanics: while the first one is promoted to an operator, $\mathbf{r} \to \hat{\mathbf{r}}$, this is *not* the case for time. Thus, when trying to absorb time into a band index, it is this fundamental property that requires the extension of the original Hilbert space.

2.2.3. Effective Hamiltonians and the Magnus expansion

Stroboscopic time-evolution of non-interacting Floquet systems

In the previous sections 2.2.1 and 2.2.2 all tools have been provided to solve a non-interacting periodically driven quantum system. However, while for some systems the temporal periodicity might be inherent, it is not yet apparent why a periodic drive might be beneficial or even desirable in the light of designing systems. In order to get a better intuition for potential advantages of Floquet systems we want to focus again on the time-evolution operator $U(t, t_0)$, see Eq. (2.20). Using the arguments from Eqs. (2.24) and (2.25) it is clear that $U(t+T, t_0+T) = U(t, t_0)$ holds. Thus, any evolution operator can be written as

$$U(t, t_0) = U(t' + t_0, t_0) U(nT + t_0, t_0) = U(t' + t_0, t_0) \left[U^F(t_0)\right]^n , \tag{2.42}$$

where $t = t' + t_0 + n\Omega$, $t' \in [0, T)$ and $n \in \mathbb{Z}$. The first operator on the right-hand side, $U(t' + t_0, t_0)$, describes the evolution within a single driving period, and is associated with the *micromotion* of the system. When being interested in evolution times that are much larger than T, i.e., $n \gg 1$, one can typically ignore this micromotion part. The knowledge about $U^F(t_0)$ is then sufficient to explore the long time dynamics of the quantum system. This is because once the Floquet operator is diagonalised such as

$$S^\dagger \, U^F(t_0) \, S = e^{-iDT} , \tag{2.43}$$

with S being a unitary matrix built from Floquet eigenstates, and D describing a diagonal matrix composed of quasienergies of the first Floquet zone $\{\varepsilon_\nu\}$, one trivially obtains the

evolution operator after n cycles to be

$$U(t_0 + nT, t_0) = S\, e^{-iDnT}\, S^\dagger\,. \tag{2.44}$$

So an arbitrary initial state $|\Psi(t_0)\rangle = \sum_\nu c_\nu\, |\phi_\nu(t_0)\rangle$, where $c_\nu = e^{i\varepsilon_\nu t_0}\, \langle\phi_\nu(t_0)|\Psi(t_0)\rangle$, is propagated in a *stroboscopic* manner by this relation. Because of the linear phase evolution given in Eq. (2.44), this stroboscopic evolution resembles the time evolution generated by a time-independent Hamiltonian. Hence, one can find[4] an *effective time-independent Hamiltonian* H^{eff} that describes this stroboscopic time evolution. It is defined as

$$e^{-iH^{\text{eff}}_{t_0}T} \equiv U^F(t_0)\,. \tag{2.45}$$

By using Eq. (2.43) this effective Hamiltonian can conveniently be expressed as

$$H^{\text{eff}}_{t_0} = SDS^\dagger = \sum_\nu \varepsilon_\nu\, |\phi_\nu(t_0)\rangle\, \langle\phi_\nu(t_0)|\ . \tag{2.46}$$

Note that the effective Hamiltonian depends parametrically on the initial time t_0.

Using the fact that the eigenstates $|\psi_\nu(t)\rangle$ (see Eq. (2.27)) form an orthonormal basis at any fixed time t, one can write the evolution operator for arbitrary times as

$$U(t, t_0) = \sum_\nu e^{-i\varepsilon_\nu(t-t_0)}\, |\phi_\nu(t)\rangle\, \langle\phi_\nu(t_0)|\ . \tag{2.47}$$

Note again that this generalizes the familiar form of propagators for time-independent systems to Floquet systems. By introducing the *micromotion operator* [17, 78, 80]

$$U^{\text{m}}(t, t_0) = \sum_\nu |\phi_\nu(t)\rangle\, \langle\phi_\nu(t_0)|\ , \tag{2.48}$$

which captures the time dependence of the Floquet states by evolving them in time, one can rewrite the time-evolution operator in terms of H^{eff} and U^{m} as [17, 78]

$$U(t, t_0) = e^{-i(t-t_0)H^{\text{eff}}_t}\, U^{\text{m}}(t, t_0) = U^{\text{m}}(t, t_0)\, e^{-i(t-t_0)H^{\text{eff}}_{t_0}}\,. \tag{2.49}$$

So knowing the effective Hamiltonian as well as the micromotion operator allows a direct formulation of the time-evolution operator for all times. However, one might still be worried about the fact that $H^{\text{eff}}_{t_0}$ has a parametric dependence on the initial time t_0. To solve this issue one can find a new unitary one-point operator $\widetilde{U}^{\text{m}}(t)$ which satisfies [17]

$$H^{\text{eff}}_{t_0} = \widetilde{U}^{\text{m}}(t_0)\ H^{\text{eff}}\ \left[\widetilde{U}^{\text{m}}(t_0)\right]^\dagger\,, \tag{2.50}$$

where H^{eff} is independent of t_0. At the same time it holds that $\widetilde{U}^{\text{m}}(t)\left[\widetilde{U}^{\text{m}}(t_0)\right]^\dagger = U^{\text{m}}(t, t_0)$, such that the propagator takes the form

$$U(t, t_0) = \widetilde{U}^{\text{m}}(t)\ e^{-i(t-t_0)H^{\text{eff}}}\ \widetilde{U}^{\text{m}}(t_0)\,. \tag{2.51}$$

So the dependence of $H^{\text{eff}}_{t_0}$ on t_0 can be understood as a simple gauge transformation. Note that promoting any $\widetilde{U}^{\text{m}}(t)$ to act on the extended Hilbert space $\mathcal{F}$, leads to an

[4] In fact, as we will point out later, see Sec. 5.1, there are limits to finding such effective Hamiltonians. One particular class of examples were this (often) fails are *interacting systems*. Here, the fact that periodically driven quantum systems are inherently not protected against heating, will cause problems in formulating *local* effective Hamiltonians [31].

operator $\bar{U}^{\mathrm{m}}$ that block diagonalises the Floquet matrix (see Fig. 2.2) with respect to its Floquet indices. The fact that this block diagonalisation is not unique represents the role of the initial time t_0. Sometimes the one-point micromotion operator is also expressed as $\widetilde{U}^{\mathrm{m}}(t) = e^{-iK(t)}$, where K is called a *kick operator* [78]. In this picture the system experiences an initial and final 'kick', and evolves according to some effective time-independent Hamiltonian in between. While the predicted long-time dynamics are the same for all effective Hamiltonians that are connected by a unitary transformation (2.50), quantitative differences may arise due to the 'kicks' (e.g., a change of band populations, see Sec. 3.2.2). Note that throughout this thesis the focus lies mainly on the long time properties of the respective Floquet systems. Hence, unless stated otherwise, the initial time is typically set to zero, $t_0 = 0$, and the micromotion is ignored. Having said this, there are actually cases where the micromotion yields interesting physical insights. For example, only recently a setup was proposed [82] in which the micromotion gives direct access to observing the topological invariant of a Floquet system.

In summary, the time evolution generated by a time periodic Hamiltonian can be described by a stroboscopic evolution of an effective time-independent Hamiltonian plus a micromotion part. It has become clear from Eqs. (2.46) and (2.48) that these operators can be built from Floquet eigenstates and quasienergies. However, it is also obvious that solving the Floquet eigenvalue problem can be an extremely hard numerical task or can even become impossible for complicated Hamiltonians, e.g., describing many-body quantum systems on a lattice. Thus, the following is a very natural and practical question to ask: how can one find or even purposely build a targeted effective Hamiltonian *without* the prior knowledge about the respective Floquet states and associated quasienergies?

If there was indeed a positive answer to this question, one could even turn the perspective around and claim that time-periodic Hamiltonians can be exploited in order to stroboscopically *simulate* the dynamics of time-independent systems. This approach is precisely the way that opened up the field of *Floquet enigneering*. Here, properties of (effective) Hamiltonians of interest are tailored by tuning the time-dependence of some original Hamiltonian $H(t)$. This powerful and novel way of engineering quantum systems has had a tremendous impact on the experimental field of ultracold atoms as well as triggered many exciting theoretical proposals. A small overview regarding these ideas will be given in Sec. 2.3. In the following it will be sketched how to determine even complicated effective Hamiltonians within a suitable approximation scheme.

Large frequency expansions of the Floquet operator

A widely used and very powerful approximation to compute effective Hamiltonians from Floquet systems goes by the name *Magnus expansion* [79,80,83,84]. This method is a high-frequency expansion, and, thus, requires that the driving frequency Ω is larger than the largest energy scale of the problem at hand. One starts again with the Floquet operator

$$\exp\left[-iTH^{\mathrm{eff}}_{t_0}\right] = U^F(t_0) = \mathcal{T}_t \exp\left[-i\int_{t_0}^{T+t_0} dt\ H(t)\right], \tag{2.52}$$

Inverting this equation then yields

$$H^{\mathrm{eff}}_{t_0} = \frac{i}{T}\log\left[\mathcal{T}_t \exp\left(-i\int_{t_0}^{T+t_0} dt\ H(t)\right)\right]. \tag{2.53}$$

Expanding the right hand side of Eq. (2.53) allows to systematically find a series representation of the effective Hamiltonian [79], i.e.,

$$H_{t_0}^{\text{eff}} = \sum_{i=0}^{\infty} H_{t_0}^{\text{eff}(i)} \,, \tag{2.54}$$

where the first few terms are given by

$$H_{t_0}^{\text{eff}(0)} = \frac{1}{T}\int_{t_0}^{T+t_0} dt_1 \; H(t_1) \,, \tag{2.55}$$

$$H_{t_0}^{\text{eff}(1)} = \frac{1}{T}\int_{t_0}^{T+t_0} dt_1 \int_{t_0}^{t_1} dt_2 \; [H(t_1), H(t_2)] \,, \tag{2.56}$$

$$H_{t_0}^{\text{eff}(2)} = \frac{1}{T}\int_{t_0}^{T+t_0} dt_1 \int_{t_0}^{t_1} dt_2 \int_{t_0}^{t_2} dt_3 \; \Big([H(t_1), [H(t_2), H(t_3)]] + (1 \leftrightarrow 3)\Big) \,. \tag{2.57}$$

Typical frequency values in this thesis are indeed large compared to all other energy scales within the respective problems. In such situations already the first two terms of the Magnus expansion, i.e. Eqs. (2.56) and (2.57), are sufficient to give a good analytical representation of the effective Hamiltonian.

After decomposing the time-periodic Hamiltonian into its Fourier components,

$$H(t) = \sum_n e^{-in\Omega t} H_n \,, \tag{2.58}$$

the expressions above can be conveniently evaluated further to yield

$$H_{t_0}^{\text{eff}(0)} = H_0 \,, \tag{2.59}$$

$$H_{t_0}^{\text{eff}(1)} = \frac{1}{\Omega}\sum_{n=1}^{\infty} \frac{1}{n}\Big([H_{-n}, H_n] - e^{-in\Omega t_0}[H_0, H_n] + e^{in\Omega t_0}[H_0, H_{-n}]\Big) \,. \tag{2.60}$$

So to lowest order, the effective Hamiltonian $H_{t_0}^{\text{eff}}$ simply equals the time-independent part of H. One observes that the initial time t_0 then enters only at the next order in Eq. (2.60). As described above, the starting time t_0 should not affect the quasienergy spectrum, and is, therefore, irrelevant for experiments where the drive is switched on adiabatically, for example. This is, however, not guaranteed by the *truncated* Magnus expansion above. To this end, one should choose to absorb the initial time dependence into additional kick-operators, see Eq. (2.51), which yields a similar series expansion of H^{eff} with slightly different looking terms for $i \geq 1$ than above [78–80]:

$$H^{\text{eff}(0)} = H_0 \qquad \text{and} \qquad H^{\text{eff}(1)} = \frac{1}{\Omega}\sum_{n=1}^{\infty} \frac{1}{n}\,[H_{-n}, H_n] \,. \tag{2.61}$$

In general, for the purpose of quantum simulation one aims to tune the external drive in such a way that this alternative truncated Magnus[5] expansion,

$$H^{\text{eff}} \approx H^{\text{eff}(0)} + H^{\text{eff}(1)} \,, \tag{2.62}$$

matches the form of a target Hamiltonian which one desires to study. A detailed example of this procedure can be found in chapter 6, where it is shown how a periodically driven

[5] Note that throughout this thesis we will somewhat loosely use the term 'Magnus expansion'. While there is a clear distinction regarding the nomenclature in the literature between the original form of the Magnus expansion and the alternative form of Eq. (2.61), in this thesis we will also call the latter one '(alternative) Magnus expansion'.

tight-binding model describing graphene gives rise to the Haldane model in the spirit of Eq. (2.62). Furthermore, if one was truly interested in a description of the evolution at all times, one would need to perform a similar series expansion also for the micromotion operator $U^F(t, t_0)$ above [79, 80].

Generally, the Magnus expansion is a powerful tool to approximately determine the effective static Hamiltonian in the high-frequency regime. In fact, the recent triumph of experimental Floquet systems, see Sec. 2.3, can mostly be attributed to this approach. Nonetheless, the success of finding a proper series expansion and being able to truncate it for practical reasons is determined by its radius of convergence. It is understood that the question of convergence of the Magnus expansion can be linked to the presence of heating in periodically driven systems [31]. For a convergent series, the resulting effective Hamiltonian must be static in the sense that it conserves energy at all (stroboscopic) times. However, a generic interacting Floquet system does fundamentally heat up (see Ch. 5). Hence, the Magnus expansion diverges in these cases indicating that there is no local effective Hamiltonian that could describe the stroboscopic time-evolution [31, 79]. In fact, many aspects of interacting Floquet systems are still not fully understood and form the ground of a very active field of research (see Sec. 5.1). The main part of this thesis is dedicated to these peculiar systems.

2.2.4. Adiabaticity in Floquet systems

So far it was assumed that the systems at hand are described by Hamiltonians which are truly time periodic, $H(t+T) = H(t)$. In most real physical situations, however, this will never be the case. The system rather drifts or changes slowly in time, which makes the Hamiltonian only approximately periodic

$$H(t+T) \approx H(t)\,. \tag{2.63}$$

If the non-periodic part of $H(t)$ is indeed slow and weak, one can absorb this behaviour into a mere time-dependent parameter. Here, the trick is to introduce a second time argument t' such that it describes the slow dependence, while the time t still captures the time-periodicity of the problem. By doing so, one can recover a perfectly time-periodic Hamiltonian that parametrically depends on t', i.e.,

$$H_{t'}(t+T) = H_{t'}(t)\,. \tag{2.64}$$

This representation is called the (t, t')-formalism[6] [85–89]. The key feature of this approach is that the time-dependent solution to the ordinary Schrödinger equation (2.19) can be determined from

$$|\psi(t)\rangle = |\Psi_{t'}(t)\rangle\,\big|_{t'=t}\,, \tag{2.65}$$

where the state $|\Psi_{t'}(t)\rangle$ fulfils the Schrödinger-type equation

$$i\frac{\partial}{\partial t'}\,|\Psi_{t'}(t)\rangle = H^F_{t'}(t)\,|\Psi_{t'}(t)\rangle\,, \tag{2.66}$$

with H^F being the Floquet Hamiltonian defined in Eq. (2.21). The initial condition needs to fulfil $|\Psi_{t_0}(t_0)\rangle = |\psi(t_0)\rangle$. So t' can be seen as a time coordinate in the extended

[6] Note that this formalism actually holds for arbitrary time-dependent Hamiltonians $H(t)$. However, the treatment always requires to rewrite the Hamiltonian into a time-periodic Hamiltonian which depends parametrically on a second time argument, $H(t) \to H_\tau(t)$. This decomposition in itself might already be an extremely demanding task. Hence, this formalism naturally describes those systems that are inherently of Floquet nature with an additional weak or slow temporal variation.

Hilbert space, and H^F generates the evolution with respect to that 'time'. The validity of Eq. (2.65) is straightforwardly shown by realising that

$$\frac{\partial}{\partial t}\left|\psi(t)\right\rangle = \frac{\partial}{\partial t}\left|\Psi_{t'}(t)\right\rangle\Big|_{t'=t} + \frac{\partial}{\partial t'}\left|\Psi_{t'}(t)\right\rangle\Big|_{t'=t}. \tag{2.67}$$

Of course, the (t,t')-method also works for cases where the original Hamiltonian is perfectly periodic at all times. At first sight, the procedure does not look very beneficial in these circumstances. However, it has been shown that this method can be very useful where standard Green's function techniques are applied to the auxiliary evolution problem in $\mathcal{F}$ of Eq. (2.66) [90–92]. We will show later how a similar Green's function technique is strongly related to this picture, see Ch. 5.

If the Hamiltonian is indeed *not* perfectly periodic as outlined above, one can argue that a simplification of the problem is not guaranteed, since the Schrödinger-type equation (2.66) still describes an evolution that is generated by a time-dependent Hamiltonian. However, because the dependence on t' is very slow, one can apply a Floquet version of the *adiabatic theorem* [86, 89, 93, 94]. First, using again the definition of Floquet states (see Eq. (2.27)) one needs to solve the parametric (or t'-instantaneous) Floquet eigenvalue problem

$$\bar{H}^F_{t'}\left|\phi_{\nu,t'}\right\rangle\!\!\right\rangle = \varepsilon_{\nu,t'}\left|\phi_{\nu,t'}\right\rangle\!\!\right\rangle. \tag{2.68}$$

In the next step the adiabatic evolution equation (2.66) is solved. We now denote the parametric time dependence of the Floquet Hamiltonian by a set of parameters $\boldsymbol{\lambda}(t) = (\lambda_1(t), ...)$, $\bar{H}^F_t \to \bar{H}^F_{\boldsymbol{\lambda}(t)}$. Assume also that the system is initially prepared in a certain Floquet state, $|\Phi_{\boldsymbol{\lambda}(t_0)}(t_0)\rangle = |\phi_\nu(t_0)\rangle$. Adiabatic evolution states that the system follows and remains in that very eigenstate, and can only acquire a phase. Hence, the time-evolved state is given by $|\Psi_{t'}(t)\rangle = e^{-i\theta_{\nu,t'}}\,|\Phi_{\boldsymbol{\lambda}(t')}(t)\rangle$. An expression for $\theta_{\nu,t}$ is obtained by substituting the ansatz into Eq. (2.66). Multiplying with the same Floquet state from the left and integrating over the fast time dependence, i.e., taking the scalar product in $\mathcal{F}$, eventually yields the expression

$$\theta_{\nu,t'} = \int_{t_0}^{t'} d\tilde{t}\;\varepsilon_{\nu,\boldsymbol{\lambda}(\tilde{t})} - i\int_{t_0}^{t'} d\tilde{t}\;\sum_i \dot{\lambda}_i(\tilde{t})\,\langle\!\langle\phi_{\nu,\boldsymbol{\lambda}(\tilde{t})}|\partial_{\lambda_i}\,\phi_{\nu,\boldsymbol{\lambda}(\tilde{t})}\rangle\!\!\rangle\,. \tag{2.69}$$

The result is familiar from the adiabatic evolution of a non-Floquet system: the first term represents the dynamical phase of the system, and the second term can be interpreted as a Floquet version of *Berry's phase* [95]. One can now identify both time arguments with each other, $t = t'$, in order to obtain the physical state

$$|\psi(t)\rangle = e^{-i\int_{t_0}^{t} dt'\,\varepsilon_{\nu,\boldsymbol{\lambda}(t')}}\;e^{i\int_{\mathcal{C}} d\boldsymbol{\lambda}\cdot\mathcal{A}^F_{\nu,\boldsymbol{\lambda}}}\;\left|\phi_{\nu,\boldsymbol{\lambda}(t)}(t)\right\rangle\,, \tag{2.70}$$

where we also introduced a Floquet version of the *Berry connection*

$$\mathcal{A}^F_{\nu,\boldsymbol{\lambda},i} = i\langle\!\langle\phi_{\nu,\boldsymbol{\lambda}}|\,\frac{\partial}{\partial\lambda_i}\left|\phi_{\nu,\boldsymbol{\lambda}}\right\rangle\!\!\rangle\,. \tag{2.71}$$

In Eq. (2.70) a line integral along a path $\mathcal{C} := \boldsymbol{\lambda}([t_0,t])$ has been introduced illustrating that the geometric phase indeed does not depend on the velocity (as long as the adiabatic condition is fulfilled), but only on the path taken in parameter space. The scalar product $d\boldsymbol{\lambda}\cdot\mathcal{A}_\nu$ indicates a summation over all parameters. Note the crucial fact that neither the Berry phase nor the Berry connection are invariant under gauge transformations. This leads to the fact that, in principle, one can always find a gauge such that these quantities

due not contribute. The scenario is, however, different for closed paths. For more details about Berry phases in general the reader is referred to [96].

In short, the results for adiabatic evolution in periodically driven quantum systems with an additional slow time dependence are similar to those obtained for conventional Hamiltonians. The main difference is that the role of the energy eigenstates of ordinary systems is now played by the Floquet states of the problem. Nonetheless, there is a peculiar issue with the Floquet adiabaticity: adiabatic transport requires a time scale which is larger than the encountered energy gaps of the system. Owing to the quasienergy structure of a Floquet system (see Sec. 2.2.1) all energies of the original problem can be folded into the first Floquet zone. Consequently, it is hard to believe that the adiabaticity condition can always be met if there is a large number of states [97]. However, it can be claimed that one is only interested in adiabatic processes for finite times. This circumvents the problem because folded eigenvalues might be close in quasienergy, but might only be connected via 'multi-photon' processes. Such processes are typically highly suppressed and set a (very long) time scale themselves. So even for systems with crowded quasienergy spectra the adiabatic principle can be well justified [89]. This is, of course, particularly true for systems that are purposely designed. The idea of solving a Floquet problem which parametrically depends on an additional slow time-dependence will be of great importance in the course of this thesis, see chapters 5, 6 and 7.

2.3. Floquet systems: experimental examples and theoretical ideas

The coherent manipulation of matter by means of time-periodic forcing using radiation is traditionally applicable to small quantum systems such as single atoms [17]. However, the fact that ultracold atoms are highly controllable and well isolated systems, as outlined in Sec. 2.1, allowed for the recent development that periodic driving can also be promisingly used for the coherent manipulation of many-body states. Here, the characteristics of the Floquet operator, $U^F(t_0) = e^{-iH^{\text{eff}}_{t_0}T}$ (see also Eq. (2.45)), play a central role: the fact that periodic driving stroboscopically simulates the dynamics of an effective static Hamiltonian H^{eff} with potentially exciting and novel properties has boosted the field of Floquet engineering using ultracold atoms and beyond. In the following, we give a small overview on major achievements of both experimental as well as theoretical nature which have shaped this field of research over recent years. Crucially, most of the examples and ideas presented in this section build on non-interacting systems. Floquet realisations and associated phenomena depending on interactions are discussed in Sec. 5.1. Furthermore, we refrain from including quantum ratchets in the discussion below, since we already dedicate chapter 3 to these systems. Note that the progress of Floquet realisations with cold atoms has been summarized only very recently in a review by Eckardt [17], which also inspired parts of this section.

First experiments with ultracold atoms conducted in the spirit of Floquet engineering showed that periodic driving can effectively change the strength as well as sign of the hopping of atoms in an optical lattice, hereby controlling the ballistic expansion of Bose-Einstein condensates [55], dynamically controlling the quantum phase transition between a bosonic Mott insulator and a superfluid [98] or implementing the simulation of frustrated classical magnetism [56], respectively. More recently, the creation of artificial gauge fields as well as the realisation of topological band structures have moved into the focus of many experimental groups. Examples of such experiments include the general realisation of strong effective magnetic fields [50], the creation of tunable gauge fields [99] to engineer

Ising-XY spin-models in triangular lattices [20], the generation of topological quantum walks [100] and of effective electric fields in a discrete quantum simulator [101], the realisation of the Harper [102] and Hofstadter Hamiltonian [103] and variants thereof [104] as well as the direct measurement of associated Chern numbers [105], and the observation of Bose-Einstein condensation in strong synthetic magnetic fields [106]. Also, the generation of spin-orbit coupling was achieved [107, 108] and chiral currents in bosonic ladders were observed [109]. Furthermore, topological quantum pumps based on periodic driving have been realised for bosonic [18] as well as fermionic [19] systems made of cold atoms. A recent experiment with cold atoms was even able to simulate the Haldane model [23], i.e., a model that demonstrates the existence of a quantum Hall state without external magnetic fields. Along these lines, Berry phases could be reconstructed from experimentally realised topological models [110] and it has been claimed that a dynamical topological phase transition was experimentally observed [111]. Note that spectacular Floquet experiments were also performed outside the field of ultracold atoms, where, for instance, a Floquet topological insulator with photons was realised [112]. In addition, circularly polarized light was used to manipulate the surface states of conventional topological insulators [113].

So far, all presented examples describe experimental achievements. However, also many proposals have been made from the theory side pointing out that periodically driven states can be used to realise a wide range of states of matter. Such proposals often have a wide range of applicability and go generally beyond potential realisations with ultracold atoms. One of the very first of such ideas was the creation of photoinduced quantum Hall states in irradiated graphene [114, 115]. Moreover, various topological Floquet states have been discussed theoretically. Examples include the proposal for a Floquet topological insulator in semiconductor quantum wells [21], the general classification [116] and characterisation [117] of periodically driven lattice systems, transport properties of Floquet topological insulators [118], Floquet topological transitions in driven topological insulators [119] and dissipative Floquet topological systems [120]. In addition, owing to the unique property of the Floquet zone being periodic in the direction of energy, anomalous topological edge states were identified in Floquet systems [121]. Recently, quantized magnetization densities in periodically driven systems as a signature of topological bulk properties have been studied [82]. Furthermore, the potential realisation of Majorana fermions in driven quantum wires [122], of non-abelian gauge fields [123], of a Floquet fractional Chern insulator [124] and various quantized pumping schemes [125–127] have been proposed. Very recently, it was further suggested how time crystals can form in Floquet systems as a consequence of spontaneously broken time translation symmetry [128] and how many-body localisation effects can survive [129] or even be imposed [130] by periodic driving.

So indeed, ideas for Floquet realisations are vast. In the following, we elaborate on the main principle that is sufficient to understand most ultracold atom experiments employing periodic forcing. Starting point is a non-interacting tight-binding lattice Hamiltonian of the form (see Sec. 2.1)

$$H = -\sum_{i,j} J_{ij}\, c_i^\dagger c_j + \sum_i \varepsilon_i\, c_i^\dagger c_i\,, \tag{2.72}$$

with J being a hopping strength, ε describes an on-site energy shift and $c^\dagger$ (c) is a creation (annihilation) operator of a bosonic or fermionic particle, respectively. Note that the respective geometry of the underlying lattice is undetermined at this point. The temporal periodicity, $H \to H(t) = H(t + T_0)$, can then be experimentally imposed in various ways (see also below), such as by direct lattice shaking [20, 23, 55, 98, 99], by including additional moving lattices [102,103,105,106] or by time-dependent external fields [131,132]. Here, immediate consequences for the initial Hamiltonian (2.72) depend specifically on

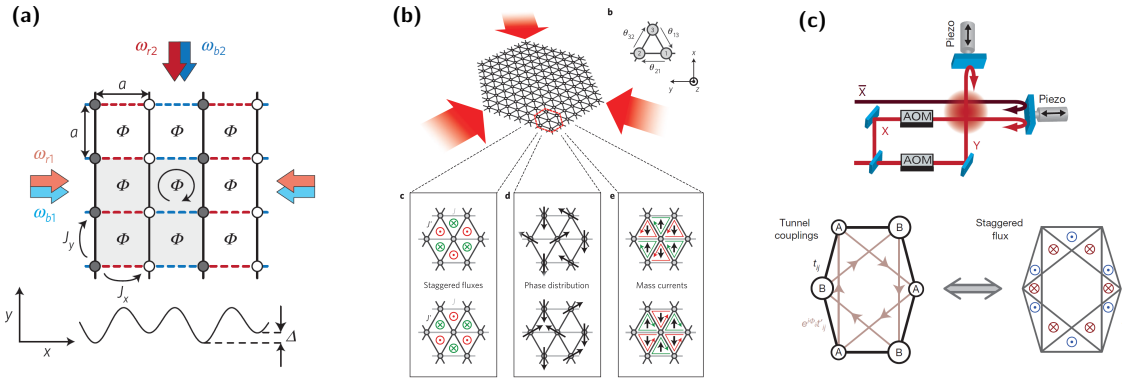

Figure 2.3.: Illustrations of prototypical experimental Floquet realisations with ultracold atoms. (a) Laser-assisted tunnelling imprints Peierls phases which leads to effective gauge potentials experienced by the used rubidium atoms [105]. Here, the smallest possible squares described by four different lattice sites define a plaquette P (see text). (b) Periodic forcing of a triangular lattice geometry allows for the realisation of tunable artificial gauge fields leading to the engineering of spin-models [20]. (c) Haldane model realised by circular shaking of a distorted honeycomb lattice and subsequent emergence of complex next-nearest-neighbour hoppings [23], see also Ch. 6. Taken from (a) [105], (b) [20] and (c) [23].

the selected method. Most crucially, however, by performing a gauge transformation $H' = U^\dagger H U - i\hbar U^\dagger \partial_t U$, with $U(t)$ encoding the introduced time-dependence, one can fully absorb the periodic forcing into a time-dependent Peierls phase $\theta_{ij}(t)$, i.e.,

$$J_{ij} \;\rightarrow\; J_{ij}(t) = e^{i\theta_{ij}(t)}\, J_{ij}\,. \tag{2.73}$$

Note that while this procedure is deliberately presented in a somewhat vague way at this point, we give an explicit detailed example of such a gauge transformation in Sec. 6.1.2. Experiments are typically conducted in the high frequency regime, $\Omega \gg J$, allowing for a Magnus expansion treatment according to Eqs. (2.61) and (2.62). This leads to the emergence of effective static hopping strengths of the form [17]

$$J_{ij}(t) \;\rightarrow\; J_{ij}^{\text{eff}} = \left|J_{ij}^{\text{eff}}\right| e^{i\theta_{ij}^{\text{eff}}} \qquad \text{and} \qquad \theta_{ij}^{\text{eff}} = \frac{1}{\hbar}\int_{\mathbf{r}_i}^{\mathbf{r}_j} d\mathbf{r}\cdot\mathbf{A}^{\text{eff}}(\mathbf{r}), \tag{2.74}$$

where the effective static Peierls phase can be written in terms on an effective vector potential $\mathbf{A}^{\text{eff}}(\mathbf{r})$.

The realisation of modified hopping strengths according to Eq. (2.74) represents the essence of most of the recently realised Floquet systems with ultracold atoms. Such experiments can be coarsely divided into two groups: those with $\theta^{\text{eff}} = 0, \pi$ and those for which $\theta^{\text{eff}} \neq 0, \pi$. In the former case, J^{eff} are real and Floquet engineering creates models with renormalized hopping strengths. For instance, considering a Bose-Einstein condensate in a shaken one-dimensional optical lattice [55,133] leads to effective tunnelling rates of $J^{\text{eff}} = J\mathcal{J}_0(K/(\hbar\Omega))$, with $\mathcal{J}_0$ being the zeroth-order Bessel function of the first kind and K parametrizes the amplitude of the shaking. For certain values of K the effective hoppings vanish leading to 'dynamical localization' [134]. Moreover, $\theta^{\text{eff}} = 0, \pi$ not only allows for modifying the amplitude of J^{eff} but also for changing its sign. Such a sign change is expected to cause frustration effects in triangular Bose-Hubbard models [135]. A quantum simulator that uses this property to study frustrated classical magnetism was indeed realised by the Sengstock group [56].

In contrast, the scenario of $\theta^{\text{eff}} \neq 0, \pi$ generates effective complex hopping strengths. Here, cases of particular interest are those where the Peierls phases (2.74) lead to an effective finite magnetic flux $\Phi_P^{\text{eff}} = \sum_P \theta_{ij}^{\text{eff}}$ through a plaquette P, see Fig. 2.3(a). Note that the emergence of such fluxes is fundamentally connected to the breaking of time-reversal symmetries[7] [17]. In recent years, particularly the Bloch group [50, 103, 105, 109] as well as the Ketterle group [102,106] has realised such systems experimentally by periodic forcing in order to study the effects of effective strong magnetic fields on charge-neutral atoms. Most recently, the Greiner group has extended respective studies also to the interacting case [104]. The remarkable aspect of these Floquet engineered systems is the fact that extremely strong magnetic fields can be simulated: in order to obtain similar fluxes for say electrons in graphene magnetic field strengths of about $B \approx 3.9 \times 10^4$T [17] would be necessary, which is about two orders of magnitude larger than experimentally realisable real magnetic fields. Moreover, even if net fluxes are zero, complex hopping strengths can still have a huge impact in triangular or honeycomb lattices, as demonstrated by the Sengstock group [20] in engineering quantum spin models, see Fig. 2.3(b). Most importantly, such scenario was used by the Esslinger group [23] to realise the Haldane model, i.e., to simulate a quantum Hall state without Landau levels [138], see Fig. 2.3(c).

The aforementioned Floquet systems with ultracold atoms are mostly realised by two different methods: laser-assisted tunnelling and shaking of the optical lattice. We will close this section by briefly elaborating on these two methods.

Laser-assisted tunnelling This technique is mainly implemented in setups that aim at the simulation of strong magnetic fields [50, 102, 103, 105, 106, 109]. Originally proposed by Jaksch and Zoller [139], this concept builds on the idea that tunnelling is prohibited in the static system, i.e., $J \ll \Delta$ in Eq. (2.72). The presence of two slightly detuned lasers of frequencies ω_1, ω_2, see Fig. 2.3(a), then gives rise to an effective shallow second lattice that moves with respect to the original one [17]. This moving lattice causes an effective time-periodic modulation that varies from site to site [51]. The temporal modulation resonantly activates tunnelling in the system thereby allowing for respective achievements. Note that extensions of this Floquet scheme for the realisation of topological insulators [140] or Weyl semimetals [141] have been proposed.

Optical lattice shaking The perhaps more direct way of implementing Floquet engineering with ultracold atoms is the global shaking of the entire lattice. The very first experiments on dynamical localisation [55] used this technique as well as the most modern versions of realising topological states [23, 110] and observing dynamical topological phase transitions [110]. Technically, the shaking is implemented, e.g., by introducing a frequency difference between the lattice beams by means of acousto-optical modulators [55] or by vibrating the mirrors that retro-reflect the lattice beams using Piezo-electric actuators [23], cf. Fig. 2.3(c). Building on this experimental technique, ideas have been recently developed in order to create topological interfaces and to detect chiral edge modes in two-dimensional lattices [142], to simulate synthetic dimension from shaking harmonic traps [143], to realise Floquet topological phases without static counterpart [144] and to control the Floquet state population in a periodically driven system [145].

We conclude by remarking that detailed examples of non-interacting Floquet realisations can be found within this thesis in the context of a quantum ratchet model in Ch. 3 and in

[7] Note that these symmetries are identical to the ones that need to be broken in order to allow for ratchet-type transport effects [136, 137], as also discussed in Ch. 3

the discussion of the effective simulation of the Haldane model in Ch. 6. We also stress that the collection of examples given in this section are far from complete. More information about many aspects of Floquet systems realised with ultracold atoms can be found in, e.g., Ref. [17], and references therein. Lastly, we stress again that all Floquet effects discussed in this section fundamentally build on the simulation of an effective Hamiltonian describing the Floquet operator, see Eq. (2.45). New qualitative behaviours, however, will emerge in the presence of heating due to the lack of energy conservation. We devote part II of this thesis to these peculiar extended Floquet systems.

3. A quantum ratchet for excitations of a bosonic Mott insulator

One of the most simple quantum machines is a Hamiltonian where parameters are changed periodically in time. Such periodically driven systems can lead to a directed motion of particles. In this chapter we present a possible blueprint for such a machine in a most simplified form by introducing a *quantum ratchet* for the excitations of a thermally activated Mott insulator [146]. We first elaborate on the concept of a ratchet in general before discussing our chosen model. We then study the dynamics of doublons and holes in such a periodically driven setting for different external potentials. We finally close the discussion by remarking on potential topological aspects of such a Floquet quantum system.

3.1. From classical ratchets to small quantum machines

Typically, the working principle of a machine is fundamentally linked to a certain transport mechanism. A very peculiar idea of such a mechanism is to convert random motion into work. This idea was put into a *Gedankenexperiment* first by Smoluchowski [147] and later with more popularity by Feynman [148]. The potential machine is depicted in Fig. 3.1(a) and is based on the following logic [149]: being surrounded by a gas at thermal equilibrium, atoms or molecules *randomly* hit paddles at one end of the machine. Attached to these paddles via an axle is a circular saw with asymmetric saw-teeth. This *ratchet* is completed by a pawl that breaks the rotational symmetry of the setup and is thought to cause a rectification of the initial random motion by letting the system only rotate in one direction. If, in addition, there was also a load attached to the rod, one might be tempted to argue that this load gets lifted and that work is indeed done by the ratchet. Of course, this thought is false and one needs to conclude that this machine cannot succeed to work, since it describes a perpetual motion machine which would be in contradiction with the second law of thermodynamics [149]. A short-cut explanation for the failure of this Feynman ratchet is the fact that in *thermal equilibrium* the pawl experiences as much thermal fluctuation as the paddles, rendering the same likelihood of rotating clockwise and anticlockwise, respectively.

Nevertheless, despite the fact that the above described perpetual motion machine is prohibited to work, the concept of witnessing directed transport in an unbiased environment based on deliberate symmetry breaking has become quite prominent, particularly for spatially periodic systems. To be precise, this *ratchet effect* requires a system that is driven away from equilibrium by *periodic driving* and all spatial inversion symmetries are broken [149, 150]. In addition, in classical systems the presence of thermal noise is crucial in order to guarantee irreversibility. Fulfilling all these conditions offers the possibility to observe directed motion in spite of the fact that the external forces driving the system vanish on average. In Fig. 3.1(b) we present a most intuitive picture of the working principle of such a ratchet: first, particles reside at the valleys of a periodic sawtooth potential. The potential is then assumed to be switched on and off at a certain frequency. During the

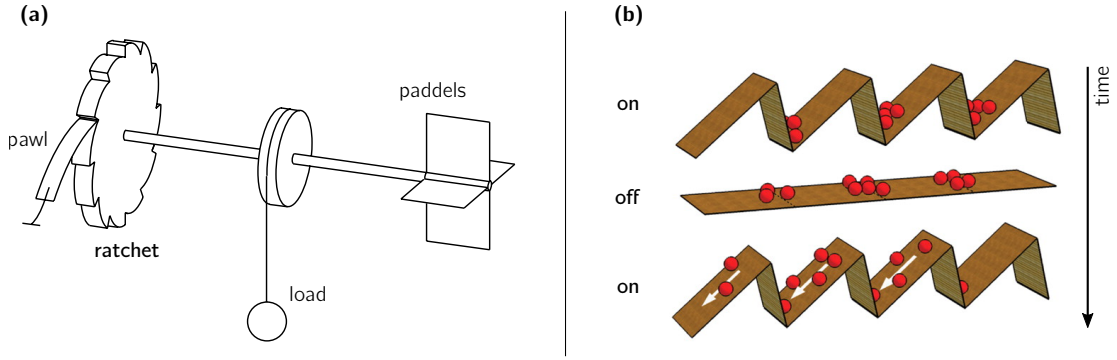

Figure 3.1.: Illustrations of (a) the Feynman ratchet and (b) 'Brownian ratchet' with classical particles. While the example in (a) cannot yield directed motion due to its nature of being a perpetual motion machine (see text), the ratchet of (b) indeed does show unidirectional transport as a consequence of the external drive. The schematics of (a) and (b) were taken and adopted from Refs. [149] and [137], respectively.

time when the potential is temporarily absent, the particles undergo Brownian motion in free space and diffuse. Switching the potential back on causes the particles to 'roll' back into the minima. However, not all particles will end up in the same minima as before, and since the potential is spatially asymmetric, this will lead to a steady particle current.

This ratchet mechanism (and variants thereof) can in general be used to explain a broad range of phenomena. For example, ratchet effects are thought to be the cause of certain types of biological motors on the micro-scale [151–153]. In these systems that are typically strongly dominated by thermal noise, the ratchet effect explains transport properties of molecules or molecular structures [154], and even entire cells [155]. In the realm of physics, the ratchet effect has been mainly exploited to create man-made machines in the spirit of Fig. 3.1. For instance, in solid state systems ratchet effects have - among others - been used to experimentally realise electron-pumps [156,157], to create spin-currents [158] or to detect asymmetries in graphene [159]. Due to their high level of controllability, systems made of cold atoms in optical lattices (see Sec. 2.1) have been an ideal test bed for implementing and investigating ratchets. The very first of these (cold atom) ratchets relied on dissipative processes breaking the time-inversion symmetry in combination with a periodic phase modulation of the optical lattice [160–162]. Note that comprehensive reading material on all aspects of (semi)classical ratchets (and their implementations) is provided by the reviews of Reimann [149] and Hänggi [150], for example.

Most importantly, however, cold atom systems do not solely offer the implementation of classical, dissipation based ratchets, but rather allow to extend the manufacturing to fully coherent quantum versions. These *quantum ratchets* are built on the property that transport is evoked by deterministic symmetry breaking instead of stochastic processes, such as thermal noise. One can therefore formulate the following two criteria for obtaining a quantum ratchet, which demands

1. coherent periodic driving with vanishing quantities on average, and
2. explicit breaking of both spatial inversion and time reversal symmetries on the Hamiltonian level.

Early experimental (cold atom) realisations of such quantum ratchets were based on 'kicked rotor models' [163–166]. A more elegant version is, however, the alternative implementation of a continuous external drive [136,167,168]. A recent experiment [137], which

was conducted in the group of M. Weitz in Bonn, demonstrated a quantum ratchet using this approach by loading an atomic Bose-Einstein condensate into a periodically changing potential. Here, once the inversion and time-reversal symmetries are broken, the atomic cloud drifts with an average velocity. Even more recently, they extended on this study by investigated the quantum ratchet effect in the presence of additional external forces [169]. Theoretically, one can describe the dynamics of such systems most conveniently within the Floquet formalism, see Sec. 2.2. Note that, in this spirit, other engineered 'quantum machines' such as quantum conveyor belts [170,171] or topological particle pumps [18,19,172] (see Sec. 3.4) are also related to the quantum ratchet systems. As outlined in Ch. 2, such quantum machines are the next logical step in utilizing the laws of quantum mechanics for our everyday lives.

Based on the criteria above, we will develop a simple model for the controlled manipulation of doubly occupied sites (doublons) or empty sites (holes) of a bosonic Mott insulator using the quantum ratchet effect in the following.

3.2. Directed motion of doublons and holes in a periodically driven 1D lattice

3.2.1. A designed ratchet model

Motivated by the capability of ultracold atom experiments (see Sec. 2.1), we consider a Bose-Hubbard Hamiltonian with time- and space-dependent hopping strengths as well as external potentials of the form

$$H(t) = -\sum_i J_i(t)\,(a_{i+1}^\dagger a_i + a_i^\dagger a_{i+1}) + \frac{U}{2}\sum_i n_i(n_i-1) + \sum_i V_i(t)\,n_i\,, \tag{3.1}$$

where $a_i^\dagger(a_i)$ creates (annihilates) a bosonic particle at site i, $n_i = a_i^\dagger a_i$ is the particle number operator, J_i is a hopping matrix element, V_i is an external potential and U describes the on-site interaction strength. Units are chosen such that $\hbar = 1$. As pointed out in Sec. 2.1 solving the static Bose-Hubbard model in its most general form is already a demanding task and yields two quantum phases depending on its parameters. If the interaction strength dominates over the hopping, $U \gg J$, such that to lowest order in J/U the latter can be neglected, the Mott-insulating phase will emerge. Because this quantum phase is very robust, it might a qood starting point for designer quantum systems in order to perform quantum computation, for instance. However, despite having great control over all experimental parameters, the effective temperature of a cold atom setup will inevitably create excitations in the Mott insulator. In the spirit of creating a reliable and reproducable quantum system these excitation might indeed be undesired.

We, thus, propose to implement a quantum ratchet mechanism in order to gain dynamical control over such excitations. In order to meet one of the criteria of a quantum ratchet *space inversion* symmetry needs to be broken (see above). Since there are no further constraints on the spatial structure, this can be done in the easiest possible way. We, therefore, demand that the system is described by staggered hopping amplitudes J_i as well as staggered potentials V_i. For example, as shown in the experiment by Salger *et al.* [137] this can be achieved by an optical lattice which is characterised by two wavelengths λ and 2λ. To be able to see a quantum ratchet effect one additionally needs to drive the system *periodically* in time. Here, the hoppings and potentials are modulated with the

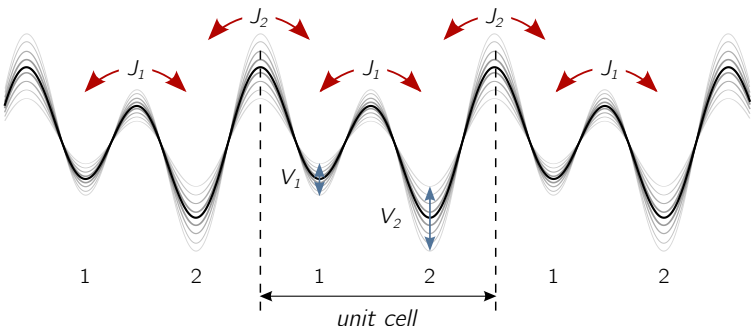

Figure 3.2.: Illustration of the lattice model causing the ratchet effect shown without external linear potential. Both the local hopping parameter and potential are staggered. The drive is implemented in such a way that time-reversal symmetry is broken, see Eq. (3.3). The parameters J_1, J_2, V_1, V_2 are defined according to Eqs. (3.2) and (3.3). The size of the unit cell is given by $a = 2a_{\mathrm{lat}}$, where we choose $a_{\mathrm{lat}} = 1$.

same frequency Ω. The resulting parameters read as

$$J_i(t) = \begin{cases} J_{s,o} + \cos(\Omega t) J_o & \text{for } i \text{ odd} \\ J_{s,e} + \cos(\Omega t) J_e & \text{for } i \text{ even} \end{cases}, \tag{3.2}$$

$$V_i(t) = \begin{cases} -g\,i + V_s + \cos(\Omega t + \varphi) V_o & \text{for } i \text{ odd} \\ -g\,i - V_s + \cos(\Omega t + \varphi) V_e & \text{for } i \text{ even} \end{cases}. \tag{3.3}$$

The first term in the expression of V_i account for the effect of a uniform force of strength g, e.g., caused by gravity or an effective 'electric field'. A sketch of the effective hoppings and potentials is given in Fig. 3.2 for $g = 0$. To fulfil the last requirement of a quantum ratchet the symmetry of *time inversion* must be broken as well. The is done by a relative phase shift φ in the time dependence of the oscillating hopping terms (J_e, J_o) and the corresponding potential terms (V_e, V_o). Throughout this chapter, all coupling constants, frequencies and times are measured in units of the average static hopping rate of doublons, i.e., $(J_{s,o} + J_{s,e})$, which is set to unity in the following (see also Tab. 3.1).

Before aiming at solving the full time-dependent problem described by Eq. (3.1) a few remarks should be made. As discussed above, we consider the limit where the on-site interaction U is considerably larger than the hopping rates, the frequency Ω and the initial temperature of the system (before the ratchet is switched on), $U \gg J_i, V_i, \Omega, T$. Furthermore, we consider an average occupation of the system of one boson per site. In this limit the main excitations of the system are doubly occupied sites (*doublons*) and empty sites (*holes*) with creation operators $d_i^\dagger$ and $h_i^\dagger$, respectively. We assume that they are so diluted that we can neglect their scattering on the time scale of the experiment.

In the considered limit one can also safely neglect all processes in which the number of doublons and holes change. In any of such annihilation or pair-creation events an energy of order U is either released or absorbed. To provide or absorb such an amount of energy, either U/Ω quanta of the driving frequency or the kinetic energy of U/J particles (or combinations thereof) is needed to meet the requirement of energy conservation. Consequently, additional excitation or relaxation processes are indeed higher-order processes which are exponentially suppressed in U/Ω and U/J, respectively. This suppression has been studied in a number of theoretical works [173–176] and was in fact also confirmed experimentally by Strohmaier *et al.* [177] by studying the hole-doublon annihilation rates. Therefore, the single-particle dynamics of doublons and holes is described by non-interacting Hamiltoni-

ans, which to leading order in $1/U$ have the simple form

$$H_d(t) = \sum_i -2\,J_i(t)\,(d_{i+1}^\dagger d_i + d_i^\dagger d_{i+1}) + V_i(t)\,d_i^\dagger d_i\,, \tag{3.4}$$

$$H_h(t) = \sum_i -J_i(t)\,(h_{i+1}^\dagger h_i + h_i^\dagger h_{i+1}) - V_i(t)\,h_i^\dagger h_i\,. \tag{3.5}$$

It becomes clear that the dynamics of doublons and holes are different in two aspects. First, the hopping rate of doublons is twice the hopping rate of holes. This is due to the fact that doublons experience an enhancement in hopping owing to their Bose statistics. Second, the potentials felt by the holes are reversed. This is easily understood by realising that a hole is indeed nothing but a missing bosonic particle.

Because the following treatment is independent of the two particle species, we focus on doublons for reasons of brevity. In the absence of external forces, $g=0$, the system can be described by a two-site unit cell (see Fig. 3.2). It is, hence, natural to define creation (and annihilation) operators acting on even or odd sites only, i.e., $d_{j,o}^\dagger = d_{2j-1}^\dagger$, $d_{j,e}^\dagger = d_{2j}^\dagger$. One can then perform a Fourier transformation with respect to the unit cell index. The transformations for the operators are defined as

$$d_{k,e/o}^\dagger = \sum_j e^{ikja}\,d_{j,e/o}^\dagger \qquad \Leftrightarrow \qquad d_{j,e/o}^\dagger = \int_{-\pi/a}^{\pi/a} \frac{dk}{2\pi/a}\; e^{-ikja}\,d_{k,e/o}^\dagger\,, \tag{3.6}$$

where the size of the unit cell is given by twice the lattice spacing, $a=2a_{lat}$. In the following we use conventions where we set the lattice spacing to unity, $a_{lat}=1$. Therefore, the first Brillouin zone is given by momentum values of $-\pi/2 \le k < \pi/2$. Using an additional temporal Fourier decomposition, the respective effective Hamiltonian can conveniently be described by simple 2×2 matrices $H_{k,n}^d$ that oscillate with $e^{-in\Omega t}$, i.e.,

$$H_d(t) = \int \frac{dk}{2\pi/a}\,\left(d_{k,o}^\dagger, d_{k,e}^\dagger\right)\left(\sum_n H_{k,n}^d\,e^{-in\Omega t}\right)\begin{pmatrix} d_{k,o} \\ d_{k,e}\end{pmatrix}\,, \tag{3.7}$$

where for *doublons*

$$H_{k,0}^d = \begin{pmatrix} V_s & -2(J_{s,o} + J_{s,e}\,e^{-2ik}) \\ -2(J_{s,o} + J_{s,e}\,e^{2ik}) & -V_s \end{pmatrix}\,, \tag{3.8}$$

$$H_{k,\pm1}^d = \frac{1}{2}\begin{pmatrix} e^{\mp i\varphi}\,V_o & -2(J_o + J_e\,e^{-2ik}) \\ -2(J_o + J_e\,e^{2ik}) & e^{\mp i\varphi}\,V_e \end{pmatrix}\,. \tag{3.9}$$

The corresponding expressions for *holes* are readily found using $J \to J/2$ and $V \to -V$.

Having reduced the initial Bose-Hubbard Hamiltonian (3.1) to the effective 2×2 time-dependent problem given by Eq. (3.7) allows now for a practicable *Floquet treatment* (for details see Sec. 2.2): the time evolution of quantum states is determined by using the Floquet theorem. First, the single-particle Floquet Hamiltonian for doublons and holes is promoted to an operator acting on the extended Hilbert space $\mathcal{F}$, i.e., $H_{d/h}^F(t) \to \bar{H}_{d/h}^F$. One can then solve the eigenvalue matrix equation (cf. Eq. (2.37))

$$\sum_m H_{k,nm}^F\,|\phi_{\nu,k}^m\rangle = \varepsilon_\nu(k)\,|\phi_{\nu,k}^n\rangle\,, \tag{3.10}$$

where the matrix elements of the k-parametrised Floquet Hamiltonian are given by

$$H_{k,nm}^F = \Big(H_{k,0} - n\Omega\Big)\,\delta_{n,m} + H_{k,+1}\,\delta_{n,m+1} + H_{k,-1}\,\delta_{n,m-1}\,. \tag{3.11}$$

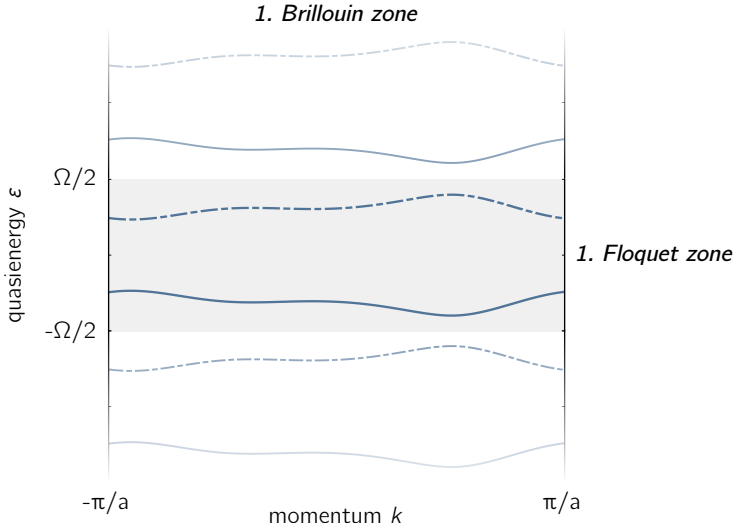

Figure 3.3.: Illustration of the quasienergy spectrum of the Floquet Hamiltonian (3.11) for an arbitrarily chosen driving frequency of $\Omega = 3$. Shown are bands of the first Floquet zone (gray shaded area). Other bands above and below the energy window $[-\Omega/2, \Omega/2)$ indicate that there are indeed infinitely many (copy) solutions (see Sec. 2.2.1). In the present case, breaking the space inversion as well as the time reversal symmetry of the system renders asymmetric bands which supports unidirectional particle transport, see Eq. (3.21).

Of course, one needs to replace each $H_{k,n}$ by $H_{k,n}^{d/h}$ depending on whether the dynamics of doublons or holes are of interest.

The number of unique physical solutions of the enlarged Floquet problem equals the dimension of the physical Hilbert space, $\dim(\mathcal{H})$. Hence, the Floquet Hamiltonian (3.11) is described by two distinct energy bands as a function of momentum (and infinitely many copies thereof). The Floquet index ν of a certain Floquet state is therefore interpreted as a *Floquet band index* for these kind of models. In Fig. 3.3 we show the resulting (Floquet) band structure for doublons that are driven with a frequency of $\Omega = 3$, which was chosen arbitrarily. Here, the truncation parameter for the Floquet matrix was set to $N_f = 5$. We stress again that, in the following, only quasienergies of the first Floquet zone and associated eigenstates $|\phi_{\nu,k}\rangle\rangle$ (or $|\phi_{\nu,k}(t)\rangle$, respectively), see Sec. 2.2, need to be considered.

This section is closed by drawing attention to the dimensionality of the system: note that the initial problem (3.1) has been written in its one-dimensional version. It is important to stress that all the results presented below apply equally also for dimensions $d > 1$ as long as the modulations of H occur only in one direction of space. In fact, an extra dimension might even be crucial for the single-particle approximation discussed in this section to hold. The reason being that in 1D, particles moving with opposite velocities will inevitably hit each other at some point in time (assuming that they do not move away from each other right from the start). In 2D, however, the second dimension can be exploited by the quasiparticles in order to smoothly pass each other.

3.2.2. Quantification of the ratchet effect

The velocity operator

The central objective of this section is to quantify the ratchet effect. A measure for the transport properties of the system is the *particle current*. Generally, the current density $\mathbf{j}$

is given by the continuity equation

$$\frac{\partial \rho(\mathbf{r},t)}{\partial t} = -\boldsymbol{\nabla}\cdot\mathbf{j}(\mathbf{r},t)\,, \tag{3.12}$$

where ρ describes the density of particles (or charge carriers for electric currents, respectively). In order to reformulate Eq. (3.12) in terms of a total current one introduces the polarization operator $\mathbf{P}(t) = \int d^3r\,\mathbf{r}\rho(\mathbf{r},t)$. It follows that [178]

$$\frac{\partial \mathbf{P}(t)}{\partial t} = \int d^3r\ \mathbf{r}\,\frac{\partial \rho(\mathbf{r},t)}{\partial t} = -\int d^3r\ \mathbf{r}\,\boldsymbol{\nabla}\cdot\mathbf{j}(\mathbf{r},t) = \int d^3r\ \mathbf{j}(\mathbf{r},t)\,, \tag{3.13}$$

where the last step requires integration by parts. This total current can now be related to a *current operator* $\mathbf{J}$ of a tight-binding type model. For now assume that the kinetic part of the system is described by a generic hopping Hamiltonian of the form $H^{\mathrm{hop}} = -\sum_{ij} J_{ij}\, a_i^\dagger a_j$. The polarization operator is defined by

$$\mathbf{P} = \sum_i \mathbf{R}_i\, n_i\,, \tag{3.14}$$

where the index i runs over all sites of a yet to be specified lattice and $\mathbf{R}_i$ is its corresponding position. Using the Heisenberg equation of motion one finds the following expression for the current operator[1]

$$\mathbf{J} = \frac{\partial \mathbf{P}}{\partial t} = i[H,\mathbf{P}] = i\sum_{n,m}\Big(\mathbf{R}_n - \mathbf{R}_m\Big)\, J_{nm}\, a_n^\dagger a_m\,. \tag{3.15}$$

Note that typical potential terms of the Hamiltonian depend on the particle number operator $n_i = a_i^\dagger a_i$ (and combinations thereof). Hence, they do not contribute to the current operator $\mathbf{J}$, because n_i commutes with H. The result for the current operator (3.15) is generic for all fermionic and bosonic tight-binding type systems (a spin index can be trivially added, as well).

For a 1D system with only nearest neighbour hopping and fixed lattice constant a_{lat} as given by the effective Hamiltonians (3.4) and (3.5), the difference of lattice vectors is $(\mathbf{R}_{n+1} - \mathbf{R}_n) = a_{\mathrm{lat}}\hat{e}$, with $\hat{e}$ being the unit vector pointing in the direction of the lattice. Thus, the projected current operator along the lattice is readily given by $\mathbf{J}\cdot\hat{e} \equiv |\mathbf{J}|$. The corresponding expectation value $\langle\mathbf{J}\rangle$ is an extensive quantity in the total number of particles of the system N. However, in order to make quantitative statements about the ratchet effect of single particles we want a quantity which is independent of N. To this end, we define the *velocity operator*

$$\mathbf{v} = \mathbf{J}/N\,, \tag{3.16}$$

or alternatively $v = |\mathbf{J}|/N$. One can then express the particle current in terms of an average velocity $\langle\mathbf{v}\rangle^{\mathrm{av}}$, i.e., $\langle\mathbf{J}\rangle = N\langle\mathbf{v}\rangle^{\mathrm{av}}$.

For the time-dependent problem at hand, the velocities of doublons and holes are then formally obtained from the corresponding operators

$$v_d(t) = \frac{i}{N_d}\sum_n 2J_n(t)\,(d_{n+1}^\dagger d_n - d_n^\dagger d_{n+1})\,, \tag{3.17}$$

$$v_h(t) = \frac{i}{N_h}\sum_n J_n(t)\,(h_{n+1}^\dagger h_n - h_n^\dagger h_{n+1})\,. \tag{3.18}$$

[1] Note that we chose the same symbol J to describe the current as well as the hopping amplitude of the Bose-Hubbard model. This is a slightly unfortunate convention, which is widely used in the context of ultracold atoms in optical lattices. One could have circumvented this issue by representing the hopping strength by the also commonly used letter t. However, since this quantity is time-dependent throughout most parts of this thesis, such a labelling appeared to be even more unlucky.

Here, $N_d = \sum_i d_i^\dagger d_i$ and $N_h = \sum_i h_i^\dagger h_i$ are the total number of doublons and holes, respectively. Note that we use conventions where a positive $\langle v_{d/h} \rangle$ describes doublons (or holes) moving to the right. Despite the fact that the operators (3.17) and (3.18) formally yield the average velocity of a single doublon or hole, respectively, the expressions (approximately) coincide with the true single particle velocity operators. The reason for this is as follows: it is assumed that initially the temperature of the system is low compared both to the bandwidth and the Mott gap. Therefore, only a few doublons and holes are present, occupying states with momenta close to zero, and, hence, they all yield approximately the same velocity.

Since the true transport properties of the system will only emerge for times $t \gg 1/\Omega$, we introduce the asymptotic velocity $\langle v_{d/h} \rangle^{\text{asy}}$, i.e., the average velocity in the limit $t \to \infty$, which is defined as

$$\langle v_{d/h} \rangle^{\text{asy}} = \lim_{t\to\infty} \frac{1}{t} \int_0^t dt' \ \langle \psi(t') |\, v_{d/h}(t') \,| \psi(t') \rangle \ . \tag{3.19}$$

Next, the current operators (3.17) and (3.18) are decomposed into their Fourier components, $v_{d/h}(t) = \sum_n e^{-in\Omega t} v^n_{d/h}$, and the time-evolved state describing the system is expressed in terms of Fourier modes of Floquet eigenstates, $|\psi(t)\rangle = \sum_{\nu,n} c_\nu \, e^{-i(\varepsilon_\nu + n\Omega)t} \, |\phi^n_\nu\rangle$ with $c_\nu = \langle \phi_\nu(0) | \psi(0) \rangle$. Note that here the initial time was set to zero for convenience, $t_0 = 0$, but that the velocity of a doublon or hole actually does parametrically depend on the initial time. We will discuss this effect below. The expression (3.19) can now be rewritten as

$$\begin{aligned}
\langle v_{d/h} \rangle^{\text{asy}} &= \lim_{t\to\infty} \frac{1}{t} \int_0^t dt' \ \sum_{\nu,\mu} \sum_{n,m,l} c_\nu c^*_\mu \, e^{i(\varepsilon_\nu - \varepsilon_\mu)t} e^{i(n-m-l)\Omega t} \, \langle \phi^n_\nu |\, v^m_{d/h} \,| \phi^l_\mu \rangle \qquad (3.20) \\
&= \sum_{\nu,\mu} \sum_{n,m,l} c_\nu c^*_\mu \, \delta_{\nu,\mu} \, \delta_{n-m,l} \, \langle \phi^n_\nu |\, v^m_{d/h} \,| \phi^l_\mu \rangle \\
&= \sum_{\nu,n} p_\nu \left(\langle \phi^n_\nu |\, v^{-1}_{d/h} \,| \phi^{n+1}_\nu \rangle + \langle \phi^n_\nu |\, v^0_{d/h} \,| \phi^l_\nu \rangle + \langle \phi^n_\nu |\, v^1_{d/h} \,| \phi^{n-1}_\nu \rangle \right) \\
&= \sum_\nu p_\nu \, \langle\!\langle \phi_\nu | \bar{v}_{d/h} | \phi_\nu \rangle\!\rangle \ ,
\end{aligned}$$

where $p_\nu = |c_\nu|^2$ describes the probability (normalised to 1) that Floquet state ν is occupied. In Eq. (3.20) it has been used that interferences of Floquet states with different quasienergies as well as interferences of different Floquet sectors average to zero in the limit $t \to \infty$. Hence, transforming the velocity operators (3.17) and (3.18) to operators that explicitly act on the extended Hilbert space $\mathcal{F}$, $v_{d/h}(t) \to \bar{v}_{d/h}$, allows to calculate these quantities by taking expectation values of single Floquet states in Floquet space. This can be straightforwardly implemented in practice as outlined in Sec. 2.2.2.

Alternatively, the asymptotic velocity can be determined by the slope of the quasienergy bands, i.e.,

$$\langle v_{d/h}(k) \rangle^{\text{asy}} = \sum_\nu p_\nu \, \frac{\partial \varepsilon_{d/h,\nu}(k)}{\partial k} \, . \tag{3.21}$$

This is fully analogous to the conventional semiclassical picture of transport associated with energy bands, and can be analytically shown by applying the Hellmann-Feynman Theorem to the Floquet theory [164]. Having expression (3.21) in mind and recalling the Floquet bands of Fig. 3.3, it becomes instantly apparent why one can expect a quantum ratchet based on a system of bands to work: breaking the symmetries of the system simultaneously breaks the symmetry of the quasienergy bands, therefore allowing for a non-zero velocity for initial states with zero momentum.

time	$t < t_0$		$t > t_0$	
parameters	$J_{s,o} = 0.67$	$V_s = 0$	$J_{s,o} = 0.67$	$V_s = 0.4$
	$J_{s,e} = 0.33$	$V_o = 0$	$J_{s,e} = 0.33$	$V_o = 0.4$
	$J_o = 0$	$V_e = 0$	$J_o = 0.67$	$V_e = -0.4$
	$J_e = 0$		$J_e = -0.17$	

Table 3.1.: Parameters of Hamiltonian $H(t)$ as used throughout this chapter. The time t_0 corresponds to the point in time when the ratchet is (fully) switched on. All parameters are measured in units of $(J_{s,e} + J_{s,o})$.

Numerical results for velocities of doublons and holes

We proceed by studying the evolution of a single-particle state with momentum $k = 0$. Again, this is justified due to the low temperature approximation mentioned above, which only allows a few excitations with momenta close to zero. We assume that both doublons and holes are present in the system with such momenta, and that for $t < t_0$ the driving as well as the staggered potential is switched off, i.e., $V_s = V_e = V_o = J_e = J_o = 0$. During that time the dynamics of the system is captured by a Hamiltonian which we call H_0 in the following. At $t = t_0$ both the static staggered potential V_s and the oscillating terms are switched on. For $t > t_0$ we use the momentum space representation of our Floquet problem as shown in Sec. 3.2.1, where one understands the Floquet state index ν in Eq. (3.20) as a collection of a (Floquet) band index and a momentum index that is set to zero, $\nu \to (\nu, k = 0)$.

In the following we want to show the transport properties of doublons and holes within the described setting. To this end, we investigate two limits: in the first case we consider a sudden switching on of the oscillating terms, $H = H_0 + \Theta(t-t_0)\big(H(t)-H_0\big)$. Secondly, we look at an adiabatic switching on, $H = H_0 + f(t-t_0)\big(H(t)-H_0\big)$ where $f(t)$ smoothly changes from 0 to 1 (for $t > t_0$) on a time scale assumed to be much larger than all other time scales of the problem. In the latter case, the system evolves adiabatically[2] into a Floquet eigenstate while in the former a superposition of Floquet eigenstates has to be considered. It is clear that in cases where such a superposition of Floquet states determines the long-time dynamics the starting time of the ratchet, t_0, can in principle play an important role. Generally, values of the parameters used throughout this chapter can be found in Tab. 3.1. Note that the parameters have been chosen arbitrarily, but we checked that all effects discussed in the following do not depend qualitatively on this choice.

Finite net velocities are generically expected whenever they are allowed by symmetry. Due to the presence of *both* staggered potential and staggered hopping all mirror symmetries are broken. So, first, we consider a suddenly switched on ratchet of fixed driving frequency and look at asymptotic velocities of a doublon as a function of the relative phase φ. From Fig. 3.4 one can see how crucial the breaking of time-reversal symmetry for the functionality of the ratchet is: for the time-reversal points $\varphi = \pm\pi, 0$ the ratchet indeed stops working. In addition, we study the effect of t_0 on the velocities of the doublon. In contrast to the role of φ, the initial time t_0 has in most cases only a small quantitative effect, see Figs. 3.4(a) and (c). Nevertheless, as can be seen from Fig. 3.4(b) for some values of the driving frequency there is a strong impact on the velocity. This can be explained

[2] While we assume that the adiabatic state preparation is possible in the present case, the notion of 'remaining adiabatic' throughout the entire initialization process is generally non-trivial for Floquet systems. For details see Sec. 2.2.4.

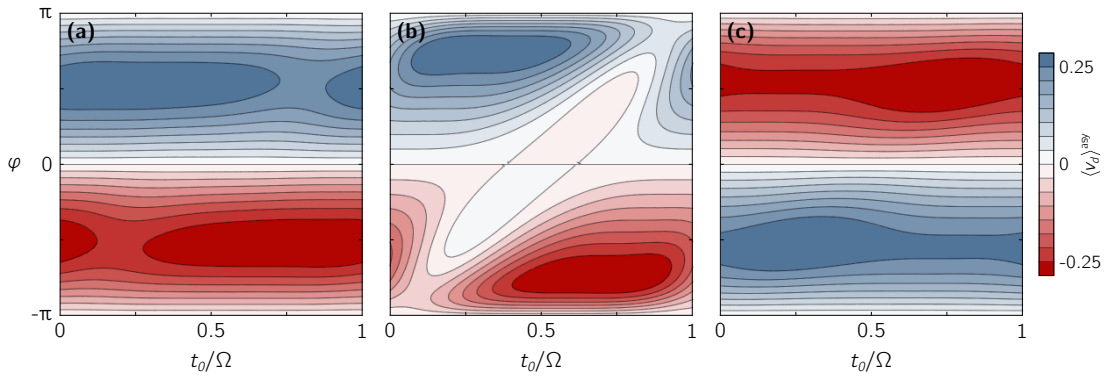

Figure 3.4.: Asymptotic doublon velocities for a suddenly switched on ratchet as function of the relative phase shift φ and initial time t_0. Values are shown for driving frequencies of (a) $\Omega = 3$, (b) $\Omega = 4$ and (c) $\Omega = 5$. Typically, velocities are almost insensitive to changes of t_0 except for situations where Ω is tuned on resonance (see Figs. 3.5, 3.6, and text).

by the presence of resonances, which will be the subject of study in the following. Bearing this in mind, we set $t_0 = 0$ and $\varphi = -\pi/2$ for the rest of this section. Note that the same discussion also holds for holes.

We continue to investigate the case where oscillating terms are switched on suddenly. In Fig. 3.5(a) we show the velocities of a doublon (solid red) and a hole (dashed blue) as a function of frequency. For both species the response is characterised by a number of resonances at frequencies $\Omega \approx \Omega_n = \Delta E/n$, with $n \in \mathbb{N}^+$ and ΔE corresponding to the energy difference between the two bands of the undriven system at $k = 0$. As doublons and holes have different hopping rates, one can see that the resonances and their corresponding frequencies are fundamentally different. In both cases, however, every resonance can be associated with a certain number of sign changes. While for $n = 1$ there is only one sign change, there are always two sign changes associated with $n \geq 2$. It can be shown that these sign changes persist even in the limit where the oscillating terms in the Hamiltonian are very weak. These effects can indeed be linked to the presence of resonances and can therefore be easily understood from perturbation theory. We will elaborate on this approach below in Sec. 3.2.3. In short, for $\Omega \approx \Delta E/n$ two entries of the Floquet matrix become degenerate leading to a pole in the response of the velocity. Since these poles have the same sign for all n, there must be an additional sign change associated with all resonances for $n \geq 2$. Furthermore, the zero crossing of the velocity right on resonance reflects the avoided level crossing occurring at each resonance, see Fig. 3.6(a). When changing from $\Omega < \Delta E/n$ to $\Omega > \Delta E/n$ one effectively changes the band for a sudden switching on of the ratchet. Right on resonance, the system is in an equal superposition of both bands. This leads to opposing contributions, and, hence, to a zero crossing of the velocity. In fact, this also explains the observed effect on the choice of the initial time t_0, as was seen in Fig. 3.4(b): on resonance the band population is very sensitive to the underlying Floquet states. Note, however, that the overall behaviour of the velocities as a function of Ω is *not* changed qualitatively when t_0 is varied.

If the ratchet is switched on adiabatically, the behaviour of the respective velocity as a function of frequency changes dramatically. This can be seen in Fig. 3.5(b). Here, for $n=1$ there is no sign change at all, but there is always one sign change for $n \geq 2$. Moreover, one observes that in contrast to the sudden switching, the velocity is strongest right on the resonance Ω_n for the adiabatic case. This is again a direct consequence of the avoided level crossing occurring at each resonance, see Fig. 3.6(b). In the adiabatic case one remains in

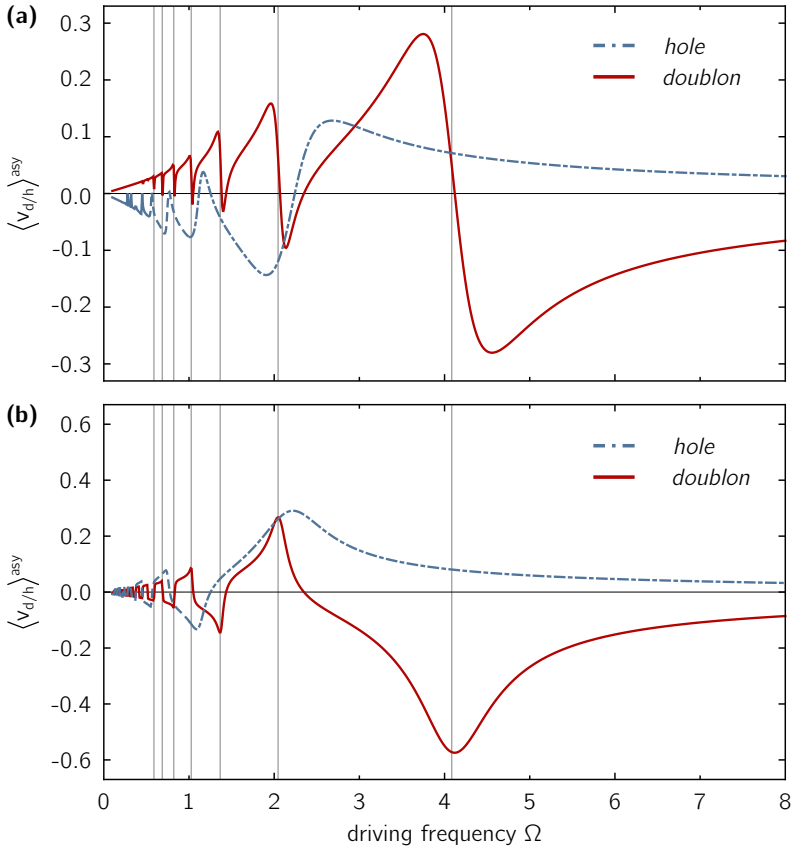

Figure 3.5.: Doublon (solid red) and hole (dashed blue) asymptotic velocity for (a) the sudden switching and (b) the adiabatic case (see text). Velocities are given in units of $a_{\mathrm{lat}}(J_{s,o}+J_{s,e})$, i.e., lattice constant times average static doublon hopping rate. The parameters used are as presented in Tab. 3.1. Vertical lines indicate the first seven doublon resonances, $\Omega_n = \Delta E/n$, $n \in \{1, ..., 7\}$.

the same band when going over a resonance. Because a single Floquet band experiences most reshaping when the resonance condition is fulfilled, the velocity is strongest for the adiabatic case. Note that we do not consider any in-between cases here, i.e., cases of a finite ramping speed of the oscillating potential. These would map to the Landau-Zener tunnelling problem in the limit when the ramping time is large compared to the oscillation period T.

Next to the resonances, the limits of large and very small frequencies can also be of great interest. The latter case describes the situation of an overall adiabatic evolution of the system. As can be seen from Fig. 3.5, this limit yields zero velocities. Nonetheless, while the adiabatic driving is seemingly not of importance for the case of (very) dilute doublon or hole excitations, it might have a huge impact on insulating states, i.e., Mott insulators or fermionic band insulators. We will discuss this matter in more depth in Sec. 3.4. In the case of large frequencies the velocities decrease as $1/\Omega$. One way to show this is to use perturbation theory again, see Sec. 3.2.3. A probably more appealing approach is to interpret this result as arising from an effective vector potential $\mathcal{A}$ in the effective Hamiltonian defined by $U(T) = \exp[-iH^{\mathrm{eff}}T]$ (see Sec. 2.2.3). A vector potential shifts the momentum giving rise to a finite velocity at $k=0$, i.e., $\varepsilon^0_\alpha(k) \to \varepsilon^0_\alpha(k-\mathcal{A}_d)$, where ε^0_α describes the eigenenergies of the undriven system. A more detailed discussion about this can be found in Sec. 3.2.4.

In conclusion, as doublons and holes are characterised by different hopping rates and

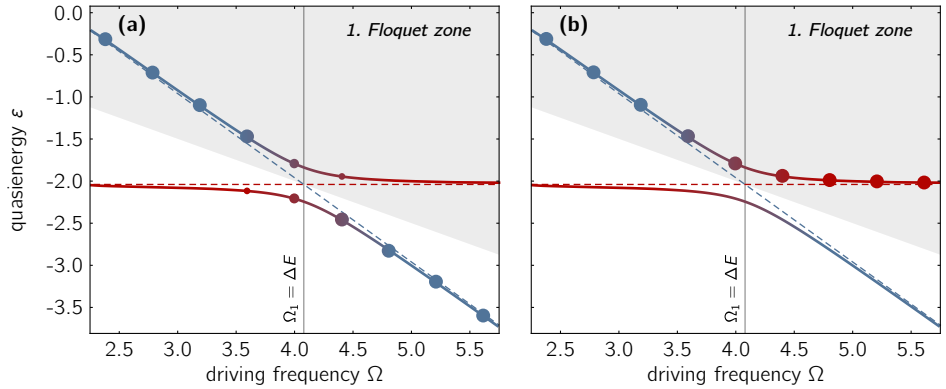

Figure 3.6.: Avoided crossing at the main resonance $\Omega_1 = \Delta E$ of the doublon bands at the lower edge of the first Floquet zone (gray shaded area). Points illustrate population of the respective band for (a) the sudden switching and (b) the adiabatic case. Dashed lines correspond to eigenenergies of H^F in the absence of time-dependent terms in the original Hamiltonian. In (a) the system changes the band as function of Ω, while in (b) it remains in the Floquet band. Parameters as in Tab. 3.1.

reversed potentials, also the relevant resonance frequencies are different. In fact, specific Floquet band shapes can be tailored by changing the parameters appropriately. Thus, by tuning the frequency of the oscillating potential, one can easily reach situations where, e.g., holes are driven to the right but doublons move in the opposite direction. Similarly, one can also reach situations where only one of the two species is moving. In cases where the ratchet is switched on in a sudden fashion the initial driving time t_0 may also be used to engineer the desired dynamics of doublons and holes. We have therefore shown that with the help of ratchets one can selectively control the various excitations of a homogeneous interacting many-particle system. One can combine this with a spatial control of where the excitations are moving to by using, e.g., focused lasers which locally change the effective resonance frequencies of the ratchet [146].

3.2.3. Resonances and Floquet perturbation theory

In Sec. 3.2.2 we have shown the behaviour of doublons and holes in the present ratchet setup in terms of their velocities. While in the previous section we described the general behaviour for strong driving strengths, we now aim at a better understanding of the origins of the observed resonances. In order to do so we assume weak external oscillations such that the Hamiltonian can be written in the form

$$H(t) = H_s + \epsilon_J H_J(t) + \epsilon_V H_V(t)\,, \tag{3.22}$$

with $\epsilon_J, \epsilon_V \ll 1$. Here, H_s describes the static part of the Hamiltonian, H_J includes all oscillating hopping parameters and H_V is characterised by time-dependent potential terms (c.f. Eqs. (3.1)-(3.3)). As before, we want to find the corresponding Floquet Hamiltonian. Promoting this Floquet Hamiltonian to an operator that explicitly acts on the extended Hilbert space yields

$$\bar{H}^F = \bar{H}^F_s + \epsilon_J \bar{H}^F_J + \epsilon_V \bar{H}^F_V\,, \tag{3.23}$$

with matrix elements $H^F_{s,nm} = (H^s - n\Omega)\,\delta_{nm}$, $H^F_{J,nm} = H^J(\delta_{n,m+1} + \delta_{n,m-1})$ and $H^F_{V,nm} = H^V(e^{-i\varphi}\delta_{n,m+1} + e^{i\varphi}\delta_{n,m-1})$. Similarly, the velocity operator acting on $\mathcal{F}$ can be expressed as

$$\bar{v} = \bar{v}_s + \epsilon_J\,\bar{v}_J\,, \tag{3.24}$$

with matrix elements $v_{s,nm} = v^s \delta_{nm}$ and $v_{J,nm} = v^J(\delta_{n,m+1} + \delta_{n,m-1})$. In the following we want to calculate the asymptotic velocity $\langle v_{d/h} \rangle^{\text{asy}}$ by means of taking expectation values in Floquet space, but now using a perturbative approach.

Floquet perturbation theory

In order to formulate this perturbation theory in Floquet space we express the Floquet states and quasienergies in terms of a respective power series, i.e.,

$$\varepsilon_{\nu n} = \varepsilon^{(0)}_{\nu n} + \epsilon_J \, \varepsilon^{(1),J}_{\nu n} + \epsilon_V \, \varepsilon^{(1),V}_{\nu n} + \epsilon_J \, \epsilon_V \, \varepsilon^{(2),JV}_{\nu n} + \ldots \, , \tag{3.25}$$

$$|\phi_{\nu n}\rangle\!\rangle = |\phi^{(0)}_{\nu n}\rangle\!\rangle + \epsilon_J \, |\phi^{(1),J}_{\nu n}\rangle\!\rangle + \epsilon_V \, |\phi^{(1),V}_{\nu n}\rangle\!\rangle + \epsilon_J \, \epsilon_V \, |\phi^{(2),JV}_{\nu n}\rangle\!\rangle + \ldots \, . \tag{3.26}$$

Since we want to calculate expectation values, we are mainly interested in corrections to the Floquet eigenstates at this point. Substituting expressions (3.25) and (3.26) into the Floquet eigenvalue problem defined by Eq. (2.37), and equating components of same power in ϵ_J, ϵ_V eventually yields

$$|\phi^{(1),J}_{\nu n}\rangle\!\rangle = \sum_{\substack{\mu m \neq \\ \nu n}} \frac{\langle\!\langle \phi^{(0)}_{\mu m} | \bar{H}^F_J | \phi^{(0)}_{\nu n} \rangle\!\rangle}{\varepsilon^{(0)}_{\nu n} - \varepsilon^{(0)}_{\mu m}} \, |\phi^{(0)}_{\mu m}\rangle\!\rangle \, , \tag{3.27}$$

$$|\phi^{(1),V}_{\nu n}\rangle\!\rangle = \sum_{\substack{\mu m \neq \\ \nu n}} \frac{\langle\!\langle \phi^{(0)}_{\mu m} | \bar{H}^F_V | \phi^{(0)}_{\nu n} \rangle\!\rangle}{\varepsilon^{(0)}_{\nu n} - \varepsilon^{(0)}_{\mu m}} \, |\phi^{(0)}_{\mu m}\rangle\!\rangle \, , \tag{3.28}$$

$$\begin{aligned} |\phi^{(2),JV}_{\nu n}\rangle\!\rangle = \sum_{\substack{\eta l \neq \\ \nu n}} \sum_{\substack{\mu m \neq \\ \nu n}} \Bigg[& \frac{\langle\!\langle \phi^{(0)}_{\eta l} | \bar{H}^F_J | \phi^{(0)}_{\mu m} \rangle\!\rangle \, \langle\!\langle \phi^{(0)}_{\mu m} | \bar{H}^F_V | \phi^{(0)}_{\nu n} \rangle\!\rangle}{(\varepsilon^{(0)}_{\nu n} - \varepsilon^{(0)}_{\eta l})(\varepsilon^{(0)}_{\nu n} - \varepsilon^{(0)}_{\mu m})} \\ & + \frac{\langle\!\langle \phi^{(0)}_{\eta l} | \bar{H}^F_V | \phi^{(0)}_{\mu m} \rangle\!\rangle \, \langle\!\langle \phi^{(0)}_{\mu m} | \bar{H}^F_J | \phi^{(0)}_{\nu n} \rangle\!\rangle}{(\varepsilon^{(0)}_{\nu n} - \varepsilon^{(0)}_{\eta l})(\varepsilon^{(0)}_{\nu n} - \varepsilon^{(0)}_{\mu m})} \Bigg] |\phi^{(0)}_{\eta l}\rangle\!\rangle \end{aligned} \, . \tag{3.29}$$

These results are structurally familiar from convential perturbation theory for non-Floquet systems. Here, however, the sum indices run over all states in the extended space, and only exclude identical copy states. While Eqs. (3.27)-(3.29) hold in general, we want to exploit the monochromaticity of the drive in the following. It is therefore convenient to realise that since $|\phi^{(0)}_{\nu n}\rangle\!\rangle$ describes an eigenstate of the Floquet matrix without a drive, only its nth Floquet entry, $|\phi^{n(0)}_{\nu n}\rangle \equiv |\nu\rangle$, is non-zero and in fact identical for all copy states.

We are interested in calculating the asymptotic velocity for a particle in a given Floquet band at $k = 0$, i.e., $\nu \to (\nu, k = 0)$. This corresponds to the adiabatic case in Sec. 3.2.2, where $\langle v_{d/h} \rangle^{\text{asy}} = \langle\!\langle \phi_\nu | \bar{v}_{d/h} | \phi_\nu \rangle\!\rangle$. One can straightforwardly verify that in this case the zeroth-order term as well as all first-order contributions vanish by construction. Furthermore, due to symmetry arguments, only second-order terms that are proportional to $\epsilon_J \epsilon_V$ yield finite contributions. Hence, restricting the calculation to second order the velocity can be approximated by the following compact form after a few steps of simplification:

$$\begin{aligned} \langle v_{d/h} \rangle^{\text{asy}} \approx -2i\epsilon_J \epsilon_V \sin(\varphi) \Bigg[& v^J_{\mu\nu} H^V_{\mu\nu} \left(\frac{1}{\Omega - \delta} - \frac{1}{\Omega + \delta} \right) \\ & + \frac{4\Omega \, v^s_{\mu\nu}}{\delta\Omega - \delta^3} \left(H^J_{\mu\nu} H^V_{\nu\nu} - H^V_{\mu\nu} H^J_{\nu\nu} \right) \Bigg] \end{aligned} \, , \tag{3.30}$$

with $\delta = \varepsilon^{(0)}_\mu - \varepsilon^{(0)}_\nu$, $H^V_{\mu\nu} = \langle \mu | H^V | \nu \rangle$, etc., and $\nu, \mu \in \{1, 2\}$ but $\nu \neq \mu$, where we understand the band label as '1' ('2') corresponding to the lower (upper) band. Clearly,

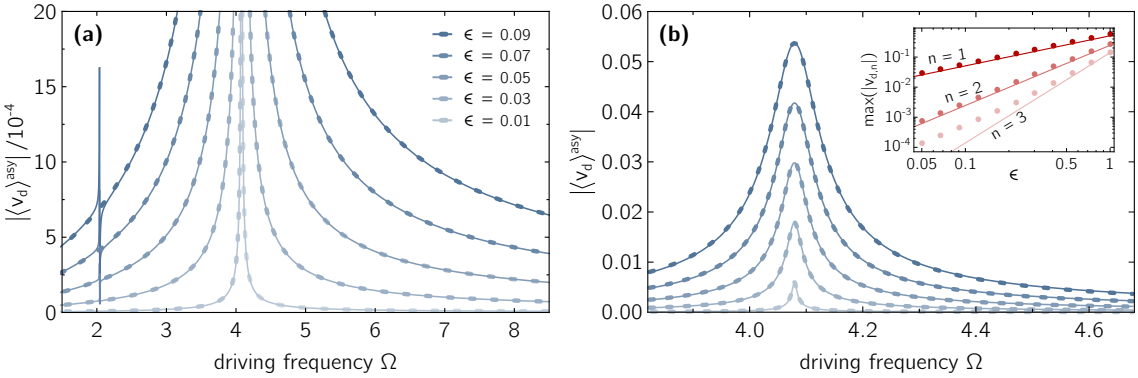

Figure 3.7.: Asymptotic doublon velocities around the main resonance Ω_1 for different values of $\epsilon = \epsilon^J = \epsilon^V$. Other parameters are as in Tab. 3.1. Coloured lines represent exact numerical data. Dashes correspond to predictions by (a) perturbation theory, Eq. (3.30), and (b) degenerate perturbation theory, Eq. (3.36). The sharp spike appearing on solid curves in (a) correspond to the second resonance at Ω_2, which is not captured by Eq. (3.30). The inset of (b) shows the height of the first three resonance peaks, $n = 1, 2, 3$, as a function of ϵ. Dots show exact numerical data and solid lines are guides to the eye representing a function $\propto \epsilon^n$.

expression (3.30) breaks down at the resonance, where it predicts a pole for the velocity. Therefore, only the 'wings' are compared to exact numerical data in Fig. 3.7(a). We compare absolute values of the velocity, because perturbation theory gives an undesired sign change. This is due to the fact that the formula for the velocity (3.30) does not keep track of the correct band labelling when sweeping through a resonance.

In the limit $\Omega \gg \varepsilon_{\nu/\mu}$, Eq. (3.30) can be used to describe the velocity for high frequencies even if $\epsilon_1 = \epsilon_2 = 1$. The expression simplifies in this case to

$$\langle v_{d/h} \rangle^{\text{asy}} \overset{\Omega \gg \varepsilon_{\nu/\mu}}{\approx} -\frac{4i\epsilon_J \epsilon_V \sin(\varphi)}{\Omega} \left[v^J_{\mu\nu} H^V_{\mu\nu} + \frac{2\, v^s_{\mu\nu}}{\delta} \left(H^J_{\mu\nu} H^V_{\nu\nu} - H^V_{\mu\nu} H^J_{\nu\nu} \right) \right]. \tag{3.31}$$

The detailed expression for the velocity of doublons or holes, respectively, is gained by diagonalising H^s and inserting the respective form of v^s, v^J, H^J, H^V into Eqs. (3.30) and (3.31). Due to the property that $H^V \to -H^V$ when switching from doublons to holes, one immediately sees that the velocities of the two species must have opposite signs in the large frequency limit. Moreover, one can indeed observe that for both species the velocity decays in this limit with $1/\Omega$.

Degenerate Floquet perturbation theory

In order to be able to describe the behaviour around the resonance correctly, one needs to apply *degenerate* perturbation theory. Degeneracies leading to the main resonance of the system are found for $\Omega = \delta$. Going into the basis that diagonalises $\bar{H}^F_s$, i.e. $\{|\phi^{(0)}_{\nu n}\rangle\rangle\}$, one defines the degeneracy subspace

$$\tilde{H}_s = \begin{pmatrix} \frac{1}{2}(\Omega - \delta) & (\epsilon_J H^J + \epsilon_V\, e^{i\varphi} H^V)_{12} \\ (\epsilon_J H^J + \epsilon_V\, e^{-i\varphi} H^V)_{21} & -\frac{1}{2}(\Omega - \delta) \end{pmatrix} \equiv \tilde{\boldsymbol{h}}_s \cdot \boldsymbol{\sigma}\,, \tag{3.32}$$

with the notation $(.)_{\nu\mu}$ referring to the respective operator in the basis $\{|\nu\rangle\}$, where again $\nu, \mu \in \{1, 2\}$ as defined above, and $\delta = (\varepsilon^{(0)}_2 - \varepsilon^{(0)}_1)$. Alternatively, one can define the Hamiltonian by a scalar product of $\tilde{\boldsymbol{h}}_s = (\tilde{h}_x, \tilde{h}_y, \tilde{h}_z)$ and the vector of Pauli matrices $\boldsymbol{\sigma} = (\sigma_x, \sigma_y, \sigma_z)$. Dividing the original Floquet Hamiltonian into a structure composed

of such degeneracy blocks, allows to define effective coupling matrices. In the following we shall only consider those which couple next-nearest degeneracy blocks, which can be written (for $k = 0$) as

$$\tilde{H}^J = H^J_{11}\,\sigma_z \qquad \text{and} \qquad \tilde{H}^V = e^{-i\varphi} H^V_{11}\,\sigma_z\,. \tag{3.33}$$

The same procedure is done for the respective parts of the velocity operator. The expressions in the degeneracy space yield

$$\tilde{v}^J = i\,v^J_{12}\,\sigma_y \qquad \text{and} \qquad \tilde{v}^s = \frac{1}{2}\,v^s_{12}\,(\sigma_x + i\sigma_y)\,. \tag{3.34}$$

In order to find the asymptotic velocity one first determines perturbatively the basis states of $\bar{H}^F$. In order to do so we use again Eqs. (3.27)-(3.27), but states are now found with respect to the degeneracy subspace, i.e., $|\tilde{\phi}^{(0)}_{\nu n}\rangle\!\rangle$, etc. Note that all arguments from above are carried over to this case in an analogous fashion. After doing the algebra, the asymptotic velocity of a particle (doublon or hole) in given band ν with momentum $k = 0$ is eventually given by

$$\begin{aligned}\langle v_{d/h}\rangle^{\text{asy}} \approx \mp\,\frac{i}{|\tilde{\boldsymbol{h}}_s|}\Big[&\epsilon^J (v^J)_{12}\tilde{h}_y - \frac{2}{\Omega}\,\epsilon^J v^s_{12} H^J_{11}\tilde{h}_y \\ &- \frac{2}{\Omega}\,\epsilon^V v^s_{12} H^V_{11}\Big(\cos(\varphi)\tilde{h}_y + \sin(\varphi)\tilde{h}_x\Big)\Big]\,,\end{aligned} \tag{3.35}$$

where the $-(+)$ refers now to the lower (upper) band of the original Floquet Hamiltonian, H^F. Using explicit relations for $\tilde{h}_x, \tilde{h}_y$ and $\tilde{h}_z$, the expression for the velocity (3.35) simplifies further to read as

$$\langle v_{d/h}\rangle^{\text{asy}} \approx \mp\,\frac{2i\epsilon_1\epsilon_2\sin(\varphi)}{\sqrt{(\delta-\Omega)^2+\Delta^2}}\Big[v^J_{21}H^V_{21} + \frac{2\,v^s_{21}}{\Omega}\Big(H^J_{21}H^V_{11} - H^V_{21}H^J_{11}\Big)\Big]\,, \tag{3.36}$$

with

$$\Delta^2 = 4\left(\left(\epsilon^J H^J_{21}\right)^2 + \left(\epsilon^V H^V_{21}\right)^2 + 2\epsilon^J\epsilon^V\cos(\varphi)H^J_{21}H^V_{21}\right). \tag{3.37}$$

Comparing Eqs. (3.36) and (3.30), one sees that the major modification in the case of degenerate perturbation theory is the appearance of the Δ-term. This term turns the naked pole into a Lorentzian-like function. In Fig. 3.7(b) exact numerical doublon velocities are shown together with plots of Eq. (3.36) for different values of ϵ.

Furthermore, in order to investigate the height of the velocity peak one sets $\Omega = \delta$. For the special case that $\epsilon^J = \epsilon^V = \epsilon$ one observes that $\langle v_{d/h}\rangle^{\text{asy}} \approx \mathcal{O}(\epsilon^2)/\mathcal{O}(\epsilon) = \mathcal{O}(\epsilon)$. Hence, the height of the main resonance is directly proportional to ϵ. Generally, the height of the n^{th} resonance is given by $\mathcal{O}(\epsilon^n)$. This dependence can be witnessed from the inset of Fig. 3.7(b). Having said this, peaks for $n \geq 3$ already seem to experience a strong cross talk with tails of more prominent peaks with $n = 1, 2$. As before, the analysis of the hole velocity is completely analogous.

3.2.4. Effective vector potentials in the large frequency limit

In the regime where the driving frequency is large compared to all other energies in the system one can understand the dynamics as emerging from an effective Hamiltonian that is derived from a truncated Magnus expansion (see Sec. 2.2.3). One can then interpret the behaviour of the velocity of doublons and holes calculated in Sec. 3.2.2 as a consequence of

an effective vector potential $\mathcal{A}$ appearing in this effective Hamiltonian. Using Eqs. (2.61) and (2.62) the effective Hamiltonian can be determined to be

$$H^{\text{eff}} = H_0 + \frac{1}{\Omega}\left[H_{-1}, H_1\right]. \tag{3.38}$$

Such a first order Magnus expansion for monochromatically driven quantum systems is commonly used for Floquet setups, see, e.g., Refs. [23,124]. The analytic form of the effective Hamiltonian (3.38) can now be straightforwardly determined by using the simplified expressions for doublons (3.4) and holes (3.5), respectively. Knowing that the calculation is fully analogous for both species, we will continue by focussing on doublons only.

After inserting the Fourier components (3.8) and (3.9) into the expression (3.38), a few steps of appropriate simplification allow to write H_d^{eff} in the following compact form

$$H_{d,k}^{\text{eff}} = \begin{pmatrix} V_s & C(k) \\ C^*(k) & -V_s \end{pmatrix}, \tag{3.39}$$

with C approximately given by

$$C(k) \approx -2\Big(J_{s,o}\, e^{-i\alpha_d} + J_{s,e}\, e^{-i\beta_d}\, e^{-2ik}\Big), \tag{3.40}$$

and where

$$\alpha_d = \frac{1}{\Omega}\sin(\varphi)(V_o - V_e)\Big(1 + \frac{J_o}{2J_{s,o}}\Big) \quad \text{and} \quad \beta_d = \frac{1}{\Omega}\sin(\varphi)(V_o - V_e)\Big(1 + \frac{J_e}{2J_{s,e}}\Big). \tag{3.41}$$

Owing to its simple structure $H_{d,k}^{\text{eff}}$ can readily be diagonalised. One can then easily verify that the eigenenergies of the effective Hamiltonian (3.39), $\varepsilon_{d,\nu}^{\text{eff}}$, are given as

$$\varepsilon_{d,\nu}^{\text{eff}}(k) = \varepsilon_{d,\nu}^{0}(k - \mathcal{A}_d), \tag{3.42}$$

where $\varepsilon_{d,\nu}^{0}(k)$ denote the energy bands of the doublon Hamiltonian *without* the drive, and

$$\mathcal{A}_d = \alpha_d - \beta_d = \frac{1}{2\Omega}\sin(\varphi)(V_o - V_e)\left(\frac{J_o}{J_{s,o}} - \frac{J_e}{J_{s,e}}\right) \tag{3.43}$$

being indeed an *effective vector potential* coupling to the momentum k. Similarly, a corresponding expression for holes can be derived using the modified parameters $V \to -V$ and $2J \to J$,

$$\mathcal{A}_h = -\frac{1}{2\Omega}\sin(\varphi)(V_o - V_e)\left(\frac{J_o}{J_{s,o}} - \frac{J_e}{J_{s,e}}\right) = -\mathcal{A}_d. \tag{3.44}$$

Thus, the effective vector potential for holes is equal, but opposite to that for doublons. Note that this property is related to the reversed sign of the potential for both species. The different hopping strengths enter only via the calculation of the respective bands $\varepsilon_{d/h,\nu}^{0}$. Also, the vector potential $\mathcal{A}_{d/h}$ becomes zero (maximal) for $\varphi = 0, \pi$ ($\varphi = -\pi/2, \pi/2$), and decays as $1/\Omega$. This is consistent with the previously discussed dependences of the dynamics of doublons and holes in Secs. (3.2.2) and (3.2.3).

The resulting asymptotic velocity associated with quasienergy band ν for both doublons and holes is then (approximately) given by (see Eq. (3.21))

$$\langle v_{d/h,\nu}(k)\rangle^{\text{asy}} \approx \frac{\partial}{\partial k}\varepsilon_{d/h,\nu}^{\text{eff}}(k) = \frac{\partial}{\partial k}\varepsilon_{d/h,\nu}^{0}(k - \mathcal{A}_{d,h}). \tag{3.45}$$

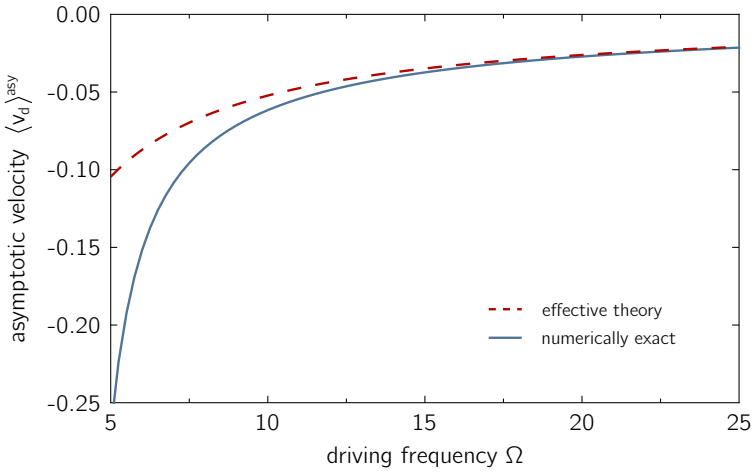

Figure 3.8.: Comparison of doublon velocities of exact numerical data (blue solid) and plots of Eq. 3.45 (red dashed) as a function of the driving frequency. For very large frequencies $\Omega \gg J_o, J_e, V_o, V_e$ the effective description reproduces the exact results. Parameters of the ratchet are as presented in Tab. 3.1.

Hence, a finite velocity at $k = 0$ is indeed realised by a shift of the momentum due to the vector potential. In Fig. 3.8, the velocity (3.45) is compared to exact numerical data for $k = 0$. It is clearly visible how Eq. (3.45), and hence Eqs. (3.38) and (3.42), becomes valid in the large frequency regime. The interpretation of phenomena in terms of such vector potentials has become very popular over recent years (for Floquet systems and beyond), where they have been intensively studied both experimentally [20, 50, 99, 102–106, 109, 179–181] and theoretically [17, 123, 182, 183] (see also Sec. 2.3).

3.3. Ratchet effects in the presence of an external force

In the previous section the ratchet effect for doublons and holes was investigated assuming that the underlying lattice potential is homogeneous. However, in most cold atom setups an external parabolic potential holds the atomic cloud together. We, thus, want to address the following question: can a ratchet perform work and move the particles 'up the hill'? To this end, we consider the effect of a constant force, $g \neq 0$ in Eq. (3.3). Note that such a force resembles the situation of electrons experiencing a static electric field. The previous analysis from Sec. (3.2) cannot be carried over to this problem straightforwardly, since the presence of the linear potential breaks the translational invariance of the original Hamiltonian.

The system is now rather characterised by the fact that the particles gain or lose energy, respectively, when hopping from one lattice site to the next. In ordinary, time-independent systems energy conservation holds. As the kinetic energy is bounded, the system cannot absorb (deposit) the potential energy it would gain (lose) in the presence of a finite net velocity. As a consequence particles perform Bloch oscillations when they experience weak external forces and obey the rules of a Wannier-Stark ladder for strong forces. Exceptions to this can be found in interacting systems, where the energy might be provided or absorbed via complex many-body processes, see, e.g., [184]. Nonetheless, the situation is completely changed for *time-dependent* systems, since energy is not conserved any more. In Floquet systems energy is provided by the external drive in multiples of Ω. Thus, the energy $n_0 g$ that is needed to move a particle uphill by n_0 lattice sites is only avail-

able in a quantised form of $m_0\Omega$ with m_0 being an integer. This argumentation yields a commensurability condition

$$n_0\, g = m_0\, \Omega\,, \tag{3.46}$$

with integer $m_0 \in \mathbb{Z}$ and even n_0, $\frac{n_0}{2} \in \mathbb{Z}$ (due to the dimerized structure of the present Hamiltonian). In the following we will argue that this relation implies that in the limit $t \to \infty$ a net motion uphill (or downhill) is only possible when the commensurability condition is indeed fulfilled. We will also show how this condition becomes more and more prominent as time evolves.

3.3.1. Dynamics in the long-time limit

We will first investigate the asymptotic dynamics of a system where the commensurability condition (3.46) is met. The reason being that in this case the problem simplifies technically in a substantial way. Here, shifting the particle by n_0 lattice sites to the left costs an energy $n_0 g$ which is exactly met by a multiple of Ω. This leads to a new 'translation invariance' in Floquet space with respect to both position *and* Floquet indices: when moving n_0 lattice sites in real space and simultaneously m_0 sectors in Floquet space, one recovers the same Hamiltonian. A more pictorial view of this is taken in Fig. 3.9, where the vector marks the translational invariance in the extended space. Consequently, the extended space eigenstates of the Floquet Hamiltonian, see Eq. (2.21), can be chosen as

$$\langle\!\langle i, m|\phi_{\nu,k}\rangle\!\rangle = e^{ikr_i}\, \langle\!\langle i, m|u_{\nu,k}\rangle\!\rangle\ , \tag{3.47}$$

with

$$\langle\!\langle i, m|u_{\nu,k}\rangle\!\rangle = \langle\!\langle i + n_0, m - m_0|u_{\nu,k}\rangle\!\rangle\ , \tag{3.48}$$

where i is the real-space index and m represents the Floquet sector. Note that a negative shift of the Floquet index is necessary due to the definition of the Fourier transformation in Eq. (2.34) (see also Fig. 2.2). Moreover, k indicates the effective momentum projected on the space coordinate for convenience, leading to $-\pi/n_0 \leq k < \pi/n_0$. One obtains now n_{0r} unique (Floquet) bands in the first Floquet zone $-\Omega/2 \leq \varepsilon_\nu < \Omega/2$ for every value of k. Here, n_{0r} is the reduced denominator of m_0/n_0.

Within this picture of an extended unit cell, the previously discussed methods to solve the problem carries over in a straightforward fashion (see Sec. 3.2). However, due to the size of this new unit cell the procedure might be quite demanding in practice. The natural first attempt to truncate the Floquet matrix is as follows: one takes the $n_0 \times n_0$ - dimensional blocks for each entry of the Floquet matrix, and fixes a certain interval of Floquet indices ranging from $-N_f$ to N_f. It is crucial that $2N_f > m_0 + 2n_f$, where n_f guarantees that the eigenstates of the first Floquet zone do not experience any finite size effects. The number of states that one includes in this procedure is given by $(2N_f+1)n_0 \gtrsim n_0 m_0$. While there is nothing false about this truncation scheme, it might indeed be highly inefficient depending on the values of n_0 and m_0. Looking at Fig. 3.9 one can find a much more effective truncation scheme: because the physics of the problem is mainly dominated by the commensurability condition (3.46), it is often enough to consider only Floquet blocks close to the line connecting $(0, 0)$ and $(n_0, -m_0)$. This leads to a total number of states of only $\sim (2n_f + 1)n_0$. Hence, the necessity of calculating a large number of redundant states can be avoided by a suitable truncation of the Floquet matrix. Once this truncated Floquet matrix is found, it again allows for the calculation of numerically exact quasienergies and Floquet eigenstates. As before, those can then be used to determine the asymptotic velocities of doublons and holes for the ratchet system with an additional external force.

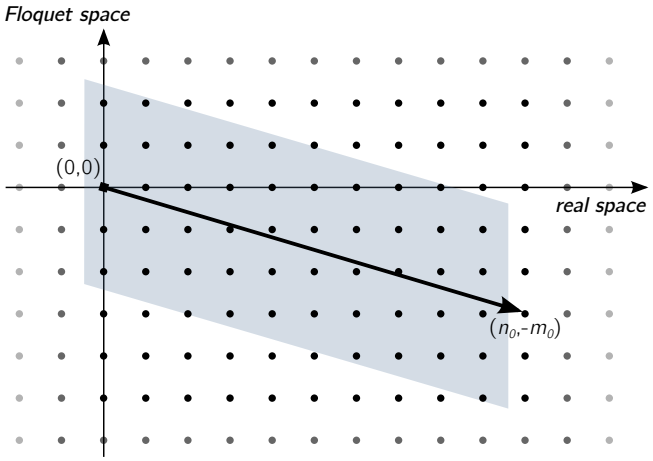

Figure 3.9.: Illustration of states in a mixed real-space/Floquet-space representation. The vector from $(0,0)$ to $(n_0,-m_0)$ fulfils the commensurability condition (3.46). The negative 'direction' with respect to the Floquet space is due to the definition of the Fourier transformation (2.34). The practical truncation of the Floquet matrix is done around this vector and only states lying in the blue shaded region are used in calculations. In most cases it is sufficient to take only a few Floquet states per real-space index into account (see Sec. 2.2.2).

Above, we have described the algorithm in a mixed real-space/Floquet-space picture. A fully equivalent formulation can also be obtained by a simple Gauge transformation which encodes the constant force (which can be viewed as an electric field) in a time-dependent vector potential. In this case, one makes the following replacements in the respective Hamiltonian (3.4) or (3.5): $d_{i+1}^\dagger d_i \rightarrow d_{i+1}^\dagger d_i e^{igt}$ and $h_{i+1}^\dagger h_i \rightarrow h_{i+1}^\dagger h_i e^{-igt}$. This leads to a Hamiltonian which is again translationally invariant in real space, but now characterized by *two* frequencies. Therefore, one can obtain a representation of the problem in terms of two independent Floquet indices (one for each frequency) instead of a single one. Nonetheless, under the condition (3.46) the two frequencies Ω and g are commensurate, allowing again for a simplified treatment equivalent to the one described above. In fact, this double frequency structure resembles a two-dimensional lattice struture in frequency space, which can be used, e.g., to investigate novel topological states [81].

We consider a quantum ratchet with the same parameters as before (see Tab. 3.1) plus an additional external potential g. Of course, this potential will be equal, but opposite for doublons and holes, respectively. We also set $\varphi = -\pi$ and $t_0 = 0$. Similar to the studies in Sec. 3.2, we are interested in the dynamics of an initial single particle excitation with zero momentum, $k = 0$. We also want to address the question again of how the dynamics are affected by 'how' the ratchet is switched on. In Sec. 3.3.2 below, we combine the cases of a non-adiabatic switching with incommensurate external forces, and investigate the dynamics in such situations. Here, however, we focus on situations where the ratchet is switched on adiabatically and where the commensurability condition (3.46) is fulfilled. First, we are interested in how the asymptotic velocity behaves as a function of frequency Ω *and* as a function of the external force g. Asymptotic velocities of doublons and holes, $\langle v_{d/h} \rangle^{\text{asy}}$, are calculated by means of Eq. (3.20) (or alternatively Eq. (3.21)). The results are shown in Figs. 3.10(a) and 3.10(b) for doublons and holes, respectively. Negative velocities describe left-moving (red) and positive velocities right-moving (blue) excitations. Within the conventions used a positive g yields a force pointing to the right. The results are given as continuous functions of Ω and g for fixed ratios m_0/n_0. The set of ratios m_0/n_0 for which results are represented is, however, limited: we combine for our plots

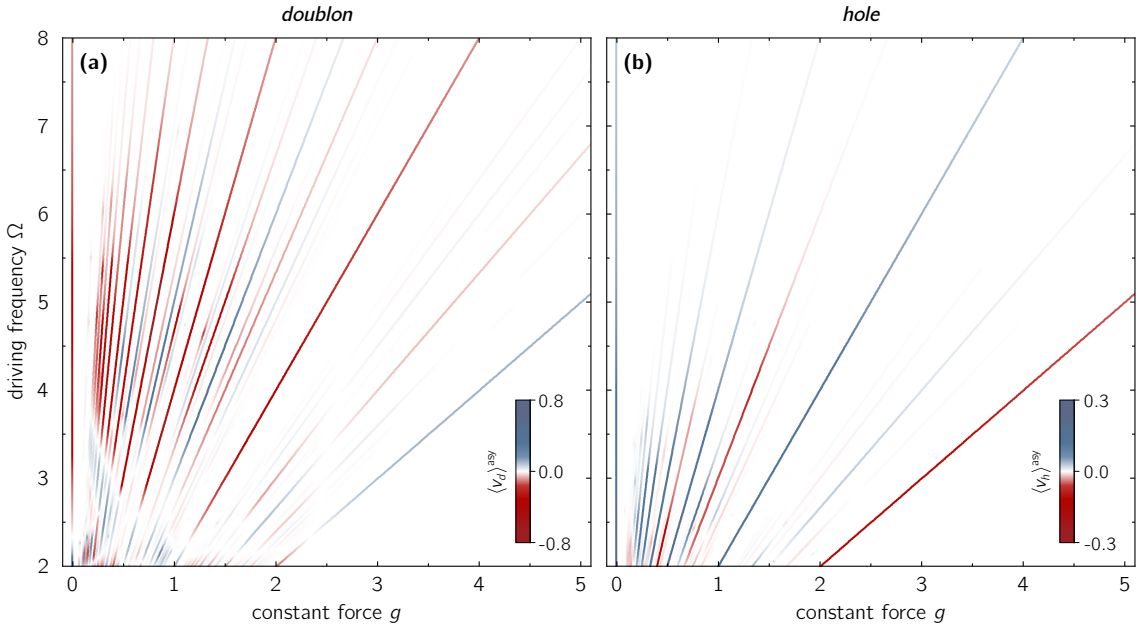

Figure 3.10.: Asymptotic (a) doublon and (b) hole velocity as function of driving frequency Ω and external force g for an adiabatically switched on ratchet. All velocities are measured in units of $a_{\mathrm{lat}}(J_{s,o}+J_{s,e})$ and system parameters are as presented in Tab. 3.1. Combined results are shown for real-space unit cell sizes $n_0 = 14, 16, 18$ and 60 and arbitrary values of m_0 (see text).

data for $n_0 = 60$ with data for $n_0 = 14, 16$ and 18 with arbitrary values of m_0 and Ω (and therefore also g). This allows to cover all fractions with $n_{0r}/2 = 1, 2, ..., 10$.

The reason for this choice of ratios being that, in general, the motion of the particles is most pronounced when $g/\Omega = m_0/n_0$ can be written as a fraction with small integers m_0 and n_0. To explain this observation, we first recall that for static band Hamiltonians a static external force does not lead to a finite net velocity of the particles; only Bloch oscillations can occur. As outlined above, this can be understood from energy conservation. In the presence of oscillating terms in the Hamiltonian, the energy is still conserved modulo Ω. This implies that an energy conserving transport process is possible if the energy gain gn_0 obtained by hopping n_0 steps to the right, is an integer multiple of Ω as described by Eq. (3.46). For large values of either m_0 or n_0, this process is, however, exponentially suppressed as the particle has to tunnel through long distances in either real- or Floquet space until the resonance condition is met. This further implies that for $t \to \infty$ a finite average velocity is only possible if g and Ω are commensurate, while it is expected to vanish for all incommensurate ratios (i.e., it is finite only on a set of measure zero).

By considering only those values of Ω and g where one can indeed observe transport, one recovers similar conclusions already drawn for the ratchet without external potential: depending on both frequency and 'electric field', the particles can move either 'up' or 'down'. Moreover, by comparing velocities, one realizes that by choosing convenient values for g and Ω, doublons and holes can be forced to move in the same or in opposite directions. Alternatively, one can tune parameters such that only one species is moving. So, indeed, the quantum ratchet seems to work for long times even when an external force is present.

3.3.2. Finite-time velocities and effective Bloch oscillations

The situation is, however, different when finite times t are considered. Here, velocities might still be detectable even though the commensurability condition (3.46) is not (well)

fulfilled. In order to study such systems where arbitrary values of g are chosen we need to compute the average velocity for finite systems. However, there is an immediate practical question arising: how can the above demonstrated Floquet space algorithm be used for arbitrary (and even non-commensurate) values of g? To circumvent this seemingly troublesome issue a modified potential is introduced

$$V(g,n) = -gn - \sum_{i\in\mathbb{Z}} \Theta(n - in_0)\left(\frac{m(g)\Omega}{n_0} - g\right)n_0\,, \tag{3.49}$$

where the Θ-function is defined by $\Theta(x) = 1$ for $x \geq 0$ and $\Theta(x) = 0$ for $x < 0$. Within the unit cell of real-space size n_0 this potential describes the true potential gn. However, by enforcing translational invariance in Floquet space the potential is simultaneously enforced to jump at the boundaries of the unit cell, $n = in_0$ with $i \in \mathbb{Z}$. Thus, the commensurate property becomes $V(g, n + n_0) = V(g, n) - m(g)\Omega$ and the size of the jump is given by $\Delta V = m(g)\Omega - n_0 g\,(< \Omega/2)$. Here, $m(g)$ is an integer which is chosen to be the best approximation to gn_0/Ω, i.e., $m(g) = \lfloor gn_0/\Omega \rceil$. The size of n_0 is set at convenience, but it is clear that the larger n_0 becomes, the smaller the potential jump ΔV is. For all studies in this section we set $n_0 = 120$.

So as soon as g cannot be written in the form $g = \frac{m_0}{n_0}\Omega$ there emerge finite size errors. Due to these jumps one cannot use the model of Eq. (3.49) together with the previously discussed Floquet space algorithm (see Sec. 3.3.1) to calculate the long-time asymptotic behaviour of the system. However, the model *is* valid for short times if one determines the velocity of the bosons only in the center of the unit cell, i.e., far away from the boundaries. This is true because it was shown by Lieb and Robinson [185] that (up to exponential precision) information propagates maximally at a fixed velocity v_{LR} through the system. This Lieb-Robinson velocity v_{LR} is on the order of twice the hopping rate, and guarantees that for short times, $t < n_0/(2v_{\mathrm{LR}})$, the result is not affected by the jumps at the edge of the unit cell.

As an initial state we consider a doublon at zero momentum $k = 0$ with wave function $|\psi(0)\rangle = 1/\sqrt{N}\sum_{i=1}^{N}|i\rangle$ in real space. At time $t_0 = 0$ the ratchet is suddenly switched on. In order to calculate $|\psi(t)\rangle$ we follow the Floquet protocol as above: first, $|\psi(0)\rangle$ is projected onto the Floquet eigenstates, $\langle\phi_\nu(0)|\psi(0)\rangle$. Second, $|\psi(t)\rangle$ is evaluated using the Floquet theorem. At every point in time the expectation value of the velocity operator (see Eq. (3.17)) can then be determined. However, to avoid finite size effects we evaluate the expectation value of the single-site velocity operator $\langle\psi(t)|v_{d,i}(t)|\psi(t)\rangle$, with $v_d(t) = \sum_i v_{d,i}(t)$, only in the middle of the unit cell, $i_m = n_0/2$. The average velocity for the interval $[0,t]$ at that lattice site is then calculated by $\langle v_{d,i_m}(t)\rangle^{\mathrm{av}} = \frac{1}{t}\int_0^t \langle v_{d,i_m}(t)\rangle$. Because the initial state of the doublon is chosen to be homogeneous in space, the total average velocity is simply given by

$$\langle v_d(t)\rangle^{\mathrm{av}} = \frac{N}{t}\int_0^t dt'\ \langle\psi(t')|v_{d,i}(t')|\psi(t')\rangle\,\Big|_{i=i_m} \tag{3.50}$$

For the chosen normalization $\langle v_d(t)\rangle^{\mathrm{av}}$ directly gives the average velocity of the doublons in the interval $[0,t]$.

The average velocity as a function of g is shown in Fig. 3.11 for a fixed frequency Ω. The plot shows how for increasing time t the average velocity (solid line) approaches the $t \to \infty$ limit (dots). The curves are characterized by oscillations with a width that shrinks with $1/t$. With shrinking width, only those external forces give a sizeable contribution which fulfil the commensurability condition (3.46) with a precision determined by $1/t$, $n_0 g = m_0(\Omega + \mathcal{O}(1/t))$. Close to each point where the commensurability condition is

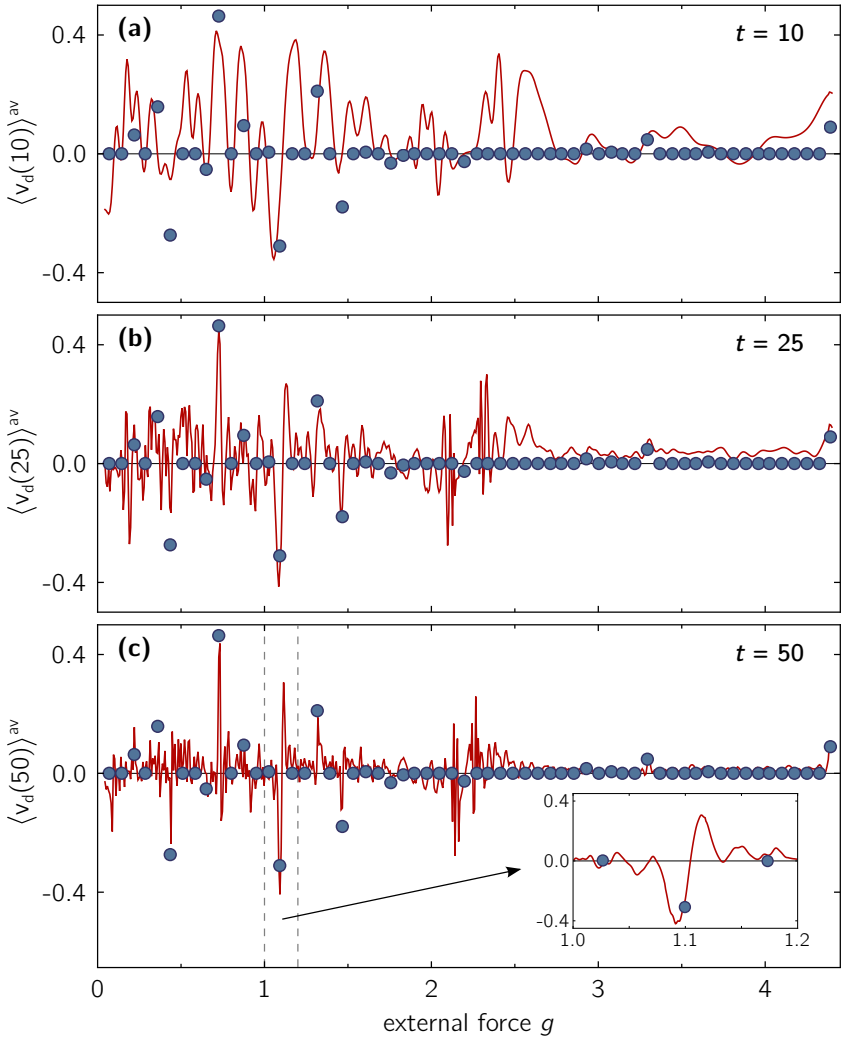

Figure 3.11.: Average doublon velocity (solid lines) at times $t = 10, 25$ and 50 after a sudden switching on of the ratchet potential as function of the external force g. The driving frequency is fixed to $\Omega = 4.4$ and the real-space unit cell size is set to $n_0 = 120$ (see text). Ratchet parameters are as in Tab. 3.1 and velocities are measured in units of $a_{\mathrm{lat}}(J_{s,o} + J_{s,e})$. The discrete points at $g_c = \frac{m_0}{60}\Omega$ show the average velocity in the limit $t \to \infty$. The inset in (c) reveals the characteristic pattern of minima and maxima caused by effective Bloch oscillations (see text) near the $\frac{m_{0r}}{n_{0r}} = \frac{1}{4}$ resonance.

fulfilled, there is a characteristic pattern of oscillations (see inset of Fig. 3.11(c)). These oscillations can be interpreted as *Bloch oscillations* of an effective Floquet band structure and an effective electric field: at a point of commensurability, $g = g_c = \frac{m_0}{n_0}\Omega = \frac{m_{0r}}{n_{0r}}\Omega$, with $\frac{m_{0r}}{n_{0r}}$ being the reduced fraction, one obtains a number of n_{0r} Floquet bands in the enlarged unit cell[3]. These bands incorporate the effect of the constant force g and of the oscillating Hamiltonian. Hence, if the external force g is tuned away from g_c, the difference $g - g_c$ can be interpreted as a small effective electric field acting on these Floquet bands. This small electric field then induces Bloch oscillations. The period of such oscillations can be computed semiclassically using $F = \partial_t p = g - g_c$ as an expression for the effective force and

[3] See, e.g., Refs. [101, 186] for a similar discussion about effective Floquet bands in the presence of a constant external force.

$T\partial_t p = \frac{2\pi}{n_{0r}}$. The last equality describes the fact that the system traces out an entire circle in the Brilouin zone over a single period T. The period of these effective Bloch oscillations is therefore given by

$$T = \frac{2\pi}{n_{0r}|g - g_c|} \,. \tag{3.51}$$

Hence, one observes peaks for $\langle v(t)\rangle^{\mathrm{av}}$ as a function of g not only close to the commensurability points g_c, but there is an emerging series of minima and maxima separated by $\Delta g \approx \frac{\pi}{n_{0r}t}$ as can be seen in the inset of Fig. 3.11(c). Note that while the calculation was done for doublons only, the results carry over to the species of holes in an analogous fashion (cf. Sec. 3.3.1). Since they do not show any qualitative difference we refrain from showing explicit results here.

3.4. Prospects of a topological quantum ratchet

While the main goal of this chapter is to investigate ratchet effects for dilute doublon and hole gases as done in the previous sections, we briefly want to review the consequences of our discussion for insulating states, i.e., Mott insulators or fermionic band insulators. In these cases one has to investigate the current (or particle velocity) when all states of a given band are occupied. Of course, the dynamical response is typically absent for these insulating materials. However, in some cases the dynamics of the system is not only composed of the sum of individual contributions, but might also be characterised by global properties. Materials that exhibit these kind of properties are said to have *topological order*. Recently, the concept and understanding of topology has become very fertile in the context of condensed matter systems. The first crucial steps along these lines was the discovery of the integer quantum Hall effect [187] and its explanation in terms of a topological invariant by Thouless and collaborators [188]. Meanwhile, there have appeared many more topological materials such as topological versions of insulators [189, 190], superconductors [190] and metals [191]. Also certain types of quasiparticles and magnetic textures have attracted a lot of scientific attention, because they exhibit a strong robustness due to their topological nature. A particularly interesting example in this context are magnetic skyrmions [192,193]. The ultimate proof of how much the notion of topology has shaped the field of condensed matter physics (and beyond) was brought in 2016 when three pioneers of this field, David Thouless, Duncan Haldane and Michael Kosterlitz, were jointly awarded the Nobel prize.

While the reader is referred to comprehensive review material in order to study the general aspects of topological matter (see, e.g., Refs. [189, 190, 194, 195]), we shall be interested in consequences of topological aspects for the dynamics of the presented ratchet setup. The main goal is to connect the notion of topology for static band Hamiltonians to the properties of Floquet systems. Here, we will strongly follow the ideas by Kitagawa *et al.* [116] and Qi *et al.* [196]. In doing so we want to address the question whether a topological pump is also achievable at large driving frequencies Ω. In other words, we want to investigate if it is possible to merge the characteristics of a quantum ratchet, as seen in Secs. 3.2 and 3.3, with potential topological properties.

3.4.1. Examples for topological transport in periodically driven systems

Thouless pump

In 1982, Thouless, Kohmoto, Nightingale and den Nijs succeeded in explaining the strange quantised behaviour of the conductivity for the integer quantum Hall effect [188]. They

considered a 2D insulating electronic (fermionic) system that has a rectangular shape and is translational invariant. Furthermore, the system is non-interacting allowing for a many-particle description by 'filling up' the single particle spectrum with associated energy eigenstates $|u_{n\mathbf{k}}\rangle$, where n is the band index and $\mathbf{k}$ describes the momentum. Having an insulator means that the Fermi energy ε_F lies in between a band gap of the system guaranteeing that bands below (above) ε_F are completely filled (empty). Applying an electric field $\mathbf{E}$ to this system creates a current density $\mathbf{j}$. Here, the Hall conductivity, $\sigma_{xy} = \partial J_x/\partial E_y$, quantifies the response of the current in x direction due to an electric field in the direction of y (see Ch. 7 for more details). Using the Kubo formula one can show [96, 197] that the Hall conductivity is eventually given by

$$\sigma_{xy} = -\frac{ie^2}{\hbar}\sum_n \int_{\mathrm{B}Z} \frac{d^2k}{(2\pi)^2}\left(\left\langle \frac{\partial u_{n\mathbf{k}}}{\partial k_x}\middle|\frac{\partial u_{n\mathbf{k}}}{\partial k_y}\right\rangle - \left\langle \frac{\partial u_{n\mathbf{k}}}{\partial k_y}\middle|\frac{\partial u_{n\mathbf{k}}}{\partial k_x}\right\rangle\right) = -\frac{e^2}{2\pi\hbar}\,C\,, \tag{3.52}$$

with e being the charge of an electron, $\hbar$ is the reduced Planck constant and $C = \sum_n C_n$ describes the sum over all *first Chern numbers* of occupied bands of the system. Note that while the first part of Eq. (3.52) does not immediately reveal the quantised nature of the conductivity, identifying its expression in terms of Chern numbers indeed does.

These Chern numbers ought to be integer values, $C_n \in \mathbb{Z}$, because they represent topological equivalence classes: they generally classify band Hamiltonians that can be deformed into each other without closing a gap [189]. They are, hence, *topological invariants* and can only be of integer form. Chern numbers are mathematical objects that are connected to the notion of fibre bundles [198]. However, they can alternatively be expressed in terms of an integration over the *Berry curvature*

$$C_n = \frac{1}{2\pi}\int_{\mathrm{B}Z} d^2k\;\Omega_{n,ij}\,, \tag{3.53}$$

where the Berry curvature is defined as

$$\Omega_{n,ij} = \frac{\partial \mathcal{A}_{n,j}}{\partial k_i} - \frac{\partial \mathcal{A}_{n,i}}{\partial k_j} \qquad \text{and} \qquad \mathcal{A}_{n,j} = i\,\langle u_{n\mathbf{k}}|\frac{\partial}{\partial k_j}|u_{n\mathbf{k}}\rangle \tag{3.54}$$

is the $U(1)$ Berry connection (cf. Eq. (2.71)). It is easily shown that with these expressions Eq. (3.52) is fulfilled. This expression of the Chern number in terms of an integration of the Berry curvature over the two-dimensional momentum torus is also known as the TKKN invariant in the literature. A more elaborate discussion of the quantised nature of Chern numbers and its deep connection to Berry curvatures can be found in, e.g., Refs. [96, 195, 199]. Chern numbers and other topological quantities have become of great importance lately, since they are the key to understanding topological insulators. We will present more on this matter in Chs. 6 and 8.

After having briefly discussed the importance of topological aspects and its consequence for the quantum Hall system, one might rightfully wonder where the connection to dynamical systems, such as Floquet systems is. Here, it is crucial to realise again that the concept of Chern numbers is not only preserved for two-dimensional Brillouin zones, but rather holds for *any* parameter space that forms a torus $\mathbf{T}^2$. The model that we want to study now is a 1D insulating lattice system which is driven periodically in time. We require that the drive is performed adiabatically such that energy bands are ensured to remain gapped throughout the driving cycle. Note that we are *not yet* introducing the notion of 'Floquet'. The system is then indeed described by a toric 2D parameter space spanned by momentum $k \in [-\pi/a, \pi/a)$ and time $t \in [0, T)$. In 1983, Thouless showed [172] that

the particle transfer of such a system without any additional forces is indeed given by the total Chern number

$$C = \frac{1}{2\pi} \sum_n \int_0^T \int_{\mathrm{BZ}} dk\ \Omega_{n,tk}\,. \tag{3.55}$$

Therefore, for $C \neq 0$ one expects to have a quantised movement of particles per driving period in the system. Due to its close analogy to the quantisation of the Hall conductivity above one can in some sense view this *Thouless pump* as a dynamical version of the integer quantum Hall effect. Note that while the above model seems very simplified, one can in principle extend the result of having a quantised pump also to the presence of (weak) disorder or interactions [200]. We stress again that a quantised and robust particle pump requires insulating states, such as fermionic band insulators or bosonic Mott insulators. Both scenarios have been demonstrated only recently in experiments with ultracold atoms [18, 19].

Quantum conveyor belts

While the Thouless pump relates a rigorous mathematical object to the occurrence of quantised transport, the picture misses out on yielding a simple physical intuition. We therefore present a different example of a quantised particle pump: the quantum *conveyor belt*. Here, one first engineers the desired transport behaviour of the system and then tries to find some underlying mathematical explanation. Note that while at first this quantum conveyor belt might seem like a purely academic problem, actual experimental realisations have been achieved by using cold atoms in optical lattices [170, 171].

We consider again a one-dimensional non-interacting lattice system. Quantum particles are positioned at lattice sites i in corresponding states $|i\rangle$ and have an $SU(2)$ spin attached to them. Assume that the lattice is very deep, i.e., that to lowest order no hopping between different sites take place, and that the lattice is spin-dependent. We require now that the potential for the spin-down part remains static, while the spin-up lattice drifts to the right. This drift has to be slow enough such that no particles are excited into higher bands of the system. After a certain time T the spin-up part of the potential will coincide with the spin-down part again. The resulting evolution operator reads as

$$U(T,0) = \sum_i |i+1,\uparrow\rangle\langle i,\uparrow| + |i,\downarrow\rangle\langle i,\downarrow| \equiv U^F(0)\,, \tag{3.56}$$

where we set the lattice constant to unity, $a_{lat} = 1$. Indeed, by assuming that the movement of the spin-up lattice is continuous we can identify this evolution operator with the Floquet operator $U^F = \exp(-iH^{\mathrm{eff}}T)$ (see Sec. 2.2.1). Clearly, the dynamics predicted by such an evolution is that particles with spin-up are pumped exactly one lattice site per driving period to the right. This is very similar to the Thouless pump above. Going to the momentum basis the system is described as

$$U_k^F = e^{-ik}\ |\uparrow\rangle\langle\uparrow| + |\downarrow\rangle\langle\downarrow| \qquad \text{and} \qquad H_k^{\mathrm{eff}} = \begin{pmatrix} k/T & 0 \\ 0 & 0 \end{pmatrix}. \tag{3.57}$$

The dynamics of the particles in this peculiar system are therefore described by the quasienergy bands of the effective Hamiltonian (3.57), which are shown in Fig. 3.12(a) below. The average velocity of a fully occupied Floquet band ν is given by (cf. Eq. (3.21))

$$\langle v\rangle^{\mathrm{av}} = \int \frac{dk}{2\pi}\ \frac{\partial\varepsilon_\nu(k)}{\partial k} = \frac{n_\nu \Omega}{2\pi} = \frac{n_\nu}{T}\,, \tag{3.58}$$

with $n_\nu \in \mathbb{Z}$. Hence, one might argue that the quantisation of the pump is linked to the winding of a quasienergy band around the Floquet zone.

After having introduced the concept and idea of topological pumps, we will look into a deeper mathematical grounding of these effects in a Floquet setting. Moreover, we will address the fundamental question whether such topological pumping processes are also applicable to large frequencies as seen for the quantum ratchet transport, see Sec. 3.2.

3.4.2. Topological invariants and dimensional reduction

In order to establish a connection between the dynamical properties of a quantised particle pump and its Floquet description we present a topological classification in terms of *homotopy* groups following closely Ref. [116]. A small general introduction to the theory of homotopies can also be found in Sec. 8.1.1.

While the discussion can in principle be extended to higher dimensions, we restrict ourselves again to a spatially one-dimensional problem that is translationally invariant (lattice constant being set to unity, $a_{\mathrm{lat}} = 1$). Here, the set of Floquet operators $\{U^F\}$ defines a map from the first Brillouin zone to the space of $m \times m$-dimensional unitary matrices, with m describing the number of bands of the system. Note that for a full description the number of bands are nominally infinite. However, in many circumstances - as it is also the case for the Bose-Hubbard model in Eq. (3.1) - the system can be projected onto some low-energy subspace. As a consequence, m becomes finite and the physics is described by an associated effective low-energy Hamiltonian.

The periodic nature of the Brillouin zone causes the map to the space of unitary matrices to trace out a loop. A topological classification can now be conducted by equating all such loops that can be smoothly deformed into each other. Each of these homotopy classes are represented by an integer-valued topological invariant $w \in \mathbb{Z}$. For the system at hand this 'winding number' is defined as [116]

$$w = \frac{i}{2\pi} \int_{\mathrm{BZ}} dk \ \mathrm{Tr}\Big[\big(U_k^F\big)^\dagger \partial_k U_k^F \Big] , \tag{3.59}$$

where the trace is taken over the m-dimensional (sub)space. Clearly, due to the cyclic nature of the trace the winding number does not alter under a similarity transformation of U^F. We can therefore gain a good intuitive picture of w by expressing the Floquet operator in terms of Floquet eigenstates. The expression reads as

$$w = \frac{T}{2\pi} \sum_\nu \int_{\mathrm{BZ}} dk \ \frac{\partial \varepsilon_\nu(k)}{\partial k} = n_\nu \, , \tag{3.60}$$

with T being the driving period. This picture of w is particularly useful as it allows the non-trivial topology to be identified through simple inspection of the quasienergy spectrum: the topological invariant is indeed nothing but the sum over all windings of individual Floquet bands[4]. We want to stress again that this is a unique property of Floquet systems. Due to the fact that the spectrum must not only be periodic in k but also in the quasienergy, one can have bands that leave the Floquet-Brillouin zone to one energy side and emerges simultaneously at the other, see Fig. 3.12. This leads to a winding of the respective band around this torus in a very literal sense. Therefore, for any local, static (non-driven) system the winding number is trivial ($w = 0$). Again, if there is a net winding of a single Floquet band, its average velocity must be quantised, and

[4]Note that when there are degeneracies in the spectrum one should choose the definitions of $\varepsilon_\nu(k)$ such that they become smooth functions of k [116].

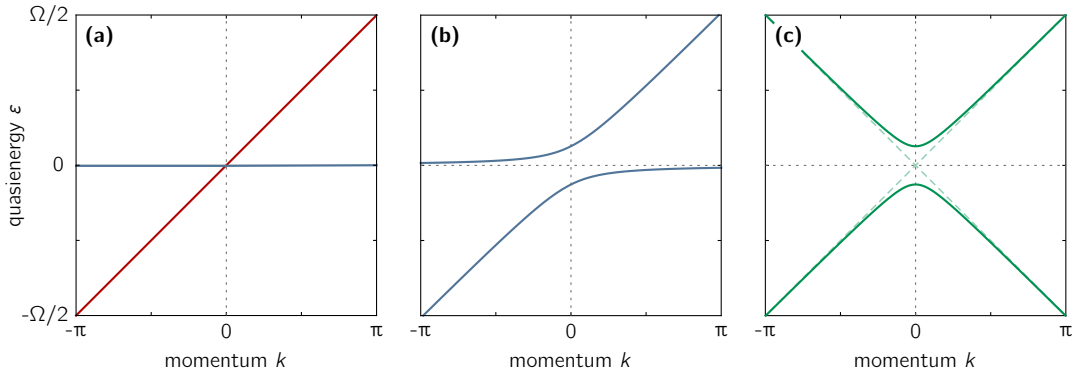

Figure 3.12.: Examples for Floquet bands that wind in quasienergy space. (a) Floquet band representation of the single spin conveyor belt, see Eq. (3.57). (b) Perturbations open a gap at $(0, 0)$, but leave the net winding unchanged. (c) Demonstration of how single band winding is not protected under perturbations. The energy gap defines an adiabaticity condition for, e.g., (approximate) quantised particle pumping in these cases.

it follows what was predicted by Thouless [172]: the displacement of particles over one driving period is exactly w unit cells, which yields a quantised charge current for charged (fermionic) particles.

Being equal to a topological invariant, the net winding of Floquet bands is topologically protected, meaning that it is insensitive to (weak) perturbations. This is best visualised by our example of a quantum conveyor belt (see above): the ideal case is described in Fig. 3.12(a), where one band is completely flat and the other one goes straight from $(-\pi, -\Omega/2)$ to $(\pi, \Omega/2)$ in the mixed Floquet-Brillouin zone. Switching on a perturbation that mixes the eigenstates will cause a band gap to open at $(0, 0)$. However, one can easily see from Fig. 3.12(b) that while the band initially corresponding to the spin-up particle loses its individual winding property, the net winding is indeed preserved.

So the nature of a quantised pump can not only be phenomenologically explained with a winding of Floquet bands, but has a deeper connection to the topological classification of the corresponding Floquet operator as outlined above. However, despite the possibility to directly create or simulate discrete Floquet operators [101, 201, 202] it is more natural to start with a static Hamiltonian and only then drive it with a time-periodic term (see Sec. 2.2). Hence, it is worthwhile to try to formally connect the homotopy classification above with a topological classification in terms of Chern numbers for time-dependent Hamiltonians as in the Thouless pump case.

This connection was established in Ref. [196] by means of *dimensional reduction*: a $2n$–1 dimensional insulator characterised by a parameter θ can be classified by a Chern number defined in $2n$ dimensions. This can be done by regarding θ as an additional component of the crystal momentum. In contrast to the single band system of the Thouless pump, we assume that the driving frequency is only adiabatic with respect to some m-dimensional band space. This means that in the course of a single driving period instantaneous energy eigenstates are allowed to mix. An example of such a system is indeed the quantum ratchet model described in Sec. 3.2. The system's property of not being adiabatic forces us to introduce the non-abelian Berry connections (cf. Eq. (3.54))

$$\mathcal{A}_{\alpha\beta,k} = i \langle u_{\alpha k}(\theta) | \frac{\partial}{\partial k} | u_{\beta k}(\theta) \rangle \qquad \text{and} \qquad \mathcal{A}_{\alpha\beta,\theta} = i \langle u_{\alpha k}(\theta) | \frac{\partial}{\partial \theta} | u_{\beta k}(\theta) \rangle \ , \tag{3.61}$$

with $|u_{\alpha k}(\theta)\rangle$ being an instantaneous eigenstate. The expression of the total first Chern

number then reads as

$$C = \frac{1}{2\pi} \oint d\theta \int_{\mathrm{BZ}} dk \ \mathrm{Tr}\Big[\frac{\partial \mathcal{A}_k}{\partial \theta} - \frac{\partial \mathcal{A}_\theta}{\partial k}\Big] . \tag{3.62}$$

We now choose a gauge such that $\mathcal{A}_\theta$ is always single valued. Also, for periodically driven systems we interpret the parametric dependence of Bloch states on θ as coming from the evolution of these states under the periodic Hamiltonian. In other words, we identify the cyclic parameter θ with the time variable t. The expression (3.62) then yields

$$C = \frac{1}{2\pi} \int_{\mathrm{BZ}} dk \ \mathrm{Tr}\big[\mathcal{A}_k(T)\big] - \mathrm{Tr}\big[\mathcal{A}_k(0)\big] . \tag{3.63}$$

As long as the adiabatic condition (with respect to the m-dimensional band space) is fulfilled the time evolution operator $U_k(t)$ mixes occupied bands only. Hence, the initial state $|u_{\alpha k}(t=0)\rangle$ evolves into the state $|u_{\alpha k}(T)\rangle = U_k^F |u_{\alpha k}(0)\rangle$ after one period T. Inserting this expression into the Berry connection (3.61) gives

$$\begin{aligned} \mathcal{A}_{\alpha\beta,k}(T) &= i \langle u_{\alpha k}(T)|\partial_k|u_{\beta k}(T)\rangle \\ &= i \langle u_{\alpha k}(0)|(U_k^F)^\dagger \partial_k (U_k^F |u_{\beta k}(0)\rangle) \\ &= \mathcal{A}_{\alpha\beta,k}(0) + i \langle u_{\alpha k}(0)|(U_k^F)^\dagger (\partial_k U_k^F)|u_{\beta k}(0)\rangle \quad . \end{aligned} \tag{3.64}$$

Finally, by substituting this expression into Eq. (3.63) the total Chern number becomes

$$C = \frac{i}{2\pi} \int_{\mathrm{BZ}} dk \ \mathrm{Tr}\Big[(U_k^F)^\dagger \partial_k U_k^F\Big] , \tag{3.65}$$

which is nothing but the expression for the topological invariant w indexing a certain homotopy class, see (3.59). Therefore, the sum of all Chern numbers equals the net winding of Floquet bands.

Both of these quantities are topologically protected. However, this protection does not hold for properties of single bands: while Chern numbers are quantities of individual bands, the winding of a single Floquet band is not protected against perturbations as can be seen from Fig. 3.12. Most crucially, it is known that all local and physical Hamiltonians possessing a finite number of bands - such as tight-binding Hamiltonians - have the following property: the sum of Chern numbers over all bands of the Hamiltonian must equal to zero [203]. It is therefore the fate of every generic periodically driven band Hamiltonian to reveal a net Floquet winding of *zero*. Of course, the obvious question now is how the working principles of Thouless' pump and of the quantum conveyor belt fit into this general statement.

Clearly, if the driving is performed adiabatically with respect to some sub-band energy scale, then there can (approximately) be some Floquet winding due to the fact that the partial sum over Chern numbers is allowed to be finite. This is the essence of the Thouless pump, and explains why quantised pumping requires some form of adiabaticity. Once this adiabaticity condition is lifted Floquet bands inevitably start hybridizing, which changes the net winding as can be seen from Fig. 3.12(c). Note that this hybridization is exponentially suppressed in Ω divided by the band gap.

Nonetheless, the quantum conveyor belt is seemingly stable. Here, however, it is crucial to realise that we directly introduced the Floquet operator without the prior formulation of a local microscopic Hamiltonian of the system. Indeed, by transforming the effective Hamiltonian (3.56) to position space one immediately sees that H^{eff} cannot be described by a local form of a Hamiltonian. It can, thus, be summarised that quantised pumping in lattice systems is only possible when either the condition of having a local Hamiltonian is broken, or an adiabaticity condition is introduced.

3.5. Summary and discussion

In this chapter, we have studied effectively non-interacting periodically driven quantum systems. Here, we focused on simple lattice models with and without the additional presence of an external force. First, we have suggested a quantum ratchet setup to gain control over the dynamics of a thermally activated homogeneous Mott insulator characterized by a small number of doublon and hole excitations. We showed that these excitations can indeed be moved across the lattice in a controlled fashion by choosing appropriate values for the driving frequency Ω and by ensuring that all mirror symmetries of the system are broken. This ratchet effect can be linked to the emergence of resonances: whenever a multiple of the driving frequency approximately equals the energy difference of bands $n\Omega \approx \Delta E$, unidirectional motion is enhanced. A thorough analysis of such resonances in terms of Floquet perturbation theory was presented. We have further shown that the particle transport characteristics qualitatively depend on *how* the ratchet is switched on: either adiabatically or instantaneously. Moreover, in the large frequency regime, $\Omega > \Delta E$, the quantum ratchet connects to a quantum simulator that mimics the dynamics of a particle in the presence of an effective vector potential $\mathcal{A}$ coupling to the momentum.

In a second study we imposed the presence of a constant external force, which naturally complicates the situation. However, introducing a unit cell in the extended space considerably simplifies the problem. We identified a commensurability condition that needs to be met in order to allow for transport in the long-time limit: only if the applied force g and the frequency Ω of the applied driving are commensurate, a net motion of doublons and holes can be observed. Here, transport is most pronounced in cases where the ratio of g and Ω is given by a fraction with small denominator. Note that such a commensurability condition is, for instance, also needed to obtain dynamical localization in kicked rotor systems [204] or to guarantee ballistic transport in electric quantum walks [101]. Nevertheless, for finite times, transport is also permitted for incommensurate frequencies. In these cases, the physics is captured by Bloch oscillations in an effective system with an enlarged unit cell and reduced force. In both cases our analysis supports motion of the particle 'up the hill'. Note that such an effect due to a quantum ratchet has also been studied experimentally in a different setup [169].

As for future prospects, it will be interesting to generally realise quantum machines by using specifically designed periodically driven systems. One natural goal in the context of our work could be the development of a cooling device. Here, such a machine could rely on the selective transport of doublons and holes to either remove the excitations from the system or to bring them close to each other for a controlled recombination of both. The latter would obviously require some additional appropriate time-dependent change of the Hamiltonian.

In addition, we have shed light on a possible stabilization of the ratchet effect by topological order. While matter with such topological order is predestined for the purpose of quantum computation due to its robustness against perturbations, we summarized the results of such robustness for dynamical properties. By means of dimensional reduction one can show that the net winding of Floquet bands must correspond to the sum of Chern numbers over all bands of the original Hamiltonian. This proves that in general there *cannot* exist a stable topological quantum ratchet for arbitrary frequencies. Having said this, there are examples that do support quantised pumping, such as the Thouless pump [172]. This type of pumping, however, requires the strict following of an adiabaticity condition. Nevertheless, particularly in designed systems such a condition might be met relatively easily. It is therefore no surprise that a topological pump was recently realised

with systems of cold atoms [18, 19] and that related forms of (topological) pumping have been proposed in such designed systems, see, e.g., Ref. [92]. We also note that while a non-zero net winding of Floquet bands is seemingly unprotected, these bands might be characterized by some Chern number themselves (cf. Ch. 6). While these systems might be particularly interesting for realising Floquet versions of topological insulators, see Sec. 2.3, they can also exhibit exotic transport properties due to anomalous edge states [121, 127]. However, this mechanism is not to be understood as a quantum machine in the spirit of our discussion above.

Lastly, the discussion about transport properties of the investigated quantum ratchet has neglected a very crucial aspect: the *interactions* of the doublons and holes among each other. We claimed that this approximation holds true for small densities of excitations, but it must fail once this density starts to grow. Generically, the presence of interactions inevitably leads to heating in the long-time limit [31, 32, 205] (for more details see Sec. 5.1): ultimately, the only possible stationary state is the infinite temperature state, which describes the situation of occupying all many-particle states with equal probability. We expect, however, that even in strongly interacting systems it will be possible to design quantum machines which on the one hand manipulate a (strongly) interacting system efficiently and on the other hand do not produce too much entropy. A possible description of interacting Floquet systems will be one of the central tasks of this thesis, which we will develop in the following.

Part II.

Interacting periodically driven quantum systems

4. From Keldysh formalism to the Boltzmann equation

In previous chapters, the characteristics and features of effectively non-interacting designed quantum systems were investigated. Now, we turn our attention to the key principle of condensed matter physics: *interacting* quantum many-body systems. It is the ultimate aim of part II of this thesis to capture interaction effects in periodically driven quantum systems. While, eventually, our description will take a semiclassical approach, the coherent and possibly strong external drive of a Floquet system makes it worthwhile to start by picturing the full quantum mechanical treatment.

In general, an arbitrary quantum system can be described on the microscopic level by a corresponding many-body Hamiltonian encoding all interactions of participating constituents [206]. However, despite knowing the microscopic structure of a system, consequences for its macroscopic behaviour can generally not be deduced. This reason for this unsatisfying situation is the sheer number of $\sim 10^{23}$ particles in systems of macroscopic size. So how is it at all possible to get theoretical access to the description of complex, interacting many-body quantum system a from a microscopic perspective? The key to answer this question is a theoretical framework that uses collective degrees of freedom in form of fields. Such *quantum fields theories* (QFT) have indeed developed into a universal common language in the context of condensed matter physics [207]. Their success is rooted in the valid formulation of a respective low-energy theory for the collective field. Perhaps the most popular QFT is based on an imaginary time technique, also called 'Matsubara formalism' [208], which is capable of describing the physics of a many-body system at thermal equilibrium. The list of available literature on this equilibrium QFT is quite extensive. Here, we highlight the book by Altland and Simons [206].

Interestingly, despite the fact that a much more powerful quantum field theory capturing also aspects beyond equilibrium situations was established around the same time, most attention has been paid to the less capable but, perhaps, more aesthetic Matsubara technique. A possible explanation for this development is the fact that true non-equilibrium situations in the realm of condensed matter physics were perceived as 'too rough' to provide delicate and interesting effects beyond equilibrium [207]. Moreover, most traditional experimental systems such as disordered metals, bulk magnets or superconductors can hardly be driven away from equilibrium [207]. Here, external disturbances are sufficiently described by 'linear response theory' [206,209], which is embedded in the equilibrium QFT formalism.

Nonetheless, recent experimental and technological developments have dramatically changed the general perception and triggered also large interest in *non-equilibrium* many-body quantum systems. Here, systems made of ultracold atoms (Sec. 2.1) are a major driving force of this field: since these quantum systems are typically well isolated, they represent an ideal testbed to study non-equilibrium many-particle physics [13,25,111,137], holding prospects to even simulate aspects of the highly non-equilibrium situation of the early universe [210, 211]. The theoretical foundations to deal with systems far from equilibrium were originally laid by Schwinger [212], Kanstantinov and Perel [213], Kadanoff and Baym [214] and, most prominently, Keldysh [215]. While initial descriptions of

non-equilibrium theories were build on the 'operator formalism', in a recent book by Kamenev [207] the language of non-equilibrium QFT was thoroughly introduced entirely in a functional integral representation. We stress again that the list of applications demanding the usage of this QFT language is growing rapidly. Most importantly, among the examples are also *Floquet systems* which are inherently out of equilibrium owing to an external drive at, in principle, arbitrary strength and frequency. Therefore, our aim is to ultimately bring together the concept of Floquet theory, see Sec. 2.2, and methods of non-equilibrium QFT.

Nevertheless, while a quantum mechanical description of many-body systems is indeed crucial for many scenarios in the field of condensed matter physics, remarkably, a much simpler approach which captures the semiclassical dynamics of the system works well in many situations. Such a *kinetic equation* was initially introduced by Boltzmann more than one hundred years ago to describe the physics of classical gases [216]. Phenomenologically, the dynamics of a many-body system is attributed to three different mechanisms: particles drift due to intrinsic imbalances, external fields couple to particles, e.g., an electric field acting on charge carriers, and scattering effects due to interactions of particles with each other or through collisions with defects. The resulting *Boltzmann equation* can thus be abstractly written as [217]

$$\dot{n}_k = \dot{n}_k\big|_{\text{drift}} + \dot{n}_k\big|_{\text{field}} + \dot{n}_k\big|_{\text{scatt}} \,, \tag{4.1}$$

with $n_{\mathbf{k}}$ describing the distribution function of particles and the three different terms on the right hand side represent the dynamics evoked by each corresponding mechanism. Boltzmann equations are a mighty tool to describe how scattering affects the semiclassical dynamics. Importantly, such kinetic equations do not aim at capturing quantum-coherent processes at short times, but instead consider the dynamics on time scales set by slow changes of external parameters and by the scattering time between particles. Thus, kinetic equations generally build on a clear separation of the associated time scales.

Clearly, any semiclassical theory must be revealed when taking the associated limit of a corresponding full quantum mechanical description. In this spirit, the Boltzmann equation (4.1) naturally emerges from a full non-equilibrium quantum-field theory. One of the central objectives of this thesis is to perform such a semiclassical approximation for an interacting periodically driven system yielding a Floquet version of a Boltzmann equation, see Ch. 5. However, in order to make this thesis self-contained, in this chapter we will present a thorough derivation of a conventional Boltzmann equation from the Keldysh approach. To this end, we mainly summarize the introductory chapters of Kamenev's book [207]: first, we give an introduction to the general Keldysh formalism and its structure. We then show how to derive quantum kinetic equations by considering the Dyson equation of the theory. Lastly, we reveal how the assumption of having weak interactions together with a clear separation of physical scales can be used to derive the infamous Boltzmann equation by exploiting associated approximation schemes. The main material, conventions as well as structure of the corresponding part of this chapter are indeed provided by Ref. [207], but complementary information can be found, among others, in the books by Rammer [218], Altland and Simons [206] and in a review article by Rammer and Smith [219]. We then finish the chapter by assembling some general remarks on semiclassical transport theory.

Note that while we particularly focus on aspects that are relevant for the Floquet case presented in Ch.5, this chapter is solely an accumulation and a review of technical aspects that have been expressed in the literature before. We, thus, invite the experienced reader in this field to continue with the next chapter, Ch. 5.

4.1. Basics of the Keldysh formalism

4.1.1. The Keldysh contour

We start by considering a most general quantum many-body system which is determined by a time-dependent Hamiltonian $H(t)$. Such a system is generally unsolvable. Nonetheless, we can formally claim that the state describing the full system at time $t_0 = -\infty$ is represented by a corresponding many-body density matrix $\rho(-\infty)$, which is known. The peculiar reference time of $t_0 = -\infty$ is deliberately chosen such that one can safely assume the system to be non-interacting at that point in time. In addition, the system is neither characterised by thermal nor by quantum fluctuations. The interaction part of H (independent of the details) is then only switched on adiabatically. Of course, besides the impact of interactions the Hamiltonian might experience some explicit time-dependence by, e.g., the presence of some external fields. In chapter 5 these fields will be time-periodic. Most importantly, it is because of these external time-dependent perturbations that the system is driven out of equilibrium.

The time evolution of the density matrix $\rho(t)$ is given by the von Neumann equation, $\partial_t \rho(t) = -i[H(t), \rho(t)]$ (with $\hbar = 1$). Hence, the evolution is given by

$$\rho(t) = U_{t,-\infty}\, \rho(-\infty)\, U_{-\infty,t}\,, \tag{4.2}$$

with $U_{t,t_0} = \mathcal{T}_t \exp[-i \int_{t_0}^{t} dt' H(t')]$ being the evolution operator and $\mathcal{T}_t$ describes the time-ordering operator. The latter must be introduced since the Hamiltonians at different times do not necessarily commute with each other. Eventually, one is interested in calculating the expectation value of some observable O at a certain time t. The expectation value is defined with respect to the density matrix as

$$\langle O \rangle(t) = \frac{\mathrm{Tr}[O\rho(t)]}{\mathrm{Tr}[\rho(t)]} = \frac{1}{\mathrm{Tr}[\rho(t)]} \mathrm{Tr}\big[U_{-\infty,+\infty}\, U_{+\infty,t}\, O\, U_{t,-\infty}\, \rho(-\infty)\big]\,, \tag{4.3}$$

where the trace is taken over the many-body Hilbert space of the problem. Note that in order to get the expression on the right-hand side of Eq. (4.3) the equality $U_{-\infty,t} = U_{-\infty,+\infty} U_{+\infty,t}$ was used as well as the cyclic nature of the trace. One can also put the evolution under the trace into a pictorial form: the density matrix at $t_0 = -\infty$ is evolved up to t, where the expectation value is evaluated, followed by an additional evolution to $+\infty$ (the reason for this 'detour' is clarified below) and finally back to $-\infty$. Thus, taking the expectation value requires a forward as well as backward evolution in time along a *closed time contour* $\mathcal{C}$, see Fig. 4.1. The trace taken in Eq. (4.3) ensures the closing of this contour.

A central object of the presented theory is the *partition function* that is defined as

$$Z \equiv \frac{\mathrm{Tr}[U_{\mathcal{C}}\rho(t)]}{\mathrm{Tr}[\rho(t)]} = 1\,, \tag{4.4}$$

with $U_{\mathcal{C}} = U_{-\infty,+\infty} U_{+\infty,-\infty}$ describing the evolution operator along the closed path $\mathcal{C}$. In realistic situations the Hamiltonian is the same on the backward and the forward branch of the evolution. Hence, an initial state is perfectly brought back to itself (without any phase factors) under the evolution of $U_{\mathcal{C}}$, and it holds that $U_{\mathcal{C}} = 1$. This enforces that the partition function Z equals unity.

In order to insert an observable at some point on the forward or backward branch, respectively, one can work with a source term that makes the Hamiltonian slightly different on both branches. Thus, by introducing the Hamiltonian $H_V^{\pm}(t) = H(t) \pm OV(t)$, where

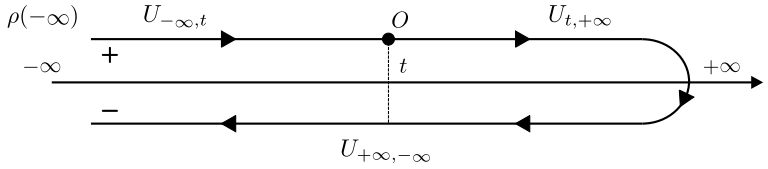

Figure 4.1.: Illustration of the time contour which is enforced by the expectation value of Eq. (4.3). This contour is frequently named *Keldysh contour*. Taking the trace as done in Eq. (4.3) additionally closes the contour at $t = -\infty$. The '+' ('-') indicates the forward (backward) time-evolving branch. Note that this picture is presented in the Schrödinger picture, i.e., it is the density matrix that is time-evolved along the contour.

the plus (minus) refers to the forward (backward) branch, the evolution operator along the contour becomes non-trivial, $U_{\mathcal{C}} \neq 1$. Equally, the partition function becomes non-trivial as well and can now be understood as the *generating function* $Z[V]$. The expectation values of an observable O can then be found from

$$\langle O \rangle(t) = \frac{i}{2} \frac{\delta Z[V]}{\delta V(t)}\bigg|_{V=0} . \tag{4.5}$$

Comparing this expression to equilibrium QFT techniques, one instantly realises that there the observables demand a derivative of a logarithm [206]. This logarithm is void in Eq. 4.5, because $Z[0] = Z = 1$.

Having started to make comparisons one might wonder how the (potentially more familiar) notion of equilibrium QFT fits into the closed time contour picture presented here. Lets consider for simplicity the zero-temperature formalism [220]. Here, expectation values are taken with respect to a ground state of the interacting many-body system, $|0_I\rangle$. Since the system is known to be in equilibrium, this ground state is connected to the ground state of the non-interacting Hamiltonian at $t_0 = -\infty$ by an adiabatic evolution, i.e., $|0_I\rangle = U_{t,-\infty} |0\rangle$. Thus, one can write $\langle O \rangle = \langle 0| U_{-\infty,t} O U_{t,-\infty} |0\rangle$. The key idea is now that one can write

$$U_{+\infty,-\infty} |0\rangle = e^{i\phi} |0\rangle , \tag{4.6}$$

meaning that evolving the non-interacting ground state while switching on and off the interactions takes the system back into that very state, up to a phase factor. Clearly, the phase is given by $e^{i\phi} = \langle 0| U_{\infty,-\infty} |0\rangle$. Excepting this argumentation and using Eq. (4.6) explicitly, one can express the expectation value as follows:

$$\langle O \rangle = e^{-i\phi} \langle 0| U_{+\infty,-\infty} U_{-\infty,t} \, O \, U_{t,-\infty} |0\rangle = \frac{\langle 0| U_{+\infty,t} \, O \, U_{t,-\infty} |0\rangle}{\langle 0| U_{+\infty,-\infty} |0\rangle} , \tag{4.7}$$

So, indeed, the expectation value can be deduced from a forward only evolution. However, the price to pay here is the evaluation of the denominator of Eq. (4.7). In a diagramatic picture this division corresponds to the subtraction of the disconnected or vacuum loop diagrams, which is known as the linked cluster theorem' [206]. Moreover, the denominator plays a major role in disordered systems. Here, it is typically desired to determine the disorder average. But since the accumulated phase depends on the disorder realisation, this phase cannot be ignored and must be included in the treatment according to Eq. (4.7). This causes a complication of the averaging procedure in a very substantial way [206]. Note that for finite-temperature equilibrium formalisms [178, 208, 220], where the evolution is performed in imaginary time by means of the equilibrium density matrix $e^{-\beta H}$ (with $\beta = 1/T$ being the inverse temperature), similar arguments as for the zero-temperature case hold.

Nevertheless, the ansatz (4.6) does *not* work for non-equilibrium situations. External influences drive the system away from equilibrium, and, hence, the non-interacting ground state is not simply evolved adiabatically as above. Consequently, the forward *and* backward evolution needs to be taken into account for generic time-dependent systems. In fact, a field theory that follows the structure of the closed time contour in Fig. 4.1 was first constructed by Schwinger [212]. Around the same time a diagramatic approach to the closed time contour was developed by Konstantinov and Perel [213]. This formalism requires an additional propagation along the imaginary time of length β. Kadanoff and Baym [214] most successfully advanced this language by deriving an associated kinetic theory. It was then Keldysh [215] who suggested a formalism that is able to abandon the imaginary time part in the steps of deriving kinetic equations. We will use the latter formalism throughout this thesis, because it yields the derivation of the kinetic theory in the most transparent way.

4.1.2. Partition function and its functional integral representation

The Keldysh formalism as we want to present it here is based on a functional integral representation for the evolution operator along the closed time contour $\mathcal{C}$, see Fig. 4.1. Before formally developing this Keldysh functional integral it is crucial to specify the particle species. Of course, one can perform the derivation for bosons as well as for fermions, but there will be differences in the formulation. In the following we will show how the theory is formulated for *fermions*, for the following reason: as we are eventually interested in the behaviour of weakly interacting systems we want to avoid bosons in order to circumvent the occurrence of Bose-Einstein condensation.

For pedagogical reasons we start by considering a single quantum level which can be occupied by fermionic particles. Due to Pauli's exclusion principle one can have either zero or one particle in a particular state. The many-body Hilbert space is therefore spanned by the two orthonormal states $|0\rangle$ and $|1\rangle$ only. We further introduce the fermionic creation (annihilation) operator $c^\dagger$ (c) with properties $c^\dagger|0\rangle = |1\rangle$, $c^\dagger|1\rangle = 0$, $c|1\rangle = |0\rangle$, $c|0\rangle = 0$ and where it holds that $\{c, c^\dagger\} = 1$ and $c^2 = (c^\dagger)^2 = 0$. One can also find eigenstates of these operators given by

$$c|\psi\rangle = \psi|\psi\rangle \qquad \text{and} \qquad \langle\psi| c^\dagger = \langle\psi|\bar{\psi}, \qquad \text{with} \qquad \langle\psi|\psi'\rangle = e^{\bar{\psi}\psi'}, \tag{4.8}$$

$|\psi\rangle$ is a fermionic coherent state and $\psi, \bar{\psi}$ represent independent Grassmann variables. The last identity of (4.8) illustrates that the set of coherent states is not orthonormal. A resolution of unity in terms of these fermionic coherent states takes the form

$$\mathbb{1} = \int d\bar{\psi} \int d\psi \; e^{-\bar{\psi}\psi} \, |\psi\rangle\langle\psi| \, . \tag{4.9}$$

Consequently, the trace of an operator O, i.e., $\mathrm{Tr}[O] = \sum_n \langle n|O|n\rangle$, can be written as

$$\mathrm{Tr}[O] = \sum_n \iint d\bar{\psi}\, d\psi \; e^{-\bar{\psi}\psi} \, \langle n|\psi\rangle \, \langle\psi|O|n\rangle = \iint d\bar{\psi}\, d\psi \; e^{-\bar{\psi}\psi} \, \langle\psi|O|-\psi\rangle \; , \tag{4.10}$$

where the minus sign in $|-\psi\rangle$ comes from commuting two coherent states, and it was used that $\sum_n |n\rangle\langle n| = \mathbb{1}$. The matrix element of a normal ordered operator appearing in Eq. (4.10) can be written as

$$\langle\psi| \, O(c^\dagger, c) \, |\psi'\rangle = O(\bar{\psi}, \psi') \, \langle\psi|\psi'\rangle = O(\bar{\psi}, \psi') \, e^{\bar{\psi}\psi'} \, . \tag{4.11}$$

We now aim at making progress in calculating the partition function Z, given in Eq. (4.4). The energy of the single quantum state under consideration is denoted by ϵ_0, and the associated Hamiltonian of this spinless model reads (in second quantised form) as[1]

$$H = \epsilon_0 \, c^\dagger c \,. \tag{4.12}$$

In order to simplify things we assume that the initial density matrix at $t_0 = -\infty$ is given in some equilibrium form $\rho(t_0) \equiv \rho_0 = \exp[-\beta(\epsilon_0 - \mu)c^\dagger c]$, with μ describing the chemical potential. The denominator of the partition function thus reads as $\mathrm{Tr}[\rho_0] = 1 + \rho_{\epsilon_0}$, where $\rho_{\epsilon_0} = e^{-\beta(\epsilon_0 - \mu)}$. In the next step, one deals with the evolution operator along the time contour. For this purpose the contour $\mathcal{C}$ is divided into $2N-2$ time intervals of equal duration $\delta_t \sim 1/N$, with $\delta_t \to 0$ for $N \to \infty$. Here, it holds that $t_1 = t_{2N} = -\infty$ and $t_N = t_{N+1} = +\infty$. This fragmentation of the contour results also in an incremental time-evolution of the system by U_{δ_t} on the forward branch and $U_{-\delta_t}$ on the backward branch, respectively. One now inserts the resolution of unity (4.9) at each point $j = 1, ..., 2N$ along $\mathcal{C}$. The numerator of Z, i.e., $\mathrm{Tr}[U_{\mathcal{C}}\rho_0]$, yields the following term

$$\langle \psi_{2N}|U_{-\delta t}|\psi_{2N-1}\rangle \ldots \langle \psi_{N+1}|\mathbb{1}|\psi_N\rangle \ldots \langle \psi_2|U_{+\delta t}|\psi_1\rangle\langle\psi_1|\rho_0| - \psi_{2N}\rangle \,, \tag{4.13}$$

where it should be understood that the term is read from right to left. So the matrix elements appearing in expression (4.13) are determined to be

$$\begin{aligned} \langle \psi_{j+1}|U_{\pm\delta t}|\psi_j\rangle &= \langle \psi_{j+1}| \, e^{\mp iH(c^\dagger, c)\delta_t} \, |\psi_j\rangle \\ &\approx \langle \psi_{j+1}| \, (1 \mp iH(c^\dagger, c)\, \delta_t) \, |\psi_j\rangle \\ &\approx e^{\bar\psi_{j+1}\psi_j} \, e^{\mp iH(\bar\psi_{j+1}, \psi_j)\delta_t} \quad . \end{aligned} \tag{4.14}$$

Note that his derivation does not only apply to more general Hamiltonians, but also to time-dependent ones. This is crucial since we eventually want to treat Floquet systems. Finally, by collecting all the exponential factors along the time contour one can write the partition function (4.4) as

$$Z = \frac{1}{\mathrm{Tr}[\rho_0]} \iint \prod_{j=1}^{2N} [d\bar\psi_j, d\psi_j] \;\; \exp\left(i \sum_{j,j'=1}^{2N} \bar\psi_j \, G^{-1}_{jj'} \, \psi_{j'} \right), \tag{4.15}$$

where the $2N \times 2N$-dimensional matrix $iG^{-1}_{jj'}$ is given by

$$iG^{-1}_{jj'} = \left(\begin{array}{cccc|cccc} -1 & & & & & & & -\rho_{\epsilon_0} \\ h_- & -1 & & & & & & \\ & \ddots & \ddots & & & & & \\ & & h_- & -1 & & & & \\ \hline & & & 1 & -1 & & & \\ & & & & h_+ & -1 & & \\ & & & & & \ddots & \ddots & \\ & & & & & & h_+ & -1 \end{array} \right), \tag{4.16}$$

and $h_\mp \equiv 1 \mp i\epsilon_0\delta_t$. The matrix (4.16) has a structure that can be divided into four sectors: The on-diagonal parts correspond to the exponentials of Eq. (4.14) for the forward and

[1] Note that throughout this section we will continue to assume the presence of this Hamiltonian. However, all results below can be analogously derived for a general, time ordered Hamiltonian, as well.

backward branch of the Keldysh contour, respectively. The upper right element of the matrix, $-\rho_{\epsilon_0}$, is due to the last element of Eq. (4.13), i.e., $\langle\psi_1|\rho_0| - \psi_{2N}\rangle$. Note that this element is in fact the only one containing information on the initial density matrix ρ_0. Furthermore, the upper right element of the bottom left sector of the matrix is due to the fact that the points N and $N+1$ on the counter are in fact indistinguishable in a physical sense. Hence, there is no evolution between these two points, see Eq. (4.13). Despite the fact that these isolated matrix elements seem to be singular for the case that $N \to \infty$ they remain crucial in order to ensure normalisation.

Before dealing with the Gaussian integral in Eq. 4.15 explicitly we take a look at the continuum limit $N \to \infty$. Using the notation $\psi_j \to \psi(t)$, one formally arrives at the following expression for the partition function:

$$Z = \int \mathbf{D}[\bar{\psi}, \psi]\; e^{iS[\bar{\psi},\psi]}\,, \tag{4.17}$$

where the short-hand notation $\int \mathbf{D}[\bar{\psi}, \psi] = (\mathrm{Tr}[\rho_0])^{-1} \iint \prod_{j=1}^{2N} [d\bar{\psi}_j, d\psi_j]$ has been introduced. According to Eqs. (4.15) and (4.16) as well as using $\delta t_j \equiv \pm\delta_t$ (depending on the branch) the *action* S reads as

$$S[\bar{\psi}, \psi] \;=\; \sum_{j=2}^{2N} \Big[i\bar{\psi}_j \,\frac{\psi_{j-1} - \psi_{j-1}}{\delta t_j} - \epsilon_0 \bar{\psi}_j \psi_{j-1} \Big] \delta t_j + i\bar{\psi}_1 \Big[\psi_1 + \rho_{\epsilon_0}\, \psi_{2N} \Big] \tag{4.18}$$

$$\overset{N\to\infty}{=} \int_{-\infty}^{+\infty} dt\; \Big[\bar{\psi}^+(t)(i\partial_t - \epsilon_0)\psi^+(t) - \bar{\psi}^-(t)(i\partial_t - \epsilon_0)\psi^-(t) \Big]\,, \tag{4.19}$$

where the contour integral has been split[2] into a forward and backward part with respectively residing Grassmann fields ψ^+ and ψ^-. Going from the discrete picture (4.18) to its continuum version (4.19) suggests that in the latter one loses the knowledge about the boundary term in the upper right corner of the matrix (4.16). If this was indeed the case, then the fields ψ^+ and ψ^- were completely uncorrelated. Of course, this is *not* true. Hence, the continuum representation should only be understood as an abbreviation of the underlying discrete description. However, for practical reasons we demand a continuum version of the theory that does also encode the information about the boundary term. This procedure goes by the name *Keldysh rotation* and is presented in the next section.

4.1.3. Green's functions and the Keldysh action

To present a continuum representation of the functional integral which encodes all information of the system we return to the discrete version of the partition function (4.4). Here, we exploit the identity of Gaussian integration for Grassmann fields [206], i.e.,

$$\int \mathbf{D}[\bar{\psi}, \psi]\; e^{-\Sigma_{ij}\bar{\psi}_i A_{ij} \psi_j} = \det A\,. \tag{4.20}$$

Using this expression the partition function (4.4) is calculated to give

$$Z = \frac{\det[iG^{-1}]}{\mathrm{Tr}[\rho_0]} = \frac{1 + \rho(\epsilon_0)(1-h^2)^{N-1}}{1+\rho(\epsilon_0)} \approx \frac{1 + \rho(\epsilon_0)\, e^{(\epsilon_0\delta_t)^2(N-1)}}{1+\rho(\epsilon_0)} \overset{N\to\infty}{=} 1\,. \tag{4.21}$$

This confirms the argued normalisation of the partition sum of $Z = 1$, Sec. 4.1.1. Moreover, Eq. (4.21) underlines once more how crucial the boundary term is: normalisation of the theory is only achieved by including the upper right matrix element of Eq. (4.16).

[2] $\int_{\mathcal{C}} \psi = \int_{-\infty}^{+\infty} \psi^+ + \int_{+\infty}^{-\infty} \psi^- = \int_{-\infty}^{+\infty} (\psi^+ - \psi^-)$.

The correlator of two Grassmann fields is defined as

$$\langle \psi_j \, \bar{\psi}_{j'} \rangle \equiv \int \mathbf{D}[\bar{\psi}, \psi] \; \psi_j \, \bar{\psi}_{j'} \; \exp\left(i \sum_{k,k'} \bar{\psi}_k \, G^{-1}_{kk'} \, \psi_{k'} \right) = i \, G_{jj'} \,, \tag{4.22}$$

where again basic properties of Gaussian integrals have been employed. Here, the indices run over the discretised version of the entire Keldysh contour. Note that the factor of Z^{-1} which appears in the equilibrium theory is absent due to $Z = 1$. It is now possible to invert the infinitely large matrix (4.16) and, hence, find explicit expressions for the correlators (4.22). As before, it is convenient to split the fields into parts residing on the forward (backward) branch indicated by ψ^+ (ψ^-). After having found the correlators in their discretised form one can take the continuum limit for convenience. Without giving explicit details of this procedure (for details the reader is once again referred to Ref. [207]), the final result is given by

$$\langle \psi^+(t) \, \psi^-(t') \rangle \equiv i \, G^<(t,t') = -n_F \, e^{-i\epsilon_0 (t-t')} \,, \tag{4.23}$$

$$\langle \psi^-(t) \, \psi^+(t') \rangle \equiv i \, G^>(t,t') = (1 - n_F) \, e^{-i\epsilon_0 (t-t')} \,, \tag{4.24}$$

$$\langle \psi^+(t) \, \psi^+(t') \rangle \equiv i \, G^{\mathcal{T}}(t,t') = i \, \theta(t-t') \, G^>(t,t') + i \, \theta(t'-t) \, G^<(t,t') \,, \tag{4.25}$$

$$\langle \psi^-(t) \, \psi^-(t') \rangle \equiv i \, G^{\widetilde{\mathcal{T}}}(t,t') = i \, \theta(t'-t) \, G^>(t,t') + i \, \theta(t-t') \, G^<(t,t') \,, \tag{4.26}$$

with $n_F = \rho_{\epsilon_0}/(1+\rho_{\epsilon_0})$ being the Fermi occupation number and $\theta(t)$ representing the Heaviside step-function, $\theta(t) = 1\,(0)$ for $t > 0\,(t < 0)$. Note that in order to be consistent with the discrete description above one finds that for *both* Eqs. (4.25) and (4.26) the first term is determined by $\theta(0) = 1$, while the second term follows $\theta(0) = 0$. The respective correlators are identified with the lesser (greater) *Green's function* $G^<$ ($G^>$) as well as with the time ordered (anti-ordered) Green's function $G^{\mathcal{T}}$ ($G^{\widetilde{\mathcal{T}}}$). Here, the symbols refer to the time-ordering with respect to the contour $\mathcal{C}$. The Green's functions have the properties

$$\left[G^{<(>)}\right]^\dagger = -G^{<(>)} \qquad \text{and} \qquad \left[G^{\mathcal{T}}\right]^\dagger = -G^{\widetilde{\mathcal{T}}} \,. \tag{4.27}$$

Note that the Green's functions are understood to be matrices in time space, and, hence, conjugation leads to an exchange of time arguments.

Most crucially, one realises that contrary to the action given by Eq. (4.19) the continuum version of the set of Green's functions (4.23)-(4.26) still carries the knowledge about the initial distribution ρ. In order to bring also the action into a desired form one continues with the inspection that

$$G^{\mathcal{T}}(t,t') + G^{\widetilde{\mathcal{T}}}(t,t') - G^<(t,t') - G^>(t,t') = 0 \,. \tag{4.28}$$

The Green's functions (4.23)-(4.26) are therefore not independent. This should allow for a transformation that eliminates this redundancy. However, note that there is a subtlety here: following the above normalisation of the step-function at equal times, $\theta(0)$, the identity of Eq. (4.28) does *not* hold in situations where $t = t'$, for which the right-hand side of Eq. (4.28) equals $-i$ rather than zero. Since $t = t'$ defines a manifold of measure zero, this subtlety is typically ignored. Nonetheless, whenever evaluating equal-time Green's functions this property should be taken into consideration, see Sec. 4.2.2.

Next, we consider a transformation that allows to make progress from Eq. (4.28). This transformation is called *Keldysh rotation*, since a set of new fermionic fields is introduced in the following manner

$$\begin{pmatrix} \psi^1 \\ \psi^2 \end{pmatrix} = \frac{1}{\sqrt{2}} \begin{pmatrix} 1 & 1 \\ 1 & -1 \end{pmatrix} \begin{pmatrix} \psi^+ \\ \psi^- \end{pmatrix} \qquad \text{and} \qquad \begin{pmatrix} \bar{\psi}^1 \\ \bar{\psi}^2 \end{pmatrix} = \frac{1}{\sqrt{2}} \begin{pmatrix} 1 & -1 \\ 1 & 1 \end{pmatrix} \begin{pmatrix} \bar{\psi}^+ \\ \bar{\psi}^- \end{pmatrix} . \tag{4.29}$$

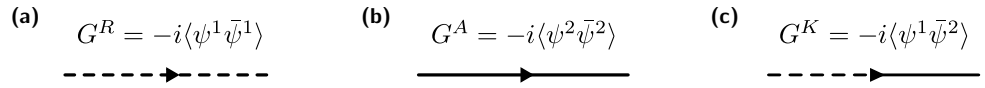

Figure 4.2.: Graphical representation of the (a) retarded, (b) advanced and (c) Keldych Green's function. The explicit forms are found by the Keldysh rotation (4.29) and are given by Eqs. (4.31)-(4.33) or Eq. (4.41), respectively.

Note that this transformation is not unitary. Since $\bar{\psi}$ is in fact not the conjugate field to ψ, but rather an independent Grassmann field, one has a certain freedom in defining the transformation. The here presented form of Eq. (4.29) was first introduced by Larkin and Ovchinnikov [221] and has some practical advantages that will become apparent later on. Employing the Keldysh rotation together with Eqs. (4.23)-(4.26) yields a new set of Green's function that can be put into the following compact form

$$\hat{G}(t,t') = \begin{pmatrix} \hat{G}^{11} & \hat{G}^{12} \\ \hat{G}^{21} & \hat{G}^{22} \end{pmatrix} = \begin{pmatrix} G^R(t,t') & G^K(t,t') \\ 0 & G^A(t,t') \end{pmatrix}, \tag{4.30}$$

where $\hat{G}^{ab}(t,t') = -i\,\langle\psi^a(t)\bar{\psi}^b(t')\rangle$, with $a,b=(1,2)$. Note that here and in the following we indicate objects by a hat that have an inherent 2×2 Keldysh structure, e.g., $\hat{G}$. The superscripts R, A, K indicate the *retarded*, *advanced* and *Keldysh* component of the Green's function. They are given by

$$G^R(t,t') = \frac{1}{2}\left(G^{\mathcal{T}} - G^{\widetilde{\mathcal{T}}} - G^< + G^>\right) = \theta(t-t')\left(G^> - G^<\right), \tag{4.31}$$

$$G^A(t,t') = \frac{1}{2}\left(G^{\mathcal{T}} - G^{\widetilde{\mathcal{T}}} + G^< - G^>\right) = \theta(t'-t)\left(G^< - G^>\right), \tag{4.32}$$

$$G^K(t,t') = \frac{1}{2}\left(G^{\mathcal{T}} + G^{\widetilde{\mathcal{T}}} + G^< + G^>\right) = G^< + G^>. \tag{4.33}$$

These Green's functions are the central objects of the Keldysh technique. A graphical representation of them is given in Fig. 4.2. Furthermore, using the properties of Eq. (4.27) one finds that

$$\left[G^R\right]^\dagger = G^A \qquad \text{and} \qquad \left[G^K\right]^\dagger = -G^K. \tag{4.34}$$

Also, from Eqs. (4.31)-(4.33) and Eqs. (4.23)-(4.26) the following equal-time correlator identities can be deduced

$$G^R(t,t) + G^A(t,t) = 0 \qquad \text{and} \qquad G^R(t,t) - G^A(t,t) = -i\,. \tag{4.35}$$

Again, it is crucial to notice that these characteristics are not unique to the toy model from Eq. (4.12), but are generally true for *any* system. To this end, we state a formal expression for the inverse retarded/advanced Green's function [206]

$$\left[G^{R/A}\right]^{-1}(t,t') = \delta(t-t')\left(i\partial_t \pm i0^+ - H(t)\right), \tag{4.36}$$

with 0^+ being an infinitesimal small, positive, real number and H is the Hamiltonian. Moreover, it is often convenient to parametrize the anti-Hermitian Keldysh Green's function (see Eq. (4.34)) with the help of a Hermitian matrix F, i.e.,

$$G^K(t,t') = \int d\tilde{t}\; G^R(t,\tilde{t})\,F(\tilde{t},t') - F(t,\tilde{t})\,G^A(\tilde{t},t') \equiv G^R \circ F - F \circ G^A, \tag{4.37}$$

where the '$\circ$' indicates convolution regarding all degrees of freedom. The matrix $F(t,t')$ is also called *distribution matrix*[3]. We remark that for general systems the fields and Green's function become functions of all degrees of freedom (not only time), i.e., $\psi(t) \to \psi_\sigma(\mathbf{r},t)$ and $\hat{G}^{ab}(t,t') \to \hat{G}^{ab}_{\sigma\sigma'}(\mathbf{r},t,\mathbf{r}',t')$, where $\mathbf{r}$ represents the position space and σ indicates a spin degree of freedom.

We continue by formulating an action associated with the new set of Green's functions. Similar to Eq. (4.22) we express the Green's functions (4.31)-(4.33) in terms of an functional integral

$$\hat{G}^{ab}(t,t') = -i \int \mathbf{D}[\bar{\psi},\psi]\ \psi^a(t)\,\bar{\psi}^b(t')\ e^{iS[\bar{\psi},\psi]}\,, \tag{4.38}$$

where the action S now reads as

$$S[\bar{\psi},\psi] = \iint_{-\infty}^{+\infty} dt\,dt'\ (\,\bar{\psi}^1,\,\bar{\psi}^2\,)_t \begin{pmatrix} [G^R]^{-1} & [G^{-1}]^K \\ 0 & [G^A]^{-1} \end{pmatrix}_{t,t'} \begin{pmatrix} \psi^1 \\ \psi^2 \end{pmatrix}_{t'} . \tag{4.39}$$

It has been used that $[G^{-1}]^{R/A} = [G^{R/A}]^{-1}$ which is a direct consequence of the triangular structure of $\hat{G}$, see Eq. (4.30). The Keldysh component of the inverse Green's function is determined by $G^R \circ [G^{-1}]^K + G^K [G^A]^{-1}$, which is, by employing Eq. (4.37), rearranged to yield

$$[G^{-1}]^K = [G^R]^{-1} \circ F - F \circ [G^A]^{-1}\,. \tag{4.40}$$

In general, it is this term that correctly regularizes the action (4.39). Finally, Eq. (4.39) achieves the goal to formulate an action in the continuum model that carries the knowledge about all boundary conditions and correlations: while the retarded and advanced Green's functions depend only on the spectrum of the underlying Hamiltonian, the Keldysh component contains information about the occupation numbers. In the following, the form of the action (4.39) allows to perform standard diagramatic perturbation theory, see Sec. 4.2.

An alternative method to the functional integral (4.38) for calculating the Green's functions G^R, G^A and G^K is given by taking the (contour ordered) operator expectation value. Using the fermionic creation and annihilation in their Heisenberg representation, $c^\dagger(t)$ and $c(t)$, the Green's functions can be determined from the following expressions [218]

$$\begin{aligned} G^R(t,t') &= -i\,\theta(t-t')\,\langle\{c(t),c^\dagger(t')\}\rangle\,, \\ G^A(t,t') &= i\,\theta(t'-t)\,\langle\{c(t),c^\dagger(t')\}\rangle\,, \\ G^K(t,t') &= -i\,\langle[c(t),c^\dagger(t')]\rangle\,, \end{aligned} \tag{4.41}$$

with $\{.\}/[.]$ describing the anti-/commutator. These expressions will be particularly useful in calculating explicit forms of non-interacting Green's functions (see Sec. 5.2.2).

We close this section by making a short remark on an alternative approach to the Keldysh time contour: instead of using a functional integral representation, one could have formulated the entire theory in terms of contour ordered operators, see, e.g., Ref. [218]. While both theories are formally equivalent, the functional integral representation is much more transparent and approachable; particularly in deriving kinetic equations from an interacting system.

[3] Using expressions (4.23) and (4.24) one can explicitly determine the form of the Keldysh Green's function (4.33). Taking the Fourier transformation yields $G^K(\epsilon) = -2\pi i F(\epsilon)\delta(\epsilon-\epsilon_0)$, with $F(\epsilon) = 1 - 2n_F(\epsilon)$ being the transformed distribution matrix.

4.2. Quantum kinetic equations

4.2.1. Dyson equation in Keldysh space

After having introduced the general structure of the functional integral approach in Keldysh space in the previous section 4.1, we will now give a practical approach to the explicit calculation of Green's functions of interacting many-body systems. First we claim that the Hamiltonian is written in the following form

$$H = H^0 + H^{\text{int}}\,, \tag{4.42}$$

with H^0 being the non-interacting part of the Hamiltonian, and H^{int} encodes all interactions in the system. Including all relevant degrees of freedom, one can find a functional integral representation for the Green's functions of the form

$$\hat{G}^{ab}_{\sigma\sigma'}(x,x') = -i\int \mathbf{D}[\bar{\psi},\psi]\ \psi^a_\sigma(x)\,\bar{\psi}^b_{\sigma'}(x')\ e^{i(S_0[\bar{\psi},\psi]+S_{\text{int}}[\bar{\psi},\psi])}\,, \tag{4.43}$$

where $x = (\mathbf{r},t)$. The non-interacting part of the Hamiltonian is absorbed into S_0, and S_{int} is the part of the action that is caused by the interactions. Crucially, the term S_{int} is not quadratic in the fields, but rather of higher order (e.g., quartic for particle-particle interactions). Hence, there exists no general scheme for the *exact* inversion of this matrix, and, indeed, it may even be impossible to invert it in practice (cf., Eq. (4.22)). Nonetheless, one can make progress by formally expanding the exponential of Eq. (4.43) in powers of S_{int}, i.e.,

$$\hat{G}^{ab}_{\sigma\sigma'}(x,x') = -i\int \mathbf{D}[\bar{\psi},\psi]\ \psi^a_\sigma(x)\,\bar{\psi}^b_{\sigma'}(x')\left(1 + iS_{\text{int}} - \frac{S^2_{\text{int}}}{2} + \dots\right) e^{iS_0[\bar{\psi},\psi]}\,. \tag{4.44}$$

Thus, the total Green's function $\hat{G}$ is expressed as a sum of higher order correlators that are all evaluated with respect to the Gaussian action S_0.

In order to tackle this seeming problem one exploits another main advantage of the functional integral formalism: the validity of *Wick's theorem*. This theorem states that an average is given by the sum of all possible pairwise contractions. In the case of Grassmann fields one should bare in mind that every commuting process yields an additional minus sign. Each combination is therefore multiplied by a factor that represents the parity of the respective permutation, e.g.,

$$\langle \psi^a\psi^b\bar{\psi}^c\bar{\psi}^d\rangle = -\langle \psi^a\bar{\psi}^c\rangle\langle \psi^b\bar{\psi}^d\rangle + \langle \psi^a\bar{\psi}^d\rangle\langle \psi^b\bar{\psi}^c\rangle\ . \tag{4.45}$$

The logic of Eq. (4.45) carries over to any correlator of arbitrarily high order. Hence, one can write the Green's function (4.44) in terms of combinations of non-interacting Green's functions $\hat{G}_0 = \hat{G}|_{S_{\text{int}}=0}$. The different combinations of Green's functions also encode various integrals over position and time as well as matrix multiplication in Keldysh space. One can now interpret these collections of Green's functions and associated integrals in terms of (Feynman) diagrams. The explicit form of these diagrams depend on the type of interaction. Examples are given in the next section, Sec. 4.2.2. Generally, one can rearrange the diagrams, i.e., the terms of the infinite sum in Eq.(4.44), into blocks of *irreducible* ones. The collection of all irreducible diagrams is named the *self-energy* $\hat{\Sigma}$. Here, the self-energy is also a matrix in Keldysh space. With this definition at hand one can rewrite Eq. (4.44) as

$$\hat{G} = \hat{G}_0 + \hat{G}_0\circ\hat{\Sigma}\circ\hat{G}_0 + \hat{G}_0\circ\hat{\Sigma}\circ\hat{G}_0\circ\hat{\Sigma}\circ\hat{G}_0 + \ldots = \hat{G}_0 + \hat{G}_0\circ\hat{\Sigma}\circ\hat{G}\,, \tag{4.46}$$

where the notion of '$\circ$' has been extended to include the Keldyh space structure. The only formal difference to the standard (equilibrium) diagramatic expansion [178, 206, 220] is indeed the additional matrix multiplication in Keldysh space.

Multiplying both sides of Eq. (4.46) with $\hat{G}_0^{-1}$ from the left followed by a rearrangement leads to the *Dyson equation*

$$\left(\hat{G}_0^{-1} - \hat{\Sigma}\right) \circ \hat{G} = \mathbb{1}\,, \tag{4.47}$$

which is an exact equation determining the full Green's function $\hat{G}$. To make progress one uses an explicit form of the self-energy. This form depends on the Keldysh rotation. In fact, the reason to choose the transformation as presented in Eq. (4.29) is to have $\hat{G}$, $\hat{G}^{-1}$ and $\hat{\Sigma}$ all possessing the same structure. Without giving the explicit proof here, the self-energy takes the form

$$\hat{\Sigma}(x,x') = \begin{pmatrix} \Sigma^R(x,x') & \Sigma^K(x,x') \\ 0 & \Sigma^A(x,x') \end{pmatrix}\,, \tag{4.48}$$

where the retarded, advanced and Keldysh parts of the self-energy exhibit similar properties as the Green's function (see Eq. (4.34)), i.e., $\Sigma^R = [\Sigma^A]^\dagger$ and $\Sigma^K = -[\Sigma^K]^\dagger$. As a result of Eq. (4.48), the Dyson equation becomes

$$\begin{pmatrix} \left[G_0^R\right]^{-1} - \Sigma^R & -\Sigma^K \\ 0 & \left[G_0^A\right]^{-1} - \Sigma^A \end{pmatrix} \circ \begin{pmatrix} G^R & G^K \\ 0 & G^A \end{pmatrix} = \mathbb{1}\,. \tag{4.49}$$

Note that it was taken into account that the Keldysh component of the inverse Green's function $\left[G^{-1}\right]^K$ is only a regularization. Thus, it can be omitted in the presence of a finite Keldysh component of the self-energy Σ^K.

The on-diagonal parts of the Dyson equation (4.49) yield for the retarded and advanced components

$$\left(\left[G_0^{R/A}\right]^{-1} - \Sigma^{R/A}\right) \circ G^{R/A} = 1\,. \tag{4.50}$$

These expressions are closed and, assuming the self-energies $\Sigma^{R/A}$ are known, might even be solved for simple systems. We, hence, want to focus on the Keldysh component of the Dyson equation. Using the parametrization of G^K in terms of the distribution matrix F, see Eq. (4.37), the expression is given by

$$\left(\left[G_0^R\right]^{-1} - \Sigma^R\right) \circ \left(G^R \circ F - F \circ G^A\right) - \Sigma^K \circ G^A = 0\,. \tag{4.51}$$

One makes progress by multiplying this expression with $\left(\left[G_0^A\right]^{-1} - \Sigma^A\right)$ from the right and by exploiting Eq. (4.50). Finally, by moving all terms that depend on self-energies to the right, and all other terms to the left, one finds

$$F \circ \left[G_0^A\right]^{-1} - \left[G_0^R\right]^{-1} \circ F \;=\; \Sigma^K - \left(\Sigma^R \circ F - F \circ \Sigma^A\right)\,. \tag{4.52}$$

This form of separation has an obvious reasoning: the left-hand side depends on the inverse of non-interacting Green's functions and therefore describes the *kinetic* terms, and the right-hand side captures interaction effects and thus called the *collision integral*. Those parts together in Eq. (4.52) describe the *quantum kinetic equation* (QKE) for the distribution matrix F. Notice at this point that the QKE is formally still an exact description of a general many-body non-equilibrium system. However, for arbitrary systems and times this equation is practically impossible to solve. The problem is two-fold: one needs to find expressions for the self-energies as well as to deal with the convolution of objects. In order to be able to make progress one therefore has to apply sensible approximation schemes to Eq. (4.52).

4.2.2. The self-energy

In order to be able to calculate self-energies explicitly the interaction part of the Hamiltonian needs to be specified. We, hence, make the first crucial assumption: in the following we shall consider two-body interactions that are static and *local* in space. In true electronic systems this assumption may only firmly hold in situations where sufficient screening yields effective short-range interactions. Having said this, we are strongly motivated to find a theoretical description of systems made of cold atoms in optical lattices (see Sec. 2.1). Here, the charge neutrality of the atoms typically excludes[4] any long-range interaction, and the interaction part of the Hamiltonian of type

$$H^{\mathrm{int}} = U \int d\mathbf{r}\; c^{\dagger}_{\mathbf{r}\uparrow} c^{\dagger}_{\mathbf{r}\downarrow} c_{\mathbf{r}\downarrow} c_{\mathbf{r}\uparrow} \qquad \xrightarrow{\mathrm{TBM}} \qquad U \sum_i c^{\dagger}_{i\uparrow} c^{\dagger}_{i\downarrow} c_{i\downarrow} c_{i\uparrow}\,, \tag{4.53}$$

is indeed the natural description of particle-particle interactions in the system. Here, we have already indicated what form this interaction type assumes in a tight-binding model (TBM). In favour of generality, however, we will (first) consider the continuous expression on the left-hand side of Eq. (4.53). In the following, we also crucially assume that the interaction strength U is sufficiently small, i.e., much smaller than the energy scale set by H^0, in order to allow for a perturbative treatment of the problem. For general situations the particle-particle interactions between electrons lead to a space-dependent interaction potential, $U \to U(\mathbf{r})$. A typical approach for a simplification of the problem is given, e.g., by a Hubbard-Stratonovich transformation [206, 207]. Nonetheless, for short-range interactions, such as the s-wave scattering of cold atoms, the interaction type (4.53) is not only valid but simplifies the yet to be developed perturbation theory substantially.

The time-evolution along the Keldysh contour under the presence of H^{int} leads to a functional integral representation that includes an associated contribution to the action, see Eq. (4.43). Considering the original form of the contour, i.e., the form of the contour before the Keldysh rotation, the interaction part of the action for the explicit interaction type (4.53) is given by

$$S_{\mathrm{int}}[\bar{\psi},\psi] = -\frac{U}{2}\int_{\mathcal{C}} dt \int d\mathbf{r} \sum_{\sigma} \bar{\psi}_{\sigma}(\mathbf{r},t)\,\bar{\psi}_{\bar{\sigma}}(\mathbf{r},t)\,\psi_{\bar{\sigma}}(\mathbf{r},t)\,\psi_{\sigma}(\mathbf{r},t) \tag{4.54}$$

$$= -\frac{U}{2}\int_{-\infty}^{\infty} dt \int d\mathbf{r} \sum_{\sigma} \left[\, \bar{\psi}^{+}_{\sigma}\bar{\psi}^{+}_{\bar{\sigma}}\psi^{+}_{\bar{\sigma}}\psi^{+}_{\sigma} \;-\; \bar{\psi}^{-}_{\sigma}\bar{\psi}^{-}_{\bar{\sigma}}\psi^{-}_{\bar{\sigma}}\psi^{-}_{\sigma} \,\right], \tag{4.55}$$

where $\bar{\sigma} = \downarrow(\uparrow)$ for $\sigma = \uparrow(\downarrow)$, and the coordinate variable has been dropped in the second line for convenience. Note that there is a subtlety regarding the temporal limits of integration: recall that in the very far past (future) it is actually required that the interactions are switched off (cf. Sec. 4.1.1). After being turned on adiabatically they remain, however, present for an arbitrarily long time.

Bearing this information in mind one now performs the Keldysh rotation given by Eq. (4.29). The action of Eq. (4.55) then acquires the form

$$S_{\mathrm{int}}[\bar{\psi},\psi] = -\frac{U}{2}\int_{-\infty}^{\infty} dt \int d\mathbf{r} \sum_{\sigma} \left[\, \bar{\psi}^{1}_{\sigma}\bar{\psi}^{1}_{\bar{\sigma}}\psi^{1}_{\bar{\sigma}}\psi^{2}_{\sigma} \;+\; \bar{\psi}^{1}_{\sigma}\bar{\psi}^{2}_{\bar{\sigma}}\psi^{2}_{\bar{\sigma}}\psi^{2}_{\sigma} \;+\; (1 \leftrightarrow 2) \,\right], \tag{4.56}$$

where the last term represents a copy of the first two terms with interchanged labels. Following the logic of Eq. (4.44) the different terms in Eq. (4.56) generate higher-order correlation functions by expanding the exponential in powers of S_{int}. Switching to a

[4] Exceptions are systems made of *Rydberg atoms*, for example.

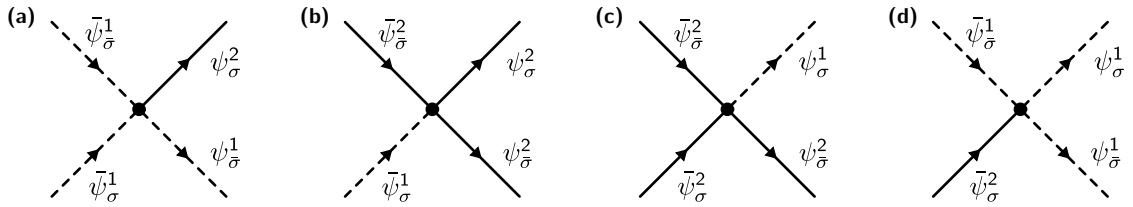

Figure 4.3.: Graphical representation of the four interaction vertices as the appear in the corresponding interaction S_{int}, see Eq. (4.56). They fundamentally arise from an on-site interaction type given by Eq. (4.53).

graphical visualisation the interaction terms are represented by a set of *vertices*. These vertices are shown in Fig. 4.3.

The full Green's function can now be determined by evaluating the self-energy diagramatically. The nth order contribution to Σ is given by all possible combinations of n number of vertices that form an irreducible diagram. Here, irreducibility describes the fact that the diagram cannot be separated into two by simply cutting a single propagator line. In the following we will exemplarily evaluate the first and second order contribution to the self-energies.

1st order

The first order expansion term of Eq. (4.44) yields four terms. Using the Wick's theorem (4.45), the first term of Eq. (4.56) describes a contribution to the full Green's function of the following form:

$$\begin{aligned}
\left(G^{ab}_{\uparrow\uparrow}(x,x')\right)^{(1,1)} &= -\frac{U}{2}\int dx_1 \sum_{\sigma} \left\langle \psi^a_{\uparrow}(x)\left(\bar{\psi}^1_{\sigma}(x_1)\,\bar{\psi}^1_{\bar{\sigma}}(x_1)\,\psi^1_{\bar{\sigma}}(x_1)\,\psi^2_{\sigma}(x_1)\right)\bar{\psi}^b_{\uparrow}(x')\right\rangle \\
&= \frac{U}{2}\int dx_1 \left(\left\langle\psi^a_{\uparrow}\bar{\psi}^1_{\uparrow}\right\rangle\left\langle\psi^1_{\downarrow}\bar{\psi}^1_{\downarrow}\right\rangle\left\langle\psi^2_{\uparrow}\bar{\psi}^b_{\uparrow}\right\rangle + \left\langle\psi^a_{\uparrow}\bar{\psi}^1_{\uparrow}\right\rangle\left\langle\psi^2_{\downarrow}\bar{\psi}^1_{\downarrow}\right\rangle\left\langle\psi^1_{\uparrow}\bar{\psi}^b_{\uparrow}\right\rangle\right) \\
&= i^3\,\frac{U}{2}\int dx_1 \left(G^{a1}_{\uparrow\uparrow}\,G^{11}_{\downarrow\downarrow}\,G^{2b}_{\uparrow\uparrow} + G^{a1}_{\uparrow\uparrow}\,G^{21}_{\downarrow\downarrow}\,G^{1b}_{\uparrow\uparrow}\right) \\
&= -\,i\,\frac{U}{2}\int dx_1 \left(G^{a1}_{\uparrow\uparrow}(x,x_1)\,G^{R}_{\downarrow\downarrow}(x_1,x_1)\,G^{2b}_{\uparrow\uparrow}(x_1,x')\right) \\
&= \int dx_1 \left(G^{a1}_{\uparrow\uparrow}(x,x_1)\,\Sigma^{K}_{\downarrow\downarrow}(x_1,x_1)\,G^{2b}_{\uparrow\uparrow}(x_1,x')\right), \qquad (4.57)
\end{aligned}$$

where the superscript '$(1,1)$' refers to the first term of the first order expansion term. In the second line it was exploited that the two-point correlators are diagonal in spin space, since the interaction does not change the spin. Note that because of this property we will shorten the double spin index of all two-point functions in the following, e.g., $\Sigma_{\uparrow} \equiv \Sigma_{\uparrow\uparrow}$. In the second and third line the space and time variable x_1 was dropped for convenience. Moreover, it was used that $G^{21} = 0$, see Eq. (4.30).

The procedure of Eq. (4.57) is repeated for all terms of the first order expansion term and for both spin configurations of G. Eventually, all first order contributions to the self-energy are found to be

$$\Sigma^{K}_{\sigma}(x,x) = -i\,\frac{U}{2}\left(G^{R}_{\sigma}(x,x) + G^{A}_{\sigma}(x,x)\right) \overset{(4.35)}{=} 0\,, \qquad (4.58)$$

$$\Sigma^{R}_{\sigma}(x,x) = \Sigma^{A}_{\sigma}(x,x) = -i\,\frac{U}{2}\,G^{K}_{\sigma}(x,x)\,. \qquad (4.59)$$

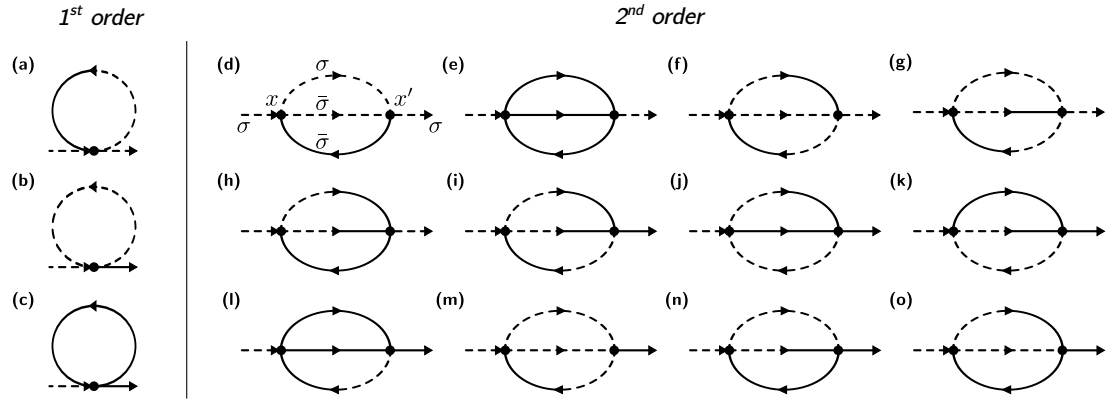

Figure 4.4.: Diagrammatic representation of (a)-(c) first-order and (d)-(o) second-order contributions to the self-energy resulting from the on-site interaction vertices of Eq. (4.56) or Fig. 4.3, respectively. First order: (a) contributes to Σ^R and (b)-(c) are associated with Σ^K, see Eqs. (4.58) and (4.59). Second order: (d)-(h) are parts of Σ^R, while (i)-(o) contribute to Σ^K, see Eqs. (4.60) and (4.61). The corresponding contributions to Σ^A are obtained by using that $\Sigma^A = \Sigma^{R\dagger}$. Note that the spin index assignment as shown in (d) is the same for all second-order contributions.

Diagramatically, Eqs. (4.58) and (4.59) are represented by Fig. 4.4(a)-(c). So the first order correction to the self-energy is seemingly proportional the Keldysh Green's function. Evaluating expression (4.41) at equal times gives $G^K = i(2\langle c^\dagger c\rangle - 1)$. Hence, due to the second term of G^K the self-energy is predicted to yield a constant offset. However, the typical mean-field approximation for Hubbard-type models, $Un_\uparrow n_\downarrow \to U\langle n_\uparrow\rangle n_\downarrow + Un_\uparrow\langle n_\downarrow\rangle$, does not have this additional contribution. So where have we gone wrong? The answer is hidden in the validity of Eq. (4.28): recall that for equal times it holds that $G^{\mathcal{T}} = G^{\widetilde{\mathcal{T}}} = G^{>}$, and, thus, the Keldysh rotation does actually not bring the Green's function into the form of Eq. (4.30) at equal times. Nevertheless, by going back to the Keldysh contour ordered Green's function given by (4.22) we see that the energy offset indeed vanishes when taking the correct properties into account. In the following, we will therefore assume that the energies of the system are simply renormalized by the Hartree corrections in the familiar sense.

2nd order

The total second order contribution to the self-energy is given by the 16 different combinations of the terms of S_{int}. Here, every term is evaluated in the spirit of Eq. (4.57). Using again that $G^{21} = 0$ as well as $G^A(x,x')G^R(x,x') = 0$, one eventually finds 12 different and independent diagrams contributing to the Keldysh or retarded component of the self-energy, respectively. These diagrams are shown in Fig. 4.4. Note that the ones contributing to Σ^A are trivially obtained from $(\Sigma^R)^\dagger$. When translating the diagrams into explicit expressions for the respective parts of the self-energy, the retarded component takes on the form

$$\begin{aligned}\Sigma^R_\sigma(x,x') = -\frac{U^2}{4}\Big[\, & G^A_{\bar\sigma}(x',x)\, G^R_{\bar\sigma}(x,x')\, G^R_\sigma(x,x') + G^A_{\bar\sigma}(x',x)\, G^A_{\bar\sigma}(x,x')\, G^A_\sigma(x,x') \\ & + G^K_{\bar\sigma}(x',x)\, G^R_{\bar\sigma}(x,x')\, G^K_\sigma(x,x') + G^K_{\bar\sigma}(x',x)\, G^K_{\bar\sigma}(x,x')\, G^R_\sigma(x,x') \\ & + G^A_{\bar\sigma}(x',x)\, G^K_{\bar\sigma}(x,x')\, G^K_\sigma(x,x')\Big], \end{aligned} \tag{4.60}$$

and the Keldysh component is given by

$$\begin{aligned}\Sigma^K_\sigma(x,x') = -\frac{U^2}{4}\Big[& G^K_{\bar\sigma}(x',x)\, G^K_{\bar\sigma}(x,x')\, G^K_\sigma(x,x') + G^R_{\bar\sigma}(x',x)\, G^A_{\bar\sigma}(x,x')\, G^K_\sigma(x,x') \\ & + G^R_{\bar\sigma}(x',x)\, G^K_{\bar\sigma}(x,x')\, G^A_\sigma(x,x') + G^K_{\bar\sigma}(x',x)\, G^A_{\bar\sigma}(x,x')\, G^A_\sigma(x,x') \\ & + G^K_{\bar\sigma}(x',x)\, G^R_{\bar\sigma}(x,x')\, G^R_\sigma(x,x') + G^A_{\bar\sigma}(x',x)\, G^K_{\bar\sigma}(x,x')\, G^R_\sigma(x,x') \\ & + G^A_{\bar\sigma}(x',x)\, G^R_{\bar\sigma}(x,x')\, G^K_\sigma(x,x')\Big], \end{aligned} \tag{4.61}$$

where still $\bar\sigma = \downarrow(\uparrow)$ when $\sigma = \uparrow(\downarrow)$. These expressions are simplified further by exploiting the following general identities for retarded and advanced Green's functions:

$$G^R(x',x)G^A(x,x') + G^A(x',x)G^R(x,x') = -(G^R - G^A)(x',x)(G^R - G^A)(x,x') \tag{4.62}$$

as well as

$$\left[G^R(x,x')\right]^2 + \left[G^A(x,x')\right]^2 = \left[(G^R - G^A)(x,x')\right]^2. \tag{4.63}$$

The advantage of expressing all quantities in terms of the difference of retarded and advanced Green's functions will become apparent in Sec. 4.3. In short, the energy representation of $G^R - G^A$ yields a sharply-peaked function for weakly interacting systems. Using the abbreviation $G^{RA} \equiv (G^R - G^A)$ one finally finds

$$\begin{aligned}\Sigma^R_\sigma(x,x') = -\frac{U^2}{4}\Big[& G^A_{\bar\sigma}(x',x)\, G^{RA}_{\bar\sigma}(x,x')\, G^{RA}_\sigma(x,x') + G^A_{\bar\sigma}(x',x)\, G^K_{\bar\sigma}(x,x')\, G^K_\sigma(x,x') \\ & + G^K_{\bar\sigma}(x',x)\, G^R_{\bar\sigma}(x,x')\, G^K_\sigma(x,x') + G^K_{\bar\sigma}(x',x)\, G^K_{\bar\sigma}(x,x')\, G^R_\sigma(x,x')\Big] \end{aligned} \tag{4.64}$$

and

$$\begin{aligned}\Sigma^K_\sigma(x,x') = -\frac{U^2}{4}\Big[& G^K_{\bar\sigma}(x',x)\, G^K_{\bar\sigma}(x,x')\, G^K_\sigma(x,x') + G^K_{\bar\sigma}(x',x)\, G^{RA}_{\bar\sigma}(x,x')\, G^{RA}_\sigma(x,x') \\ & - G^{RA}_{\bar\sigma}(x',x)\, G^{RA}_{\bar\sigma}(x,x')\, G^K_\sigma(x,x') - G^{RA}_{\bar\sigma}(x',x)\, G^K_{\bar\sigma}(x,x')\, G^{RA}_\sigma(x,x')\Big]. \end{aligned} \tag{4.65}$$

Note again that $\Sigma^A = (\Sigma^R)^\dagger$.

Generally, one can extend this discussion to higher-order contributions of the self-energy. Note that all terms at all orders are either calculated in the spirit of Eq. (4.57) or, alternatively, by finding the corresponding diagrams and translating them to explicit expressions as done above. Again, this perturbative approach assumes a small interaction strength U compared to, e.g., the characteristic energy scale J of a Hubbard-type model, see Sec. 2.1. This assumption is also necessary for a semiclassical derivation of the Boltzmann equation, as presented in the next section. Hence, we refrain from calculating higher-order diagrams and focus on the ones given above in the following.

Before continuing with the main agenda we briefly discuss a crucial aspect of the chosen approximation to simplify the self-energy: the way how the perturbation theory was presented assumes that the Green's functions appearing in the diagrams of Fig. 4.4 are in fact of non-interacting nature. The issue with this is that the resulting Dyson equation (4.47) is not a closed equation any more for a selected subset of diagrams. This leads to an uncontrolled method to approximate the Green's function of the system. In order to circumvent this problem we claim that the Green's function is calculated *self-consistently*. This leads to the understanding of the self-energy being a functional of the full interacting Green's function, i.e.,

$$\hat\Sigma \;\to\; \hat\Sigma[\hat G]. \tag{4.66}$$

Indeed, it was shown by Baym and Kadanoff [222] that macroscopic conservation laws are not violated when approximating the Green's function in the correct way. Further, it was also proven by Baym [223] that *conserving approximations* are always guaranteed when the self-energy can be written as

$$\hat{\Sigma}[\hat{G}] = \frac{\delta\hat{\Phi}[\hat{G}]}{\delta\hat{G}}\,, \tag{4.67}$$

where $\hat{\Phi}[\hat{G}]$ describes a (truncated) *Luttinger-Ward functional* [224]. The Luttinger-Ward functional is the sum of all closed, two-particle irreducible diagrams. Examples for conserving approximation schemes are the (self-consistent) Hartree-Fock, second Born or the T-matrix approximation. For an in-depth view on this matter we refer the reader to the references given above as well as to the recent book by Stefanucci and van Leeuwen [225].

Consequently, the above derivation of the first and second order contribution to the self-energy is understood to encode an implicit re-summation of the perturbative expansion of the full Green's function: the propagator lines appearing in Fig. 4.4 ought to be full ones. Finally, we conclude that the equations for the self-energies (4.64) and (4.65) as functions of the interacting Green's function together with the Dyson equation (4.47) and a suitable initial condition define a quantum kinetic equation.

4.3. Semiclassical approximations: deriving the Boltzmann equation

4.3.1. Wigner transformation and Moyal expansion

The quantum kinetic equation (4.52) is an equation that determines the dynamics of the distribution matrix $F(x,x') = F(\mathbf{r},t,\mathbf{r}',t')$. Owing to its two-point character with respect to space and time as well as its associated matrix structure the quantum kinetic equation (4.52) is impossible to solve in most circumstances. However, one might take advantage from a separation of microscopic and macroscopic space and time scales. Assuming that the latter scales are much larger than the former ones allows for a significant simplification of the kinetic equations. In the following, we will present a semiclassical representation of the QKE for ordinary, time-independent systems. To this end, we will introduce the *Wigner transformation* [207, 218]. Note that later (see Ch. 5) we will combine the separation of (time-)scales with the rapid periodic oscillations of a Floquet system.

At first we introduce the Wigner or mixed space-coordinates

$$\bar{\mathbf{r}} = \frac{\mathbf{r}+\mathbf{r}'}{2} \qquad \text{and} \qquad \Delta\mathbf{r} = \mathbf{r}-\mathbf{r}' \tag{4.68}$$

and time variables

$$\bar{t} = \frac{t+t'}{2} \qquad \text{and} \qquad \Delta t = t-t'\,. \tag{4.69}$$

Note that in the following we use sometimes the abbreviated notation $\bar{x} = (\bar{\mathbf{r}},\bar{t})$ indicating the central coordinate and $\Delta x = (\Delta\mathbf{r},\Delta t)$ describing the relative coordinate. One can then express any two-point function, $A(x,x')$, in terms of these variables and perform a

Fourier transformation[5] with respect to the relative coordinate, i.e.,

$$A(\bar{x},p) = \int d\Delta x\; e^{-ip\Delta x}\, A\big(\bar{x}+\tfrac{\Delta x}{2},\bar{x}-\tfrac{\Delta x}{2}\big)\,, \tag{4.70}$$

with the relative momentum $p=(\mathbf{k},\omega)$ and $p\bar{x}=\mathbf{kr}-\omega t$. The associated inverse Wigner transformation is then given by

$$A(x,x') = \int dp\; e^{ip(x-x')}\, A\big(\tfrac{x+x'}{2},p\big)\,, \tag{4.71}$$

where $\int dp = \int d\mathbf{k}/(2\pi)^d \int d\omega/(2\pi)$. Considering the expressions for the Green's functions, see Eqs. (4.64) and (4.65), it is apparent that a Wigner transformation of an algebraic product of the form $A(x,x')=B(x,x')C(x,x')$ is required. Using the definitions of Eqs. (4.70) and (4.71) one finds

$$A(\bar{x},p) = \int dq\; B(\bar{x},p-q)\, C(\bar{x},q)\,. \tag{4.72}$$

In addition, it is interesting how a convolution $A=B\circ C=\int dx_1 B(x,x_1)C(x_1,x')$ transforms. Using again the expressions given by Eqs. (4.70) and (4.71) as well as performing a convenient change of variables eventually yields

$$A(\bar{x},p) = \iint dx_1\, dx_2 \iint dp_1\, dp_2\; e^{i(p_2x_1-p_1x_2)}\, B\big(\bar{x}+\tfrac{x_1}{2},p+p_1\big)\, C\big(\bar{x}+\tfrac{x_2}{2},p+p_2\big)\,. \tag{4.73}$$

One now proceeds by expanding the objects B and C in terms of a Taylor series in the momenta p_1 and p_2. The integrals over the momenta can then be evaluated by using the identity $\int dp\, e^{\pm ipx}p^n = (\mp i)^n\delta^{(n)}(x)$, with $\delta^{(n)}$ denoting the nth derivative of the delta-function. Following this, the integrals over the spatial coordinates are also evaluated. The formal expression finally takes the form

$$A(\bar{x},p) = e^{\frac{i}{2}(\partial_{\bar{x}}^B\partial_p^C-\partial_p^B\partial_{\bar{x}}^C)}\; B(\bar{x},p)\, C(\bar{x},p)\,, \tag{4.74}$$

where the differential operator $\partial^{B(C)}$ acts on two-point function $B\,(C)$ only, and it holds that $\partial_{\bar{x}}\partial_p = \nabla_{\mathbf{r}}\nabla_{\mathbf{k}} - \partial_t\partial_\omega$. Note that more details about the derivation can be found in Sec. 5.3.2, where an analogous expression is derived in a Floquet setting. The expression (4.74) is formally exact and called the *Moyal product*. Every matrix product indicated by '$\circ$' can thus be formally replaced by this Moyal product.

It is now intuitive why a representation in terms of Eq. (4.74) might be desirable: an expansion of the exponential function yields terms with increasing order of derivatives. A physical separation of scales allows to truncate this expansion. This is because under the above assumptions a general two-point function depends only slowly on the central coordinates, i.e., the associated derivatives give small contributions. The most extreme example is given by translationally invariant systems. Here, only the zeroth order expansion term of the Moyal product survives. Generic systems that follow a clear separation of scales are typically already well described by a first order expansion

$$A(\bar{x},p) \approx B(\bar{x},p)\, C(\bar{x},p) + \frac{i}{2}\Big(\partial_{\bar{x}}B(\bar{x},p)\,\partial_p C(\bar{x},p) - \partial_p B(\bar{x},p)\,\partial_{\bar{x}}C(\bar{x},p)\Big)\,, \tag{4.75}$$

where the respective derivative acts on its neighbouring function B,C only. The *Moyal expansion* given by Eq. (4.75) is a powerful tool to simplify the quantum kinetic equation (4.52), provided that a separation of scales is indeed physical reality.

[5] Note that when dealing with spatially periodic lattice systems where spatial coordinates are replaced by discrete lattice sites, $A(x,x')\to A_{ij}$, the Fourier transformation is altered correspondingly. Here, translationally invariant objects, $A_{ij}=A_{i-j}\equiv A_{\Delta j}$, are transformed as $A(k)=\sum_{\Delta j} e^{-ika\Delta j}A_{\Delta j}$ and $A_{\Delta j}=\int_{\mathrm{BZ}}\frac{dk}{(2\pi/a)^d}e^{ika\Delta j}A(k)$, with a being the lattice constant. While we shall leave this aspect aside for now, we will discuss such systems at length in chapter 5.

4.3.2. Kinetic terms and the mass-shell distribution function

By using the approximative expression (4.75) we are finally in a position to proceed with the quantum kinetic equation (4.52). Note again, however, that this procedure decouples micro- from macroscopic scales in a crude way, and is, thus, a *semiclassical* approach. We will elaborate a bit further on the associated consequences in Sec. 4.4.

We continue by considering the general non-interacting form of the inverse retarded and advanced Green's function $G_0^{-1} \equiv \left[G_0^{R/A}\right]^{-1}$, see Eq. (4.36), which Wigner-transforms as

$$G_0^{-1}(x,x') = \delta(x-x')\,(\,i\partial_t - h(x)\,) \quad \xrightarrow{\text{WT}} \quad G_0^{-1}(\bar{x},p) = \omega - \varepsilon_{\mathbf{k}} - V(\bar{x})\,, \tag{4.76}$$

where $h(x)$ is some single-particle Hamiltonian that is decoupled into an energy spectrum part $\varepsilon_{\mathbf{k}}$ and an external potential $V(\bar{x})$. For pedagogical reasons we demand a simplified spectrum at this point. However, one can imagine to have a spectrum that is additionally characterized by other quantum numbers, such as band or spin indices (see above). In fact, we implicitly assumed some kind of diagonalization of $h(x)$ in order to express it (after Wigner transformation) in terms of the single-particle spectrum $\varepsilon_{\mathbf{k}}$. We remark that there is a deep connection between this diagonalization procedure and some Berry phase corrections to the final result. In order to focus on the main results we will ignore this aspect for now, but we will elaborate on it in chapter 5 below.

Finally, substituting Eq. (4.76) into the expression describing the quantum kinetic equation (4.52) yields for the left-hand side

$$\left[\, F \,\circ\, G_0^{-1} \,\right] \xrightarrow{\text{WT}} i\left(\,\partial_{\bar{x}}F(\bar{x},p)\,\partial_p G_0^{-1}(\bar{x},p) - \partial_p F(\bar{x},p)\,\partial_{\bar{x}}G_0^{-1}(\bar{x},p)\,\right) \tag{4.77}$$

$$= i\left(\,-\nabla_{\bar{\mathbf{r}}}F\,\nabla_{\mathbf{k}}\varepsilon_{\mathbf{k}} - \partial_{\bar{t}}F + \nabla_{\mathbf{k}}F\,\nabla_{\bar{\mathbf{r}}}V(\bar{r},\bar{t}) - \partial_\omega F\,\partial_{\bar{t}}V(\bar{r},\bar{t})\,\right), \tag{4.78}$$

where it was used that $\partial_\omega G_0^{-1} = 1$. Again, differentiation is only assumed with respect to neighbouring objects and in the second line we abbreviated the distribution function as $F = F(\bar{x},p)$. Analogously, the right-hand side takes the form

$$\begin{aligned} &\Sigma^K - F\left(\,\Sigma^R - \Sigma^A\,\right) - \frac{i}{2}\left(\partial_{\bar{x}}\Sigma^R\,\partial_p F - \partial_p\Sigma^R\,\partial_{\bar{x}}F - \partial_{\bar{x}}F\,\partial_p\Sigma^A + \partial_p F\,\partial_{\bar{x}}\Sigma^A\,\right) \\ =\;& \Sigma^K - 2i\,F\,\mathrm{Im}(\Sigma^R) - i\,\partial_{\bar{x}}\mathrm{Re}(\Sigma^R)\,\partial_p F + i\,\partial_p\mathrm{Re}(\Sigma^R)\,\partial_{\bar{x}}F\,, \end{aligned} \tag{4.79}$$

where the property $\Sigma^R(\bar{x},p) = \left[\Sigma^A(\bar{x},p)\right]^*$ was used.

Upon equating Eqs. (4.78) and (4.79) the following result eventually emerges:

$$\left(\,(1-\partial_\omega\mathrm{Re}\Sigma^R)\,\partial_t + \partial_t\widetilde{V}\,\partial_\omega + \tilde{\mathbf{v}}_{\mathbf{k}}\,\nabla_{\mathbf{r}} - \nabla_{\mathbf{r}}\widetilde{V}\,\nabla_{\mathbf{k}}\,\right)F = \,I_{\text{coll}}[F]\,. \tag{4.80}$$

Note that we dropped the 'bar' as an indication for central coordinates in favour of notational brevity. Here, all gradient terms have been collected on the left-hand side and the potential, $\widetilde{V} = V + \mathrm{Re}\Sigma^R$, as well as the velocity, $\tilde{\mathbf{v}}_{\mathbf{k}} = \nabla_{\mathbf{k}}(\varepsilon_{\mathbf{k}} + \mathrm{Re}\Sigma^R)$, are renormalized according to the real part of the self-energy. Note that to lowest order these corrections are associated with the Hartree diagrams of Sec. 4.2.2. Moreover, the so-called *collision integral* on the right-hand side is given by

$$I_{\text{coll}}[F] \;=\; i\,\Sigma^K + 2\,F\,\mathrm{Im}(\Sigma^R)\,. \tag{4.81}$$

Eq. (4.80) together with the collision integral (4.81) describes the Wigner transformation of the QKE, which already greatly simplifies all intended calculations. However, the set

of equations for different energies and momenta is still coupled, which makes the problem at hand still difficult to solve. It is, thus, natural to demand yet another simplification scheme. Generally, the choice of this method depends on the properties and details of the system. In the following, we will employ the *quasiparticle approximation* [218]. Within this method we make use of the fact that the considered system is only *weakly interacting*. This property allows the spectral function, $A = i(G^R - G^A)$, to be approximated by non-interacting Green's functions, i.e.,

$$A(\bar{x},p) \approx i\,(G_0^R(\bar{x},p) - G_0^A(\bar{x},p)) = 2\pi\,\delta(\omega - \varepsilon_{\mathbf{k}} - \widetilde{V}(\bar{x}))\,. \tag{4.82}$$

Generally, the spectral function has the property $A > 0$ as well as obeys the normalization condition $\int d\omega/(2\pi)\,A(\omega) = 1$. This allows for an interpretation of A as being a probability distribution [206]. For weakly interacting systems the spectral function is sharply peaked and, thus, can be viewed as describing a well defined quasiparticle. So even if weak interactions are fully taken into account, the δ-function appearing on the right-hand side of Eq. (4.82) is only broadened by the self-energy, $\delta \to \delta_\Sigma$. The width Γ of the generated Lorentzian describes then the inverse lifetime of the quasiparticle, $\tau_{\mathrm{qp}} \sim 1/\Gamma$. Finally, for the assumption of Eq. (4.82) to hold, we require that the energy scale $\delta\omega$ on which individual objects vary (like the distribution function F, for instance) is much larger than the width of the spectral function, i.e., $\delta\omega \gg \Gamma$.

Furthermore, we consider a Wigner transformation of the Keldysh Green's function to lowest order. One observes that by construction of Eq. (4.37) the distribution function $F(\bar{x},p)$ steadily shows up in a product with the spectral function $A(\bar{x},p)$, i.e., $G^K = F(G^R - G^A) = -iFA$. Hence, one can formally restrict the energy argument of F to the position of the quasiparticle peak by means of energy integration. To this end, we introduce the *mass-shell* distribution function

$$\widetilde{F}(\mathbf{r},t,\mathbf{k}) \equiv \int d\omega\; F(\mathbf{r},t,\mathbf{k},\omega)\,\delta(\omega - \varepsilon_{\mathbf{k}} - \widetilde{V}(\bar{x})) \approx \int \frac{d\omega}{2\pi}\; F(\mathbf{r},t,\mathbf{k},\omega)\,A(\mathbf{r},t,\mathbf{k},\omega)\,. \tag{4.83}$$

By using the expression for the Keldysh Green's function the mass-shell distribution function is reformulated to read as

$$\widetilde{F}(\mathbf{r},t,\mathbf{k}) \approx i\int \frac{d\omega}{2\pi}\; G^K(\mathbf{r},t,\mathbf{k},\omega) = i\,G^K(\mathbf{r},\mathbf{k},t,t) \overset{(4.41)}{=} 1 - 2\,n_{\mathbf{k}}(\mathbf{r},t)\,, \tag{4.84}$$

where $n_{\mathbf{k}}$ describes the fermionic occupation number. Let us stress again that writing the mass-shell distribution function in terms of the equal time Keldysh Green's function is only an approximation that is controlled by the condition $\delta\omega\,\tau_{\mathrm{qp}} \gg 1$.

The kinetic equations for different energies are decoupled by multiplying Eq. (4.80) with the spectral function (4.82) followed by an integration over energies. If in addition it is assumed that Eq. (4.84) holds, a closed kinetic equation for the fermionic occupation number n is deduced of the form[6]

$$\Big(\partial_t + \widetilde{\mathbf{v}}_{\mathbf{k}}\,\nabla_{\mathbf{r}} - \nabla_{\mathbf{r}}\widetilde{V}\,\nabla_{\mathbf{k}}\Big)\,n_{\mathbf{k}}(\mathbf{r},t) = I_{\mathrm{coll}}[n_{\mathbf{k}}(\mathbf{r},t)]\,, \tag{4.85}$$

where we modified the collision integral such that $I_{\mathrm{coll}}[n] = -\frac{1}{2}I_{\mathrm{coll}}[\widetilde{F}]$. Note also the absence of the $\partial_t V \partial_\omega n$ term on the left-hand side of Eq. (4.85) as a consequence of the on-shell projection procedure.

[6]Note that we set the inverse of the quasiparticle weight $\widetilde{Z}^{-1} = 1 - \partial_\omega \mathrm{Re}\Sigma^R|_{\omega=\varepsilon-\tilde{V}}$ to unity for convenience, i.e., $\widetilde{Z}^{-1}\partial_t \to \partial_t$.

Indeed, Eq. (4.85) coincides with the celebrated *Boltzmann equation* [217]. We conclude by restating a couple of remarks: first, while it was the aim to keep the derivation of Eq. (4.85) as simple as possible, the result is straightforwardly extended to potentially more complex systems that are characterized by band and spin indices, i.e., $n_{\mathbf{k}}(\mathbf{r},t) \to n_{\mathbf{k},\alpha,\sigma}(\mathbf{r},t)$. Second, the velocity $\mathbf{v_k}$ and force $\mathbf{F_k} = -\nabla_{\mathbf{r}} V$ appearing on the left hand side of Eq. (4.85) experience corrections due to possible Berry curvatures. Formally, this was derived recently by Wickles and Belzig [226]. A discussion for Floquet systems is presented in Sec. 5.4.2. Lastly, note that considering only diagonal, on-shell contributions implies that Boltzmann-type equations cannot describe coherent quantum oscillations. The resulting equations are therefore only valid on time scales longer than the decay time of such oscillations.

4.3.3. The collision integral

The first step in calculating the collision integral (4.81) is to determine the self-energies in their respective Wigner-transformed forms. As mentioned above, the first-order diagrams are purely real, and, thus, only renormalise the quantities on the left-hand side of the Boltzmann equation (4.85). We assume that this is implicitly done and focus for the collision integral on the second-order contributions, see Eqs. (4.64) and (4.65). Note again that in the end we look for a lowest order approximation to the initial QKE. The Green's functions that appear in the expressions of the self-energies are self-consistently determined by the Dyson equation (4.47), which encodes a Moyal product. So determining the collision integral to lowest order also allows to determine the Green's functions within a zeroth-order Moyal expansion. Furthermore, since interactions are weak and the second order self-energy contributions are already $\propto U^2$, we refrain from considering further self-energy corrections to the Green's functions appearing in Σ. Consequently, it is sufficient to evaluate the non-interacting Green's functions in order to calculate the collision integral to lowest order.

We assume for now that the fermionic system is spin-less, but still has short-range interactions of type (4.53). We then consider the Wigner transformations of objects that appear in Eqs. (4.64) and (4.65), i.e.,

$$(G_0^R - G_0^A)(\bar{x},p) = -2\pi i\,\delta(\omega-\varepsilon_{\mathbf{k}}) \quad \text{and} \quad G_0^K(\bar{x},p) = -2\pi i\,\widetilde{F}(\mathbf{k})\,\delta(\omega-\varepsilon_{\mathbf{k}})\,, \tag{4.86}$$

where we dropped central coordinates for convenience and assumed that the energies are renormalized to the external potential as well as to the real part of the (retarded) self-energy, Eq. 4.82. With the help of expressions (4.86) and by using the identity (4.72) to deal with the Wigner transformation of the product of two two-point functions, the respective self-energies can eventually be found in their Wigner representation, $\Sigma(\mathbf{k},\omega)$. Similar to above, we want to find the associated on-shell expressions. So multiplying with the (non-interacting) spectral function plus a subsequent integration over energies yield the desired result, $\widetilde{\Sigma} = \int d\omega/(2\pi)\, A\,\Sigma$.

After putting all elements together and evaluating trivial integration over delta-functions the Keldysh component of the self-energy takes the form (cf. Sec. 5.4)

$$\begin{aligned}\widetilde{\Sigma}^K(\mathbf{k}) = &-\frac{\pi i U^2}{2}\int\frac{d\mathbf{p}}{(2\pi)^d}\int\frac{d\mathbf{q}}{(2\pi)^d}\;\delta(\varepsilon_{\mathbf{k}}+\varepsilon_{\mathbf{p}-\mathbf{q}}+\varepsilon_{\mathbf{p}}+\varepsilon_{\mathbf{k}-\mathbf{q}}) \\ &\times\Big[\widetilde{F}(\mathbf{k}-\mathbf{q})\widetilde{F}(\mathbf{p}-\mathbf{q})\widetilde{F}(\mathbf{p}) + \widetilde{F}(\mathbf{p}-\mathbf{q}) - \widetilde{F}(\mathbf{p}) - \widetilde{F}(\mathbf{k}-\mathbf{q})\Big]\,,\end{aligned} \tag{4.87}$$

and the imaginary part of the retarded component reads as

$$\begin{aligned}\mathrm{Im}[\widetilde{\Sigma}^R(\mathbf{k})] = \frac{\pi U^2}{4}\int\frac{d\mathbf{p}}{(2\pi)^d}\int\frac{d\mathbf{q}}{(2\pi)^d}\;\delta(\varepsilon_{\mathbf{k}}+\varepsilon_{\mathbf{p}-\mathbf{q}}+\varepsilon_{\mathbf{p}}+\varepsilon_{\mathbf{k}-\mathbf{q}}) \\ \times\left[\widetilde{F}(\mathbf{k}-\mathbf{q})\widetilde{F}(\mathbf{p})-\widetilde{F}(\mathbf{p}-\mathbf{q})\widetilde{F}(\mathbf{p})-\widetilde{F}(\mathbf{k}-\mathbf{q})\widetilde{F}(\mathbf{p}-\mathbf{q})+1\right].\end{aligned} \tag{4.88}$$

One can now compute the collision integral for short-ranged particle-particle interactions by substituting Eqs. (4.87) and (4.88) into the expression for $I_{\mathrm{coll}}[\widetilde{F}]$, see Eq. (4.81). Finally, using further that $I_{\mathrm{coll}}[n]=-\frac{1}{2}I_{\mathrm{coll}}[\widetilde{F}]$ and $\widetilde{F}=1-2n$ the final result is obtained as

$$\begin{aligned}I_{\mathrm{coll}}[n_{\mathbf{k}}] = 2\pi U^2\int\frac{d\mathbf{q}_1}{(2\pi)^d}\int\frac{d\mathbf{q}_2}{(2\pi)^d}\int d\mathbf{q}_3\;\delta(\mathbf{k}+\mathbf{q}_1-\mathbf{q}_2-\mathbf{q}_3)\,\delta(\varepsilon_{\mathbf{k}}+\varepsilon_{\mathbf{q}_1}+\varepsilon_{\mathbf{q}_2}+\varepsilon_{\mathbf{q}_3}) \\ \times\left[n_{\mathbf{q}_2}n_{\mathbf{q}_3}(1-n_{\mathbf{k}})(1-n_{\mathbf{q}_1})-n_{\mathbf{k}}n_{\mathbf{q}_1}(1-n_{\mathbf{q}_2})(1-n_{\mathbf{q}_3})\right].\end{aligned} \tag{4.89}$$

In order to acquire this expression an additional momentum variable was introduced and one had to add and subtract the term $n_{\mathbf{k}}n_{\mathbf{q}_1}n_{\mathbf{q}_2}n_{\mathbf{q}_3}$. Note also that central coordinates are still suppressed and that the collision integral is indeed a functional of $n_{\mathbf{k}}(\mathbf{r},t)$.

The form of the collision integral given by Eq. (4.89) concludes the derivation of the semiclassical Boltzmann equation from the initial quantum kinetic equation (4.52). The δ-functions appearing in Eq. 4.89 guarantee momentum and energy conservation, respectively. The expression in the parentheses corresponds to a combination of in- an outgoing scattering channels. Here, a factor of $(1-n_{\mathbf{k}})$ ensures that scattering into an occupied state is suppressed. This is, of course, a manifestation of the Pauli principle. In general, the matrix element weighting a scattering process is not constant, but rather depends on the participating momentum states. In fact, one could consider a semiclassical approximation scheme that goes beyond lowest order, but its only effect is the change of this matrix element. An example is the *T-matrix* approach [227] in which the full two-particle scattering problem determines the matrix elements of the collision integral (4.89).

4.4. General remarks on kinetic equations and transport

As seen above, in this chapter we have deliberately put emphasis on the systematic *derivation* of the Boltzmann equation (4.85). The reason for this choice is twofold: first, we will strongly benefit from a clear understanding of the basic notations and methods when deriving a Floquet version of the Boltzmann equation in the next chapter, and, second, it gives us a good intuitive understanding for applied (semiclassical) approximations and its limitations. In particular, this could be valuable for future prospects where one might be interested in extending the formalism to regimes of different approximations.

As well known, the Boltzmann formalism naturally gives rise to the description of macroscopic transport theory. While aspects of the latter will also be highly relevant for the work of this thesis, see Ch. 7, we refrain from giving a more in-depth discussion on transport theory at this point. Instead, we refer the reader to comprehensive texts in the literature, e.g., to the book by Ziman [217]. In this section, we only briefly present some core ideas about the semiclassical Boltzmann formalism and associated transport theory as well as comment on some general aspects of (quantum) kinetic equations. Later, in Ch. 7, we will in detail present an earmarked transport formalism.

Phenomenological interpretation of the Boltzmann equation Having obtained a semiclassical approximation to the full quantum kinetic equation we connect this Boltzmann

equation to the phenomenological expression of Eq. (4.1). Here, we identify

$$\dot{n}_{\mathbf{k}}\big|_{\text{drift}} = -\mathbf{v}_{\mathbf{k}}\,\nabla_{\mathbf{r}} n_{\mathbf{k}}\,, \qquad \dot{n}_{k}\big|_{\text{field}} = -\mathbf{F}_{\mathbf{k}}\,\nabla_{\mathbf{k}} n_{\mathbf{k}}\,, \qquad \dot{n}_{k}\big|_{\text{scatt}} = I_{\text{coll}}[n_{\mathbf{k}}]\,. \tag{4.90}$$

At first sight individual terms indeed appear as if purely deduced from phenomenological arguments [217], i.e., gradients in spatial profiles cause drifts, external forces evoke changes in the momentum distribution and the collision of particles can give rise to a scattering dependent change of the distribution function.

However, we stress that the version of the kinetic equation which is approximated from a full quantum theory, see Eq. (4.85), is indeed more powerful in the sense that it knows naturally about additional corrections from Berry phases and interaction effects. This is, for instance, crucial in situation where the dynamics of the system is fully described by quasiparticles obeying strong energy renormalisations such as in the Landau Fermi liquid theory [228]. Here, it is crucial to keep track of the energy corrections in order to obtain a contribution due to a 'drag' or 'backflow' effect. Note that this effect is embedded in the structure of the spectral function of the system, or likewise in the self-energy, and therefore encoded in Eq. (4.85) but *not* in the phenomenological version of Eq. (4.1). The key message here is that despite being powerful descriptions, Boltzmann equations can indeed miss out on crucial details of the underlying full interacting and quantum mechanical system. In fact, later in Ch. 7 we encounter a scenario where the results from a pure Boltzmann treatment are incomplete and need to be modified *a posteriori*.

We also stress once more that while the Boltzmann equation is a powerful tool describing non-equilibrium dynamics and being successful in, e.g., predicting conductivities of metals, it still remains a semiclassical approximations with severe limitations. While we discussed the main limitations related to interaction strengths above, we note that the validity might also be restricted by dimensional arguments [229].

Equilibration and steady states The scattering term or collision integral, see Eq. (4.89), typically encodes a high level of complexity in the Boltzmann equation in the sense that it renders an integro-differential equation. However, there is a simple situation - *equilibrium* - which is defined by $I_{\text{coll}}[n^0_{\mathbf{k}}] = 0$ and for which we denote $n_{\mathbf{k}} = n^0_{\mathbf{k}}$. This relation is a consequence of the principle of detailed balance [217]. Additionally, it must obviously also be a direct consequence of the Boltzmann equation itself, since this is the only scenario allowed in the absence of external fields. In fact, for the example of having an atomic cloud confined to a parabolic potential, equilibrium is obtained by a gradient in the chemical potential counteracting the non-vanishing external linear force, cf. Ch. 7.

Another characteristic situation predicted by the Boltzmann equation is the case where the time derivative of the occupation function vanishes, but both fields and collision integral remain finite. This situation is called *steady state*.

Transport Assuming that the Boltzmann equation could be solved, i.e., the distributions functions are available for all momenta $\mathbf{k}$ (and possibly other quantum numbers), one can calculate the associated particle and energy current densities. To this end, one defines (cf. Sec. 3.2.2) [217]

$$\mathbf{j}_n(\mathbf{r},t) = \int \frac{d\mathbf{k}}{(2\pi)^d}\; \mathbf{v}_{\mathbf{k}}\, n_{\mathbf{k}}(\mathbf{r},t) \qquad \text{and} \qquad \mathbf{j}_e(\mathbf{r},t) = \int \frac{d\mathbf{k}}{(2\pi)^d}\; \mathbf{v}_{\mathbf{k}}\, \varepsilon_{\mathbf{k}}\, n_{\mathbf{k}}(\mathbf{r},t)\,, \tag{4.91}$$

where $(2\pi)^d$ indicates the corresponding volume of the Brillouin zone and we set $e = 1$. The expressions of Eq. (4.91) can then be used to obtain macroscopic transport coefficients.

For instance, the electrical conductivity σ_n can be obtained from Ohm's law (cf. Eq. 7.28)

$$\mathbf{j}_n = \sigma_n \mathbf{E} \, . \tag{4.92}$$

Techniques to approximate the Boltzmann equation It is, however, only rarely possible to solve the Boltzmann equation exactly due to its integro-differential structure. Hence, if one wants to make progress and quantitatively determine, e.g., conductivities, further approximation schemes need to be applied. The crudest simplification goes by the name 'relaxation time approximation' and approximates the collision integral effectively by a single parameter in terms of a scattering rate τ [217]. At the same time, it is assumed that the full occupation functions only differ marginally from corresponding equilibrium solution. Then, the collision integral can be approximated by $I_{\text{coll}} \approx -(n_{\mathbf{k}} - n^0_{\mathbf{k}})/\tau$.

The next better approximation captures the characteristics of the collision integral more seriously, but still relies on small deviations from equilibrium. Since scattering always drives the system back into equilibrium, one can safely linearise the collision integral in $\delta n_{\mathbf{k}}$, with $\delta n_{\mathbf{k}} = n_{\mathbf{k}} - n^0_{\mathbf{k}}$. By doing so, one obtains the *linearised Boltzmann equation*, which has the huge advantage of not being an integro-differential equation any more, but simply an integral equation. This equation is then much easier to solve and eases numerical efforts tremendously. One common approach to obtain information from the linearised Boltzmann equation is the 'variational ansatz'. Essentially, this approach reduces the problem to the momentum channels which deviate from equilibrium most. For more information about this technique see Refs. [217, 230]. Under some circumstance, the linearised Boltzmann equation can even be fully solved. An example for such an approach is given in Ch. 7 of this thesis.

Still, particularly for inhomogeneous systems solving not just the collision integral within some approximation but the full (linearised) Boltzmann equation can remain a formidable task. One further route can be to reduce the Boltzmann equation to hydrodynamic or diffusion equations. These equations then do not describe the dynamics of individual occupation functions any more, but rather determine the dynamical behaviour of conserved quantities of the system. This method will be key in respective quantitative calculations in Ch. 7. Again, more details about general aspects of these approximation schemes can be found, e.g., in Refs. [217] and [230].

Reversibility of kinetic equations As seen above, a fundamental aspect of semiclassical kinetic equations is the description of equilibration. This behaviour is fundamentally linked to the intrinsic irreversibility of the Boltzmann equation. In contrast, a fundamental property of many quantum systems *is* the presence of time reversal symmetry. In fact, it was recently shown analytically [231] that also associated quantum kinetic equations can still fulfil this symmetry. By embedding time reversal symmetry with the help of an explicit anti-unitary transformation, $H = THT^{-1}$ (with T being the time reversal, anti-unitary operator and H describes the many-particle Hamiltonian, cf. Eq. 4.42), one can demonstrate [231] that all many-particle approximations preserve time reversal symmetry, if self-energies can be written in a Φ-derivable way, i.e., for all conserving approximations (see above). We therefore stress that it is solely the projection onto on-shell processes that breaks time-reversal symmetry and not the approximations to the self-energy.

Solving quantum kinetic equations numerically Lastly, we make a remark on the practicability of the full quantum theory. We recall that the quantum kinetic equation (4.52) is an exact description of the interacting many-body system at hand. As discussed above,

though, due to its matrix structure and the fact that self-energies need to be computed self-consistently, solving the QKE for arbitrary systems and times is practically impossible. Nevertheless, using the 'nonequilibrium Green's function (NEGF) method' [232] indeed allows for finding numerical solutions for finite times. Being related to the operator formalism by Kadanoff and Baym [214], the NEGF is a variant of the QKE in the sense that it is an explicit equation of motion for Green's functions. Here, the full information about the system is encoded via a certain hierarchy of equations. Practically, this hierarchy needs to be truncated, which can be done by introducing a self-energy approximation scheme respecting conserving approximations (see above). Details about the NEGF method can be found in Ref. [232] and reference therein. Recently, the NEGF method has been successfully used to numerically describe systems from very different fields of physics. Examples include the dynamics of strongly correlated fermions [233], the laser excitation of small atoms [234], the analysis of nuclear collisions [235], strong laser plasma interactions [236] and many others. Most recently, one has also seen an increasing interest in the generalized Kadanov-Baym ansatz (GKBA) [237], which is a method related to the NEGF but numerically less costly.

5. The Floquet-Boltzmann equation

In this chapter, we finally return to the discussion of Floquet systems. However, in contrast to part I of this thesis, where we dealt with non-interacting Floquet systems, we now include the presence of interactions and describe the system by a many-particle Hamiltonian of the form

$$H = H^0(t) + H^{\text{int}}\,, \qquad \text{with} \qquad H^0(t+T_0) \approx H^0(t) \tag{5.1}$$

being approximately periodic and H^{int} (H^0) describes the (non-)interacting part of the Hamiltonian. Here, the time-periodic property results from the external drive, as seen above, but we now also allow for an additional variation on a time-scale τ_{slow} much longer compared to T_0. This separation of time-scales, $\tau_{\text{slow}} \gg T_0$, together with the assumption of having only weak interactions in the system marks the backbone of the theory discussed in this chapter. Motivated by experimental ultracold atom realisations, see Sec. 2.1, we choose non-interacting *fermionic* lattice models paired with a particle-particle interaction mechanism as the basis of our theoretical description.

Starting from the Keldysh approach, see Ch. 4, we develop a formalism, the *Floquet-Boltzmann equation* [238], to describe the dynamics and the scattering of quasiparticles in such systems. Here, periodic oscillations occurring on a time scale $T_0 = 2\pi/\Omega$ are treated using the Floquet formalism of Sec. 2.2 and quasiparticles are defined as eigenstates of a non-interacting Floquet Hamiltonian. The dynamics on much longer time scales, however, is modelled by a Boltzmann equation which describes the semiclassical dynamics of Floquet quasiparticles and their scattering processes. Most importantly, since in these circumstances the energy is conserved only modulo $\hbar\Omega$, the formalism supports a heating up of the interacting system in the long-time limit.

In other words, this chapter will deal with the temporal properties of an interacting driven system and is constructed in the following way. First, we will give a general introduction to interacting Floquet systems, where we will elaborate on their characteristics and give various examples. We then start to develop our semiclassical formalism. To this end, we present a few definitions that concern two-point functions of systems that are perfectly periodic in time. In the following, we introduce how the Wigner transformation and Moyal product, see Sec. 4.3, can be extended to a Floquet version of theirs and what conditions need to be fulfilled to guarantee their validity. In the last step, we run a semiclassical approximation protocol and eventually derive the Floquet-Boltzmann equation for fermionic systems. Since many steps are structurally similar as in Ch. 4, we will focus in this chapter on aspects that are unique to the Floquet character.

5.1. An introduction to interacting Floquet systems

In the first part of this thesis, we discussed the capabilities and advantages of periodically driven non-interacting quantum systems. In particular, we expressed the huge potential of Floquet systems in the spirit of quantum simulators. We explicitly showed and gave examples of how a (many-body) quantum system equipped with a periodic drive can exhibit a broad range of exotic behaviour and even realise novel states of matter. Here,

the essence being the formulation of an effective static Hamiltonian describing the long-term physics of the system at hand. However, it can be shown [31] that this description will eventually break down, if the quantum system is characterized by *interactions*. Of course, if a system is interacting, its complexity - particularly regarding an appropriate theoretical description - is considerably enhanced. As discussed above, non-interacting Floquet systems have moved into the focus of research only over the last two decades. Hence, also interacting periodically driven systems have received only little attention until recently.

Nevertheless, since all experimental systems are ultimately interacting - either inherently or with an environment - successful and stable Floquet engineering requires a good understanding of the role of these interactions. One peculiar feature of such interacting Floquet systems becomes immediately apparent: energy is generally *not* conserved; only modulo the driving frequency Ω for monochromatically driven systems. Most importantly, one can expect that in the long-time limit, $t \to \infty$, a generic interacting Floquet system approaches the state with the highest entropy allowed by the remaining conservation laws [239]. For closed systems, it is thus believed that generic interacting Floquet systems eventually approach an *infinite temperature* state [31, 32, 205, 240]. One way to picture this behaviour is in terms of a circular ensemble of the random matrix theory, which can be interpreted as such an infinite temperature state [31]. Another approach is the explanation in terms of the eigenstate thermalization hypothesis (ETH) [241]. Here, one considers the pure *many-particle* state $|\Psi(t)\rangle$ and the associated time-evolution of the expectation value $O(t) = \langle\Psi(t)|\hat{O}|\Psi(t)\rangle$ of some observable $\hat{O}$. Decomposing the quantum state into Floquet eigenstates (cf. Eq. (2.29)) allows to write the latter quantity as

$$O(t) = \sum_{\nu,\nu'} c_\nu^* c_{\nu'}\, e^{i(\varepsilon_\nu - \varepsilon_{\nu'})t} \left\langle \phi_\nu(t)|\hat{O}|\phi_{\nu'}(t)\right\rangle \overset{t\to\infty}{\simeq} \sum_\nu |c_\nu|^2 \left\langle \phi_\nu(t)|\hat{O}|\phi_\nu(t)\right\rangle , \tag{5.2}$$

where the relaxation to a diagonal Floquet ensamble is expected in the long-term limit due to destructive interference in time [242]. In the spirit of eigenstate thermalization, it is conjectured that all many-body Floquet states appearing in Eq. (5.2) yield the same infinite-temperature expectation values $\langle\phi_\nu(t)|\hat{O}|\phi_\nu(t)\rangle \simeq O$ independent of ν [17, 32]. In short, in order to compute statistically the properties of many-body Floquet states, these states need to be formed by the hybridization of many eigenstates with different mean energies, since energy is not conserved. All infinite temperature states are trivial in the sense that they are described by a density matrix which is given by the identity matrix, expressing the fact that all states contribute with equal likelihood. At the same time, all interesting and novel aspects of Floquet systems are washed out in this $T \to \infty$ limit. In general, there are three possible routes to avoid this situation of having all correlations vanished due to heating: one constrains the system in such a way that it will fundamentally change its long-time behaviour, one tries to delay the thermalization at an infinite temperature by fine-tuning the system or one cools the system as much as it heats up.

One possible robust solution for the former aspect is provided by *many-body localisation* (MBL) [243]. Here, the addition of sufficiently strong disorder to an interacting, ergodic system leads to vanishing transport. Indeed, recent studies [129, 244–248] have shown that even in the presence of periodic driving the property of many-body localisation does not necessarily vanish. The ETH argument from above does therefore not apply, and the infinite temperature state is avoided. In fact, it was even suggested [129] that Floquet systems might be the ideal test grounds for studying MBL phases due to their strong distinction to thermal, i.e., infinite temperature phases. Another idea is to provoke the emergence

of many-body localization by driving a previously delocalized static system [130]. Experimentally, the emergence of a many-body localised phase in a periodically driven setting was investigated only recently by means of ultracold atoms in optical lattices by the Bloch group [16].

Another approach to avoid the infinite temperature fate of an interacting Floquet system is to impose additional constraints on the entropy increase mentioned above. Such a realisation is given by a Floquet-integrable system [249], which offers conserved quantities even in the presence of driving [239]. The result is a state synchronised with the drive that has maximal entropy constrained by the conserved quantities of the integrable system. Hence, the system does not equilibrate into the infinite temperature state, but is rather described by a *Floquet generalized Gibbs ensemble* [239, 250, 251] (in analogy to the generalized Gibbs ensemble of static systems [252]). Generally, the interplay of integrable models and periodic driving does not only prevent heating, but can lead to interesting phenomena itself, such as strong pumping effects [253]. A third possibility to avoid infinite temperatures in an interacting Floquet system is the presence of a cooling mechanism. Such mechanism can, e.g., either be caused by emitting radiation, or by an external bath [254, 255]. While general cold atomic systems are inherently closed, cooling mechanisms might be naturally available in conventional condensed matter systems due to the coupling to phonons [254, 256] or by means of cryostats.

Nevertheless, even if the ultimate fate of producing an infinite temperature state in the long-term cannot be avoided, one can aim for tuning the system in such a way that for experimental relevant time scales strong heating is suppressed. Since such Floquet systems might still be largely characterized by its interactions, one interprets this regime as a form of *prethermalization*. For example, consider a Floquet system being subject to a quantum quench. The prethermal regime then represents the time scale on which the system was able to relax to an equilibrium-like state *without* having experienced too much heating. Since this regime promisingly combines the notion of interaction effects with Floquet engineering of novel and exotic phenomena, it has recently been subject to numerous theoretical studies [92, 257–262]. One particular route to suppress heating effects in this context is to employ driving frequencies that are large compared to all other microscopic time scales [79, 80, 263–265].

Besides understanding and characterizing the different limits and regimes of interacting Floquet systems, one naturally also desires to investigate specifically designed models and explicit realisations of such Floquet systems. Most of the associated studies have been conducted only very recently and range from investigating quench dynamics in Floquet systems [266] over Floquet fractional Chern insulators [124] to the Floquet realization of one-dimensional anyons in optical lattices [267]. It was further suggested [268] that periodic driving can be used to change the interparticle interactions from repulsive to attractive, leading to a simulation of an effectively attractive Hubbard model with a temperature below the superconducting transition temperature of the equilibrium system. Moreover, in Refs. [269, 270], the stability of Bose-Einstein condensates in periodically driven systems was studied, and general transport properties through leads [254, 271] and of a 2D electron gas [272] in a Floquet setting were investigated. Further examples are recent studies of periodically driven quantum dots yielding strong renormalization effects [273] or revealing two-channel Kondo physics when coupled to metallic leads [274]. In addition, aspects of interacting Floquet topological insulators were analysed including the effect of dissipation [120, 275, 276]. Along these lines, transport signatures in topological systems coupled to time-periodic fields were recently studied [277]. Generally, non-equilibrium steady states in the context of coupling a Floquet system to an external bath have been

identified and analysed [278, 279]. Also, exotic states such as chiral quasisteady states in periodically driven many-body systems have been found [92]. Most recently, the effect of driving-enhanced superconductivity was thoroughly studied [256, 280]. Another fascinating realisation of interacting periodically driven systems are Floquet time crystals [128, 281], which are associated with a spontaneous breaking of the discrete time translational symmetry.

While most of these studies regarding interactions in periodically driven systems are of theoretical nature, also experimental works have recently started to investigate the consequences of such interactions in a controlled and systematic way. At first, this was mostly done by building on priorly achieved non-interacting Floquet realisations [23, 110, 282]. However, there also exist experiments that are specifically designed for studying interacting Floquet systems [16, 145].

Since finding an appropriate theoretical description of an interacting Floquet system is generally a demanding task, there are various techniques of both numerical and analytical form to deal with such systems under specifically given circumstances. For instance, in situations where interactions can be viewed as perturbations, one can establish a 'Floquet Fermi golden rule' [115,283,284] estimating the rates of Floquet scattering events. Another fruitful approach is a formalism that merges the notion of Floquet with dynamical mean field theory (DMFT) [285]. This allows, for example, to study correlated electron systems that are periodically driven out of equilibrium. A general overview about non-equilibrium DMFT including its Floquet version can be found in Ref. [286] (and references within). Furthermore, a Schrieffer-Wolff transformation for periodically driven systems was introduced dealing with strongly interacting Fermi-Hubbard models [287]. More recently, even functional renormalization group (FRG) techniques were applied in Floquet space [288] and density-matrix renormalization group (DMRG) studies of many-body localization in Floquet eigenstates were presented [289]. Most prominently, a non-equilibrium transport formalism was established for a Floquet setting [114, 115, 256, 262, 277, 278] by using associated Green's functions [90, 91] (see also below).

Our approach builds on the concept of deriving a kinetic equation, the *Floquet-Boltzmann equation*, which can be used to describe the dynamics of weakly interacting Floquet systems. As shown in chapter 4, such kinetic equations can be found from a semiclassical approximation of a full quantum field theoretical description. Here, however, the question emerges of how to combine the required separation of these time scales with the fast periodic drive of the Floquet system. We will resolve this issue by decoupling the fast oscillations from the slow variations by means of Floquet theory that was presented in Sec. 2.2. Note that a similar semiclassical kinetic equation was also derived for a different context based on an equation-of-motion approach in a recent paper of Seetharam *et al.* [254].

5.2. Floquet definitions for many-body objects

Before developing the right tools to derive the Floquet-Boltzmann equation the non-interacting, but time-dependent part of the Hamiltonian, $H^0(t) = \sum H_n^0(t) e^{-i\Omega n t}$, shall be considered. Here, the Fourier mode of the Hamiltonian, $H_n^0(t)$, varies only on time scales $\tau_{\text{slow}} \gg T_0$, where τ_{slow} is set either by the variation of some external parameter or by intrinsic heating mechanisms[1], and T_0 is the driving period. As an approximation to the

[1] Note that we intrinsically assume to absorb all possible Hartree-Fock corrections into the non-interacting part of the Hamiltonian by an according renormalisation of the single-particle energies.

relation (5.1), we assume that the Hamiltonian has the property

$$H^0_{t_0}(t+T_0) = H^0_{t_0}(t) \tag{5.3}$$

for times t close to (set by τ_{slow}) some reference time t_0. The non-interacting part of the Hamiltonian can then be written in its second quantised form as follows

$$H^0_{t_0}(t) = \sum_{n,i,j} \left[h^0_n(t_0)\right]_{ij} c_i^\dagger c_j \, e^{-in\Omega t}\,, \tag{5.4}$$

where $h^0(t)$ describes the single-particle Hamiltonian expressed in first quantisation language. Such time-periodic, non-interacting Hamiltonians were discussed extensively in Sec. 2.2 with the focus being on the single-particle description. Using conventions which were introduced in Sec. 2.2 the Floquet Hamiltonian associated with (5.4) is given by

$$H^F_{t_0}(t) = H^0_{t_0}(t) - i\partial_t \qquad \text{and} \qquad H^F_{t_0,nm} = h^0_{n-m}(t_0) - n\Omega\,\delta_{nm}\,\mathbb{1} \tag{5.5}$$

is its matrix representation in the extended Hilbert space $\mathcal{F}$. Note again that we consider mainly those Hamiltonians that describe an underlying spatial lattice structure.

In general, there are two strategies how periodic driving can be incorporated in the description of many-body systems. One option is to already formulate the action, see Eq. (4.56), in Floquet language. Another approach is to use known results from standard descriptions, as seen in the previous section, and apply an appropriate transformation to the respective objects. In this section we will build on the latter approach. In doing so, we will extend the single-particle Floquet formalism of Sec. 2.2 to definitions that allow for a Floquet representation of two-point objects that are associated with the quantum field formalism shown in Ch. 4, such as Green's functions.

5.2.1. Floquet transformation of two-point functions

We start by considering a general two-point function $A(t,t')$. Note that we restrict the arguments of the function A to the time variables only. So the entire discussion within this section will deal with the time coordinates only, since the spatial treatment remains largely identical to the one presented in Ch. 4. Due to the assumed perfect temporal periodicity, see Eq. (5.3), the two-point functions are also periodic, but under a simultaneous shift of both time arguments by T_0, i.e.,

$$A(t+T_0, t'+T_0) = A(t,t')\,. \tag{5.6}$$

Next, one can formally express A in terms of its Fourier decomposition. The two-point function is then written as

$$A(t_1,t_2) = \int_{-\infty}^{\infty} \frac{d\omega_1}{2\pi} \int_{-\infty}^{\infty} \frac{d\omega_2}{2\pi}\; e^{-i\omega_1 t_1}\, e^{i\omega_2 t_2}\, A(\omega_1,\omega_2) \tag{5.7}$$

and the corresponding representation in energy space, $A(\omega,\omega')$, is given by the associated inverse Fourier transformation. Exploiting the property (5.6) one finds the following convenient condition for $A(\omega,\omega')$:

$$\begin{aligned} A(\omega_1,\omega_2) &= \int dt_1 \int dt_2\; e^{i\omega_1 t_1}\, e^{-i\omega_2 t_2}\, A(t_1,t_2) \\ &= \int dt_1 \int dt_2\; e^{i\omega_1 (t+T_0)}\, e^{-i\omega_2 (t_2+T_0)}\, A(t_1+T_0, t_2+T_0) \\ &= e^{i(\omega_1-\omega_2)T_0} \int dt_1 \int dt_2\; e^{i\omega_1 t}\, e^{-i\omega_2 t_2}\, A(t_1,t_2) \\ &= e^{i(\omega_1-\omega_2)T_0}\, A(\omega_1,\omega_2)\,. \end{aligned} \tag{5.8}$$

Hence, the condition $e^{i(\omega_1-\omega_2)T_0} = 1$ is enforced. This leads to the fact that the phase of the exponential must equal to an integer multiple of 2π, i.e., $(\omega_1-\omega_2)T_0 = 2\pi\bar{n}$ with $\bar{n} \in \mathbb{Z}$. Consequently, one can rewrite

$$\omega_1 = \omega + n\Omega \qquad \text{and} \qquad \omega_2 = \omega + m\Omega\,, \tag{5.9}$$

where $n, m \in \mathbb{Z}$ and $\omega \in [-\Omega/2, \Omega/2)$, with $\Omega = 2\pi/T_0$. We can therefore express the Fourier transform of $A(t_1, t_2)$ in terms of a single continuous frequency ω within the first Floquet zone plus two discrete indices n, m. The latter ones are *Floquet indices* and their meaning is identical to the ones introduced in Sec. 2.2. Recall further that the position of the Floquet zone can be chosen arbitrarily. However, for a many-particle system this choice should be made in such a way that all quantities are maximally conserved.

The *Floquet transformation* of a two-point function and its inverse is then defined as

$$A_{nm}(\omega) = \frac{1}{T_0}\int dt_1 \int dt_2 \; e^{i(\omega+n\Omega)t_1}\, e^{-i(\omega+m\Omega)t_2}\, A(t_1, t_2)\,, \tag{5.10}$$

$$A(t_1, t_2) = \sum_{n,m}\int \frac{d\omega}{2\pi}\; e^{-i(\omega+n\Omega)t_1}\, e^{i(\omega+m\Omega)t_2}\, A_{nm}(\omega)\,, \tag{5.11}$$

where we call $A_{nm}(\omega)$ the Floquet representation[2] of $A(t_1, t_2)$. Due to its matrix structure the object $A_{nm}(\omega)$ is defined in the extended space that was introduced in Sec. 2.2. Note that the factor $1/T_0$ appearing in Eq. (5.10) ensures correct normalisation of the set of transformations. The advantage of this Floquet representation is indeed its inherent matrix structure. This makes it numerically relatively easy to compute combinations of different Floquet-represented objects. For example, using Eqs. (5.10) and (5.11) it is easily shown that a convolution of two perfectly periodic two-point functions, $A = B \circ C$, can be converted into a matrix multiplication in Floquet space, i.e.,

$$A(t, t') = \int d\tilde{t}\; B(t, \tilde{t})\, C(\tilde{t}, t') \qquad \Leftrightarrow \qquad A_{nm}(\omega) = \sum_l B_{nl}(\omega)\, C_{lm}(\omega)\,. \tag{5.12}$$

5.2.2. Non-interacting Floquet Green's functions

While the ultimate goal is to describe a fully interacting Floquet system by means of Green's functions, we first focus on the non-interacting and perfectly periodic case as described by the Hamiltonian (5.4). The associated Green's functions possess the property $G(t, t') = G(t + T_0, t' + T_0)$. Hence, it is natural to demand a Floquet representation of these objects, $G_{nm}(\omega)$. In this section we will follow the virtue of Sec. 5.2.1 and present the retarded, advanced and Keldysh Green's function in Floquet space by means of the transformation (5.10).

Floquet creation and annihilation operator

For the non-interacting case it is most convenient to calculate the corresponding Green's function by using the operator expressions (4.41). In order to switch directly to a Floquet picture one has to follow two steps: first, the creation (annihilation) operator $c_i^\dagger$ (c_i) is

[2] Note that sometimes the literature, e.g., Refs. [256, 285], chooses slightly different conventions for the 'Floquet transformation': in those cases, the central time coordinate of a Wigner transformed object (see Sec. 4.3.1) is expressed in terms of its discrete Fourier modes, i.e., $A_n(\omega) = \int dt\, e^{-in\Omega t} A(t, \omega)$. However, one can switch forth and back between both conventions by realising that one recovers the matrix representation in Floquet space, Eq. (5.10), via $A_{nm}(\omega) = A_{n-m}(\omega + \frac{n+m}{2}\Omega)$ [286].

expressed in terms of its Floquet counterpart $f_\nu^\dagger$ (f_ν). Here, the Floquet creation operator creates a fermion in a Floquet eigenstate, i.e.,

$$f_\nu^\dagger(t)\,|0\rangle = |\phi_\nu(t)\rangle\ , \tag{5.13}$$

with $|0\rangle$ being the quasiparticle vacuum. Second, $f_\nu^\dagger$ and f_ν are found in their Heisenberg representations.

For the first step we use single-particle Floquet eigenstates $|\phi_{t_0,\nu}(t)\rangle$ that are associated with the Hamiltonian $H^0_{t_0}(t)$, see Eq. 5.4. Recall that ν encodes all usual quantum numbers such as momentum, spin and the bandindex. Note further that we will drop the t_0-index in favour of notational clarity, keeping in mind, though, that all respective quantities do depend parametrically on it. We now use the property that at equal times the Floquet states form a complete set in the physical Hilbert space $\mathcal{H}$, i.e., $\mathbb{1} = \sum_\nu |\phi_\nu(t)\rangle\langle\phi_\nu(t)|$ (for details see Sec. 2.2). With this relation one finds the expressions

$$c_i^\dagger = \sum_\nu \bar{\phi}_\nu(t,i)\ f_\nu^\dagger(t) \qquad \text{and} \qquad c_i = \sum_\nu \phi_\nu(t,i)\ f_\nu(t)\,, \tag{5.14}$$

where the amplitude $\phi_\nu(t,i) = \langle i|\phi_\nu(t)\rangle$ describes the projection of the respective Floquet eigenstate onto a state that is created by $c_i^\dagger$, with i representing a set of initial indices such as lattice site and spin. We denote its corresponding complex conjugate as $\bar{\phi}_\nu(t,i)$. Note again that the sum in Eq. (5.14) only runs over states of the first Floquet zone (not over all replica states). Using the mode expansion of the Floquet states, $|\phi_\nu(t)\rangle = \sum_n e^{-in\Omega t}\,|\phi_\nu^n\rangle$, the Floquet creation and annihilation operators are eventually given by

$$f_\nu^\dagger(t) = \sum_{i,n} e^{-in\Omega t}\,\phi_\nu^n(i)\ c_i^\dagger \qquad \text{and} \qquad f_\nu(t) = \sum_{i,n} e^{in\Omega t}\,\bar{\phi}_\nu^n(i)\ c_i\,, \tag{5.15}$$

where $\phi_\nu^n(i) = \langle i|\phi_\nu^n\rangle$. Notice that the operators $f_\nu^\dagger$ and f_ν, which are represented in their Schrödinger picture, have an explicit time-dependence. Furthermore, one clearly observes that by using different replica states one still receives the same creation and annihilation operator given by Eq. (5.15).

This brings us to the next issue: finding the Heisenberg form of $f_\nu^\dagger$ and f_ν. The Heisenberg equation of motion for the Floquet annihilation operator is given by

$$\frac{d}{dt}\Big(f_\nu(t)\Big)_H = i\left([H^0(t), f_\nu(t)]\right)_H + \left(\frac{\partial f_\nu(t)}{\partial t}\right)_H\,, \tag{5.16}$$

where the $(.)_H$ indicates the Heisenberg picture. By using the second quantized form of the Hamiltonian in the basis of Floquet states,

$$H^0(t) = \sum_{\mu\eta} H^0_{\mu\eta}(t) f_\mu^\dagger(t) f_\eta(t)\,, \tag{5.17}$$

one straightforwardly evaluates the commutator appearing in the first term on the right hand side of Eq. 5.16 to read as $[H^0(t), f_\nu(t)] = -\sum_\lambda H^0_{\nu\lambda}(t) f_\lambda(t)$. Also, remembering the Floquet eigenvalue problem, $(H(t) - i\partial/\partial t)\,|\phi_\nu(t)\rangle = \varepsilon_\nu\,|\phi_\nu(t)\rangle$, one finds that $\partial f_\nu(t)/\partial t = i\sum_\eta (H^0_{\nu\eta}(t) - \varepsilon_\nu\delta_{\nu\eta}) f_\eta(t)$. With these expressions Eq. (5.16) simplifies to the simple differential equation $\frac{d}{dt}(f_\nu)_H = -\varepsilon_\nu (f_\nu)_H$ which is readily solved by

$$\big(f_\nu(t)\big)_H = e^{-i\epsilon_\nu t}\,f_\nu\,, \tag{5.18}$$

where $f_\nu \equiv (f_\nu(0))_H = (f_\nu(0))_S$, with $(.)_S$ indicating the Schrödinger representation of the respective object. In order to make this identification we fixed the initial time to $t = 0$.

A similar equation also holds for the Floquet creation operator, i.e., $(f_\nu^\dagger(t))_H = e^{i\epsilon_\nu t} f_\nu^\dagger$. One can therefore state that the Floquet creation and annihilation operators in their Heisenberg form are simply time-evolved by the respective quasienergy. The original creation and annihilation operators can now be expressed in terms of Eq. (5.18). Using Eqs. (5.14) and (5.15) one can write the Heisenberg form of $c_i, c_i^\dagger$ as

$$c_i(t) = e^{-i\epsilon_\nu t} \sum_{\nu,n} e^{-in\Omega t}\, \phi_\nu^n(i)\, f_\nu \qquad \text{and} \qquad c_i^\dagger(t) = e^{i\epsilon_\nu t} \sum_{\nu,n} e^{in\Omega t}\, \bar{\phi}_\nu^n(i)\, f_\nu^\dagger\,, \tag{5.19}$$

where $c_i(t) = (c_i)_H$, etc. Finally, the expressions (5.19) can be used to explicitly express the non-interacting Green's functions given in Eqs. (4.41) in terms of Floquet creation and annihilation operators.

Retarded and advanced Floquet Green's function

We continue by substituting the expressions (5.19) into the formal operator form of the retarded Green's function, see Eq. (4.41). Note again that we have switched to a discrete spatial structure, which naturally leads to $G(x,x') \to G_{ij}(t,t')$ (where indices i,j do not only describe space but also encode other quantum numbers, e.g., spin). The retarded Green's function can then be written as

$$\begin{aligned} G_{ij}^R(t,t') &= -i\theta(t-t')\,\langle\{c_i(t), c_j^\dagger(t')\}\rangle \\ &= -i\theta(t-t') \sum_{\nu,\mu}\sum_{n,m} e^{-i\varepsilon_\nu t} e^{-in\Omega t} e^{i\varepsilon_\mu t'} e^{im\Omega t'} \phi_\nu^n(i)\bar{\phi}_\mu^m(j)\,\langle\{f_\nu, f_\mu^\dagger\}\rangle \\ &= -i\theta(t-t') \sum_{\nu}\sum_{n,m} e^{-i\varepsilon_\nu (t-t')} e^{-in\Omega t} e^{im\Omega t'} \phi_\nu^n(i)\bar{\phi}_\nu^m(j)\,, \end{aligned} \tag{5.20}$$

where it was used in the second line that $\{f_\nu, f_\mu^\dagger\} = \delta_{\nu\mu}$, representing fermionic anti-commutator rules. One immediately spots that the Green's function indeed possesses the property $G^R(t,t') = G^R(t+T_0, t'+T_0)$. Hence, the object naturally calls for a representation in Floquet space according to the definition given by Eq. (5.10). In order to simplify the appearing time-integration we express the θ-function in its integral representation

$$\theta(t-t') = -\frac{1}{2\pi i}\int_{-\infty}^{\infty} dz\; \frac{e^{-iz(t-t')}}{z+i0^+}\,, \tag{5.21}$$

with 0^+ being an infinitesimal small, positive, real number. After substituting this expression into Eq. (5.20) one finds that the Floquet transformation of G^R takes the following form:

$$\begin{aligned} G_{\substack{ij\\nm}}^R(\omega) &= \frac{1}{T_0}\int dt \int dt'\; e^{i(\omega+n\Omega)t} e^{-i(\omega+m\Omega)t'}\, G_{ij}^R(t,t') \\ &= \frac{1}{T_0}\sum_\nu\sum_{s,l}\int dt\int dt'\int\frac{dz}{2\pi}\;\frac{\phi_\nu^s(i)\,\bar{\phi}_\nu^l(j)}{z+i0^+}\, e^{-i(\varepsilon_\nu-\omega+z)(t-t')} e^{-i(s-n)\Omega t} e^{i(l-m)\Omega t'} \\ &= \frac{1}{T_0}\sum_\nu\sum_{s,l}\int dt\int dz\;\frac{\phi_\nu^s(i)\,\bar{\phi}_\nu^l(j)}{z+i0^+}\,\delta\big(\varepsilon_\nu-\omega+(l-m)\Omega+z\big)\, e^{-i(\varepsilon_\nu-\omega+(s-n)\Omega+z)t} \\ &= \frac{1}{T_0}\sum_\nu\sum_{s,l}\int dt\;\frac{\phi_\nu^s(i)\,\bar{\phi}_\nu^{m+l}(j)}{\omega-\varepsilon_\nu-l\Omega+i0^+}\, e^{-i(s-n-l)\Omega t} \\ &= \sum_{\nu,l}\frac{\phi_\nu^{n+l}(i)\,\bar{\phi}_\nu^{m+l}(j)}{\omega-\varepsilon_\nu-l\Omega+i0^+}\,, \end{aligned} \tag{5.22}$$

where $\omega \in [-\Omega/2, \Omega/2)$. In the course of evaluating Eq. (5.22) it was used that $\int dt\, e^{-izt} = 2\pi\delta(z)$ and it was exploited that Floquet indices can be appropriately shifted under the infinite sum.

While Eq. (5.22) yields the general result for a perfectly time-periodic system, it is worthwhile to reintroduce the parameter t_0 at this point. So, finally, the retarded Green's function for a system given by Eq. (5.4) is given by

$$G^R_{\substack{t_0,ij\\nm}}(\omega) = \sum_{\nu,l} \frac{\phi^{n+l}_{t_0,\nu}(i)\, \bar{\phi}^{m+l}_{t_0,\nu}(j)}{\omega - \varepsilon_{t_0,\nu} - l\Omega + i0^+}\,. \tag{5.23}$$

The expression for the corresponding advanced Green's function can be obtained in a similar fashion. The derivation is fully analogous as outlined above. Alternatively, one can exploit the relation $G^A = (G^R)^\dagger$. The expression for the advanced Green's function is then straightforwardly found to read as

$$G^A_{\substack{t_0,ij\\nm}}(\omega) = \left(G^R_{\substack{t_0,ji\\mn}}(\omega)\right)^* = \sum_{\nu,l} \frac{\phi^{n+l}_{t_0,\nu}(i)\, \bar{\phi}^{m+l}_{t_0,\nu}(j)}{\omega - \varepsilon_{t_0,\nu} - l\Omega - i0^+}\,. \tag{5.24}$$

So the Floquet representation of the *non-interacting* retarded and advanced Green's functions (5.23) and (5.24) resembles the typical form of spectrally decomposed Green's functions. However, there is a crucial peculiarity here: the additional sum over the Floquet index l means that the non-interacting Green's functions are actually an infinite sum of single-particle propagators in the following sense. Due to the special structure of Floquet space (see Sec. 2.2) the propagator does not only take the system directly from the 'm' to the 'n'-photon sector, but rather offers the possibility to pass every possible sector on its way. In a more pictorial sense this means that the system does not necessarily emit n–m photons only, but can also incorporate an additional number of l photons in the total process. It is precisely this property that will eventually lead to heating in the system.

Keldysh Floquet Green's function and distribution function

The Keldysh Green's function is found analogously to the procedure above. Using again the operator form of G^K given by Eq. (4.41) as well as the expression of $c_i, c_i^\dagger$ in terms of Floquet creation and annihilation operators, one finds

$$\begin{aligned} G^K_{t_0,ij}(t,t') &= -i\,\langle [c_i(t), c_j^\dagger(t')]\rangle \\ &= -i \sum_\nu \sum_{n,m} e^{-i\varepsilon_{t_0,\nu}(t-t')} e^{-in\Omega t} e^{im\Omega t'} \phi^n_{t_0,\nu}(i) \bar{\phi}^m_{t_0,\nu}(j)\, \langle [f_\nu, f_\mu^\dagger]\rangle \\ &= -i \sum_\nu \sum_{n,m} e^{-i\varepsilon_{t_0,\nu}(t-t')} e^{-in\Omega t} e^{im\Omega t'} \phi^n_{t_0,\nu}(i) \bar{\phi}^m_{t_0,\nu}(j)\, (1 - 2n_{t_0,\nu})\,, \end{aligned} \tag{5.25}$$

where it is assumed that the many-body state of the system has the property $\langle f_\nu^\dagger, f_\mu\rangle = \delta_{\nu\mu}$. Moreover and most importantly, the Floquet occupation number n_ν has been introduced. The latter is defined by

$$n_{t_0,\nu} = \langle f^\dagger_{t_0,\nu}(t) f_{t_0,\nu}(t)\rangle \tag{5.26}$$

and is *time independent* for non-interacting, periodic Floquet Hamiltonians such as given by Eq. (5.4). We stress that a single function $n_{t_0,\nu}$ describes the occupation of one physical Floquet state. It is therefore not necessary to introduce individual occupation numbers for every 'Floquet copy' of that state, which again reflects the fact that every Floquet

copy state describes the same physical state. So while the retarded and advanced Green's functions, see Eqs. (5.23) and (5.24), only provide information about the Floquet spectrum, the Keldysh component of the Green's function carries knowledge about the occupation of the system. Because we chose to switch to the basis of Floquet states, also the occupation is given in this language. Later we will show that even in slowly varying and weakly interacting systems these Floquet occupation functions, $n_{t_0,\nu}$, still capture the dynamics of the system. Hence, it will be our main goal to find a semiclassical description for the time evolution of the Floquet occupation, i.e., for $n_\nu(t)$.

As long as the system is non-interacting and n_ν does not depend on time, the Keldysh Green's function also possesses the property that it is invariant under a simultaneous shift of both time argument by a single driving period, $G^K(t+T_0,t'+T_0) = G^K(t,t')$. One can therefore transform Eq. (5.25) to a representation in Floquet space as done for G^R and G^A. Following the same logic as in Eq. (5.22) the Floquet Keldysh Green's function is obtained in the form

$$\begin{aligned} G^K_{\substack{t_0,ij\\nm}}(\omega) &= \frac{1}{T_0}\int dt \int dt'\; e^{i(\omega+n\Omega)t} e^{-i(\omega+m\Omega)t'}\, G^K_{t_0,ij}(t,t') \\ &= -2\pi i \sum_{\nu,l} \delta\big(\omega-\varepsilon_{t_0,\nu}-l\Omega\big)\, \phi^{n+l}_{t_0,\nu}(i)\, \bar{\phi}^{m+l}_{t_0,\nu}(j)\, \big(1-2n_{t_0,\nu}\big)\,, \end{aligned} \tag{5.27}$$

where the summation over the Floquet index l has the same interpretation as before. Additionally, recalling the parametrization of the Keldysh Green's function, $G^K = G^R \circ F - F \circ G^A$, and using the identity for algebraic products given by Eq. (5.12) one can interpret the right hand side of Eq. (5.27) in terms of G^R, G^A and F. In fact, since the Green's functions above are all diagonal in the space of Floquet eigenstates, we can alternatively write the relation between Keldysh Greens function and distribution matrix as $G^K = (G^R - G^A)\circ F$. Hence, it is worthwhile to mention that

$$\Big(G^R - G^A\Big)_{\substack{t_0,ij\\nm}}(\omega) = \sum_{\nu,l} \delta\big(\omega-\varepsilon_{t_0,\nu}-l\Omega\big)\, \phi^{n+l}_{t_0,\nu}(i)\, \bar{\phi}^{m+l}_{t_0,\nu}(j)\,, \tag{5.28}$$

which is straightforwardly obtained from Eqs. (5.23) and (5.24). From this expression one finds that the Floquet representation of the distribution matrix $F(t,t')$ is given by

$$F_{\substack{t_0,ij\\nm}}(\omega) = \sum_{\nu,l} \phi^{n+l}_{t_0,\nu}(i)\, \bar{\phi}^{m+l}_{t_0,\nu}(j)\, \big(1-2n_{t_0,\nu}\big)\,. \tag{5.29}$$

The distribution matrix is an object that is diagonal in the basis of Floquet states with entries $(1-2n_\nu)$. In other words, in the non-interacting case $F(\omega)$ only has support at quasienergies of single-particle Floquet states, and can thus be already understood as being in a mass-shell form (see Sec. 4.3.2). Note once more that the occupation number n_ν is the same for every replica state.

We stress that the reason why we could find Green's functions in the simplified forms above and also determine a concise expression for F is the fact that the system is *non-interacting* as well as perfectly *time-periodic*. The immediate consequence of this setting is that all objects are diagonal in the basis of Floquet states. This will, of course, not be the case if interactions are present or additional time variations are introduced. Nevertheless, in the following we will assume that interactions are sufficiently small such that we can to good approximation still assume a form of the distribution function as given by Eq. (5.29).

However, before studying how the system behaves under these circumstances we make a few further remarks on the Floquet character of the considered objects. We stress

again that in order to calculate the non-interacting Green's functions one simply needs to solve the Floquet eigenvalue problem in the extended Hilbert space $\mathcal{F}$, i.e., $\bar{H}^F |\phi_{\nu n}\rangle\!\rangle = \varepsilon_{\nu n} |\phi_{\nu n}\rangle\!\rangle$ (for details see Sec. 2.2). Obtaining Floquet eigenstates and quasienergies (as done, e.g., in Ch. 3) is already sufficient for finding Floquet expressions of G^R and G^A. For G^K additional information about some initial condition is required. In that sense it should be no surprise that all the Floquet transformed Green's functions above, see Eqs. (5.23), (5.24) and (5.27), are solutions to the *Floquet-Dyson equation*

$$\sum_{m'} \left(\omega\, \delta_{nm'} - H^F_{t_0,nm'}\right) G_{t_0,m'm}(\omega) = \delta_{nm} \mathbb{1}\,, \tag{5.30}$$

with $H^F_{t_0,nm}$ being the Floquet Hamiltonian represented in the extended Hilbert space (see Eq. (2.40)), ω is still restricted to the first Floquet zone and we have omitted all Hilbert space indices for convenience.

So while our chosen route started with the general physical definition of Green's functions and aimed at a suitable Floquet transformation of such, one could have tried to incorporate the Floquet structure right from the beginning of the derivation. In fact, there are many examples in the literature, e.g., Refs. [90–92, 290], where Floquet Green's functions are determined directly from Eq. (5.30) rather than from transforming Eqs. (4.41). A possible advantage might be that a prior diagonalisation of H^F is not required to obtain explicit results for G. However, one should bear in mind that those Floquet Green's functions carry redundant information, since they treat all replicas independently. One possible way to recover physical reality is the $(t, t')-$formalism[3] presented in Sec. 2.2.

Having said this, the huge advantage of using a Floquet transformation approach as presented here is that one can very closely follow already developed theoretical methods and strategies. Nowadays, the Floquet representation of Green's functions is indeed a widely used tool in the context of non-equilibrium, periodically driven quantum systems [114, 115, 256, 277, 278, 285, 286, 288, 291–294].

5.3. Semiclassical Floquet approximation schemes

Having Floquet definitions of general two-point functions at hand, see Eq. (5.10), as well as having calculated explicit expressions for Floquet versions of non-interacting Green's functions, Eqs. (5.23), (5.24) and (5.27), we start tackling our main question of this chapter: how do interacting Floquet systems that are inherently *out of equilibrium* behave as a function of time? Ultimately, we want to capture the dynamics of the system described by Eq. (5.1) by a semiclassical approximation of the quantum kinetic equations introduced in Ch. 4. This requires, as described above, the assumption of having weak interactions as well as a clear separation of scales in the system. For Floquet systems we additionally demand that one can cleanly separate the slow dynamics treated within a semiclassical approach from the rapid, periodic oscillations that shall be treated fully quantum mechanically. While the starting point for the former is the use of a Wigner representation (see Sec. 4.3.1), the fast oscillations are conveniently handled by the Floquet theory (see Sec. 2.2).

These two approaches can therefore indeed be combined in the following situation: we require that the oscillation period T_0 is much smaller than all time scales τ_{slow} on which

[3] In fact, there is also a deep connection between the $(t, t')-$formalism and the present Hamiltonian $H^0_{t_0}(t)$, which is time-periodic as well as depends parametrically on some central time t_0. We will comment on this at a later stage in Sec. 5.3.1.

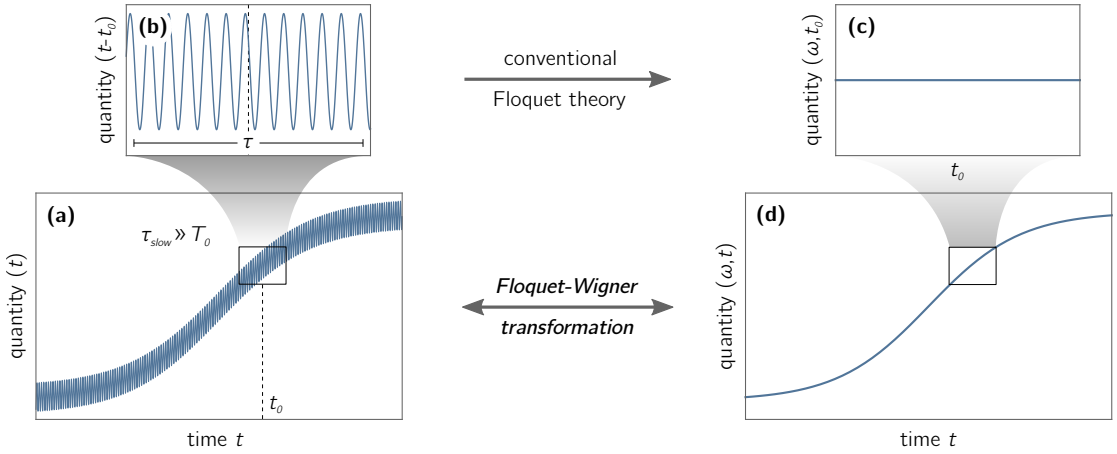

Figure 5.1.: Cartoon illustrating a separation of time scales determined by Eq. (5.31). (a) The original time-dependent problem is characterised by a fast oscillation of period T_0 and a slow variation given by τ_{slow}. We illustrate this dependence by showing some expressive quantity such as an external parameter or a single instantaneous eigenenergy. (b) A time-window of length τ around some reference time t_0 then only shows perfect oscillations, which can be dealt with standard by Floquet theory, see Sec. 2.2. (c) The resulting energy representation still depends on t_0. (d) Identifying t_0 with t, which is controlled by τ/τ_{slow}, reveals a time-dependent quantity that has been Floquet transformed 'locally' in time. The Floquet-Wigner transformation, see Eq. (5.32), formally connects (a) and (d).

the occupation function changes or on which the oscillating Hamiltonian is modified. To be precise, we demand that one can always find a time scale τ which fulfills

$$T_0 \ll \tau \ll \tau_{\text{slow}} \,. \tag{5.31}$$

In words, τ defines a time window that appears very broad from the point of view of the fast oscillations, but very narrow from the perspective of slowly changing quantities. In Fig. 5.1 we give a pictorial interpretation of τ as well as of the general philosophy of the separation of time scales: despite the fact that quantities are changing both rapidly and slowly, within the time scale τ only the periodic behaviour can be witnessed (cf. Eq. (5.3)). Floquet theory allows for an exact analysis of the system, which parametrically depends on the chosen time-window. Repeating this procedure for all possible time-windows reveals a Floquet quantity that depends slowly on time. First, we will show how this picture is formalised using the Floquet-Wigner transformation. We will then exploit this newly introduced transformation in order to derive a Floquet analogue of the Moyal product given by Eq. (4.74).

5.3.1. The Floquet-Wigner transformation

A conventional Wigner transformation of two-point functions (such as Green's functions or self-energies) of type (4.70) has the drawback for Floquet systems that the central time still shows fast oscillations at frequency Ω. However, the separation of time scales (5.31) allows us to extend the Floquet transformation given by Eq. (5.10) and formally introduce the *Floquet-Wigner transformation*

$$A_{nm}(\bar{t},\omega) = \frac{1}{T_0}\int dt \int dt'\; \delta_\tau(\bar{t} - \tfrac{t+t'}{2})\; e^{i(\omega+n\Omega)t}\, e^{-i(\omega+m\Omega)t'}\, A(t,t')\,, \tag{5.32}$$

where the object $A_{nm}(\bar{t},\omega)$ still depends on the central time coordinate despite being transformed into Floquet space. This is because we introduced the *filter function* $\delta_\tau(\bar{t}-t)$.

This function is normalized to unity, centred at $\bar{t}$ and is broadened on the time scale τ. The latter is chosen much larger than the period T_0, but much smaller than the time scale of slow modifications $\tau_{\rm slow}$, see Eq. (5.31). As long as these properties are manifest the actual form of $\delta_\tau(t)$ is irrelevant. The use of the filter function then guarantees that the object $A_{nm}(\bar{t},\omega)$ is *not* oscillating on the time scale T_0. In order to be more specific we choose

$$\delta_\tau(\bar{t}-t) = \frac{1}{\tau\sqrt{\pi}}\, e^{-\left(\frac{\bar{t}-t}{\tau}\right)^2} \tag{5.33}$$

being a broadened version of the $\delta-$function. One then observes that oscillating terms get transformed as $\int dt\, \delta_\tau(t)\, e^{i\Omega t} = e^{-(\Omega\tau)^2/4}$. Hence, all oscillating components at driving frequency Ω are *exponentially suppressed* by the factor $e^{-\pi^2(\tau/T_0)^2}$. Below, $\bar{t}$ will adopt the role of t_0 of the previous section, which will consequently become a dynamical parameter.

The inverse transformation of the Floquet-Wigner representation is given by

$$A(t,t') \approx \sum_{n,m} \int \frac{d\omega}{2\pi}\; e^{-i(\omega+n\Omega)t}\, e^{i(\omega+m\Omega)t'}\, A_{nm}\big(\tfrac{t+t'}{2},\omega\big)\,. \tag{5.34}$$

It is crucial to realise that this back-transformation is *not* exact due to the finite width of $\delta_\tau(t)$. Hence, Eq. 5.34 is only valid up to exponential precision in cases where relation (5.31) holds. In order to see this, it is instructive to plug expression (5.34) into Eq. (5.32):

$$\begin{aligned} A_{nm}(\bar{t},\omega) \;&= \frac{1}{T_0}\int dt \int dt'\; \delta_\tau(\bar{t}-\tfrac{t+t'}{2})\; e^{i(\omega+n\Omega)t}\, e^{-i(\omega+m\Omega)t'} \\ &\qquad \times \sum_{n',m'} \int \frac{d\omega'}{2\pi}\; e^{-i(\omega'+n'\Omega)t}\, e^{i(\omega'+m'\Omega)t'}\; A_{n'm'}\big(\tfrac{t+t'}{2},\omega'\big) \\ &\approx \frac{1}{T_0}\sum_{n',m'} \int \frac{d\omega'}{2\pi}\, A_{n'm'}(\bar{t},\omega') \\ &\qquad \times \int dt \int dt'\; \delta_\tau(\bar{t}-\tfrac{t+t'}{2})\, e^{i(\omega-\omega')(t-t')}\, e^{i(n-n')\Omega t}\, e^{-i(m-m')\Omega t'} \\ &\approx \sum_{n',m'} \int d\omega'\, A_{n'm'}(\bar{t},\omega')\, \delta(\omega-\omega')\, \delta_{nn'}\, \delta_{mm'} \\ &= A_{nm}(\bar{t},\omega)\,. \end{aligned} \tag{5.35}$$

In the second line it was used that the condition $\tau_{\rm slow} \gg \tau$ allows to approximate $\delta_\tau(t)$ as a true δ-function for the slowly varying object $A_{nm}(\frac{t+t'}{2},\omega)$. The third equation line of (5.35) then used that due to $\tau \gg T_0$ the integration of fast oscillations (approximately) do not lead to a mixing of Floquet modes. By considering further that ω is still bound to the first Floquet zone the integration over both time arguments yields the combination of δ-function and Kronecker δ's.

Having established the Floquet-Wigner transformation and its limitations, one can, for instance, ask how an algebraic product of two two-point functions, $A(t,t') = B(t,t')C(t,t')$, transforms according to Eq. (5.32). This will be important for the computation of the self-energies, see Eqs. (4.64) and (4.65). Plugging $A(t,t') = B(t,t')C(t,t')$ into Eq. (5.32), expressing B, C in terms of their inverse transformation (5.34) and following the same arguments as done for Eq. (5.35) yields the following identity

$$\begin{aligned} & A(t,t') = B(t,t')\, C(t,t') \\ \Leftrightarrow \qquad & A_{nm}(\bar{t},\omega) = \sum_{n',m'} \int \frac{d\omega'}{2\pi}\; B_{n'm'}(\bar{t},\omega')\, C_{n-n',m-m'}(\bar{t},\omega-\omega')\,. \end{aligned} \tag{5.36}$$

A respective result for transforming a temporal convolution of two two-point functions is derived in the following section.

Before doing so we make a general remark on the presented formalism. While the filter function $\delta_\tau(t)$ allowed for a formal manifestation of the separation of fast oscillations and other slow temporal dependencies along the direction of time, one could have viewed the procedure from a slightly different perspective: due to the exponentially suppressed cross-talk of slow and fast modulations both scales were treated independently. Such an independent treatment was already encountered in Sec. 2.2: the $(t,t')-$formalism. Within this formalism one artificially introduces a new time coordinate. The time-evolution of the system is then evaluated in a coordinate system where both time-axes are orthogonal to each other. A similar setup was introduced here where the 'new' time coordinate is given by the central time $\bar{t}$ of $\delta_\tau(\bar{t}-t)$. Again, the main difference is that within the formalism of the present section one always remains in a physical picture, while the (t,t')-formalism needs the identification of both time arguments at the end to become physical. Nonetheless, both pictures are deeply connected and, thus, aspects of one (e.g., the discussion about geometrical phases in Sec. 2.2.4) can be carried over to the other.

5.3.2. The Floquet-Moyal product

In the following we sketch the explicit derivation of the Floquet analogue of the Moyal product (4.74). Starting point is the question how a time-convolution of two two-point functions given by

$$A(t,t') = \int dt_1 \; B(t,t_1)\, C(t_1,t') \tag{5.37}$$

transforms under the set of Floquet-Wigner transformations (5.32) and (5.34). In order to find the explicit form of $A_{nm}(\bar{t},\omega)$ one inserts the inverse Floquet-Wigner expressions (see. Eq. (5.34)) for B and C into Eq. (5.37). The formula then becomes

$$\begin{aligned} A(t,t') \approx \sum_{n',m'} \sum_{n'',m''} \int \frac{d\omega'}{2\pi} \int \frac{d\omega''}{2\pi} \; e^{-i(\omega'+n'\Omega)t}\, e^{i(\omega''+m''\Omega)t'} \\ \times \int dt_1 \; e^{i(\omega'+m'\Omega)t_1} \; e^{-i(\omega''+n''\Omega)t_1} \, B_{n'm'}(\omega', \tfrac{t+t_1}{2}) \; C_{n''m''}(\omega'', \tfrac{t_1+t'}{2}) \,. \end{aligned} \tag{5.38}$$

If the objects B and C do not depend slowly on time, one recovers the simple matrix multiplication in Floquet space given by Eq. (5.12). However, since B, C *do* show some slow temporal variation, the first technical challenge enters now via the convolution in the time-argument t_1. To make progress here, one formally expands the functions B and C around $t_1 = t'$ and $t_1 = t$, respectively. This leads to the following expression

$$\begin{aligned} A(t,t') \approx \sum_{n',m'} \sum_{n'',m''} \sum_{l,l'} \frac{1}{l!l'!} \frac{1}{2^{l+l'}} \int \frac{d\omega'}{2\pi} \int \frac{d\omega''}{2\pi} \; e^{-i(\omega'+n'\Omega)t}\, e^{i(\omega''+m''\Omega)t'} \\ \times \int dt_1 \; e^{i(\omega'-\omega''+(m'-n'')\Omega)t_1} \, (t_1-t')^l \, (t_1-t)^{l'} \, B^{(l,0)}_{n'm'}(\tfrac{t+t'}{2}, \omega') \; C^{(l',0)}_{n''m''}(\tfrac{t+t'}{2}, \omega'') \,, \end{aligned} \tag{5.39}$$

where $B^{(l,0)}$ describes the lth (0th) derivative of the function B with respect to central time (frequency), etc. In the next step one substitutes the identity $(t_1-t)^l = \sum_{k=0}^{l} \binom{l}{k} (-1)^k t_1^{l-k} t^k$ into Eq. (5.39). Subsequently, the t_1 integral can be evaluated by using that $\int dt_1 e^{i\omega_1 t_1} t_1^\alpha = (-1)^\alpha \alpha!/(i\omega_1)^\alpha \int dt_1 e^{i\omega_1 t_1} = 2\pi(-1)^\alpha \alpha!/(i\omega_1)^\alpha \delta(\omega_1)$. One can then exploit the identity for derivatives of the δ-function, $\delta^{(n)}(x) = (-1)^n n!/x^n \delta(x)$. At

the same time, we desire to remove the differentiation of δ-functions by means of an integration by parts. The expression for A can eventually be written as

$$\begin{aligned} A(t,t') \approx & \sum_{n',m'} \sum_{n'',m''} \sum_{l,l'} \frac{1}{l!l'!} \frac{1}{2^{l+l'}} \int \frac{d\omega'}{2\pi} \int d\omega'' \sum_{k=0}^{l} \sum_{k'=0}^{l'} \binom{l}{k} \binom{l'}{k'} \\ & \times (-1)^{l-k'} \, i^{l+l'-k-k'} \, t^k \, t'^{k'} \, \delta\big(\omega' - \omega'' + (m'-n'')\Omega\big) \\ & \times \Big(e^{-i(\omega'+n'\Omega)t} \, B^{(l,0)}_{n'm'}(\omega', \bar{t})\Big)^{(0,l'-k')} \Big(e^{i(\omega''+m''\Omega)t'} \, C^{(l',0)}_{n''m''}(\omega'', \bar{t})\Big)^{(0,l-k)} . \end{aligned} \tag{5.40}$$

Due to the fact that $-\frac{\Omega}{2} \leq \omega < \frac{\Omega}{2}$, the argument of the δ-function above can only be zero if $\omega' = \omega''$ and $m' = n''$. Hence, the energy integration $\int d\omega'' \sum_{n''}$ can be straightforwardly performed. In the following, one wants to use the identity $(fg)^{(n)} = \sum_{k=0}^{n} \binom{n}{k} f^{(n-k)} g^{(k)}$ and simplify summations. Eventually, after some steps a relabeling of indices yields the form

$$A(t,t') \approx \sum_{n,m} \int \frac{d\omega}{2\pi} \, e^{-i(\omega+n\Omega)t} \, e^{i(\omega+m\Omega)t'} \left[\sum_{l,l'} \frac{(-1)^l}{2^{l+l'}} \frac{i^{l+l'}}{l!l'!} \sum_{m'} B^{(l,l')}_{nm'}(\bar{t}, \omega) \, C^{(l',l)}_{m'm}(\bar{t}, \omega) \right] . \tag{5.41}$$

The explicit form of $A_{nm}(\bar{t}, \omega)$ can now be simple read off by comparing Eq. (5.41) with expression (5.34). After a few more steps of simplification, one finally finds an expression for the *Floquet-Moyal product* that reads as[4]

$$A_{nm}(\bar{t}, \omega) = e^{-\frac{i}{2}(\partial^B_{\bar{t}} \partial^C_{\omega} - \partial^B_{\omega} \partial^C_{\bar{t}})} \sum_{m'} B_{nm'}(\bar{t}, \omega) \, C_{m'm}(\bar{t}, \omega) \, , \tag{5.42}$$

where $\partial^{B/C}$ is an operator acting only on object B or C, respectively. The *Floquet-Moyal expansion* is obtained by expanding the exponential function in Eq. (5.42). One can see that the form of this expression is very similar to the ordinary Moyal product. Indeed, the derivation of Eq. (4.74) is philosophically the same as outlined here. In the Floquet case, however, the expression is supplemented by an additional matrix multiplication of the Floquet indices, which is taking care of the fast oscillations.

Notice that all manipulation steps throughout the presented derivation are exact. What is, however, *not* exact is the definition of the inverse Floquet-Wigner transformation (5.34) that was used in Eq. (5.38), i.e., in the very first step of the derivation. Thus, the Floquet-Moyal product (5.42) - per definition - only holds in the limit where the inverse Floquet-Wigner transformation is valid to good approximation.

5.4. A semiclassical Floquet approximation of quantum kinetic equations

5.4.1. General procedure

In formulating the Floquet-Wigner transformation (5.32) we succeeded in separating slow, semiclassical dynamics from quantum-coherent processes that are captured by the Floquet theory. At the same time, we have all the tools ready to derive a semiclassical approximation of the quantum kinetic equation (4.52) that respects all identified time scales

[4] Note that Eq. (5.42) corrects a small typo in the form of the Floquet-Moyal product presented in Ref. [238].

and self-consistently determines the dynamics of the occupation functions: the *Floquet-Boltzmann equation*. Similar to the procedure in Ch. 4 the derivation of the Floquet version of the Boltzmann equation can generally be divided into four steps:

1. One starts again by considering the quantum kinetic equation (4.52), which is still an exact expression. This starting point is paired with an appropriate calculation of self-energy diagrams, which are functionals of the Green's function. Depending on the system's characteristics one chooses an appropriate approximation scheme to find explicit forms of the self-energy. In the present case, we restrict the discussion to self-consistent second order diagrams owing to assumed *weak interactions*, see Eqs. (4.64) and (4.65).

2. The next goal is to formally incorporate the *separation of time scales*, $\tau_{\text{slow}} \gg T_0$. Therefore, one applies the Floquet-Wigner representation discussed in Sec. (5.3.1) for all Green's functions and self energies appearing in the QKE. Algebraic products of type $A(t,t') = B(t,t')C(t,t')$ that appear naturally within the self-energy expressions are transformed by means of the identity (5.36). Convolutions, indicated by '$\circ$', can be rewritten in terms of a Floquet-Moyal product (5.42). Again, such a Floquet-Wigner representation of the quantum kinetic equation is only valid when the time scales are well separated.

3. An immediate consequence of the separation of time scales is that terms proportional to ∂_t give small contributions. Hence, the exponential of the *Floquet-Moyal product*, $e^{-\frac{i}{2}(\partial_t^B \partial_\omega^C - \partial_\omega^B \partial_t^C)}$, is well approximated by a leading order Taylor expansion in the gradients $\partial_t \partial_\omega$. Therefore, the left hand side of the quantum kinetic equation (4.52) needs to be expanded to first order, since the zero order contribution vanishes due to its commutator structure $[F \mathbin{\circ\!\!\!,} G_0^{-1}]$ and due to the assumption that in the weakly interacting case the distribution matrix remains its non-interacting form, see Eq. (5.29). On the other hand, a zeroth-order expansion of the right-hand side of the QKE is sufficient. Note that such a zeroth-order expansion does not only apply to the term $\Sigma^R \circ F - F \circ \Sigma^A$, but also to the evaluation of the Green's function: G is now self-consistently determined from a lowest order Floquet-Moyal expansion of the Dyson equation $(\hat{G}_0^{-1} - \hat{\Sigma}) \circ \hat{G} = \mathbb{1}$. At the same time, for problems which are not spatially homogeneous the discussion regarding spatial coordinates remains the same as outlined in Ch. (4), where the conventional Moyal product was used.

4. Finally, the resulting equation is projected onto on-shell processes. In the present case this is done by a matrix multiplication of the equation with the *Floquet spectral function* $A_{\nu,nm}(\omega)$ and a subsequent combination of integration over frequencies and tracing over Floquet indices. For weakly interacting systems the Floquet spectral function is approximately given by (cf. Eqs. (4.82) and (5.28))

$$\underset{\nu,nm}{A_{t_0,ij}}(\omega) \approx 2\pi\delta(\omega - \varepsilon_{t_0,\nu})\, \phi^n_{t_0,\nu}(i)\, \bar{\phi}^m_{t_0,\nu}(j)\,. \tag{5.43}$$

   This ensures the projection of the kinetic equation onto a Floquet state with quantum number ν. In other words, we follow a quasiparticle approximation (see Sec. 4.3.2) where the quasiparticles are determined to good approximation by non-interacting Floquet eigenstates. Hence, the final result of these steps is an equation that describes the occupation functions $n_\nu(\mathbf{r}, t)$ of the corresponding Floquet eigenstates at time t.

Note that these steps are generally applicable for all fermionic Floquet systems as long as the discussed approximations hold, i.e., interactions are weak and the separation of time scales is manifest. The corresponding Floquet states at time t are given by the eigenstates of the Floquet Hamiltonian (5.5), where one subsequently equates $t_0 = t$.

For a *periodically driven lattice model* with n_u sites per (spatial) unit cell, the eigenfunctions are calculated in momentum space by diagonalizing a $n_u(2N_f+1) \times n_u(2N_f+1)$ dimensional matrix, with N_f being the truncation size of the Floquet matrix (see Sec. 2.2). So for a Hamiltonian where the non-interacting part is of type (5.4) the Floquet state index ν can be understood as a collection of a momentum quantum number $\mathbf{k}$, a Floquet band index ξ and a spin index σ, i.e., $\nu = (\mathbf{k}, \xi, \sigma)$. In addition, similar to the treatment of the variable t_0, which was introduced to deal with slow time dependencies, we also allow that the Hamiltonian depends smoothly on the spatial parameter $\mathbf{r}_0$. In complete analogy to the temporal case where the full time dependence of the Floquet states are recovered by setting $t_0 = t$, we identify $\mathbf{r}_0 = \mathbf{r}$ in order to describe the states also as functions of space. In the following we will, thus, denote the Floquet components of the corresponding eigenfunctions by $\phi^n_{t,\mathbf{r},\mathbf{k},\xi,\sigma}(i)$, where $n = -N_f, -N_f+1, ..., N_f$ is the Floquet index and $i = 1, \ldots, n_u$ describes the structure of the Bloch-Floquet wave function within the unit cell. Note that below we will sometimes omit the slowly varying indices, i.e., t and $\mathbf{r}$, in order to simplify notations and just write, e.g., $\phi^n_{\mathbf{k},\xi,\sigma}(i)$.

For the following discussion of deriving the Floquet-Boltzmann equation, we will put emphasis on the parts that are either unique to Floquet systems or have not been dealt with in Ch. 4. So for parts of the derivation that are identical for Floquet systems and conventional cases one can view the following discussion as being complementary to Ch. 4. This applies particularly to the treatment of the space variable. In favour of structural clarity we will first discuss the left-hand side of the Floquet-Boltzmann equation before we analyse the right-hand side.

5.4.2. Semiclassical dynamics and Floquet Berry-phase corrections

We now closely follow the 4-step protocol above to discuss the left-hand side of the quantum kinetic equation (4.52) within a Floquet semiclassical approximation. The first task is to find a Floquet-Wigner representation of $[F \,\overset{\circ}{,}\, G_0^{-1}]$. For that purpose we write the temporal part of the convolution in terms of a Floquet-Moyal product (5.42), which introduces a matrix multiplication in Floquet space, as discussed above. The spatial part is still resolved with the ordinary Moyal product (4.74) and, thus, does not introduce further additional indices. Suppressing all indices except for the Floquet ones, the Floquet-Wigner transformation (FWT) of the left-hand side to lowest order in $\partial_x \partial_p$ is given by (cf. Eq. (4.78))

$$\left[F \overset{\circ}{,} G^{-1}\right] \xrightarrow{\text{FWT}} \frac{i}{2} \sum_{m'} \Big[\left(\partial_x F_{nm'}\right)\left(\partial_p G^{-1}_{m'm}\right) - \left(\partial_p F_{nm'}\right)\left(\partial_x G^{-1}_{m'm}\right) - \left(\partial_x G^{-1}_{nm'}\right)\left(\partial_p F_{m'm}\right) + \left(\partial_p G^{-1}_{nm'}\right)\left(\partial_x F_{m'm}\right) \Big], \tag{5.44}$$

where it is still understood that $\partial_x \partial_p = \nabla_{\mathbf{r}} \nabla_{\mathbf{k}} - \partial_t \partial_\omega$ and that $G^{-1} \equiv [G_0^{R/A}]^{-1}$ is the inverse non-interacting (retarded/advanced) Green's function. Note that we also suppressed the matrix product in the spatial index running over sites within a single unit cell in Eq. (5.44).

Since we aim at deriving a lowest order simplification of the original QKE in the spirit described above, we are allowed to find the non-interacting Green's function from a similar

lowest order approximation to the Dyson equation. Within this approximation the Dyson equation in Floquet representation takes exactly the form of Eq. (5.30). Hence, we are allowed to use directly the Green's functions that were derived in Sec. 5.2.2. The inverse Green's function in Floquet representation is therefore given by $G^{-1}_{ij,nm} = \sum_{\nu,l}(\omega - \varepsilon_\nu - l\Omega)\phi^{n+l}_\nu(i)\bar{\phi}^{m+l}_\nu(j)$, where again all additional variables have been suppressed. In addition, since interactions are weak, we assume that also the distribution matrix F is given by its non-interacting form (5.29) with $n_\nu = n_\nu(t)$. For instance, the first term of Eq. 5.44 therefore takes the form (up to a factor of $i/2$)

$$\sum_{m',j'} \Big(\nabla_{\mathbf{r}} F_{\substack{ij'\\nm'}}\Big)\Big(\nabla_{\mathbf{k}} G^{-1}_{\substack{j'j\\m'm}}\Big) = \sum_{m',j'} \nabla_{\mathbf{r}}\Big(\sum_{\xi,l} \phi^{n+l}_{\mathbf{k},\xi}(i)\,\bar{\phi}^{m'+l}_{\mathbf{k},\xi}(j')\,(1-2n_{\mathbf{k},\xi})\Big) \tag{5.45}$$

$$\times\ \nabla_{\mathbf{k}}\Big(\sum_{\xi',l'} \phi^{m'+l'}_{\mathbf{k},\xi'}(j')\,\bar{\phi}^{m+l'}_{\mathbf{k},\xi}(j)\,(\omega - \varepsilon_{\mathbf{k},\xi'} - l'\Omega)\Big)$$

$$= 2\sum_{\xi,l} \phi^{n+l}_{\mathbf{k},\xi}(i)\,\bar{\phi}^{m+l}_{\mathbf{k},\xi}(j)\,(\nabla_{\mathbf{r}} n_{\mathbf{k},\xi})(\nabla_{\mathbf{k}}\varepsilon_{\mathbf{k},\xi}) \;+\; \dots \quad , \tag{5.46}$$

where it was used that $\sum_{n,i} \phi^{n+l}_\nu(i)\bar{\phi}^{n+l'}_\mu(i) = \langle\!\langle \phi_{\nu l}|\phi_{\mu l'}\rangle\!\rangle = \delta_{\nu\mu}\delta_{ll'}$ and slow variables $t, \mathbf{r}$ have been suppressed. We have further absorbed the spin index σ into the band index ξ (and will stay with this convention for the rest of this section). The partial derivatives in Eq. (5.45) yield a contribution from acting on the respective diagonal entries in Floquet band space, see Eq. (5.46). Note crucially that the derivatives give additional contributions from acting on the Floquet eigenstates. We will, however, ignore these latter contributions indicated by $'\dots'$ in (5.46) for the time being, but discuss them later on.

In the next step we project the quantum kinetic equation onto on-shell processes. This is done by following the above advice of multiplying the transformed QKE with the Floquet spectral function and performing a subsequent integration over frequencies. We show this again exemplarily for the first term of the left-hand side, which becomes[5]

$$\int \frac{d\omega}{2\pi}\ \mathrm{Tr}\Big[A_{\mathbf{k},\xi} \circ (5.46)\Big] = 2\Big(\nabla_{\mathbf{r}} n_{\mathbf{k},\xi}(\mathbf{r},t)\Big)\Big(\nabla_{\mathbf{k}}\varepsilon_{\mathbf{k},\xi}(\mathbf{r},t)\Big) \;+\; \dots\,, \tag{5.47}$$

where again it was used that $\langle\!\langle \phi_{\nu l}|\phi_{\mu l'}\rangle\!\rangle = \delta_{\nu\mu}\delta_{ll'}$. Repeating this procedure for every term of Eq. (5.44) then yields a similar form of the left-hand side (lhs) as in the ordinary case (cf. Sec. 4.3.2), i.e.,

$$\mathrm{lhs} \;\propto\; \Big(\partial_t - (\nabla_{\mathbf{r}}\varepsilon_{\mathbf{k},\xi}(\mathbf{r},t))\nabla_{\mathbf{k}} + (\nabla_{\mathbf{k}}\varepsilon_{\mathbf{k},\xi}(\mathbf{r},t))\nabla_{\mathbf{r}}\Big)\, n_{\mathbf{k},\xi}(\mathbf{r},t)\,. \tag{5.48}$$

The main difference to the non-Floquet case, however, is that $n_\xi(t)$ now describes occupation numbers of Floquet eigenstates and ε_ξ are the quasienergies of the system. Note that corrections due to the real parts of self-energies are absent here. This is due to the fact that we assumed to have incorporated the leading order corrections (Hartree-Fock) by renormalizing the energies of the Floquet system (see Sec. 5.2). Nonetheless, while expression (5.48) looks already promising in the sense that it resembles the standard Boltzmann equation, it only represents one part of the final result. In order to obtain the latter we need to include the so far neglected corrections due to differentiation of Floquet states.

In order to proceed we rephrase the problem in the following way: how can one efficiently combine a Floquet-Moyal product and a band projection procedure? In fact, this is not a unique problem for Floquet systems, but rather applies to band models in general. The

[5] Note that the $'\circ'$ on the left-hand side of Eq. (5.47) does not describe a Floquet-Moyal product but only refers to a simple matrix multiplication in Floquet and space indices.

solution to this issue was presented quite recently by Wickles and Belzig [226]. They argued that the correct way to think about diagonalising an object of interest, e.g., F, is

$$F_\Lambda = \Lambda \circ F \circ \Lambda^\dagger \,, \tag{5.49}$$

with $\Lambda \circ \Lambda^\dagger = \mathbb{1}$. Here, the crucial point is that the diagonalising object Λ is required to be unitary under the Moyal product and, hence, cannot be straightforwardly determined. However, one can systematically calculate corrections by choosing the ansatz $\Lambda = \Lambda_0(\mathbb{1} + \Lambda_1 + \ldots)$. Here, $\Lambda_0(\mathbf{r}, t, \mathbf{k})$ describes the transformation that diagonalises the object of interest in its Wigner form with respect to the band space, e.g., $F_{\Lambda_0} = \Lambda_0 F \Lambda_0^\dagger$. Wickles and Belzig showed that such a trivial diagonalisation via simple matrix multiplication still respects Eq. (5.49) to lowest order, if at the same time the exponent of the Moyal product appearing in (5.49) gets corrections from *Berry phases*. Thus, also the left-hand side of the kinetic equation experiences these corrections, since the on-shell projection is preceded by a diagonalisation procedure in the respective band space. The final result is that velocities and forces of Eq. (4.85) are modified according to these Berry-phases. The resulting semiclassical equation of motion coincide with expressions that were derived before in a different context considering the explicit description of semiclassical wavepackets by Niu *et al.* [295].

One can now repeat the calculation by Wickles and Belzig explicitly for Floquet systems. We present only the core ideas here and refer for details to Ref. [226] due to the following reason: as discussed above, since the entire Floquet character of the system can be absorbed into a simple matrix structure (assuming that a separation of time scales is given), the derivation for ordinary band systems carries directly over to periodically driven systems. To be more specific, it becomes immediately apparent from Sec. (5.2.2) that in a Floquet case the transformation Λ_0 is given by the matrix of Floquet eigenstates. An expansion of the Floquet-Moyal product $\Lambda \circ \Lambda^\dagger$ therefore yields expressions of the form

$$\Lambda_0 \, \partial_\alpha \, \Lambda_0^\dagger = \partial_\alpha - i \mathcal{A}_\alpha^F \,, \tag{5.50}$$

where we used that $\alpha = (\mathbf{r}, t, \mathbf{k}, \omega)$ and $\mathcal{A}_\alpha^F$ is the matrix of Floquet-Berry connections, see Eq. (2.71). One can now study how the combination of both evaluating the Floquet-Moyal product and projecting onto Floquet bands can be represented in terms of Eq. (5.50). The result is a modification of the Floquet-Moyal product in terms of Floquet-Berry connections. For the procedure of multiplying the object of interest with the Floquet spectral function (5.43) followed by tracing over Floquet indices and integrating over energies, one finds that a projected convolution $B \circ C$ can be reformulated as

$$\int \frac{d\omega}{2\pi} \, \mathrm{Tr}\big[A_\xi \, (B \circ C)\big] \quad \to \quad \big[\, B \,\tilde{\circ}\, C \,\big]_\xi \,, \tag{5.51}$$

where the modified Moyal product $\tilde{\circ}$ is defined as

$$\big[\, B \,\tilde{\circ}\, C \,\big]_\xi = \exp\Big[\frac{i}{2}\Big(\partial_x^B \partial_p^C - \partial_p^B \partial_x^C\Big) + \frac{i}{2} \, \partial_{\bar{\alpha}}^B \, \Omega_{\xi,\alpha\beta} \, \partial_{\bar{\beta}}^C \Big] \, B_{\Lambda_0,\xi} \, C_{\Lambda_0,\xi} \Big|_{\omega=\varepsilon_\xi} \,. \tag{5.52}$$

One understands $B_{\Lambda_0,\xi}$ as being the ξ-component of the Floquet-Wigner representation of B that has been diagonalised by Λ_0. The first term of the exponential is the same as in the ordinary Moyal product (4.74) with $x = (\mathbf{r}, t)$ and $p = (\mathbf{k}, \omega)$. The second term is the correction coming from Eq. (5.50). Note that the indices are generally given by $\alpha, \beta = (t, r_1, r_2, r_3, k_1, k_2, k_3)$ and $\bar{\alpha}, \bar{\beta}$ are determined from α, β using the rules $\mathbf{r} \leftrightarrow \mathbf{k}$ and $t \leftrightarrow \omega$. Also, the rule $\partial_{\bar{\alpha}} = (\partial_\mathbf{r}, -\partial_\mathbf{k}, \partial_\omega)$ needs to be applied. Most importantly, we have

introduced the Floquet version of the *Berry-curvature tensor* $\Omega_{\xi,\alpha\beta}$ in Eq. (5.52). The explicit form (for non-crossing Floquet bands) reads as

$$\begin{aligned}\Omega_{\xi,\alpha\beta} &= \partial_\alpha \mathcal{A}^F_{\xi,\beta} - \partial_\beta \mathcal{A}^F_{\xi,\alpha} \\ &= i\left[\langle\langle \partial_\alpha \phi_\xi | \partial_\beta \phi_\xi \rangle\rangle - \langle\langle \partial_\beta \phi_\xi | \partial_\alpha \phi_\xi \rangle\rangle\right] \\ &= i \sum_{i,n} \left[\left(\partial_\alpha \bar{\phi}^n_\xi(i)\right)\left(\partial_\beta \phi^n_\xi(i)\right) - \left(\partial_\beta \bar{\phi}^n_\xi(i)\right)\left(\partial_\alpha \phi^n_\xi(i)\right)\right],\end{aligned} \tag{5.53}$$

where it should be understood that most variables have been suppressed, i.e., $\phi_\xi = \phi_{t,\mathbf{r},\mathbf{k},\xi}$, etc. Here, it becomes clear why the indices $\alpha, \beta = (\mathbf{r}, t, \mathbf{k})$ only run over space, time and momentum variables, but *not* over frequency: it is assumed that Floquet eigenstates do not depend on ω, i.e., $\partial_\omega \phi_\xi = 0$.

By setting $B_{\Lambda_0,\xi} = F_{\Lambda_0,\xi} = (1 - 2n_\xi)$ and $C_{\Lambda_0,\xi} = G^{-1}_{\Lambda_0,\xi} = (\omega - \varepsilon_\xi)$ one can straightforwardly determine the left-hand side of the quantum kinetic equation in terms of its Floquet-Wigner transformation that respects Berry-phase corrections at the same time. One finds that for Floquet systems the respective Berry curvatures modify the semiclassical equations of motion in a similar way as done in the ordinary case [226, 295]. The only difference is that now Berry curvatures are calculated from Floquet eigenstates.

The left-hand side of the Floquet-Boltzmann equation can thus be written in the following compact form[6]

$$\left(\partial_t + \boldsymbol{\mathcal{F}}_{\mathbf{k},\xi} \nabla_{\mathbf{k}} + \mathbf{v}_{\mathbf{k},\xi} \nabla_{\mathbf{r}}\right) n_{\mathbf{k},\xi}(\mathbf{r}, t) = I_{\text{coll}}[n_{\mathbf{k},\xi}] \tag{5.54}$$

with

$$\boldsymbol{v}_{\mathbf{k},\xi} = (\mathbb{1} + \boldsymbol{\Omega}_{\xi,rk}) \cdot \nabla_{\mathbf{k}} \epsilon_\xi - \boldsymbol{\Omega}_{\xi,kt} + \boldsymbol{\Omega}_{\xi,kk} \cdot \nabla_{\mathbf{r}} \epsilon_\xi \quad , \tag{5.55}$$

$$\boldsymbol{\mathcal{F}}_{\mathbf{k},\xi} = -(\mathbb{1} + \boldsymbol{\Omega}_{\xi,rk}) \cdot \nabla_{\mathbf{r}} \epsilon_\xi + \boldsymbol{\Omega}_{\xi,rt} + \boldsymbol{\Omega}_{\xi,rr} \cdot \nabla_{\mathbf{k}} \epsilon_\xi \quad , \tag{5.56}$$

where, in general, the effective forces and velocities also depend smoothly on time and space, $\boldsymbol{\mathcal{F}}_{\mathbf{k},\xi} = \boldsymbol{\mathcal{F}}_{\mathbf{k},\xi}(\mathbf{r}, t)$ and $\mathbf{v}_{\mathbf{k},\xi} = \mathbf{v}_{\mathbf{k},\xi}(\mathbf{r}, t)$. The collision integral I_{coll} corresponds to the projected right-hand side of the QKE and will be discussed in the following section 5.4.3.

Note that $\boldsymbol{\Omega}_{rk}$, $\boldsymbol{\Omega}_{rr}$ and $\boldsymbol{\Omega}_{kk}$ are matrices with $r, k = (1, 2, 3)$, and can be related to effective magnetic fields in phase space. On the other hand, $\boldsymbol{\Omega}_{rt}$ and $\boldsymbol{\Omega}_{kt}$ are vectors and referred to effective electric fields. Since many modern applications of Floquet Hamiltonians (see Sec. 2.3) have the goal to realize systems with non-trivial Berry phases, it is important to keep track of these effects on the left-hand side of the Floquet-Boltzmann equation (see also Ch. 7).

5.4.3. Scattering of Floquet quasiparticles

The right-hand side (rhs) of the quantum kinetic equation is mainly described by the self-energies of the interacting system, see Eq. (4.52). So in order to calculate

$$\Sigma^K - \left(\Sigma^R \circ F - F \circ \Sigma^A\right), \tag{5.57}$$

in its Floquet-Wigner representation, we start from the second-order expressions of the self-energies (4.64) and (4.65). In order to find explicit forms of Σ^R and Σ^K corresponding

[6] Note that by bringing the left-hand side into the form of Eq. (5.54) we absorbed a factor of $-\frac{i}{2}$ into the collision integral (cf. discussion below Eq. (4.85)).

expressions for the Green's functions are needed: as discussed above, due to the assumed separation of time scales it is sufficient to evaluate the Green's function using a zeroth-order Floquet-Moyal expansion of the Dyson equation $(\hat{G}_0^{-1} - \hat{\Sigma}) \circ \hat{G} = \mathbb{1}$, see also Eq. (4.47). Furthermore, despite the fact that Green's functions are calculated self-consistently, here, we do not have to include any further self-energy corrections to the Green's functions within our perturbative approach. This is because all self-energies are already $\propto U^2$ and further corrections will be small as interactions are weak. Making the same argument as in the previous section, the Dyson equation, which describes the Green's functions that appear in each self-energy diagram, effectively reduces to the simplified form of Eq. (5.30). This implies again that we are allowed to directly use the non-interacting Floquet Green's functions of Sec. 5.2.2. Here, however, all quantities are replaced by their versions with full dependencies on space and time, e.g., $n_\nu = n_{\mathbf{k},\xi,\sigma}(\mathbf{r},t)$ and $\epsilon_\nu = \epsilon_{\mathbf{k},\xi,\sigma}(\mathbf{r},t)$, etc. Note that we will drop the slow changing variables $\mathbf{r}, t$ at convenience throughout this section.

To evaluate the Floquet-Wigner representation of the self-energies Σ^R and Σ^K we are going to consider every term of the respective expressions individually. However, in order to avoid redundancies we will present the transformation in detail only for a single term. Due to no particular reason we will first focus on the first term of the expression for the Keldysh self-energy, i.e.,

$$\Sigma_\sigma^{K(1)}(x,x') = -\frac{U^2}{4}\left[\, G_{\bar{\sigma}}^K(x',x)\, G_{\bar{\sigma}}^K(x,x')\, G_\sigma^K(x,x') \,\right], \tag{5.58}$$

where $\bar{\sigma} = \downarrow (\uparrow)$ for $\sigma = \uparrow (\downarrow)$ and the superscript '(1)' indeed refers to the first term of Eq. (4.65). To make progress one needs to apply *twice* the identities (4.72) and (5.36) to transform an algebraic product of two-point functions. Here, the first expression deals with the spatial coordinate and the second one encodes the Floquet structure in the temporal transformation. The Floquet-Wigner transformation of Eq. (5.58) then becomes

$$\begin{aligned}\Sigma_{\substack{ij,\sigma\\nm}}^{K(1)}(\mathbf{k},\omega) = -\frac{U^2}{4}\sum_{n',m'}\sum_{n'',m''}\int\frac{d\omega'}{2\pi}\int\frac{d\omega''}{2\pi}\int\frac{d\mathbf{p}}{(2\pi/a)^d}\int\frac{d\mathbf{q}}{(2\pi/a)^d} \\ \times\; G_{\substack{ji,\bar{\sigma}\\m''-m'n''-n'}}^K(\mathbf{q}-\mathbf{p},\omega''-\omega')\; G_{\substack{ij,\bar{\sigma}\\n''m''}}^K(\mathbf{q},\omega'')\; G_{\substack{ij,\sigma\\n-n'm-m'}}^K(\mathbf{k}-\mathbf{p},\omega-\omega')\,,\end{aligned} \tag{5.59}$$

with all frequencies being restricted to the first Floquet zone, $\omega, \omega', \omega'' \in [-\Omega/2, \Omega/2)$. Due to the underlying lattice model the momentum space integral only runs over the first Brillouin zone, $\int d\mathbf{p} \equiv \int_{\mathrm{BZ}} d\mathbf{p}$. Also, to have a set of normalised Fourier transformations (cf. (3.6)) we demand that every momentum integral is divided by the volume of the Brillouin zone $(2\pi/a)^d$, with d indicating the number of spatial dimensions and a denotes the lattice constant. Notice further that there is a little subtlety involved in finding Eq. (5.59): once the form of the object with reversed indices, e.g., $G^K(x',x)$, is fixed under the transformation, one has a certain liberty in assigning the variables to the other two remaining objects. In general one therefore wants to choose a symmetrised version of the transformation, meaning that different configurations are weighted equally[7].

Using the explicit Floquet form of the non-interacting Keldyh Green's function, see

[7] In the present example, in fact, one should symmetrise with respect to the spin index of the forward flowing objects. However, in order to present a slightly shortened form of the derivation we assume that the system is degenerate with respect to the spin index. Notationally, this allows for a 'locking' of the spin and momentum label.

Eq. (5.27), the expression above can be written as

$$\begin{aligned}\Sigma^{K(1)}_{\substack{ij,\sigma\\nm}}(\mathbf{k},\omega) = &-\frac{i\pi U^2}{2}\sum_{n',m'}\sum_{n'',m''}\int d\omega'\int d\omega''\int\frac{d\mathbf{p}}{(2\pi/a)^d}\int\frac{d\mathbf{q}}{(2\pi/a)^d} \\ &\times\sum_{\mu,s}\delta(\omega''-\omega'-\varepsilon_{\mathbf{q}-\mathbf{p},\mu,\bar\sigma}-s\Omega)\,\phi^{m''-m'+s}_{\mathbf{q}-\mathbf{p},\mu,\bar\sigma}(j)\,\bar\phi^{n''-n'+s}_{\mathbf{q}-\mathbf{p},\mu,\bar\sigma}(i)\,\widetilde F_{\mathbf{q}-\mathbf{p},\mu,\bar\sigma} \\ &\times\sum_{\lambda,u}\delta(\omega''-\varepsilon_{\mathbf{q},\lambda,\bar\sigma}-u\Omega)\,\phi^{n''+u}_{\mathbf{q},\lambda,\bar\sigma}(i)\,\bar\phi^{m''+u}_{\mathbf{q},\lambda,\bar\sigma}(j)\,\widetilde F_{\mathbf{q},\lambda,\bar\sigma} \\ &\times\sum_{\eta,l}\delta(\omega-\omega'-\varepsilon_{\mathbf{k}-\mathbf{p},\eta,\sigma}-l\Omega)\,\phi^{n-n'+l}_{\mathbf{k}-\mathbf{p},\eta,\sigma}(i)\,\bar\phi^{m-m'+l}_{\mathbf{k}-\mathbf{p},\eta,\sigma}(j)\,\widetilde F_{\mathbf{k}-\mathbf{p},\eta,\sigma}\,,\end{aligned} \tag{5.60}$$

where we introduced $\widetilde F_{\mathbf{k},\xi,\sigma} = (1-2n_{\mathbf{k},\xi,\sigma})$, and omitted $\mathbf{r}$ and t labels. Note for clarification that s, u, l, n, m, etc. are Floquet indices, while μ, λ, η are (Floquet) band indices and i, j denote sites within the unit cell. When simplifying Eq. (5.60) by integration over frequencies and summing over Floquet indices, one has to be cautious regarding the domains of frequency arguments. The general strategy is to use the replica structure of the Floquet states: one absorbs the indices (n', n'') into the δ-functions by an appropriate relabelling of other Floquet indices. Consequently, a combined frequency integration of $\int d\omega' \sum_{n'}$ and $\int d\omega'' \sum_{n''}$ can be performed, respectively. In fact, it is mainly this careful treatment of frequency domains and tracking of Floquet indices which distinguishes this derivation from the ordinary one in Sec. 4.3. Nevertheless, after a successive evaluation of such frequency integrations accompanied by convenient shifts of respective Floquet indices one eventually succeeds in rewriting Eq. (5.60) in the simplified form of

$$\begin{aligned}\Sigma^{K(1)}_{\substack{ij,\sigma\\nm}}(\mathbf{k},\omega) = &-\frac{i\pi U^2}{2}\sum_{\mu,\lambda,\eta}\sum_{s,u,l}\int\frac{d\mathbf{p}}{(2\pi/a)^d}\int\frac{d\mathbf{q}}{(2\pi/a)^d}\;\Phi^{sul}_{\substack{\mu\lambda\eta,\sigma\\\mathbf{kpq}}}(n,m,i,j) \\ &\times\;\delta\big(\omega+\varepsilon_{\mathbf{q}-\mathbf{p},\mu,\bar\sigma}-\varepsilon_{\mathbf{q},\lambda,\sigma}-\varepsilon_{\mathbf{k}-\mathbf{p},\eta,\bar\sigma}+\Delta_{sul}\Omega\big) \\ &\times\;\widetilde F_{\mathbf{q}-\mathbf{p},\mu,\bar\sigma}\,\widetilde F_{\mathbf{q},\lambda,\bar\sigma}\,\widetilde F_{\mathbf{k}-\mathbf{p},\eta,\sigma}\,,\end{aligned} \tag{5.61}$$

with $\Delta_{sul} = s-u-l$, and

$$\begin{aligned}\Phi^{sul}_{\substack{\mu\lambda\eta,\sigma\\\mathbf{kpq}}}(n,m,i,j) = &\sum_{m',m''}\phi^{m'+s}_{\mathbf{q}-\mathbf{p},\mu,\bar\sigma}(j)\,\bar\phi^{m''+s}_{\mathbf{q}-\mathbf{p},\mu,\bar\sigma}(i)\,\phi^{m''+u}_{\mathbf{q},\lambda,\bar\sigma}(i) \\ &\times\;\bar\phi^{m+u}_{\mathbf{q},\lambda,\bar\sigma}(j)\,\phi^{n+l}_{\mathbf{k}-\mathbf{p},\eta,\sigma}(i)\,\bar\phi^{m'+l}_{\mathbf{k}-\mathbf{p},\eta,\sigma}(j)\,.\end{aligned} \tag{5.62}$$

Now, the last remaining step is to evaluate the resulting formula on shell: we multiply the right-hand side of the quantum kinetic equation (5.57) by the Floquet-spectral function of a certain Floquet state with quantum numbers $\mathbf{k}$ and ξ, see Eq. (5.43), integrate over frequencies and finally trace over Floquet as well as space indices. In the following, we shall use a short-hand notation (cf. Eq. (5.51)) incorporating this procedure

$$\Big[(..)(\mathbf{k})\Big]_\xi \equiv \int\frac{d\omega}{2\pi}\;\mathrm{Tr}\Big[A_{\mathbf{k},\xi}(\omega)\,(..)(\mathbf{k},\omega)\Big]\,, \tag{5.63}$$

where (..) denotes any two-point object in Floquet-Wigner representation. Applying this transformation to the specific term of the Keldysh Green's function given by Eq. (5.61) then yields

$$\begin{aligned}\Big[\Sigma^{K(1)}_\sigma(\mathbf{k})\Big]_\xi = &-\frac{i\pi U^2}{2}\sum_{\mu,\lambda,\eta}\sum_{s,u,l}\int\frac{d\mathbf{p}}{(2\pi/a)^d}\int\frac{d\mathbf{q}}{(2\pi/a)^d}\;\Phi^{sul}_{\substack{\mu\lambda\eta,\sigma\\\mathbf{kpq}}}(\xi) \\ &\times\;\delta\big(\varepsilon_{\mathbf{k},\xi,\sigma}+\varepsilon_{\mathbf{q}-\mathbf{p},\mu,\bar\sigma}-\varepsilon_{\mathbf{q},\lambda,\bar\sigma}-\varepsilon_{\mathbf{k}-\mathbf{p},\eta,\sigma}+\Delta_{sul}\Omega\big) \\ &\times\;\widetilde F_{\mathbf{q}-\mathbf{p},\mu,\bar\sigma}\,\widetilde F_{\mathbf{q},\lambda,\bar\sigma}\,\widetilde F_{\mathbf{k}-\mathbf{p},\eta,\sigma}\,,\end{aligned} \tag{5.64}$$

where the transformed matrix element reads as

$$\Phi^{sul}_{\substack{\mu\lambda\eta,\sigma\\ \mathbf{kpq}}}(\xi) = \sum_{i,j}\sum_{n,m} \bar{\phi}^{n}_{\mathbf{k},\xi,\sigma}(i)\, \Phi^{sul}_{\substack{\eta\mu\lambda,\sigma\\ \mathbf{kpq}}}(n,m,i,j)\, \phi^{m}_{\mathbf{k},\xi,\sigma}(j)\,. \tag{5.65}$$

One then repeats this entire calculation in order to find all other terms of Σ^K in their respective Floquet-Wigner representation. Next to G^K one now also uses explicit Floquet representations of $G^R - G^A$, see Eq. (5.28). By respecting initial symmetrisations, performing frequency integrals and projecting onto Floquet state $(\mathbf{k},\xi)$ one eventually obtains an expression for the full contribution to the second order Keldysh self-energy

$$\begin{aligned}\left[\Sigma^K_\sigma(\mathbf{k})\right]_\xi = &-\frac{i\pi U^2}{2}\sum_{\mu,\lambda,\eta}\sum_{s,u,l}\int\frac{d\mathbf{p}}{(2\pi/a)^d}\int\frac{d\mathbf{q}}{(2\pi/a)^d}\;\Phi^{sul}_{\substack{\mu\lambda\eta,\sigma\\ \mathbf{kpq}}}(\xi)\\ &\times\;\delta\big(\varepsilon_{\mathbf{k},\xi,\sigma}+\varepsilon_{\mathbf{q}-\mathbf{p},\mu,\bar{\sigma}}-\varepsilon_{\mathbf{q},\lambda,\bar{\sigma}}-\varepsilon_{\mathbf{k}-\mathbf{p},\eta,\sigma}+\Delta_{sul}\Omega\big)\\ &\times\;\Big[\widetilde{F}_{\mathbf{q}-\mathbf{p},\mu,\bar{\sigma}}\,\widetilde{F}_{\mathbf{q},\lambda,\bar{\sigma}}\,\widetilde{F}_{\mathbf{k}-\mathbf{p},\eta,\sigma}+\widetilde{F}_{\mathbf{q}-\mathbf{p},\mu,\bar{\sigma}}-\widetilde{F}_{\mathbf{q},\lambda,\bar{\sigma}}-\widetilde{F}_{\mathbf{k}-\mathbf{p},\eta,\sigma}\Big]\,.\end{aligned} \tag{5.66}$$

In the next step we consider $\Sigma^R\circ F - F\circ\Sigma^A$, i.e., the second term of the QKE's right-hand side. One also starts by finding individual terms of the retarded and advanced self-energies in Floquet-Wigner representation, similar to Eq. (5.60). Here, however, one notices that frequency integration cannot be performed straightforwardly. This is because retarded and advanced non-interacting Green's functions of type (5.23) and (5.24) appear explicitly instead of their difference $G^R - G^A$. Nevertheless, one can still find a simplified expression by first recalling that the right-hand side (5.57) requires only a zeroth order expansion of the Floquet-Moyal product. Hence, the Floquet-Wigner representation approximately takes on the from

$$\big(\,\Sigma^R\circ F - F\circ\Sigma^A\,\big) \quad\xrightarrow{\text{FWT}}\quad \sum_{m'}\big(\Sigma^R_{nm'}\,F_{m'm} - F_{nm'}\,\Sigma^A_{m'm}\,\big)\,, \tag{5.67}$$

where all indices but Floquet ones have been suppressed such that objects on the right are to be understood as $\Sigma^R_{nm} = \Sigma^R_{nm,ij,\sigma}(\mathbf{r},t,\mathbf{k},\omega)$, etc. Applying the projection (5.63), it can be straightforwardly shown that Eq. (5.67) is further reduced to[8]

$$\Big[\Sigma^R\circ F - F\circ\Sigma^A\Big]_\xi = \widetilde{F}_{\mathbf{k},\xi,\sigma}\sum_{i,j}\sum_{n,m}\phi^{m}_{\mathbf{k},\xi,\sigma}(j)\,\bar{\phi}^{n}_{\mathbf{k},\xi,\sigma}(i)\;\big(\Sigma^R-\Sigma^A\big)^{ij,\sigma}_{nm}(\mathbf{k},\varepsilon_{\mathbf{k},\xi,\sigma}) \tag{5.68}$$

by using the explicit form of F given by (5.29) as well as properties of Floquet states. Since the expression now depends on the difference $(\Sigma^R-\Sigma^A)$, also G^R and G^A appear in form of $G^R - G^A$ throughout the individual terms. This allows then a straightforward integration over frequencies as shown above. The final result for the projected Floquet-Wigner form of the second term of (5.57) is then calculated to be

$$\begin{aligned}\Big[\Sigma^R\circ F - F\circ\Sigma^A\Big]_\xi = &\frac{i\pi U^2}{2}\sum_{\mu,\lambda,\eta}\sum_{s,u,l}\int\frac{d\mathbf{p}}{(2\pi/a)^d}\int\frac{d\mathbf{q}}{(2\pi/a)^d}\;\Phi^{sul}_{\substack{\mu\lambda\eta,\sigma\\ \mathbf{kpq}}}(\xi)\\ &\times\;\delta\big(\varepsilon_{\mathbf{k},\xi,\sigma}+\varepsilon_{\mathbf{q}-\mathbf{p},\mu,\bar{\sigma}}-\varepsilon_{\mathbf{q},\lambda,\sigma}-\varepsilon_{\mathbf{k}-\mathbf{p},\eta,\bar{\sigma}}+\Delta_{sul}\Omega\big)\\ &\times\;\widetilde{F}_{\mathbf{k},\xi,\sigma}\Big[\,1+\widetilde{F}_{\mathbf{q},\lambda,\bar{\sigma}}\,\widetilde{F}_{\mathbf{k}-\mathbf{p},\eta,\sigma}-\widetilde{F}_{\mathbf{q}-\mathbf{p},\mu,\bar{\sigma}}\,\big(\widetilde{F}_{\mathbf{q},\lambda,\bar{\sigma}}+\widetilde{F}_{\mathbf{k}-\mathbf{p},\eta,\sigma}\big)\Big]\,.\end{aligned} \tag{5.69}$$

[8] Note that the discussion from Sec. 5.4.2 about a modified Floquet-Moyal product does not need to be applied here, because both procedures are identical to zeroth order.

Having calculated the expressions (5.66) and (5.69) allows now to find an explicit form of the *collision integral*. As defined in Sec. 5.4.2 the collision integral is proportional to the projected right-hand side of the QKE (see Eq. (5.54) and cf. Eq. (4.81)), and is given as

$$I_{\mathrm{coll}}[n_{\mathbf{k},\xi,\sigma}(\mathbf{r},t)] = -\frac{i}{2}\left[\Sigma^K - \left(\Sigma^R \circ F - F \circ \Sigma^A\right)\right]_\xi . \tag{5.70}$$

Here, the prefactor is due to the fact that the entire kinetic equation was divided by $2i$ in order to bring the left-hand side into the from of Eq. (5.54). One can now find a concrete expression for the collision integral in terms of the Floquet occupation functions $n_{\mathbf{k},\xi,\sigma}$. First, Eqs. (5.66) and (5.69) are substituted into Eq. (5.70) and the $\widetilde{F}$'s are re-expressed as $\widetilde{F}_{\mathbf{k},\xi,\sigma} = (1-2n_{\mathbf{k},\xi,\sigma})$. Next, in order to simplify the combination of occupation functions in a most convenient way, one adds and subtracts an additional term which is proportional to $n_\xi n_\mu n_\lambda n_\eta$. We shall also assume that quasienergies do not depend on spin. Moreover, it is convenient to introduce an individual momentum variable for each occupation function. At the same time, quasimomentum conservation is guaranteed by a corresponding δ-function. Note crucially that momentum is only conserved modulo reciprocal lattice vectors $\mathbf{G}_a$ due to the underlying lattice structure.

Performing the entire outlined procedure and allowing for yet another transformation of the matrix element (5.65), one eventually finds an expression for the collision integral which reads as

$$\begin{aligned} I_{\mathrm{coll}}[n_{\mathbf{k},\xi,\sigma}] = \sum_{\mu,\lambda,\eta}\sum_{\alpha,n}\int\frac{d\mathbf{q}_1}{(2\pi/a)^d}\int\frac{d\mathbf{q}_2}{(2\pi/a)^d}\int\frac{d\mathbf{q}_3}{(2\pi/a)^d} \\ \times\, W^n_{\substack{\xi\mu\lambda\eta,\sigma\\ \mathbf{k}\mathbf{q}_1\mathbf{q}_2\mathbf{q}_3}}\,(2\pi/a)^d\,\delta\big(\mathbf{k}+\mathbf{q}_1-\mathbf{q}_2-\mathbf{q}_3+\alpha\mathbf{G}\big) \\ \times\,\delta\big(\epsilon_{\mathbf{k},\xi,\sigma}+\epsilon_{\mathbf{q}_1,\mu,\bar\sigma}-\epsilon_{\mathbf{q}_2,\lambda,\bar\sigma}-\epsilon_{\mathbf{q}_3,\eta,\sigma}+n\Omega\big) \\ \times\,\Big[n_{\mathbf{q}_2,\lambda,\bar\sigma}\,n_{\mathbf{q}_3,\eta,\sigma}\,(1-n_{\mathbf{k},\xi,\sigma})\,(1-n_{\mathbf{q}_1,\mu,\bar\sigma}) \\ -\,n_{\mathbf{k},\xi,\sigma}\,n_{\mathbf{q}_1,\mu,\bar\sigma}\,(1-n_{\mathbf{q}_2,\lambda,\bar\sigma})\,(1-n_{\mathbf{q}_3,\eta,\sigma})\Big], \end{aligned} \tag{5.71}$$

where we have introduced the integers $\alpha, n \in \mathbb{Z}$ to account for umklapp scattering in momentum and frequency space, respectively. The matrix element W^n describes the scattering rate for a process involving a quantized energy transfer *to* the system of $n\Omega$, i.e., the system absorbs (emits) energy[9] for $n > 0$ (< 0). We obtain

$$W^n_{\substack{\xi\mu\lambda\eta,\sigma\\ \mathbf{k}\mathbf{q}_1\mathbf{q}_2\mathbf{q}_3}} = 2\pi\,U^2\,\left|\,V^n_{\substack{\xi\mu\lambda\eta,\sigma\\ \mathbf{k}\mathbf{q}_1\mathbf{q}_2\mathbf{q}_3}}\,\right|^2, \tag{5.72}$$

where the amplitude reads as

$$V^n_{\substack{\xi\mu\lambda\eta,\sigma\\ \mathbf{k}\mathbf{q}_1\mathbf{q}_2\mathbf{q}_3}} = \sum_i\sum_{\substack{n_1,n_2\\ n_3,n_4}}\delta_{n-(n_1+n_2-n_3-n_4)}\;\bar\phi^{n_1}_{\mathbf{k},\xi,\sigma}(i)\,\bar\phi^{n_2}_{\mathbf{q}_1,\mu,\bar\sigma}(i)\,\phi^{n_3}_{\mathbf{q}_2,\lambda,\bar\sigma}(i)\,\phi^{n_4}_{\mathbf{q}_3,\eta,\sigma}(i)\,. \tag{5.73}$$

We remark once more that space and time play two fundamentally different roles for the presented discussion. This can be directly seen from Eqs. (5.72) and (5.73). Here, the Floquet and momentum indices enter the matrix elements, and therefore the collision integral, in a completely different way: occupation functions depend on momentum and band indices, but do not depend on the Floquet indices. Correspondingly, we sum over Floquet indices in Eq. (5.73), but not over momentum or band indices.

[9] Note that this is in fact only true for non-winding Floquet bands. If the Floquet bands indeed wind around the Floquet-zone, a 'labelling' of the bands solely depending on the energy becomes impractical.

5.5. Discussion and Outlook

In this chapter, we have derived the *Floquet-Boltzmann equation* for periodically driven Fermi systems starting from the Keldysh dynamics of Green's functions. Based on conventional Floquet theory and a clear physical separation of time scales, we were able to formulate the Floquet-Wigner representation (and variants thereof) in order to find a semiclassical approximation to quantum kinetic equations in the presence of a fast periodic drive. The final result is an equation determining the dynamics of Floquet occupation functions given as

$$\Big(\partial_t + \boldsymbol{\mathcal{F}}_{\mathbf{k},\xi}(\mathbf{r},t)\,\nabla_{\mathbf{k}} + \boldsymbol{v}_{\mathbf{k},\xi}(\mathbf{r},t)\,\nabla_{\mathbf{r}}\Big)\, n_{\mathbf{k},\xi,\sigma}(\mathbf{r},t) = I_{\mathrm{coll}}[n_{\mathbf{k},\xi,\sigma}(\mathbf{r},t)]\,, \tag{5.74}$$

where the (effective) forces and velocities are given by Eqs. (5.55) and (5.56), and the collision integral forming the right-hand side is described by Eqs. (5.71)-(5.73). In the following we shall summarize and discuss the characteristics of this Floquet version of a Boltzmann equation, sketch its limitations as well as further potentials and, most importantly, shed light on prospects of applications.

Heating Comparing the formulas that determine the collision integral of the Floquet-Boltzmann equation, see Eqs. (5.71)-(5.73), with the result from the ordinary case, see Eq. (4.89), one observes strong structural resemblance. Nevertheless, there are two main differences:

1. The Floquet-Boltzmann equation is formulated for occupation functions of Floquet eigenstates n_ξ of the periodically driven many-body system. Indeed, also the matrix element W reflects the Floquet nature of the quasiparticles: scattering occurs between different Floquet states.

2. It was argued from the beginning that a Floquet system does preserve energy only up to integer multiplies of Ω. This property is formally embedded in the collision integral of the Floquet-Boltzmann eqation: every collision of Floquet quasiparticles may change the energy of the system in a discrete way, as given by the δ-function of Eq. (5.71).

Generally, the system relaxes to a state with maximal entropy allowed by the remaining conservation laws, see Sec. 5.1. If the system is closed, the latter property will therefore typically heat the system to an *infinite temperature* state in the long term. The dynamics described by the full Floquet-Boltzmann equation is therefore expected to depend strongly on this heating effect, which is in clear distinction to the conventional case. The ideal test ground for studying these Floquet-heating effects are homogeneous systems, i.e., such systems where all gradients are assumed to vanish. We will, thus, apply the Floquet-Boltzmann equation in a first approach to such a homogeneous system in chapter 6.

Since the Floquet-Boltzmann equation (5.74) was eventually determined in a lowest order (Born) approximation, the captured interaction effects are solely of two-particle nature. Hence, one could argue that the presented from of the collision integral, see Eq. (5.71), does not necessarily contain more information than scattering rates predicted by a Floquet version of Fermi's golden rule [115,262,284] in combination with an educated guess about the corresponding statistical factor. We want to stress, however, that the here developed Floquet-Boltzmann equation is a much more powerful tool than a simple 'golden rule' description. The reason being that our formalism indeed gives us control

over the semiclassical approximations in the sense that limitations of semiclassics can be investigated. Furthermore, our formalism allows for a systematic study beyond the lowest order approximation. In fact, these arguments are also the reason why we believe that our description yields advantages over a recently used equation-of-motion approach to derive a similar semiclassical kinetic equation in Floquet form [254]. We will extend the discussion about the capabilities of the Floquet-Boltzmann equation in the following.

Berry phase corrections The Floquet-Boltzmann equation does not only describe by its left-hand side the dynamics due to forces in an inhomogeneous system, see Eq. (5.74), but also manages to capture corrections due to Berry phases as pointed out above. While these corrections can also be incorporated in the conventional Boltzmann equation [226], a potential interplay between these Berry corrections and intrinsic heating effects seems to be unique to Floquet systems. The effects can be two-fold: first, heating dependent behaviour of the Floquet occupation functions can lead to anomalous effects. These effects could be mainly associated with effective 'magnetic fields' in phase space, represented by the Berry curvatures $\mathbf{\Omega}_{rr}$, $\mathbf{\Omega}_{kk}$ and $\mathbf{\Omega}_{rk}$, respectively. Second, due to heating Floquet systems are intrinsically time-dependent (in addition to the external drive). This might lead to time-dependent Floquet eigenstates (via some Hartree correction, for instance) which in turn could give rise to effective 'electric' fields, $\mathbf{\Omega}_{rt}$ or $\mathbf{\Omega}_{kt}$, in the problem. The presence of Berry curvatures can generally induce macroscopic transport effects of the system, e.g., a rotation of an atomic cloud in a harmonic trap. Indeed, since many modern cold atom experiments (see Sec. 2.3) strive to realise systems with non-trivial Berry phases, the discussion of such is important even in an interacting system. We will investigate aspects of these intriguing Berry-phase effects in chapter 7.

Strongly interacting systems Many-body systems that are strongly interacting are generically beyond the applicability of our approach. Nevertheless, one can hope to be able to extend the perturbative results derived by us to the limit of strong interactions in situations where the number of excitations remains small. For example, such a situation is given by a Mott insulator, for which $U \gg J$, that is only weakly thermally activated, as discussed in Ch. 3. When the system is characterised by a dilute density of quasiparticles, the transition rates on the right-hand side of the Floquet-Boltzmann equation have to be computed from the solution of the two-particle scattering problem in the presence of periodic driving. In fact, this two-particle Floquet scattering problem was solved for excitations of a truly one-dimensional Mott insulator in the Bachelor thesis of Matthias Pukrop [296]. Moreover, such T-matrix approach was, for example, also used to estimate interaction effects in a (strongly) interacting Thouless pump scenario [92]. Such a T-matrix formulation can generally also be directly obtained from the quantum kinetic equation [227].

Higher-order scattering processes The collision integral in the form of Eq. (5.71) is characterized by an energy conservation modulo Ω. However, since all quasienergies ε_ξ are defined such that they lie within the first Floquet zone, it follows that $|\epsilon_\xi+\epsilon_\mu-\epsilon_\lambda-\epsilon_\eta| < 2\Omega$. Hence, there exists a frequency threshold at which energy-violating processes due to two-particle collisions ought to die out. We will discuss this feature quantitatively for a specific example in Sec. 6.3. Therefore, even in the limit for which the present form of the Floquet-Boltzmann equation is fully valid, i.e., weak interactions, etc., a description in terms of higher-order scattering processes might be required in order to capture heating effects. Note that one would solely enter this regime by increasing the driving frequency.

The opposite scenario, i.e., where the driving frequency is lowered to approach some adiabatic regime, might also be relevant for a description including higher-order processes. Such a system was recently investigated by, e.g., Lindner *et al.* [92]: here, an interacting Thouless pump type system was analysed at a finite driving frequency. While interactions heat up the system within the Floquet band describing this pump quite rapidly (cf. Sec. 3.4), one can additionally consider heating mechanisms to higher lying bands that will eventually relax the pump characteristics of the system. For more details on the system's setup we refer the reader to Ref. [92]. Due to the exponential decay of Floquet eigenstates in energy space (see Sec. 3.2.3) the matrix elements for two-particle scattering events W, see Eq. (5.72), might be highly suppressed. In such situations the leading order processes might be determined by a certain 'magic order' [92], which is given by a minimal trade-off between increasing powers of the interaction strength U and a decreasing total overlap of Floquet eigenstates. Indeed, one could try to capture such higher order processes in an extended version of the Floquet-Boltzmann equation (5.74).

Formally, one might be able to incorporate these higher-order processes by a systematic treatment of corresponding diagrams within the self-energy expressions (cf. Sec. 4.2.2). However, the feasibility of such treatment depends strongly on the characteristics of the system under consideration: since the number of diagrams grows exponentially with the order of interest, one would need to carefully select the relevant ones. If such a selection was indeed possible and assuming that the Floquet character is treated with corresponding care, a systematic simplification of the quantum kinetic equation up to higher orders could be done as in the non-driven case [227]. Note that a low density limit simplifies this discussion considerably, as for these situations often an effective two-particle description of the interacting problem is sufficient, see above.

Phonon coupling and open systems The Floquet-Boltzmann equation (5.74) was derived under the consideration of a closed many-body quantum system characterized by fermion-fermion interactions, motivated by ultracold atomic systems. However, one could also extend the language to other interaction types. In order to be able to capture aspects of real solid state systems it is often crucial to include the role of *phonons*. An extension of our formalism to such systems should be possible in a straightforward manner. Indeed, in a recent study by Seetharam *et al.* the transport properties of periodically coupled leads where investigated by an equation of motion approach (see above). So our formalism should be able to reproduce the obtained results as well as be applicable to comparable setups.

Moreover, even more complex scenarios can be explained by variants of our presented formalism. For example, in a recent comprehensive study by Babadi *et al.* [256] the notion of Floquet-Boltzmann kinetic equations were used to analyse the phenomenon of light-induced electron-phonon superconductivity [297]. Here, however, the authors had to loosen the quasiparticle approximation, since electronic and phononic quasiparticle coherence is an important factor in the analysis. A detailed study of changes in the Floquet spectral function is therefore crucial in these type of theories. Note, however, that their thorough study is fundamentally based on the same Floquet-Wigner transformation as shown in Sec. 5.3 (and already in Ref. [238]).

In general, the perspective of engineering quantum many-body states by means of dissipation appears to be highly promising [298]. In the context of periodically driven systems, coupling to a thermal reservoir can lead to non-equilibrium (time-periodic) steady states with unconventional properties [118,253,254,275,278]. The mixture of coherent and dissipative quantum dynamics can also be most promisingly described by Keldysh field

theories [299]. One can, hence, imagine to merge aspects of this chapter with such a field theoretical description of *open* periodically driven quantum systems.

In conclusion, it is evident that for the design of Floquet systems, which are generally interacting, it will be crucial to understand and control heating processes. Such systems are typically quantum simulators in form of ultracold atoms in optical lattices or standard-type solid state systems that show light-induced effects, respectively. We hope that the Floquet-Boltzmann equation and variants thereof can be a useful future tool in this context.

6. Heating effects in the interacting Haldane model

In this chapter we apply the Floquet-Boltzmann equation derived in the previous chapter to a first concrete example. In a recent experiment with ultracold fermionic atoms in an optical lattice by Jotzu *et al.* [23] the *Haldane model* was realized by means of periodic shaking of the lattice. Since this experiment is one of the most prominent Floquet realisations in recent years, it represents a natural starting point to study interactions in a periodically driven (closed) quantum system. Moreover, the experimental setup allows for a controlled and tunable way to study the additional effect of interactions, which makes the development of a corresponding theory worthwhile.

The Haldane model is the prototypical example of a topological insulator: Haldane showed [138] that an integer quantum Hall state can be realized *without* any external magnetic field on average, but just by arranging complex hopping parameters on a hexagonal lattice. The arrangement of the parameters is such that nearest-neighbour hoppings are real and only next-nearest-neighbour hoppings are complex. The corresponding non-interacting Hamiltonian for this spinless model reads

$$H_{\text{Haldane}} = -\sum_{\langle ij\rangle} J_{ij} c_i^\dagger c_j - \sum_{\langle\langle ij\rangle\rangle} e^{i\Phi_{ij}} J'_{ij} c_i^\dagger c_j + \sum_i \Delta_{\mathcal{AB}}\, c_i^\dagger c_i \,, \tag{6.1}$$

where Φ_{ij} are phases and $\Delta_{\mathcal{AB}}$ is an energy difference between both sublattices of the hexagonal lattice (see below).

Before investigating the role of interactions in such a system we will first give an introduction to the experimental realisation of the Hamiltonian (6.1) by the Esslinger group [23] followed by a discussion about the topological properties of the Haldane model. Following this, interactions are turned on in the model and we study the associated heating effects by using the Floquet-Boltzmann equation. Ultimately we present results that predict how a corresponding system changes its temperature or entropy, respectively, as a function of time [238]. Within the present chapter we mainly focus on the calculation of scattering effects, i.e., on the right-hand side of the Floquet-Boltzmann equation. Effects due to inhomogeneities are discussed in chapter 7.

6.1. An experimental realisation of the Haldane model with ultracold atoms

The experimental realisation of the Haldane model was recently achieved with fermionic ultracold atoms in a periodically modulated optical potential, see Ref. [23]. The novel aspect of this experiment was that the desired complex next-nearest-neighbour amplitudes, see Eq. (6.1), were obtained by - literally - shaking the optical lattice. Nevertheless, the basis for these achievements was the prior realisation of an artificial form of graphene by means of cold atoms combined with a hexagonal optical lattice [68,300]. In this section we summarize the journey from a static hexagonal lattice to this realisation of the Haldane model by driving. While we aim to focus on the (non-interacting) theory describing the

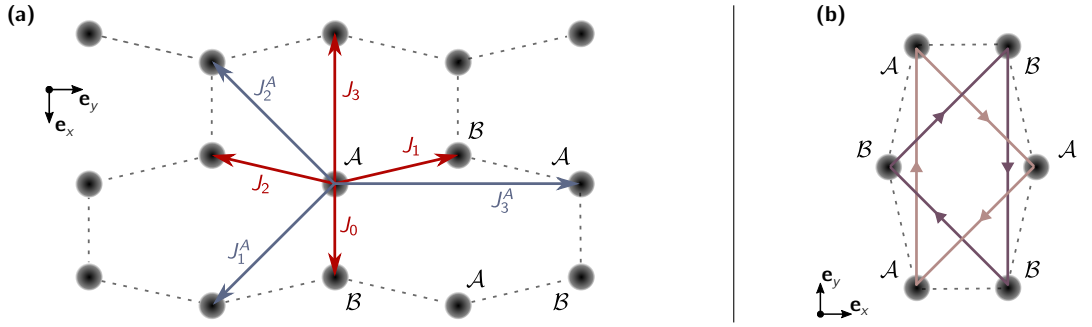

Figure 6.1.: Schematic of the hexagonal lattice employed in realising the Haldane model in Ref. [23]. (a) Every tunnelling amplitude J_j (J_j^A) is associated with a corresponding lattice vector $\mathbf{v}_j$ ($\mathbf{u}_j$). Note that we choose $J_j^A = J_j^B$. (b) The respective phase of a complex hopping strength is defined along the direction of the respective vector in this figure.

system, we remain close to experimental details: all parameters employed throughout this section are also effectively used in the respective experimental realisation, see Refs. [68] and [23]. Moreover, we largely follow the same notations as in Ref. [23] and its associated supplementary material.

6.1.1. Artificial graphene with cold atoms

In this section we will introduce the static artificial graphene system by a theoretical description and by giving experimental parameters, which extend their validity also to the driven setup. The experimental details are collected from Refs. [23,68,300] and associated supplementary materials, and more information can be found therein.

The starting point is a 2D lattice geometry[1] which is generated by three retro-reflected laser beams of wavelength $\lambda = 1064\text{nm}$. Two of the beams are at exactly the same frequency and orthogonal to each other giving rise to a chequerboard lattice of spacing $\lambda/\sqrt{2}$. The third laser beam, running parallel to one of the two and being slightly red-detuned, forms its own standing wave. Since the latter interferes with the former chequerboard, this gives rise to an entire zoo of potentially realisable two-dimensional lattice structures. One of these structures is the *honeycomb* lattice which is familiar from, e.g., graphene [301]. Conventional graphene can be understood as a triangular lattice with a basis of two atoms per unit cell. In contrast, the present honeycomb lattice is distorted, as shown by Fig. 6.1. Here, the two sites of the unit cell form two chequerboard sublattices $\mathcal{A}$ and $\mathcal{B}$ with associated mutually orthogonal Bravais lattice vectors $\mathbf{u}_1 = \lambda(0.5, -0.5)$ and $\mathbf{u}_2 = \lambda(-0.5, -0.5)$, respectively. Other relevant vectors connecting lattice sites are $\mathbf{u}_3 = \lambda(0, 1)$, $\mathbf{v}_0 = \lambda(0.438, 0)$, $\mathbf{v}_1 = \lambda(-0.062, 0.5)$, $\mathbf{v}_2 = \lambda(-0.062, -0.5)$ and $\mathbf{v}_3 = \lambda(-0.562, 0)$. As can also be seen from Fig. 6.1(a), while vectors $\mathbf{u}_j$ connect points on the same sublattice, vectors $\mathbf{v}_j$ connect points on different ones. Note that this structure will eventually give rise to a quadratic Brillouin zone.

In the experiment, fermionic ^{40}K atoms are loaded into the optical lattice of Fig. 6.1(a) after being evaporatively cooled to about $0.2\,T_F$, where T_F is the Fermi temperature. The number of atoms used varies from 5×10^4 for a spin-polarised Fermi gas to about 2×10^5 for a balanced spin mixture. In the former case the atoms are all prepared in the

[1] In fact, an additional laser beam is used for confinement in the third spatial direction. In typical experimental situations parameters are chosen in such a way that different 2D layers are weakly coupled. Here, however, we assume within our analysis that the third spatial direction is frozen out and that the system truly follows a 2D description.

$|F, m_F\rangle = |9/2, -9/2\rangle$ Zeeman state, where F denotes the hyperfine manifold and m_F the magnetic sub-level of the respective potassium isotope. For the spin mixture half of the atoms are prepared in the $|9/2, -9/2\rangle$ state and the other half are initialised in the $|9/2, -5/2\rangle$ state. Note that in order to investigate non-interacting properties the first setup is sufficient, as presented in the main text of Ref. [23], for instance. However, once interaction effects are of interest - as they indeed are for the main part of this section - a spin-mixture is required to ensure the occurrence of s-wave scattering between the fermionic particles.

Furthermore, experimental parameters are chosen such that the optical lattice is deep. This allows for a tight-binding description of the problem, see Sec. 2.1, capturing nearest-neighbour (NN) and next-nearest-neighbour (NNN) hopping mechanisms only. Allowing also for some energy difference, $\Delta_{\mathcal{AB}}$, between both sublattices, the non-interacting system can be described by the following lattice Hamiltonian

$$\begin{aligned} H_{\text{lat}} = \sum_{\mathbf{u}\in\mathcal{A},\sigma} \Big[& \frac{\Delta_{\mathcal{AB}}}{2} \left(a^\dagger_{\mathbf{u}\sigma} a_{\mathbf{u}\sigma} - b^\dagger_{\mathbf{u}+\mathbf{v}_0,\sigma} b_{\mathbf{u}+\mathbf{v}_0,\sigma} \right) \\ & - \sum_{j,\sigma} \left(J_j \, b^\dagger_{\mathbf{u}+\mathbf{v}_j,\sigma} a_{\mathbf{u}\sigma} + \text{h.c.} \right) \\ & - \sum_{j,\sigma} \left(J^A_j \, a^\dagger_{\mathbf{u}+\mathbf{u}_j,\sigma} a_{\mathbf{u}\sigma} + J^B_j \, b^\dagger_{\mathbf{u}+\mathbf{v}_0-\mathbf{u}_j,\sigma} b_{\mathbf{u}+\mathbf{v}_0,\sigma} + \text{h.c.} \right) \Big] , \end{aligned} \tag{6.2}$$

with σ being a spin index and $a^\dagger_{\mathbf{u}}\,(b^\dagger_{\mathbf{u}'})$ creates a fermion on sublattice $\mathcal{A}\,(\mathcal{B})$ at the corresponding position $\mathbf{u}\,(\mathbf{u}')$. The index j runs over all available corresponding bonds as depicted in Fig. 6.1. As can be seen from Eq. (6.2), the amplitudes J_j correspond to hoppings between different sublattices, while J^A_j and J^B_j describe hopping strengths within each sublattice. We choose that J_j is always real, but $J^{A/B}_j$ may be complex. We assume further that $J'_j = J^A_j = J^B_j$, where complex phases are indeed equal but defined in opposite directions with respect to the two sublattices $\mathcal{A}$ and $\mathcal{B}$, see Fig. 6.1(b) and last line of Eq. (6.2). Note that all hopping amplitudes are assumed to be independent of the spin species.

We proceed by performing a Fourier transformation of the creation and annihilation operators according to (cf. Eq. (3.6))

$$a^\dagger_{\mathbf{k}\sigma} = \sum_{\mathbf{u}\in\mathcal{A}} e^{i\mathbf{k}\cdot\mathbf{u}} \, a^\dagger_{\mathbf{u}\sigma} \qquad \Leftrightarrow \qquad a^\dagger_{\mathbf{u}\sigma} = \int \frac{d\mathbf{k}}{(2\pi/a)^2} \, e^{-i\mathbf{k}\cdot\mathbf{u}} \, a^\dagger_{\mathbf{k}\sigma} \, , \tag{6.3}$$

$$b^\dagger_{\mathbf{k}\sigma} = \sum_{\mathbf{u}'\in\mathcal{B}} e^{i\mathbf{k}\cdot\mathbf{u}'} \, b^\dagger_{\mathbf{u}'\sigma} \qquad \Leftrightarrow \qquad b^\dagger_{\mathbf{u}'\sigma} = \int \frac{d\mathbf{k}}{(2\pi/a)^2} \, e^{-i\mathbf{k}\cdot\mathbf{u}'} \, b^\dagger_{\mathbf{k}\sigma} \, , \tag{6.4}$$

with $(2\pi/a)^2$ being the volume of the quadratic Brillouin zone and $a = |\mathbf{u}_1| = |\mathbf{u}_2| = \lambda/\sqrt{2}$ describes the length of the Bravais lattice vectors. It is straightforwardly shown that this brings the Hamiltonian (6.2) into the form

$$H_{\text{lat}} = \sum_\sigma \int \frac{d\mathbf{k}}{(2\pi/a)^2} \left(a^\dagger_{\mathbf{k}\sigma}, b^\dagger_{\mathbf{k}\sigma} \right) h(\mathbf{k}) \begin{pmatrix} a_{\mathbf{k}\sigma} \\ b_{\mathbf{k}\sigma} \end{pmatrix} , \tag{6.5}$$

where the quasimomentum part of the Hamiltonian can be written as

$$h(\mathbf{k}) = h_i(\mathbf{k}) \, \mathbb{1} + h_x(\mathbf{k}) \, \sigma_x + h_y(\mathbf{k}) \, \sigma_y + h_z(\mathbf{k}) \, \sigma_z \, , \tag{6.6}$$

with $\sigma_{x,y,z}$ being the Pauli matrices and individual coefficients read as

$$h_i(\mathbf{k}) = -2\sum_j \mathrm{Re}[J'_j]\,\cos\left(\mathbf{k}\cdot\mathbf{u}_j\right) \tag{6.7}$$

$$h_x(\mathbf{k}) = -\sum_j J_j\,\cos\left(\mathbf{k}\cdot\mathbf{v}_j\right) \tag{6.8}$$

$$h_y(\mathbf{k}) = \sum_j J_j\,\sin\left(\mathbf{k}\cdot\mathbf{v}_j\right) \tag{6.9}$$

$$h_z(\mathbf{k}) = \frac{\Delta_{\mathcal{AB}}}{2} - 2\sum_j \mathrm{Im}[J'_j]\,\sin\left(\mathbf{k}\cdot\mathbf{u}_j\right) \tag{6.10}$$

The eigenvalues, i.e., the energy bands of the Hamiltonian (6.6) are then straightforwardly calculated to be

$$\varepsilon_\pm(\mathbf{k}) = h_i(\mathbf{k}) \pm \left[h_x(\mathbf{k})^2 + h_y(\mathbf{k})^2 + h_z(\mathbf{k})^2\right]^{1/2}. \tag{6.11}$$

In the experiment two *static* versions of this model can be achieved: either only nearest-neighbour hoppings are present, or fermionic particles are allowed to hop to their next-nearest neighbours with purely real tunnelling amplitudes. For the remainder of the this chapter we assume the former situation to hold for all our theoretical discussions. The reason is two-fold: first, a reduction of the number of relevant parameters simplifies the problem. (Note that the main results of this chapter do only depend quantitatively on this choice.) Second, experimentally a spinful, interacting system was indeed studied with the simpler set of parameters, as discussed in the supplemental material of Ref. [23]. To be precise, in the experiment the hopping strengths to nearest neighbours were set to $J/\hbar = J_{0,1,2}/\hbar = 2\pi\times 172\,\mathrm{Hz}$, and $J_3 = 0$. All next-nearest-neighbour hoppings, on the other hand, were frozen out, i.e., $J'_j = 0$. Additionally, also the on-site energy offset between the two sublattices was put to zero, i.e., $\Delta_{\mathcal{AB}} = 0$. With such choice of parameters Eqs. (6.7)-(6.10) simplify even further. The resulting 2D band structure of Eq. (6.11) is shown in Fig. 6.2(b). The characteristic Dirac points can be calculated to reside at momenta $\mathbf{k}_\mathrm{D}^\pm = \pm\frac{4\pi}{3\lambda}(0,1)$. Note that the discrepancy between these position and the one in typical graphene [301] again stems from the distortion of the honeycomb lattice in the present case. Furthermore, the total bandwidth of the static system can be calculated to be $D = 6J$. While this static system was experimentally already subject to earlier studies [68, 300] the ultimate goal in order to simulate the Haldane model was to accomplish *complex* next-nearest-neighbour tunnelling amplitudes. How this is achieved by means of periodic shaking is outlined in the following section.

We conclude this section by making an important side remark: Note that the Hamiltonian (6.2) fails to capture the weak harmonic confinement potential that is present in most cold atom experiments, see Sec. 2.1. This approximation is maintained throughout this chapter, rendering the system with a discrete translation symmetry. Eventually, however, we will investigate how the interplay of interactions and lattice inhomogeneities gives rise to transport phenomena in a periodically driven version of Eq. (6.2), see Ch. 7.

6.1.2. Periodic lattice modulation

The Haldane model was realised experimentally in the Esslinger group by means of shaking the optical lattice. In the following, we will therefore present the general description of having a lattice Hamiltonian as in Eq. (6.2) paired with some external driving at frequency Ω. To this end, we keep the discussion general in the following sense: we assume that

$J'_j = J_j^{\mathcal{A}} = J_j^{\mathcal{B}}$ and that all hopping amplitudes J_j, J'_j are real. Note that this section is inspired by as well as complementary to the supplemental material of Ref. [23].

In the experiment[2], the lattice position is periodically modulated in the plane of the lattice itself. The motion of the lattice is along the two orthogonal axes $(\mathbf{e}_x, \mathbf{e}_y)$ (cf. Fig. 6.1) with equal amplitude α and relative phase $\varphi \in (-\pi, \pi]$. This leads to an elliptical trajectory

$$\mathbf{r}_{\mathrm{el}}(t) = -\,\alpha\left(\cos\left(\Omega t\right)\mathbf{e}_x + \cos\left(\Omega t - \varphi\right)\mathbf{e}_y\right). \tag{6.12}$$

Here, the amplitude is chosen such that a certain combination of experimental parameters and natural constants is kept at a fixed value, i.e., $K_0 = \alpha m \Omega \lambda/(2\hbar) = 0.7778$, with m being the mass of a ^{40}K atom. As can be seen from Eq. (6.12), the phase-shift φ determines both the aspect ratio of the elliptical trajectory (linear for $\varphi = 0, \pi$ and circular for $\varphi = \pm\pi/2$) as well as its direction (clockwise for $-\pi < \varphi < 0$ and anticlockwise for $0 < \varphi < \pi$).

Generally, such a periodic shaking of the lattice leads to an acceleration of all atoms. The time-dependent, homogeneous force associated with this acceleration is given by $\mathbf{F}(t) = m\ddot{\mathbf{r}}(t)$. Clearly, this force is periodic in time, $\mathbf{F}(t) = \mathbf{F}(t + T_0)$, due to the periodic shaking. Consequently, in the frame of reference that is comoving with the lattice a spatially constant inertial force $\mathbf{F}_{\mathrm{lat}}(t) = -\mathbf{F}(t) = -m\ddot{\mathbf{r}}(t)$ is felt by the atoms. Considering the general lattice Hamiltonian (6.2), the presence of the force changes this Hamiltonian in the following way

$$H(t) = H_{\mathrm{lat}} - \sum_{i \in \mathcal{A},\mathcal{B}} \left(\mathbf{F}_{\mathrm{lat}}(t) \cdot \mathbf{r}_i\right) c_i^\dagger c_i \,, \tag{6.13}$$

where for brevity we used that $c_i = a_i\,(b_i)$ for $i \in \mathcal{A}\,(\mathcal{B})$ and $\mathbf{r}_i = \mathbf{u}\,(\mathbf{u} + \mathbf{v}_0)$ is the corresponding lattice site vector (cf. Eq. 6.2). Of course, the Hamiltonian (6.13) is time-periodic due to the external modulation, $H(t + T_0) = H(t)$. Note, however, that H is *not* translationally invariant any more. It is therefore convenient to view the force as emerging from a vector potential

$$\mathbf{A}(t) = -\frac{2\hbar K_0}{\lambda}\left[\sin(\Omega t)\mathbf{e}_x + \sin(\Omega t - \varphi)\mathbf{e}_y\right], \tag{6.14}$$

according to $\mathbf{F}_{\mathrm{lat}}(t) = \partial_t \mathbf{A}(t)$. One can then use this vector potential in order to find the gauge transformed Hamiltonian $H' = U^\dagger H U - i\hbar U^\dagger \partial_t U$, where the unitary transformation is given by $U = \exp[i\sum_i (\mathbf{A}\cdot\mathbf{r}_i) c_i^\dagger c_i]$. Then, the second term of Eq. (6.13) is cancelled by the second term of the unitary transformation restoring the property of discrete translational invariance. At the same time, a generic hopping term of the original lattice Hamiltonian H_{lat} gets transformed according to

$$\sum_{i,j} J_{ij}\, c_i^\dagger c_j \qquad \xrightarrow[\text{trans.}]{\text{gauge}} \qquad \sum_{i,j} e^{-i\mathbf{A}(t)\cdot\mathbf{r}_{ij}} J_{ij}\, c_i^\dagger c_j \equiv \sum_{i,j} J_{ij}(t)\, c_i^\dagger c_j \,, \tag{6.15}$$

where the indices i, j run again over all lattice sites, and we defined $\mathbf{r}_{ij} = \mathbf{r}_i - \mathbf{r}_j$ being the vector that connects both sites. It is now understood that every tunnelling term of Eq. (6.2) transforms as shown in Eq. (6.15), where hopping strength and lattice vectors need to be identified accordingly. Moreover, on-site terms of the Hamiltonian, as given by the first line of Eq. (6.2), are left unchanged by the gauge transformation. Note that in the following we will simplify notations by omitting the apostrophe of H' and will refer to $H(t)$ as the gauge transformed Hamiltonian of the shaken lattice.

[2] Note that for the remainder of this chapter the notion 'the experiment' refers to the experimental work of Ref. [23].

So the sole consequence of the periodic modulation of the lattice is the modification of all hopping amplitudes by complex phases in form of an associated vector potential $\mathbf{A}(t)$. This leads to a description of the system by a Hamiltonian that is structurally identical to Eq. (6.2) but contains complex hopping amplitudes that depend periodically on time, i.e., $J_j(t+T_0) = J_j(t)$ and $J'_j(t+T_0) = J'_j(t)$. In fact, it is convenient to represent the phase factor appearing in Eq. (6.15) in a different form such that the hopping strengths can be written as

$$J_j(t) = e^{iz_j \sin(\Omega t+\phi_j)} J_j \qquad \text{and} \qquad J'_j(t) = e^{iz'_j \sin(\Omega t+\phi'_j)} J'_j \,, \tag{6.16}$$

where J_j, J'_j describe the static tunnelling amplitudes, and we defined

$$\begin{aligned} z_j(z'_j) &= \frac{2\hbar K_0}{\lambda}\, \rho_j(\rho'_j)\,, \\ \rho_j\, e^{i\phi_j} &= \mathbf{v}_j \cdot \mathbf{e}_x + \mathbf{v}_j \cdot \mathbf{e}_y\; e^{-i\varphi}\,, \\ \rho'_j\, e^{i\phi'_j} &= \mathbf{u}_j \cdot \mathbf{e}_x + \mathbf{u}_j \cdot \mathbf{e}_y\; e^{-i\varphi}\,, \end{aligned} \tag{6.17}$$

and $\rho_{j/j'} \geq 0$. Note that all objects in (6.16) and (6.17) are defined for a hopping process of a particle that was initially placed on sublattice $\mathcal{A}$. The quantities above are determined according to the direction of corresponding lattice vectors as given in Fig. 6.1, i.e., $z_j = z_{j,\mathcal{A}}$ etc. When considering a hopping process that starts on the sublattice $\mathcal{B}$ the direction of the lattice vectors is reversed (cf. Fig. 6.1 and Eq. (6.2)), i.e., $\mathbf{v}_j \to -\mathbf{v}_j$ and $\mathbf{u}_j \to -\mathbf{u}_j$, leading to $\rho_j\, e^{i\phi_j} = \rho_{j,\mathcal{A}}\, e^{i\phi_{j,\mathcal{A}}} = -\rho_{j,\mathcal{B}}\, e^{i\phi_{j,\mathcal{B}}}$, etc. Thus, it follows that $\rho_j = \rho_{j,\mathcal{A}} = \rho_{j,\mathcal{B}}$ and $\phi_j = \phi_{j,\mathcal{A}} = \phi_{j,\mathcal{B}} + \pi$.

Since the Hamiltonian of the shaken system is time-periodic, $H(t+T_0) = H(t)$, we desire ultimately a Floquet analysis of the problem as discussed in Sec. 2.2. The advantage of bringing the time-dependent hopping strengths into the form of Eq. (6.16) is that they can be easily decomposed into their frequency Fourier modes. This is done by means of the Jacobi-Anger expansion, $e^{iz\sin(\theta)} = \sum_n (-1)^n \mathcal{J}_n(z) e^{-in\theta}$, where $\mathcal{J}_n$ describes the nth order Bessel function of the first kind with property $\mathcal{J}_{-n} = (-1)^n \mathcal{J}_n$. All time-periodic tunnelling amplitudes of type (6.16) are therefore rewritten as

$$J_j(t) = \sum_{n=-\infty}^{\infty} e^{-in\Omega t}\, (-1)^n\, \mathcal{J}_n(z_j)\, J_j\, e^{-in\phi_j} \tag{6.18}$$

Consequently, the oscillating terms H_n of the non-interacting, periodically driven Hamiltonian, $H(t) = \sum e^{-in\Omega t} H_n$, can be straightforwardly identified using Eqs. (6.2), (6.15) and (6.18). In short, in order to find $H(t)$ one simply replaces all hopping strengths appearing in Eq. (6.2) by respective variants of Eq. (6.18). The explicit expressions for H_n can then be simply read off. In addition, by performing a position-space Fourier transformation identical to the one presented in Eqs. (6.3)-(6.5) all oscillating parts of the Hamiltonian can be written in terms of k-dependent 2×2 matrices (cf. Eq. (6.6))

$$h_n(\mathbf{k}) = h_{n,i}(\mathbf{k})\, \mathbb{1} + h_{n,x}(\mathbf{k})\, \sigma_x + h_{n,y}(\mathbf{k})\, \sigma_y + h_{n,z}(\mathbf{k})\, \sigma_z \,, \tag{6.19}$$

and the coefficients are calculated to read as[3]

$$h_{n,i}(\mathbf{k}) = -\sum_j J'_j\, \mathcal{J}_n(z'_j)\, e^{-in\phi'_j} \left(e^{i\mathbf{k}\cdot\mathbf{u}_j} + (-1)^n e^{-i\mathbf{k}\cdot\mathbf{u}_j} \right), \tag{6.20}$$

[3]The discrepancies between the formulas presented here, Eqs. (6.20)-(6.23), and corresponding ones in the supplemental material of [23], arise due to a few of reasons: first, we correct a typo in the formula for $h_{n,i}$. Second, the frequency Fourier transformation presented in [23] is inconsistent with the one given here in the sense that both differ by $n \to -n$. Third, we believe that the formulas in [23] need to experience a mapping $\mathbf{k} \to -\mathbf{k}$ in order to be consistent with the presented Fourier transformation of momentum space.

$$h_{n,x}(\mathbf{k}) = -\frac{1}{2}\sum_j J_j\,\mathcal{J}_n(z_j)\,e^{-in\phi_j}\left(e^{i\mathbf{k}\cdot\mathbf{v}_j} + (-1)^n e^{-i\mathbf{k}\cdot\mathbf{v}_j}\right), \tag{6.21}$$

$$h_{n,y}(\mathbf{k}) = -\frac{i}{2}\sum_j J_j\,\mathcal{J}_n(z_j)\,e^{-in\phi_j}\left(e^{i\mathbf{k}\cdot\mathbf{v}_j} - (-1)^n e^{-i\mathbf{k}\cdot\mathbf{v}_j}\right), \tag{6.22}$$

$$h_{n,z}(\mathbf{k}) = \frac{\Delta_{\mathcal{AB}}}{2}\,\delta_{n0}\,, \tag{6.23}$$

where the index j again runs over all corresponding nearest or next-nearest neighbour sites, respectively. Also, recall that $J_j' = J_j^{\mathcal{A}} = J_j^{\mathcal{B}}$ and that all tunnelling amplitudes of the static system are real. Note that $H_n(\mathbf{k})$ can be found from $h_n(\mathbf{k})$ according to Eq. (6.5).

Obtaining the Haldane model from a first-order Magnus expansion

We continue by performing a first-order *Magnus expansion* of the problem, see Sec. (2.2.3), and set the parameters as discussed above ($J/\hbar = J_i/\hbar = 2\pi \times 172\,\mathrm{Hz}$, $J_i' = 0, \Delta_{\mathcal{AB}} = 0$). Experimentally, such an expansion is justified by tuning the driving frequency larger than all other energy scales of the problem. For now, we set $\Omega = 2\pi\times 1080\mathrm{Hz} \approx 6.3J$, which was also used in the experiment studying a spinful, interacting system [23].

Applying the above set of parameters the components of the Hamiltonian given by (6.19) simplify to $h_n = h_{n,x}\sigma_x + h_{n,y}\sigma_y$. Substituting this form into the expressions of Eq. (2.61), i.e., the zeroth and first order term of the Magnus expansion, one finds that the corresponding *effective Hamiltonian* can be written as

$$\begin{aligned} h^{\mathrm{eff}}(\mathbf{k}) &= h_0(\mathbf{k}) + \frac{1}{\Omega}\sum_{n=1}^{\infty}\frac{1}{n}\left[h_{-n}(\mathbf{k}), h_n(\mathbf{k})\right] \\ &= h_{0,x}\sigma_x + h_{0,y}\sigma_y + \frac{2i}{\Omega}\sum_{n=1}^{\infty}\frac{1}{n}\left(h_{-n,x}h_{n,y} - h_{n,x}h_{-n,y}\right)\sigma_z \\ &\equiv h_x^{\mathrm{eff}}\sigma_x + h_y^{\mathrm{eff}}\sigma_y + h_z^{\mathrm{eff}}\sigma_z\,. \end{aligned} \tag{6.24}$$

So while the off-diagonal elements of $h^{\mathrm{eff}}(\mathbf{k})$ are given by renormalised static contributions, i.e., $h_x^{\mathrm{eff}} = h_{0,x}$ and $h_y^{\mathrm{eff}} = h_{0,y}$, the periodic drive imposes an additional term that is proportional to σ_z. By using the explicit expressions for $h_{n,x}$ and $h_{n,y}$ from Eqs. (6.21) and (6.22), respectively, one eventually finds h_z^{eff} to take the form

$$h_z^{\mathrm{eff}} = -\frac{2i}{\Omega}\sum_{n=1}^{\infty}\frac{1}{n}\sum_{j_1,j_2}\widetilde{J}_{n,j_1}\,\widetilde{J}_{n,j_2}\,e^{-in\phi_{j_1 j_2}}\sin\left(\mathbf{k}\cdot\mathbf{v}_{j_1 j_2}\right), \tag{6.25}$$

where we introduced $\widetilde{J}_{n,j} = J_j\mathcal{J}_n(z_j)$, $\phi_{ij} = \phi_i - \phi_j$ and $\mathbf{v}_{ij} = \mathbf{v}_i - \mathbf{v}_j$. One then realises that $\mathbf{v}_{j_1 j_2}$ always corresponds to a lattice vector $\pm\mathbf{u}_j$ (see Fig. 6.1). Thus, one can rewrite the double sum over $\mathbf{v}$-indices as a sum over a single $\mathbf{u}$-index. One obtains

$$h_z^{\mathrm{eff}} = -2\sum_j \widetilde{J}_j'\sin\left(\mathbf{k}\cdot\mathbf{u}_j\right) \qquad \text{with} \qquad \widetilde{J}_j' = \frac{2}{\Omega}\sum_{n=1}^{\infty}\frac{1}{n}\widetilde{J}_{n,j_1}\widetilde{J}_{n,j_2}\sin\left(n\phi_{j_1 j_2}\right), \tag{6.26}$$

where it is understood that the $\mathbf{v}$-indices j_1, j_2 are uniquely determined by $\mathbf{u}_j$.

Upon substituting expression (6.26) into Eq. (6.24) and using explicit expressions for $h_{0,x}, h_{0,y}$, the effective Hamiltonian is evaluated to read as

$$h^{\mathrm{eff}}(\mathbf{k}) = -\sum_j \widetilde{J}_j\cos\left(\mathbf{k}\cdot\mathbf{v}_j\right)\sigma_x + \sum_j \widetilde{J}_j\sin\left(\mathbf{k}\cdot\mathbf{v}_j\right)\sigma_y - 2\sum_j \widetilde{J}_j'\sin\left(\mathbf{k}\cdot\mathbf{u}_j\right)\sigma_z\,, \tag{6.27}$$

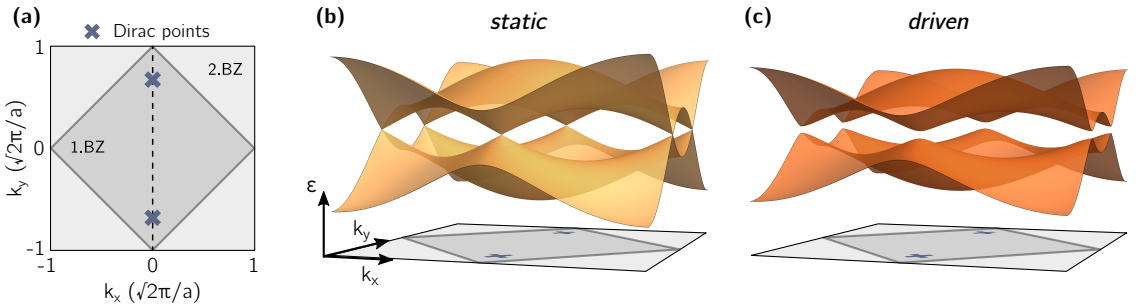

Figure 6.2.: (a) Brillouin zone associated with translationally invariant lattice shown in Fig. 6.1. The two Dirac points are indicated by blue crosses. The dotted line marks the $k_x = 0$ cut through the Brillouin zone. (b) Band structure of static graphene-like system given by Hamiltonian (6.2) and $J_i' = \Delta_{\mathcal{AB}} = 0$, etc. (see text). (c) Floquet band structure of periodically driven system, where gaps open at Dirac points. The driving frequency is $\Omega = 6.3J$.

where $\widetilde{J}_j = \widetilde{J}_{0,j}$ and the sum index runs over possible sites connected by $\mathbf{v}_j$ or $\mathbf{u}_j$, respectively. Comparing Eq. (6.27) to the discussion of the static lattice model above, see Eqs. (6.6)-(6.10), leads to a couple of crucial observations: first, the next-nearest hopping strengths of the driven system are the same as in the static case but normalised by a Bessel function[4], i.e., $J_j \to \widetilde{J}_j = J_j \mathcal{J}_0(z_j)$. Second, the term proportional to σ_z purely caused by the driving corresponds to next-nearest-neighbour hopping of the particles. Most importantly, one realises that the hopping strength $\widetilde{J}_j'$ must be identified with a purely *imaginary* part of a NNN-tunnelling amplitude of a corresponding static lattice Hamiltonian (6.2), i.e., $\widetilde{J}_j' = \mathrm{Im}[J_j']$. Hence, one can indeed realise to first order in $1/\Omega$ a (honeycomb) lattice Hamiltonian that contains real nearest-neighbour and imaginary next-nearest-neighbour hopping amplitudes, which is nothing but the *Haldane model* of Eq. (6.1) (with $\Delta_{\mathcal{AB}} = 0$). Note that since the on-site energy shift is not affected by the gauge transformation, see Eq. (6.15), an initial non-zero sublattice shift $\Delta_{\mathcal{AB}}$ can be trivially added to the effective Hamiltonian of Eq. (6.27), i.e., $h_z^{\mathrm{eff}} \to h_{z,\Delta}^{\mathrm{eff}} = h_z^{\mathrm{eff}} + \frac{\Delta_{\mathcal{AB}}}{2}$, allowing for a deliberate breaking of inversion symmetry (see below).

The band structure of the effective Hamiltonian is then also calculated using Eq. (6.11), and is shown in Fig. 6.2 for a circularly shaken lattice with $\varphi = \pi/2$. One clearly sees that the additional complex hopping amplitudes open a gap at the previous Dirac points. The size of the gap is $\Delta_G/\hbar \approx 2\pi \times 50\mathrm{Hz}$. Moreover, the entire band structure changed slightly in shape due to the renormalisation of the static hoppings. The total bandwidth of the effective Hamiltonian is given by $D/\hbar = 2\sum_j \widetilde{J}_j/\hbar \approx 2\pi \times 892\mathrm{Hz}$. In fact, the most prominent consequence of the complex hoppings is not solely the presence of the band gap, but rather the emerging topological properties and related phenomena. So having shown that driving a static honeycomb lattice can indeed lead to the realisation of the Haldane model, we will investigate its properties in the next section, Sec. 6.2.

We close this section by making an important remark. Despite the fact that the description of the system in terms of the effective Hamiltonian (6.27) captures the physics of the system well in a non-interacting environment, it has a huge drawback: energy non-conserving processes cannot be treated with a simple Magnus expansion or by its resulting effective Hamiltonian (see Sec. 2.2). Since our goal is to add interactions to the description of this section, and to eventually apply the Floquet-Boltzmann equation (5.74), we ultimately need to find Floquet eigenstates and quasienergies.

[4] Such renormalisations in terms of Bessel functions are very typical for shaken lattices. In fact, one of the pioneering Floquet realisations with cold atoms already proved this effect experimentally [55].

6.2. Topological properties of the Haldane model

In the previous section, we conceptually showed in much detail how the model Hamiltonian (6.1) with complex next-nearest neighbour hopping amplitudes can be engineered by means of periodic driving. In the present section, we elaborate on some of the peculiar properties of this system. First, it is apparent from Fig. 6.2 that the Haldane model describes a gapped system. It therefore describes an insulator, assuming that the system is half-filled. Nevertheless, the main characteristics of the model only reveal themselves when going beyond a mere analysis of the bandstructure: the Hamiltonian (6.1) in fact features topologically distinct phases of matter [138]. Hence, the Haldane model represents a 'Chern insulator' with topological charge given by the Chern number [195]. As shown in Sec. 3.4, non-zero Chern numbers are the reason for an emerging quantised Hall conductance in the context of the integer quantum Hall effect. We therefore emphasize that such a quantum Hall state is also described by the Haldane model but without any external magnetic fields and associated Landau levels [138]. Complex NNN-tunnelling amplitudes, see Fig. 6.1(b), evoke a structure of staggered fluxes that sum to zero over the total unit cell, hereby encoding the quantum Hall effect as an intrinsic property of the respective band structure.

In the following, we discuss specific topological properties of the effectively engineered Haldane model, see Eq. (6.27). For more general details about topological matter we refer the reader to Secs. 3.4 and, in particular, 8.1 (and references therein). Moreover, a detailed view on the (integer) quantum Hall effect can be obtained from, e.g., Ref. [197] (and references therein).

6.2.1. Berry-phases and Chern numbers

In order to study the effects of topology in the Haldane model we consider Berry curvatures as given in Sec. 3.4. Using the respective definition for the Berry connection of Eq. (3.54) the Berry curvature (3.54) can be written as

$$\Omega_{\nu,xy}(\mathbf{k}) = -2\,\mathrm{Im}\left[\left\langle \frac{\partial u_{\nu\mathbf{k}}}{\partial k_x}\middle|\frac{\partial u_{\nu\mathbf{k}}}{\partial k_y}\right\rangle\right], \tag{6.28}$$

with $|u_{\nu\mathbf{k}}\rangle$ being eigenstates of the effective Hamiltonian (6.27) and ν denoting the band index. If the Hilbert space of the considered system is finite, the expression (6.28) can generally be brought into an equivalent but numerically more accessible form [96], which in the present two-band case reads as[5]

$$\Omega_{\nu,xy}(\mathbf{k}) = -2\,\mathrm{Im}\left[\frac{\langle u_{\nu\mathbf{k}}|\frac{\partial h^{\mathrm{eff}}}{\partial k_x}|u_{\bar{\nu}\mathbf{k}}\rangle\langle u_{\bar{\nu}\mathbf{k}}|\frac{\partial h^{\mathrm{eff}}}{\partial k_y}|u_{\nu\mathbf{k}}\rangle}{\left(\varepsilon_{\bar{\nu}}(\mathbf{k})-\varepsilon_{\nu}(\mathbf{k})\right)^2}\right], \tag{6.29}$$

where $\nu = \{-,+\}$ with '$-$' ('$+$') indicating the respective lower (upper) band, cf. Fig. 6.2, and $\bar{\nu} = +(-)$ when $\nu = -(+)$. The Berry curvatures can now be readily computed, where the numerical advantage of Eq. 6.29 stems from the fact that the U(1)-freedom of every eigenstate drops out by construction. In Fig. 6.3(a) we show such Berry curvatures of the bottom band, Ω_-, evaluated over the entire first Brillouin zone (cf. Fig. 6.2(a)). Here, we vary the phase-shift φ as well as the on-site energy offset $\Delta_{\mathcal{AB}}$, leading to a *gapped* band

[5] Note that Eq. (6.29) can be straightforwardly extended to a full Floquet version by replacing the band index of the effective model by a band index of the extended Floquet space.

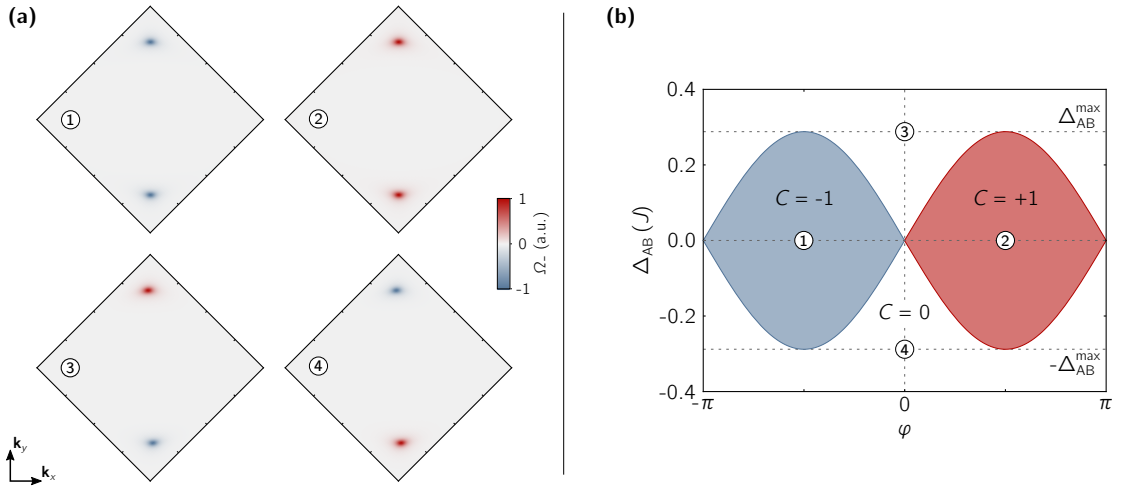

Figure 6.3.: (a) Berry curvatures associated with bottom band of effective Hamiltonian (6.27) evaluated over first Brillouin zone (cf. Fig. 6.2(a)) for four different situations either breaking TRS or IR. (b) Topological phase diagram of the Haldane model realisation (6.27). Number labels indicate integrated Berry curvatures of corresponding representations in (a).

structure in every case. At the same time, corresponding *Chern numbers* can be computed by integrating the Berry curvature over the Brillouin zone as, see Eq. (3.53),

$$C_\nu = \frac{1}{2\pi} \int d\mathbf{k}\; \Omega_{\nu,xy}(\mathbf{k})\,. \tag{6.30}$$

So indeed, for parameters of $\varphi = \pi/2$ and $\Delta_{\mathcal{AB}} = 0$ the lowest band of the Hamiltonian is topologically non-trivial, describing a topological Chern insulator with $C = +1$, see Fig. 6.3(b). For some other configurations, however, conventional insulators are found. In order to understand this behaviour it is favourable to interpret φ and $\Delta_{\mathcal{AB}}$ as parameters that break time-reversal symmetry (TRS) or inversion symmetry (IS), respectively. So while breaking the inversion symmetry only yields trivial insulating states at half-filling, time-reversal symmetry breaking causes a gap that separates bands with non-zero Chern numbers. The gap size in the latter case is easily evaluated from Eq. (6.27) assuming that the positions of the Dirac points, $\mathbf{k}_\mathrm{D}^\pm = \pm\frac{4\pi}{3\lambda}(0,1)$, remain stable. Here, it holds that $h_x^\mathrm{eff}(\mathbf{k}_\mathrm{D}^\pm) = h_y^\mathrm{eff}(\mathbf{k}_\mathrm{D}^\pm) = 0$, and the gap due to TRS breaking is given by

$$\Delta_T = -4\sum_j \widetilde{J}'_j \sin\left(\mathbf{k}_\mathrm{D}^+ \cdot \mathbf{u}_j\right) = \Delta_T^\mathrm{max} \sin\left(\varphi\right), \tag{6.31}$$

with $\Delta_T^\mathrm{max}/\hbar \simeq 0.3J/\hbar \simeq 2\pi \times 50\mathrm{Hz}$ being calculated using Eq. (6.26), etc. When both symmetries are fulfilled, i.e., $\varphi = \Delta_{\mathcal{AB}} = 0$, the system maps to a renormalised gapless Dirac system as depicted in Fig. 6.2(b).

In contrast, when both symmetries are broken, i.e., $\varphi \neq 0$ as well as $\Delta_{\mathcal{AB}} \neq 0$, a topological phase transition must take place to connect topologically distinct regions in parameter space characterized by Chern numbers C. The topological phase diagram is shown in Fig. 6.3(b). Note that right on the transition line where the topological phase transition takes place, one of the Dirac points is required to become gapless. Once IS is explicitly broken, the total band gap results from a competition of $\Delta_{\mathcal{AB}}$ and the gap emerging from breaking TRS, i.e.,

$$\Delta_G^\pm \simeq \left|\Delta_{\mathcal{AB}} \pm \Delta_T^\mathrm{max} \sin\left(\varphi\right)\right|. \tag{6.32}$$

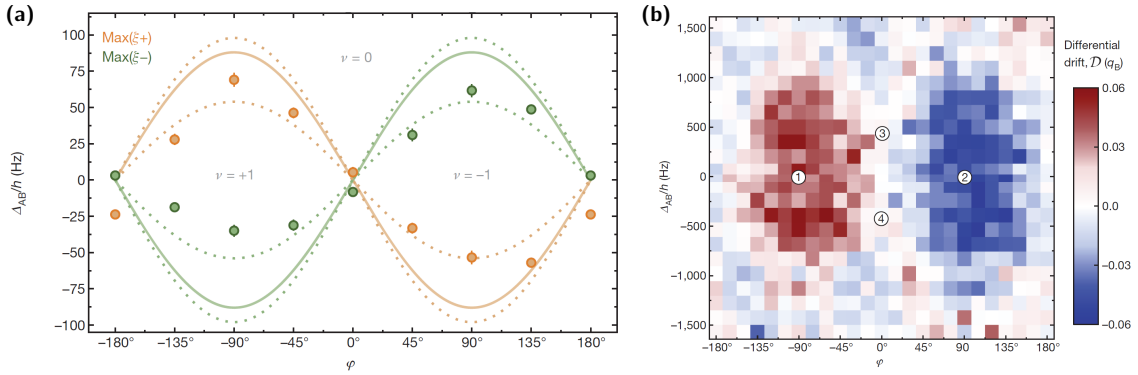

Figure 6.4.: Experimental results verifying the successful simulation of the Haldane model. (a) Topological phase diagram obtained by measuring the fraction of atoms that change to the upper band after a Bloch cycle (see text). (b) Measured differential drifts or anomalous velocities as a consequence of Berry curvatures. Over a full Bloch cycle a net contribution can only emerge if Berry curvatures of bottom band carry the same sign around both Dirac points, i.e., when $C = \pm 1$. Note that Chern numbers are reversed compared to Fig. 6.3, which results from an alternative definition of the Berry curvature in Ref. [23] including an additional minus sign. Taken from Ref. [23].

Note that the sign change results from the fact that the sine-function in Eq. (6.31) is mapped to $-\sin(\cdot)$ when considering the Dirac point at $\mathbf{k}_{\mathrm{D}}^{-}$. Thus, the phase transition line is expected to reside at $\Delta_{\mathcal{AB}} \simeq \Delta_T^{\max} \sin(\varphi)$. Note that we elaborate on the connection between symmetries and topological states from a different point of view in Sec. 8.1, where we also explain in more detail the necessity of closing band gaps during topological phase transitions.

Experimental verification of the successful realisation of the Haldane model was obtained by measuring gap sizes as well as by directly observing Berry phase effects [23]. In order to map out the topological phase transition line of Fig. 6.3 the associated closing of an energy gap was detected by means of evoking Landau-Zener transitions [68]. To this end, using a magnetic field gradient atoms are accelerated by a constant force inducing Bloch oscillations. After one full Bloch cycle the fraction of atoms in the upper band, ξ, is then determined from a specific band-mapping procedure [23]. Generally, a vanishing energy gap leads to a significant enhancement of the upper band population. Here, ξ becomes maximal for $\Delta_G^{\pm} = 0$. Experimental data [23] for a corresponding phase transition line is given in Fig. 6.4(a).

Nevertheless, the closing of an energy gap cannot provide sufficient proof for the existence of a *topological* phase transition. To this end, the effect of Berry curvatures (6.28) were directly measured in the experiment [23]. As seen in the previous section, Berry curvatures are expected to change the semiclassical equations of motion, see Eqs. (5.55) and (5.56) (cf. [199, 295]). For a force $\mathbf{F}$ which leaves the local system unchanged causing only Bloch oscillations, the velocity $\boldsymbol{v}$ of a particle in band ν carrying quasimomentum k is then given by

$$\boldsymbol{v}_{\mathbf{k},\nu}(\mathbf{r}) = \nabla_{\mathbf{k}} \varepsilon_{\mathbf{k},\nu} - \boldsymbol{\Omega}_{\nu} \cdot \mathbf{F}(\mathbf{r}, t)\,, \tag{6.33}$$

where $\boldsymbol{\Omega}$ is a matrix with entries given by Eq. (6.28). Most interestingly, the second term of Eq. (6.33) produces an *anomalous velocity*, i.e., a contribution to $\boldsymbol{v}$ that is perpendicular to the direction of the applied force. In the experiment, a net drift in the x-direction is measured as a response to a force applied along y after a full Bloch cycle. The results of such measurements [23] are shown in Fig. 6.4(b). Here, it is convenient to introduce a 'dif-

ferential drift' $\mathcal{D}$ which describes the difference of two drift results from equal but opposite forces. For example, choosing $\varphi = \pi/2$ and $\Delta_{\mathcal{AB}} = 0$ the lowest band produces positive Berry curvatures, see Fig. 6.3(a), which leads to a negative drift for a force pointing along the positive y-direction. In contrast, for a parameter choice that describes a conventional insulator, $C = 0$, the drifts due to both Dirac points are expected to cancel each other over a full Bloch period. In other words, this detection scheme measures the anomalous Hall response of the system. Note that this effect will be the central subject of study in chapter 7.

Lastly, we note that while topological properties are largely irrelevant for the following discussion on heating effects, they do play a major role in the next chapter where we consider an inhomogeneous Floquet realised Haldane model. Moreover, creating this Haldane model by Floquet techniques on a finite geometry will lead to corresponding edge channels consistent with the integer quantum Hall effect. How such edge states depend on interactions, i.e., heating effects in the Floquet system is left as an open question.

6.3. The Floquet realised Haldane model with weak interactions

6.3.1. Model and parameters

In this section, we present a theoretical analysis of interaction effects in the Haldane model discussed in the previous sections. To this end, we add to the periodically driven lattice Hamiltonian (6.13) the on-site interaction term (cf. Sec. 2.1)

$$H_{\text{int}} = U \sum_{i\in\mathcal{A},\mathcal{B}} n_{i\uparrow} n_{i\downarrow} \,, \tag{6.34}$$

with U being the interaction strength and $n_{i\sigma} = a^\dagger_{\mathbf{u}_i\sigma} a_{\mathbf{u}_i\sigma}$ ($n_{i\sigma} = b^\dagger_{\mathbf{u}_i+\mathbf{v}_0,\sigma} b_{\mathbf{u}_i+\mathbf{v}_0,\sigma}$) on the $\mathcal{A}$ ($\mathcal{B}$) sublattice, respectively. Here, we require the model to become spinful, as otherwiese an on-site interaction mechanism of type (6.34) would be prohibited for fermions due to Fermi-statistics. As discussed in Sec. 5.1, such an interacting Floquet system is bound to heat up as time evolves, and therefore *cannot* be sufficiently described by an effective Hamiltonian deduced from a Magnus expansion as presented in Sec. 6.1. Thus, we ultimately require a full Floquet description of the problem, see below.

To achieve such an *interacting Haldane model* experimentally, a repulsively interacting Fermi gas being composed of a spin mixture is loaded into the optical honeycomb lattice discussed above. While in Ref. [23] mainly the non-interacting spinless case was considered, the authors also briefly studied the spinful limit. Here, they indeed tried to look at the interplay of interactions and periodic modulations for a balanced spin mixture of $|9/2,-9/2\rangle$ and $|9/2,-5/2\rangle$ states of ^{40}K (see Sec. 6.1.1). In order to make our analysis as approachable as possible regarding the experiment performed, we continue to use experimental parameters and the experimental lattice geometry as presented in Sec. 6.1 throughout this section: $J/\hbar = J_{0,1,2}/\hbar = 2\pi\times 172\,\text{Hz}$ and $J_3 = J'_j = \Delta_{\mathcal{AB}} = 0$. In addition we set $\varphi = \pi/2$, thus describing a situation where the ground state is in the topological phase with Chern number $C = +1$ (see Sec. 6.2). Moreover, we only consider the case of a translationally invariant system at half filling.

Our ultimate goal is to capture the interplay of periodic driving and interactions by the Floquet-Boltzmann equation (5.74). As outlined in Ch. 5 we require two conditions for this approach to be applicable:

1. Since the Floquet-Boltzmann equation is based on a perturbative treatment, we require weak interaction strengths. For the present lattice model this puts an up-

per bound to the value of U, which should not exceed the order of the hopping strength, i.e., $\max(U) \sim \mathcal{O}(J)$. Consequently, this approach cannot be applied to, e.g., fermionic Mott-insulating states, as studied experimentally in [23].

2. The central aspect of the Floquet-Boltzmann formalism is the clear separation of time scales. Here, the time scale set by the driving frequency ought to be much smaller than times representing changes triggered by interactions. It is therefore required that $\Omega \gg U$.

Another aspect of the Floquet-Boltzmann equation is that all Hartree corrections are assumed to be absorbed into the original Hamiltonian by a appropriate renormalisation of single-particle energies. So in order to clarify what precise Floquet system needs to be solved, we discuss a potential Hartree correction to the non-interacting Hamiltonian first. In fact, it turns out that the Hartree correction only gives tiny contributions. An imbalance of particles on the sublattices leads to an oscillating term of the form $\Delta_{\mathcal{AB}}(t) \approx cU\cos(\Omega t)$, where c depends on the occupation function of all states. It was found that $c \lesssim 0.2$ for a ground state as discussed above. The Hartree contribution therefore remains small compared to all other terms for values of $U \lesssim J$. The single-particle gap, for example, changes only by 0.2% for $U = J$ and $c = 0.2$. We will therefore neglect the Hartree correction in all calculations in the following. This considerably simplifies the numerical efforts, since the scattering matrix elements W on the right-hand side of the Floquet-Boltzmann equation (being essentially the overlap of different Floquet states) do not depend on time. Thus, these matrix elements only have to be computed once. Furthermore, this approximation implies that the dependence of U can be absorbed into a redefinition of the time, see below.

To determine the Floquet eigenstates and quasienergies it is therefore sufficient to diagonalize the matrix representation of the non-interacting Floquet Hamiltonian given in its general form by Eq. (2.40). In the present case the Floquet matrix is readily built by using the expressions (6.19)-(6.23), which yield

$$H^F_{nm}(\mathbf{k}) = h_{n-m}(\mathbf{k}) - n\Omega\delta_{nm}\mathbb{1}\,, \tag{6.35}$$

with $h_n = h_{n,x}\sigma_x + h_{n,y}\sigma_y$, etc. By numerically diagonalizing this Floquet Hamiltonian, i.e., solving the Floquet eigenvalue problem in the extended space, one obtains the Floquet states $|\phi_{\mathbf{k},\xi}\rangle\rangle$ and quasienergies $\varepsilon_{\mathbf{k},\xi}$, see Eq. (2.37). Recall from Sec. 2.2.2 that a rigorous truncation of the Floquet matrix is often practicable due to the condition $\Omega N_f \gg E_{\max}$, where N_f is the largest Floquet index before truncation and $E_{\max}$ corresponds to the largest energy scale of the undriven system. In the present case it holds that $E_{\max} = D = 6J$, with D being the total bandwidth (see Sec. 6.1.1). Because driving frequencies are typically selected to be larger, e.g., $\Omega = 6.3J$, N_f can be indeed chosen on the order of one. We have checked that for driving frequencies of $\Omega/\hbar \gtrsim 3J/\hbar \approx 2\pi \times 500\text{Hz}$ it is sufficient to keep track of a few Floquet modes only, i.e., $N_f \geq 3$. So once Floquet eigenstates and quasienergies are found, all quantities entering the Floquet-Boltzmann equation can be calculated numerically exactly (within the presented approximations). Nevertheless, the FBE is in general still an integro-differential equation for the occupation function of Floquet states $n_{\mathbf{k},\nu}$ that is typically non-trivial to solve.

6.3.2. Heating rate and quasiequilibrium

We start by considering the full Floquet-Boltzmann equation given by Eq. (5.74). Furthermore, we assume that the system can indeed be described by a time-dependent lattice

Hamiltonian of type (6.2) imposing a translationally invariant situation. An immediate consequence of this property is the vanishing of all terms involving spatial derivatives on the left-hand side of Eq. (5.74). This applies to the spatial derivative of the Floquet occupation function $n_{\mathbf{k},\xi}$ itself as well as to all remaining Berry-phases corrections. Consequently, the Floquet-Boltzmann equation is reduced to the simplified form of

$$\partial_t \, n_{\mathbf{k},\xi,\sigma}(t) = I_{\mathrm{coll}}[n_{\mathbf{k},\xi,\sigma}(t)] \, . \tag{6.36}$$

Note that because the non-interacting driven part of the system is independent of the spin and, since the interaction part of Eq. (6.34) conserves the spin, it holds that the occupation function of both spin species is identical for the chosen initial configuration, i.e., $n_{\mathbf{k},\xi,\uparrow}(t) = n_{\mathbf{k},\xi,\downarrow}(t) = n_{\mathbf{k},\xi}(t)$.

While an interacting time-independent system preserves energy, the collision integral of the Floquet-Boltzmann equation allows for a violation of energy conservation in a discrete fashion, see Eq. (5.71). It is this very property that shall be the focus of our investigations now: how does the interacting Haldane model *heat up* over the course of time. In order to study such heating of the system, we consider the change of the (quasi)energy per lattice site defined by

$$e(t) = \frac{1}{2} \sum_{\xi,\sigma} \int \frac{d\mathbf{k}}{(2\pi/a)^2} \; \varepsilon_{\mathbf{k},\xi} \, n_{\mathbf{k},\xi,\sigma}(t) \, , \tag{6.37}$$

where the factor $1/2$ arises due to the fact that there are two lattice sites per unit cell. Here, $\varepsilon_{\mathbf{k},\xi}$ are the quasienergies of the non-interacting Floquet Hamiltonian (6.35), the sum index ξ indicates Floquet states of the first Floquet-zone only (see Sec. 5.2.2) and the sum over spins yields a global factor of 2 due to the argument above. The corresponding *heating rate*, $\Gamma = de/dt$, is then given by the temporal derivative of Eq. (6.37), and therefore reads as

$$\Gamma(t) = \frac{de(t)}{dt} \approx \sum_{\xi} \int \frac{d\mathbf{k}}{(2\pi/a)^2} \; \varepsilon_{\mathbf{k},\xi} \, \dot{n}_{\mathbf{k},\xi}(t) \, . \tag{6.38}$$

Note that we assumed $\partial_t \varepsilon_{\mathbf{k},\xi} \approx 0$, because we neglect the potential time-dependence of quasienergies arising from Hartree corrections as in the discussion above. Hence, the heating rate is fully determined by the temporal change of the Floquet occupation functions.

One can make progress now by realising that this variation over time is described by the simplified Floquet-Boltzmann equation (6.36). So using the explicit expression for the collision integral, see Eq. (5.71), the heating rate can be expressed as

$$\begin{aligned} \Gamma(t) = \sum_{\xi,\mu,\lambda,\eta} \sum_{n,\alpha} \int & \frac{d\mathbf{k}}{(2\pi/a)^2} \, \frac{d\mathbf{q}_1}{(2\pi/a)^2} \, \frac{d\mathbf{q}_2}{(2\pi/a)^2} \, \frac{d\mathbf{q}_3}{(2\pi/a)^2} \\ & \times \; n\Omega \; W^{n}_{\substack{\xi\mu\lambda\eta \\ \mathbf{k}\mathbf{q}_1\mathbf{q}_2\mathbf{q}_3}} \; \delta(\varepsilon_{\mathbf{k},\xi} + \varepsilon_{\mathbf{q}_1,\mu} - \varepsilon_{\mathbf{q}_2,\lambda} - \varepsilon_{\mathbf{q}_3,\eta} + n\Omega) \\ & \times \; \frac{1}{2} \; (2\pi/a)^2 \; \delta(\mathbf{k} + \mathbf{q}_1 - \mathbf{q}_2 - \mathbf{q}_3 + \alpha\mathbf{G}) \\ & \times \; n_{\mathbf{k},\xi}(t) \, n_{\mathbf{q}_1,\mu}(t) \, \big(1 - n_{\mathbf{q}_2,\lambda}(t)\big) \, \big(1 - n_{\mathbf{q}_3,\eta}(t)\big) \, . \end{aligned} \tag{6.39}$$

Note that in order to obtain this result one exploits some symmetry properties of the scattering rates: since the integration is over all momentum indices, one can conveniently symmetrize with respect to each of theses labels. One further uses that

$$W^{n}_{\substack{\xi\mu\lambda\eta \\ \mathbf{k}\mathbf{q}_1\mathbf{q}_2\mathbf{q}_3}} = W^{n}_{\substack{\mu\xi\eta\lambda \\ \mathbf{q}_1\mathbf{k}\mathbf{q}_3\mathbf{q}_2}} \qquad \text{and} \qquad W^{n}_{\substack{\xi\mu\lambda\eta \\ \mathbf{k}\mathbf{q}_1\mathbf{q}_2\mathbf{q}_3}} = W^{-n}_{\substack{\lambda\eta\xi\mu \\ \mathbf{q}_2\mathbf{q}_3\mathbf{k}\mathbf{q}_1}} \, , \tag{6.40}$$

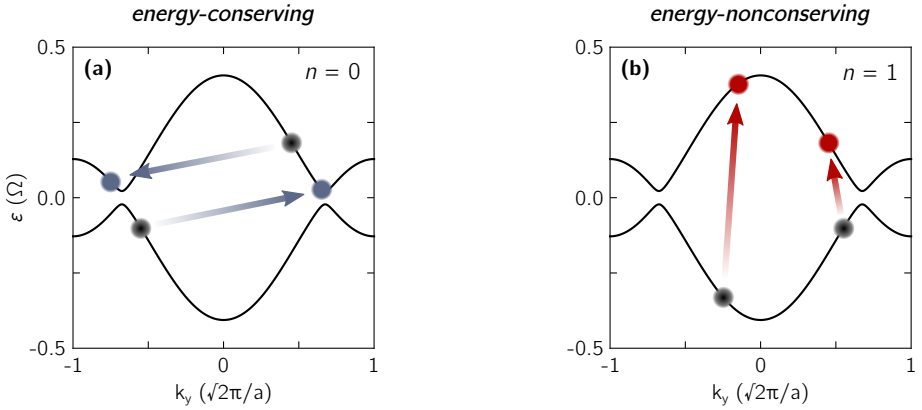

Figure 6.5.: Schematic of two-particle collision processes for (a) the energy conserving case ($n = 0$) and (b) the energy violating case ($n = 1$). The energy bands are shown along the diagonal of the quadratic Brillouin zone, see cut along $k_x = 0$ in Fig. 6.2(a) (dashed line). Scattering is indicated by arrows from initial states (black) into final states (blue/red). Parameters of the system are as described in the main text ($\Omega = 6.3J = 2\pi \times 1080\text{Hz}$).

where the latter expression follows from the principle of microscopic reversibility of transition rates. Using Eq. (6.40) one straightforwardly finds the form of Eq. (6.39). Indeed, the energy changes in quanta of $n\Omega$ determined by the Floquet matrix elements W^n. Note, however, that W^n with $|n| \geq 2$ cannot contribute to Eq. (6.39) as $|\varepsilon_{\mathbf{k}\xi}| \leq \Omega/2$ (see also Sec. 5.5).

As discussed above, Floquet states entering the matrix element W as well as quasienergies are readily calculated from the non-interacting Floquet Hamiltonian (6.35). The Floquet occupation functions $n_{\mathbf{k},\xi}$ are then determined from the solution of the Floquet-Boltzmann equation. This is in general a formidable task due to the integro-differential structure of the latter together with the multi-dimensional integrals appearing in the collision integral (5.71). Nevertheless, the problem can be dramatically simplified in situations where one can identify yet another separation of time scales. Considering the expression for the heating rate (6.39) there exists two types of scattering processes: either energy is *conserved* during a collision with $n = 0$, or the scattering *violates* energy conservation with $n \neq 0$. If the associated scattering time scales τ_{con} and τ_{vio}, respectively, fulfil the condition

$$\frac{1}{\tau_{\text{con}}} \gg \frac{1}{\tau_{\text{vio}}}, \tag{6.41}$$

the heating rate (6.39) can be calculated with a strongly reduced (numerical) effort. The nature of the two processes of Eq. (6.41) is depicted in Fig. (6.5). Note that this additional separation of time scales is indeed given by the chosen experimental parameters, where both rates differ by much more than an order of magnitude, see Sec. 6.3.3 below.

The essence of Eq. (6.41) is now the following: if energy-violating processes occur only rarely, the system behaves like a time-independent interacting system within a time window of τ_{vio}. In such systems scattering processes lead to an *equilibration* of the system. Condition (6.41) implies that the system undergoes many energy-conserving collisions before the energy is changed. Hence, the system equilibrates locally in time at a certain time-dependent temperature $T(t)$ and is approximately described by the thermal occupation function

$$n_{\mathbf{k},\xi}(t) \approx n^0_{\mathbf{k},\xi}(T(t)) = \left[\exp\left(\frac{\varepsilon_{\mathbf{k},\xi} - \mu(T(t))}{T(t)}\right) + 1\right]^{-1}, \tag{6.42}$$

where $\mu(T)$ is generally determined from the condition that the total number of particles remains constant. For the chosen set of parameters, though, the system is equipped with a particle-hole symmetry, and therefore $\mu(T) = 0$ for all temperatures and times. Note also that we set $k_B = \hbar = 1$ for convenience, with k_B being the Boltzmann constant. The situation in which condition (6.41) holds and the occupation function can be approximated by (6.42) is called *quasiequilibrium*, since the temperature still varies as a function of time.

The huge advantage of Eq. (6.42) for practical implementations is that all dependences of the occupation function on respective quantum numbers are approximately reduced to a single, yet time-dependent parameter: the temperature $T(t)$. Thus, to leading order in $\tau_{\mathrm{vio}}/\tau_{\mathrm{con}}$, we can replace all occupation functions in the expressions for the heating rate, Eqs. (6.38) and (6.39), by Fermi functions of type (6.42), i.e., $n(t) \to n^0(T(t))$. Consequently, we obtain the relation

$$\frac{dT(t)}{dt}\,\frac{de}{dT} \approx \Gamma(T(t))\,. \tag{6.43}$$

This simple differential equation can be directly solved to yield

$$t = \int_{T_i}^{T(t)} dT'\; \frac{c(T')}{\Gamma(T')}\,, \tag{6.44}$$

where we introduced the specific heat $c(T) = de/dT$.

In summary, under condition (6.41) we do not have to solve the coupled integro-differential equations given by the Floquet-Boltzmann equation in order to obtain $n_{\mathbf{k},\xi}(t)$. Instead, it is sufficient to calculate the heating rate Γ and the quasienergy per lattice site e as functions of temperature in combination with solving a simple one-parameter differential equation given by Eq. (6.43). The quasienergy density is straightforwardly obtained using Eq. (6.37), once the quasienergies are known. The heating rate (6.39), however, is determined by a high-dimensional integral that might remain numerically demanding. Lastly, we remark that the general notion of a 'temperature' for periodically driven systems is actually quite subtle. The reason being that the Floquet zone is not uniquely defined, see Sec. 2.2. We therefore demand a definition of the Floquet zone such that all quantities are maximally conserved. The temperature T used throughout is then understood to refer to this quasienergy setting. In the present, weakly interacting case where also the driving frequency is large, the Floquet zone is safely fixed by the single-particle picture of the bands, see Figs. 6.2 and 6.5, together with an initial (thermal) many-body state preparation.

6.3.3. Numerical aspects

In order to calculate heating rates given by Eq. (6.39) the multi-dimensional integrals need to be solved. In this section we elaborate upon the technical aspects of calculating this general expression. First, we introduce the algorithm that approximates the multi-dimensional integral. Then, we will argue numerically why the quasiequilibrium assumption of Eq. (6.42) is indeed a good one.

Multi-dimensional momentum integral

Generally, the task to numerically solve a multi-dimensional integral can be very demanding. For the present example, we need to evaluate an integral over four momentum indices, where every index is d-dimensional, yielding in total $4d$ degrees of freedom. The situation is simplified by physical constraints of having momentum as well as energy conservation

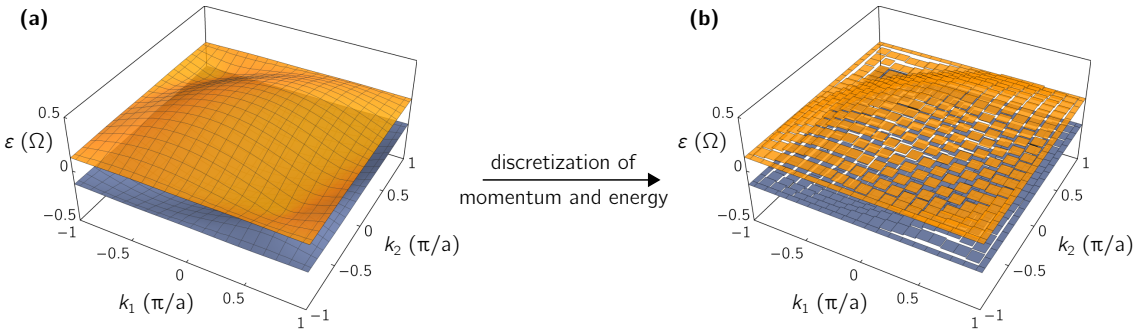

Figure 6.6.: Graphical illustration of discretisation of momentum and energy space (see text). (a) Continuous Floquet bands of first Brillouin zone (cf. Fig. 6.2). (b) Brillouin zone is discretized by a 20×20 mesh. Here, energy discretization is chosen to be $\Delta\varepsilon = \Omega/90$. Note that grid lines of (a) mark the discretisation islands of (b).

(up to multiple integers of $\mathbf{G}$ and Ω, respectively). These conservations are represented by respective δ-functions in, e.g., Eq. (6.39). The remaining $2d = 4$ integrals are, however, generally still challenging. To this end, we introduce a *discretisation* of momentum as well as energy by letting

$$\mathbf{k} \;\to\; \lfloor \mathbf{k}/\Delta k \rceil\, \Delta k = (i\Delta k, j\Delta k) \qquad \text{and} \qquad \varepsilon \;\to\; \lfloor \varepsilon/\Delta\varepsilon \rceil\, \Delta\varepsilon = l\,\Delta\varepsilon\,, \tag{6.45}$$

with $\Delta k, \Delta\varepsilon$ being discretization steps, $i, j, l \in \mathbb{Z}$ and $\lfloor x \rceil$ denotes the nearest integer function. The effect of such a discretisation on the bandstructure of the present Floquet Haldane system (isotropic lattice parameter choice and $\Omega/2\pi = 1080\,\mathrm{Hz}$) is seen in Fig. 6.6. Here, we discretise the first Brillouin zone, see Fig. 6.2(a), by a 20×20 mesh, i.e., $\Delta k = |\mathbf{G}|/20 = \pi/(10a)$, and rounded associated parts of the quasienergy bands to multiples of $\varepsilon/2\pi = 12\,\mathrm{Hz} \approx 0.07J$. Note that it is in fact advantageous to have a quadratic Brillouin zone resulting from the distorted honeycomb lattice, see Fig. 6.1.

Assuming a discrete nature of momenta and energies appearing in an expression such as Eq. (6.39), all integrals are converted into summations, i.e., $\int d\mathbf{k} \to \sum_{i,j} \Delta k$. At the same time, delta-functions representing momentum and energy conservation transform as $\delta(\mathbf{k}) \to \frac{1}{\Delta k}\delta_i\delta_j$ and $\delta(\varepsilon) \to \frac{1}{\Delta\varepsilon}\delta_l$, respectively. The algorithm to calculate corresponding multi-dimensional integrals is determined by the following steps:

1. For a given pair of incoming momenta $(\mathbf{k}, \mathbf{q_1})$, a list of all allowed scattering events including their associated energies is created. These scattering events are determined considering that momentum is conserved up to multiples of the reciprocal lattice vector $\mathbf{G}$.

2. The list of scattering events is filtered according to the energy constraint. For calculating heating rates this corresponds to rejecting all elements from the list except for the ones that change the energy by $\pm\Omega$.

3. Steps 1 and 2 are repeated for all possible (discretised) ingoing momenta $(\mathbf{k}, \mathbf{q_1})$. This reveals a complete list of relevant processes under the summation over incoming and outgoing momenta.

4. For every entry of this complete list, the matrix element W^n ($n = \pm1$ for heating rates) as well as the statistical factor $n_\xi n_\mu (1-n_\eta)(1-n_\lambda)$ is calculated. The final result is then obtained by summing over all these entries and weighting them by associated factors ($d\mathbf{k} \to \Delta k$, etc.).

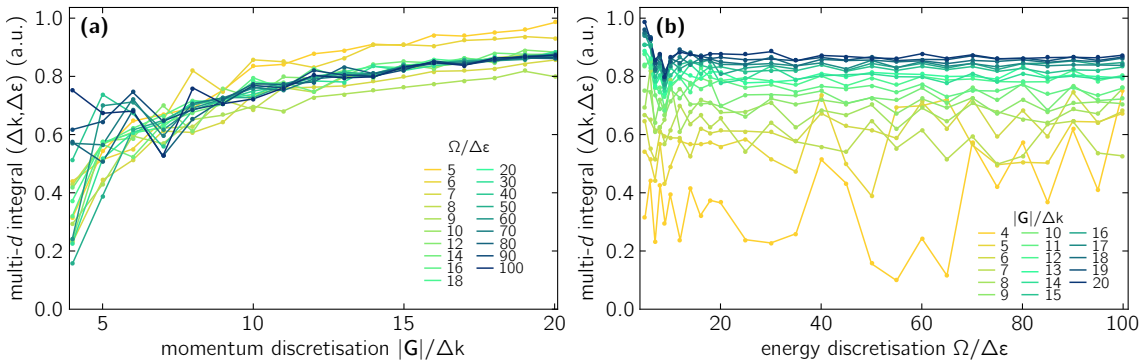

Figure 6.7.: Numerically solved multi-dimensional integral appearing in a variant expression of the heating rate Γ (see text). Results are shown (a) as a function of momentum discretisation for different values of $\Delta\varepsilon$ and (b) depending on energy discretisation for various momentum grid sizes. Dots are numerical data points. The temperature was set to $T = J$, but for $n = \pm 1$ discretisation effects are indeed independent of T.

The calculated discretised integral can obviously not be exact, but is rather a function of Δk and ΔE. Thus, the goal is to find a setting in which (e.g., for the heating rate Γ) it holds that

$$\Gamma(T, \Delta k, \Delta\varepsilon) \approx \lim_{\Delta k \to 0} \lim_{\Delta\varepsilon \to 0} \Gamma(T, \Delta k, \Delta\varepsilon) = \Gamma(T)\,. \tag{6.46}$$

In order to find a combination of $\Delta k, \Delta\varepsilon$ that approximates the true integral sufficiently well, we calculate an object similar to the heating rate (6.39) for $n = \pm 1$, but with $n\Omega \to 1$ for the factor outside the δ-function. We repeat the calculation for a range of discretised momenta as well as energies. In doing so, we first fix a certain Brillouin zone discretisation and vary $\Delta\varepsilon$ over a broad range. It is the aim to tune Δk and $\Delta\varepsilon$ in such a way that the considered quantity does not depend on $\Delta k/\Delta\varepsilon$. To fulfil this condition we look for stable plateaus in the object of interest calculated for different discretisation steps. Results for a temperature of $T = J$ are shown in Fig. 6.7, where the convergence of the multi-dimensional integral is indeed confirmed.

First of all, when choosing Δk too large, i.e., the Brillouin zone grid too coarse, no convergence of the calculated integral is to be expected, as can be seen from Fig. 6.7(a). Increasing the grid size to $|\mathbf{G}|/\Delta k \sim 15$ then allows for the desired convergence depending on the chosen energy spacing. Clearly, when the energy discretisation step becomes comparable to the band width of a single band, rounding errors are dramatic and cannot yield good approximate results. However, for $\Delta\varepsilon$ chosen smaller than this extreme limit, as considered in Fig. 6.7, one finds that results converge quickly for $\Omega/\Delta\varepsilon \sim 10$.

A surprising observation is that for a sufficiently small momentum grid size of, e.g., $|\mathbf{G}|/\Delta k = 16$, calculated values of the integral appear to be stable over a broad range of energy discretisations, $\Omega/\Delta\varepsilon \sim \mathcal{O}(10) - \mathcal{O}(100)$, see Fig. 6.7(b). In fact, the reason for this is that for cases of $n = \pm 1$ scattering processes are supported by the entire *Fermi sea*. Here, most of the individual scattering processes contribute in a similar way and details of the states are not significant in a qualitative sense. So despite the fact that the list of scattering events (see point (3) above) decays linearly in length with decreasing $\Delta\varepsilon$, which is straightforwardly understood from probabilistic arguments, there is still enough statistics 'surviving' from (3) to approximately fulfil Eq. (6.46), even for very small values of $\Delta\varepsilon$ compared to the momentum grid, $\Omega/\Delta\varepsilon \ll |\mathbf{G}|/\Delta k$. We checked that the plateau shown in Fig. 6.7(b) extends to discretisations of about $\Omega/\Delta\varepsilon \sim 1000$.

Moreover, the same Fermi sea argument can be used to explain the heating rate's sensi-

tivity on the discretisation as a function of temperature: since all particles of the Fermi sea contribute to heating, the quantitative discretisation step discussion above applies likewise to arbitrary temperatures. We also checked this numerically. However, the situation is fundamentally different when energy conserving processes, $n = 0$, are considered. Here, the scattering at low temperatures, $T \ll J$, is dominated by states near the Fermi surface due to the respective form of Fermi functions. This additional selection of states leads to a strong sensitivity of a sufficient discretisation on temperature. While within this chapter we are solely interested in heating rates, the $n = 0$ case will be relevant in Ch. 7. There, however, the stability of calculations is guaranteed by demanding at least moderate temperatures of $T \sim J$.

For the actual calculation of heating rates Γ in this chapter, we choose the same discretisation as used in Fig. 6.6, i.e., $\Delta k = |\mathbf{G}|/20 = \pi/(10a)$ and $\Delta\varepsilon = \Omega/90 = 2\pi \times 12\,\mathrm{Hz}$. Note again that choosing $\Delta\varepsilon$ as small as possible is numerically beneficial, since it reduces the amount of total scattering processes that need to be considered. In general, we trust that for the respectively chosen parameters discretisation errors are negligible up to uncertainties on the percent level $\sim \mathcal{O}(1\%)$, cf. Fig. 6.7.

Applicability of the quasiequilibrium approximation

We have to check whether experimental circumstances can ever allow the separation of scattering time scales (6.41). Ultimately, all generic Floquet systems heat up to infinite temperature. Thus, we compare the ratio of the scattering rates averaged over all bands and momenta in the limit $T \to \infty$, where all Fermi functions become constants $n^0 \to \frac{1}{2}$. We therefore define

$$\begin{aligned}\mathcal{W}^n = \sum_{\xi,\mu,\lambda,\eta} \sum_{\alpha} \int \frac{d\mathbf{k}}{(2\pi/a)^2} \frac{d\mathbf{q}_1}{(2\pi/a)^2} \frac{d\mathbf{q}_2}{(2\pi/a)^2} \frac{d\mathbf{q}_3}{(2\pi/a)^2} \\ \times W^n_{\substack{\xi\mu\lambda\eta,\sigma \\ \mathbf{k}\mathbf{q}_1\mathbf{q}_2\mathbf{q}_3}} \delta(\varepsilon_{\mathbf{k},\xi} + \varepsilon_{\mathbf{q}_1,\mu} - \varepsilon_{\mathbf{q}_2,\lambda} - \varepsilon_{\mathbf{q}_3,\eta} - n\Omega) \\ \times \delta(\mathbf{k} + \mathbf{q}_1 - \mathbf{q}_2 - \mathbf{q}_3 - \alpha\mathbf{G})\,,\end{aligned} \tag{6.47}$$

where $n = 0$ corresponds to an energy-conserving process and $n = \pm 1$ denotes a process that violates energy conservation by absorbing or emitting a photon of energy Ω, respectively. We then estimate the ratio of scattering times by

$$\frac{\tau_{\mathrm{con}}}{\tau_{\mathrm{vio}}} \approx \frac{\mathcal{W}^{+1} + \mathcal{W}^{-1}}{\mathcal{W}^0}\,. \tag{6.48}$$

So to check whether condition (6.41) is indeed fulfilled we apply the numerical technique presented above in order to obtain the averaged scattering rates $\mathcal{W}^0, \mathcal{W}^{\pm 1}$. In Fig. 6.8 we show numerical values for the ratio (6.48) as a function of the driving frequency Ω. For the smallest experimental values of about $\Omega \approx 2\pi \times 1000\,\mathrm{Hz}$ one observes that the energy conserving processes dominate by about two orders of magnitude, which justifies the approximation of Eq. (6.41) with high precision. As will be discussed in more detail below, the ratio vanishes for a certain value of the frequency, $\Omega_{\max}/2\pi \approx 1778.5\,\mathrm{Hz}$, and all two-particle processes violating energy conservation die out with $(\Omega_{\max} - \Omega)^3$ for $\Omega \to \Omega_{\max}$, see inset of Fig. 6.8.

6.3.4. Temporal behaviour of temperatures and entropies

Applying the technique presented in Sec. 6.3.3 to solve the multi-dimensional momentum integral now allows for an explicit calculation of the heating rate (6.39). Note that

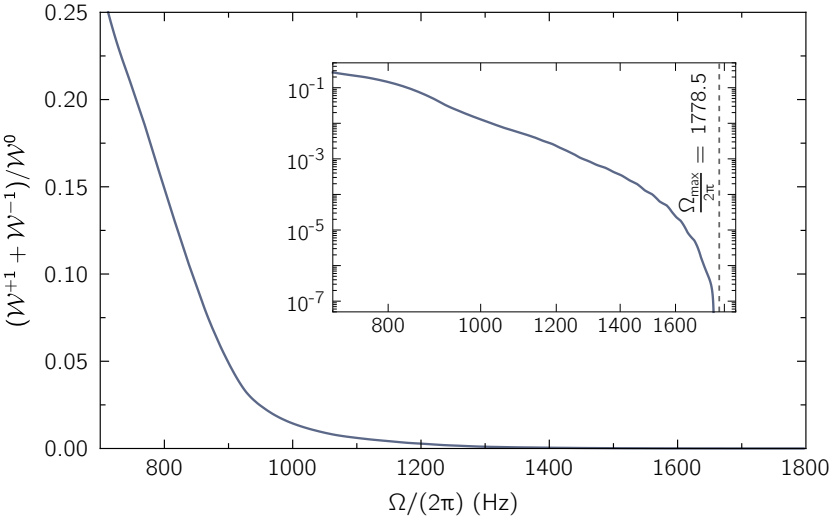

Figure 6.8.: The ratio $\tau_{\rm con}/\tau_{\rm vio}$ of scattering times for energy non-conserving ($W^{\pm 1}$) and energy conserving processes (W^0), see Eq. (6.48), plotted as a function of the driving frequency ($\Omega/2\pi$ is given in units of Hz). For large frequencies, $\Omega > 6J \approx 2\pi \times 1000$Hz energy conserving scattering dominates by several orders of magnitude. Inset shows a double-logarithmic plot. Ratio dies out as $\Omega \to \Omega_{\max} \simeq 1778.5$Hz (see text).

throughout this section we refrain from varying the lattice parameters of the system and stay with the isotropic choice made above. In Fig. 6.9 the heating rate $\Gamma(T)$ is plotted as a function of temperature for different driving frequencies Ω. First of all we note that all calculated heating rates follow (in dimensionless units) $\Gamma \ll 1$. This yields already a good self-consistency check for the applicability of the chosen approximations. To be more specific, one observes that all heating rates show the qualitative same behaviour: Γ starts out at some maximal value at $T = 0$ and then approaches $\Gamma = 0$ for $T \to \infty$. The initial plateau of the heating rate (see inset of Fig. 6.9) can be linked to the band gap of the Haldane model which is given by about $\Delta_G \approx 0.3\, J$ for $\Omega = 2\pi \times 1080\,\text{Hz}$. As long as the temperature is not of the order of Δ_G, the system cannot bridge the gap and, hence, the heating rate (along with all other quantities) is unaffected up to exponentially small corrections. Once the temperature is considerably larger than the band gap, the heating rate starts to drop. To analyse the limit $T \to \infty$, it is useful to realize that in situations where (6.41) holds a *detailed balance* condition relates the rate Γ^+ to Γ^- as

$$\frac{\Gamma^+}{\Gamma^-} \;=\; e^{\Omega/T}\,, \tag{6.49}$$

where Γ^+ is defined by the terms in Γ proportional to W^{+1} and Γ^- contains the terms proportional to W^{-1}. Recall that $W^n = 0$ for $|n| \geq 2$. Eq. (6.49) follows from the property of Fermi functions (6.42) that for $\epsilon_\xi + \epsilon_\mu - \epsilon_\eta - \epsilon_\lambda = \Omega$ it holds that

$$n^0_\eta\, n^0_\lambda\, (1 - n^0_\xi)\, (1 - n^0_\mu) = n^0_\xi\, n^0_\mu\, (1 - n^0_\eta)\, (1 - n^0_\lambda)\, e^{\Omega/T}\,. \tag{6.50}$$

Using Eq. (6.49) the heating rate is given by $\Gamma = \Gamma^+ - \Gamma^- = \Gamma^-(e^{\Omega/T} - 1)$. In the high temperature limit, i.e., for $T \gg \Omega$, $e^{\Omega/T}$ can be Taylor expanded and one obtains

$$\Gamma(T) \;\propto\; \frac{1}{T}\,, \tag{6.51}$$

as is also confirmed by the numerical results shown in Fig. 6.9.

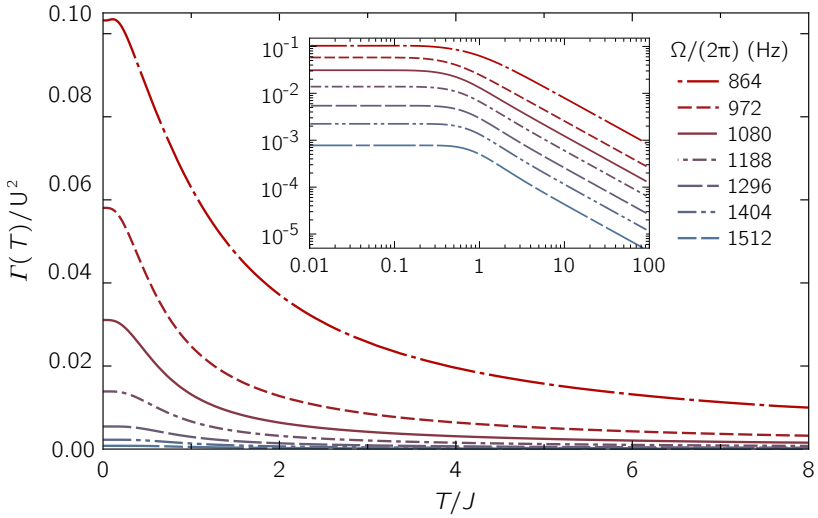

Figure 6.9.: Heating rate per lattice site (in units of $1/U^2$), see Eq. (6.39), plotted against dimensionless temperature T/J, with $J = 2\pi\times172$Hz being the hopping amplitude of the isotropic Hubbard model at hand. Different curves describe different driving frequencies Ω, ranging from $5J = 2\pi \cdot 864\,\mathrm{Hz}$ to $8.8J = 2\pi \times 1512$Hz, see legend. The inset shows a double logarithmic plot indicating different regimes.

While the heating rate Γ drops for increasing temperatures according to Eq. (6.51), it also decreases rapidly for increasing driving frequencies, as can be seen from Fig. 6.9. The reasons for this are two-fold: first, the matrix elements $W^{\pm1}$ drop for increasing Ω with $W^{\pm1} \propto 1/\Omega^2$ for $\Omega \to \infty$. In fact, this can be simply understood from perturbation theory as presented in Sec. 3.2.3, where it is shown that Floquet eigenstates decay with $1/\Omega$ in Floquet space (for $\Omega \to \infty$). Second, the phase space for two-particle scattering with energy transfer $\pm\Omega$ vanishes due to the restrictions on energy conservation. As denoted above, since every quasienergy is restricted to the first Floquet-zone, $|\varepsilon_{\mathbf{k},\xi}| \leq \Omega/2$, the maximal energy that can possibly be absorbed during a two-particle collision is $\max(\Delta E) = 2D(\Omega)$, with $D(\Omega) = \max_{\mathbf{k},\xi} \varepsilon_{\mathbf{k},\xi} - \min_{\mathbf{k},\xi} \varepsilon_{\mathbf{k},\xi}$ being the total bandwidth of the two Floquet bands of the first Floquet zone. Considering Fig. 6.5(b), this corresponds to a process that brings two particles at the bottom of the lower band simultaneously to the top of the upper band. It is now clear that as soon as the driving frequency exceeds the energy needed for this process, i.e. $\Omega > 2D(\Omega)$, heating is no longer supported by the formalism presented here. So approaching this threshold $\Omega_{\max} = 2D(\Omega_{\max})$ and expanding around the band minimum and maximum, one obtains the following behaviour for the heating rate

$$\Gamma(\Omega) \propto (\Omega_{\max} - \Omega)^3 , \tag{6.52}$$

for $\Omega \to \Omega_{\max}$ and $\Omega < \Omega_{\max}$. We also checked the validity of Eq. (6.52) numerically, see Fig. 6.8, where within our model we obtain $\Omega_{\max} = 2\pi \times 1778.5\,\mathrm{Hz}$.

Again, as for $\Omega > \Omega_{\max}$ two-particle scattering *cannot* contribute to heating, one has to consider higher-order scattering events for a proper analysis of this regime. In general, the matrix elements of these higher-order processes are expected to be small (at least for at most moderate interaction strengths) due to a further reduced overlap of corresponding Floquet states. We, hence, remark that increasing the driving frequency might be useful to bring the system into a prethermal regime where interactions do play a role with respect to the existing Floquet band structure, but at the same time heating might be suppressed on a time scale set by higher-order scattering processes. Such prethermalizing Floquet systems

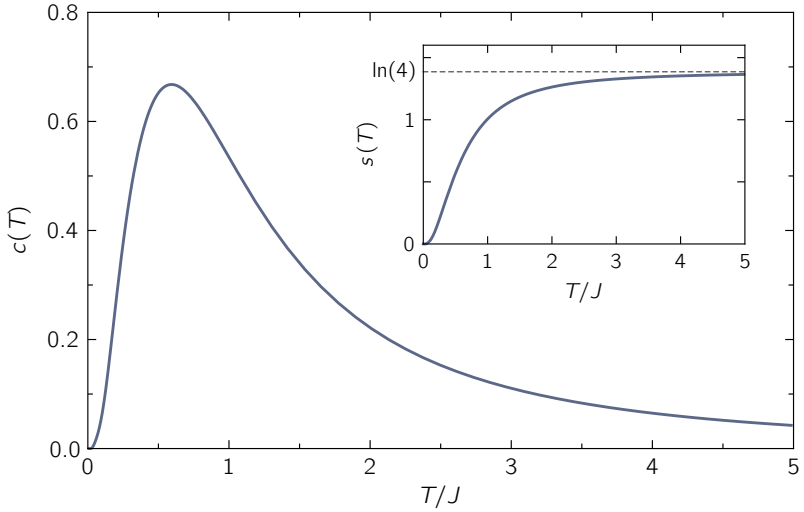

Figure 6.10.: Specific heat per lattice site, $c(T)$, plotted as function of dimensionless temperature T/J for a driving frequency of $\Omega = 6.3J = 2\pi\times 1080\text{Hz}$. The inset shows the corresponding entropy per lattice site ($k_B = 1$).

have only recently been considered in different circumstances, e.g., in Refs. [79, 92, 262].

Having discussed the heating rate as a function of time, one can now proceed by solving the simple equation (6.44). To this end, the heat capacity is determined from

$$c(T) = \frac{de(T)}{dT} \overset{(6.37)}{=} \sum_{\xi} \int \frac{d\mathbf{k}}{(2\pi/a)^2}\, \varepsilon_{\mathbf{k},\xi}\, \frac{d}{dT}\, n^0_{\mathbf{k},\xi}(T) \tag{6.53}$$

$$\overset{(6.43)}{=} \sum_{\xi} \int \frac{d\mathbf{k}}{(2\pi/a)^2}\, \left(\varepsilon_{\mathbf{k},\xi}\beta\right)^2 \frac{e^{\varepsilon_{\mathbf{k},\xi}\beta}}{\left(1+e^{\varepsilon_{\mathbf{k},\xi}\beta}\right)^2}\,, \tag{6.54}$$

with $\beta = 1/T$ being the inverse temperature. Since the specific heat (6.54) solely depends on the quasienergies, it can be calculated in a straightforward fashion. Fig. 6.10 shows the specific heat as a function of temperature. Generally, the curve can be divided into three different temperature regimes:

$$c(T) \propto \begin{cases} e^{-\frac{\Delta_G}{T}} & \text{for} \quad T \ll \Delta_G \\ T^2 & \text{for} \quad \Delta_G < T < J \\ \frac{1}{T^2} & \text{for} \quad J \ll T \end{cases}. \tag{6.55}$$

For $T \to 0$ the specific heat is exponentially suppressed due to the band gap Δ_G as already discussed for the heating rate. Note that we have checked that over the investigated frequency range, $5J < \Omega < 9J$, the band gap does not close and, thus, the system remains in the same topological state throughout. When the temperature becomes larger than the gap, but is still small compared to the bandwidth of a quasienergy band, i.e., $\Delta_G < T < J$, the specific heat is dominated by the (gapped) Dirac cones near $\mathbf{k}_D = \pm\frac{4\pi}{3\lambda}(0,1)$. Hence, the system is approximately described by a Dirac equation [301] and $c(T)$ grows with T^2. Here, notice the fundamental difference between the behaviour of the heat capacity in this regime and the heating rate: while the former is dominated by a Fermi surface effect, Γ is mostly insensitive to the specific details of the band structure. For large temperatures, $T \gg J$, the specific heat changes its behaviour and one obtains $c(T) \propto 1/T^2$.

Finally, using Eq. (6.44) and having numerically calculated the heating rate Γ as well as the specific heat c, we can directly compute the temperature as a function of time.

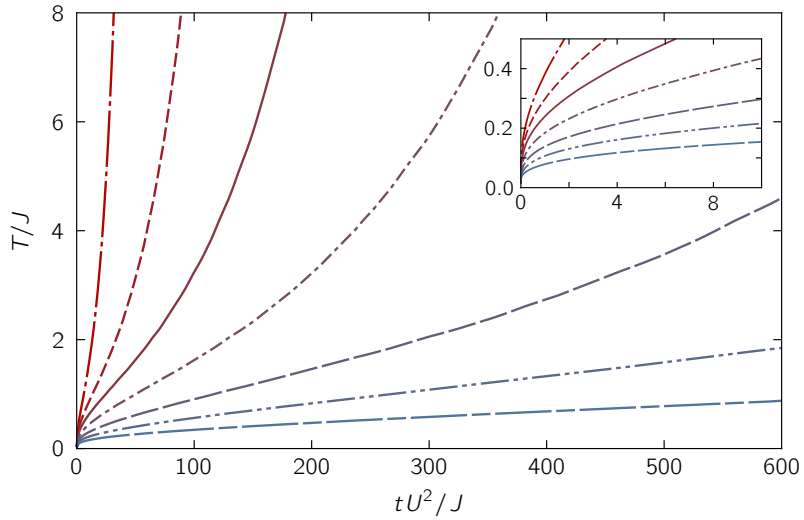

Figure 6.11.: Dimensionless temperature T/J of the interacting system as a function of time t for different driving frequencies Ω ($\Omega = 2\pi \times 864, \ldots, 1512$Hz). Curves are defined corresponding to the legend of Fig. 6.9. The inset clarifies the fact that the temperatures undergo two distinct regimes before rising with exponential speed, cf. Eq. (6.56).

We assume $T_i = 0$ as the initial temperature. The results are shown in Fig. 6.11 for different values of the driving frequency Ω. Because of the piecewise behaviour of c given by Eq. (6.55) as well as the discussed dependence of the heating rate on T (see Fig. 6.9), also the temperature shows three distinct regimes as a function of time:

$$T(t) \propto \begin{cases} \ln(1/t)^{-1} & \text{for} \quad T(t) \ll \Delta_G \\ t^{1/3} & \text{for} \quad \Delta_G < T(t) < J \\ e^{\alpha t} & \text{for} \quad T(t) \gg J, \Omega \end{cases} , \tag{6.56}$$

where α is a factor that depends, e.g., on the driving frequency. Due to the exponential suppression of $c(T)$ for $T \to 0$, initially $T(t)$ rises very rapidly as $1/\log(1/t)$ for $T(t)$ being small compared to the band gap Δ_G. This is followed by $T(t) \propto t^{1/3}$ for $\Delta_G < T < J$ as can be seen from the inset of Fig. 6.11. Because the curvature of the curves will have to change, there is an approximately linear intermediate regime before the temperature eventually starts to grow exponentially $T(t) \propto e^{\alpha t}$ for $T \gg \Omega$. The latter behaviour is immediately obtained from Eq. (6.43) by considering the results of Eqs. (6.51) and (6.55), i.e., $\Gamma \propto 1/T$ and $c \propto 1/T^2$, for $T \gg J, \Omega$, and also confirmed numerically, see Fig. 6.11. Moreover, the strong dependence of Γ on the driving frequency Ω propagates also into a similar behaviour of the temperature $T(t)$. For instance, when the driving frequency comes close to its 'critical value', i.e., $\Omega \to \Omega_{\max}$, the prefactor α in Eq. (6.56) decreases rapidly, $\alpha \propto (\Omega_{\max} - \Omega)^3$, see Eq. (6.52). This in turn enforces a strong slow down of the heating.

In ultracold atom experiments, however, it is not trivial to determine the temperature of the system. A way to circumvent this issue is often that the entropy is measured, which is a much more accessible observable for these kind of experiments. The reason being that the entropy remains approximately constant when all optical lattices and interactions are slowly switched off. These processes are often necessary to extract the desired information from the experimental system. In fact, also in the experiment by Jotzu *et al.* such an entropy measurement was performed (see extended data section of Ref. [23]). We therefore show in Fig. 6.12 also the entropy as a function of time. Here, the entropy was calculated

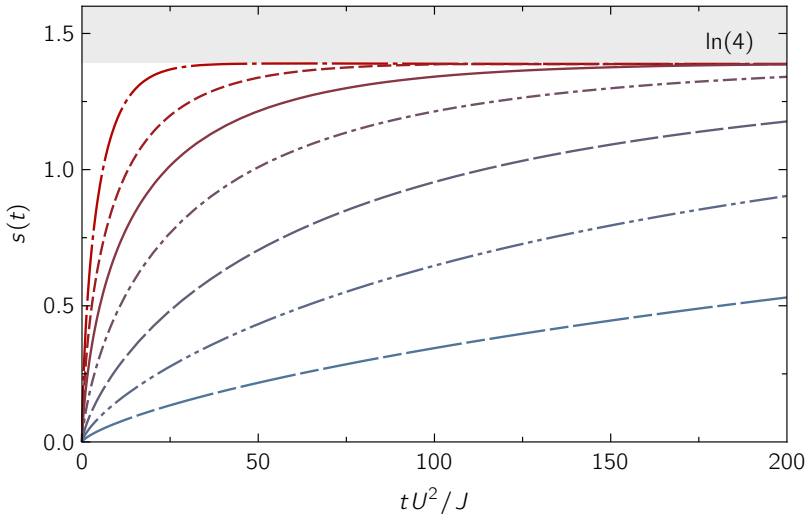

Figure 6.12.: Entropy per lattice site (i.e., per particle) as a function of time for different driving frequencies Ω ($= 2\pi \times 864, \ldots, 1512$Hz), see legend of Fig. 6.9. The solid curve ($\Omega = 6.3J = 2\pi \times 1080\,$Hz) is the typical frequency used in the experiment by Jotzu *et al.* [23]. Gray shaded area indicates the maximal entropy per particle (see text).

by using

$$S(T) = \int_0^T dT' \, \frac{c(T')}{T'} \qquad \text{or} \qquad S(t) = \int_0^t dt' \, \frac{\gamma(T(t))}{T(t)} \,, \tag{6.57}$$

respectively. Due to the exponential rise of T with time, see Eq. (6.56), the entropy (per lattice site) approaches its $T \to \infty$ limit with exponential speed

$$S(t) \approx \ln(4) - \kappa \, e^{-2\alpha t} \qquad \text{for} \qquad t \to \infty \,, \tag{6.58}$$

with κ being a prefactor depending on the system settings. Note that the maximally attainable value for the entropy per lattice site is $\ln(4)$, since for the system at hand - a spinful, fermionic lattice model at half filling - there exist only four possible microscopic configurations, i.e., $\{0, \uparrow, \downarrow, \uparrow\downarrow\}$.

6.4. Discussion and Conclusion

In this chapter, we have successfully applied the Floquet-Boltzmann equation to a Floquet realisation of the Haldane model. Here, the main result describes the behaviour of the system's temperature as a function of time. Ultimately, periodically driven closed quantum systems heat up to infinite temperature due to the absence of energy conservation. Our calculations presented in Sec. 6.3.4 have shown that for experimentally relevant parameters, as used in Ref. [23], this heating effect can be quite strong on typical time-scales of the experiment $\sim \mathcal{O}(10\text{ms})$. For example, we consider the situation where driving the system at a frequency of $\Omega = 6.3J = 2\pi \times 1080$Hz and having moderate interaction strengths of $U = J$. In this case, the entropy per site rises from $0.5\, k_B \ln(4)$ to $0.75\, k_B \ln(4)$ within $\Delta t \approx 18/J \approx 20$ms, as seen from Fig. 6.12. This is in fact short compared to typical loading times $\sim \mathcal{O}(100\text{ms})$ used in the experiment of Ref. [23], revealing the importance of the heating effects.

Nevertheless, a direct quantitative comparison with experimentally observed heating rates by Jotzu *et al.* is not possible. In Ref. [23] results are presented for rather large

values of the interaction strength, $U = 10J$ ($U = 20J$). This means that the system was experimentally investigated close to (or in) the Mott insulating regime, which is far beyond the applicability of our approach. Another aspect neglected by us is that a finite coupling between two-dimensional layers of atoms was present in this experiment. Moreover, in order to be able to describe experimental heating rates and associated behaviour of the system, it would also be necessary to treat the harmonic potential present in the experimental setup. This additional confinement is expected to lead to inhomogeneous heating as well as to heat transport through the trap. We will investigate this more complex situation in the next chapter, see Ch. 7.

We further note that the entropy growth of only a few k_B/s reported in Ref. [23] seems to be rather small in comparison to the values calculated by us in Sec. 6.3.4, where small initial entropies were assumed. We believe that these discrepancies are mainly explained by the fact that experimental entropies per lattice site were rather high on a scale set by $\ln(4)$. Indeed, studies of the non-driven artificial graphene system [300] revealed entropies *per particle* of $1.5\,k_B \approx k_B \ln(4)$ and $2.5\,k_B \approx 1.8 k_B \ln(4)$ before and after loading the atomic cloud into the optical lattice, respectively.

We have shown that moderate changes of the driving frequency can be used to effectively gain control over the amount of heating in the system. Here, heating by two-particle collisions is fully absent if Ω is tuned to larger values than twice the total bandwidth. In these cases higher-order processes, which are not included in our present analysis, need to be taken into account (see also discussion in Sec. 5.5). However, these effects are generally expected to be highly suppressed due to the Pauli principle forbidding three particles to reside on the same lattice site. However, increasing the driving frequency does not only cause a suppression of the heating mechanism, but likewise reduces all other effects associated with the periodic modulation. For example, the gap of the present simulated Haldane model scales with $1/\Omega$ for large Ω. To be concrete, increasing the driving frequency from say $6.3J \approx 2\pi \times 1080\text{Hz}$ to $\Omega \approx 10.3J \approx 2\pi \times 1800\text{Hz}$, where two-particle processes are completely suppressed, reduces the band gap $0.3\,J$ to $0.15\,J$.

Lastly, we remark that the results discussed in this chapter do not depend qualitatively on the parameter choice of the underlying lattice model. A corresponding numerical study of an alternative set of parameters (where, e.g., $J_j' \neq 0$) is presented by the author in the appendix of Ref. [238]. Again, what *is* expected to have a strong qualitative effect on the physics of the system is the presence of inhomogeneities. This will be subject of our investigations in the following chapter. Here, we will start to couple the topological properties of the model with the effects associated with Floquet heating presented in this chapter.

7. Transport in an inhomogeneous Floquet-engineered Haldane model

Understanding the mechanisms and properties of transport in many-body systems such as solids has been a long-standing question in the field of condensed matter systems. In fact, due to an enhanced controllability and implementability of designed non-equilibrium quantum system (such as ultracold atoms in optical lattices) finding appropriate transport descriptions is of more relevance than ever. As shown in previous chapters, semiclassical descriptions in terms of Boltzmann equations are powerful tools to capture the dynamics of (weakly) interacting many-body systems. Conventionally, such Boltzmann equations and variants thereof are very successful in estimating electric charge as well as heat conductivities and associated transport properties [217]. Nevertheless, in spite of their already simplified form compared to a full quantum description (cf. Ch. 4), Boltzmann equations quickly become numerically difficult to solve in the presence a spatial inhomogeneities. However, these are precisely the scenarios in which transport is generated either by some external force acting on the particles or by internal mechanisms, such as a spatially non-uniform density profile giving rise to diffusion.

Recently, many experiments with ultracold quantum gases were conducted in order to study many-body transport properties [302]. Examples encompass, among others, the measurements of universal spin-transport aspects in strongly interacting Fermi gases [303], the study of light-cone-like spreadings of correlations in many-body systems [13] and the observation of quantized conductance [304]. Moreover, the transport and out-of-equilibrium dynamics of a fermionic quantum gas in a Hubbard model was studied [14]. From a theoretical perspective, Boltzmann equations can also yield insights into aspects of these specific transport scenarios [230]. Here, however, a Boltzmann-like approach needs to be modified, since realisations with ultracold gases describe well isolated many-body quantum systems, i.e., systems that are *not* coupled to an external bath. These systems are typically characterized by spatially depending filling factors and energy densities, which needs to be embedded in the formalism accordingly [230].

In this chapter, we will present transport properties of a quantum gas system that is inherently out of equilibrium. To be precise, we address the question of how currents develop in a Floquet realised interacting Haldane model, as discussed in the previous chapter, in the presence of an additional parabolic confining potential. Most crucially, while other cold atom transport setups rely, for instance, on (quantum) quenches [13, 14] or on atom reservoir imbalances [304], transport properties of our proposal are fundamentally based on Floquet heating effects. In a static version, the system would simply remain in a corresponding equilibrium state. Including the external periodic drive, however, allows for a development of temperature gradients in the trap and for the emergence of associated currents. Most interestingly, since the underlying system is a quantum Hall state with non-trivial topological properties, see Sec. 6.2, the expected currents are bound to show anomalous effects. The study of this anomalous *Floquet-Nernst effect*, i.e., of the anomalous particle flow as a response to the presence of temperature gradients, is the central objective of this chapter (see, e.g., Ref. [305] for a discussion of a non-Floquet version of this effect). In other words, the investigations presented within this chapter are grounded

on three fundamental aspects: macroscopic transport due to diffusion, intrinsic heating owing to Floquet scattering processes and Berry phase effects related to the anomalous Hall effect.

Inspired by the formulation of hydrodynamics for cold atom systems by Mandt [230], we develop a transport formalism based on the previously derived Floquet-Boltzmann equation, see Ch. 5, to capture the physics of the system of interest. At first, we will introduce the setting by expanding the periodically driven system from the previous chapter to the presence of an additional parabolic confining potential. Following this, we will present a systematic derivation of a set of diffusion equations which describe the system in its hydrodynamic limit in terms of particle and energy densities. At the same time, we explain how Berry phase corrections can be incorporated into the formalism. Then, we give a detailed description of associated conductivities and diffusion constants can be obtained numerically before discussing the Floquet-Nernst effect quantitatively as well as qualitatively at the end of this chapter.

7.1. Confining potential and local density approximation

As indicated in Sec. 2.1, optical potentials for cold atoms provide confinement due to the intensity profile of the employed laser beams. For experimentally relevant cloud sizes, the additional confinement is harmonic to good approximation. In the previous chapter, we discussed consequences of interactions for a Floquet realisation of the Haldane model. We now extend the above used formalism by incorporating the external parabolic potential.

To this end, we first modify the initial static *non-interacting* lattice Hamiltonian H_{lat} given by Eq. (6.2) such that

$$H_{\mathrm{lat}}^{V} = H_{\mathrm{lat}} + V_{\mathrm{ho}}\,, \qquad \text{with} \qquad V_{\mathrm{ho}}(\mathbf{r}) = V_0 \sum_i \mathbf{r}_i^2\, c_i^\dagger c_i \tag{7.1}$$

describing the parabolic potential by shifting on-site energies accordingly (cf. Eq. (2.16)). Here, $V_0 = m\omega^2/2$ is an energy density, with m being the mass of the trapped particle and ω is the associated trapping frequency, and $\mathbf{r}_i$ denotes respective lattice positions. Note that we assume the trap to be rotationally invariant. Moreover, all lattice parameters of the homogeneous lattice Hamiltonian are the same as stated in the previous section, $J/\hbar = 2\pi \times 172\mathrm{Hz}$, etc. The central objective of this chapter is to eventually study the interplay of Berry phase effects and Floquet heating mechanisms. Therefore, we choose $\varphi = \pi/2$ and $\Delta_{\mathcal{AB}} = 0$ to consider a non-interacting system deep in the quantum Hall regime with $C = +1$, see Sec. 6.2. Also, we further continue to assume an applied driving frequency of $\Omega = 6.3J = 1080\mathrm{Hz}$.

In the following, we crucially assume that the external potential is *shallow* which allows for a treatment within the *local density approximation* (LDA) [65]. The essence of this approximation is that the system is presumed to be *locally* translationally invariant such that (quasi)momentum is still a good quantum number. For equilibrium situations, the effect of the potential is then incorporated by simply shifting the chemical potential according to

$$\mu \;\rightarrow\; \mu(\mathbf{r}) = \mu_c - V(\mathbf{r}) = \mu_c - V_0\,\mathbf{r}^2\,, \tag{7.2}$$

where μ_c corresponds to the value of the chemical potential at the center of the trap. For the present case of a particle-hole symmetric Haldane model we set $\mu_c = 0$ (cf. Sec. 6.3). The key advantage of the LDA is that all information can be obtained from a diagonalisation of the homogeneous lattice Hamiltonian H_{lat} in combination with Eq. (7.2).

Most importantly, the LDA is preserved when activating the external periodic drive: implementing the drive by globally shaking the entire lattice as done, e.g., in Ref. [23] the external potential acquires no time dependence in the co-moving frame of the atoms, cf. Sec. 6.1.2. This allows for a straightforward application of the LDA also within the Floquet description of the problem. Therefore, all methods and tools developed in the previous chapters to obtain Floquet eigenstates and quasienergies of the non-interacting Floquet Hamiltonian identically carry over to the present chapter. The general strategy for the interacting system is thus as follows: first, the non-interacting Floquet Hamiltonian is solved in the same way as above. This has to be done only once for a given set of parameters. Then, the *inhomogeneities* of the system are solely encoded on the level of the Floquet-Boltzmann equation in combination with information about the initial state of the atomic cloud.

We assume that such an *initial state* is described by an equilibrium state of the system. Here, the situation is captured by local Fermi functions[1] ($k_B = \hbar = 1$),

$$f^0_{\mathbf{k},\xi}(\mathbf{r}) = \frac{1}{1 + e^{(\varepsilon_{\mathbf{k},\xi} - \mu(\mathbf{r}))/T}} \,, \tag{7.3}$$

that are characterised by an initial temperature T_{ini} and by the spatially varying chemical potential $\mu(\mathbf{r})$, see Eq. (7.2). Note that we use an initial temperature of $T_{\mathrm{ini}} = 1.5J$ throughout this chapter. The fact that the initial equilibrium state is indeed given in this from can also be understood from the following argument: every equilibrium state must nullify the right-hand side of the Boltzmann equation, cf. Sec. 4.4. Hence, in order for equilibrium to be present it must hold that $\mathbf{F} = \nabla_{\mathbf{r}}\mu$, which is just a restatement of Eq. (7.2).

Note, however, that within an interacting theory Hartree corrections need to be taken into account, which renormalise the energies. For a particle-particle interaction type as described by Eq. (6.34), this correction is given by $Un(\mathbf{r})$, see Sec. 4.2.2. Here, $n(\mathbf{r}) = \sum_\xi \int d\mathbf{k}\, f^0_{\mathbf{k},\xi}(\mathbf{r})$ describes the spatially varying particle density (see below). The effective force is therefore a combination of the external force, which results from the parabolic confining potential, and a corresponding Hartree term, $\mathbf{F} = -\nabla_{\mathbf{r}} V - U\nabla_{\mathbf{r}} n$. Thus, the true initial equilibrium state is characterised by the effective chemical potential given by

$$\mu_{\mathrm{eff}}(\mathbf{r}) = -V(\mathbf{r}) - Un(\mathbf{r}) \approx -V(\mathbf{r})\,. \tag{7.4}$$

Generally, the initial particle densities $n(\mathbf{r})$ therefore need to be computed self-consistently using the expression for μ_{eff} in Eq. (7.3) (see Ref. [230] for details). Nevertheless, throughout this chapter we are mostly interested in interaction strengths that are at most of moderate strength, $U \sim J$, and we checked that for these situations Hartree corrections are indeed negligible.

In summary, this section introduced a harmonic confining potential to the shaken hexagonal lattice model of the previous chapter. We claimed that this additional potential can be dealt with employing an LDA treatment and that initial equilibrium states are found accordingly. Having clarified these non-interacting aspects of the theory, we will now begin to develop the effects of *interactions* associated with the presence of V_{ho} building on a Floquet-Boltzmann treatment in the next section.

[1] Note that we relabelled the distribution function as $n_{\mathbf{k},\xi} \to f_{\mathbf{k},\xi}$ (compared to the notation of Ch. 5) in order to not confuse the reader with the commonly used notation for particle densities n, see below.

7.2. From Floquet-Boltzmann formalism to hydrodynamics

Considering the Floquet realisation of the Haldane model with weak interactions, as discussed in Ch. 6, and assuming that the LDA applies, allows for a natural treatment of the system within a Floquet-Boltzmann equation approach, see Ch. 5. In contrast to the previous chapter, where the homogeneous Haldane system was characterised by the right-hand side of the Floquet-Boltzmann equation, i.e., by the collision integral, now the spatial inhomogeneities activate also all terms on the left-hand side - including Berry phase correction terms. Nevertheless, a treatment of the system within a full Floquet-Boltzmann equation picture keeping track of every local Fermi function is practically impossible. Hence, the idea is to simplify the problem by considering a set of quantities with much fewer degrees of freedom [230], i.e., taking the hydrodynamic limit. To this end, one expresses the initial Boltzmann equation as a set of coupled equations - the diffusion equations - describing the flow of conserved quantities. For a typical ultracold atom setup, these conserved quantities are the particle number and the total energy. While the latter is not fully conserved in our Floquet setting, we will base the derivation on these two quantities. We stress that the following systematic derivation of the diffusion equations is strongly inspired by the work of Mandt [230]. Nonetheless, aspects of energy violation in terms of heating rates as well as the discussion on anomalous effects are unique to the here presented work.

7.2.1. Continuity equations

The hydrodynamic or diffusive limit of the conventional Boltzmann equation given in Ch. 4, see Eq. (4.85), emerges from the presumption of remaining close to thermal equilibrium at all times [230]. This demands that the Boltzmann equation is dominated by the collisions on the right-hand side, which prevents the forces to drive the system much out of the equilibrium state. So while one still requires that interactions are not too large such that a well-defined quasiparticle picture is applicable, see Ch. 4, interactions as well as particle densities cannot be too small either in the spirit of the statement above. For the Floquet case, see Ch. 5, the *same* requirements apply. In addition, one needs to keep in mind that the Floquet-Boltzmann equation allows for energy nonconserving processes which might drive the system quickly out of equilibrium - even for relatively small interaction strengths. One therefore demands for the Floquet case that conventional equilibrium processes dominate over those that violate energy conservation. This claim leads to the notion of a quasiequilibrium as already discussed in Sec. 6.3.2.

We start by making the same quasiequilibrium ansatz for the occupation function as above, see Eq. (6.42). Here, however, we add a small correction, because forces - be they of mechanical or statistical nature - drive the system inherently out of equilibrium. We write

$$f_{\mathbf{k},\xi}(\mathbf{r},t) = f^0_{\mathbf{k},\xi}(\mu(\mathbf{r},t), T(\mathbf{r},t)) + \delta f_{\mathbf{k},\xi}(\mathbf{r},t)\,, \tag{7.5}$$

where ξ is a Floquet band index that also encodes the spin information and δf describes the small deviation from quasiequilibrium. The spatial dependence of the equilibrium distribution function f^0 is a consequence of the inhomogeneity of the system and is captured by a spatially varying temperature $T(\mathbf{r})$ as well as chemical potential $\mu(\mathbf{r})$. We stress again that the total occupation function f obtains its dynamics from an interplay of the response to external forces as well as 'Floquet heating' processes.

We now introduce the *particle density* n as well as the *(quasi)energy density* e associated with the distribution function given by Eq. (7.5). We sometimes write these quantities also in a combined way as $\mathbf{n} = (n, e)$. They are defined by an appropriate integration over

the Brillouin zone of the form[2]

$$n(\mathbf{r},t)=\sum_{\xi}\int\frac{d\mathbf{k}}{(2\pi)^d}\;f_{\mathbf{k},\xi}(\mathbf{r},t)\qquad\text{and}\qquad e(\mathbf{r},t)=\sum_{\xi}\int\frac{d\mathbf{k}}{(2\pi)^d}\;\varepsilon_{\mathbf{k},\xi}\,f_{\mathbf{k},\xi}(\mathbf{r},t)\,. \tag{7.6}$$

The aim is to develop a formalism that describes the behaviour of the system in terms of the quantities n and e instead of the occupation functions f. The reason for this ambition is easily understood: the densities $\mathbf{n}(\mathbf{r},t)$ being functions of space and time only, while the occupation number additionally depends on a large amount of quantum numbers (momentum, spin, etc.).

One continues by integrating the Floquet-Boltzmann equation (5.74) in the following way:

$$\sum_{\xi}\int\frac{d\mathbf{k}}{(2\pi)^d}\;\left(\partial_t+\boldsymbol{\mathcal{F}}_{\mathbf{k},\xi}\,\nabla_{\mathbf{k}}+\boldsymbol{v}_{\mathbf{k},\xi}\,\nabla_{\mathbf{r}}\right)\left(f^0_{\mathbf{k},\xi}+\delta f_{\mathbf{k},\xi}\right)=0\,, \tag{7.7}$$

$$\sum_{\xi}\int\frac{d\mathbf{k}}{(2\pi)^d}\;\varepsilon_{\mathbf{k},\xi}\left(\partial_t+\boldsymbol{\mathcal{F}}_{\mathbf{k},\xi}\,\nabla_{\mathbf{k}}+\boldsymbol{v}_{\mathbf{k},\xi}\,\nabla_{\mathbf{r}}\right)\left(f^0_{\mathbf{k},\xi}+\delta f_{\mathbf{k},\xi}\right)=\Gamma(\mathbf{r},t)\,, \tag{7.8}$$

where we omitted the dependence on the central coordinates $(\mathbf{r},t)$ on the left-hand side for convenience. Most importantly, it was used that the collision integral guarantees *particle conservation* and only allows for Floquet heating under the quasiequilibrium assumption made above (cf. Eq. (6.39)), i.e.,

$$\sum_{\xi}\int\frac{d\mathbf{k}}{(2\pi)^d}\;I_{\text{coll}}[n_{\mathbf{k},\xi}]=0\qquad\text{and}\qquad\sum_{\xi}\int\frac{d\mathbf{k}}{(2\pi)^d}\;\varepsilon_{\mathbf{k},\xi}\,I_{\text{coll}}[n_{\mathbf{k},\xi}]=\Gamma(\mathbf{r},t)\,. \tag{7.9}$$

Here, Γ is the heating rate as already encountered in Sec. 6.3.2, which now depends on space $\mathbf{r}$ as well as on time t. In conventional situations, where interactions perfectly conserve energy, one has $\Gamma=0$. The presence of this energy violating contribution in the Floquet case naturally complicates the discussion. Having said this, a non-zero Γ can also *trigger* physical phenomena, such as heat currents, for instance. Indeed, the ultimate goal of this section is to analyse effects that are fundamentally linked to a spatially dependent heating rate.

Next, using the definitions of the local particle and energy densities, Eq. (7.6), one can rewrite Eqs. (7.7) and (7.8) as

$$\dot{n}(\mathbf{r},t)=-\sum_{\xi}\int\frac{d\mathbf{k}}{(2\pi)^d}\;\left(\boldsymbol{\mathcal{F}}_{\mathbf{k},\xi}\,\nabla_{\mathbf{k}}+\boldsymbol{v}_{\mathbf{k},\xi}\,\nabla_{\mathbf{r}}\right)\left(f^0_{\mathbf{k},\xi}+\delta f_{\mathbf{k},\xi}\right), \tag{7.10}$$

$$\dot{e}(\mathbf{r},t)=-\sum_{\xi}\int\frac{d\mathbf{k}}{(2\pi)^d}\;\varepsilon_{\mathbf{k},\xi}\left(\boldsymbol{\mathcal{F}}_{\mathbf{k},\xi}\,\nabla_{\mathbf{k}}+\boldsymbol{v}_{\mathbf{k},\xi}\,\nabla_{\mathbf{r}}\right)\left(f^0_{\mathbf{k},\xi}+\delta f_{\mathbf{k},\xi}\right)\;+\;\Gamma(\mathbf{r},t)\,, \tag{7.11}$$

where central coordinates have again been omitted for all objects appearing under the momentum integral. We proceed by explicitly using the local density approximation as discussed above: since the system is considered to be locally translationally invariant, it holds that the quasienergy spectrum is time and space independent, i.e., $\partial_t\varepsilon\approx 0$ and $\nabla_{\mathbf{r}}\varepsilon\approx 0$. Therefore, one obtains for some of the Berry curvatures that $\boldsymbol{\Omega}_{rr}=\boldsymbol{\Omega}_{rk}=$

[2] Note that for the lattice system at hand densities are given per lattice site. Thus, the correct normalisation of the momentum integrals appearing in Eq. (7.6) is $(2\pi/a)^{-d}/2$ (cf., e.g, Eq. (6.37)). The factor of $(2\pi)^{-d}$ must therefore be understood as a notational abbreviation.

$\boldsymbol{\Omega}_{rt} = \boldsymbol{\Omega}_{kt} = 0$. The expressions for the forces $\boldsymbol{\mathcal{F}}$ and velocities $\boldsymbol{v}$ including Berry phase corrections then become (cf. Eqs. (5.55) and (5.56))

$$\boldsymbol{\mathcal{F}}_{\mathbf{k},\xi}(\mathbf{r},t) = \mathbf{F}(\mathbf{r},t) \qquad \text{and} \qquad \boldsymbol{v}_{\mathbf{k},\xi}(\mathbf{r},t) = \underbrace{\nabla_{\mathbf{k}}\varepsilon_{\mathbf{k},\xi}}_{\equiv \mathbf{v}^0_{\mathbf{k},\xi}} - \underbrace{\boldsymbol{\Omega}_{\xi,kk}\cdot\mathbf{F}(\mathbf{r},t)}_{\equiv -\mathbf{v}^{\mathrm{an}}_{\mathbf{k},\xi}(\mathbf{r},t)}, \tag{7.12}$$

with $\mathbf{v}^0$ denoting the conventional velocity and $\mathbf{v}^{\mathrm{an}}$ describes the *anomalous velocity* being a direct consequence of non-zero Berry curvatures and therefore an intrinsic property of the system (cf. Sec. 6.2). Often [199] the anomalous velocity is expressed in a different but equivalent way as $\mathbf{v}^{\mathrm{an}} = -\mathbf{F}\times\boldsymbol{\Omega}$, where $\boldsymbol{\Omega} = \Omega_{\xi,k_xk_y}\hat{e}_z$ for our 2D system at hand (cf. Eq. (5.53)). Note further that $\mathbf{F}(\mathbf{r},t) = -\boldsymbol{\nabla}V(\mathbf{r},t)$ has in principle a static part owing to the external parabolic potential and a time-dependent Hartree contribution (see above).

Upon substituting the expressions of Eq. (7.12) into Eqs. (7.10) and (7.11) and using the above described assumptions one eventually finds

$$\dot{n}(\mathbf{r},t) = -\nabla_{\mathbf{r}}\Big[\sum_{\xi}\int\frac{d\mathbf{k}}{(2\pi)^2}\,\Big(\mathbf{v}^0_{\mathbf{k},\xi}\,\delta f_{\mathbf{k},\xi} + \mathbf{v}^{\mathrm{an}}_{\mathbf{k},\xi}\,f^0_{\mathbf{k},\xi}\Big)\Big], \tag{7.13}$$

$$\begin{aligned}\dot{e}(\mathbf{r},t) = &-\nabla_{\mathbf{r}}\Big[\sum_{\xi}\int\frac{d\mathbf{k}}{(2\pi)^2}\,\varepsilon_{\mathbf{k},\xi}\,\Big(\mathbf{v}^0_{\mathbf{k},\xi}\,\delta f_{\mathbf{k},\xi} + \mathbf{v}^{\mathrm{an}}_{\mathbf{k},\xi}\,f^0_{\mathbf{k},\xi}\Big)\Big] \\ &+ \mathbf{F}\Big[\sum_{\xi}\int\frac{d\mathbf{k}}{(2\pi)^2}\,\Big(\mathbf{v}^0_{\mathbf{k},\xi}\,\delta f_{\mathbf{k},\xi} + \mathbf{v}^{\mathrm{an}}_{\mathbf{k},\xi}\,f^0_{\mathbf{k},\xi}\Big)\Big] + \Gamma(\mathbf{r},t)\,.\end{aligned} \tag{7.14}$$

To obtain these equations one needs to exploit a few properties: first, since $f_{\mathbf{k}}$ and $\delta f_{\mathbf{k}}$ are periodic functions with respect to the Brillouin zone, boundary terms are absent leading to $\int d\mathbf{k}\nabla_{\mathbf{k}} f_{\mathbf{k}} = 0$ and $\int d\mathbf{k}\nabla_{\mathbf{k}}\delta f_{\mathbf{k}} = 0$, respectively. Second, using integration by parts one can use that $\int d\mathbf{k}\,\varepsilon_{\mathbf{k}}\nabla_{\mathbf{k}}\delta f_{\mathbf{k}} = -\int \mathbf{v}^0_{\mathbf{k}}\delta f_{\mathbf{k}}$. Third, despite the fact that the anomalous velocity depends on the spatial coordinate $\mathbf{r}$ it does commute with the spatial derivative operator $\nabla_{\mathbf{r}}$. The reason being that the divergence of the anomalous velocity is always zero for the present 2D case, as can easily be shown[3]. In addition, we ignore terms that are cubic in the force and/or in gradients, respectively, such as $\nabla_{\mathbf{r}}\mathbf{v}^{\mathrm{an}}_{\mathbf{k},\xi}\delta f_{\mathbf{k},\xi}$, etc., because they are small. Moreover, it is convenient to introduce the associated particle and energy current densities defined as

$$\mathbf{j}^0_n(\mathbf{r},t) = \sum_{\xi}\int\frac{d\mathbf{k}}{(2\pi)^2}\,\mathbf{v}^0_{\mathbf{k},\xi}\,\delta f_{\mathbf{k},\xi}\,, \qquad \mathbf{j}^0_e(\mathbf{r},t) = \sum_{\xi}\int\frac{d\mathbf{k}}{(2\pi)^2}\,\varepsilon_{\mathbf{k},\xi}\,\mathbf{v}^0_{\mathbf{k},\xi}\,\delta f_{\mathbf{k},\xi}\,, \tag{7.15}$$

$$\mathbf{j}^{\mathrm{an}}_n(\mathbf{r},t) = \sum_{\xi}\int\frac{d\mathbf{k}}{(2\pi)^2}\,\mathbf{v}^{\mathrm{an}}_{\mathbf{k},\xi}\,f^0_{\mathbf{k},\xi}\,, \qquad \mathbf{j}^{\mathrm{an}}_e(\mathbf{r},t) = \sum_{\xi}\int\frac{d\mathbf{k}}{(2\pi)^2}\,\varepsilon_{\mathbf{k},\xi}\,\mathbf{v}^{\mathrm{an}}_{\mathbf{k},\xi}\,f^0_{\mathbf{k},\xi}\,, \tag{7.16}$$

where $\mathbf{j}^0$ denote conventional currents and $\mathbf{j}^{\mathrm{an}}$ are anomalous currents. With these definitions one can reformulate Eqs. (7.13) and (7.14) as follows:

$$\dot{n}(\mathbf{r},t) = -\nabla_{\mathbf{r}}\Big[\mathbf{j}^0_n(\mathbf{r},t) + \mathbf{j}^{\mathrm{an}}_n(\mathbf{r},t)\Big], \tag{7.17}$$

$$\dot{e}(\mathbf{r},t) = -\nabla_{\mathbf{r}}\Big[\mathbf{j}^0_e(\mathbf{r},t) + \mathbf{j}^{\mathrm{an}}_e(\mathbf{r},t)\Big] + \mathbf{F}(\mathbf{r},t)\,\mathbf{j}^0_n(\mathbf{r},t) + \Gamma(\mathbf{r},t)\,. \tag{7.18}$$

This set of equations is a variant of celebrated *continuity equations*. We learnt above that the divergence of the anomalous velocity in the present case is zero. In a true equilibrium

[3] Note that $-\nabla_{\mathbf{r}}\mathbf{v}^{\mathrm{an}}_{\mathbf{k}} = \nabla_{\mathbf{r}}(\mathbf{F}\times\boldsymbol{\Omega}) = \epsilon_{ijk}\partial_k F_i\Omega_j = (\partial_x F_y - \partial_y F_x)\Omega_z = (\partial_y\partial_x V - \partial_x\partial_y V)\Omega_z = 0$. Here it was used that $\mathbf{F} = -\nabla_{\mathbf{r}}V$ and $\boldsymbol{\Omega} = (0,0,\Omega_z)$, see text.

situation ($\delta f = 0$) Eqs. (7.17) and (7.18) are bound to vanish, and thus it holds that $\nabla \mathbf{j}_n^{\mathrm{an}} = \nabla \mathbf{j}_e^{\mathrm{an}} = 0$. Due to the fact that these currents (to lowest order) depend solely on f^0, i.e., represent an *intrinsic* property of the system, this condition remains approximately[4] true even for $\delta f \neq 0$. Hence, we can write Eqs. (7.17) and (7.18) in the more simplified and familiar form of

$$\dot{n}(\mathbf{r},t) = -\nabla_{\mathbf{r}}\, \mathbf{j}_n^0(\mathbf{r},t)\,, \qquad \dot{e}(\mathbf{r},t) = -\nabla_{\mathbf{r}}\, \mathbf{j}_e^0(\mathbf{r},t) + \mathbf{F}(\mathbf{r},t)\, \mathbf{j}_n^0(\mathbf{r},t) + \Gamma(\mathbf{r},t)\,. \tag{7.19}$$

We stress that while the change of particle densities is solely determined from particle currents, the energy evolution has additional contributions. Here, the energy currents are accompanied by the 'Floquet heating rate', Γ, as well as by a 'Joule heating' term, $\mathbf{F}\mathbf{j}_n^0$. The latter represents the possibility of converting potential energy into kinetic energy and vice versa. While anomalous currents do not (significantly) contribute to adjustments of densities $\mathbf{n}$ in the present setup, they mark an important feature of the theory, which we will discuss in Sec. 7.2.4 below. In order to simplify notations, however, we will neglect them where allowed by virtue of Eqs. (7.19).

We conclude by remarking that the dynamics predicted by the Floquet-Boltzmann equation are equally captured by the continuity equations (7.19). Here, we assumed a slightly perturbed quasiequilibrium situation of type (7.5). To make further progress, though, one needs to calculate individual quantities of Eq. (7.19). Following the assumptions made above, the heating rate Γ can be determined in exactly the same way as presented in Sec. (6.3.2). The conventional particle and energy currents on the other hand demand the knowledge of δf. To this end, we calculate these small deviations from a simplified version of the Boltzmann equation presented in the next section.

7.2.2. The linearised Boltzmann equation

Generally, a full (Floquet-)Boltzmann treatment is very challenging, often impossible due to its integro-differential structure. In cases, however, where the system is in a quasiequilibrum, or is only marginally separated from equilibrium, the discussion of the problem simplifies substantially (as already partially seen in Sec. (6.3.2)). For the present situation described by Eq. (7.5) one can consider a *linearised* version of the Boltzmann equation [217, 230].

We start by claiming that small deviations from an equilibrium position are mainly determined by the dominant scattering processes. In other words, we assume that δf can be solely calculated from energy conserving processes, i.e., $n = 0$ in the Floquet-Boltzmann equation, see Eq. (5.71). Indeed, this is consistent with the quasiequilibrium assumption made above. We then introduce a new function $\phi_{\mathbf{k},\xi}$ that parametrises $\delta f_{\mathbf{k},\xi}$ and is defined as [217]

$$\delta f_{\mathbf{k},\xi} = -\frac{\partial f^0_{\mathbf{k},\xi}}{\partial \varepsilon_{\mathbf{k},\xi}}\, \phi_{\mathbf{k},\xi} = \beta f^0_{\mathbf{k},\xi}(1 - f^0_{\mathbf{k},\xi})\, \phi_{\mathbf{k},\xi}\,, \tag{7.20}$$

with $\beta = 1/T$ being the inverse temperature ($k_B = 1$). Since $\delta f_{\mathbf{k},\xi} = f_{\mathbf{k},\xi} - f^0_{\mathbf{k},\xi}$ is demanded to be small, so is $\phi_{\mathbf{k},\xi}$ and one can linearise the Boltzmann equation with respect to this quantity. Notice that the construction of (7.20) reflects the typical property that forces only deform the system's Fermi surface, where the function $-\partial f^0_{\mathbf{k},\xi}/\partial \varepsilon_{\mathbf{k},\xi} = \beta f^0_{\mathbf{k},\xi}(1 - f^0_{\mathbf{k},\xi})$ is sharply peaked.

[4] Note that for a rotationally invariant system the divergence of anomalous currents vanishes exactly. For the present case, where transport properties are expected to be different along x- and y-directions, we checked that contributions from $\nabla \mathbf{j}_n^{\mathrm{an}}$ and $\nabla \mathbf{j}_e^{\mathrm{an}}$ are negligible for the discussion below.

Now, the general goal is to find a corresponding lowest order representation of the Floquet-Boltzmann equation (5.74). Using Eq. (7.20) one finds that the FBE is approximated as

$$(\partial_t + \mathbf{F}\,\nabla_{\mathbf{k}} + \mathbf{v}^0_{\mathbf{k},\xi}\,\nabla_{\mathbf{r}})\, f^0_{\mathbf{k},\xi} = I^{\mathrm{lin}}_{\mathrm{coll}}[\phi_{\mathbf{k},\xi}]\,, \tag{7.21}$$

where $I^{\mathrm{lin}}_{\mathrm{coll}}$ is a linearised version of the collision integral (5.71). Note crucially that for the left-hand side one assumes $f_{\mathbf{k},\xi} \approx f^0_{\mathbf{k},\xi}$, since here already the mere equilibrium distribution yields non-zero contributions. Furthermore, all Berry phase corrections have been neglected in Eq. (7.21). In contrast, the right-hand side cannot solely depend on f^0, since the equilibrium distribution nullifies the collision integral. In order to linearise I_{coll} one considers the statistical factor, see Eq. (5.71), which becomes

$$\begin{aligned}
&[f_{\mathbf{q}_2,\eta} f_{\mathbf{q}_3,\lambda}(1-f_{\mathbf{k},\xi})(1-f_{\mathbf{q}_1,\mu}) - f_{\mathbf{k},\xi} f_{\mathbf{q}_1,\mu}(1-f_{\mathbf{q}_2},\eta)(1-f_{\mathbf{q}_3,\lambda})] \qquad (7.22)\\
&\quad\approx\ -\beta\,\phi_{\mathbf{k},\xi}\, f^0_{\mathbf{k},\xi}(1-f^0_{\mathbf{k},\xi})[f^0_{\mathbf{q}_2,\eta} f^0_{\mathbf{q}_3,\lambda}(1-f^0_{\mathbf{q}_1,\mu}) + f^0_{\mathbf{q}_1,\mu}(1-f^0_{\mathbf{q}_2,\eta})(1-f^0_{\mathbf{q}_3,\lambda})] \ +\ \dots\\
&\quad=\ -\beta\,\phi_{\mathbf{k},\xi}\,[f^0_{\mathbf{k},\xi} f^0_{\mathbf{q}_1,\mu}(1-f^0_{\mathbf{q}_2,\eta})(1-f^0_{\mathbf{q}_3,\lambda})] \ +\ \dots\ ,
\end{aligned}$$

where all terms beyond linear order in $\phi_{\mathbf{k},\xi}$ have been ignored and '…' indicates terms proportional to $\phi_{\mathbf{q}_1,\mu}$, etc., which are determined in the same way as outlined here for $\phi_{\mathbf{k},\xi}$. Note that the detailed balance condition (6.50) was used in the first line to eliminate the zeroth order term and in the second line for rearrangement. The linearized collision integral can thus be written as

$$I^{\mathrm{lin}}_{\mathrm{coll}}[\phi_{\mathbf{k},\xi}] = -\beta \sum_{\mu,\lambda,\eta} \int \frac{d\mathbf{q}_1}{(2\pi)^2}\frac{d\mathbf{q}_2}{(2\pi)^2}\frac{d\mathbf{q}_3}{(2\pi)^2}\ \mathcal{P}^{\xi\mu\lambda\eta}_{\mathbf{k}\mathbf{q}_1\mathbf{q}_2\mathbf{q}_3}\ (\phi_{\mathbf{k}\xi} + \phi_{\mathbf{q}_1\mu} - \phi_{\mathbf{q}_2\eta} - \phi_{\mathbf{q}_3\lambda})\,, \tag{7.23}$$

where we redefined the transition elements as

$$\mathcal{P}^{\xi\mu\lambda\eta}_{\mathbf{k}\mathbf{q}_1\mathbf{q}_2\mathbf{q}_3} = 4\pi^2 \sum_{\alpha} W^0_{\xi\mu\lambda\eta\,\mathbf{k}\mathbf{q}_1\mathbf{q}_2\mathbf{q}_3}\ \delta(\Delta\mathbf{k}+\alpha\mathbf{G})\,\delta(\Delta\varepsilon_{\mathbf{k}})\,[f^0_{\mathbf{k},\xi} f^0_{\mathbf{q}_1,\mu}(1-f^0_{\mathbf{q}_2,\eta})(1-f^0_{\mathbf{q}_3,\lambda})]\,, \tag{7.24}$$

with short-hand notations $\Delta\mathbf{k} = \mathbf{k}+\mathbf{q}_1-\mathbf{q}_2-\mathbf{q}_3$ and $\Delta\varepsilon = \epsilon_{\mathbf{k},\xi}+\epsilon_{\mathbf{q}_1,\mu}-\epsilon_{\mathbf{q}_2,\lambda}-\epsilon_{\mathbf{q}_3,\eta}$. The collision integral given by Eq. (7.23) completes the linearised form of the Floquet-Boltzmann equation (7.21). We stress again that the Floquet character of the description is partly gone, because it does not allow for heating any more ($n = 0$). Nevertheless, the quasiparticles are still assumed to be described by Floquet states. Therefore, the rates (7.24) are still calculated from non-interacting Floquet eigenstates of the locally homogeneous Floquet Hamiltonian. The biggest advantage gained by the procedure above is that the Boltzmann equation has been reduced to a mere integral equation. This equation can therefore be formally inverted to obtain an explicit expression for $\phi_{\mathbf{k},\xi}$.

Before doing so, however, we briefly discuss the role of the spin index. So far, we considered σ to be implicitly contained in the Floquet band index ξ. For the following steps the spin needs to be taken into account explicitly, though. To this end, we assume that the spin index is locked to the respective Floquet band label in the order $(\sigma\bar{\sigma}\bar{\sigma}\sigma)$, where still $\bar{\sigma}$ indicates the opposite spin of σ. It is in fact the latter property of not having free sums running over the spin indices that makes the discussion of such important. Since it is still presumed that quasienergies as well as Floquet states are spin-independent, the only effect arises via some statistical weight of the scattering processes and one can re-expresses Eq. (7.23) as

$$I^{\mathrm{lin}}_{\mathrm{coll}}[\phi_{\mathbf{k},\xi,\sigma}] \equiv \sum_{\xi',\sigma'} \int d\mathbf{k}'\ M_{\mathbf{k}\mathbf{k}',\xi\xi',\sigma\sigma'}\ \phi_{\mathbf{k}'\xi'\sigma'}\,, \tag{7.25}$$

with M being defined according to Eqs. (7.23)-(7.24) and reads as

$$M_{\mathbf{k}\mathbf{k}',\xi\xi',\sigma\sigma'} = -\beta \sum_{\mu,\lambda,\eta} \int \frac{d\mathbf{q}_1}{(2\pi)^2} \frac{d\mathbf{q}_2}{(2\pi)^2} \frac{d\mathbf{q}_3}{(2\pi)^2} \, \mathcal{P}^{\xi\mu\lambda\eta}_{\mathbf{k}\mathbf{q}_1\mathbf{q}_2\mathbf{q}_3} \times \left[\delta_{\mathbf{k}\mathbf{k}'}\delta_{\xi\xi'}\delta_{\sigma\sigma'} + \delta_{\mathbf{q}_1\mathbf{k}'}\delta_{\mu\xi'}\delta_{\bar{\sigma}\sigma'} - \delta_{\mathbf{q}_2\mathbf{k}'}\delta_{\eta\xi'}\delta_{\bar{\sigma}\sigma'} - \delta_{\mathbf{q}_3\mathbf{k}'}\delta_{\lambda\xi'}\delta_{\sigma\sigma'}\right], \tag{7.26}$$

where for momenta we employed the short-hand notation $\delta_{\mathbf{k}\mathbf{k}'} = \delta(\mathbf{k}-\mathbf{k}')$, etc. Assuming that the inverse of this matrix is known one can formally solve the linearised FBE of Eq. (7.21) for $\phi_{\mathbf{k},\xi}$ to obtain

$$\begin{aligned}
\phi_{\mathbf{k},\xi}(\mathbf{r},t) &\approx \sum_{\xi'} \int d\mathbf{k}' \; M^{-1}_{\mathbf{k}\mathbf{k}',\xi\xi'} \Big(\mathbf{F}\,\nabla_{\mathbf{k}'} + \mathbf{v}^0_{\mathbf{k}',\xi'}\nabla_{\mathbf{r}}\Big) f^0_{\mathbf{k}',\xi'} \\
&= \sum_{\xi'} \int d\mathbf{k}' \; M^{-1}_{\mathbf{k}\mathbf{k}',\xi\xi'} \Big(\mathbf{F}\,\nabla_{\mathbf{k}'} f^0_{\mathbf{k}',\xi'} + \mathbf{v}^0_{\mathbf{k}',\xi'} \frac{\partial f^0_{\mathbf{k}',\xi'}}{\partial\mu}\,\nabla_{\mathbf{r}}\mu + \mathbf{v}^0_{\mathbf{k}',\xi'} \frac{\partial f^0_{\mathbf{k}',\xi'}}{\partial T}\,\nabla_{\mathbf{r}} T\Big) \\
&= \sum_{\xi'} \int d\mathbf{k}' \; M^{-1}_{\mathbf{k}\mathbf{k}',\xi\xi'} \mathbf{v}^0_{\mathbf{k}',\xi'} \frac{\partial f^0_{\mathbf{k}',\xi'}}{\varepsilon_{\mathbf{k}',\xi'}} \Big((\mathbf{F} - \nabla_{\mathbf{r}}\mu) - \frac{1}{T}\,(\varepsilon_{\mathbf{k}',\xi'} - \mu)\nabla_{\mathbf{r}} T\Big),
\end{aligned} \tag{7.27}$$

where we reabsorbed the spin index σ into the Floquet band index for notational brevity. In the first line we neglect the temporal derivative ∂_t, as it can be understood [230] as a second order spatial derivative which we ignore within our discussion. Furthermore, we used that $\partial f/\partial T = (\mu-\varepsilon)/T \cdot \partial f/\partial\varepsilon$ as well as $\partial f/\partial\mu = -\partial f/\partial\varepsilon$, and recalled that the spatial dependencies of the equilibrium function are encoded in the chemical potential and the temperature, $(\mu(\mathbf{r},t), T(\mathbf{r},t))$. The corrections to the equilibrium state, $\delta f = \beta f^0(1-f^0)\phi$, are essentially the response to mechanical as well as statistical forces. In the following, we will extract respective conductivities from these individual parts.

7.2.3. Generalized conductivities and diffusion equations

Knowing - at least formally - the explicit forms of $\delta f_{\mathbf{k},\xi}$ and $\phi_{\mathbf{k},\xi}$, see Eqs. (7.20) and (7.27), the currents defined in Eqs. (7.15) can be represented in terms of conductivities of the form

$$\begin{pmatrix} \mathbf{j}^0_n \\ \mathbf{j}^0_e \end{pmatrix} = \underbrace{\begin{pmatrix} \sigma_n & \alpha_n \\ \sigma_e & \alpha_e \end{pmatrix}}_{\equiv\hat{\boldsymbol{\sigma}}} \begin{pmatrix} \mathbf{F} - \nabla_{\mathbf{r}}\mu \\ -\nabla_{\mathbf{r}} T \end{pmatrix}, \tag{7.28}$$

with $\hat{\boldsymbol{\sigma}}$ defining the 2×2 matrix of *generalised conductivities*, where the individual components are given by

$$\sigma_n = \sum_{\xi,\xi'} \int d\mathbf{k} \int d\mathbf{k}' \; \mathbf{v}^0_{\mathbf{k},\xi} \, \widetilde{M}^{-1}_{\mathbf{k}\mathbf{k}',\xi\xi'} \, \mathbf{v}^0_{\mathbf{k}',\xi'}, \tag{7.29}$$

$$\sigma_e = \sum_{\xi,\xi'} \int d\mathbf{k} \int d\mathbf{k}' \; \varepsilon_{\mathbf{k},\xi} \, \mathbf{v}^0_{\mathbf{k},\xi} \, \widetilde{M}^{-1}_{\mathbf{k}\mathbf{k}',\xi\xi'} \, \mathbf{v}^0_{\mathbf{k}',\xi'}, \tag{7.30}$$

$$\alpha_n = \frac{1}{T} \sum_{\xi,\xi'} \int d\mathbf{k} \int d\mathbf{k}' \; \mathbf{v}^0_{\mathbf{k},\xi} \, \widetilde{M}^{-1}_{\mathbf{k}\mathbf{k}',\xi\xi'} \, \mathbf{v}^0_{\mathbf{k}',\xi'} \, (\varepsilon_{\mathbf{k}',\xi'} - \mu), \tag{7.31}$$

$$\alpha_e = \frac{1}{T} \sum_{\xi,\xi'} \int d\mathbf{k} \int d\mathbf{k}' \; \varepsilon_{\mathbf{k},\xi} \, \mathbf{v}^0_{\mathbf{k},\xi} \, \widetilde{M}^{-1}_{\mathbf{k}\mathbf{k}',\xi\xi'} \, \mathbf{v}^0_{\mathbf{k}',\xi'} \, (\varepsilon_{\mathbf{k}',\xi'} - \mu). \tag{7.32}$$

Here, we have re-defined the inverse scattering matrix as

$$\widetilde{M}^{-1}_{\mathbf{k}\mathbf{k}',\xi\xi'} = -\frac{1}{4\pi^2} \frac{\partial f^0_{\mathbf{k},\xi}}{\partial\varepsilon_{\mathbf{k},\xi}} \frac{\partial f^0_{\mathbf{k}',\xi'}}{\partial\varepsilon_{\mathbf{k}',\xi'}} M^{-1}_{\mathbf{k}\mathbf{k}',\xi\xi'}. \tag{7.33}$$

The diagonal entries of $\hat{\boldsymbol{\sigma}}$, i.e., σ_n and α_e, are typical particle and energy conductivities in the following sense: the former measures the drift of particles as a response to an external mechanical force $\mathbf{F}$ or some gradient in the chemical potential. The second describes the energy flow as a consequence of a temperature gradient. The off-diagonal terms σ_e and α_n, on the other hand, represent the strength of thermoelectric effects, e.g., how much a spatial variation of the temperature affects the particle flow. Note that all conductivities given by Eqs. (7.29)-(7.32) are 2×2 matrices by themselves representing the two spatial dimensions. All conductivities above are *symmetric* matrices with respect to the spatial structure.

Ultimately, we desire a description in terms of particle and energy densities of the system as outlined in Sec. 7.2.1. To this end, we need to perform the change of variables

$$(\mu, T) \;\rightarrow\; (n, e)\,, \tag{7.34}$$

which is established by the definitions for the particle and energy densities: here, we *define* the temperature T and chemical potential μ for a given $\mathbf{n}$ in such a way that they produce the correct densities when using $f(\mathbf{r},t) = f^0(\mu(\mathbf{r},t), T(\mathbf{r},t))$ in Eq. (7.6). We apply this change of variables to the equation describing the currents above, see Eq. (7.28), as well as interpret the conductivities as functions of $\mathbf{n}$, i.e., $\sigma_n(\mathbf{n})$, etc. Then, the continuity equations (7.19) describe indeed a closed set of equations for $\mathbf{n}$. Clearly, using the chain rule of differentiation one finds

$$\nabla_{\mathbf{r}}\mu = \frac{\partial\mu}{\partial n}\nabla_{\mathbf{r}} n + \frac{\partial\mu}{\partial e}\nabla_{\mathbf{r}} e \qquad \text{and} \qquad \nabla_{\mathbf{r}} T = \frac{\partial T}{\partial n}\nabla_{\mathbf{r}} n + \frac{\partial T}{\partial e}\nabla_{\mathbf{r}} e\,. \tag{7.35}$$

This allows to establish *'susceptibilities'* [230] which relate the two sets of variables of (7.34) in the following way:

$$\hat{\boldsymbol{\chi}}(\mathbf{n}) = \begin{pmatrix} \frac{\partial n}{\partial \mu} & \frac{\partial n}{\partial T} \\ \frac{\partial e}{\partial \mu} & \frac{\partial e}{\partial T} \end{pmatrix} \qquad \text{and} \qquad \hat{\boldsymbol{\chi}}^{-1}(\mathbf{n}) = \begin{pmatrix} \frac{\partial \mu}{\partial n} & \frac{\partial \mu}{\partial e} \\ \frac{\partial T}{\partial n} & \frac{\partial T}{\partial e} \end{pmatrix}. \tag{7.36}$$

These susceptibilities describe the sensitiveness of n and e on changes in the chemical potential or temperature, respectively (and vice versa for $\hat{\boldsymbol{\chi}}^{-1}$). Using the generalised conductivities as well as the matrix of inverse susceptibilities we now introduce a matrix of *diffusion constants* [230]

$$\hat{\mathbf{D}}(\mathbf{n}) = \hat{\boldsymbol{\sigma}}(\mathbf{n})\hat{\boldsymbol{\chi}}^{-1}(\mathbf{n}) \equiv \begin{pmatrix} D_{nn}(\mathbf{n}) & D_{ne}(\mathbf{n}) \\ D_{en}(\mathbf{n}) & D_{ee}(\mathbf{n}) \end{pmatrix}. \tag{7.37}$$

Finally, merging all parts of the discussion allows to re-write the continuity equations (7.19) in their closed form of generalized *diffusion equations* yielding

$$\begin{pmatrix} \dot{n} \\ \dot{e} \end{pmatrix} = -\nabla_{\mathbf{r}} \left[\begin{pmatrix} \sigma_n(\mathbf{n}) \\ \sigma_e(\mathbf{n}) \end{pmatrix} \mathbf{F} - \hat{\mathbf{D}}(\mathbf{n}) \begin{pmatrix} \nabla_{\mathbf{r}} n \\ \nabla_{\mathbf{r}} e \end{pmatrix} \right] + \begin{pmatrix} 0 \\ \mathbf{F}\,\mathbf{j}_n^0(\mathbf{n}) \end{pmatrix} + \begin{pmatrix} 0 \\ \Gamma(\mathbf{n}) \end{pmatrix}, \tag{7.38}$$

where $n(\mathbf{r},t)$ and $e(\mathbf{r},t)$ are understood as functions of space and time. The particle and energy current densities, Eq. (7.15), are now expressed as

$$\begin{aligned} \mathbf{j}_n^0(\mathbf{n}) &= \sigma_n \mathbf{F} - D_{nn}\nabla_{\mathbf{r}} n - D_{ne}\nabla_{\mathbf{r}} e\,, \\ \mathbf{j}_e^0(\mathbf{n}) &= \sigma_e \mathbf{F} - D_{en}\nabla_{\mathbf{r}} n - D_{ee}\nabla_{\mathbf{r}} e\,. \end{aligned} \tag{7.39}$$

Most crucially, we note that the diffusion equations (7.38) are a set of highly non-linear differential equations. This nonlinearity is fundamentally rooted in the properties of the collision integral (7.23). Before elaborating on a strategy to numerically solve this set of equations in Sec. 7.3, we first comment on the role of the transverse currents as given by Eq. (7.16).

7.2.4. Transverse currents and anomalous transport effects

While the diffusion equations (7.38) only carry knowledge about the conventional current densities given by Eqs. (7.39), transversal or anomalous currents can still be observed macroscopically. Following the spirit of Eq. (7.28), we use $\mathbf{v}^{\mathrm{an}} = -\mathbf{F} \times \boldsymbol{\Omega}$, where $\boldsymbol{\Omega} = \Omega_{\xi,k_xk_y}\hat{e}_z$, in order to write the transverse currents given by Eqs. (7.16) also in terms of corresponding conductivities, i.e.,

$$\mathbf{j}_n^{\mathrm{an}} = \underbrace{\begin{pmatrix} 0 & \sigma_{n,xy} \\ -\sigma_{n,xy} & 0 \end{pmatrix}}_{\equiv \sigma_n^{\mathrm{an}}} \mathbf{F} \qquad \text{and} \qquad \mathbf{j}_e^{\mathrm{an}} = \underbrace{\begin{pmatrix} 0 & \sigma_{e,xy} \\ -\sigma_{e,xy} & 0 \end{pmatrix}}_{\equiv \sigma_e^{\mathrm{an}}} \mathbf{F}\,, \tag{7.40}$$

where the 'xy'-components of the anomalous conductivities $\sigma_{n/e}^{\mathrm{an}}$ read as

$$\sigma_{n,xy}^{\mathrm{an}} = -\sum_{\xi} \int \frac{d\mathbf{k}}{(2\pi)^2}\, f_{\mathbf{k},\xi}^0\, \Omega_{\xi,k_xk_y} \qquad \text{and} \qquad \sigma_{e,xy}^{\mathrm{an}} = -\sum_{\xi} \int \frac{d\mathbf{k}}{(2\pi)^2}\, \varepsilon_{\mathbf{k},\xi}\, f_{\mathbf{k},\xi}^0\, \Omega_{\xi,k_xk_y} \tag{7.41}$$

and the momentum space Berry curvature Ω_{ξ,k_xk_y} is given by Eq. (5.53). Here, the *anti-symmetric* structure of $\sigma_{n/e}^{\mathrm{an}}$ is a direct consequence of $\Omega_{k_xk_y} = -\Omega_{k_yk_x}$. The conductivities $\sigma_{n/e}^{\mathrm{an}}$ are also called 'Hall conductivities', because they are responsible for the intrinsic contribution to the *anomalous Hall effect* [199, 306, 307]. Note that while this intrinsic contribution to the effect is based on the presence on Berry phases, it does not require a non-zero Chern number as in the case of the integer quantum Hall effect, see Sec. 3.4. Having said this, for $T = 0$ and μ lying in the band gap of an insulating material the expression for $\sigma_{n,xy}^{\mathrm{an}}$ above coincides with Eq.(3.52) and the IQHE is recovered. In general, the anomalous quantum Hall effect has three contributions: intrinsic, skew-scattering and side-jump [307]. The latter two also emerge from a full semiclassical Botzmann equation treatment of the problem, but only at third order in corrections to the collision integral [96, 307–310]. Within the here presented assumptions and approximations, we therefore restrict the discussion to the contribution from Berry phases only. The anomalous quantum Hall effect has been an intriguing effect in the field of condensed matter systems, and consequently there exists an exhaustive list of literature on this topic. For more details the reader is referred to, e.g., Refs. [96, 307] (and references therein).

In the following, we shall be solely interested in the macroscopic transport properties that are associated with the anomalous currents. To be specific, we focus on the anomalous particle current $\mathbf{j}_n^{\mathrm{an}}$ for now. By inspection of Eq. (7.40) one immediately realises that the Boltzmann formalism predicts transverse currents that couple to external, mechanical forces $\mathbf{F}$ only. Thermoelectric components as seen in Eq. (7.28) above are entirely absent, which predicts a vanishing of anomalous currents as soon as $\mathbf{F} = 0$. Within the presented formalism, this scenario is even expected to hold if there are non-zero *statistical forces*, i.e., gradients of thermodynamic quantities μ and T. This, however, contradicts results from standard transport theory [217, 305] where there exists a fixed relation between individual microscopic transport coefficients. In other words, Eq. (7.37) describing the diffusion constants would *not* be generally fulfilled.

To be precise, Eq. (7.40) would render an effect due to mechanical forces which is distinct from such imposed by a gradient of the chemical potential. This violates the *Einstein relation*, which states that both type of forces should be indistinguishable by the system and their macroscopic properties [217, 305]. Similarly, the *Mott relation* typically establishes a relation between particle (or electrical) and thermoelectric conductivities [217, 305, 311]. The latter relation argues that if one can expect an anomalous Hall effect,

then there should also emerge a similar effect in the presence of a temperature gradient, which is known as the *Nernst effect*. This is not expected from the present expression for $\mathbf{j}_n^{\mathrm{an}}$, see Eq. (7.40). Nevertheless, the effect of Berry phases in thermoelectric transport can be introduced such that Einstein and Mott relations continue to hold. To clarify this we mainly follow the corresponding argumentation by Xiao *et al.* [305]. Complimentary information can also be found in, e.g., Refs. [199, 312–314].

The reason why only anomalous velocities emerge from a semiclassical Boltzmann approach is because the mechanical force exists already on the microscopic level and, hence, is naturally encoded in the Hamiltonian. Statistical forces, on the other hand, only manifest themselves on the macroscopic level and enter the description with the introduction of statistical distributions of the particles [305]. So where do things go wrong then? It turns out that the Boltzmann picture is too naïve in the sense that it treats the quasiparticles as structureless objects. To solve this issue one needs to take into account the intrinsic magnetic moment as well as orbital magnetization. For an explicit calculation and a detailed discussion of these quantities we refer the reader to Refs. [199, 295, 305]. Eventually, one finds (to lowest order) an expression for the total *transport current* density which yields[5] [305]

$$\mathbf{j}_n^{\mathrm{tr}}(\mathbf{r},t) = \sum_\xi \int \frac{d\mathbf{k}}{(2\pi)^2} \, \Big[\boldsymbol{v}_{\mathbf{k},\xi} \, f_{\mathbf{k},\xi} + \nabla_{\mathbf{r}} \times \boldsymbol{\Omega}_\xi(\mathbf{k}) \, \ln\big[1 + e^{-\beta(\varepsilon_{\mathbf{k},\xi}-\mu)}\big] \Big] \,, \tag{7.42}$$

where we again introduced $\boldsymbol{\Omega}_\xi(\mathbf{k}) = \Omega_{\xi,k_xk_y}\hat{e}_z$ (cf. discussion below Eq. (7.12)). The first term of Eq. (7.42) is the total current that also appears in the Boltzmann formalism above. The second term is an additional Berry phase contribution which only contributes to the anomalous current. Thus, after using the chain rule of differentiation followed by a few steps of simplification the *anomalous transport current* takes the form

$$\begin{aligned} \mathbf{j}_n^{\mathrm{an,tr}}(\mathbf{r},t) = \sum_\xi \int \frac{d\mathbf{k}}{(2\pi)^2} \, \Big[& - (\mathbf{F} - \nabla_{\mathbf{r}}\mu) \times \boldsymbol{\Omega}_\xi(\mathbf{k}) \, f^0_{\mathbf{k},\xi} \\ & - \nabla_{\mathbf{r}} T \times \boldsymbol{\Omega}_\xi(\mathbf{k}) \Big(\ln\big[1 + e^{-\beta(\varepsilon_{\mathbf{k},\xi}-\mu)}\big] + \frac{\varepsilon_{\mathbf{k},\xi}-\mu}{T} \, f^0_{\mathbf{k},\xi} \Big) \Big] \,. \end{aligned} \tag{7.43}$$

After evaluating the cross product and introducing

$$\alpha_{n,xy} = -\sum_\xi \int \frac{d\mathbf{k}}{(2\pi)^2} \, \Big(\ln\big[1 + e^{-\beta(\varepsilon_{\mathbf{k},\xi}-\mu)}\big] + \frac{\varepsilon_{\mathbf{k},\xi}-\mu}{T} \, f^0_{\mathbf{k},\xi} \Big) \, \Omega_{\xi,k_xk_y} \,, \tag{7.44}$$

which is the 'xy'-components of the anomalous thermoelectric conductivity, Eq. (7.43) can be written in the simplified form

$$\mathbf{j}_n^{\mathrm{an,tr}}(\mathbf{r},t) = \begin{pmatrix} 0 & \sigma_{n,xy} \\ -\sigma_{n,xy} & 0 \end{pmatrix} (\mathbf{F} - \nabla_{\mathbf{r}}\mu) + \underbrace{\begin{pmatrix} 0 & \alpha_{n,xy} \\ -\alpha_{n,xy} & 0 \end{pmatrix}}_{\equiv \alpha_n^{\mathrm{an}}} (-\nabla_{\mathbf{r}} T) \,, \tag{7.45}$$

where $\sigma_{n,xy}^{\mathrm{an}}$ is given by Eq. (7.41) and we will abbreviate $\mathbf{j}_n^{\mathrm{an,tr}} \equiv \mathbf{j}_n^{\mathrm{an}}$ in the following. It is obvious that with this definition of the anomalous current Eq. (7.28) also holds for total currents, $\mathbf{j}_n = \mathbf{j}_n^0 + \mathbf{j}_n^{\mathrm{an}}$. Note that the discussion can be straightforwardly extended to anomalous energy currents [305]. Therefore, also the general validity of $\hat{\mathbf{D}}(\mathbf{n}) = \hat{\boldsymbol{\sigma}}(\mathbf{n})\hat{\boldsymbol{\chi}}^{-1}(\mathbf{n})$ is restored together with conventional Einstein and Mott relations.

[5] Eq. (7.42) is already adjusted to our present 2D Floquet system with $\hbar = k_B = -e = 1$, where e is the electric charge.

We want to conclude this section by remarking that the derived diffusion equations, see Eq. (7.38), are in fact not altered by this discussion on anomalous currents. Since the newly introduced term in Eq. (7.42) is proportional to a curl, possible contributions of the form $\nabla_{\mathbf{r}}\mathbf{j}_n^{\mathrm{an}}$ are nullified. So one can combine the results from the Boltzman equation with the additional Berry phase modifications to establish a formalism that meets all requirements for macroscopic transport - even in the presence of anomalous terms.

7.3. Numerical implementation of the diffusion equations

In the previous section 7.2 we have presented the analytical framework to analyse, e.g., the dynamics of particles in a Floquet realised Haldane model in the presence of a parabolic potential. The general strategy for practical purposes is therefore the following: first, we aim at solving the diffusion equations (7.38). Once particle and energy densities are known, we use $\mathbf{n}$ to calculate anomalous transport currents by means of Eq. (7.45) yielding the emergence of an anomalous Hall effect or anomalous Nernst effect, respectively.

However, as pointed out above, the diffusion equation is a highly non-linear differential equation which is generally impossible[6] to solve analytically beyond its representation in Eq. (7.38). So the diffusion equations need to be solved numerically. This section is devoted to technical details of finding numerical expressions for all conductivities which subsequently allows for solving the diffusion equations.

7.3.1. General procedure

Besides actually solving the diffusion equation (7.38), the majority of the practical afford needs to go into converting all objects, which can be easily initialized for some combination of μ and T, into functions of $\mathbf{n}$. The general procedure performed by us involves a certain number of steps which are summarized as follows:

1. At first, we calculate the scattering matrix M of the linearised Floquet-Boltzmann equation, see Eq. (7.26), for a fixed set of μ and T using the same technical procedure as described in Sec. 6.3.3. For more details see Sec. 7.3.2.

2. Next, inversion of the scattering matrix is performed to find $\widetilde{M}^{-1}$, see Eq. (7.33). Here, one needs to pay special attention to zero-modes corresponding to physical conservation laws of the system, as also discussed in Sec. 7.3.2. Subsequently, conventional conductivities, see Eqs. (7.29)-(7.32), are straightforwardly obtained.

3. Repeating steps (1) and (2) for a grid of both the chemical potential and the temperature then yields conductivities as a function of μ and T for a finite range. In addition, in the limits of $T\to\infty$ and $|\mu|\to\infty$ one can deduce values for $\hat{\boldsymbol{\sigma}}(\mu,T)$ from a semi-analytical treatment.

4. Anomalous conductivities are also determined from a finite $\mu-T$ grid in combination with their asymptotic behaviour. Since these conductivities are simply intrinsic properties of the homogeneous system, they can be easily computed, see Sec. 7.3.2.

5. At the same time, the local heating rates Γ are determined as a function of μ and T. This calculation is identical to the one used in the homogeneous system described in Sec. 6.3.

[6] In fact, analytical progress can be made in situations where one is specifically interested in a high temperature limit, see, e.g., Ref. [230].

6. Finally, one introduces particle $n(\mu, T)$ and energy densities $e(\mu, T)$. Susceptibilities (7.36) are then found by inverting these quantities, allowing for a conversion of all conductivities into functions of $\mathbf{n}$. Here, a $n-\frac{e}{n}$ representation is actually convenient to simplify the treatment of small densities. For details see Sec. 7.3.2.

7. Having completed all previous steps then allows for a straightforward calculation of all diffusion constants $\hat{\mathbf{D}}(\mathbf{n})$. These expressions combined with an explicit form of the external force $\mathbf{F}$ complete the diffusion equations (7.38). Note that we approximate the parabolic confining potential with a form that guarantees finite particle densities at all positions removing issues of divergence near the edge of the trap, see Sec. 7.3.3.

8. Due to the fact that all objects are smooth functions of space and time the diffusion equations can eventually be solved with relatively little numerical effort. We therefore solve these differential equations with built-in functions of the programme *Mathematica*. Lastly, found solutions then also allow to calculate anomalous currents indicating the presence of a Floquet-triggered macroscopic anomalous effect. Results for varying parameters are discussed in Secs. 7.4 and 7.5.

7.3.2. Numerical calculation of conductivities and heating rates

The calculation of conductivities in the present case splits into two tasks: first, one needs to calculate the conventional conductivities, σ_n, etc. These can also be viewed as *extrinsic*, since they depend on the particle-particle interactions of the system. Second, the *intrinsic* or anomalous contributions have to be calculated. Moreover, we have to determine the heating rate Γ, cf. Sec. 6.3.2, as a function of μ and T.

Conventional conductivities

As outlined above, the conventional conductivities require a calculation of the scattering matrix M, see Eq. (7.26). To this end, we apply the same discretization scheme for momentum and quasienergy space as presented in Sec. 6.3.3. Note that we slightly adjusted the discretisation by choosing a momentum grid of 16×16 and a fixed energy spacing of $\Delta\varepsilon = \Omega/15$. The protocol is identical to above except for the fact that now we are interested in energy conserving processes with $n = 0$. The latter aspect leads to a crucial consequence: since solely energy conserving processes are considered, the statistical factor $f^0 f^0 (1-f^0)(1-f^0)$ appearing in the expression for $\mathcal{P}$, see Eq. (7.24), is a sharply peaked function near the Fermi surface for $T/J \ll 1$. Consequently, the numerical procedure becomes much more sensitive to the discretisation of the Floquet and Brillouin zone, respectively. A relatively rough discretisation as presented above would in fact not be sufficient and special caution needs to be taken, if one was truly interested in investigating a $T \to 0$ limit. Nevertheless, we circumvent the problem by initializing the system at a temperature that is comparable to the hopping amplitude. We checked that for values of $T \sim J/2$ the Fermi distributions f^0 are smeared out sufficiently strongly in energy space such that remaining numerical errors are negligible. While for generic systems this approach might not be justified, we rely on the fact that ultracold atoms in optical lattices are in fact quite 'hot' with respect to the effective energy landscape, see discussion of Sec. 6.4.

Next, the matrix M needs to be inverted numerically, which is not straightforwardly achieved due to the presence of zero modes. One can technically solve this issue by projecting the problem onto a subspace that is orthogonal to the one spanned by these

modes[7]. We continue by rewriting the linearized Boltzmann equation, see Eqs. (7.21) and (7.25), as a true (discretised) matrix equation of the form

$$\mathbf{L}\,\mathbf{f}^0 = \mathbf{M}\,\boldsymbol{\phi}\,. \tag{7.46}$$

Here, $\boldsymbol{\phi}$ is a vector with entries $\phi_{\tilde{\xi}}$ where the index $\tilde{\xi} \in \{1,\ldots,N\}$ comprises (discretised) momentum, band index and spin, and $N \equiv \#\text{bands}\times\#\text{spins}\times\#\text{momentum-grid-points}$. While $\mathbf{f}^0 = (f_1^0, f_2^0, \ldots)^T$ also describes a vector, $\mathbf{L}$ and $\mathbf{M}$ denote corresponding matrices. One now introduces a set of vectors $\mathbf{c}_i$, each corresponding to a different conservation law of the system. For the present case where we have particle, quasienergy[8] and total spin conservation, we define

$$\mathbf{c}_1 = \big(1,1,\ldots,1\big)^T\,, \tag{7.47}$$

$$\mathbf{c}_2 = \big(\varepsilon_1,\varepsilon_2,\ldots,\varepsilon_N\big)^T\,, \tag{7.48}$$

$$\mathbf{c}_3 = \big(\underbrace{1,\ldots,1}_{\uparrow},\underbrace{-1,\ldots,-1}_{\downarrow}\big)^T\,, \tag{7.49}$$

with N being the length of each vector. It can be easily seen that each of these vectors $\mathbf{c}_i$ nullifies the left-hand side of Eq. (7.46), i.e., $\mathbf{c}_i\cdot(\mathbf{L}\mathbf{f}^0) = 0$, due to the argumentation of Eqs. (7.7) and (7.8).

We now define a projector onto the subspace of the zero-modes $\mathbf{c}_i$, which is given by

$$\mathbf{P} = \sum_i \mathbf{c}_i \otimes \mathbf{c}_i \qquad \text{and} \qquad \mathbf{Q} = \mathbb{1} - \mathbf{P} \tag{7.50}$$

being its complementary. The scattering matrix has the property $\mathbf{PM}=\mathbf{MP}=0$. Instead of determining $\boldsymbol{\phi}$ by the inversion of $\mathbf{M}$, one technically uses now the $\mathbf{Q}$-projected inversion matrix which is defined by [315]

$$\mathbf{M}_{\mathbf{Q}}^{-1} = \mathbf{Q}\,\mathbf{M}^{-1}\,\mathbf{Q} \equiv \mathbf{Q}\,\big(\mathbf{QMQ} + \mathbf{PaP}\big)^{-1}\,\mathbf{Q}\,, \tag{7.51}$$

with $\mathbf{a}$ being an arbitrary auxiliary matrix. The trick is that $\mathbf{M}_{\mathbf{Q}}^{-1}$ does in fact not depend on $\mathbf{a}$, since $\mathbf{P}$ and $\mathbf{Q}$ are projectors onto orthogonal subspaces. Thus, one can lift the zero eigenvalues of $\mathbf{M}$ 'by hand' using matrix $\mathbf{a}$ and subsequently invert the matrix $(\mathbf{QMQ}+\mathbf{PaP})$. The final projection onto $\mathbf{Q}$ ensures that results are indeed not affected by this procedure. The numerical solution to $\boldsymbol{\phi}$ is then given by

$$\boldsymbol{\phi} = \mathbf{M}_{\mathbf{Q}}^{-1}\,\mathbf{L}\,\mathbf{f}^0\,. \tag{7.52}$$

Once the vector $\boldsymbol{\phi}$ is determined, the conductivities can be straightforwardly found by virtue of Eqs. (7.29)-(7.33). The resulting expressions are 2×2 matrices according to the two-dimensional structure of the present Haldane system. Note that the conventional conductivities are in fact not necessarily diagonal. However, due to the symmetric structure of the matrices (see above) the contributions to the respective xy-component of σ_n, etc., are understood as 'sheer conductivities'. These can always be eliminated by an appropriate rotation[9] of the system [96]. In Fig. 7.1 we show numerical results for xx-components of

[7] The author is indebted to Zala Lenarčič for her assistance on this matter.

[8] As pointed out above, on the level of the linearized Boltzmann equation quasienergy is fully conserved. The full picture, of course, still supports energy violation due to Floquet heating.

[9] In fact, the origin for the emergence of sheer conductivities in the present case is that the edges of the Brillouin zone are rotated by $\pi/4$ with respect to its symmetry axes, see Fig. 6.2.

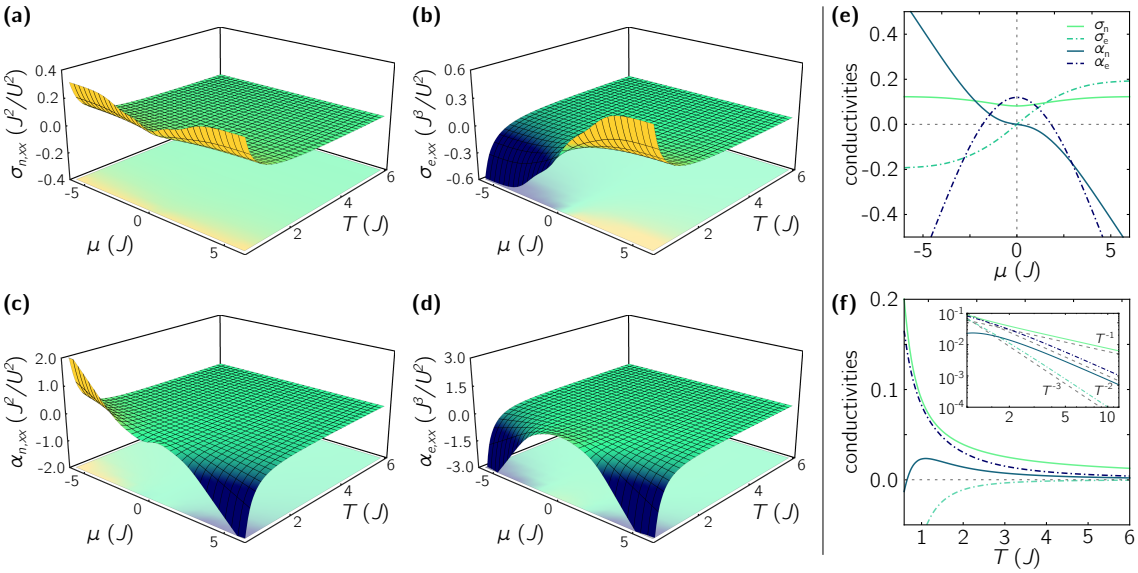

Figure 7.1.: (a)-(d) The xx-components of conventional conductivities $\hat{\boldsymbol{\sigma}}$ as functions of chemical potential μ and temperature T. Each individual conductivity is presented in dimensionless units (cf. Sec. 7.3.4). Joint representation of all four conductivities as a function (e) of μ for $T = J$ and (f) of T for $\mu = J$. The inset of (f) numerically confirms the analytical considerations of Eq. (7.54).

all four conductivities of $\hat{\boldsymbol{\sigma}}$ as functions of μ and T. One observes that all conductivities fall off rapidly as a function of temperature. The behaviour with respect to the chemical potential is different for σ_n, σ_e and α_n, α_e: while the former ones settle to a constant value as μ grows to large absolute values, the latter ones seem to depend linearly on μ in the same limit. Note that the yy-components of the conductivities are qualitatively identical, but are decreased by a factor of ~ 2.9. This discrepancy results from the fact that the system is not rotationally invariant, cf. Fig. 6.1.

The asymptotic behaviour of the conductivities can be easily understood from an analytical treatment of expressions (7.29)-(7.32). To this end, one considers the Fermi function in the respective limits, i.e.,

$$f^0_{\mathbf{k}} \overset{|\mu|\gg T}{\approx} \frac{1}{2} + s\left(\frac{1}{2} - e^{-\beta|\mu|}e^{s\beta\varepsilon_{\mathbf{k}}} + e^{-2\beta|\mu|}e^{2s\beta\varepsilon_{\mathbf{k}}}\right), \qquad f^0_{\mathbf{k}} \overset{T\gg|\varepsilon_{\mathbf{k}}-\mu|}{\approx} \frac{1}{2} - \frac{1}{4}\frac{\varepsilon_{\mathbf{k}}-\mu}{T}, \quad (7.53)$$

where $s = \mathrm{sgn}(\mu)$. For $T \to \infty$ one thus realises by considering Eqs. (7.20), (7.26) and (7.33) that to leading order $M \propto 1/T$, $\partial f^0/\partial\varepsilon \propto 1/T$ and therefore $\widetilde{M}^{-1} \propto 1/T$. One eventually obtains[10]

$$\sigma_n \overset{T\gg|\mu|}{\propto} \frac{1}{T}, \qquad \sigma_e \overset{T\gg|\mu|}{\propto} \frac{1}{T^3}, \qquad \alpha_n \overset{T\gg|\mu|}{\propto} \frac{1}{T^2}, \qquad \alpha_e \overset{T\gg|\mu|}{\propto} \frac{1}{T^2}. \quad (7.54)$$

When considering the large μ limit one finds that all factors $e^{-\beta|\mu|}$ appearing in the leading order correction to f^0, see Eq. (7.53), actually cancel in the expression for $\widetilde{M}^{-1}$. Hence, the conductivities σ_n and σ_e indeed approach a constant value, which we define as

$$\sigma_n^{\mathrm{asy}}(T) = \lim_{\mu\to-\infty}\sigma_n \qquad \text{and} \qquad \sigma_e^{\mathrm{asy}}(T) = \lim_{\mu\to-\infty}\sigma_e\,. \quad (7.55)$$

[10] The behaviour of all conductivities for $T \gg |\mu|$ can be explained by leading order considerations, except for σ_e. For the latter, the associated integral over $\varepsilon_{\mathbf{k},\xi}$, see Eq. 7.30, leads to a vanishing of leading order contributions. Next-leading-order contributions to the Fermi function f^0, an hence to σ_e, then only appear at T^{-3}.

The asymptotic behaviour is then found by taking the next-to-leading order term of $f^0_{\mathbf{k}}$ into account. One finally obtains

$$\sigma_n \overset{|\mu|\gg T}{\propto} \sigma_n^{\mathrm{asy}}(1-\zeta e^{-\beta|\mu|}) \qquad \text{and} \qquad \sigma_e \overset{|\mu|\gg T}{\propto} \mathrm{sgn}(\mu)\,\sigma_e^{\mathrm{asy}}(1-\zeta e^{-\beta|\mu|}) \tag{7.56}$$

where ζ is some *a priori* unknown constant. The asymptotic behaviour of α_n and α_e is dominated by their linear dependence on μ, cf. Eqs. (7.31) and (7.32). Leading order contributions yield

$$\alpha_n \overset{|\mu|\gg T}{\propto} -\mu\,\sigma_n^{\mathrm{asy}} \qquad \text{and} \qquad \alpha_e \overset{|\mu|\gg T}{\propto} -|\mu|\,\sigma_e^{\mathrm{asy}}\,. \tag{7.57}$$

The discussion of Eqs. (7.54)-(7.57) is fully supported by numerical findings, as can be seen from Fig. 7.1.

In practice, we combine numerical calculations of conductivities $\hat{\boldsymbol{\sigma}}$ for a finite range of $\mu \in [-12J, 12J]$ and $T \in [0.6J, 12J]$ with an 'analytic continuation' according to the limits above. This allows us to obtain $\hat{\boldsymbol{\sigma}}$ for arbitrarily large values of μ and T. Note that information about $T < 0.6J$ is not readily available due to reasons discussed above. Most importantly, having presented a way to obtain conductivities for large values of μ, we remark that results must actually be *false* by construction in this regime. The reason being that large values of μ correspond to very diluted densities ($\mu < 0$ for particles, $\mu > 0$ for holes). Here, the approach to accurately capture the physics by a linearised Boltzmann equation is *not* justified. As explained above, the Boltzmann equation can only be linearised in circumstances where it is dominated by scattering events on the right-hand side. This is clearly not the case for very small densities. Bearing this in mind, we will later ensure (see Secs. 7.4 and 7.5) that the results of our simulations are actually independent of the tails of the atomic cloud where $\mu \to -\infty$.

Anomalous conductivities

In the next step, we calculate the anomalous conductivities. For pedagogical reasons we restrict the discussion to $\sigma^{\mathrm{an}}_{n,xy}$ and $\alpha^{\mathrm{an}}_{n,xy}$, i.e., to the ones responsible for anomalous particle flow. Note again, since these quantities are connected to intrinsic properties of the system, they can be easily computed from a simple diagonalisation of the non-interacting homogeneous system.

First, one calculates the Berry curvatures Ω_{ξ,k_xk_y} following Eq. (6.29). The expressions for $\sigma^{\mathrm{an}}_{n,xy}$ and $\alpha^{\mathrm{an}}_{n,xy}$ are then obtained from Eqs. (7.41) and (7.44), respectively. The respective results for anomalous conductivities are depicted in Fig. 7.2(a) and 7.2(b) as functions of μ and T. One observes that for low temperatures the anomalous conductivities are largest, and spread out in μ quickly as T is increased. As described above, for $T=\mu=0$ one recovers the physics of the integer quantum Hall effect and therefore a finite $\sigma^{\mathrm{an}}_{n,xy}$. As done above, we only calculate the conductivities for a finite window in the μ–T parameter space and complement them with an analytical treatment for $|\mu| \to \infty$ and $T \to \infty$. Using the leading order terms of $f^0_{\mathbf{k}}$, see Eq. (7.53), one finds

$$\sigma^{\mathrm{an}}_{n,xy} \overset{T\gg|\mu|}{\propto} \frac{1}{T} \qquad \text{and} \qquad \alpha^{\mathrm{an}}_{n,xy} \overset{T\gg|\mu|}{\propto} \frac{1}{T^2} \tag{7.58}$$

as well as

$$\sigma^{\mathrm{an}}_{n,xy} \overset{|\mu|\gg T}{\propto} e^{-\beta|\mu|} \qquad \text{and} \qquad \alpha^{\mathrm{an}}_{n,xy} \overset{|\mu|\gg T}{\propto} \mathrm{sgn}(\mu)\,e^{-\beta|\mu|}\,. \tag{7.59}$$

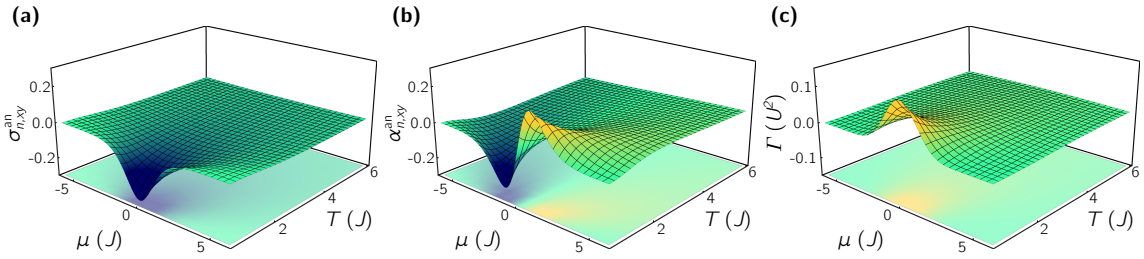

Figure 7.2.: Anomalous particle conductivities, (a) $\sigma^{\mathrm{an}}_{n,xy}$ and (b) $\alpha^{\mathrm{an}}_{n,xy}$, as functions of μ and T. Note that here physical units of $e = h = 1$ were chosen. (c) Dependence of heating rate Γ on chemical potential and temperature. Asymptotic behaviours for all quantities, see Eq. (7.58), (7.59) and (7.60), are numerically confirmed.

Here, we also used that $\ln[1+e^{-x}] \approx \ln[2] - x/2$ and that $\Omega_\xi = -\Omega_{-\xi}$ (where '$-\xi$' denotes the inversion of the band index). The latter property leads to a vanishing of constant contributions.

Note that while Ω_{ξ,k_xk_y} is independent of μ and T, it does depend on the discretization of the Brillouin zone. Since the Berry curvatures are confined only to small areas in $\mathbf{k}$ close to the gapped Dirac points, see Fig. 6.3, we numerically checked the dependence of anomalous conductivities on discretisation grid sizes as well as on temperatures. Here we find that at very low temperatures $T/J \ll 1$ (much lower than considered in the calculation of the conventional conductivities above) discretisation does play a role. However, for moderate temperatures, $T \sim J$, as used for starting values in the simulations below, discretisation effects are negligible.

Heating rate

The calculation of the heating rate Γ as a function of μ and T, see Fig. 7.2(c), is performed in the same way as described for the conductivities: exact numerical calculation is paired with a semi-analytical treatment. The protocol to calculate Γ follows precisely the one presented in Sec. 6.3.3. The behaviour of the heating rate as $|\mu|, T \to \infty$ can also be straightforwardly determined using again the approximate forms of $f^0_{\mathbf{k}}$ given in Eq. (7.53). One obtains

$$\Gamma \overset{|\mu|\gg T}{\propto} e^{-2|\mu|\beta} \qquad \text{and} \qquad \Gamma \overset{T\gg|\mu|}{\propto} \frac{1}{T}\,. \tag{7.60}$$

In addition, the heating rate is a function of the driving frequency, $\Gamma(\Omega)$. As shown in Sec. 6.3 (e.g., in Fig. 6.8), this dependence on Ω is quite strong and also changes its character due to phase-space restrictions on scattering processes. Note that, in the following, we restrain from a detailed discussion of the results regarding the dependence on Ω. Instead, we set the driving frequency to the experimentally relevant value of $\Omega_{\mathrm{exp}} = 6.3J = 2\pi \times 1080\mathrm{Hz}$ (cf. Ch. 6 and Ref. [23]). At the same time, we crucially understand that the effect of a possible variation of Ω on the heating rate can be absorbed into an effective rescaling of the interaction strength, $U \to U_\Omega$.

Lastly, we remark that $\Gamma \propto U^2$ while the conventional conductivities behave as $\sigma_n \propto 1/U^2$, etc. So while in each individual case the interaction strength can be reabsorbed into a redefinition of the time coordinate (cf. Ch. 6), this is not possible any more once diffusion and heating are present together. Thus, the role of Γ within the diffusion equations (7.38) is indeed determined by the combination of Ω and U. Nevertheless, we show below, see Sec. 7.3.4, that the diffusion equations can be effectively parametrised by a single

parameter only, therefore indeed allowing for a restricted discussion of the explicit role of the driving frequency Ω.

Changing variables and the n-e/n-grid

All objects discussed above need to be expressed as functions of densities $\mathbf{n}$ to be usable for the diffusion equation (7.38). To this end, we use the definitions of n and e, see Eqs. 7.6, with $f = f^0$ to obtain $n(\mu, T)$ and $e(\mu, T)$, respectively. In practice, we calculate the densities numerically for a broad parameter window (e.g., $\mu \in [-50J, 50J]$ and $T \in [J/20, 15J]$) and accompany this with an analytical treatment of the limits (as above). For example, one realises that

$$\begin{aligned} n(\mu,T) &\overset{\mu\to-\infty}{\approx} e^{\beta\mu} \sum_{\xi} \int \frac{d\mathbf{k}}{(2\pi)^2}\; e^{-\varepsilon_{\mathbf{k},\xi}\beta}\,, \\ e(\mu,T) &\overset{\mu\to-\infty}{\approx} e^{\beta\mu} \sum_{\xi} \int \frac{d\mathbf{k}}{(2\pi)^2}\; \varepsilon_{\mathbf{k},\xi}\, e^{-\varepsilon_{\mathbf{k},\xi}\beta}\,. \end{aligned} \tag{7.61}$$

By inverting the two functions n and e numerically one finally obtains expressions for $\mu(n, e)$ and $T(n, e)$. However, since this transformation is obviously non-linear, there exist certain peculiarities regarding the n-e-grid for which the functions μ and T are determined. Notice that the previously semi-infinite parameter space of μ and T is contracted to a finite region in the n-e-space. Here, the lines for $\mu \to \pm\infty$ are contracted to points at $(n, e) = (0, 0)$ and $(2, 0)$, respectively, in the n-e representation. This is, however, not beneficial for numerical purposes, since special care needs to be taken for $n \to 0$: as mentioned above, the correct physics in the low n limit is in fact not described by our method, which, however, is a natural limit for atomic clouds at the edges of the trap.

We, thus, make yet another variable transformation, and 'over-represent' the regime of low particle densities by instead expressing all quantities on an n-$\frac{e}{n}$-grid. Here, one can also easily verify using Eq. 7.61 that $\lim_{\mu\to-\infty} n/e = const.$ Eventually, knowing $\mu(n, \frac{e}{n})$ and $T(n, \frac{e}{n})$ readily allows for the determination of corresponding susceptibilities given by Eq. (7.36) as well as for a calculation of all conductivities on an evenly discretized n-$\frac{e}{n}$-grid. Using Eq. (7.37), associated diffusion constants are then straightforwardly computed.

7.3.3. Approximating the small density regime

Confining the atomic cloud by means of a harmonic potential, see Sec. 7.1, enforces arbitrarily small densities when moving away from the centre of the trap. Despite the fact that we introduced the n-$\frac{e}{n}$-grid to better deal with small particle densities numerically, arbitrarily small values of n still cause numerical challenges. The reason being that all diffusion constants diverge for $n \to 0$, see Fig. 7.3(a).

To circumvent this problem we introduce an approximation to the true parabolic potential of the form

$$V(\mathbf{r}) = c\,J\left(1 - \exp\Big[-\frac{\mathbf{r}^2}{l^2 c}\Big]\right) \overset{|\mathbf{r}|/l\sqrt{c}\ll 1}{\approx} V_0\,\mathbf{r}^2 + \mathcal{O}(\mathbf{r}^4)\,, \tag{7.62}$$

where $V_0 = J/l^2$, J is the characteristic hopping strength of the model and the regime $|\mathbf{r}|/l\sqrt{c} \ll 1$ corresponds to being close the centre of the trap. This construction of the potential in terms of the two parameters c and l is convenient in the following sense: the height of the potential far away from the centre of the trap is solely given by cJ. In other words, the parameter c represents some auxiliary dimensionless energy cut-off and

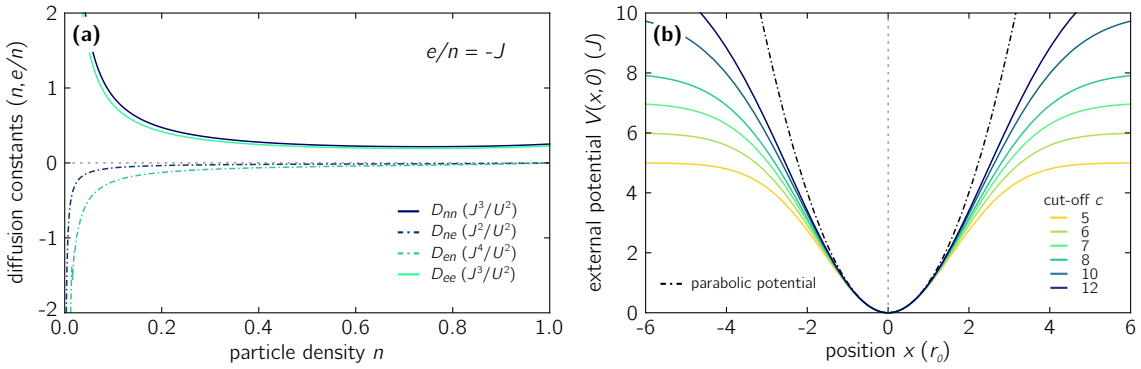

Figure 7.3.: (a) Diffusion constants $\hat{\mathbf{D}}(n, \frac{e}{n})$ as a function of particle density for fixed ratio of $e/n = -J$. All diffusion constants are given in their dimensionless form, cf. Eq. (7.65). All components of $\hat{\mathbf{D}}$ diverge in the small density limit, $n \to 0$, causing numerical issues in solving the diffusion equations. (b) Approximations to the true harmonic potential of form (7.62) to avoid the strongly diverging regime of (a). Potentials are shown for cut along x ($y = 0$). While the cut-off parameter c indeed determines the tails of the trap, the center of the potential, $|x| \lesssim r_0$, is unaffected.

therefore controls the regime of low particle densities. In fact, for $c \to \infty$ one recovers the original parabolic potential for arbitray $\mathbf{r}$, see Fig. 7.3(b). The chemical potential is approximately given as $\mu \approx -V$. The goal is therefore to choose c as small as possible in order to guarantee not too small densities at the edge of the trap for numerical convenience, but at the same time to ensure that c is large enough (densities small enough) to exclude an associated effect on the observed physics.

In contrast, the physics in the center of the trap is exclusively described by l. This parameter is physically relevant and determines the strength of the external force $\mathbf{F}_{\text{ext}} = -\nabla V$ by describing the shallowness of the trap. We further write

$$l = r_0 \, a_{\text{lat}} \,, \tag{7.63}$$

where $a_{\text{lat}} = 1$ as throughout this chapter and r_0 describes a characteristic dimensionless length scale of the potential (7.62) which determines the width of the atomic cloud (in the initial state). In combination with the initial temperature of the cloud, the characteristic length also defines the total particle number in the system. As described above, we initialize the cloud at a temperature of $T_{\text{ini}} = 1.5J$. We therefore introduce $r_{0,\text{exp}} \simeq 160$ as being the value that reproduces the experimental number of total atoms in the trap of $N_{\text{exp}} \simeq 2 \times 10^5$, see Ref. [23].

7.3.4. Dimensional analysis of the diffusion equations

Above we have discussed all necessary details to successfully implement the diffusion equations (7.38). It has become apparent that the solution of the equation depends on the choice of the interaction strength U, on the driving frequency Ω and on the potential shape represented by r_0. In order to allow for a systematic discussion of the system's dependence on the collection of all these parameters in the following, we aim at introducing a form of the diffusion equations that is described by dimensionless versions of conductivities, diffusion constants and heating rate.

To this end, we write conductivities (cf. Eq. (7.28)) as

$$\sigma_n = \frac{J^2}{U^2} \widetilde{\sigma}_n \,, \quad \sigma_e = \frac{J^3}{U^2} \widetilde{\sigma}_e \,. \tag{7.64}$$

The respective diffusion constants, see Eq. (7.37), are expressed as

$$D_{nn} = \frac{J^3}{U^2}\,\widetilde{D}_{nn}\,, \quad D_{ne} = \frac{J^2}{U^2}\,\widetilde{D}_{ne}\,, \quad D_{en} = \frac{J^4}{U^2}\,\widetilde{D}_{en}\,, \quad D_{ee} = \frac{J^3}{U^2}\,\widetilde{D}_{ee}\,. \tag{7.65}$$

At the same time we write

$$\mathbf{r} = r_0\,\widetilde{\mathbf{r}}\,, \quad \nabla_{\mathbf{r}} = \frac{1}{r_0}\,\widetilde{\nabla}_{\mathbf{r}}\,, \quad \mathbf{F} = \frac{J}{r_0}\,\widetilde{\mathbf{F}}\,, \quad \Gamma = U^2\,\widetilde{\Gamma}\,. \tag{7.66}$$

Importantly, the densities themselves are *not* rescaled, i.e., are still measured with respect to the volume given by a single lattice site ($a_{\rm lat} = 1$). The diffusion constants are understood in units of the same volume. In addition, one introduces time scales associated with diffusion and heating, respectively, which read as

$$t_d = \frac{U^2 r_0^2}{J^3} \qquad \text{and} \qquad t_h = \frac{J}{U^2} \tag{7.67}$$

with

$$\kappa = \frac{t_h}{t_d} = \frac{J^4}{U^4}\frac{1}{r_0^2} \tag{7.68}$$

being their ratio. Finally, with the aid of Eqs. (7.64)-(7.67) we reformulate the diffusion equations as

$$\frac{dn_\kappa}{d\widetilde{t}} = \kappa\left[-\widetilde{\nabla}_{\mathbf{r}}\left(\widetilde{\sigma}_n\,\widetilde{\mathbf{F}} - \widetilde{D}_{nn}\widetilde{\nabla}_{\mathbf{r}} n_\kappa - \widetilde{D}_{ne}\widetilde{\nabla}_{\mathbf{r}}\widetilde{e}_\kappa\right)\right], \tag{7.69}$$

$$\frac{d\widetilde{e}_\kappa}{d\widetilde{t}} = \kappa\left[-\widetilde{\nabla}_{\mathbf{r}}\left(\widetilde{\sigma}_e\,\widetilde{\mathbf{F}} - \widetilde{D}_{en}\widetilde{\nabla}_{\mathbf{r}} n_\kappa - \widetilde{D}_{ee}\widetilde{\nabla}_{\mathbf{r}}\widetilde{e}_\kappa\right) + \widetilde{\mathbf{F}}\,\widetilde{\mathbf{j}}^0_n\right] + \widetilde{\Gamma}\,. \tag{7.70}$$

Here, we have introduced the dimensionless energy densities $\widetilde{e} = e/J$ and the dimensionless time $\widetilde{t} = t/t_h$, which measures the time in units of the heating time scale[11]. We emphasise that all conductivities and diffusion constants are functions of n and $\widetilde{e}$, e.g., $\widetilde{D}_{nn} = \widetilde{D}_{nn}(n,\widetilde{e})$, etc. Furthermore, the dimensionless particle current is given by $\widetilde{\mathbf{j}}^0_{\kappa,n} \equiv \kappa\,\widetilde{\mathbf{j}}^0_n = \kappa(\widetilde{\sigma}_n\widetilde{\mathbf{F}} - \widetilde{D}_{nn}\widetilde{\nabla}_{\mathbf{r}} n_\kappa - \widetilde{D}_{ne}\widetilde{\nabla}_{\mathbf{r}}\widetilde{e}_\kappa)$, with a similar expression being found for $\widetilde{\mathbf{j}}^0_{\kappa,e}$. Note that the dimensionless currents are connected to the physical ones (in units of $a_{\rm lat}$) via

$$\mathbf{j}^0_n(\mathbf{r},t) = r_0\,t_h^{-1}\,\widetilde{\mathbf{j}}^0_{\kappa,n}(\mathbf{r}/r_0, t/t_h) = J\,\kappa^{1/2}\,\widetilde{\mathbf{j}}^0_n(\mathbf{r}/r_0, t/t_h)\,, \tag{7.71}$$

$$\mathbf{j}^0_e(\mathbf{r},t) = J\,r_0\,t_h^{-1}\,\widetilde{\mathbf{j}}^0_{\kappa,e}(\mathbf{r}/r_0, t/t_h) = J^2\,\kappa^{1/2}\,\widetilde{\mathbf{j}}^0_e(\mathbf{r}/r_0, t/t_h)\,, \tag{7.72}$$

showing that the (longitudinal) currents are also determined by κ only.

So, indeed, the diffusion equations can be written as a pair of coupled equations that effectively depend on a *single* parameter κ only[12]. This parameter determines the relative strength of the diffusion term compared to the heating rate $\widetilde{\Gamma}$. Hence, every effect caused by changing one of the parameters (U, r_0) can be compensated by a corresponding adjustment of the other one. Likewise, varying the driving frequency Ω can be simply captured by $t_h \to$

[11] Alternatively, one could measure the time in units of t_d. However, considering experimental values (see below) suggests that the system is dominated by the limit where local heating rates exceed diffusion strengths.

[12] Crucially, this description neglects corrections originating from a Hartree energy renormalisation, see Sec. 7.1. When these corrections are included, the external force $\mathbf{F}$ obtains an additional contribution linear in U that cannot be absorbed into κ in the spirit above. However, below we mainly consider parameter regimes for which Hartree effects can be ignored to good approximation, $U < J$.

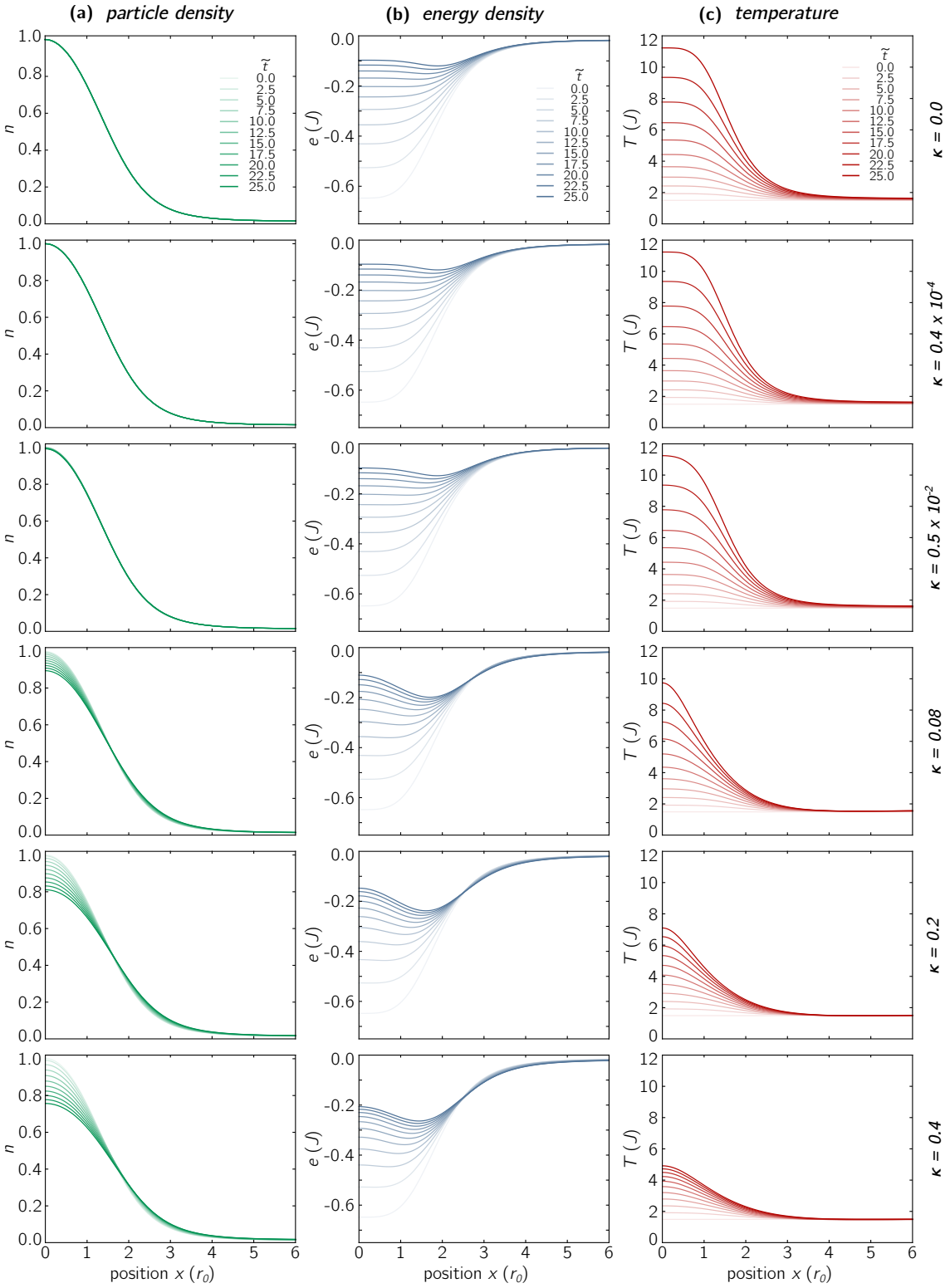

Figure 7.4.: (a) Particle densities n, (b) energy densities e and (c) temperatures T as a function of the position x at different times t and for different relative diffusion strengths κ. Results are shown for a cut along the x-axis, where $y = 0$ and $n(x, 0, t)$, etc., and an initial temperature of $T_{\text{ini}} = 1.5J$. Same quantities are arranged vertically and different rows represent different values of κ. The potential cut-off parameter, see Eq. (7.62), is $c = 8$.

$t_{h,\Omega}$ and $\kappa \to \kappa_\Omega$, yielding the same set of diffusion equations as above. In the following, we will therefore base our analysis of the diffusion equations on a systematic study of the parameter κ only. Nevertheless, in a potential experimental realisation the parameters are typically not freely selectable, but rather bound by experimental capabilities, such as the total particle number, etc. Moreover, one needs to ensure that κ does not correspond to a parameter set that contradicts the approximations made in developing the theory (i.e., LDA, assuming weak interactions, etc.).

7.4. Diffusion from inhomogeneous Floquet heating

In this section, we finally present a quantitative analysis of the solutions to the diffusion equations (7.38). As mentioned above, we will investigate the behaviour of the particle and energy densities as a function of the dimensionless parameter κ, see Eq. (7.67). Here, we test the results for a range of parameters and cut-off values. Our findings show how particle densities, energy densities and temperatures vary over times as a direct consequence of Floquet heating in the system. In the next section, see Sec. 7.5, we will present how anomalous effects arise due to this behaviour.

7.4.1. Time evolution of densities and temperatures

At first, we investigate particle densities n, energy densities e and the corresponding system's temperatures T as a function of relative diffusion strength κ and dimensionless time $\widetilde{t}$. The results obtained from solving the diffusion equations by means of built-in functions of the programme *Mathematica* are shown in Fig. 7.4. Data is given for a cut along the x-axis. We vary κ over a broad range of $\sim [0.4 \times 10^{-4}, 0.4]$. Assuming that the driving frequency and the characteristic length are fixed to experimental values of $\Omega_{\mathrm{exp}}/2\pi = 1080\mathrm{Hz}$ and $r_{0,\mathrm{exp}} = 160$, this range corresponds to a variation of the interaction strength from $U = J$ to $U = 0.1J$. In addition, we investigate the case of $\kappa = 0$, i.e. where diffusion is completely switched off, for benchmark reasons. We further set the cut-off value of the auxiliary potential, see Eq. (7.62), to $c = 8$ guaranteeing particle densities as low as $n \sim 0.015$ far away from the center of the trap, see Fig. 7.4(a). Moreover, for practical purposes we restrict the solutions to a spatial range of $x/r_0, y/r_0 \in [-w, w]$, with $w = 8.5$. At the same time, we impose periodic boundary conditions on the solutions at the edges of this slab, e.g., $n(w, y, t) = n(-w, y, t)$.

As shown by the first two rows of Fig. 7.4, for small diffusion strengths, $\kappa \ll 1$, hardly any particle diffusion is visible within the investigated duration of time of $t = 25t_h$. Instead, the system is heated locally by interactions, and energy densities as well as local temperatures freely rise. Since the heating is also strongly dependent on the particle densities, the temperature at the center of the trap increases rapidly while it is barely affected in the tails of the atomic cloud. Note that this property will cause significant temperature gradients. For increasing values of κ, diffusion of the atoms is enhanced resulting in a significant change of the spatial particle density profile, as can be seen from Fig. 7.4(a). At the same time, by driving the particles against the potential, i.e., further away from the center of the trap, diffusion allows particles to convert the provided energy into potential energy instead of heating. Consequently, one finds that the energy densities e and, more prominantly, the temperatures T increase much slower as a function of the dimensionless time $\widetilde{t}$, see 7.4(b) and (c), respectively. So systems with $\kappa \sim 1$ are characterised by stronger particle currents but also by weaker temperature gradients.

In order to investigate the behaviour of the system's temperature in more detail we

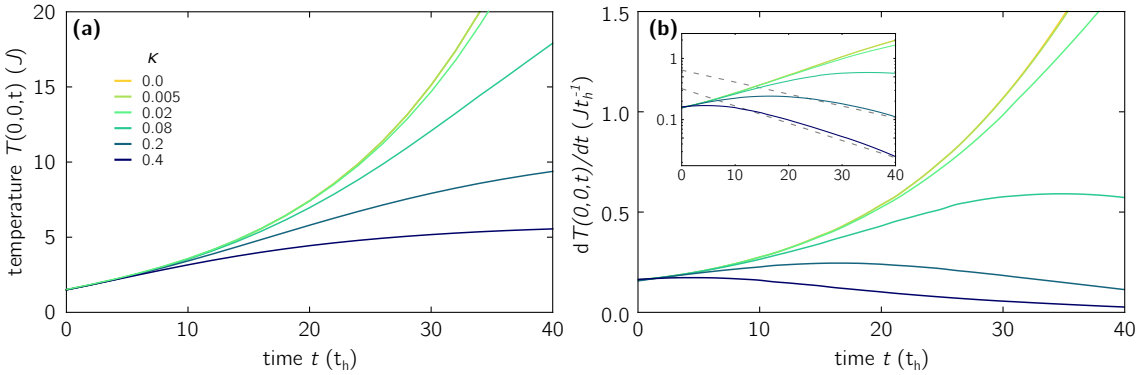

Figure 7.5.: Temporal temperature evolution at the center of the trap, $T(0,0,t)$. (a) Expected temperatures as a function of time for different diffusion strengths κ and an initial temperature of T_{ini}. (b) Corresponding derivatives, $dT(t)/dt$, indicating a strong qualitative change of the heating behaviour of the different systems. The inset shows a logarithmic plot. Gray dashed lines represent exponential functions which are understood to be guide to the eyes indicating exponential decay. Note that results for $\kappa = 0$ and $\kappa = 0.005$ are indistinguishable in (a) and (b).

consider the temporal development of T at the center of the trap, see Fig. 7.5. Importantly, the growth of the temperature does not only change quantitatively as κ is varied, but also qualitatively. This is particularly revealed by Fig. (7.5)(b), which shows dT/dt versus time. For $\kappa \ll 1$, the temperature is growing fast according to $dT(t)/dt \propto T(t)$. Hence, for values as small as $\kappa \simeq 0.01$ the system shows the same *exponential* heating characteristics as seen in Sec. 6.3.4, and the temperature can be written as

$$T(\mathbf{r},t) \overset{\kappa\to 0}{=} T_{\mathrm{ini}} + c_1(\mathbf{r})\, e^{c_2(\mathbf{r})t} \overset{c_2 t\gg 1}{\approx} c_1(\mathbf{r})\, e^{c_2(\mathbf{r})t}\,, \tag{7.73}$$

where $c_1(\mathbf{r}), c_2(\mathbf{r})$ are variables that depend on space but not on time. For this regime, it is therefore expected that the physics is entirely dominated by the local Floquet heating mechanism. The diffusion equations, Eqs. (7.69)-(7.70), can be approximated in this limit by the simple set of equations

$$\frac{dn}{d\widetilde{t}} \overset{\kappa\to 0}{\approx} 0 \qquad \text{and} \qquad \frac{d\widetilde{e}}{d\widetilde{t}} \overset{\kappa\to 0}{\approx} \widetilde{\Gamma}\,. \tag{7.74}$$

On the contrary, strengthening diffusion to $\kappa \sim 1$ not only causes a slower increase of the temperature but rather changes the heating characteristics fundamentally: as shown by Fig. (7.5)(b), the temperature gain starts to *decrease* as a function of time. The respective figure inset even conjectures that the temperature growth decays exponentially. Later, the (anomalous) current characteristics will depend strongly on this behaviour of the system's temperature.

We close this section be remarking a few technical aspects. As mentioned above, due to the lack of rotational symmetry the conductivities, and therefore the diffusion constants, yield different values for x- and y-directions. However, we checked, see Fig. 7.6(a)-(b), that for diffusion strengths of up to $\kappa \sim 0.4$ the results along both directions only show marginal differences. Finally, we have to check whether the results are indeed stable against the choice of unphysical cut-off values modelling the trapping potential, as discussed in Sec. 7.3.3. Here, the diffusion constants diverge for $n \to 0$, see Fig. 7.3(a), which could lead to an undesired and uncontrolled behaviour of the numerics. In Fig. 7.6(c)-(d) we show resulting particle and energy densities for different values of the potential cut-off parameter c. We show initial and time-evolved densities at $t = 25t_h$ for a moderately

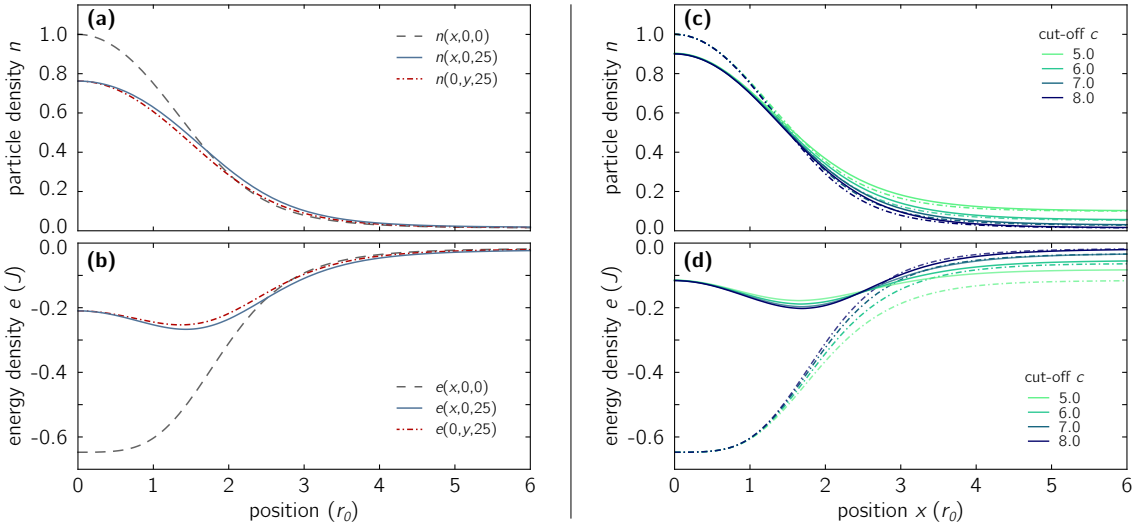

Figure 7.6.: (a)-(b) calculated densities along the x and y-direction, respectively. Initially, a symmetric cloud is prepared (gray dashed line), i.e., $n(x,0,0) = n(0,y,0)$, etc. The diffusion strength is set to $\kappa = 0.4$. (c)-(d) behaviour of the respective density as a function of the potential cut-off parameter c, see Eq.(7.62). Dashed lines correspond to initial configurations at $t = 0$ and solid lines represent time-evolved densities at $\widetilde{t} = 25$. Here, we chose $\kappa = 0.08$.

diffusing system of $\kappa = 0.08$. While c does mainly have a quantitative impact if chosen too small, results indeed converge for $c \sim 10$. For reasons of numerical performance we choose to set $c = 8$.

7.4.2. The role of heating

In the previous section it was discussed how densities and temperatures develop as a function of time. Again, the only mechanism that is available to bring the system out of equilibrium, and thereby trigger diffusion, is Floquet heating. In this section, we aim at quantifying the effect of heating relatively to other energy currents in the system.

To this end, we introduce the fraction $\dot{e}/\Gamma$ which measures the heating rate's local share of the change of the energy density. Using obtained results for particle and energy densities in combination with the expression of the longitudinal currents, see Eqs. (7.71) and (7.72), allows for a straightforward determination of $\dot{e}/\Gamma$. In Fig. 7.7, we show results of this ratio as a function of space and time for different values of κ. Of course, the net effect is already captured by κ: the smaller this parameter is, the more is diffusion suppressed, and $\dot{e}/\Gamma \sim 1$ for $\kappa \ll 1$. For $\kappa \to 0$ the behaviour is indeed described according to Eq. (7.74). Nonetheless, one can make further observations regarding the local property of heating. Generally, the relative role of heating gets more pronounced when moving away from the trapping center. Note, however, that numerical results given in Fig. 7.7(a)-(b) become unreliable when considering ratios deep in the tails of the cloud, since energy densities as well as heating rates become both small valued in this regime (see above). Moreover, one importantly finds that the local relevance of heating decreases as time evolves. Another interesting aspect is the fact that even for small values of $\kappa \simeq 0.05$ a relatively strong decrease of the local heating rate is to be expected, i.e., $\dot{e}/\Gamma(x = 2r_0, t = 20t_h) \sim 50\%$.

To give yet more insight into the system's heating behaviour, we also calculate the total amount of (kinetic) energy in a circular region of radius r_0 centred around the bottom of

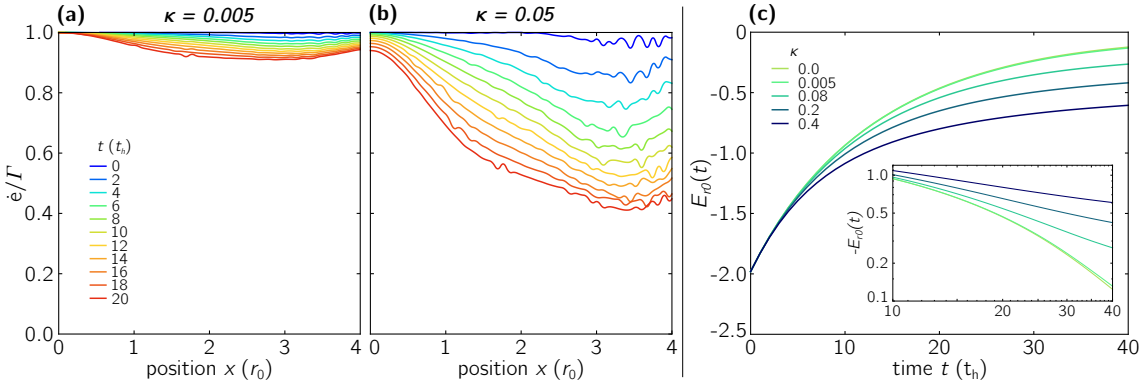

Figure 7.7.: (a)-(b) Relative contribution of the heating rate to the local temporal change of energy densities for $\kappa = 0.005$ and $\kappa = 0.05$, respectively. We used $T_{\text{ini}} = 1.5J$ and $c = 6$, respectively. For very small values of κ, changes in the energy are solely determined from Γ, see Eq. (7.74). For an increasing diffusion strength the relative strength of Γ is not only globally decreased but also shows an additional dependence on the position of the trap. Emerging wiggles for large x are numerical artefacts. (c) Total energy E_{r_0} of area with radius r_0, see Eq. (7.75), as a function of time. Inset shows a double logarithmic plot conjecturing an algebraic growth of energies in strongly diffusive cases ($\kappa \sim 1$).

the trap. We define

$$E_{r_0}(t) = \int_{A_{r_0}} d\mathbf{r}\; e(\mathbf{r}, t)\,, \tag{7.75}$$

with $A_{r_0} = \pi r_0^2$ describing the area of interest. We plot the temporal evolution of this quantity in Fig. 7.7(c). In the diffusionless case, $\kappa = 0$, the total energy grows quickly and approaches the limiting value[13] of $E_{r_0}(t \to \infty) = 0$ in an exponential fashion. However, when diffusion is present, the total energy growth in the center of the trap experiences an 'algebraic slow-down' and the limiting value is approached in terms of a power law $E_{r_0}(t) \propto -t^{-c(\kappa)}$, as suggested by the inset of Fig. 7.7(c). Here, $c(\kappa)$ is some κ-dependent exponent that needs to be determined from numerics. This behaviour can be linked to the characteristics of local energy densities, as presented in Fig. 7.4(b).

7.5. Verification of the anomalous Floquet-Nernst effect

After having studied conventional diffusion of the atomic cloud as a consequence of intrinsic Floquet heating in the previous section, we will now present results on signatures of associated anomalous transport properties. As shown in Sec. 7.2.4, Einstein relations are guaranteed to hold even in situations with non-trivial contributions to intrinsic conductivities if Berry phase corrections are respected carefully. The general validity of $\hat{\mathbf{D}}(\mathbf{n}) = \hat{\boldsymbol{\sigma}}(\mathbf{n})\hat{\boldsymbol{\chi}}^{-1}(\mathbf{n})$ then allows for a calculation of the anomalous (transport) currents according to

$$\begin{aligned}\mathbf{j}_n^{\text{an}}(\mathbf{r}, t) &= \sigma_n^{\text{an}}\mathbf{F} - D_{nn}^{\text{an}}\nabla_{\mathbf{r}} n - D_{ne}^{\text{an}}\nabla_{\mathbf{r}} e \\ &= \frac{J}{r_0}\left(\sigma_n^{\text{an}}\,\widetilde{\mathbf{F}} - \frac{1}{J}D_{nn}^{\text{an}}\widetilde{\nabla}_{\mathbf{r}} n_\kappa - D_{ne}^{\text{an}}\widetilde{\nabla}_{\mathbf{r}}\widetilde{e}_\kappa\right) \equiv \frac{J}{r_0}\,\widetilde{\mathbf{j}}_n^{\text{an}}(\mathbf{r}, t)\,,\end{aligned} \tag{7.76}$$

where in the second line we introduced the dimensionless form of $\mathbf{F}$ and $\nabla_{\mathbf{r}}$, see Eq. (7.66), and we explicitly indicated that the densities are determined from the dimensionless dif-

[13] Note that this limit is a consequence of the particle-hole symmetric underlying model. Here, the energybands are symmetric with respect to $\varepsilon = 0$, and therefore in the limit of $T \to \infty$, i.e., the limit where all energyeigenstates are populated identically, the total energy must be zero.

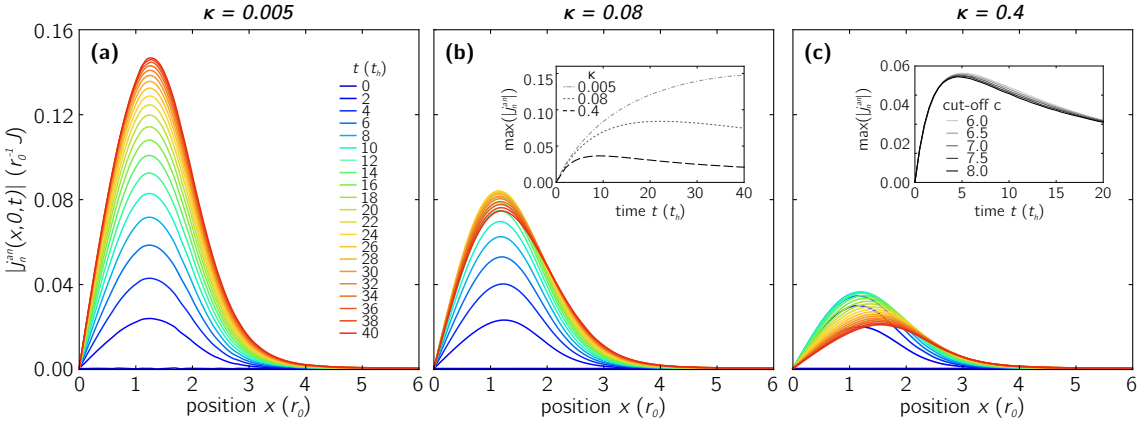

Figure 7.8.: The Floquet-Nernst effect emerging from local Floquet heating mechanisms. Anomalous particle current densities are shown as functions of space and time for diffusion strengths of (a) $\kappa = 0.005$, (b) $\kappa = 0.08$ and (c) $\kappa = 0.4$. Currents decrease in size when the role of diffusion is enhanced. Inset of (b) shows peak value of $|\mathbf{j}_n^{\mathrm{an}}(x,0)|$ as a function of time. The same quantity is also shown in the inset of (c) for $\kappa = 0.4$ only and different cut-off parameters c. Effects due to edges indeed appear to be negligible, cf. Fig. 7.9(c).

fusion equations, see Eqs. (7.69) and (7.70), for a specific choice of the parameter κ. Note, however, that we refrain from expressing, e.g., the anomalous conductivities in a similar form as used in Eqs. (7.64). The reason being that these contributions are intrinsic to the system and therefore already independent of the interaction strength U, as discussed above. Hence, while the longitudinal currents, see Eqs. (7.71) and (7.72), are solely determined by κ, the transversal currents are characterized by r_0. Having said this, the density gradients producing the anomalous currents are obtained from solutions that inherently are characterized by the parameter κ.

In Fig. 7.8, we show results for transversal currents as the system heats up as a function of time. Numerical results are evaluated for a range of diffusion strengths κ and times t. Note that we set $r_0 = 160$. We observe that anomalous currents indeed emerge as a consequence of inhomogeneous heating in the trap, yielding an anomalous *Floquet-Nernst effect*. For short times (in respective units of t_h) the spatial heating of the system is alike for investigated values of κ, see Fig. 7.4. Hence, also initially developing transversal particle currents are independent of κ. However, as time evolves the behaviour changes quantitatively as well as qualitatively for different diffusion strengths. It appears that anomalous currents are strongest when the system is dominated by local heating. This is due to the fact that ultimately temperature gradients are the driving force of this phenomenon. As seen above, less diffusion corresponds to a stronger growth of the temperature at the center of the trap, see Fig. 7.4(c) and 7.5, leading to larger temperature gradients in those cases. However, maximally attainable currents are fundamentally constrained by the absence of diffusion: switching back to a (μ, T)-description of the problem, the anomalous current can be approximated by $\mathbf{j}_{\mathbf{n}}^{\mathrm{an}}(\mathbf{r},\mathbf{t}) \approx -\alpha_n^{\mathrm{an}} \nabla_{\mathbf{r}} T$ for $\kappa \to 0$, see Eq. (7.45). At the same time, the temperature grows exponentially in this limit as discussed above. Using the explicit expression for the temperature of Eq. (7.73) as well as the associated behaviour[14] of α_n^{an},

[14] Note that particle number conservation requires a simultaneous adjustment of the chemical potential when taking $T \to \infty$. Thus, α_n^{an} needs to be evaluated in the limit $T \to \infty$ with $T/\mu = const.$, which is given by $\alpha_n^{\mathrm{an}} \propto -\frac{1}{T}$ (instead of $\propto 1/T^2$ as for fixed μ, see Eq. (7.58)).

the anomalous current is found to read as

$$\begin{aligned}\mathbf{j}_n^{\mathrm{an}}(\mathbf{r},t) &\overset{\kappa\to 0}{\approx} -\alpha_n^{\mathrm{an}}\nabla_{\mathbf{r}}T \overset{(7.73)}{=} -\alpha_n^{\mathrm{an}}\left(\nabla_{\mathbf{r}}c_1 + c_1\nabla_{\mathbf{r}}c_2\right)e^{c_2 t} \\ &\approx -\alpha_n^{\mathrm{an}}\left(\frac{1}{c_1}\nabla_{\mathbf{r}}c_1 + \nabla_{\mathbf{r}}c_2\right)T(t) \overset{\alpha_n^{\mathrm{an}}\propto -T^{-1}}{=} \mathbf{K}(\mathbf{r})\,,\end{aligned} \tag{7.77}$$

with $\mathbf{K}(\mathbf{r})$ being time-independent and solely depending on the initial properties of the atomic cloud, i.e., $(\mu_{\mathrm{ini}}, T_{\mathrm{ini}})$. In fact, $|\mathbf{K}|$ is the limiting value for the local anomalous current for $c_2 t \gg 1$, and therefore $|\mathbf{j}_n^{\mathrm{an}}(\mathbf{r},t)|$ approaches a given spatial profile as a function of time, as seen in Fig. 7.8(a).

Nevertheless, if arbitrary values of κ are considered and T does not simply grow exponentially, cf. Fig. 7.5, the estimate of Eq. (7.77) loses its validity. As discussed above, diffusion has a strong qualitative impact on the temperature of the system. We observe that attainable anomalous current densities drop in size as κ is increased, see Figs. 7.8(a)-(c). Moreover, increasing κ also has a qualitative impact on the obtained anomalous currents. As can be particularly seen from Fig. 7.8(c), particle diffusion eventually causes the Floquet-Nernst effect to decay. In order to quantify this effect we introduced the integrated anomalous current along the transversal direction

$$\mathrm{J}_{n,x}^{\mathrm{an}}(t) = \int_0^\infty dx\ \hat{\mathbf{y}}\cdot\mathbf{j}_n^{\mathrm{an}}(\mathbf{r},t) = J\int_0^\infty d\widetilde{x}\ \hat{\mathbf{y}}\cdot\widetilde{\mathbf{j}}_n^{\mathrm{an}}(\mathbf{r},t)\,, \tag{7.78}$$

measuring the amount of particle current flowing through a cut of the trap along the x-axis. Furthermore, Eq. (7.78) indeed reveals the intrinsic nature of the total anomalous current: the final form of $\mathrm{J}_{n,x}^{\mathrm{an}}$ does *not* depend on parameters (r_0, U, Ω) but solely on intrinsic ones. Thus, the total anomalous current is expected to be fundamentally bound by the Berry curvature of the non-interacting system in the sense that an external linear force causes a total current of $\int d\mathbf{r}\,\sigma_{n,xy}(\mathbf{r})F = -\int d\mu\,\sigma_{n,xy}(\mu)|_T$. This integral of the xy-component of σ^{an} gives $\approx 0.4J$ in the present case, cf. Fig. 7.2. In other words, the net anomalous current is expected to be comparable to the effect caused by an edge mode of a conventional quantum Hall setting with slab geometry [197, 316].

In Fig. 7.9 we show various aspects of the integrated anomalous current (7.78). The curve of $\mathrm{J}_{n,x}^{\mathrm{an}}(t)$ as a function of time confirms the impression of Fig. 7.8 and can generally be divided into three different regimes with the following limiting behaviour:

$$\mathrm{J}_{n,x}^{\mathrm{an}}(t) \propto \begin{cases} t & \text{for} \quad t/t_h \lesssim 1 \\ e^{-d\sqrt{\kappa}t/t_h} & \text{for} \quad \sqrt{\kappa}\,t/t_h \gg 1/d \end{cases}, \tag{7.79}$$

with d being a constant that is independent of κ. So initially, $t/t_h \lesssim 1$, the total anomalous current (7.78) grows linearly as a function of time, $\mathrm{J}_n^{\mathrm{an}}(t) \propto t$, see Fig. 7.9(a), seemingly independent of κ, see Fig. 7.9(b). This is due to the fact that for arbitrarily small times the system solely depends on the initial configuration of the cloud and begins to heat up locally independent of κ (cf. also Fig 7.5). Subsequently, the system enters an intermediate regime, where the quantitative behaviour strongly depends on κ. The inset of Fig. 7.9(a) suggests that this intermediate regime approximately marks the range of $1 \lesssim \sqrt{\kappa}\,t/t_h \lesssim 10$. Within this regime, the total transversal current peaks before starting to decay at large times. This decay is conjectured by numerics to be of exponential type following $\mathrm{J}_{n,x}^{\mathrm{an}}(t) \propto e^{-d\sqrt{\kappa}t/t_h}$, see inset of Fig. 7.9(a). Here, d describes a universal decay behaviour when systems are measured in time units of the geometric mean of t_h and t_d, i.e., $t_h/\sqrt{\kappa} = (t_h t_d)^{-1}$. Since diffusion becomes more prominent over the course of time, see Sec. 7.4.2, every system (except for $\kappa = 0$) will eventually enter this decay regime. Nevertheless,

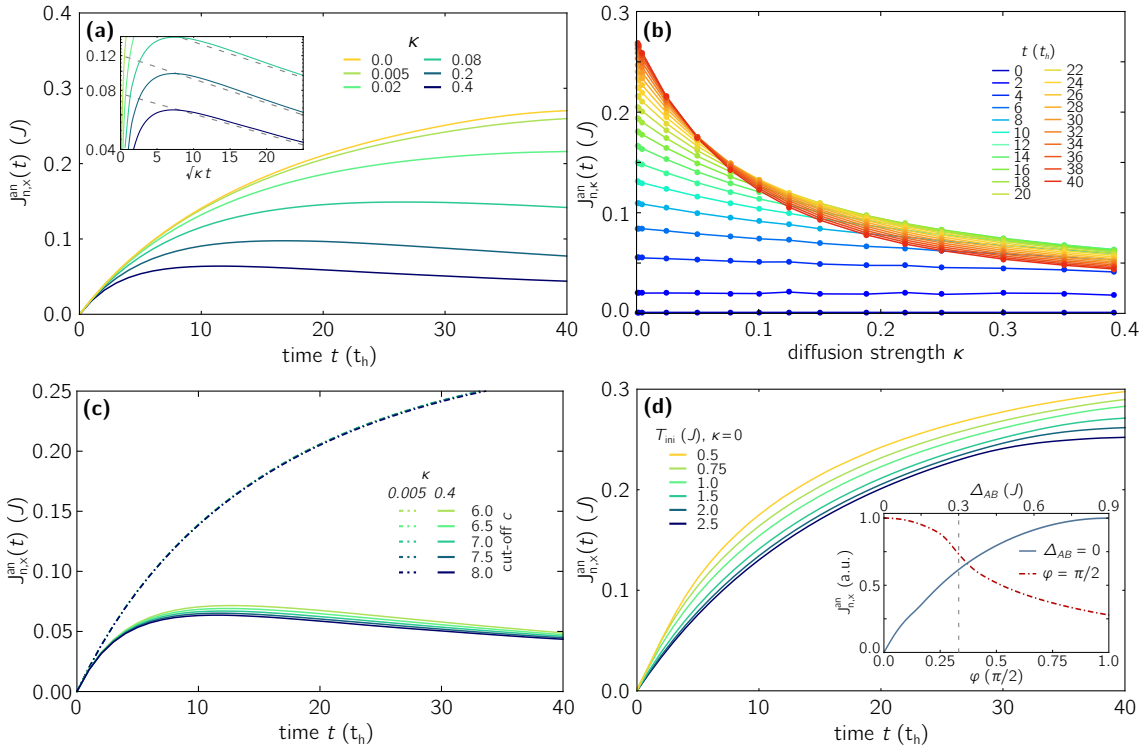

Figure 7.9.: (a) Integrated anomalous current $J^{an}_{n,x}$ as a function of time for various diffusion strengths κ. Curves show different regimes according to Eq. (7.79). The inset shows a log-plot indicating exponential decay of the anomalous currents. (b) Anomalous currents for different times as function of κ. Dots represent actual numerical data. Initial currents are independent of κ. Maximal anomalous currents decay with increasing diffusion strengths. (c) $J^{an}_{n,x}$ plotted for different trapping potential cut-off values c, see Eq. (7.62), for $\kappa = 0.4$ and $\kappa = 0.005$, respectively. Even in the strong diffusive case of $\kappa = 0.4$, results converge for the investigated parameter range. (d) Anomalous currents $J^{an}_{n,x}$ for $\kappa = 0$ and various initial temperatures T_{ini}. Lower initial temperatures support larger temperature gradients leading to larger attainable anomalous currents. The inset shows the effect of tuning φ and $\Delta_{\mathcal{AB}}$ on the anomalous current. Vertical dashed line marks topological phase transition point for varying $\Delta_{\mathcal{AB}}$.

note that it is not guaranteed that this exponential decay is the true $t \to \infty$ limit. Here, numerical limitations prohibited an investigation of much larger times than presented in Fig. 7.9. Moreover, when transversal currents decay due to diffusion, the relevance of low density regimes at the tails of the cloud is inevitably enhanced. We once more ensured, see Fig. 7.9(c), that the system's behaviour is not changed qualitatively by the chosen cut-off c.

While above we focused on the role of the 'extrinsic' parameter κ, we shall now also investigate the impact of intrinsic quantities. In Fig. 7.9(d) we show how $J^{an}_{n,x}$ depends on the initial (homogeneous) temperature of the system, T_{ini}. Results are given for the limit $\kappa \to 0$. Here, lowering the initial temperature produces larger anomalous currents. This can be explained by the fact that decreasing the initial temperature simulateously lowers the heating rate for areas of $|\mu|/J \gg 1$. Consequently, the tails of the cloud are expected to heat up slower, which leads to larger temperature gradients.

Importantly, we also consider the current depending on the Berry curvature. So far, we chose $\varphi = \pi/2$ and $\Delta_{\mathcal{AB}} = 0$ as parameters of the simulated Haldane model in order to place the system deep in the quantum Hall phase, see Sec. 6.2. In the inset of Fig. 7.9(d)

we show results for $\mathrm{J}^{\mathrm{an}}_{n,x}$ as a function of the relative phase φ controlling the time-reversal symmetry breaking of the system as well as $\Delta_{\mathcal{AB}}$. Crucially, one finds that anomalous conductivities are globally affected by tuning the intrinsic parameters $\varphi, \Delta_{\mathcal{AB}}$. Hence, the insights of Fig. 7.9(d) are applicable to all anomalous currents at all times. By varying φ from $\pi/2$ to 0 (with $\Delta_{\mathcal{AB}} = 0$) one approaches the topological phase transition, cf. Sec. 6.2, and the Floquet-Nernst effect is steadily decreased in magnitude. For $\varphi = \Delta_{\mathcal{AB}} = 0$, where the system fulfils time reversal as well as inversion symmetry, the anomalous effect is then expected to disappear completely. In contrast, setting $\varphi = \pi/2$ and increasing the energy shift between both sublattices from $\Delta_{\mathcal{AB}} = 0$ results in a slow decay of anomalous currents. As shown by the inset of Fig. 7.9(d), the Floquet-Nernst effect persists even when crossing the topological phase transition at $\Delta_{\mathcal{AB}} \simeq 0.3J$ (see Sec. 6.2). The reason for this behaviour is the fact that a finite $\Delta_{\mathcal{AB}}$ renders different gap sizes associated with both Dirac points of the underlying Haldane model.

So independent of the extrinsic parameters discussed above, tuning the intrinsic parameters $\varphi = \pi/2$ and $\Delta_{\mathcal{AB}}$ allows for an *independent* quantitative as well as qualitative adjustment of the Floquet-Nernst effect.

7.6. Discussion

In conclusion, we have demonstrated how inhomogeneous heating of a Floquet system in combination with topological properties can lead to anomalous transport effects resulting from temperature gradients in the system. Fig. 7.10 pictorially summarises the results of this chapter, yielding once again the emergence of the Floquet-Nernst effect and simultaneously expressing its dependence on all discussed parameters, $(U, r_0, \Omega, \varphi, \Delta_{\mathcal{AB}})$. Here, we show local particle currents, $\mathbf{j}_n = \mathbf{j}^0_n + \mathbf{j}^{\mathrm{an}}_n$, as vector fields for a fixed value of κ but for varying compositions of extrinsic parameters. Yet, the results once more underline the intrinsic property of anomalous effects: the relative significance of $\mathbf{j}^{\mathrm{an}}_n$ over $\mathbf{j}^0_n$ can be tuned by adjusting extrinsic parameters, e.g., by shrinking the size of the atomic cloud or by increasing the interaction strength. The probably most natural parameter to tune in a Floquet experiment is the driving frequency Ω. While the discussion of Fig. 7.10(a)-(c) only revolves around U and r_0, the consequences of Ω can be straightforwardly embedded by rescaling the interaction strength, $U \to U_\Omega = Ug(\Omega)$ with g being a function incorporating the dependence of Γ on Ω. We have excluded a specific discussion of Ω, though, since the coresponding scaling behaviour of Γ is non-trivial and undergoes many regimes, as seen in Sec. 6.3. Alternatively, the results of Fig. 7.10 could qualitatively also emerge from the following three scenarios: (a) a topologically trivial system respecting time-reversal symmetry, a quantum Hall state that is either (b) characterized by diffusion or (c) dominated by by strong local heating. The manifestation of the Floquet-Nernst effect also varies here from non-existent over weak to strong.

Nevertheless, we stress again that a simple rescaling of parameters is often not realisable in experimental circumstances. Here, the total number of particles, i.e., the size of the atomic cloud, and attainable interaction strengths are limited. Most crucially, the running time of the experiment is typically restricted due to decoherence and other relaxation processes. Since κ reacts quite sensitively to changes of individual parameters, the experimentally relevant parameter space is expected to be strongly constrained. Having said this, the choice of parameters for generating all presented data in this chapter was highly inspired by actual experimental values used by the authors of Ref. [23]. Therefore, here investigated effects are indeed expected to be observable in an experiment based on the Haldane model realisation by the Esslinger group [23]. We additionally remark that

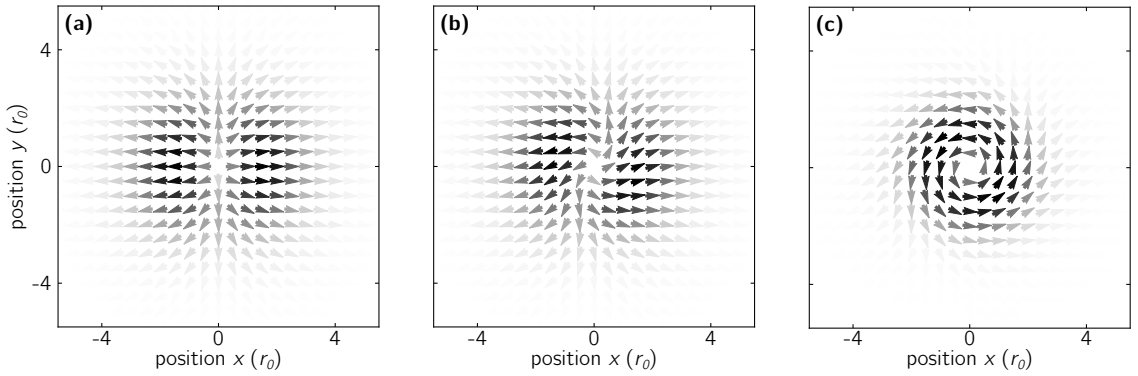

Figure 7.10.: Local particle currents, $\mathbf{j}_n = \mathbf{j}_n^0 + \mathbf{j}_n^{\mathrm{an}}$, for a fixed value of diffusion strength $\kappa = 6{\times}10^{-4}$ and time $t = 10t_h$. Intensity of shown arrows correspond to $|\mathbf{j}_n|$, normalised to the maximal current strength in the respective figure. Relative role of anomalous to longitudinal currents is tuned by the choice of extrinsic parameters: (a) $U = 0.1J, r_0 = 25r_{0,\mathrm{exp}}$, (b) $U = 0.5J, r_0 = r_{0,\mathrm{exp}}$ and (c) $U = 1.5J, r_0 = r_{0,\mathrm{exp}}/9$. The same qualitative current pattern can also be obtained by alternatively varying, e.g., κ and φ (see text).

some parameter constellation might be realisable, but contradict crucial assumptions made above. For instance, the Floquet-Nernst effect seemingly prefers a strong local heating and a development of large temperature gradients. This limit is, however, restricted as our Floquet-Boltzmann formalism requires weak interactions. Here, it is promising that our data above suggests that associated effects are already obtained for moderate interaction strengths, $U \lesssim 1$. Moreover, too little cloud sizes are also not too favourable in the spirit of our theoretical considerations.

Generally, one can interpret the physics discussed in the chapter as the interplay of two aspects: the emergence of anomalous currents from some topologically non-trivial structure and the presence of Floquet heating. As suggested in Sec. 6.3, the latter (at least to the order of our discussion) is independent of underlying topological structures and insensitive to minor quantitative changes of the system, e.g., the closing of the small present band gap, $\Delta_G < J, T$. In combination with inhomogeneities, however, the two characteristics are coupled leading to an interesting phenomenon in its own right. In addition to the exciting macroscopic manifestation of a non-trivial Berry phase effect, the Floquet-Nernst effect can be used to monitor the dynamical heating of a closed many-body Floquet system. Turning the logic around, Floquet heating holds prospects to detect topological properties of a system. This might be particularly interesting in cases where parameters of the system are changed dynamically. Hereby, one could observe the transition from a topologically trivial to a non-trivial phase.

We finish this discussion by remarking that it has yet to be clarified how to actually measure the rotation of the cloud and therefore quantify the Floquet-Nernst effect in an experiment. One possible idea could be the elongation of the harmonic trap in one spatial direction. The resulting 'cigar shaped' trapped cloud would remain its shape assuming the trap is switched off in a designed way. Most importantly, anomalous currents should be mapped to free transversal currents under the same (de)ramping procedure. This would cause the cloud to macroscopically rotate in space which should also be tractable by means of standard time-of-flight techniques [5].

Part III.

Signature and stability of a 1D edge state with ultracold atoms

8. A topologically protected edge state with ultracold atoms

Ultracold atoms in optical lattices have recently been proven to be a powerful tool to simulate a wide range of complex (many-body) systems by means of appropriate confinement and coherent manipulation, see Sec 2.1. In the previous parts of this thesis, we mainly focussed on aspects of designing quantum systems using external periodic driving and particularly on the respective role of interactions as well as associated phenomena. This chapter is devoted to the investigation of a topologically protected edge state with ultracold atoms in a static lattice system.

Topological states of matter, such as quantum Hall systems (cf. Ch. 6), are generally indistinguishable from ordinary matter by local measurements in the bulk of the material, but instead are characterised by global properties [189, 190]. In this context, topological insulators are materials that possess a band gap such as an ordinary insulator but at the same time reveal protected conducting states on their surface [189]. Such edge states were experimentally first observed in transport experiments on HgTe/CdTe quantum wells [317, 318]. Generally, these edge states emerge at the interface of any two topologically distinct materials . As seen in Ch. 6, ultracold gases in optical lattices are also promising tools for the creation and investigation of topological states of matter [18,19,22,23,49,105,110,111]. Here, however, the observation of edge states has so far been restricted to the state space imposed by the internal atomic structure [22, 183, 319, 320].

In this chapter, we present results from a close collaboration with the experimental group of M. Weitz from the University of Bonn, who were able to observe an edge state between two topologically distinct phases of an atomic physics system in real space using optical microscopy [53, 321]. Technically, this is realised by a one dimensional optical lattice with a spatially chirped amplitude. Their setup gives rise to an effective Dirac system with emergent chiral symmetry, which is closely related to the SSH model by Su, Schrieffer and Heeger (SSH) explaining soliton-type edge states in polyacetylene chains [322, 323].

While the actual experiment was conducted by M. Weitz, M. Leder and collaborators [53,321,324], the entire corresponding theoretical description was developed by us. In the following chapter, we thus want to give an overview on experimental achievements but focus on theoretical aspects necessary to understand the physics of the observations. To this end, we start by introducing the concept of topological states protected by symmetry. Along those lines we sketch the topological properties of the SSH model and explain how the physics at the interface of two topologically distinct phases can be captured by a massive Dirac equation. Subsequently, we thoroughly study this Dirac equation and elaborate on how such a system is realised experimentally. We then discuss at length possible interaction effects on the mean-field level, which are crucial to justify the experimental findings. Finally, we compare numerical simulations provided by us to experimental results, which indeed suggest that a topologically protected edge state has been observed experimentally.

We want to acknowledge experimental efforts made by our collaborators from Bonn and stress again that all experimental aspects (parameters, data, etc.) presented in this chapter are related to the work of M. Leder *et al.* [53, 321, 324].

8.1. Symmetry protected topology in 1D

As already indicated in the context of quantized pumping, Sec. 3.4, and by realising the Haldane model, Sec. 6.2, the notion of *topology* plays a major role in analysing and understanding modern condensed matter systems. In previous chapters, we mainly discussed the emergence and importance of Berry curvatures and (first) Chern numbers for topologically non-trivial states. Complementary to this approach, topological properties of gapped many-body quantum systems such as topological insulators and superconductors can be classified in terms of *symmetry classes*. This classification scheme of matter goes back to works by Wigner [325] and Dyson [326] and was thoroughly developed further in the context of superconductors by Altland and Zirnbauer [327, 328] by means of random matrix theory. Eventually, Schnyder, Ryu, Furusaki and Ludwig [329] linked the tenfold symmetry classes to topological properties of ground states in various dimensions. Generally, all such classes are built from combinations of three fundamental symmetries: time-reversal, charge conjugation (partice-hole) and a combination of both named chiral symmetry. A corresponding table [329] summarizes the entire zoo of topological states of matter that can be classified by their respective symmetries. Note that every aspect of this table has experienced a high level of scientific interest lately. In the following, however, we refrain from giving a general overview of corresponding physical systems and refer the reader for details to, e.g., Refs. [189, 190, 195, 196, 329]. Instead, we will consider only one particular symmetry class with restricted dimensionality: a one-dimensional system with chiral symmetry belonging to the BDI-class. We will briefly elaborate on the topological properties of such a system using *homotopies* and explain the emergence of a bound-state at the interface of two topologically distinct regions. We restrict the discussion to this specific situation, because this symmetry class is ultimately simulated by the here considered experimental system of cold atoms in a one-dimensional optical lattice.

8.1.1. Homotopies and winding numbers

In the following, we will analyse the topological properties of a generic one-dimensional lattice Hamiltonian belonging to the BDI-symmetry class. To this end, we consider a yet to be specified two-band Hamiltonian, which can be written in momentum space as (cf. Secs. 3.2 and 6.1)

$$H(k) = n_x(k)\,\sigma_x + n_y(k)\,\sigma_y + n_z(k)\,\sigma_z = \mathbf{n}(k)\cdot\boldsymbol{\sigma}\,, \tag{8.1}$$

with k being the one-dimensional momentum variable and we defined $\mathbf{n} = (n_x, n_y, n_z)$ as well as $\boldsymbol{\sigma} = (\sigma_x, \sigma_y, \sigma_z)$, where σ_i are the typical Pauli matrices. Despite having a one-dimensional Hamiltonian one can establish a one-to-one correspondence between a point $\mathbf{n}(k) \in \mathbb{R}^3$ and $H(k)$. Recall that the eigenenergies of Hamiltonian (8.1) are given by $E_\pm(k) = \pm|\mathbf{n}(k)|$ (cf. Eq. (6.11)), and, thus, the origin of $\mathbb{R}^3$ corresponds to the point where the band gap closes. Based on this picture we will formulate a topolocial analysis, where we closely follow the work and notations by Ryu and Hatsugai [330] and also Ref. [331]. The argumentation is based on homotopies and introduced only very briefly. For more (mathematical) depth on this issue the reader is referred to, e.g., Refs. [194,195].

We begin by imposing no restrictions on $H(k)$ (or equivalently on the behaviour of $\mathbf{n}(k)$) except for demanding that the Brillouin zone is periodic (where we set the lattice constant to unity $a = 1$). Consequently, the one-dimensional momentum space is topologically equivalent to the unit circle, i.e., $k \in [-\pi, \pi) = S^1$. For every lattice Hamiltonian (8.1) one can then identify a *loop* that is traced out by the path taken by $\mathbf{n}(k)$ when going

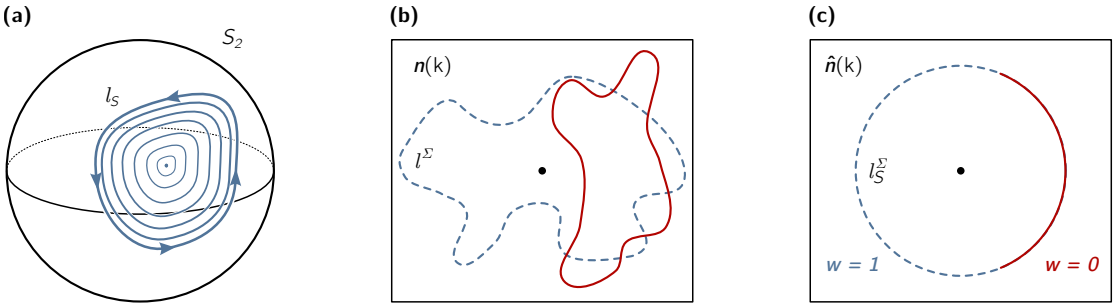

Figure 8.1.: Graphical illustration of possible loops l traced out by the Hamiltonian $H(k)$, see Eq. (8.1), when going around the one-dimensional circular Brillouin zone. (a) The unit vector $\hat{\mathbf{n}}(k)$ traces out paths on the surface of the two-dimensional unit sphere S^2. Here, all loops can be contracted to a point, and are therefore topologically trivial. (b) Chiral symmetry (8.4) reduces parameter space to $\mathbb{R}^2$, where loops are topologically distinguished whether they enclose the origin, or not. (c) Homotopies deform all loops of (b) to lie on unit circle S^1. Topological classification is done in terms of winding numbers w. Figure (a) is adopted from Ref. [96].

around this Brillouin zone. This loop can be formally defined as

$$l : S^1 \to \mathbb{R}^3 \ , \ k \mapsto \mathbf{n}(k) \, . \tag{8.2}$$

The main idea is now to classify the Hamiltonian $H(k)$ in terms of these loops (8.2). This is done by considering *homotopies*, i.e., continuous deformations of H. All Hamiltonians $H(k)$ that can be continuously deformed into each other are then said to be topologically equivalent. So in a first step we continuously deform the vector $\mathbf{n}(k)$ to the corresponding unit vector $\hat{\mathbf{n}}(k)$. The vector $\hat{\mathbf{n}}(k)$ then always points to a point on the surface of the unit sphere S^2 centred around the origin. Thus, we identify a new loop, $l_S : S^1 \to S^2$, that maps the Brillouin zone to a cyclic path on the S^2 sphere. The formal connection between this loop and Eq. (8.2) is established by defining

$$l : S^1 \to \mathbb{R}^3 \ , \ k \mapsto \mathbf{n}(k) \quad \overset{\mathfrak{H}}{\longleftrightarrow} \quad l_S : S^1 \to S^2 \ , \ k \mapsto \hat{\mathbf{n}}(k) \, , \tag{8.3}$$

where $\mathfrak{H} : S^1 \times [0,1] \to \mathbb{R}^3$ is a homotopy on the product space of the unit circle S^1 with the unit interval $[0,1]$ into the 3D space $\mathbb{R}^3$, such that $\mathfrak{H}(k,0) = l(k)$ and $\mathfrak{H}(k,1) = l_S(k)$ [331]. Here, it is crucial to assume that the loop l does *not* cross the origin during the deformation, since the unit vector $\hat{\mathbf{n}}(k)$ is ill-defined for $|\mathbf{n}(k)| = 0$.

From a topological point of view it is sufficient to study the characteristics of loops l_S instead of discussing properties of the original Hamiltonian $H(k)$ with associated vector $\mathbf{n}(k)$. All loops l_S that can be continuously deformed into each other are topologically equivalent. It is precisely due to the latter fact that Hamiltonians of form Eq. (8.1) are generically trivial in a topological sense. This is because all possible loops on the surface of a sphere can be contracted to a single point, see Fig. 8.1(a). The story is changed, however, when the system is restricted by additional *symmetries*. To this end, we finally introduce the chiral symmetry[1] that has the property

$$\{\Sigma, H(k)\} = 0 \qquad \forall \ k \in S^1 \, , \tag{8.4}$$

with $\{.\}$ describing the anti-commutator. The immediate consequence of this symmetry is that the eigenenergies of the system come in pairs according to $E(k) = -E(k)$ as well

[1] Note that despite the fact that the literature often uses the nomenclature 'symmetry', the Hamiltonian rather *anti-commutes* under the action of Σ, and, thus, is strictly speaking not a true symmetry of the system.

as $E(k) = E(-k)$. Thus, we can write $\Sigma = \mathbf{s} \cdot \boldsymbol{\sigma}$, where $\mathbf{n}(k) \cdot \mathbf{s} = 0$, and identify the loop $l^{\Sigma} : S^1 \to \mathbb{R}^2$, which lies now in the 2D plane that is normal to the vector $\mathbf{s}$. The unit vector $\hat{\mathbf{n}}(k)$ is therefore restricted to a respective plane cutting the previous unit sphere S^2 and containing the origin. Hence, the loop l_S^{Σ} is a mapping from the Brillouin zone to a closed path on a unit circle, i.e.,

$$l_S^{\Sigma} : S^1 \to S^1 \ , \ k \mapsto \hat{\mathbf{n}}(k) \, . \tag{8.5}$$

This mapping of a circle to a circle does not have to be trivial in the sense that it cannot be generally contracted to a point. This scenario can be classified by an integer *winding number* that counts how many times the loop l_S^{Σ} winds around the unit circle as one goes once around the Brillouin zone. For a Hamiltonian of form (8.1) a general expression for the winding number is given by [195]

$$w = \frac{1}{2\pi} \int_{-\pi}^{\pi} dk \ \hat{\boldsymbol{s}} \cdot \left(\hat{\boldsymbol{n}}(k) \times \partial_k \hat{\boldsymbol{n}}(k) \right) , \tag{8.6}$$

with $\hat{\boldsymbol{s}}$ being the corresponding unit vector of $\boldsymbol{s}$. Note that this winding number assumes a different form if the considered system differs from the here discussed Hamiltonian. An example for such a different situation is given in Sec. 3.4.2, where the winding number classifies different mappings of Floquet operators. Mathematically, a more rigorous way of classifying mappings above goes by the means of homotopy groups of spheres, $\pi_n(S^m)$. In the simplest case, $n = m = 1$, the corresponding group coincides with the winding number defined above yielding $\pi_1(S^1) = \mathbb{Z}$. Again, for more details the reader is referred to Refs. [194, 195] (and references within).

We conclude with a physical consequence of the discussion above: due to the fact that all Hamiltonians within the same topological class are connected by a continuous transformation, one needs to undergo some discontinuous procedure to go from one topological phase to a different one. For the discussion above, the only singular event that could possibly happen is that the vector $\mathbf{n}(k)$ is not defined. This will precisely happen once the loop runs into the origin, or - in other words - the energy gap between the bands closes at zero energy. Hence, it is necessary to close the energy gap, if one wants to change the topological phase. The bulk-boundary correspondence [195] then implies that if two systems with different winding numbers w_1, w_2 share a common interface, there exist $|w_1 - w_2|$ localized bound states at zero energy.

8.1.2. The SSH model: topological phases and edge states

A prototypical one-dimensional system that features the emergence of distinct topological phases is the so called Su-Schriefer-Heeger (SSH) model [322, 323, 332]. In this section, we briefly introduce this model and, most importantly, sketch how the associated topological properties can be likewise captured by a 1D Dirac equation. The SSH model was originally used by the respective authors of Ref. [322] in order to describe a mobile defect in polyacetylene chains, $(\mathrm{CH})_x$. Here, they assumed two degenerate energy configurations that are characterized by two different topological phases. An immediate consequence was the emergence of a soliton-type edge state located at the boundary between two regions of different configurations. While a detailed discussion of the physics of this peculiar polymer can be found, e.g., in Ref. [332], we want to focus on a reduced and simplified description, which still contains all topological aspects.

To this end, we consider the *trans*-$(\mathrm{CH})_x$ configuration of polyacetylene, see Fig. 8.2(a), and start by assuming that all bonds of the polymer are equally strong. Such a system is,

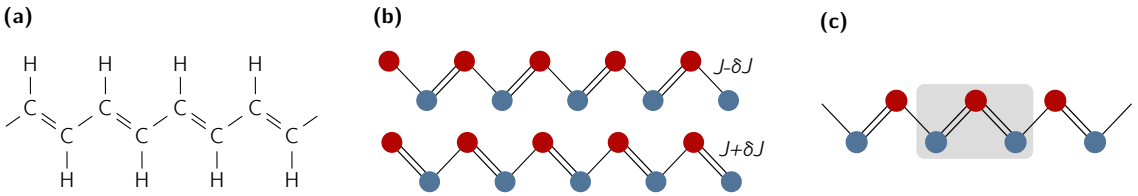

Figure 8.2.: Various schematics of polyacetylene. (a) The chemical trans-$(CH)_x$ configuration [332], where differences in bond strength between carbon atoms results from a Peierls instability. (b) An illustration of the simple tight-binding Hamiltonian (8.7) in its (b) 'wsws' (top) and 'swsw' (bottom) configuration. Here, red (blue) points indicate even (odd) lattice sites. (c) Appearance of a domain wall (gray box) by merging both energetically degenerate configurations of (b).

however, unstable with respect to a dimerization according to a Peierls instability [332]. Hence, there are two possible ground states the system can settle into: either it prefers an 'wsw' or an 'sws' configuration, where 'w' ('s') represents a weak (strong) bond, see Fig. 8.2(b). The simplest model describing this situation is a tight-binding Hamiltonian of the following form

$$H(t) = -\sum_j \left(J + (-1)^j \delta J\right) \left(c_{j+1}^\dagger c_j + c_j^\dagger c_{j+1}\right), \tag{8.7}$$

with J being some static hopping parameter, δJ encodes the dimerization and $c^\dagger, c$ are creation and annihilation operators. By changing the sign of δJ one can go back and forth between the two ground state configurations, while it is assumed that the dimerization is small, i.e., $|\delta J|/J < 1$.

In fact, Eq. (8.7) is nothing but a fermionic version of the non-interacting, static part of the quantum ratchet model given in Eq. (3.1). One can therefore introduce a similar even-odd labelling of the creation and annihilation operators representing the underlying sublattice structure. Performing a Fourier transformation defined by Eq. (3.6), one obtains the Hamiltonian

$$H = \int \frac{dk}{2\pi/a} \left(d_{k,o}^\dagger, d_{k,e}^\dagger\right) H(k) \begin{pmatrix} d_{k,o} \\ d_{k,e} \end{pmatrix}, \tag{8.8}$$

with

$$H(k) = -\left[(J - \delta J) + (J + \delta J)\cos(k)\right] \sigma_x - (J + \delta J)\sin(k)\, \sigma_y \tag{8.9}$$

being of the form $H(k) = \mathbf{n}(k) \cdot \boldsymbol{\sigma}$, see Eq. (8.1). Moreover, since the vector $\mathbf{n}(k)$ lies solely in the xy-plane, the vector $\mathbf{s} = (0, 0, 1)$ fulfils $\mathbf{n}(k) \cdot \mathbf{s} = 0\ \forall k \in \mathrm{BZ}$. Hence, we find indeed a chiral symmetry of type (8.4) with symmertry operator $\Sigma = \sigma_z$, yielding

$$\sigma_z H \sigma_z = -H\,. \tag{8.10}$$

The corresponding energy bands are now straightforwardly calculated to be $E_\pm(k) = \pm|\mathbf{n}(k)| = \pm\sqrt{2}J[(1+\cos(k)) + (\delta J/J)^2(1-\cos(k))]^{1/2}$ with the corresponding energy gap $E_{\mathrm{gap}} = 4|\delta J|$, measured at the edges of the Brillouin zone. This pairwise appearence of the energy is a direct consequence of the chiral symmetry (8.10). Note that the energies are independent of the sign of δJ, proving that both discussed polymer configurations are indeed energetically degenerate. Additionally, one can calculate the winding number according to Eq. (8.6) and obtains

$$w = \begin{cases} 1 & \text{for} \quad \delta J > 0 \\ 0 & \text{for} \quad \delta J < 0 \end{cases}. \tag{8.11}$$

The reason for this difference is shown in Fig. 8.1(b) and (c). When δJ is chosen to be positive the origin is enclosed by the loop traced out by $\mathbf{n}(k)$. However, when $\delta J < 0$ the origin lies outside the loop and all mappings are topologically trivial. As discussed above, the only way to get from one topologically distinct phase into the other is going through the origin, i.e., closing the energy gap of the system.

A natural question to ask now is what happens at the interface of two topologically distinct regions. In terms of the underlying polyacetylene this simply means the appearance of a domain wall [332]. Technically, one can encode this into the model (8.9) by letting the dimerization strength become spatially depended, i.e., $\delta J \to \delta J(z)$. Due to the discussion above, also the energy gap will then become a function of space, $E_{\mathrm{gap}} \to E_{\mathrm{gap}}(z)$. In order to model a situation that is shown in Fig. 8.2(c) one assumes that δJ flips its sign on the scale of the lattice constant a.

But why is it that the physics at the interface is dominated by the *difference* of both topological phases to each side as described in Sec. 8.1.1? To answer this question we take a look at the parameter space at hand, which is given by the space of $S^1 \times \mathbb{R}^1$, i.e., the product space of the Brillouin zone and the one-dimensional position space. This space corresponds to the surface of an infinitely stretched cylinder, see Fig. 8.3. For a given point in space this cylinder is cut by a horizontal plane. The so identified unit circle is then mapped onto another unit circle according to Eq. 8.5, and the system is characterised in terms of homotopies (8.3). We shall assume that δJ is varied in such a way that the winding number of the system corresponds to $w = 0$ on the lower half of the cylinder ($x < 0$) and $w = 1$ on the upper half ($x > 0$). Right at the interface ($x = 0$) we let $\delta J = 0$, and therefore the energy gap closes at the edge of the Brillouin zone, $E_{\mathrm{gap}}(0) = 0$. As outlined in Sec. 8.1.1, the classification in terms of winding numbers is not defined in the presence of this singularity.

So to understand the behaviour at the interface we consider two systems on the cylinder, both placed away from the singularity but one with $w = 0$ and the other one with $w = 1$, see Fig. 8.3(a). Again, one cannot continuously deform one into the other. However, a general continuous deformation is still allowed as long as the parameter space is smooth. The two systems can therefore be brought into contact, see Fig. 8.3(b). Since at this point both systems are identical, they can be merged and be further deformed in the sense of Fig. 8.3(c). This procedure visualizes that the combination of two systems with different winding numbers can be - in a topological sense - reduced to the discussion of a small loop around the topological singularities, or topological defects, which cannot be contracted to a point, see Fig. 8.3(d).

Hence, to analyse the physics at the boundary that can be linked to topological properties one can refrain from considering the two systems in its full description. Instead, an effective Hamiltonian acting on the mixed parameter space (here given by z and k) can be studied close to the point where the energy gap closes. Thus, a Taylor expansion around $k = \pi$ of the Hamiltonian (8.9) and an additional rotation[2] around the σ_x-axis by $\pi/2$, $e^{-i\sigma_x \pi/4} H e^{i\sigma_x \pi/4}$, then yields

$$H_{\mathrm{D}} = K(z)\,\sigma_x + q\,c_{\mathrm{eff}}\,\sigma_z\,, \tag{8.12}$$

which is the (1+1)-dimensional *Dirac Hamiltonian* with $c_{\mathrm{eff}} = J + \delta J$ and spatially dependent 'mass' $K(x) = 2\delta J$. Further, it is used that $q = \hbar k$. Note that for the discussion above to be applicable, the electrons of the system obviously need to occupy the states

[2] Note that this rotation is solely performed in order to bring Eq. (8.12) into a form that is consistent with large parts of the respective literature.

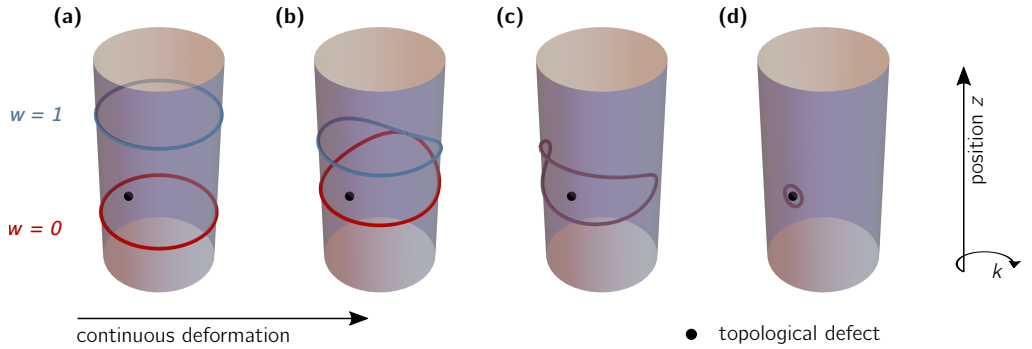

Figure 8.3.: Visualization of a topological defect at the boundary of two topologically distinct regions. (a)-(c) By continuously deforming two systems initially placed in regions of opposite winding number w, it becomes apparent (d) that all topological information are encoded in a loops close to the topological defects. See also text.

near the band maximum (for the lower band). Thus, we assume a system that is half-filled, i.e., that the Fermi energy lies exactly in the middle of the gap at $E_F = 0$.

The Hamiltonian of Eq. (8.12) was studied by Jackiw and Rebbi [333] in the context of one-dimensional relativistic field theories even before the SSH-model was introduced. They already reported on the existence of a bound state at zero energy given by

$$\psi(z) \propto e^{-\int_0^z dz' \, K(z')} \begin{pmatrix} 1 \\ -i \end{pmatrix} , \tag{8.13}$$

for $K(z \to \pm\infty) \gtrless 0$. In the light of the discussion above, this bound state is understood as a state that needs to be pinned to the topological defect, see Fig. 8.3. Moreover, the zero energy property is a consequence of the chiral symmetry given by Eq. (8.4). In the context of the underlying polyacetylene structure, this bound state can be seen a a *soliton* with a certain topological charge. However, in contrast to, e.g., the Hall conductivity (see Sec. 3.4), this charge takes on only half-integer values $\pm 1/2$ [332, 333]. The reason being that the solid angle swept out by a closed loop around the circumference (cf., Fig. 8.1) only covers half of the surface of the unit sphere [334].

In conclusion, in order to study the topological properties of a boundary of two topologically distinct phases belonging to the BDI symmetry class, it is sufficient to study the Dirac Hamiltonian given by Eq. (8.12). In the following section, we will therefore focus on a deeper analysis of the Dirac Hamiltonian and will describe how this model Hamiltonian is realised in an experiment with ultracold atoms in an optical lattice.

8.2. 1D Dirac equation with spatially varying mass

Initially, the simulation of the one dimensional Dirac equation was suggested [335] and also experimentally implemented [336] in systems with single trapped ions. More recently, the Dirac Hamiltonian was also successfully simulated in experiments with ultracold atoms in optical lattices by means of specifically tailored Bloch bands in combination with an appropriate preparation of the atomic cloud. This was prominently achieved in the group of M. Weitz at the University of Bonn, where for a homogeneous mass, cf. Eq. (8.12), Klein-tunnelling effects were studied [52] and experiments regarding a negative refractive index were conducted [337].

In this section, we will first discuss analytically the (1+1)-dimensional Dirac Hamiltonian introduced above, see Eq. (8.12). Following this, we briefly summarize how the group

of M. Weitz was able to experimentally realise the Dirac Hamiltonian with a spatially dependent mass in order to simulate the above discussed topological edge state [53]. We want to stress that, unless stated otherwise, all experimental work presented here was conducted by our collaborators from Bonn.

8.2.1. Theoretical description

First, we will study the spectrum of the one-dimensional Dirac Hamiltonian. To this end, we rewrite Eq. (8.12) as

$$H_{\mathrm{D}} = m_{\mathrm{eff}}(z)\, c_{\mathrm{eff}}^2\, \sigma_x - i\hbar\, c_{\mathrm{eff}}\, \partial_z\, \sigma_z\,, \tag{8.14}$$

where we introduced the momentum operator as $q = -i\hbar\partial_z$. We shall also assume that the effective mass $m_{\mathrm{eff}}(z)$ changes linearly as a function of space, i.e.,

$$m_{\mathrm{eff}}(z) = \alpha\, z/c_{\mathrm{eff}}^2\,, \tag{8.15}$$

which simplifies the problem significantly. As described above, the Dirac equation (8.14) possesses an emergent chiral symmetry

$$\sigma_y H_{\mathrm{D}} \sigma_y = -H_{\mathrm{D}}\,. \tag{8.16}$$

Note that for a mass of type (8.15) the problem is equivalent to the solution of the 2D Dirac equation in a magnetic field well known from graphene [301] or from the description of 2D surface states of a 3D topological insulator in a magnetic field [331].

In general, in order to solve the Hamiltonian (8.14) it is convenient to calculate the square of this Dirac Hamiltonian, H_{D}^2. Ordinary matrix multiplication yields

$$H_{\mathrm{D}}^2 = \left[(\alpha z)^2 - (\hbar c_{\mathrm{eff}})^2\, \partial_z^2\right] \mathbb{1} - \alpha\hbar c_{\mathrm{eff}}\, \sigma_y\,, \tag{8.17}$$

where the identity for Pauli matrices $\sigma_i\sigma_j = \delta_{ij} + i\epsilon_{ijk}\sigma_k$ (with ϵ_{ijk} being the Levi-Civita symbol) as well as the canonical commutation relation for position and momentum, $[z, \partial_z] = -1$, has been used. The squared Hamiltonian H_D^2 has both a term proportional to z^2 as well as ∂_z^2, and thus resembles a conventional quantum harmonic oscillator. To this end, we introduce typical raising and lowering operators for harmonic oscillators

$$b^\dagger = \frac{1}{\sqrt{2c_{\mathrm{eff}}\hbar\alpha}} \left(\alpha z - c_{\mathrm{eff}}\hbar\, \partial_z\right) \qquad \text{and} \qquad b = \frac{1}{\sqrt{2c_{\mathrm{eff}}\hbar\alpha}} \left(\alpha z + c_{\mathrm{eff}}\hbar\, \partial_z\right), \tag{8.18}$$

which fulfil the bosonic commutation relation $[b, b^\dagger] = 1$. With the help of these operators the square of the Dirac Hamiltonian can be brought into the from

$$H_D^2 = (\hbar\,\omega_0)^2 \left[\left(b^\dagger b + \frac{1}{2}\right) \mathbb{1} - \frac{1}{2}\,\sigma_y\right], \tag{8.19}$$

with $\omega_0 = \sqrt{2c_{\mathrm{eff}}\alpha/\hbar}$. Additionally, one can perform a rotation of the basis to find new basis states of the form

$$|\uparrow\rangle = \frac{1}{\sqrt{2}}\left(|+\rangle - i\,|-\rangle\right) \qquad \text{and} \qquad |\downarrow\rangle = \frac{1}{\sqrt{2}}\left(|-\rangle - i\,|+\rangle\right), \tag{8.20}$$

where $|+\rangle = (1,0)^T$ and $|-\rangle = (0,1)^T$ are the basis states of the original Dirac Hamiltonian (8.14). Using the corresponding unitary transformation matrix Λ, i.e., $(|\uparrow\rangle, |\downarrow\rangle)^T = \Lambda \cdot (|+\rangle, |-\rangle)^T$, one obtains

$$\widetilde{H}_D^2 = \Lambda\, H_D^2\, \Lambda^{-1} = (\hbar\,\omega_0)^2 \left[\left(b^\dagger b + \frac{1}{2}\right) \mathbb{1} - \frac{1}{2}\,\sigma_z\right]. \tag{8.21}$$

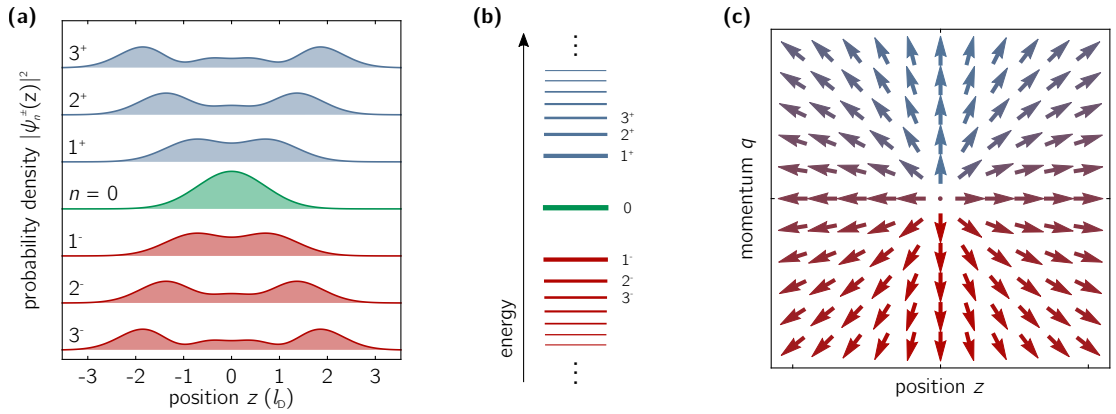

Figure 8.4.: Schematics of various properties of the Dirac Hamiltonian (8.14). (a) Probability densities of the edge state ($n = 0$) and first few excited states with $n \leq 3$. (b) Sketch of corresponding energies with $E_n = \pm\sqrt{n}\hbar\omega_0$. (c) Visualisation of the winding of the unit vector $\hat{\mathbf{n}}_{\mathrm{D}}$, where $H_{\mathrm{D}} = \mathbf{n}_{\mathrm{D}} \cdot \boldsymbol{\sigma}$ (cf. Eq. (8.1) and Fig. 8.1).

Most importantly, the expression for the Dirac Hamiltonian in the basis $\{|\uparrow\rangle, |\downarrow\rangle\}$ is found by inspection of Eq. (8.21) to read as

$$\widetilde{H}_D = \hbar\omega_0 \begin{pmatrix} 0 & b^\dagger \\ b & 0 \end{pmatrix} . \tag{8.22}$$

The eigenstates of this Hamiltonian can then also be readily found to read as

$$|\psi_0\rangle = |0\rangle\,|\uparrow\rangle \qquad \text{and} \qquad |\psi_n^{\pm}\rangle = \frac{1}{\sqrt{2}}\left(\pm|n\rangle\,|\uparrow\rangle + |n-1\rangle\,|\downarrow\rangle\right), \tag{8.23}$$

where $n \in \mathbb{N}$ and $|n\rangle$ are harmonic oscillator eigenstates, i.e., $b^\dagger b\,|n\rangle = \hbar\omega_0\,|n\rangle$. Note that due to the chiral symmetry of H_{D}, see Eq.(8.16), it holds that $|\psi_n^+\rangle = \sigma_y\,|\psi_n^-\rangle$. Moreover, using the spatial representation of harmonic oscillator eigenstates

$$\phi_n^{\mathrm{ho}}(z) = \langle z|n\rangle = \frac{1}{\sqrt{2^n n!}}\left(\frac{\alpha}{\pi c_{\mathrm{eff}}\hbar}\right)^{1/4} \exp\Big[-\frac{\alpha z^2}{2c_{\mathrm{eff}}\hbar}\Big]\, H_n\big(\sqrt{\alpha/\hbar c_{\mathrm{eff}}}\, z\big), \tag{8.24}$$

where $H_n(z)$ represent Hermite polynomials, one can alternatively write the expressions of Eq. (8.23) in terms of spinor wavefunctions of the form

$$\psi_0(z) = \phi_0^{\mathrm{ho}}(z)\,|\uparrow\rangle \qquad \text{and} \qquad \psi_n^{\pm}(z) = \frac{1}{\sqrt{2}}\left(\pm\phi_n^{\mathrm{ho}}(z)\,|\uparrow\rangle + \phi_{n-1}^{\mathrm{ho}}(z)\,|\downarrow\rangle\right). \tag{8.25}$$

Here, the length of the oscillator is given by $l_{\mathrm{D}} = \sqrt{c_{\mathrm{eff}}\hbar/\alpha}$ and the corresponding eigenenergies read as

$$E_n = \begin{cases} 0 & \text{for} \quad n = 0 \\ \pm\sqrt{n}\,\hbar\omega_0 & \text{for} \quad n \geq 1 \end{cases}, \tag{8.26}$$

where all energies come in pairs except for a single one at zero energy. This latter property is explained by the chiral symmetry of Eq. (8.4). Also, the zero energy eigenvalue is associated with an eigenstate that corresponds to the discussed topological edge state above. Using Eqs. (8.24) and (8.25), the spinor associated to the edge state is given as (in the $\{|+\rangle, |-\rangle\}$ basis)

$$\psi_0(z) = \frac{1}{\sqrt{2}}\Big[\frac{\alpha}{\pi c_{\mathrm{eff}}\hbar}\Big]^{1/4} \exp\Big[-\frac{\alpha z^2}{2c_{\mathrm{eff}}\hbar}\Big] \begin{pmatrix} 1 \\ -i \end{pmatrix} . \tag{8.27}$$

This confirms the expression by Jackiw and Rebbi introduced in the previous section, see Eq. (8.13). Finally, we show in Fig. 8.4 the spatial variation of the first few probability densities $|\psi_n(z)|^2$ as well as give a pictorial presentation of the spectrum (8.26).

8.2.2. Realisation with cold atoms in an optical lattice

The Dirac Hamiltonian (8.14) can be successfully simulated in experiments with ultracold atoms in optical lattices by a combination of designing corresponding Bloch bands (or rather band crossings) and an appropriate initial preparation of the atomic cloud. A spatially dependent mass in such a Dirac equation, i.e., an interface between two spatial regions of different topological order, is realised by spatially varying the amplitude of the optical lattice trapping the atoms. The optical lattice is created by means of four-photon processes in an atomic rubidium three-level system. This level structure is sensitive to magnetic fields, allowing for the implementation of a spatial variation of the effective lattice.

We now present a summary of the experimental setup that was used by M. Weitz and collaborators in order to simulate the 1D Dirac Hamiltonian with spatially varying mass, and therefore enabled the experimentalists to eventually observe the above discussed topological edge state [53]. Here, we briefly shed light on technical aspects as well as experimental procedures. Note that actual experimental results will be shown in Sec. 8.4. Furthermore, the following description of the experimental realisation is far from complete. Information about extensive experimental details can be found in Ref. [53] or in the Ph.D. thesis by M. Leder [321].

Rubidium BEC The experiment is based on a Bose-Einstein-condensate (BEC) made of rubidium atoms (^{87}Rb). Initially, a dilute cloud of this isotope is prepared in the $F = 1$, $m_F = -1$ state of its hyperfine ground state manifold. The rubidium atoms are first cooled in a magneto-optical trap and then loaded into a combination of a dipole and magnetic trap. Here, the dipole trapping potential is generated by a CO_2-laser at 10.6μm wavelength and the magnetic trap is present due to a quadrupole field. By means of evaporative cooling a BEC is created, which contains $\sim 15,000$ atoms. In addition, a magnetic field gradient of $b = m_{\mathrm{Rb}} g/(\mu_g |g_F|) \simeq 30.5\mathrm{Gcm}^{-1}$ is present, with $m_{\mathrm{Rb}} = 1.44 \times 10^{-25}$kg being the mass of the rubidium isotope, μ_B is the Bohr magneton and $g_F = -1/2$ denotes the gyromagnetic factor for the used $F = 1$ hyperfine component of the electronic ground state. The gradient b points along the vertical spatial axis. Note that the resulting force is tuned in such a way that it compensates the Earth's gravitational force on the rubidium atoms, see Fig. 8.5(a). This gravitational force can be compensated to within 1 part in 10^4 in the here summarized experiment.

Four-photon lattice The optical lattice evoking the spatial periodicity of the system is established by a four-photon process. Here, a rubidium atomic three-level configuration with two ground states of different spin projections and one spontaneously decaying excited state are used [338]. As can be seen from the schematic of Fig. 8.5(b), the atoms experience two absorption as well as two stimulated emission processes. The frequency of the light triggering these processes is tuned such that emission and absorption come from photons of opposite direction. Hence, the momentum transfer to each atom is $4\hbar k_0$, with $\hbar k_0 = h/\lambda$ being the momentum of a single photon, where h is Planck's constant and $\lambda = 783.5$nm describes the wavelength of the laser. From this discrete momentum transfer one can deduce a spatially periodic lattice structure. The periodicity of the resulting lattice is

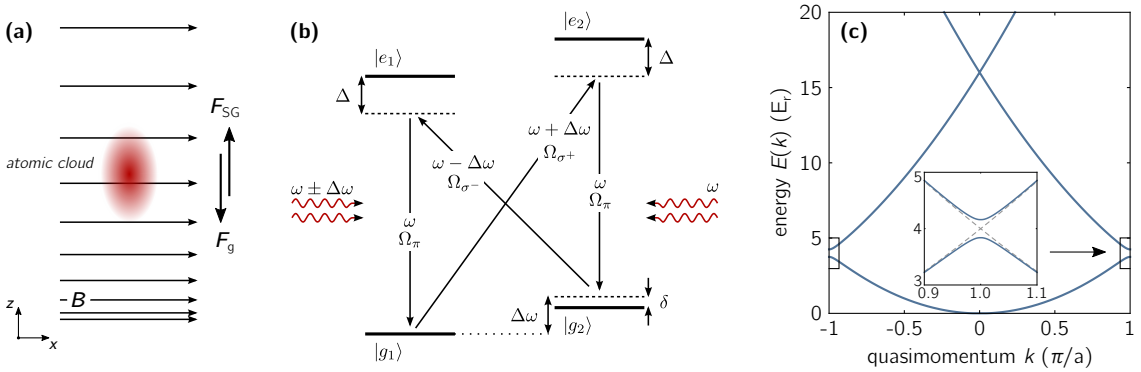

Figure 8.5.: (a) Schematic of the atomic cloud in the presence of the quadrupole field $\mathbf{B}$. While the gracitational force $\mathbf{F}_\mathrm{g}$ pulls the cloud downwards, an emergent 'Stern-Gerlach force' $\mathbf{F}_\mathrm{SG}$ compensates for this effect (see text). (b) Four-photon scheme for generating the spatially dependent optical lattice. Here, $(\Delta, \delta, \Delta\omega)$ denote detunings, and Ω indicate respective Rabi frequencies. Figs. (a) and (b) are adopted from Ref. [321]. (c) First few energy bands (blue solid) as resulting from Hamiltonian $H(k)$, see Eq. (8.29), for $V_0 = 1E_r$. The inset shows how the Diract point for $V_0 = 0$ (gray dashed) is gapped out by the presence of the additional potential.

given by $a = \lambda/4$, which is by a factor 2 smaller than conventional two-photon optical lattices with lattice spacing $\lambda/2$. One can further show [321] that the strength of the resulting potential is given by $V_0 = \hbar\Omega^+_\mathrm{eff}\Omega^-_\mathrm{eff}/\delta_0$, i.e., is proportional to the product of both effective Rabi frequencies, $\Omega^\pm_\mathrm{eff} = \Omega_{\sigma^\pm}\Omega^*_\pi/2\Delta$, coupling the respective ground states to virtual excited states and is inversely proportional to the Raman detuning from the $m_F = 0$ ground state, $\delta_0 \simeq 200\mathrm{kHz}$. Using experimental parameters this potential strength can be calculated to be $V_0 \simeq 0.36E_r$, with $E_r = \hbar^2 k_0^2/(2m)$ being the recoil energy. The spatially varying effective one-dimensional potential then takes the form

$$V(z) = \frac{V_0}{2}\cos\left(4k_0 z + \varphi_z\right), \tag{8.28}$$

where the phase shift corresponds to spatial translation of the lattice with respect to a reference point, and will be set to zero form here on, $\varphi_z = 0$. The associated reciprocal lattice vector of Eq. (8.28) is given by $G = 4k_0$. The corresponding single-particle Hamiltonian $H = -\hbar^2\partial_z^2/2m + V(z)$ can then be expressed in the basis of plane waves $\{e^{-i(k+lG)z}\}$ with $k \in [-\pi/a, \pi/a)$ and $l \in \mathbb{Z}$. The respective matrix elements read as

$$H_{ll'}(k) = \frac{\hbar^2}{2m}\left(k + l\,G\right)^2\delta_{ll'} + \frac{V_0}{4}\left(\delta_{l,l'-1} + \delta_{l,l'+1}\right). \tag{8.29}$$

A sensible truncation allows for the diagonalisation of the Hamiltonian (8.29), yielding an energy spectrum as depicted for the first few bands in Fig. 8.5(c). We focus now on the two lowest bands at the edge of the Brillouin zone, $k = -\pi/a\,(\pi/a)$. One realises that if the off-diagonal elements of Hamiltonian (8.29) are small compared to the band width of the lowest band, $V_0/4 \ll \hbar^2G^2/(8m)$, the system is described to a good approximation by the degenerate subspace of those two bands (cf. Sec. 3.2.3). By letting $k = \tilde{k} - G/2$, with $|\tilde{k}|/G \ll 1$ one can rewrite the Hamiltonian (8.29) as (where $l, l' \in \{-1, 0, 1\}$ for reasons of readability)

$$H(k) = \begin{pmatrix} \frac{\hbar^2}{2m}(k+G)^2 & \frac{V_0}{4} & 0 \\ \frac{V_0}{4} & \frac{\hbar^2}{2m}k^2 & \frac{V_0}{4} \\ 0 & \frac{V_0}{4} & \frac{\hbar^2}{2m}(k-G)^2 \end{pmatrix} \quad \rightarrow \quad \widetilde{H}(\tilde{k}) = \begin{pmatrix} \frac{\hbar^2 G}{2m}\tilde{k} & \frac{V_0}{4} \\ \frac{V_0}{4} & -\frac{\hbar^2 G}{2m}\tilde{k} \end{pmatrix}, \tag{8.30}$$

where in the expression on the right-hand side we ignored the constant energy shift $\hbar^2 G^2/(8m) = 4E_r$ as well as all terms $\mathcal{O}(\tilde{k}^2)$. In addition, by introducing the new momentum variable $q = \hbar\tilde{k}$, the effective velocity $c_{\text{eff}} = G\hbar/(2m) = 2\hbar k_0/m \simeq 1.1\, cm\, s^{-1}$ and an effective mass $m_{\text{eff}} = V_0/(4c_{\text{eff}}^2)$ the right-hand side of Eq. (8.30) becomes

$$H_{\text{D}}(q) = m_{\text{eff}}\, c_{\text{eff}}^2\, \sigma_x + q\, c_{\text{eff}}\, \sigma_z\,. \tag{8.31}$$

So indeed, close to the edges of the first Brillouin zone, where the lowest and second lowest band interfere, one can describe the system effectively in terms of a Dirac Hamiltonian of type (8.14), but with *homogeneous* mass for the current setup.

B-field gradient In order to implement the spatial dependency of the effective mass in the Dirac Hamiltonian (8.31) the characteristics of the four-photon optical lattice outlined above are exploited. Here, one needs to realise that the potential which is inversely proportional to the Raman detuning δ_0 can be shifted by means of magnetic fields. To achieve the effective mass with the desired properties given by Eq. (8.12) one superimposes *two* four-photon potentials $V_1(z), V_2(z)$ in the presence of the above mentioned quadrupole field to compensate the Earth's gravitational field. The initial respective Raman detunings $\delta_{1/2}$ are chosen to be the same in magnitude for both lattices but with opposite sign. On top of that, both detunings get an equal correction from the magnetic field gradient, yielding $\delta_{1/2} = \pm\delta_0 - \mu_B \Delta B(z)/(2\hbar)$. Here, the magnetic field is assumed to change linearly as a function of space in the desired region, i.e., $\Delta B(z) = B(z) - B(0) \simeq z\, dB/dz$. The amplitude of the respective lattice potential is then given as

$$V_{1/2,0}(z) = \frac{\hbar\Omega_{\text{eff}}^{+}\Omega_{\text{eff}}^{-}}{\delta_{1/2}} \approx \pm V_0 + 2\frac{V_0\mu_B}{4\hbar\delta_0}\frac{dB}{dz}\, z + \mathcal{O}(z^3) \approx \pm V_0 + 2\alpha z\,, \tag{8.32}$$

where one expanded the expression to first order around $z = 0$, and in the last step we defined $\alpha = V_0\mu_B(dB/dz)/(4\hbar\delta_0) \simeq 19.0\text{E}_\text{r}\text{cm}^{-1}$. The full lattice is again given by Eq. (8.28), but here we replace $V_0 \to (V_1(z) + V_2(z)) = 4\alpha z$, i.e., $V(z) = 2\alpha z \cos(4k_0 z)$. Since spatially homogeneous parts of $V_{1/2}$ vanish by construction, the total lattice potential experiences a zero crossing at $z = 0$. The total as well as the individual lattices are depicted in Fig. 8.6, where it can also be seen that for $z > 0$ ($z < 0$) the maxima (minima) of the total potential are located at integer multiples of $\lambda/4$.

Most crucially, upon replacing $V_0 \to 4\alpha z$ in Eq. (8.30) one finds that the Dirac Hamiltonian (8.31) acquires an effective mass as

$$m_{\text{eff}} \;\to\; m_{\text{eff}}(z) = \alpha z/c_{\text{eff}}^2\,, \tag{8.33}$$

hereby realising a system that can indeed be effectively described by the one-dimensional Dirac equation with spatially varying mass of Eq. (8.14). Note since we assume weak magnetic fields, also the effective mass changes slowly as a function of space. Therefore, one can indeed analyse the problem at a given point in space z_0 by considering the bandstructure for an associated fixed effective mass $m_{\text{eff}}(z) \approx m_{\text{eff}}(z_0)$, see Fig. 8.6(b). The two-component Hamiltonian (8.31) with $m_{\text{eff}}(z)$ then acts on spinors of the form $\psi(z) = \big(\Psi_1(z), \Psi_2(z)\big)^T$. Here, Ψ_1 and Ψ_2 are understood to correspond to wavefunctions of atoms with momenta close to $\pm\hbar G/2 = \pm 2\hbar k_0$. The spatial representation of the total wavefunction associated with the spinor ψ is then given by

$$\phi(z) = \Psi_1(z)\, e^{2ik_0 z} + \Psi_2(z)\, e^{-2ik_0 z}\,. \tag{8.34}$$

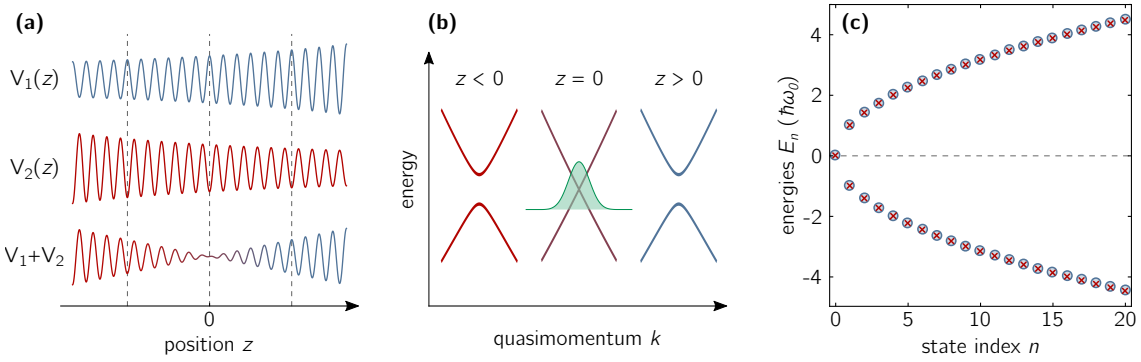

Figure 8.6.: (a) Resulting potentials $V_{1/2}(z)$ from the four-photon processes shown in Fig. 8.5(b). The increasing (decreasing) behaviour of the respective lattice depth for increasing z is due to a positive (negative) Raman detuning, see Eq. (8.32). The combined potential, $V_1 + V_2$, yields a zero crossing. (b) Illustration of the spatial variation of the lowest two bands near the (gapped) Dirac point (cf. Fig. 8.5). The shown bands can be seen as representations of vertical cuts in Fig. 8.4(c). (c) The eigenvalues of the microscopic 1D Hamiltonian (circles) close to the band crossing agree with a precision higher than 1% with the energies (crosses) of the Dirac equation given by Eq. 8.26.

Furthermore, using the expression for the Dirac spectrum (8.26) one expects the experimental system to possess a characteristic frequency of about $\omega_0 \simeq 163\,\mathrm{Hz}$. Even for the cold atom setup at hand this is a rather small energy scale, $\omega_0/E_r \approx 0.04$, and therefore the experiment appears to be highly sensitive to noise, particularly to fluctuations in the magnetic field. Thus, in order to suppress this respective noise the experiment is placed within a single layer μ-metal shielding.

We stress again that the presented effective description of the system only holds for atoms that have been prepared in momentum states close to the edge of the Brillouin zone. In fact, we have numerically checked[3] that the spectrum of the full 1D Hamiltonian, $H = -\hbar^2\partial_z^2/2m + V(z)$, coincides with the Dirac one of Eq. (8.26) for the first twenty states or so $n \lesssim 20$, see Fig. 8.6. The reason for this good agreement is the fact that the width of the most confined bound state, i.e., the topological edge state, $l_\mathrm{D} \simeq 16.2\,\mu\mathrm{m}$ is of about two orders of magnitude larger than the lattice spacing $a \simeq 196\,\mathrm{nm}$. This guarantees that relevant momenta are small. Nevertheless, one should bear in mind that the system only simulates the spatially-dependent Dirac Hamiltonian (8.12), and that the relevant chiral symmetry of the latter is only *emergent* and not a true symmetry of the (experimental) system.

8.2.3. Experimental procedure: preparation and detection

While tailoring the lattice potential as presented above leads to an effective description in terms of an Dirac Hamiltonian of type (8.14), the system at hand does not naturally occupy the desired quantum states at the edge of the Brillouin zone. Hence, the rubidium BEC needs to be engineered in an appropriate way in order to allow for the targeted effective description. We continue to briefly summarize the engineering process in this section. A more in-depth description can be found in Refs. [53, 321].

After the production of the BEC as sketched above, the cloud is adiabatically expanded in the z-direction. The reason for this is that the ultimate population of the simulated

[3] Technically, this was done by using box potential eigenfunctions of form $\sqrt{\frac{2}{L}}\sin[\frac{m\pi}{L}(z+\frac{L}{2})]$, with $m \in \mathbb{Z}$, and ensuring that results are stable under enlarging the box size, $L \to \infty$.

topological edge state at (shifted) energy $E = 0$ is maximised by spatial matching of the respective wavefunctions. Technically, the expansion is performed by further lowering the dipole trapping beam. At the end of the sequence, the atomic cloud is composed of $\sim 10,000$ atoms and has a typical spatial extension in the vertical direction of about $\Delta z_{\mathrm{rms}} \sim 10\mu$m. This compares to the root mean square (rms) width of the edge state of $\Delta z_0 = l_{\mathrm{D}}/\sqrt{2} \simeq 11.5\mu$m. At the end of the adiabatic expansion, the trapping frequency along this lattice beam axis is $\omega_z/2\pi \simeq 4$Hz, and magnetic trapping frequencies in orthogonal directions are $\omega_x/2\pi \simeq 28.5$Hz and $\omega_y/2\pi \simeq 10$Hz. The associated momentum width of the atomic cloud along the lattice beam axis is determined to be $\Delta p_z \simeq 0.01\hbar k_0$. This corresponds to an effective (1D) temperature of about 35pK. After these first steps of preparation, the cloud of atoms in z-direction is described by the corresponding part of the wavefunction, $\phi_a(z)$.

Following the adiabatic expansion of the BEC, the dipole trapping beam is extinguished and the atoms are irradiated with the laser light creating the periodic potential of form (8.28). Most importantly, at the same time the atoms are also subject to two simultaneously performed Bragg pulses of opposite direction (for more details on this Bragg-pulse technique, see Ref. [339]). These pulses imprint a momentum transfer of $\pm G/2 = \pm 2k_0$ onto the rubidium atoms. Therefore, the initialised wavefunction in z-direction ϕ_i reads as

$$\phi_i(z) = \frac{1}{\sqrt{2}}\,\phi_a(z)\left(e^{2ik_0 z} + e^{-i\varphi}\,e^{-2ik_0 z}\right), \tag{8.35}$$

with φ being a phase shift that can be conveniently imprinted by an appropriate adjustment of the Bragg pulses. After the momentum transfer, the wavefunction (8.35) can indeed be understood in terms of an associated spinor $\psi_i(z) = \left(\Psi_1, \Psi_2\right)^T$, which is acted on by the Dirac Hamiltonian (8.14), with $\Psi_1 = e^{i\varphi}\Psi_2 = \phi_a(z)/\sqrt{2}$. Eventually, the experimental system should therefore follow the physics predicted by the set of eigenstates and eigenenergies presented in Sec. 8.2.1. Here, the detailed occupation of the eigenstates is determined by the spatial shape of the initial cloud as well as the phase shift φ. We assume a spatially symmetric initial cloud with respect to the zero crossing of the lattice at $z = 0$, see Fig. 8.6(a). By comparing the emerging structure of ψ_i with the explicit form of the eigenstates, see Eq. (8.23), it is apparent that a maximal population of the edge state can only be obtained for $\varphi = \pi/2$. In contrast, for $\varphi = -\pi/2$ the overlap with ψ_0 is nullified, and, in fact, also for all other spinor eigenstates ψ_n with $n/2 \in \mathbb{N}$. Instead, eigenstates with odd indices n are populated according to the spatial shape of ϕ_a. Note that a symmetric initial cloud generally populates all $\pm$-pairs of eigenspinors equally. So, ultimately, the experimental verification of the edge state is achieved by comparing dynamical evolutions of the system depending on the initial preparation parameter φ: while atoms occupying the zero energy state are expected to remain pinned as time evolves, an equal population of, e.g., the first excited states leads to a subsequent detectable beating of the density profile of frequency $2\omega_0$, see Sec. 8.4.

The detection of the atomic cloud following the interaction with the optical lattice is done by recording a shadow image of such. This procedure images the spatial distribution of the cloud in the xz-plane, $n(x, z)$. The final image is obtained by standard absorption imaging techniques in the absence of the lattice beams [53]. Note that the size of the recorded cloud along the x-axis is dominated by the spatial resolution of 4.8μm of the used imaging system.

Lastly, we note the following crucial aspect: the rubidium atoms used in the experiment are *bosons*, while the Dirac Hamiltonian naturally describes the dynamics of fermions. In a purely non-interacting case those two descriptions are similar. However, the situation

changes fundamentally once interactions are taken into account. Since the rubidium BEC is indeed a (weakly) interacting many-particle system they *cannot* be blindly ignored, but rather have to be analysed in detail. In the same spirit, it is not directly obvious whether the effective one-dimensional description discussed here is sufficient to correctly capture the physics of the 3D cloud. Nevertheless, we will show in the next section that in the end interaction effects are negligible to good approximation, and thus the effective 1D formalism presented here is indeed applicable.

8.3. Mean-field interaction effects and theoretical predictions

So far all interaction effects have been neglected. Nevertheless, in typical experiments with ultracold bosonic atoms captured in harmonic traps interactions *cannot* be simply ignored. Due to small densities of atoms (see Sec. 2.1), interactions are typically treated well by a mean-field description in terms of the celebrated *Gross-Pitaevskii equation* (GPE) [340–342], see below. So before showing experimental results as well as theoretical interpretations of the simulated Dirac Hamiltonian, we will thoroughly study mean-field interaction effects in this section by analysing the corresponding Gross-Pitaevskii equation as well as an effective Dirac version thereof. Later, in chapter 9 we will go beyond this mean-field approach and show effects that are unique to the realisation of the Dirac Hamiltonian (8.12) with an interacting bosonic gas of cold atoms.

Bose-Einstein condensation was the first milestone reached in the field of ultracold atoms [58, 59]. Ever since these accomplishments were reported in the mid 90's, ultracold (bosonic) degenerate quantum gases have been the major building block of an entire generation of novel types of experiments, see Sec. 2.1. There exist an extensive list of comprehensive studies of Bose-Einstein condensation both in general as well as addressing the role of interactions. Thus, we refrain from presenting a detailed analysis of the effects of interactions in BECs, but rather highlight aspects that are relevant to the specific experimental setup presented in this chapter, see above. For more details, though, the reader is referred to, e.g., Refs. [343–347], and references within.

8.3.1. The Gross-Pitaevskii equation

Ultracold atoms typically only exhibit s-wave scattering due to low thermal energies of the particles. The system of N particles is well described in these situations by the following many-body Hamiltonian [343]

$$H = \int d\mathbf{r}\ \hat{\Psi}^\dagger(\mathbf{r})\Big[-\frac{\hbar^2}{2m}\nabla^2 + V_{\text{ext}}(\mathbf{r})\Big]\hat{\Psi}(\mathbf{r}) + \frac{g}{2}\,\hat{\Psi}^\dagger(\mathbf{r})\hat{\Psi}^\dagger(\mathbf{r})\hat{\Psi}(\mathbf{r})\hat{\Psi}(\mathbf{r})\,, \tag{8.36}$$

where $\hat{\Psi}^\dagger(\mathbf{r})$ and $\hat{\Psi}(\mathbf{r})$ are bosonic field operators that create and annihilate a particle at position $\mathbf{r}$, respectively, and

$$V_{\text{ext}}(\mathbf{r}) = \frac{m}{2}(\omega_x^2 x^2 + \omega_y^2 y^2 + \omega_z^2 z^2) \tag{8.37}$$

being the external harmonic confining potential. Furthermore, $g = 4\pi\hbar^2 a_s/m$ is the interaction strength parametrized by the s-wave scattering length a_s. For the rubidium isotope ^{87}Rb this scattering length is given by $a_s \approx 100 a_0$, where $a_0 = 5,29\times10^{-11}$m describes the Bohr radius. The Hamiltonian (8.36) therefore also describes the system at hand after the adiabatic expansion discussed above, see Sec. 8.2.3, with associated harmonic trapping frequencies ω_x, ω_y and ω_z.

Next, it is assumed that the population of a certain single-particle state is very large $N_0 \gg 1$, and that indeed the majority of the particles condense in this state, $N_0/N \sim 1$. One can then write the field operator in its Heisenberg form approximately as $\hat{\Psi}(\mathbf{r},t) \simeq \Phi(\mathbf{r},t) + \delta\hat{\Psi}(\mathbf{r},t)$, with $\delta\hat{\Psi}$ being a small perturbation. Impoartantly, $\Phi(\mathbf{r},t)$ is a complex function that is defined as the expectation value of the field operator, $\Phi(\mathbf{r},t) \equiv \langle\Psi(\mathbf{r},t)\rangle$ [344]. The aim is then to determine an equation of motion for the classical field Φ. One way[4] to proceed is to use the Heisenberg equation of motion and subsequently replace all field operators $\hat{\Psi}$ by its classical counter part Φ. Letting $\Phi(\mathbf{r},t) = \sqrt{N}\phi(\mathbf{r},t)$, with $\int d\mathbf{r}|\phi(\mathbf{r},t)|^2 = 1$, one finally finds the time-dependent Gross-Pitaevskii equation [340–344]

$$i\hbar\,\partial_t\phi(\mathbf{r},t) = \Big[-\frac{\hbar^2}{2m}\nabla^2 + V_{\text{ext}}(\mathbf{r}) + gN\,\big|\phi(\mathbf{r},t)\big|^2\Big]\,\phi(\mathbf{r},t)\,. \tag{8.38}$$

Again, the validity of this equation is controlled by the condition that the s-wave scattering length ought to be much smaller than the average distance between atoms, and that the number of atoms in the condensate is much larger than one [344]. If these conditions are fulfilled, Eq. (8.38) describes powerfully the dynamics of the BEC in its ground state.

In order to determine this ground state, one makes the ansatz $\phi(\mathbf{r},t) = e^{-i\mu t/\hbar}\phi(\mathbf{r})$, where μ is the chemical potential and $\phi(\mathbf{r})$ is now a real function that is still normalised to unity. By substituting this ansatz into Eq. (8.38) one obtains the static GPE [343,344]

$$\Big[-\frac{\hbar^2}{2m}\nabla^2 + V_{\text{ext}}(\mathbf{r}) + gN\,\big|\phi(\mathbf{r})\big|^2\Big]\,\phi(\mathbf{r}) = \mu\,\phi(\mathbf{r})\,. \tag{8.39}$$

In general, this time-independent Schrödinger-like equation can only be solved numerically due to the *nonlinear* term proportional to the particle density. Nonetheless, one can analytically investigate the two limits of $g \to 0$ and $gN \to \infty$: if the interaction strength vanishes, $g = 0$, Eq. (8.39) obviously reduces to the Schrödinger equation of a single-particle. Hence, with the form of the external potential given in Eq. (8.37) the problem simply becomes a three-dimensional harmonic oscillator. The ground state wavefunction of the BEC in such a scenario is therefore proportional to a Gaussian wavepacket

$$\phi_0^{\text{ho}}(\mathbf{r}) \propto \exp\Big[-\frac{m}{2\hbar}(\omega_x x^2 + \omega_y y^2 + \omega_z z^2)\Big]\,. \tag{8.40}$$

On the other hand, in the limit of very large N the nonlinear term in Eq. (8.39) dominates over the kinetic term (except at the edges of the cloud). Thus, the density profile (normalised to N) is approximately given by $n(\mathbf{r}) = N|\phi(\mathbf{r})|^2 = \frac{1}{g}[\mu - V_{\text{ext}}(\mathbf{r})]$ for the region where $\mu > V_{\text{ext}}(\mathbf{r})$ and $n(\mathbf{r}) = 0$ everywhere else. This situation is also called the Thomas-Fermi limit.

8.3.2. An effective 1D Gross-Pitaevskii-Dirac equation

Right before the optical lattice is switched on and the atoms are irradiated with Bragg pulses, the atomic cloud in its harmonic trap is described by the GPE (8.38) or (8.39), respectively. As for the non-interacting case, we will now show that also the interacting system is effectively described by an emergent Hamiltonian *after* the optical beams are switched on. To this end, we assume that after the two Bragg pulses have imprinted a momentum change of $\pm 2k_0\hbar$ in z-direction the wavefunction of the BEC can be written as (cf. Eq.(8.34))

$$\phi(\mathbf{r},t) = \Psi_1(\mathbf{r},t)\,e^{2ik_0 z} + \Psi_2(\mathbf{r},t)\,e^{-2ik_0 z}\,, \tag{8.41}$$

[4] A different approach is to proceed by some variational procedure with respect to the energy functional. In this case, the Gross-Piaevskii equation coincides with the Euler-Lagrange equation for the respective problem [343].

where again a spinor ψ associated with the wavefunction ϕ is defined as

$$\psi(\mathbf{r},t) = \Big(\Psi_1(\mathbf{r},t), \Psi_2(\mathbf{r},t)\Big)^T . \tag{8.42}$$

Here, the normalisation condition $\int d\mathbf{r}|\psi(\mathbf{r})| = 1$ holds. Note that in the following we will drop the time variable for notational convenience. Upon substituting this ansatz for the wavefunction into expression (8.38), the *non-interacting* part of the GPE becomes

$$\Big[-\frac{\hbar^2}{2m}\nabla^2 + V_{\mathrm{ext}}(\mathbf{r})\Big]\,\phi(\mathbf{r}) \quad \rightarrow \quad \Big[H_\perp^{\mathrm{ho}}\,\mathbb{1} + H_{\mathrm{D}}\Big]\,\psi(\mathbf{r}) \tag{8.43}$$

which is just a reformulation of the non-interacting part of the Hamiltonian in each spatial direction in terms of the two-dimensional harmonic oscillator Hamiltonian

$$H_\perp^{\mathrm{ho}} = \Big[-\frac{1}{2m}(\partial_x^2 + \partial_y^2) + \frac{m}{2}(\omega_x^2 x^2 + \omega_y^2 y^2)\Big] \tag{8.44}$$

and of the Dirac Hamiltonian H_{D} given by Eq. (8.14) describing the non-interacting dynamics in z-direction. Note that if there were no interactions, the wavefunctions Ψ_1, Ψ_2 would factorize into parts corresponding to each spatial direction, e.g., $\Psi_1(\mathbf{r}) = \Psi_1(x)\Psi_1(y)\Psi_1(z)$. Here, every part of the wavefuntion could be efficiently expressed in eigenstates associated with the respective spatial direction, i.e., harmonic oscillator states in xy-direction and eigenstates of type (8.25) in z-direction. Such a straightforward decomposition is, however, not readily allowed, since interactions couple the dynamics along orthogonal spatial directions.

Using Eq. (8.41) the nonlinear *interaction* part of the Gross-Pitaevskii equation can be written as

$$\begin{aligned}\big|\phi(\mathbf{r})\big|^2\,\phi(\mathbf{r}) &= \big(\big|\Psi_1\big|^2 + \big|\Psi_2\big|^2 + \Psi_1^*\Psi_2\,e^{-4ik_0z} + \Psi_2^*\Psi_1\,e^{4ik_0z}\big)\big(\Psi_1\,e^{2ik_0z} + \Psi_2\,e^{-2ik_0z}\big)\\ &\approx \big(\big|\Psi_1\big|^2 + 2\big|\Psi_2\big|^2\big)\Psi_1\,e^{2ik_0z} + \big(\big|\Psi_2\big|^2 + 2\big|\Psi_1\big|^2\big)\Psi_2\,e^{-2ik_0z}\,,\end{aligned} \tag{8.45}$$

where we neglected all contributions to the parenthesis proportional to $e^{\pm 4ik_0z}$. This is justified since large transfers of momenta are suppressed, i.e., the overlap of a spatially smooth with a fast oscillating function averages to zero. Thus, we can represent the interaction term after the Bragg pulses as

$$\big|\phi(\mathbf{r})\big|^2\,\phi(\mathbf{r}) \quad \rightarrow \quad \begin{pmatrix}\big|\Psi_1\big|^2 + 2\big|\Psi_2\big|^2 & 0\\ 0 & \big|\Psi_2\big|^2 + 2\big|\Psi_1\big|^2\end{pmatrix}\psi(\mathbf{r})\,. \tag{8.46}$$

Merging Eqs. (8.43) and (8.46) renders an effective description of an interacting BEC that is close to momenta $\pm 2\hbar k_0$. The resulting *Gross-Pitaevskii-Dirac equation* (GPDE) eventually takes on the form

$$i\hbar\partial_t\psi(\mathbf{r},t) = \Big[H_\perp^{\mathrm{ho}} + H_{\mathrm{D}} + \frac{gN}{2}\Big(3\,|\psi(\mathbf{r},t)|^2\,\mathbb{1} - \big(\psi^\dagger(\mathbf{r},t)\,\sigma_z\,\psi(\mathbf{r},t)\big)\,\sigma_z\Big)\Big]\,\psi(\mathbf{r},t)\,. \tag{8.47}$$

In order to estimate the importance of interaction effects on the dynamics of the effective Dirac system, and thus letting Eq. (8.47) become more accessible to a numerical analysis, we continue by making a crude assumption: we presume that the wavefunction (8.41) does indeed factorize as

$$\phi(\mathbf{r}) = \phi_\perp(x,y)\,\phi(z) = \phi_{\perp,0}^{\mathrm{ho}}(x,y)\,\phi(z)\,. \tag{8.48}$$

Most importantly, here we assume that in perpendicular direction the condensate is trapped in the *ground state* of the harmonic oscillator described by Eq. (8.44). The

trapping frequencies of this harmonic oscillator are still given by $\omega_x/2\pi = 28.5$Hz and $\omega_y/2\pi = 10$Hz, respectively. The Dirac spinor associated with the wavefunction (8.48) is then given by

$$\psi(\mathbf{r}) = \phi^{\mathrm{ho}}_{\perp,0}(x,y) \times \Big(\Psi_1(z), \Psi_2(z)\Big)^T = \phi^{\mathrm{ho}}_{\perp,0}(x,y) \times \psi(z)\,. \tag{8.49}$$

Formally, this assumption is correct in the limit where the energy scale of the perpendicular harmonic oscillator is much larger than the characteristic frequency of the Dirac spectrum, i.e., $\min(\omega_x, \omega_y) \gg \omega_0 = \sqrt{2c_{\mathrm{eff}}\alpha/\hbar}$. In fact, this is *not* the case for the described experimental setup, where $\omega_0/2\pi \approx 163$Hz. We note, however, that the approximation (8.48) overestimates interaction effects, since it neglects their importance for the perpendicular directions leading to an underestimated size of the wavefunction in those directions. While this treatment can therefore not be used to give precise quantitative predictions, it is still sufficient to estimate an upper bound on the interaction effects.

Time-dependent GPDE

After having made an ansatz for the wavefunction, we substitute (8.49) into the GPDE (8.47) and multiply from the left by $(\phi^{\mathrm{ho}}_{\perp,0})^*$. This is followed by an integration over the x- and y-direction. Due to the spatial decoupling of Eqs. (8.48) and (8.49) these integrals can be trivially evaluated. By using the identities $\int dxdy\, |\phi^{\mathrm{ho}}_{\perp,0}|^2 = 1$ and $\int dxdy\, |\phi^{\mathrm{ho}}_{\perp,0}|^4 = (2\pi l_x l_y)^{-1}$ one obtains an *effective one-dimensional* GPDE of the form

$$i\hbar\partial_t\psi(z,t) = H_{\mathrm{D}}\,\psi(z,t) + g^{1\mathrm{d}}\left[\,3\,|\psi(z,t)|^2\,\mathbb{1} - \big(\psi(z,t)^\dagger\sigma_z\psi(z,t)\big)\,\sigma_z\,\right]\psi(z,t)\,, \tag{8.50}$$

where $g^{1\mathrm{d}} = gN/(4\pi l_x l_y)$ describes the effective one-dimensional interaction strength with $l_{x/y} = \sqrt{\hbar/(m\omega_{x/y})}$ being the respective harmonic oscillator length. Note also that the constant energy shift due to $\int dxdy\,(\phi^{\mathrm{ho}}_{\perp,0})^* H^{\mathrm{ho}}_\perp \phi^{\mathrm{ho}}_{\perp,0}\psi = E_\perp\psi$ was 'gauged away' by letting $\psi(t) \to \psi(t)e^{-iE_\perp t/\hbar}$.

One can now study Eq. (8.50) with relatively little numerical afford (e.g., by a built-in function of the programme *Mathematica*). Fig. 8.7 shows the dynamical evolution of the density profile[5], $n(z) = |\psi(z,t)|^2$, of differently prepared initial atomic clouds and for varying interaction strengths $g^{1\mathrm{d}}$. As explained in Sec. 8.2.3, the atomic cloud is initially expanded adiabatically to match the Gaussian envelope of the topological edge state given by Eq. (8.27). Hence, we choose an initial state with spatial profile given by $\phi_a(z) = \phi^{\mathrm{ho}}_0(z)$ and investigate two distinct relative phases imprinted by the Bragg pulses, $\varphi^\alpha = \pi/2$ and $\varphi^\beta = -\pi/2$, respectively. The two studied initial states are thus $\psi^\alpha_i(z) = \psi_0(z)$ and $\psi^\beta_i(z) = -\frac{i}{\sqrt{2}}(\psi^+_1(z) + \psi^-_1(z))$, respectively, where ψ_i is the spinor associated with the initial wavefunction $\phi_i(z)$, see Eq. (8.35), and $\psi^\pm_n(z)$ are eigenstates of the non-interacting Dirac problem, see Sec. 8.2.1. The system's behaviour in the non-interacting limit, $g \to 0$, is shown in Figs. 8.7(a) and (d): if the system is already prepared in the edge state, it will remain static as a function of time. In contrast, if the state is prepared as a pair of first excited states, it will show a clean beating pattern with an oscillation period of $T = \pi/\omega_0 \approx 3$ms.

The situation obviously changes when interactions are taken into account. The experiment is typically conducted with $\sim 10,000$ rubidium atoms [53], which leads to an

[5] In fact, in Fig. 8.7 we only plot $|\Psi_1(z)|^2 + |\Psi_1(z)|^2$, since rapidly oscillating interference fringes arising from $2\mathrm{Re}[\Psi^*_1(z)\Psi_2(z)e^{-4ik_0 z}]$ cannot be resolved within the experimental resolution.

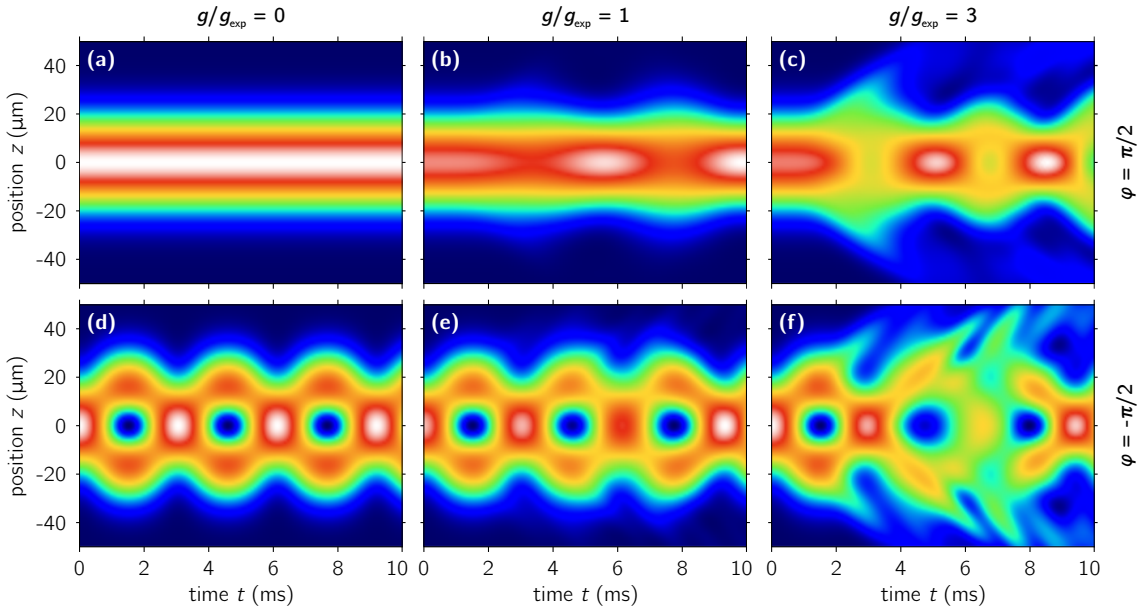

Figure 8.7.: Time evolution of a one-dimensional cloud of atoms according to the time-dependent Gross-Pitaevskii-Dirac equation, see Eq. (8.50). Interaction strength increases from left to right, $g/g_{\mathrm{exp}} = 0, 1, 3$. (a)-(c) Relative phase imprint of $\varphi = \pi/2$ (see Eq. (8.35)) allowing for a population of the zero energy state. (d)-(f) An equal superposition of first excited states $\psi_1^{\pm}$ initialised by choosing $\varphi = -\pi/2$ causes an oscillatory behaviour of the cloud. Interaction effects for experimentally expected interaction strengths appear to be negligible.

associated effective interaction strength of $g_{\mathrm{exp}}^{\mathrm{1d}}/\hbar \approx 5.6 \times 10^{-3}\mathrm{m/s}$. However, when considering this experimental value, interactions only seem to have a negligible impact on the density's time evolution, as can be seen from Figs. 8.7(b) and (d). Over the time scale of 10ms one can only witness a small amount of newly emerging beatings for an initial state ψ_i^{α}. If the system is initially prepared in the state ψ_i^{β}, one observes a shift in the beating frequency that is also tiny in size. Importantly, the actual experiment can only be run for times of about $\sim$2ms, see Sec. 8.4. For such small time scales the results show indeed no observable effect that could be resolved experimentally, see Fig. 8.7. Again, recall that these discussed interaction effects are already overestimated and that the true experimental signatures are expected to be even smaller.

Nonetheless, when increasing the interaction strength further, e.g., by trapping more atoms or increasing the scattering length by means of Feshbach resonances (see Sec. 2.1), the time evolution starts to behave non-trivially, In Figs. 8.7(c) and (f) we show, for example, interaction strengths that are three times larger than used in the experiment. Despite the fact that interactions still seem to play a minor role during the first beating period, they do become dominant very quickly. Already for $g/g_{\mathrm{exp}} = 3$ and $t > 2$ms the dynamics of the system cannot be straightforwardly explained by the non-interacting Dirac Hamiltonian any more.

Stationary GPDE

Complementary to the approach of solving the time-dependent GPDE (8.50), one can also solve a stationary energy eigenvalue problem in the spirit of Eq. (8.39) in order to find the ground state of the problem. To this end, we make a similar ansatz as above, i.e., $\psi(z,t) = e^{-i\mu t/\hbar}\psi(z)$. Substituting this expression into Eq. (8.50) then gives rise to the

time-independent one-dimensional Gross-Pitaevskii-Dirac equation of the from

$$H_{\mathrm{D}}\,\psi(z) + g^{1\mathrm{d}}\left[\,3\,|\psi(z)|^2\,\mathbb{1} - (\psi^\dagger(z)\sigma_z\psi(z))\,\sigma_z\,\right]\psi = \mu\,\psi(z)\,. \tag{8.51}$$

Note that the notion 'ground state' is actually quite delicate here: by ground state we refer to the state that is adiabatically (in the interaction strength) connected to the zero-energy state of the non-interacting system. However, the zero-energy state is in fact *not* a true ground state of the system. While for fermions the system might still be stabilized by Pauli blocking, this fact leads to an immediate qualitative effect of interactions in the present case: the bosonic system, which is unbound from below, is intrinsically *unstable*. To investigate this instability we study the Bogoliubov spectrum describing the fluctuations around the stationary solution of the GPDE in chapter 9. We indeed find a pairwise decay of atoms into higher and lower levels of same, but opposite energy differences. However, the rates of this decay channel are on the per cent level of the typical oscillation frequency ω_0, see Sec. 9.3. Moreover, spontaneous decay of the condensate into lower lying states is suppressed on the mean-field level due to energy conservation. These circumstances indeed allow us to straightforwardly proceed with an analysis of Eq. (8.51).

In order to numerically solve Eq. (8.51) we apply a standard iterative self-consistency loop: first we prepare a test state $\psi^{s=0}$ being a randomly chosen combination of ψ_0 and $\psi_1^\pm$, where s denotes the step index. We then express the GPDE of Eq. (8.51) in the basis of non-interacting Dirac eigenstates $\psi_n^\pm$ and numerically diagonalise the resulting matrix. Here, we check that results are unaffected by the truncation size given by some maximal index value $n_{\max}$. We then select the eigenstate associated with the eigenvalue lying in the center of the obtained spectrum and identify this state with $\psi^{s=1}$. We repeat this procedure until we reach the condition $(1-|\,\langle\psi^s|\psi^{s-1}\rangle\,|) < \epsilon$, where $\epsilon \ll 1$ is a threshold set by hand (with typical values of 10^{-7}). When performing this self-consistency loop, it is possible that the evaluation gets trapped in some subspace of the space of solutions, which prohibits convergence of the finial state. This behaviour can either be a numerical artefact of the used procedure or might happen due to construction. The latter aspect is mainly related to symmetry arguments. Note that owing to the identity matrix appearing in the interacting part of Eq. (8.51) conventional SU(2) symmetries (such as the chiral symmetry of Eq. (8.4)) are destroyed by the GPDE. However, the basis of Dirac states that we use to solve the problem has the mentioned symmetry naturally encoded, which potentially constrains the space of attainable solutions. To circumvent associated issues we do the following: first, we choose a random initial state configuration as mentioned above. Second, we admix a previously calculated state at step $s-1$ to the current state at step s, i.e., $\psi^s = c\psi^s + (1-c)\psi^{s-1}$ with c being chosen such that $\langle\psi^s|\psi^s\rangle = 1$. Third, it emerged to be numerically beneficial to use a different but equivalent representation of the interaction part of the GPDE:

$$g^{1\mathrm{d}}\left[3|\psi|^2\mathbb{1} - (\psi^\dagger\sigma_z\psi)\sigma_z\right]\psi = g^{1\mathrm{d}}\left[2|\psi|^2\mathbb{1} + (\psi^\dagger\sigma_x\psi)\sigma_x + (\psi^\dagger\sigma_y\psi)\sigma_y\right]\psi\,. \tag{8.52}$$

We investigate the spectrum of the stationary GPDE (8.51) as a function of interaction strength g. Fig. 8.8(a) shows the part of the spectrum that connects to non-interacting energies $E_n^\pm$ with $n \leq 3$. One observes that all considered energies experience a relatively strong shift, $\sim\mathcal{O}(1)$, for an interaction strength comparable to experimental values. Furthermore, this shift of energies is linear and appears to be the dominant effect of g. In contrast, the shape of the edge state is affected only weakly, $\sim\mathcal{O}(0.01)$, by experimental interaction strengths, as can be seen from Fig. 8.8(b). This is consistent with the previous findings of Fig. 8.7. When increasing the interaction strength to $g = 3g_{\mathrm{exp}}$ the state still

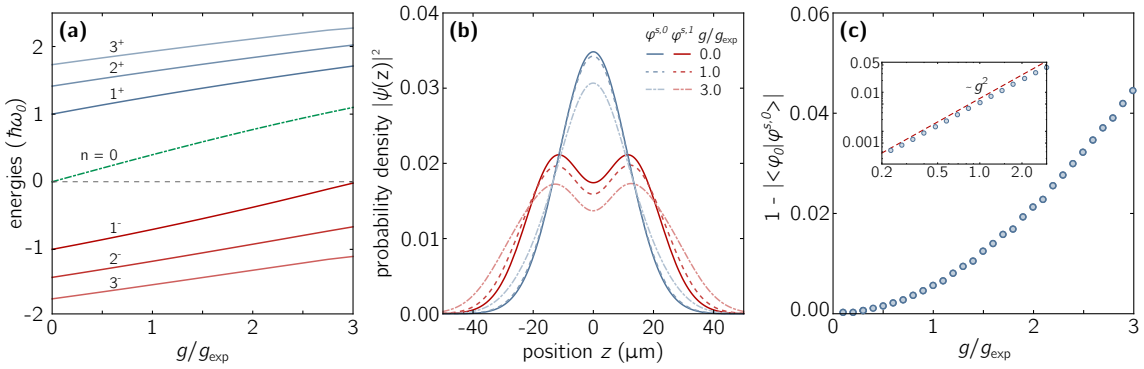

Figure 8.8.: Spectrum and eigenstates of the stationary Gross-Pitaevskii-Dirac equation, see Eq. (8.51). (a) Spectrum of the GPDE is dominantly shifted linearly in g, and effects are of order one for $g/g_{\mathrm{exp}} = 1$. (b) Density profiles of the edge state $n = 0$ (blue) and first excited state $n = 1$ (red) for different interactions strengths. Here, experimental values of g only cause changes of the order of 1%. (c) Overlap of calculated eigenstate $\psi^{s,0}$ with corresponding non-interacting bound state ψ_0. The inset shows a double logarithmic plot revealing the quadratic dependence on g. Here, the red, dashed line is a guide to the eye.

retains its shape, but the change is now significant. We also calculated the eigenstate associated with the $n = 1$ excited state of the Dirac spectrum. Here, the observation is similar as for the $n = 0$ edge state, see Fig. 8.8(b). In order to quantify the effect of g on the eigenstates, and hence on the density profiles, we calculate the overlap with the associated non-interacting state, $|\langle\psi_n^{\pm}|\psi^s\rangle|$. Fig. 8.8(c) reveals that density profiles are affected only to quadratic order in g. In fact, all observables studied in the experiment depend quadratically on g. The reason for this behaviour is a reminiscence of the chiral symmetry (8.4) of the Dirac Hamiltonian H_{D}: when evaluating observables, linear contributions to wavefunctions are cancelled by equal but opposite contributions associated with ψ_n^+ and ψ_n^-, yielding a net effect that is proportional to g^2.

In conclusion, the performed quantitative analysis shows that all experimentally relevant interaction effects turn out to be on the per cent level only and thus negligible, since they are not within experimental resolution. This statement is even enhanced by recalling that interaction effects are expected to be overestimated by construction. Hence, for the analysis of the final experimental results presented in Sec. 8.4 it will be sufficient to work with the set of non-interacting eigenstates of the Dirac Hamiltonian H_{D} as described in Sec. 8.2.1.

8.3.3. Dimensionless analysis of the interaction strength

In order to get an immediate understanding about the relative strength of the interactions in a Gross-Pitaevskii equation one typically expresses the GPE in natural length and energy scales of the problem [344, 348]. So going back to the general form of the three-dimensional GPE given by Eq. (8.38) we introduce $\omega_m = \min(\omega_x, \omega_y, \omega_z)$ and $l_m = \sqrt{\hbar/m\omega_m}$ as these natural scales. Also, we give a list of variable changes: $\mathbf{r} \to l_m\tilde{\mathbf{r}}$, $t \to \tilde{t}/\omega_m$ and $\phi \to \widetilde{\phi}/l_m^{3/2}$. This leads to the dimensionless GPE

$$i\widetilde{\partial}_t\widetilde{\phi} = \Big[-\frac{1}{2}\widetilde{\nabla}^2 + V_{\mathrm{ext}} + \beta|\widetilde{\phi}|^2 \Big]\,\widetilde{\phi}\,, \tag{8.53}$$

with dimensionless interaction parameter

$$\beta = \frac{4\pi a_s N}{l_m}\,. \tag{8.54}$$

Note that in the present case, where the GPE describes the experimental situation before the Bragg pulses and the lattice is switched on, we have $\omega_m = \omega_z = 2\pi\times 4\text{Hz}$, and $l_m = l_z = 5.4\mu\text{m}$ being the corresponding harmonic oscillator length in z-direction.

We repeat the same treatment for the effective one-dimensional GPDE of Eq. (8.50). Here, we measure frequencies in units of ω_0 and the natural length scale of the problem is $l_\text{D} = \sqrt{c_\text{eff}\hbar/\alpha} = 15.6\mu\text{m}$, see Sec. 8.2.1. Hence, we introduce the variables $z \to l_\text{D}\tilde{z}$, $t \to \tilde{t}/\omega_0$ and $\psi \to \widetilde{\psi}/l_\text{D}^{1/2}$. The dimensionless 1D Gross-Pitaevskii-Dirac equation then reads as

$$i\widetilde{\partial}_t\widetilde{\psi} = \Big[\frac{1}{\sqrt{2}}\,\tilde{z}\,\sigma_x - \frac{i}{\sqrt{2}}\,\widetilde{\partial}_z\,\sigma_z + \beta_\text{D}\left(3|\widetilde{\psi}|^2\,\mathbb{1} - (\widetilde{\psi}^\dagger\sigma_z\widetilde{\psi})\sigma_z\right)\Big]\widetilde{\psi}\,, \tag{8.55}$$

where[6]

$$\beta_\text{D} = \frac{Nma_s}{\hbar k_0}\sqrt{\frac{\omega_x\omega_y}{8}}\,. \tag{8.56}$$

First of all, one crucially realises that the dimensionless GPDE does *not* depend on the parameter α that parametrizes the mass of the initial Dirac system, see Eqs. (8.14) and (8.15). Hence, interactions are *exactly marginal* in 1D as they are neither made more prominent nor are they suppressed by an appropriate scaling of the theory [206].

Finally, calculating expressions (8.54) and (8.56) using experimental parameters one obtains

$$\beta \simeq 123.3 \qquad \text{and} \qquad \beta_\text{D} \simeq 0.3 \tag{8.57}$$

for a condensate of $N = 10^4$ rubidium atoms. Generally, these values parametrize the ratio of the interaction energy and the kinetic energy in the respective case. So interactions in the experimental Dirac system are indeed expected to be on the order of $\mathcal{O}(10^{-1}) - \mathcal{O}(1)$. This reflects the observed effect of interactions on the energies, see Fig. 8.8(a), which depend linearly on g. At the same time, we recall that observables are only affected quadratically in g. Here, the value of β_D also supports the small corrections to the numerically observed density profiles, see Fig. 8.8(b). This again underlines the suggestion that interactions are negligible for calculating observables, despite the fact that interactions are indeed of order one, $\sim\mathcal{O}(1)$.

However, the dimensionless interaction strength of the system in the initial trap is very strong , $\beta\sim\mathcal{O}(10^2)$, and by no means negligible. So when imprinting the initially prepared cloud onto the effective Dirac system, one effectively reduces the relevance of interactions by approximately two orders of magnitudes. This effect is understood from kinetic energy arguments: with an initial momentum width of $\Delta p_z \approx 0.01\hbar k_0$ (see above) typical initial energies of particles in the cloud are proportional to $\Delta p^2/\hbar^2 \approx 10^{-4}k_0$. In the Dirac system, on the other hand, the kinetic energy term yields $c_\text{eff}\Delta p/\hbar^2 \approx 4\times 10^{-2}k_0$. This nicely matches the discrepancy of the values given in Eq. (8.57). Thus, the importance of interactions is indeed reduced in the course of the experiment, since the Bragg pulses pump a large amount of (kinetic) energy into the system. It is therefore important to note that while in the Dirac system the dynamics of the condensate (in z-direction) is not dominated by interactions and hence can be effectively described by an non-interacting theory, interaction effects are indeed expected to be *crucial* for the shape of the atomic cloud in the initial harmonic trap.

[6] Note that this parameter differs from the one given in [53] by a factor of $\frac{1}{\sqrt{2}}$. This stems from a slightly different definition of the natural scales in both cases.

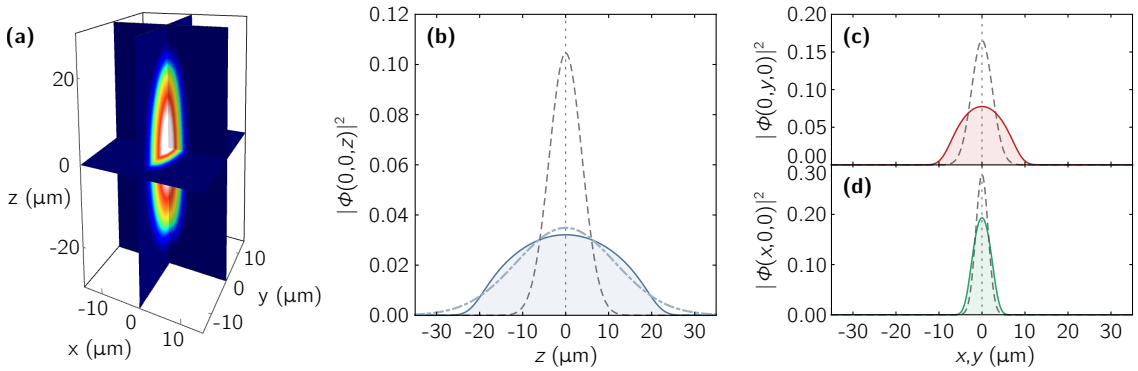

Figure 8.9.: Atomic cloud size calculated from Gross-Pitaevskii equation (8.39). (a) The shape of a BEC of about 10^4 rubidium atoms in the initial harmonic trap, see Eq. (8.37), with trapping frequencies $\omega_{x,y,z}/2\pi = (28.5, 10.0, 4.0)$Hz. (b) A cut along $x = y = 0$ reveals associated 1D density profiles for the true interacting initial cloud (blue solid), the Gaussian ground state of a corresponding non-interacting system (gray dashed), see Eq. (8.40), and the expected form of the topological edge state (blue dashed), see Eq. (8.27). All density profiles are normalised to one. The huge mismatch between the Gaussian state and the GPE state expresses the significance of interactions for the initial cloud shape. (c)-(d) Density profiles along the y- and x-direction, respectively. Again, GPE results are compared to non-interacting Gaussian states. Here, relative interaction strengths decrease due to larger respective trapping frequencies.

8.3.4. Numerical calculation of the initial atomic cloud

As described at length above, interaction effects do not play a role for the time evolution along the spatial direction of interest. However, they do affect the initial state substantially. So in order to gain a quantitative theoretical description of the experiment we proceed in the following way. First, we need to *include* interactions to calculate $\phi_a(x, y, z)$, which is the wavefunction describing the final form of the atomic cloud in the initial harmonic trap, i.e. after the adiabatic expansion, but before the Bragg pulses and the external lattice is switched on, see above. To this end, we numerically solve the stationary three-dimensional Gross-Pitaevskii equation (8.39). We then imprint the momentum change $\pm 2\hbar k_0$ due to the Bragg pulses and consider a switched on lattice potential. For the subsequent time evolution, we *neglect* interaction effects and use the non-interacting Dirac Hamiltonian given by (8.14) in combination with a simple harmonic oscillator Hamiltonian of type (8.44) for the perpendicular directions, i.e., we assume that the dynamics are described by

$$H \approx H^0 = H_{\mathrm{D}} + H_{\perp}^{\mathrm{ho}} \,. \tag{8.58}$$

So eventually we need to calculate the overlap of the calculated initial wavefunction ϕ_a with the corresponding basis states of H, which are just product states of eigenstates of H_{D} and $H_{\perp}^{\mathrm{ho}}$.

The static solution ϕ_a of the three-dimensional Gross–Pitaevskii equation is calculated using the *Matlab* toolbox *GPELab* by Antoine and Duboscq [348, 349]. This programme is quite powerful in the sense that can be applied to a large class of systems of Gross-Pitaevskii equations. For the case of stationary problems that are of interest to us, the toolbox uses an iterative procedure to find numerical solutions to an energy minimization problem. Here, the starting point is the solution of the non-interacting problem (similar to the approach explained above). For details about the algorithm and, in particular, about 'how to use GPELab' we refer the reader to Refs. [348, 349].

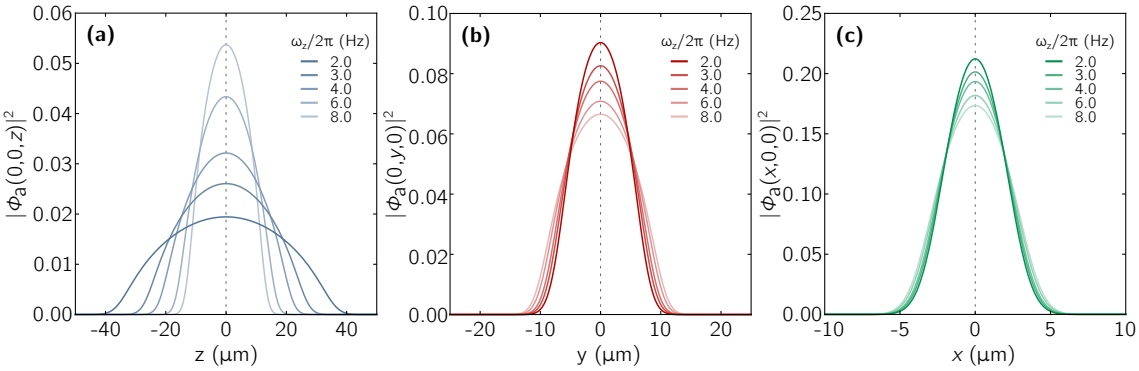

Figure 8.10.: Atomic cloud shape as a function of the trapping frequency in z-direction, ω_z. Density profiles are shown for a cut along the (a) z-, (b) y- and (c) x-direction. Here, $\omega_z/2\pi$ is varied from 2.0Hz to 8.0Hz. Changing the trapping potential in z-direction also affects the cloud in x- and y-direction, since relative interaction strengths are increased or decreased, respectively.

In Fig. 8.9 we show the density profile associated with the initial wavefunction ϕ_a, which was calculated using the trapping parameters $\omega_x/2\pi = 28.5$Hz, $\omega_y/2\pi = 10$Hz, $\omega_z/2\pi = 4$Hz and an atom number of $N = 10^4$. For the given set of parameters the resulting cloud has a cigar shape, see Fig. 8.9(a). While this shape would also be qualitatively present in a purely non-interacting system due to the respective ratios of trapping frequencies, the presence of interactions leads to an even more pronounced elongation along the z-direction. In Fig. 8.9(b) we investigate the expected shape of the atomic cloud by considering $|\phi_a(0,0,z)|^2$, i.e., the particle density along a cut at $x = y = 0$. We compare the results to a three-dimensional harmonic oscillator groundstate wavefunction $\phi_0^{\mathrm{ho}}(x,y,z)$, see Eq. (8.40), along the same spatial cut. One indeed observes that the cloud is significantly broadened by the interactions along the z-direction. In fact, the full width at half maximum is enlarged by a factor of ~ 3.7. This huge discrepancy reflects the demand to incorporate interactions in the description of the initial wavefunction. Furthermore, due to smaller relative interaction strengths along the perpendicular spatial directions, the associated broadening of the wavefunction is less dominant in the x- and y-directions. This is shown in Fig 8.9(c) and (d), where the densities $|\phi_a(0,y,0)|^2$ and $|\phi_a(x,0,0)|^2$ are depicted, respectively. Nevertheless, the interaction effects in those directions are still too strong to be negligible.

In addition, we plot the spatial distribution of the zero-energy edge mode of the Dirac Hamiltonian, $|\psi_0(z)|^2$, in Fig. 8.9(b). While the ground state of the harmonic trap is in fact much narrower than the edge state, spatial matching is considerably enhanced by the broadening of the state due to interactions. However, since the determined solution of the GPE is *not* of Gaussian shape any more, there is a limit to how much this overlap can be optimised. Generally, the size matching of the wavefunctions in z-direction is done by varying the respective trapping frequency. In Fig. 8.10 we therefore show the dependence of the densities along all three spatial directions on ω_z. Note that changing only ω_z has also an impact on the densities of the cloud along the x- and y-direction, since the relative strength of the interactions is increased (decreased) for higher (lower) values of ω_z, see Figs. 8.10(b) and (c). Nonetheless, as shown by Fig. 8.10(a), the shape of the wavefunction along the z-direction is affected most dominantly.

After the Bragg pulses have been shone onto the atoms and after the lattice potential has been switched on, we trust that the wavefunction is described by $\phi_i(x,y,z) = \frac{1}{\sqrt{2}}\phi_a(x,y,z)(e^{2ik_0 z} + e^{-i\varphi}e^{-2ik_0 z})$ with corresponding spinor $\psi_i(x,y,z)$, see Eq. (8.35) and

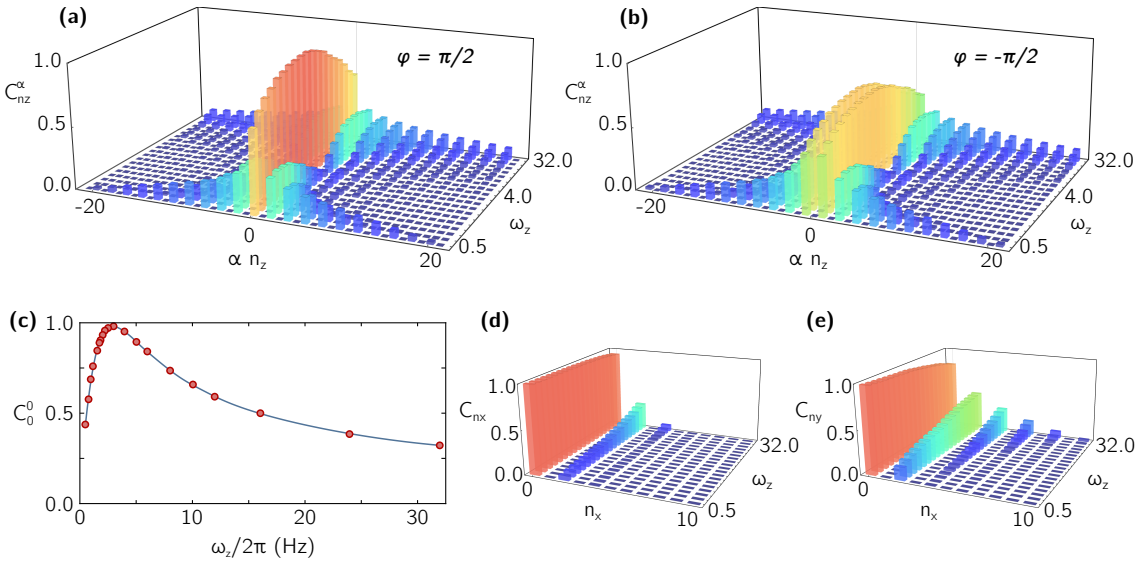

Figure 8.11.: Representation of calculated effective coefficients (see text) indicating the population of the associated quantum state. (a)-(b) Population of the non-interacting Dirac eigenstate, see Eq. (8.25), depending on the relative phase. For $\varphi = \pi/2$ ($\varphi = -\pi/2$) only states with n_z being even (odd) are occupied. Note that the frequency axis is not homogeneously discretized but rather as shown by the dots in (c). (c) Expected population of the topological edge state as a function of ω_z for $\varphi = \pi/2$. Here, dots are calculated values and the solid line is a guide to the eye. (d)-(e) Population coefficients of harmonic oscillator eigenfunctions in x- and y-direction, respectively.

Sec. 8.2.3. As mentioned above, in order to evaluate the time evolution we express ψ_i in terms of eigenstates of $H_{\rm D}$ and $H_\perp^{\rm ho}$, i.e.,

$$\psi_i(x,y,z) = \sum_{n_x n_y n_z} \sum_{\alpha} c^{\alpha}_{n_x n_y n_z}\, \phi^{\rm ho}_{n_x}(x)\, \phi^{\rm ho}_{n_y}(y)\, \psi^{\alpha}_{n_z}(z)\,, \tag{8.59}$$

with $\alpha \in \{+,-\}$ (except for $n_z = 0$), $n_x, n_y, n_z \in \mathbb{N}_0$, and where $\phi^{\rm ho}_n$ are harmonic oscillator functions of type (8.24). The Dirac spinors $\psi^{\pm}_n$ are still given by Eq. (8.25). The overlap coefficients are calculated from

$$c^{\alpha}_{n_x n_y n_z} = \frac{1}{\sqrt{2}} \int dx \int dy \int dz\ \left(\phi^{\rm ho}_{n_x}(x)\right)^* \left(\phi^{\rm ho}_{n_y}(y)\right)^* \phi_a(x,y,z)\ \left(\psi^{\alpha}_{n_z}(z)\right)^{\dagger} \cdot \begin{pmatrix} 1 \\ e^{-i\varphi} \end{pmatrix}. \tag{8.60}$$

Note that since $\phi_a(x,y,z)$ is an even function with respect to all three spatial coordinates, only specific combinations of (n_x, n_y, n_z, α) yield finite contributions to the sum (8.59). Here, it holds that $c^{\alpha}_{n_x n_y n_z} = 0$ when n_x, n_y are odd. The possible values for n_z and α are determined by the phase shift φ, since Dirac spinors contain spatially even as well as odd parts. For convenience we also define the probabilities

$$P^{\alpha}_{n_z} = \sum_{n_x,n_y} \left|c^{\alpha}_{n_x n_y n_z}\right|^2, \quad P_{n_y} = \sum_{n_x,n_z} \sum_{\alpha} \left|c^{\alpha}_{n_x n_y n_z}\right|^2, \quad P_{n_x} = \sum_{n_x,n_y} \sum_{\alpha} \left|c^{\alpha}_{n_x n_y n_z}\right|^2, \tag{8.61}$$

where it holds that $\sum_{n_z,\alpha} P^{\alpha}_{n_z} = 1$ etc., since $\int |\phi_a|^2 = 1$ is normalised to unity. In Fig. 8.11 we show how the associated effective coefficients $C^{\alpha}_{n_z} = (P^{\alpha}_{n_z})^{1/2}$, $C_{n_y} = (P_{n_y})^{1/2}$, $C_{n_x} = (P_{n_x})^{1/2}$ behave as a function of the trapping frequency ω_z. While C_{n_y}, C_{n_x} are in fact independent of the phase shift φ, the coefficient $C^{\alpha}_{n_z}$ is shown for the two scenarios of $\varphi = \pi/2$ and $\varphi = -\pi/2$, respectively. For the investigated range of $\omega_z/2\pi \in \{0.5, ..., 32\}$Hz

we observe a strong population of the ground state of the harmonic traps in x- and y-direction, see Figs. 8.11(d) and (e). In contrast, the population of the respective Dirac eigenstates is much more sensitive and also depends crucially on the relative phase shift, as can be seen from Figs. 8.11(a) and (b). In spite of the presence of interactions, one witnesses a certain parity of the population of $\psi_n^{\pm}$: if $\varphi = +\pi/2$ $(= -\pi/2)$, then only Dirac states with n_z being odd (even) can be occupied. So, most importantly, the topological edge state can indeed only be occupied if $\varphi = \pi/2$. How much this state is populated by the interaction dominated initial cloud obviously strongly depends on ω_z. Nevertheless, despite some residual spatial mismatch as explained above (see Fig. 8.9) we expect that the edge state can be populated by up to $\sim 98\%$ for $\omega_z \sim 3$Hz, see Fig. 8.11(c). For the given experimental setup with $\omega_z \simeq 4$Hz we expect a population of the edge state of about $\sim 95\%$. Note that experimentally there are limits on going to even lower frequencies, since the apparatus becomes very sensitive to (low frequency) noise.

8.4. Experimental signature of a 1D topological edge state

In this section, we finally present experimental results measured by M. Weitz and collaborators confirming the existence of the associated edge state in a system with ultracold atoms in an optical lattice [53,321]. Here, the outlined discussion will emphasize the comparison to theoretical predictions made by us. In order to verify the successful simulation of the topological edge state the experiment focusses on recording the dynamical evolution of the atomic cloud. Having calculated the overlaps given by Eq. (8.60) for all relevant quantum numbers, we are now able to perform any non-interacting time evolution for arbitrarily long times. In the following, we will first compare such a theoretical simulation to actual experimental data [53]. In a second step we will then further examine how the measurable signature of the edge state depends on initial conditions (cf. Sec. 8.3). We will show that all experimental findings agree very well with our numerical analysis.

8.4.1. Time evolution

The experiment starts by centring the atomic cloud at the position $z = 0$. Bragg pulses are then used to imprint the desired momentum change and the lattice beams are switched on. Again, we assume that these processes occur instantaneously and do not change the spatial profile of the cloud. Experimentally, the subsequent time evolution of the cloud is measured by repeating the experiment numerous times and taking a set of absorption images for different waiting times t. In Fig. 8.12 we show two different series of experimentally obtained absorption images [53, 324] and compare them to a respective theoretical simulation. Both sets are for two distinct phase shifts between Bragg pulses, $\varphi = \pi/2$ and $\varphi = -\pi/2$, respectively. The wavefunction of the system at time t from which simulation results are obtained is calculated by a simple non-interacting time evolution. Using Eqs. (8.58) and (8.59) the wavefunction takes on the form

$$\begin{aligned} \psi(x,y,z,t) &= e^{-iH^0 t}\,\psi_i(x,y,z) \\ &= \sum_{n_x n_y n_z} \sum_{\alpha} c^{\alpha}_{n_x n_y n_z}\, e^{-i(E^{\mathrm{ho}}_{n_x}+E^{\mathrm{ho}}_{n_y}+E^{\alpha}_{n_z})t}\,\phi^{\mathrm{ho}}_{n_x}(x)\,\phi^{\mathrm{ho}}_{n_y}(y)\,\psi^{\alpha}_{n_z}(z)\,, \end{aligned} \tag{8.62}$$

where $E^{\mathrm{ho}}_n = \hbar\omega(n+\frac{1}{2})$ are typical eigenenergies of a harmonic oscillator, energies $E^{\alpha}_{n_z}$ are given by Eq. (8.26) and all coefficients $c^{\alpha}_{n_x n_y n_z}$ were calculated in the previous section, see Sec. 8.3.4.

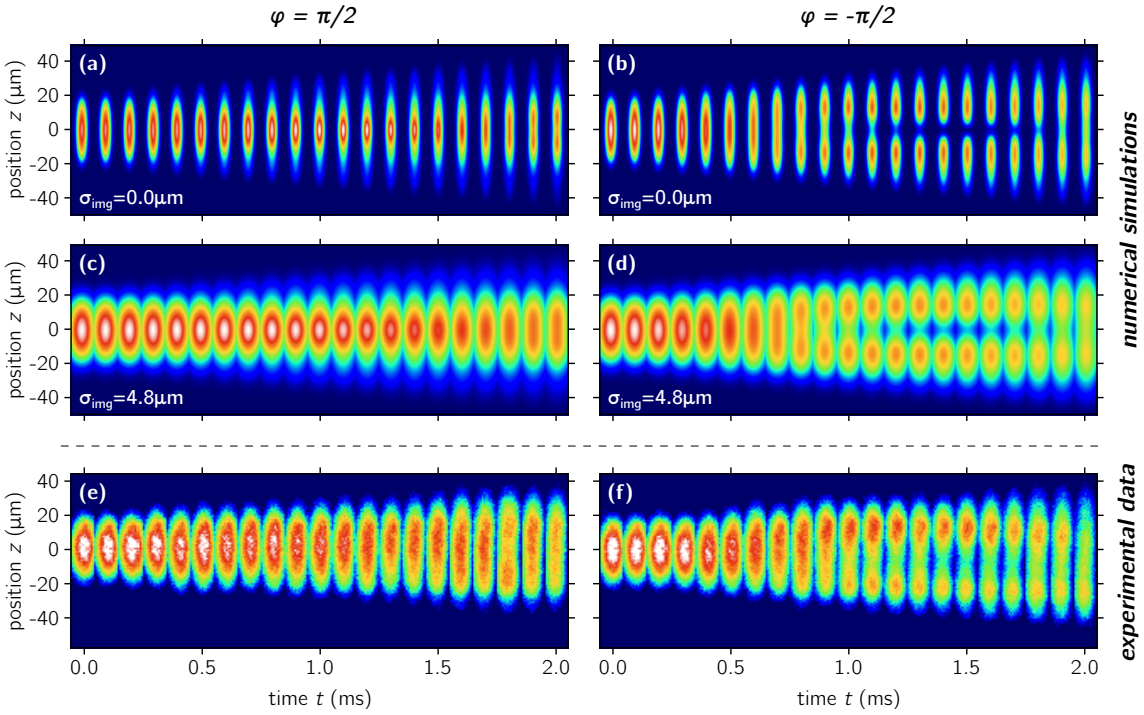

Figure 8.12.: Comparison between (a)-(d) numerical simulations and (e)-(f) experimental data of temporal evolutions of atomic clouds. Each figure shows a series of (absorption) images for a relative phase of the initially prepared wavefunction of $\varphi = \pi/2$ (left) or $\varphi = -\pi/2$ (right), respectively. The temporal step size between images in each figure is 0.1ms, and the spatial width is 14μm. While (a)-(b) show true sizes of the numerically determined clouds, (c)-(d) take into account the experimental resolution of 4.8μm. Numerical simulations agree well with experimental data: a clear trapping of the atomic cloud in the edge state is seen for $\varphi = \pi/2$, as predicted by theory. For $-\varphi = \pi/2$ a beating pattern is (partially) resolved. Here, a fit to experimental data (see text) agrees with the predicted characterstic frequency of $\omega_0/2\pi = 163$Hz. All experimental data presented here is provided by Refs. [53, 321, 324].

In the experiment, the atomic cloud is pictured by an absorption image in the xz-plane. In order to compare our theoretical expectations to this detection procedure we plot y-integrated densities associated with the calculated wavefunction $\psi(x, y, z, t)$, i.e.,

$$n(x, z, t) = \int dy \, |\psi(x, y, z, t)|^2 \approx \int dy \, |\Psi_1(x, y, z, t)|^2 + |\Psi_2(x, y, z, t)|^2 , \tag{8.63}$$

which is normalised to one. Here, we again assume that the experimental setup cannot resolve the rapidly oscillating interference fringes $2\mathrm{Re}\big[\Psi_1(x, y, z, t)^* \Psi_2(x, y, z, t) e^{-i4k_0 z}\big]$, which arise from a mixing of two spinor components. Recall further that the experimental setup has an intrinsic broadening of the imaging detection signal by about $\sigma_{\mathrm{img}} \sim 4.8\mu$m. We, thus, convolve the 'image' obtained from Eq. (8.63) by a Gaussian of rms-width given by this uncertainty. The impact of this convolution can be seen by comparing Figs. 8.12(a) and (b) to Figs. 8.12(c) and (d).

As explained above, the phase shift φ determines whether one maximally populates the edge state during the initial procedure or if it is left empty, respectively. For $\varphi = \pi/2$ the simulation predicts, see Figs. 8.12(a) and (c), that most of the atoms are trapped in the region of the edge state. Due to the fact that the edge state is only populated by $\sim 95\%$ of the atoms (see Fig. 8.11) the system is not purely stationary (cf. Fig. 8.7). Most importantly, this spatial confinement is nicely observed also from the experimental data, see Fig. 8.12(e).

By contrast, when the relative phase between the two momentum states is set to $\varphi = -\pi/2$ there is no overlap with the emergent topological edge state. Instead, the atomic cloud is mainly projected onto the first pair of excited states of the Dirac spectrum which are separated in energy by $2\omega_0 = 2\times 163$Hz. Hence, the simulation yields an associated beating pattern, as seen in Figs. 8.12(b) and (d). Note again that interactions cause a small population of higher excited states, which, however, do not have a significant quantitative impact on the oscillation frequency. Most notably, the experimental data follows the theoretical prediction, as seen from Fig. 8.12(f). However, the experimentally accessible interaction times are limited to ~ 2ms, for which an oscillation of the atoms with predicted period $T = \pi/\omega \simeq 3$ms could only be partially resolved. Nevertheless, a fit to the experimental data (see Methods section of Ref. [53]) yields a period of $T = 3.16(32)$ms. This oscillation period can be converted into an experimental value for the characteristic energy of the Dirac spectrum of $\omega_0^{\mathrm{exp}}/2\pi = 158(16)$Hz. This value is in very good agreement with our theoretical prediction of $\omega_0/2\pi = 163$Hz.

Unfortunately, the possible duration of the experiment is limited. The observed 'lifetime' of about 2ms is mainly assigned to unwanted resonant photon scattering events involving the Raman beams that create the optical lattice. It is further believed that the main visual mismatch between experiment and theory - the residual expansion of the atomic cloud trapped in the edge state, compare Figs. 8.12(c) and (e) - can be traced back to such photon scattering events. Due to this temporal restriction it was not possible to test the system's dynamics for longer times. Here, one might be particularly interested in the potential long time effects caused by (strong) interactions, cf. Fig. 8.7(c) and (f), as well as by additional interaction mechanisms, as discussed in Ch. 9.

8.4.2. Loading efficiency

Above, the emergence of the topological edge state is discussed by varying the relative phase φ and studying the dynamical evolution of the atomic cloud, see Fig. 8.12. For the present system the two distinct phases $\varphi = \pi/2$ and $\varphi = -\pi/2$ correspond to situations in which the edge state is either as much as possible or not at all populated. For all other phases φ the occupation smoothly connects between these two most extreme cases. This obvious dependence was also seen in the experiment [53]. In this section we want to focus on a different aspect of populating the edge state: how does the loading efficiency depend on the initial cloud width along the z-direction, and how do the results from Sec. 8.3.4 connect to actual experimental observables?

To study the loading efficiency experimentally the value of ω_z is varied. Since measuring precise values of this trapping frequency is not straightforward [324], the experiment instead determines the momentum width Δp_z of the cloud along the z-direction by means of Bragg spectroscopy [53, 321] at the end of the preparation sequence. For our numerical simulations the momentum width $\Delta p_z = \sqrt{\langle p_z^2 \rangle}$ (for a wavepacket centred around $p_z = 0$) is obtained from a direct calculation using the initial wavefunction ϕ_a. The expression for the rms-width then reads as

$$\Delta p_z = \sqrt{\langle p_z^2 \rangle} = \left[\int dx \int dy \int dp_z \; p_z^2 \, |\phi_a(x,y,p_z)|^2 \right]^{1/2} = \left[\int dp_z \; p_z^2 \, n(p_z) \right]^{1/2}, \quad (8.64)$$

where we introduced the partially Fourier transformed initial wavefunction

$$\phi_a(x,y,p_z) = \int dz \; e^{-ip_z z} \, \phi_a(x,y,z) \quad (8.65)$$

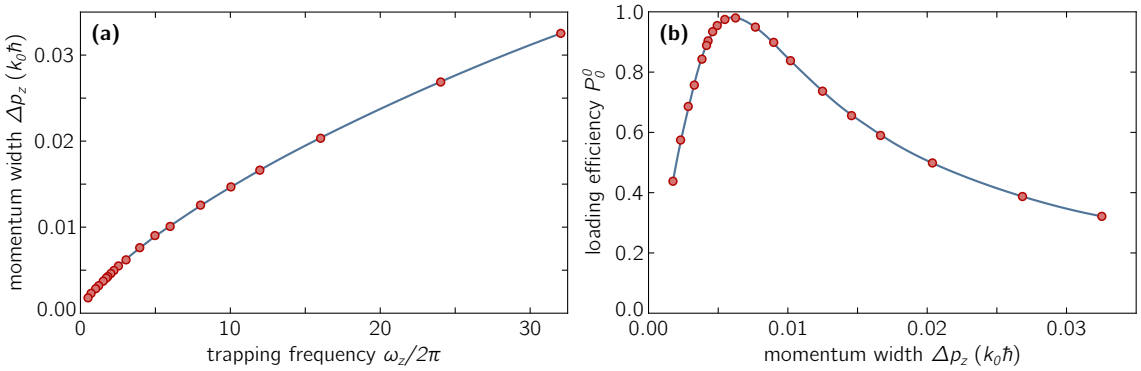

Figure 8.13.: (a) Relation between momentum width p_z and trapping frequency ω_z of an initial atomic cloud according to a GPE analysis of Eq. (8.39). Perpendicular trapping frequencies are set to $\omega_{x,y}/2\pi = (28.5, 10.0)$Hz. Momentum widths are calculated using Eq. (8.64). (b) Expected loading efficiency into the topological edge state (for $\varphi = \pi/2$) depending on the initial momentum width. Populations are calculated as described in Sec. 8.3.4, see also Fig. 8.11(c).

as well as the xy-integrated momentum densities

$$n(p_z) = \int dx \int dy \ \left|\phi_a(x, y, p_z)\right|^2 . \tag{8.66}$$

We have repeated the GPE calculation, see Eq. (8.39) and Sec. 8.3.4, for several values of ω_z. The resulting wavefunctions ϕ_a are then used to calculate the expressions of Eq. (8.65) and Eq. (8.66). Eventually, we use Eq. (8.64) to determine the momentum width of the atoms on the trapping frequency in z-direction. This dependence is depicted in Fig. 8.13(a). Furthermore, one can now also express the theoretically expected loading efficiency into the topological edge state as a function of Δp_z, see Fig. 8.13(b).

Next, the non-interacting time evolution procedure as explained above is performed. In order to be able to quantify final differences between different configurations, one measures the spatial width of the cloud along the z-direction using (cf. Eq. 8.64)

$$\Delta z(t) = \sqrt{\langle z^2 \rangle} = \left[\int dz \ z^2 \, n(z, t) \right]^{1/2} , \tag{8.67}$$

where $n(z,t) = \int dx\, dz\, n(x, y, z, t)$ is the xy-integrated density profile, see also Eq. (8.63). To distinguish between resulting time evolutions for different phase shifts ($\varphi = \pi/2$ and $\varphi = -\pi/2$) as well as for different initial cloud widths one defines the following 'contrast' for a given time t

$$\Upsilon(\omega_z, t) = \frac{\Delta z_-(t) - \Delta z_+(t)}{\Delta z_-(t) + \Delta z_+(t)} . \tag{8.68}$$

Here, Δz_- (Δz_+) describes the rms-width of a cloud at time t which was initially prepared with a phase shift $\varphi = -\pi/2$ ($= \pi/2$). Since the numerator of Eq. (8.68) is most pronounced if most of the system is captured in the edge state, the contrast Υ is an appropriate experimental measure for the loading efficiency into this very state. Note, however, that one can check that the contrast does not peak at the momentum width for which the loading into the edge state is expected to be largest (compare Figs. (8.13)(b) and (8.14)).

Finally, Fig. 8.14 shows the contrast (8.68) given at time $t_\Upsilon = 1.7$ms as a function of the initial momentum width Δp_z. One finds that the experimentally measured values [53] are in good agreement with our numerical simulation (solid curve). As described above, the experiment allows for initial atomic clouds with a momentum width of about $\sim 0.01\hbar k_0$,

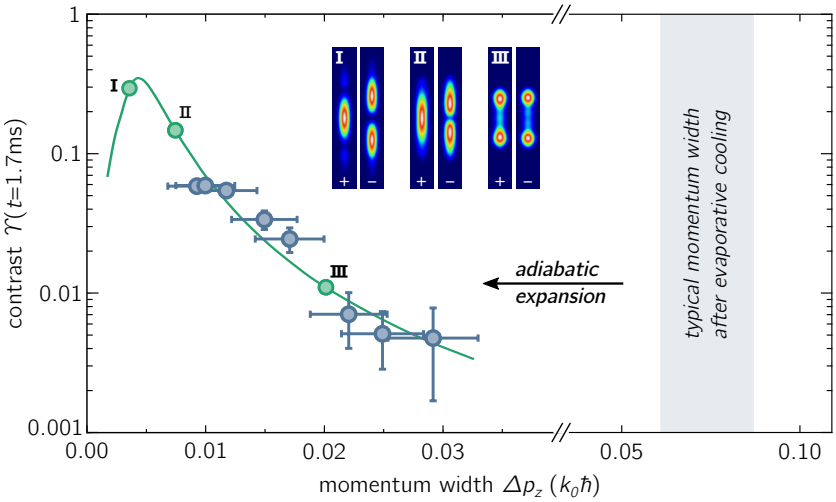

Figure 8.14.: Comparing the numerically calculated contrast of Eq. (8.68) (solid green curve) to experimentally obtained results (blue dots) [53, 321, 324] at a given time $t_\Upsilon = 1.7$ms. Experimentally, the momentum width of the atomic cloud is decreased by an adiabatic expansion in the trap, see Sec. 8.2.3. Inset images (I)-(III) indicate associated numerically expected atomic clouds. Note that while the calculated contrast does take into account experimental resolution of 4.8μm, the inset images are not broadened due to reasons of visual clarity.

which corresponds to effective 1D temperatures in the pK regime. While clouds of even smaller momentum width cannot be achieved due to experimental limitations, initially broader wavepackets in momentum space are easily engineered by putting an earlier halt to the adiabatic expansion of the cloud. Generally, one finds that a larger initial momentum spread corresponds to a smaller measured contrast. This is, of course, attributed to an enhanced population of excited Dirac states with $n > 0$ which is accompanied by a reduced population of the edge state ψ_0, see Fig. 8.11. Despite the fact that a comparison of experimental data with our numerical simulation suggests that the contrast can still be improved quite significantly, $\sim\mathcal{O}(10)$, we want to stress again that our theoretical analysis predicts that more than 90% of the condensate already populates the topological edge state.

8.5. Conclusion and Outlook

Using a synergy of experimental data and numerical simulations we have shown that an edge state at the interface of two distinct topological phases has been observed by real-space imaging of an atomic cloud [53]. Experimental evidence for the successful population of this edge state has been obtained from excellent qualitative as well as quantitative agreement with the theoretical description formulated by us. This evidence is three-fold: first, the dependence on the initial relative phase φ has been confirmed. Second, the dependence of the initial momentum width on the loading efficiency agrees with theoretical expectations. Third, an experimental measurement of the characteristic frequency ω_0 agrees within the margin of error with the value obtained from a corresponding non-interacting theory.

We stress that this agreement is far from trivial due to two main reasons: knowing that the initial cloud is strongly affected by interactions, it is *a priori* not obvious that final results are in fact not changed by these interactions. Hence, the mean-field discussion as done above takes a crucial role in approving the correctness of the interpretation of

experimental results. Moreover, experimental circumstances enforce a small characteristic frequency ω_0 (compared to the recoil energy) and likewise large spatial extensions of the eigenstates of the effective Dirac system (compared to the lattice spacing). This prohibits an unquestionable distinction in behaviour depending on whether the system populates the edge state or not. In other words, while we expect to load 90% of the BEC into the topological state, the contrast given by Eq. (8.68) is measured to be on the order of 10% only. At the same time, of course, the experiment is constrained by error sources, such as unwanted resonant photon scattering events.

Nevertheless, to boost the prominence of the topological edge state, e.g., in a real-space time evolution measurement as shown here, one could further adjust the form of the effective Hamiltonian (8.31). For example, replacing the potential by the alternative form

$$V(z) \to V(z) = \frac{2}{\beta} \tanh\left(\alpha\beta z\right) \cos\left(4k_0 z\right), \tag{8.69}$$

with β being some yet to be specified parameter, leads to finite potentials as $|z| \to \infty$, and therefore to an energetically bounded Hamiltonian. Here, we expect that parameters can - in principle - be tuned such that only the edge state is a true bound state of the system, while other eigenstates of the Dirac system become running wave solutions. In such situations, no beating of 'excited states' would be expected (cf. Fig. 8.12) and the edge state could potentially be detected in a more prominent fashion. Here, one would like to be able to investigate the experiment for longer times as presented above. To this end, changing the atomic species to, e.g., erbium could enhance coherent times [321].

Longer investigatable time scales also hold prospects for studying novel Berry phase effects: by realising a spatially dependent *complex* mass in the Dirac Hamiltonian, one explicitly breaks the emergent chiral symmetry of the system. This is due to the emergence of an additional term in Eq. (8.31) being proportional to σ_y. At the same time, the topological singularity, see Fig. 8.4(c), 'smears out' and generates Berry curvatures in phase space away from the origin. Such Phase-space Berry curvatures have an impact on the semiclassical equation of motion [96, 199] (cf. Secs. 5.4.2 and 7.2.4), which should be observable in an otherwise similar setup as studied here.

For the future, it will also be most important as well as highly interesting to study the role of interactions on the topological edge state. In order to do so the intrinsic interaction strength needs to be enhanced either by means of Feshbach resonances, see Sec. 2.1, or by using a different atom species with a larger scattering length to mass ratio. As shown in Fig. 8.7, even mean-field effects are rapidly expected to become non-trivial. Such study of interactions in the present setup holds the prospect to simulate general aspects of interacting quantum matter [350]. Another perspective of an interacting system is the realisation of relativistic wave equation predictions [351].

So far, the role of interactions has only been mentioned on a mean-field level. However, it is worthwhile to study interaction effects also beyond this leading order description. Since the Dirac Hamiltonian has an unbounded spectrum, even weak fluctuations are expected to yield a qualitative effect: a pairwise decay of bosonic particles into higher and lower states of equal but opposite energies leads to dynamical instabilities. This intriguing effect which is, of course, genuine for bosonic systems only, will be the central objective of the next chapter.

9. Intrinsic instabilities of the bosonic Dirac Hamiltonian

In the previous chapter, interaction effects of the bosonic quantum gas were estimated by incorporating such interactions in terms of a mean-field discussion. Indeed, for weakly interacting many-body systems mean-field descriptions are generally powerful in capturing the ground state physics of the system, e.g., the emergence of Bose-Einstein condensation. By including *fluctuations* around this mean-field solution physical phenomena such as superfluidity can be explained [206]. Moreover, a study of such fluctuations can reveal interesting instability behaviours of a BEC [352]. One type of these instabilities are said to be dynamically unstable and are associated with imaginary eigenvalues appearing in the fluctuation spectrum. They emerge as a consequence of degeneracies, which require a mirror-type spectrum of the system. Therefore, also the Gross-Pitaevskii-Dirac equation, which was introduced in the previous section, see Eq. (8.50), is believed to show these kind of instabilities.

In the following, we will shortly elaborate on the general derivation of the fluctuation spectrum and why the emergence of complex eigenvalues is at all possible. We will then give a simple pedagogical example of how a dynamical instability results from a 'mirror' spectrum in combination with a bosonic particle bath. Eventually, we will export these ideas to identify such instabilities also in the effective 1D Gross-Pitaevskii-Dirac equation. We will indeed show that the presented bosonic version of the Dirac Hamiltonian is dynamically unstable for *all* interaction strengths. Having said this, we find that expected effects are negligible for an experimental setup as in Ref. [53]. Nevertheless, such intriguing effects could be studied experimentally in similar setups with stronger relative interaction strengths.

9.1. Fluctuations around mean-field solution

In this section, we present a typical fluctuation analysis that goes beyond the mean-field description of the previous section 8.2.3. Here, we particularly focus on the formal emergence of *dynamical instabilities* resulting from imaginary eigenvalues of the Bogoliubov-de Gennes equations. In doing so, we closely follow the logic of Nakamura *et al.* [353] as well as use related works presented in Refs. [343, 352, 354–357].

9.1.1. The Bogoliubov de-Gennes equations

We start by considering again the time-dependent Gross-Pitaevskii equation of Eq. (8.38). Here, we view V_{ext} as a yet to be specified external potential and still assume that the stationary solution to Eq. (8.38) is given by $\phi(\mathbf{r},t) = e^{-i\mu t}\phi_{\text{MF}}(\mathbf{r})$, with $\int|\phi|^2 = 1$. The function $\phi_{\text{MF}}(\mathbf{r})$ describes the mean field solution that satisfies the stationary GPE given by Eq. (8.39) (we introduced the additional label for reasons of clarity). In order to study the excitation spectrum of the condensate we allow small field fluctuations around the mean-field solution of the form

$$\phi(\mathbf{r},t) \;\rightarrow\; \phi(\mathbf{r},t) = e^{-i\mu t}\left(\,\phi_{\text{MF}}(\mathbf{r}) + \delta\phi(\mathbf{r},t)\,\right). \tag{9.1}$$

We proceed by substituting Eq. (9.1) into the the GPE (8.38). Since it is presumed that fluctuations are small, $\delta\phi \ll \phi$, it is justified to linearise the resulting equation with respect to the fluctuation fields $\delta\phi$. Abbreviating the non-interacting part of the Hamiltonian as $H_0 = -(\hbar^2/2m)\nabla^2 + V_{\text{ext}}$, one straightforwardly finds

$$i\partial_t \delta\phi(t) = \left(H_0 - \mu + 2g\left|\phi_{\text{MF}}\right|^2\right)\delta\phi(t) + gN\phi_{\text{MF}}^2\,\delta\phi^*(t)\,, \tag{9.2}$$

where we dropped the position label $\mathbf{r}$ for convenience. Since this equation does not only depend on the fluctuation field but also on its complex conjugate $\delta\phi^*$, we complete the set of coupled equations by determining

$$-i\partial_t \delta\phi^*(t) = \left(H_0 - \mu + 2g\left|\phi_{\text{MF}}\right|^2\right)\delta\phi^*(t) + gN\left(\phi_{\text{MF}}^*\right)^2\delta\phi(t)\,, \tag{9.3}$$

which is indeed just the complex conjugate of Eq. (9.2). Alternatively, we can rephrase these coupled equations as a general matrix equation

$$i\partial_t \begin{pmatrix} \delta\phi(t) \\ \delta\phi^*(t) \end{pmatrix} = \begin{pmatrix} \mathcal{M} & \mathcal{G} \\ -\mathcal{G}^* & -\mathcal{M}^* \end{pmatrix} \begin{pmatrix} \delta\phi(t) \\ \delta\phi^*(t) \end{pmatrix}\,, \tag{9.4}$$

where in the present case

$$\mathcal{M} = H_0 - \mu + 2gN\left|\phi_{\text{MF}}\right|^2 \qquad \text{and} \qquad \mathcal{G} = gN\phi_{\text{MF}}^2\,, \tag{9.5}$$

which possess the general properties $\mathcal{M}^\dagger = \mathcal{M}$ and $\mathcal{G}^T = \mathcal{G}$, respectively.

Next, one assumes that the fluctuation fields $\delta\phi$ can be written in terms of fluctuation modes $\delta\phi_\alpha$, which are decomposed as

$$\delta\phi_\alpha(\mathbf{r},t) = e^{-iE_\alpha t}\,u_\alpha(\mathbf{r}) + e^{iE_\alpha^* t}\,v_\alpha^*(\mathbf{r})\,. \tag{9.6}$$

Substituting this expression into Eq. (9.4) and equating parts that oscillate in the same way eventually yields the infamous *Bogoliubov-de Gennes equations* (BdG) [354, 358, 359]

$$E_\alpha\,\xi_\alpha(\mathbf{r}) = H_{\text{BdG}}\,\xi_\alpha(\mathbf{r})\,, \tag{9.7}$$

where we have introduced the 'doublet' notation

$$\xi_\alpha(\mathbf{r}) = \begin{pmatrix} u_\alpha(\mathbf{r}) \\ v_\alpha(\mathbf{r}) \end{pmatrix} \qquad \text{and} \qquad H_{\text{BdG}} = \begin{pmatrix} \mathcal{M} & \mathcal{G} \\ -\mathcal{G}^* & -\mathcal{M}^* \end{pmatrix}\,. \tag{9.8}$$

Notice that *if* the eigenvalues of the BdG (9.7) are real, the functions $u_\alpha(\mathbf{r}), v_\alpha(\mathbf{r})$ describe a conventional Bogoliubov quasiparticle transformation. Here, the normalization condition $\int d\mathbf{r}|u_\alpha|^2 - |v_\alpha|^2 = 1$ holds - or rather can be met - guaranteeing the quantized nature of quasiparticles [343], see below. However, the condition $E_\alpha \in \mathbb{R}$ is *not* necessarily fulfilled, leading to intrinsic instabilities of the condensate in respective situations.

9.1.2. General properties and dynamical instabilities of the BdG

In order to get a better intuition for the Bogoliubiv-de Gennes equations (9.7) as well as its associated objects (9.8) and to understand how instabilities can emerge from this structure we now discuss general properties of the BdG. First of all, one instantly realises that the eigenvalues E_α of the BdG do not have to be real, since

$$H_{\text{BdG}} = \sigma_z\,H_{\text{qp}} \tag{9.9}$$

is indeed *not* Hermitian. Here, we introduced the quasiparticle Hamiltonian $H_{\rm qp}$ and σ_z is the third Pauli matrix. The characteristics of the eigenvalues already yield a plausible definition of stability: if E_α is a real value for all modes α then the system is dynamically stable. For emerging complex eigenvalues, however, the system is said to be *dynamically unstable*.

Moreover, it is easily shown that the object $H_{\rm BdG}$ possesses the symmetry properties

$$\sigma_x \, H_{\rm BdG} \, \sigma_x = -\big(H_{\rm BdG}\big)^* \,, \tag{9.10}$$

$$\sigma_z \, H_{\rm BdG} \, \sigma_z = \big(H_{\rm BdG}\big)^\dagger \,. \tag{9.11}$$

These symmetry relations then also determine the characteristics of the associated eigenstates ξ_α of the BdG. From relation (9.10) it follows that if ξ_α is an eigendoublet of $H_{\rm BdG}$ with E_α, then

$$H_{\rm BdG} \, \widetilde{\xi}_\alpha = \widetilde{E}_\alpha \, \widetilde{\xi}_\alpha \qquad \text{with} \qquad \widetilde{\xi}_\alpha = \sigma_x \xi_\alpha^* \qquad \text{and} \qquad \widetilde{E}_\alpha = -E_\alpha^* \tag{9.12}$$

also holds. Furthermore, using relation (9.11) it can be shown [356] that if E_α is an eigenvalue of $H_{\rm BdG}$, then also E_α^* is an eigenvalue with corresponding eigenstate $\xi'_\alpha = \sigma_z \xi_{*\alpha}$. Here, $\xi_{*\alpha}$ is the dual parter to ξ_α fulfilling

$$\big(H_{\rm BdG}\big)^\dagger \, \xi_{*\alpha} = E_\alpha^* \, \xi_{*\alpha} \,. \tag{9.13}$$

Clearly, if $E_\alpha \in \mathbb{R}$ then $\xi'_\alpha = \xi_\alpha$, i.e., $\xi_{*\alpha} = \sigma_z \xi_\alpha$. So whenever eigenvalues E_α are purely real or imaginary they come in pairs $\{E_\alpha, -E_\alpha\}$. If eigenvalues are complex, on the other hand, they appear as a quartet of the form $\{E_\alpha, E_\alpha^*, -E_\alpha, -E_\alpha^*\}$.

We also remark that the BdG contain eigenfunctions ξ_0 that belong to eigenvalues $E_0 = 0$ [357,360]. The number of these modes is connected to the number of spontaneously broken symmetries. The concept of such *Goldstone modes* is widely used in the context of condensed matter physics (and beyond), and can be understood in the present case as follows: since in a BEC system the global U(1) gauge symmetry is spontaneously broken, one can generate fluctuations by

$$\phi_{\rm MF} \;\to\; e^{i\theta} \, \phi_{\rm MF} \;\overset{\theta \ll 1}{\approx}\; \phi_{\rm MF} + \underbrace{i\theta \phi_{\rm MF}}_{=\delta\phi} \,. \tag{9.14}$$

Hence, one can explicitly show that

$$H_{\rm BdG} \, \xi_0(\mathbf{r}) = 0 \qquad \text{with} \qquad \xi_0(\mathbf{r}) \propto \begin{pmatrix} \phi_{\rm MF}(\mathbf{r}) \\ -\phi_{\rm MF}^*(\mathbf{r}) \end{pmatrix} \tag{9.15}$$

being the Goldstone mode.

In order to make statements about the normalisation of a general doublet ξ_α it is convenient to introduce the following 'inner product' of two arbitrary doublets [361]

$$(\xi_\alpha, \xi_\beta) = \int d\mathbf{r} \; \xi_\alpha^\dagger(\mathbf{r}) \, \sigma_z \, \xi_\beta(\mathbf{r}) \,, \tag{9.16}$$

where the relevance of this form is motivated by the non-Hermitian structure of $H_{\rm BdG}$, see Eq. (9.9), as well as by the relation (9.11). The associated 'norm' of a doublet is then defined as

$$\|\xi_\alpha\|^2 \equiv (\xi_\alpha, \xi_\alpha) = \int d\mathbf{r} \; |u_\alpha(\mathbf{r})|^2 - |v_\alpha(\mathbf{r})|^2 \,. \tag{9.17}$$

Further, by using Eq. (9.11) one deduces that the relation $(\xi_\alpha, H_{\mathrm{BdG}}\xi_\beta) = (H_{\mathrm{BdG}}\xi_\alpha, \xi_\beta)$ is fulfilled. Most crucially, this leads to

$$(E_\beta - E_\alpha^*)\,(\xi_\alpha, \xi_\beta) = 0\,, \tag{9.18}$$

from which follows that

$$\mathrm{Im}(E_\alpha)\,\|\xi_\alpha\|^2 = 0\,. \tag{9.19}$$

So if the eigenvalues of the Bogoliubov-de Gennes equations are indeed real, then $\mathrm{Im}(E_\alpha) = 0$ and the condition (9.19) is automatically fulfilled. In these cases the norm can in principle be set to arbitrary values, but is typically set to unity. The reason is that for this choice Eq. (9.17) becomes $\int d\mathbf{r}|u_\alpha|^2 - |v_\alpha|^2 = 1$. This result is nothing but the correct normalisation of a typical Bogoliubov quasiparticle transformation, where a unity norm conserves the commutation relation in the quasiparticle picture [354]. Note that the partner states $\widetilde{\xi}_\alpha$ possess in fact a norm of $\|\widetilde{\xi}_\alpha\|^2 = -1$. These states correspond to anti-modes in this spirit and do not represent independent physical degrees of freedom [352, 355].

Most interestingly, if eigenvalues E_α *do* have an imaginary part, then the only way to fulfil the necessary condition (9.19) is by demanding that $\|\xi_\alpha\|^2 = 0$. At the same time, this means that modes corresponding to these kind of eigenvalues *cannot* be treated in the spirit of Bogoliubov quasiparticles. In other words, the lack of a proper normalisation of such a Bogoliubov transformation prohibits the quantization of corresponding excited modes. Instead, one expects an exponential growth (decay) of respective modes [352]. It is precisely this situation that is phrased as *dynamical instability*.

While we have discussed the possible emergence of instabilities, it is yet not clear what the conditions and circumstances are under which the eigenvalues E_α become complex. Generally, the emergence of complex eigenvalues is the result of a mode with positive norm becoming degenerate with a mode with negative norm [352,353,362] (where the norm is still defined according to Eq. (9.17)). One can capture these degeneracies by, e.g., perturbation theory to derive explicit conditions for the emergence of complex eigenvalues [353]. Loosely speaking, such degeneracies can only occur when the fluctuation spectrum has states with energies that lie above as well as below the 'ground state' energy μ. This is obviously not the typical case, since the mean-field solution ϕ_{MF} often describes a true ground state of the system (e.g., a BEC at the bottom of a harmonic trap). Nonetheless, for the system at hand, in particular for the fluctuation spectrum of the GPDE in Sec. 9.3.3, ϕ_{MF} does *not* describe a true ground state. In the following, we will hence derive specific conditions that reveal the emergence of complex eigenvalues in the GPDE.

9.2. Coupling a two-level system to a coherent bosonic bath

Before focussing on the main problem of this section we aim at gaining some deeper intuition for the emergence of dynamical instabilities and their associated degeneracies. To this end, we consider a most simplified toy-model that only consists of two quantum levels. We assume that a coherent bosonic particle bath, such as a BEC, is coupled to this two-level quantum system allowing for a description by the following Hamiltonian:

$$H = (\varepsilon + \Delta\varepsilon)\,u^\dagger u - (\varepsilon - \Delta\varepsilon)\,d^\dagger d + g\,(u^\dagger d^\dagger + u\,d)\,, \tag{9.20}$$

where $u^\dagger$ ($d^\dagger$) create a bosonic particle in the upper (lower) quantum state. The operators u, d annihilate particles in the respective state correspondingly. Eq. (9.20) describes a situation where the particle source lies energetically in between those two levels $|u\rangle, |d\rangle$, and allows for a pairwise creation or annihilation of particles in the system. The latter

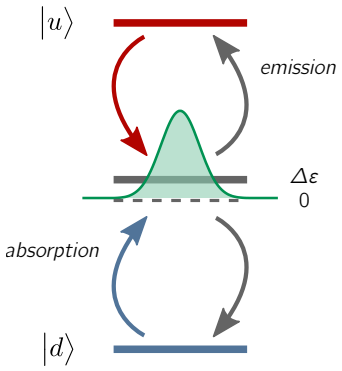

Figure 9.1.: Sketch of the simple toy model described by the Hamiltonian (9.20). Particle source is energetically shifted by $\Delta\varepsilon$. Emission (gray arrows) and absorption (coloured) of particles can only occur pairwise. Hamiltonian (9.20) describes dynamics of effective two-level system $\{|u\rangle, |d\rangle\}$.

property is captured by typical particle number violating terms parametrized by a coupling strength g. A schematic of this system can be found in Fig. 9.1. Complementary to our discussion in Sec. 9.1.2, here, we briefly want to elaborate on a typical Bogoliubov transformation and want to show explicitly why it fails in the present case. We then present how an analytic discussion of the problem is still possible when one loosens the constraint of having a canonical transformation preserving bosonic commutation relations.

9.2.1. Breakdown of the conventional Bogoliubov transformation

First of all, we bring the Hamiltonian (9.20) into a Bogoliubov-type form of

$$H = \left(u^\dagger, d\right) \begin{pmatrix} \varepsilon + \Delta\varepsilon & g \\ g & -\varepsilon + \Delta\varepsilon \end{pmatrix} \begin{pmatrix} u \\ d^\dagger \end{pmatrix} \equiv \Psi^\dagger \, h \, \Psi \,, \tag{9.21}$$

where we introduced the 'vector' $\Psi = (u, d^\dagger)$ and ignored the constant energy offset coming from $[d, d^\dagger] = 1$. One can now (try to) solve the quadratic Hamiltonian (9.21) by means of a typical Bogoliubov transformation procedure [206]. To this end, we introduce the transformation T defining $\widetilde{\Psi} = T\Psi$. This leads to

$$H = \widetilde{\Psi}^\dagger \widetilde{T}^\dagger \, h \, \widetilde{T} \widetilde{\Psi} \,, \tag{9.22}$$

with $\widetilde{T} = T^{-1}$. It is the goal to choose $\widetilde{T}$ in such a way that it diagonalises h. However, this has to be done under the condition that T preserves the commutation relations for the new set of creation and annihilation operators, $\widetilde{u}^\dagger$, etc. The commutation relations are expressed in terms of components of Ψ as $[\Psi_i, \Psi_j^\dagger] = (\sigma_z)_{ij} \overset{!}{=} [(T\Psi)_i, (T\Psi)_j^\dagger]$. This leads directly to the condition $\sigma_z = T\sigma_z T^\dagger$. Instead of considering $\widetilde{h} = \widetilde{T}^\dagger h \widetilde{T}$ one uses that

$$\sigma_z \widetilde{h} = \sigma_z \widetilde{T}^\dagger \sigma_z \sigma_z h \widetilde{T} = \widetilde{T}^{-1} \sigma_z h \widetilde{T} \,, \tag{9.23}$$

where $(\sigma_z)^2 = \mathbb{1}$ was applied. Note that Eq. (9.23) is simply a similarity transformation. Hence, all information about the original diagonalisation problem (9.22) are obtained by diagonalizing $\sigma_z h$. This, however, corresponds to the same issue as above: $\sigma_z h$ is *not* a Hermitian matrix, and therefore is not guaranteed to have real eigenvalues. The eigenvalues $\lambda_\pm$ of $\sigma_z h$ are readily computed to read as

$$\lambda_\pm = \varepsilon \pm \sqrt{\Delta\varepsilon^2 - g^2} \,. \tag{9.24}$$

Thus, whenever $\Delta\varepsilon < g$ the eigenvalues become indeed complex. At the same time, one can check[1] that

$$\sigma_z \stackrel{?}{=} T\sigma_z T^\dagger \quad : \quad \begin{cases} \text{true} & \text{for} \quad \mathrm{Im}(\lambda_\pm) = 0 \\ \text{false} & \text{for} \quad \mathrm{Im}(\lambda_\pm) \neq 0 \end{cases} . \tag{9.25}$$

Hence, the condition that guarantees the preservation of bosonic commutation relations cannot be fulfilled if the eigenvalues $\lambda_\pm$ are complex. So we conclude that as soon as $\sigma_z h$ yields complex eigenvalues the conventional Bogoliubov protocol is not consistent any more. In these circumstances no proper Bogoliubov transformation can be performed, meaning that fluctuation modes cannot be expressed in terms of quantised quasiparticles (see also above).

In Fig. 9.2(a) we show numerical results for the time evolution of the total particle number in the two-level system, i.e., $N(t) = \langle u^\dagger(t)u(t) + d^\dagger(t)d(t)\rangle$, with $u^\dagger(t)$ being in its Heisenberg form. Here, the initial state is the vacuum state containing no particles, see also below. For not too large times and coupling strengths the simple Hamiltonian (9.20) can be calculated numerically exactly. The results are shown for different values of $\Delta\varepsilon$. For $\Delta\varepsilon > g$ the number of particles in the system oscillates, corresponding to an absorption and subsequent emission of particles. The oscillation frequency is obviously given by the difference of the two calculated modes above, $\omega_{\mathrm{osc}} = \lambda_+ - \lambda_- = 2\sqrt{\Delta\varepsilon^2 - g^2}$. For $\Delta\varepsilon < g$ the number of particles becomes unstable and starts to grow exponentially in time. So, again, while the concept of a quantized Bogoliubov transformation fails for certain scenarios regarding the Hamiltonian (9.21), it still seems rightful and justified to calculate the physical modes from the non-Hermitian object $\sigma_z h$. This is in full agreement with the discussion of the Bogoliubov-de Gennes equations above, see Sec. 9.1.

9.2.2. Non-quantized Bogoliubov transformation

To make analytical progress, we now loosen the initial constraint of preserving the conical commutation relations. Instead, we will be guided by the premise of having to diagonalise $\sigma_z h$ (cf. Eq. (9.9)). In order to simplify notations we consider the special case where $\Delta\varepsilon = 0$. The transformed vector $\widetilde{\Psi}$ is then given by

$$\widetilde{\Psi} = \begin{pmatrix} \widetilde{u} \\ \widetilde{d}^\dagger \end{pmatrix} = T \begin{pmatrix} u \\ d^\dagger \end{pmatrix} = \frac{1}{\sqrt{2}} \begin{pmatrix} i & 1 \\ -i & 1 \end{pmatrix} \begin{pmatrix} u \\ d^\dagger \end{pmatrix} . \tag{9.26}$$

Alternatively, one can write the transformed creation and annihilation operators as

$$\widetilde{u}^\dagger = \frac{1}{\sqrt{2}}\left(d - iu^\dagger\right) , \quad \widetilde{u} = \frac{1}{\sqrt{2}}\left(d^\dagger + iu\right) , \quad \widetilde{d}^\dagger = \frac{1}{\sqrt{2}}\left(d^\dagger - iu\right) , \quad \widetilde{d} = \frac{1}{\sqrt{2}}\left(d + iu^\dagger\right) . \tag{9.27}$$

Using these expressions for the respective operators yields the Hamiltonian (9.22) in the rather peculiar form of

$$H = \widetilde{\Psi}\,\widetilde{h}\,\widetilde{\Psi} = \left(\widetilde{u}^\dagger, \widetilde{d}\right) \begin{pmatrix} 0 & -\varepsilon - ig \\ -\varepsilon + ig & 0 \end{pmatrix} \begin{pmatrix} \widetilde{u} \\ \widetilde{d}^\dagger \end{pmatrix} = \widetilde{E}_1\, \widetilde{u}^\dagger \widetilde{d}^\dagger + \widetilde{E}_1^*\, \widetilde{d}\,\widetilde{u} , \tag{9.28}$$

with $\widetilde{E}_1 = -(\varepsilon + ig)$ being the 'eigenvalue'. Here, the fact that even the transformed Hamiltonian depends (solely) on particle number violating terms reflects the situation

[1] The contradictory case is most easily seen for the situation where $\Delta\varepsilon = 0$. Here, it holds that $T^\dagger = T^{-1}$, i.e. the transformation becomes unitary. Consequently, it follows that $\sigma_z = T\sigma_z T^\dagger = T\sigma_z T^{-1} \Rightarrow [\sigma_z, T] = 0$. This is only true for a diagonal T, which it is *not*.

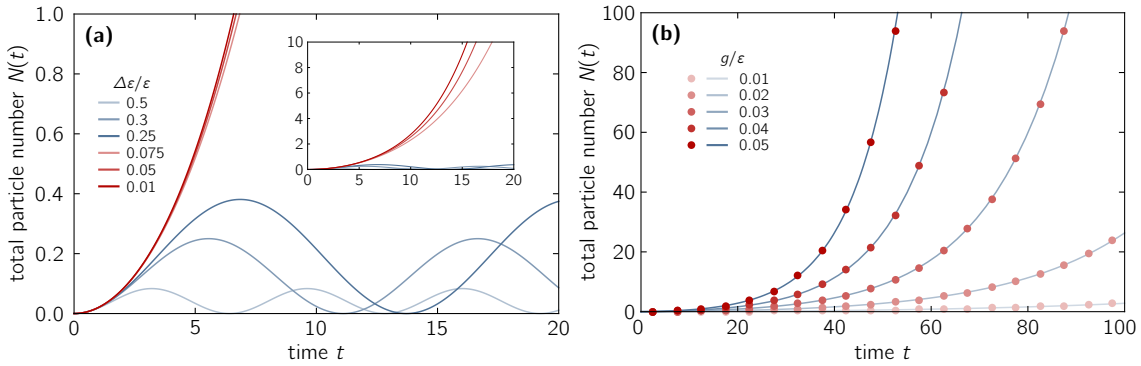

Figure 9.2.: Total particle number of function of time in simple toy model of Eq. (9.20). (a) Numerical exact calculation for different $\Delta\varepsilon$ at fixed interaction strength $g/\varepsilon = 0.1$. For $g < \Delta\varepsilon$ the number of particles (blue) oscillates with frequency $\omega_{\text{osc}} = 2\sqrt{\Delta\varepsilon^2 - g^2}$. When $g > \Delta\varepsilon$ the number of particles in the system (red) becomes unstable and grows exponentially with time, see inset. (b) Comparison of numerically exact data (red dots) and analytical expression of Eq. (9.34) (blue lines) for different interaction strengths. Despite the fact that Bogoliubov is not quantized the imaginary eigenvalues of Eq. (9.28) capture the correct exponential growth of N.

that well-defined quasiparticles do not exist when eigenvalues are complex. Moreover, using Eq. (9.27) and bosonic commutation relations for $u^\dagger, d^\dagger$, etc., one finds the following relations for the transformed operators:

$$[\widetilde{u}^\dagger, \widetilde{d}^\dagger] = [\widetilde{d}, \widetilde{u}] = 1\,, \quad [\widetilde{u}, \widetilde{u}^\dagger] = [\widetilde{d}, \widetilde{u}^\dagger] = 0\,, \quad [\widetilde{u}, \widetilde{u}] = [\widetilde{u}^\dagger, \widetilde{u}^\dagger] = 0\,, \tag{9.29}$$

where the last relations equally hold for $\widetilde{d}$ and $\widetilde{d}^\dagger$, respectively. It is therefore confirmed that the commutation relations for $\widetilde{u}, \widetilde{u}^\dagger$, etc., are not of bosonic type.

Next, in order to obtain the instability characteristics of the system explicitly we consider an observable as a function of time. To this end, we introduce the total particle number operator, $N = (u^\dagger u + d^\dagger d)$, which measures the sum of the particles in the lower and the upper state. Exploiting the expressions for the transformed operators of Eq. (9.27) as well as the associated commutation relations (9.29) one finds that

$$\begin{aligned} N(t) &= \langle u^\dagger(t)u(t) + d^\dagger(t)d(t)\rangle \\ &\overset{(9.27)}{=} \frac{1}{2}\left\langle (\widetilde{u}^\dagger(t) - \widetilde{d}(t))(\widetilde{u}(t) - \widetilde{d}^\dagger(t)) + (\widetilde{u}(t) - \widetilde{d}^\dagger(t))(\widetilde{d}(t) - \widetilde{u}^\dagger(t))\right\rangle \\ &\overset{(9.29)}{=} \langle \widetilde{u}^\dagger(t)\widetilde{u}(t)\rangle + \langle \widetilde{d}^\dagger(t)\widetilde{d}(t)\rangle - 1\,, \end{aligned} \tag{9.30}$$

where all operators are in their Heisenberg representation and can be evaluated using the Heisenberg equation of motion. For example, this yields for the operator $\widetilde{u}^\dagger(t)$ the following expression (with $\hbar = 1$):

$$\frac{d}{dt}\widetilde{u}^\dagger = i\,[H, \widetilde{u}^\dagger] = i\left(\widetilde{E}_1\,[\widetilde{u}^\dagger\widetilde{d}^\dagger, \widetilde{u}^\dagger] + \widetilde{E}_2\,[\widetilde{d}\,\widetilde{u}, \widetilde{u}^\dagger]\right) \overset{(9.29)}{=} -i\,\widetilde{E}_1\,\widetilde{u}^\dagger \tag{9.31}$$

$$\Rightarrow \qquad \widetilde{u}^\dagger(t) = e^{-i\widetilde{E}_1 t}\,\widetilde{u}\,. \tag{9.32}$$

One then finds $\widetilde{u}(t) = e^{i\widetilde{E}_1^* t}\widetilde{u}$, $\widetilde{d}(t) = e^{-i\widetilde{E}_1^* t}\widetilde{d}$ and $\widetilde{d}^\dagger(t) = e^{i\widetilde{E}_1 t}\widetilde{d}^\dagger$ in a similar fashion. With the help of these expressions one can simplify Eq. (9.30) to

$$N(t) = e^{-2gt/\hbar}\,\langle \widetilde{u}^\dagger\widetilde{u}\rangle + e^{2gt/\hbar}\,\langle \widetilde{d}^\dagger\widetilde{d}\rangle - 1\,. \tag{9.33}$$

We now evaluate the expectation values with respect to the vacuum state $|0\rangle$ containing no particles. Using Eq. (9.27) and recalling the typical actions of a creation (annihilation) operator on a Fock state yields

$$N(t) = \langle 0|u^\dagger(t)u(t) + d^\dagger(t)d(t)|0\rangle = \frac{1}{2}\left(e^{-2gt} + e^{2gt}\right) - 1\,. \tag{9.34}$$

To check this analytical result, which was obtained from a rather peculiar, non-quantized Bogoliubov transformation, we compare it to exact numerical data. In Fig. 9.2(b) we plot Eq. (9.34) for various coupling strengths g. As described above, numerical results are acquired with little effort due to the simplicity of the investigated quantum system. The agreement between numerics and the analytical form (9.34) again suggests that the eigenvalues of $\sigma_z h$ describe physical reality and that a system becomes dynamically unstable once these eigenvalues have imaginary components.

9.3. Dynamical instabilities of the Gross-Pitaevskii-Dirac equation

In this section, we finally analyse the fluctuation spectrum of the Gross-Pitaevskii-Dirac equation given by Eq. (8.50). After having gained some further intuition for dynamical instabilities in the previous section, we discuss fluctuations thoroughly by means of adjusted Bogoliubov-de Gennes equations. We first apply general aspects of Sec. 9.1 to the GPDE, followed by a numerical study of the corresponding BdG showing indeed the emergence of dynamical instabilities. Lastly, we analytically investigate these instabilities from a perturbation theory approach.

9.3.1. The quasiparticle Hamiltonian

The first goal is to present the Bogoliubov-de Gennes equations, see Eq. (9.7), associated with the system that is effectively described by the effective 1D Gross-Pitaevskii-Dirac equation, see Eq. (8.50). This can technically be done in two ways: one option is to start from Eq. (9.2) and consider fluctuations of type $\delta\phi(z,t) = \delta\Psi_1(z,t)e^{2ik_0 z} + \delta\Psi_2(z,t)e^{-2ik_0 z}$ (cf. Eq. (8.34)), where the full spatial dependence is encoded and the spinor structure is introduced only at the end, see Sec. 8.3. The second approach is to introduce the fluctuations already on the spinor level by making the ansatz $\delta\psi(z,t) = (\delta\Psi_1(z,t), \delta\Psi_2(z,t))^T$ such that

$$\begin{aligned}\psi(z,t) &= e^{-i\mu t}\left(\psi_{\mathrm{MF}}(z) + \delta\psi(z,t)\right) \\ &= e^{-i\mu t}\left(\Psi_1(z) + \delta\Psi_1(z,t), \Psi_2(z) + \delta\Psi_2(z,t)\right)^T,\end{aligned} \tag{9.35}$$

and use the previously derived one-dimensional Gross-Pitaevskii-Dirac equation given by Eq. (8.50). Here, we will follow the notation of the latter approach for no particular reasons. Note that by writing $\psi_{\mathrm{MF}} = (\Psi_1, \Psi_2)$ we have dropped the 'mean-field' label (MF) of the respective components.

We proceed by substituting the spinor (9.35) into the 1D GPDE (8.50) and subsequently linearise with respect to $\delta\psi$. By dropping space and time indices for notational brevity one obtains the following equation describing the fluctuations $\delta\psi$ to linear order:

$$\begin{aligned}i\partial_t\delta\psi =& (H_{\mathrm{D}} - \mu\mathbb{1})\,\delta\psi + g\Big[3(\psi^\dagger\psi)\mathbb{1} - (\psi^\dagger\sigma_z\psi)\sigma_z\Big]\,\delta\psi \\ &+ g\Big[3(\delta\psi^\dagger\psi)\mathbb{1} + 3(\psi^\dagger\delta\psi)\mathbb{1} - (\psi^\dagger\sigma_z\delta\psi)\sigma_z - (\delta\psi^\dagger\sigma_z\psi)\sigma_z\Big]\,\psi\,,\end{aligned} \tag{9.36}$$

where H_D is the Dirac Hamiltonian (8.31) and $g = g^{1\mathrm{D}}$. For the following discussion it is convenient to switch to a component representation of the spinors ψ and $\delta\psi$. Using Eq. (9.35) one finds after a few steps of simplification that expression (9.36) acquires the form

$$i\partial_t \delta\psi = H_\mathrm{D}^\mu\, \delta\psi + \underbrace{4g \begin{pmatrix} |\Psi_1|^2+|\Psi_2|^2 & \Psi_1\Psi_2^* \\ \Psi_1^*\Psi_2 & |\Psi_1|^2+|\Psi_2|^2 \end{pmatrix}}_{\equiv H_\mathrm{int}^1} \delta\psi + \underbrace{4g \begin{pmatrix} \frac{1}{2}\Psi_1^2 & \Psi_1\Psi_2 \\ \Psi_1\Psi_2 & \frac{1}{2}\Psi_2^2 \end{pmatrix}}_{\equiv H_\mathrm{int}^2} \delta\psi^* \,, \quad (9.37)$$

where we introduced the short hand notation $H_\mathrm{D}^\mu = H_\mathrm{D} - \mu\mathbb{1}$. After finding an equivalent expression for $\delta\psi^*$ by complex conjugation of Eq. (9.37), one can express the set of coupled equations (cf. Eqs. (9.2) and (9.3)) as

$$i\partial_t \delta\psi = H_\mathrm{D}^\mu\, \delta\psi + H_\mathrm{int}^1\, \delta\psi + H_\mathrm{int}^2\, \delta\psi^* \,, \quad (9.38)$$

$$-i\partial_t \delta\psi^* = H_\mathrm{D}^{\mu*}\, \delta\psi^* + H_\mathrm{int}^{1*}\, \delta\psi^* + H_\mathrm{int}^{2*}\, \delta\psi \,. \quad (9.39)$$

where we used the notation $H_\mathrm{D}^{\mu*} \equiv \left(H_\mathrm{D}^\mu\right)^*$, etc.

We make now a similar ansatz as in Sec. 9.1 by expressing the fluctuations in terms of modes of the form (cf. Eq. (9.6))

$$\delta\psi_\alpha(t) = e^{-E_\alpha t}\, \mathbf{u}_\alpha + e^{E_\alpha^* t}\, \mathbf{v}_\alpha^* \,, \quad (9.40)$$

where $\mathbf{u}$ and $\mathbf{v}$ are understood as to have inherited the spinor structure of $\delta\psi$. Following closely the procedure of Sec. 9.1 then yields the Bogoliubov-de Gennes equations which are given in the present case as

$$E_\alpha \begin{pmatrix} \mathbf{u}_\alpha \\ \mathbf{v}_\alpha \end{pmatrix} = H_\mathrm{BdG}^\mathrm{D} \begin{pmatrix} \mathbf{u}_\alpha \\ \mathbf{v}_\alpha \end{pmatrix} \qquad \text{with} \qquad H_\mathrm{BdG}^\mathrm{D} = \sigma_z^\mathrm{D} H_\mathrm{qp}^\mathrm{D} \,, \quad (9.41)$$

where the 'D' shall remind the reader of the additional intrinsic 2×2 Dirac structure. Hence, it holds that $(\sigma_z)_{11} = 1 \to (\sigma_z^\mathrm{D})_{11} = \mathbb{1}_{2\times 2}$, etc. Using the explicit expressions of Eq. (9.37) the *quasiparticle Hamiltonian* H_qp^D can be written as

$$H_\mathrm{qp}^\mathrm{D} = \begin{pmatrix} H_\mathrm{D}^\mu + H_\mathrm{int}^1 & H_\mathrm{int}^2 \\ \left(H_\mathrm{int}^2\right)^* & \left(H_\mathrm{D}^\mu\right)^* + \left(H_\mathrm{int}^1\right)^* \end{pmatrix} \equiv H_\mathrm{qp}^0 + H_\mathrm{qp}^\mathrm{int} \,, \quad (9.42)$$

with

$$H_\mathrm{qp}^0 = \begin{pmatrix} H_\mathrm{D} - \mu\mathbb{1} & 0 \\ 0 & \left(H_\mathrm{D}\right)^* - \mu\mathbb{1} \end{pmatrix} , \quad (9.43)$$

and

$$H_\mathrm{qp}^\mathrm{int} = 4g \begin{pmatrix} |\Psi_1|^2+|\Psi_2|^2 & \Psi_1\Psi_2^* & \frac{1}{2}\Psi_1^2 & \Psi_1\Psi_2 \\ \Psi_1^*\Psi_2 & |\Psi_1|^2+|\Psi_2|^2 & \Psi_1\Psi_2 & \frac{1}{2}\Psi_2^2 \\ \frac{1}{2}\left(\Psi_1^2\right)^* & \Psi_1^*\Psi_2^* & |\Psi_1|^2+|\Psi_2|^2 & \Psi_1^*\Psi_2 \\ \Psi_1^*\Psi_2^* & \frac{1}{2}\left(\Psi_2^2\right)^* & \Psi_1\Psi_2^* & |\Psi_1|^2+|\Psi_2|^2 \end{pmatrix} . \quad (9.44)$$

The numerical as well as analytical study of the Bogoliubov-de Gennes equations (9.41), and particularly of the 'interaction Hamiltonian' $H_\mathrm{qp}^\mathrm{int}$ will be the remaining objective of this chapter.

9.3.2. Numerical evidence for dynamical instabilities

As outlined above and in Sec. 9.1, diagonalizing $\sigma_z^{\mathrm{D}} H_{\mathrm{qp}}^{\mathrm{D}}$ yields the fluctuation spectrum. Owing to the structure of H_{qp}^0 it is natural as well as favourable for numerical applications to express the quasiparticle Hamiltonian in the basis of eigenstates of the original Dirac Hamiltonian H_{D}, see Eq. (8.14), as well as by eigenstates of its complex conjugate $(H_{\mathrm{D}})^*$. To this end, one expresses the mode vectors $\mathbf{u}$ and $\mathbf{v}$ in terms of these sets of eigenstates $\{|\psi_n^{\pm}\rangle\}$ and $\{|\psi_n^{\pm *}\rangle\}$, respectively. Hence, one writes

$$\mathbf{u}_\alpha = \sum_{n,\gamma} u_\alpha^{\gamma n} \, |\psi_n^{\gamma}\rangle \qquad \text{and} \qquad \mathbf{v}_\alpha = \sum_{n,\gamma} v_\alpha^{\gamma n} \, |\psi_n^{\gamma *}\rangle \ , \tag{9.45}$$

where $\gamma \in \{+,-\}$ (except for $n=0$) and the eigenstates $|\psi_n^{\gamma}\rangle$ are given by Eq. (8.23). Consequently, the doublet spinor $(\mathbf{u},\mathbf{v})^T$ can be expressed as

$$\left(\mathbf{u}_\alpha, \mathbf{v}_\alpha \right)^T \quad \rightarrow \quad \left(\dots, u_\alpha^{-1}, u_\alpha^0, u_\alpha^1, \dots, \dots, v_\alpha^{-1}, v_\alpha^0, v_\alpha^1, \dots \right)^T , \tag{9.46}$$

and the noninteracting part of the quasiparticle Hamiltonian, H_{qp}^0, becomes diagonal, yielding

$$H_{\mathrm{qp}}^0 \ \rightarrow \ \hbar\omega_0 \, \mathrm{diag}(\dots, -\sqrt{1}, 0, \sqrt{1}, \dots, \dots, -\sqrt{1}, 0, \sqrt{1} \dots) - \mu \mathbb{1} \, . \tag{9.47}$$

The main numerical task to obtain the fluctuation spectrum is to find $H_{\mathrm{qp}}^{\mathrm{int}}$ in the basis according to Eqs. (9.45) and (9.46) such as

$$H_{\mathrm{qp}}^{\mathrm{int}} = \begin{pmatrix} \langle \psi_n^{\gamma} | H_{\mathrm{int}}^1 | \psi_m^{\zeta} \rangle & \langle \psi_n^{\gamma} | H_{\mathrm{int}}^2 | \psi_m^{\zeta *} \rangle \\ \langle \psi_n^{\gamma *} | H_{\mathrm{int}}^{2*} | \psi_m^{\zeta} \rangle & \langle \psi_n^{\gamma *} | H_{\mathrm{int}}^{1*} | \psi_m^{\zeta *} \rangle \end{pmatrix} , \tag{9.48}$$

where $\langle \psi_n^{\gamma} | \, . \, | \psi_m^{\zeta} \rangle$, etc., are understood to be matrices expressed in the respective basis.

In order to calculate expression (9.48) and, subsequently, the spectrum of the fluctuations around the mean-field solution one follows a couple of steps:

1. At first, one needs to determine the mean-field solution to the interacting bosonic problem, i.e., find the (close to) zero energy state of the Gross-Pitaevskii-Dirac equation (8.50). As explained in Sec. (8.3), this 'ground state' solution ψ_{MF} is calculated in a iterative fashion together with its eigenenergy μ.

2. Assuming the convergence of the mean-field protocol, the resulting components of the spinor $\psi_{\mathrm{MF}} = (\Psi_1, \Psi_2)^T$ are substituted into Eq. (9.48). In fact, one can boost the numerical evaluation by realising that $i\Psi_1 = \Psi_2^*$, which is a reminiscence of the property of the basis states $\{|\uparrow\rangle, |\downarrow\rangle\}$, see Eq. (8.20). With the aid of this property one can show that
$$\langle \psi_n^{\gamma} | H_{\mathrm{int}}^2 | \psi_m^{\zeta *} \rangle = \langle \psi_n^{\gamma} | H_{\mathrm{int}}^1 | \psi_m^{\zeta} \rangle \tag{9.49}$$
This simplifies the numerical costs, since the solution from the first step can be recycled in calculating $H_{\mathrm{qp}}^{\mathrm{int}}$.

Note that the size of the submatrices are determined by the interaction strength. For values of g that are comparable to experimentally accessible values, i.e., $g \sim \mathcal{O}(1)$, truncation is typically possible at $n_{\max} \sim \mathcal{O}(10) - \mathcal{O}(100)$, where $n_{\max}$ is inversely proportional to g, see Sec. 9.3.3. The fluctuation spectrum is finally obtained from diagonalizing $\sigma_z H_{\mathrm{qp}}$, which is a $2(2n_{\max}+1) \times 2(2n_{\max}+1)$ dimensional matrix.

In Fig. 9.3 we show the resulting fluctuation spectrum for various interactions strengths g. The real part of the spectrum is given in Fig. 9.3(a). If there were no interactions, all

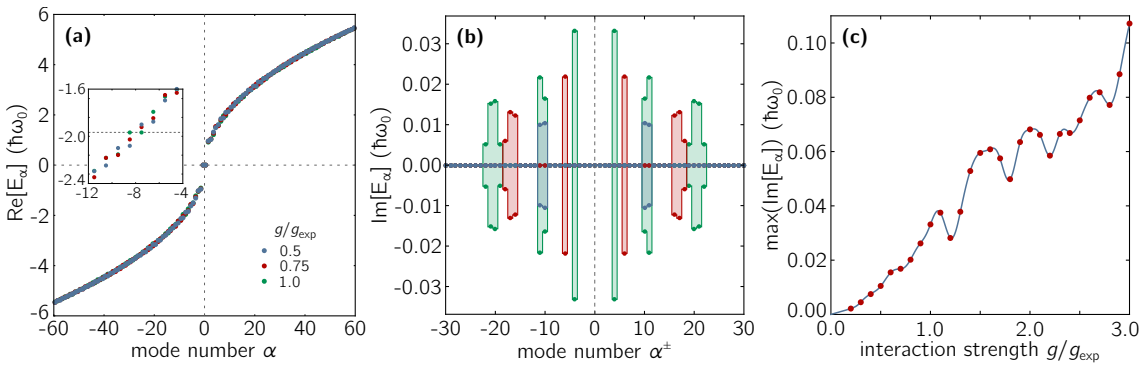

Figure 9.3.: Fluctuation spectrum of effective Gross-Pitaevskii-Dirac equation. (a) Real part of spectrum for different interaction strengths. Inset reveals occurring degeneracies (dashed line). (b) Imaginary part of spectrum, where mode numbers are divided by two (compared to (a)) in order to combine '±-pairs'. Different interaction strengths are as indicated in (a). Imaginary contributions decay for larger mode numbers. (c) Maximum imaginary eigenvalue as a function of interaction strength. Red dots mark calculated values and blue line is a guide to the eye.

eigenvalues would come exactly in pairs according to Eq. (9.47). With interactions, however, the two mirrored Dirac spectra are modified and most energies lose their 'partner'. Nonetheless, if two states are pushed into resonance at certain interaction strengths, they form a degenerate pair with respect to the real part of the eigenvalues. This is visualized in the inset of Fig. 9.3(a). At the same time, they acquire an equal but opposite imaginary part, see Fig. 9.3(b). Note that due to the property $E_\alpha = -E_{-\alpha}$ of the fluctuation spectrum, see Sec. 9.1.2, the emergence of complex eigenvalues always occurs in a quartet as already argued above. This is also seen in Fig. 9.3(b). Moreover, the expected pair of Goldstone modes (cf. Eq. (9.15)) is also clearly visible from Fig. 9.3(a).

There are two main observations associated with the complex eigenmodes representing dynamical instabilities: first, while for moderate interactions strengths, $g \sim \mathcal{O}(1)$, dynamical instabilities can be found for small mode numbers, $\alpha \sim \mathcal{O}(1) - \mathcal{O}(10)$, for decreasing interaction strengths the emergence of $\mathrm{Im}[E_\alpha] \neq 0$ only happens for steadily growing mode numbers. This important property can be clearly observed from Fig. 9.3(b) and will be explained in the next section by means of perturbation theory. Second, the largest imaginary value of all fluctuation modes, i.e., the fastest growing rate of an unstable mode, seems to be directly proportional to the interaction strength, $\max(\mathrm{Im}[E_\alpha]) \propto g$, as suggested by Fig. 9.3(c) (having said this, the behaviour for $g \ll 1$ is quadratic in g, see Sec. 9.3.3). One further observes that for experimentally relevant interaction strengths the growth rate is given by $\max(\mathrm{Im}[E_\alpha]) \approx 0.03\,\omega_0\hbar$, which is only on the per cent level of the characteristic frequency ω_0 of the effective Dirac system. For typical experimental running times of $t_{\mathrm{exp}} \sim 2\mathrm{ms}$ this leads to a contribution from instabilities of about $e^{\max(\mathrm{Im}[E_\alpha])t_{\mathrm{exp}}/\hbar} \simeq 1.063$. Hence, the probability conservation is expected to be violated only on the per cent level, as well. We therefore conclude that within experimental errors the effect of dynamical instabilities are *not* detectable and therefore negligible for the setup presented in the previous chapter 8. It is, nevertheless, a very interesting effect that is unique to bosonic systems. Since running times of the experiment is limited by photon scattering the most direct way to study these effects is by increasing the s-wave scattering between the atoms. This could be done by, e.g., means of Feshbach resonances, or by substituting the rubidium atoms with a different species that interacts more strongly with each other for the given experimental parameters.

9.3.3. Analytic expressions from perturbation theory

The emergence of complex eigenvalues in the fluctuation spectrum as seen above can be explained by degeneracies between two modes of the Bogoliubov-de Gennes equations represented by H_{BdG}. As explained in Sec. 9.1.2, one of these modes should have negative norm, while the other one has positive norm. Such degeneracies can be analysed by means of perturbation theory for small interaction strengths. In the following, we thus shall assume that $g \ll 1$. We further consider the lowest order perturbation picture: whenever two on-diagonal entries become approximately degenerate one can restrict the discussion to the 2×2 subspace spanned by the respective basis states. The effective 2×2 matrix has the same structure as the toy-model of Sec. 9.2. Generally, such degeneracies are possible as long as the stationary solution ψ_0 is not a true ground state of the problem. For the course of this section we utilize the property of H_{D} of being truly unbound[2]. This allows for the situation that the negative branch of the unperturbed Dirac spectrum can interfere with the positive partner and vice versa (due to the multiplication with σ_z).

We shall again express H_{BdG} in terms of single-particle Dirac eigenstates, see Eqs. (9.45) and (9.46). Using now lowest order perturbation theory and reducing the problem to a 2×2 submatrix one straightforwardly obtains the following condition to have complex eigenvalues (cf. Eqs. (9.21) and (9.24)):

$$\frac{1}{4}\left(\langle\psi_n^\gamma|H_{\mathrm{D}}^\mu + H_{\mathrm{int}}^1|\psi_n^\gamma\rangle + \langle\psi_m^{\zeta*}|H_{\mathrm{D}}^{\mu*} + H_{\mathrm{int}}^{1*}|\psi_m^{\zeta*}\rangle\right)^2 < \left|\langle\psi_n^\gamma|H_{\mathrm{int}}^2|\psi_m^{\zeta*}\rangle\right|^2 . \tag{9.50}$$

Exploiting respective properties of the original Hamiltonian, i.e., using Eq. (9.49) as well as $\langle\psi_m^{\zeta*}|H_{\mathrm{D}}^{\mu*}+H_{\mathrm{int}}^{1*}|\psi_m^{\zeta*}\rangle = \langle\psi_m^{\zeta}|H_{\mathrm{D}}^{\mu}+H_{\mathrm{int}}^{1}|\psi_m^{\zeta}\rangle$, one can rewrite Eq. (9.50) as

$$\frac{1}{4}\left(E_n^\gamma + E_m^\zeta - 2\mu + \langle\psi_n^\gamma|H_{\mathrm{int}}^1|\psi_n^\gamma\rangle + \langle\psi_m^\zeta|H_{\mathrm{int}}^1|\psi_m^\zeta\rangle\right)^2 < \left|\langle\psi_n^\gamma|H_{\mathrm{int}}^1|\psi_m^\zeta\rangle\right|^2 . \tag{9.51}$$

To proceed we first assume to lowest order that $\mu \approx \mu^0 = \frac{1}{2}\langle\psi_0|H_{\mathrm{int}}^1|\psi_0\rangle$. This relation stems from the fact that $\frac{1}{2}H_{\mathrm{int}}^1$ indeed coincides with the nonlinear term of the GPDE, see Eq. (8.52). Furthermore, when evaluating the matrix elements appearing in Eq. (9.51) using lowest order perturbation theory one must keep in mind that H_{int}^1 depends self-consistently on ψ_{MF}. Here, we presume that $\psi_{\mathrm{MF}} \approx \psi_0$ holds. One can therefore express the interaction part of the quasiparticle Hamiltonian to lowest order, $H_{\mathrm{int}}^{1(0)}$, as

$$H_{\mathrm{int}}^{1(0)}(z) = 4g\,(\phi_0^{\mathrm{ho}}(z))^2\,(\,\mathbb{1} - \frac{1}{2}\,\sigma_y\,)\,. \tag{9.52}$$

The matrix elements can be determined correspondingly to read as

$$\langle\psi_n^\gamma|H_{\mathrm{int}}^{1(0)}|\psi_m^\zeta\rangle = 4g\int dz\;(\phi_0^{\mathrm{ho}}(z))^2\Big[\psi_n^{\gamma\dagger}(z)\psi_m^\zeta(z) - \frac{1}{2}\psi_n^{\gamma\dagger}(z)\,\sigma_y\,\psi_m^\zeta(z)\Big]\,, \tag{9.53}$$

where the position space representations of the Dirac eigenspinors are given by Eq. (8.25). Due to the fact that their entries are given by simple harmonic oscillator eigenfunctions the integral of Eq. (9.53) can be solved analytically for all combinations of (n,m,γ,ζ) using the identities

$$\int dz\;(\phi_0^{\mathrm{ho}}(z))^4 = \frac{1}{\sqrt{2\pi}\,l_{\mathrm{D}}}\,, \tag{9.54}$$

$$\int dz\;(\phi_0^{\mathrm{ho}}(z))^2\phi_n^{\mathrm{ho}}(z)\,\phi_m^{\mathrm{ho}}(z) = \frac{1}{\sqrt{2\pi}\,l_{\mathrm{D}}}\frac{(-1)^{(n-m)/2}}{\sqrt{2^{(n+m)}n!m!}}(n+m-1)!!\,,$$

[2] This is, however, *not* true in the actual experimental system. We will comment on this issue in Sec. 9.4.

where $(n+m)/2 \in \mathbb{Z}$, since $\phi_0^{\mathrm{ho}}(z)$ is an even function of space, and $('!!')'!'$ indicates the (double) factorial. Finally, using Eqs. (9.53) and (9.54) one can rewrite the inequality of Eq. (9.51) after a few steps of simplification in the form

$$\begin{aligned}\gamma\sqrt{n}+\zeta\sqrt{m}-6g'+g'\Big[\frac{(2n-1)!!}{2^n n!}\Big(3+\frac{2n}{2n-1}\Big)\Big]+g'\Big[\frac{(2m-1)!!}{2^m m!}\Big(3+\frac{2m}{2m-1}\Big)\Big]\\ <\quad g'^2\Big[\frac{3\gamma\zeta}{\sqrt{2^{n+m}n!m!}}(n+m-1)!!+\frac{(n+m-3)!!}{\sqrt{2^{n+m-2}(n-1)!(m-1)!}}\Big],\end{aligned} \tag{9.55}$$

where γ,ζ should be understood as $\in\{+1,-1\}$. Furthermore, we divided the inequality by $\hbar\omega_0$ and redefined the interaction strength such as $g'/g'_{\mathrm{exp}}=1$, with $g'_{\mathrm{exp}}=g_{\mathrm{exp}}/(\omega_0\hbar\sqrt{2\pi}l_{\mathrm{D}})=\beta_{\mathrm{D}}/\sqrt{2\pi}$ (cf. Eq.(8.57)). Using experimental parameters as introduced in Ch. 8 this dimensionless interaction strength is given by $g'_{\mathrm{exp}}\approx 0.13$.

Note that the inequality (9.55) only has a chance to hold for arbitrary values of g' if $(\gamma\sqrt{n}+\zeta\sqrt{m})/g'\sim 1$. So for this to be true in the limit of $g'\to 0$ two conditions need to be fulfilled: $n,m\gg 1$ as well as $\gamma n\approx -\zeta m$. One can, however, show that the inequality is never fulfilled for exactly $\gamma n=-\zeta m$, i.e., $n=m$ and $\gamma=-\zeta$, meaning that instabilities can never occur due to a mixing of a state with its original 'negative partner'. Thus, we let $m=n-k$ and $\zeta=-\gamma$, where $n\gg k$ and $k/2\in\mathbb{N}$ (due to the symmetry of the integrand in Eq. (9.54)). Considering first the left-hand side (lhs) of Eq. (9.55), and assuming the conditions above to be present, one can employ two following simplifications. First, we obtain $\sqrt{n}-\sqrt{n-k}\approx 2/(k\sqrt{n})$, where we also assumed that $\gamma=+1$ (and therefore $\zeta=-1$) in favour of simplicity. Second, using *Stirling's formula* one can reduce the factorial expressions to $(2n-1)!!/(2^n n!)\approx 1/\sqrt{\pi n}$. Eventually, the lhs of Eq. (9.55) reads as

$$\mathrm{lhs}\approx\Big[\frac{k}{2\sqrt{n}}+g'\Big(\frac{4}{\sqrt{\pi n}}+\frac{4}{\sqrt{\pi(n-k)}}-6\Big)\Big]^2\approx\Big[\frac{k}{2\sqrt{n}}-3g'\Big]^2. \tag{9.56}$$

Since the lhs is desired to be smaller than the right-hand side (rhs) of Eq.(9.55), one aims at tuning n such that Eq. (9.56) becomes minimal, i.e.,

$$n_{\mathrm{min}}\approx\frac{1}{36g'^2}\Big(\frac{k}{2}+\frac{4g'}{\sqrt{\pi}}\Big)^2\approx\frac{k^2}{4}\frac{1}{36g'^2}\,. \tag{9.57}$$

Of course, n_{min} cannot be a continuous variable but must rather be an integer number. This is formally enforced by an a rounding procedure of the form

$$n^r_{\mathrm{min}}=n_{\mathrm{min}}+\epsilon_r\,, \tag{9.58}$$

where $\epsilon_r\in[-\frac{1}{2},\frac{1}{2})$ is a corresponding rounding error. Substituting Eq. (9.58) back into the expression for the lhs, Eq. (9.56), yields

$$\mathrm{lhs}_{\mathrm{min}}\approx\frac{k^2}{64}\frac{\epsilon_r^2}{n_{\mathrm{min}}^3}\approx\frac{\epsilon_r^2\,3^6\,2^6}{k^4}g'^6\,. \tag{9.59}$$

Using the same assumptions as above for the rhs (i.e., $n,m\gg 1, m\approx n$), one finds the simplified approximative expression

$$\mathrm{rhs}\approx\frac{1}{\pi}\frac{g'^2}{n}\qquad\to\qquad\mathrm{rhs}_{\mathrm{min}}\approx\frac{1}{\pi}\frac{g'^2}{n_{\mathrm{min}}}=\frac{3^2\,2^4}{\pi k^2}g'^4\,. \tag{9.60}$$

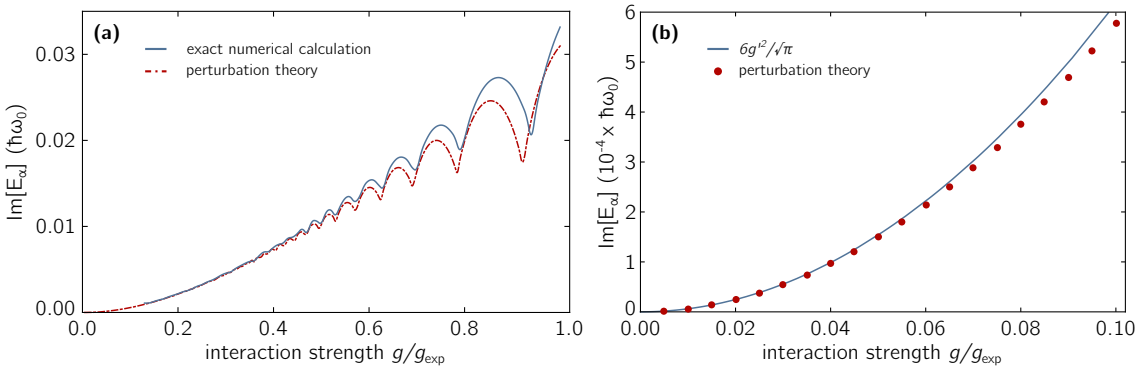

Figure 9.4.: Largest imaginary eigenvalue of the fluctuation spectrum as a function of the interaction strength g. (a) Comparison of exact numerical data with a perturbation theory treatment according to Eq. (9.55). (b) Full lowest-order perturbation theory versus analytical results of Eq. 9.63 for $g/g_{\mathrm{exp}} \ll 1$.

Note that the quantity 'rhs$_{\mathrm{min}}$' does not refer to a minimal value of the right-hand side, but is understood to be connected to a minimal value of the lhs via Eq. (9.57). Looking at lhs$_{\mathrm{min}}$ < rhs$_{\mathrm{min}}$ allows to finally derive the inequality

$$g'^2 < \frac{1}{3^4\pi}\frac{k^2}{\epsilon_r^2}\,, \tag{9.61}$$

which states self-consistently that for $g' \to 0$, i.e., where perturbation theory is believed to be valid, one can indeed always fulfil this inequality. In other words, for infinitesimally small interaction strengths g, there will *always* be unstable modes predicted by the fluctuation analysis of the GPDE. How fast these modes grow/decay depends on the imaginary part of the respective eigenvalues, $\mathrm{Im}(E_\alpha)$. Within our perturbative treatment these are just given by

$$\mathrm{Im}(E_\alpha) = \pm\left(\mathrm{rhs} - \mathrm{lhs}\right)^{1/2}, \tag{9.62}$$

where the maximal complex value is determined by lhs$_{\mathrm{min}}$ and rhs$_{\mathrm{min}}$, respectively, i.e.,

$$\max(\mathrm{Im}[E_\alpha]) = \pm\left(\mathrm{rhs}_{\mathrm{min}} - \mathrm{lhs}_{\mathrm{min}}\right)^{1/2} \approx \pm\left(\mathrm{rhs}_{\mathrm{min}}\right)^{1/2} = \pm\frac{12}{k\sqrt{\pi}}\,g'^2\,. \tag{9.63}$$

Hence, the magnitude of the instability is expected to behave quadratically on the interaction strength for small values of g. Also, the strongest unstable mode is predicted for the smallest available value for k, i.e., $k = 2$.

In Fig. 9.4 we confirm our analytical results of Eq. (9.63) numerically. First, we ensure that the inequality expression derived directly from perturbation theory, see Eq. (9.55), yields good agreement with a full numerical calculation of the eigenvalue with the largest imaginary part as discussed in Sec. 9.3.2. We calculate $\mathrm{Im}(E_\alpha)$ according to Eq. (9.62) using the full expressions of Eq. (9.55). The results are shown in Fig. 9.4(a), where for $g/g_{\mathrm{exp}} \lesssim 0.5$ perturbation theory delivers reliable results. In the regime of $g' \ll 1$, where Eq. (9.63) is applicable, it is hence justyfied to compare the analytical expression of Eq. (9.63) to the results obtained from full expressions of lowest order perturbation theory. We do this because the mode number at which complex eigenvalues emerge scales as $1/g'^2$, see Eq. (9.57). Thus, the full calculation of the fluctuation spectrum up to a point where the emergence of unstable modes is detectable becomes numerically costly quite rapidly for $g' \to 0$. Nonetheless, Fig. 9.4(b) confirms the applicability of Eq. (9.63)

for small values of g', and therefore the quadratic behaviour of the unstable mode on the interaction strength, $\mathrm{Im}(E_\alpha) \overset{g' \ll 1}{\propto} g^2$.

9.4. Outlook

In this chapter, we have studied the emergence of dynamical instabilities in the Gross-Pitaevskii-Dirac equation by analysing the corresponding fluctuation spectrum. Numerical results and analytical discussions revealed that such instabilities are present for all interaction strengths. The key principle of these instabilities is the occurrence of degeneracies in the mirror-type spectrum of the Dirac Hamiltonian.

For an experimental setup as presented in Ref. [53] a system with positive and equal but opposite negative branch of eigenvalues is simulated well for mode numbers close to the edge state, $n \sim \mathcal{O}(10)$. We therefore believe that the dynamical instability of pairwise decaying atoms should be within the scope of the discussed experiment. Nevertheless, we also showed that expected decaying rates are only on the per cent level compared to the characteristic frequency ω_0, which should prohibit an observation of the decay on the time scale of the experiment of ~ 2ms. In order to boost the dynamical instability effect one could enhance interaction effects by means of Feshbach resonances or by using an atom species with stronger relative interactions strength, as already discussed in Sec. 8.5.

However, effects are expected to change qualitatively as soon as cases of even smaller interaction strengths, g/g_{exp}, are considered. This is because the true Hamiltonian describing the experiment is energetically bound and deviates from the Dirac Hamiltonian as absolute values of mode numbers increase. Thus, we conjecture that lowering g and thereby increasing the mode number, $n \propto 1/g^2$, ultimately leads to a vanishing of the dynamical instability.

In addition, it is unclear how a dynamical instability behaves when changing the set of discrete excited energy levels to a continuum of states, as discuss in Sec. 8.5. Such a continuum is achieved by forcing the external potential to stay finite when $|z| \to \infty$. We conjecture that the instability mechanism remains unchanged, but leave the analysis of such a situation as an open question to be answered.

10. Summary and Outlook

The desire for controlling, manipulating and creating quantum matter is a concern at the forefront of research holding exciting prospects for everyday life purposes in the future. In recent years, ultracold atoms in optical lattices have emerged as a versatile tool for studying and engineering complex many-body systems in the laboratory. Both their high level of controllability and their unique property of essentially being isolated quantum systems have also triggered an enormous amount of theoretical proposals and ideas.

Within this thesis we mainly focussed on the exciting concept of quantum engineering by studying periodically driven versions of these systems. Here, large parts of our efforts revolved around the central question about the role of interactions in these intriguing Floquet systems. The unique and, at the same time, intellectually challenging property in this context is the discrete violation of energy conservation and its consequences. Next to the description of heating effects, we were strongly concerned with the role of dynamics in these essentially out-of-equilibrium systems. We studied both transport as a response to the external drive itself as well as dynamical effects as a consequence of intrinsic heating mechanisms. In addition, we investigated the fascinating aspects of topology in these Floquet systems and beyond. Here, we also provided the theoretical framework of a specifically designed system showing associated properties. Due to their reliable role as quantum simulators, ultracold atoms can indeed be used to mimic aspects of this contemporary research field of condensed matter physics.

In part I, we showed that coherent periodic driving can be used to establish directed motion of particles in quantum systems when combined with an adequate breaking of associated mirror symmetries. We studied such ratchet effects for excitations of a bosonic Mott insulator by using a full Floquet treatment of the effectively non-interacting system. We explicitly studied how the dynamics of doublons and holes can be manipulated and designed by a suitable choice of parameters. Furthermore, we extended our discussion to the scenario of operating a quantum ratchet in the presence of an external static homogeneous force. Identifying translational symmetries in a mixed position/Floquet space allows us both to study such system using conventional Floquet methods and to understand transport properties in a long-time limit: directed motion of particles is only expected to be possible if the external potential strength g and the driving frequency Ω fulfil the commensurability condition $n_0 g = m_0 \Omega$, with $n_0/2, m_0 \in \mathbb{Z}$. We also discuss the general idea of stabilizing ratchet transport effects by means of topological order. Here, however, we had to conclude that such mechanism is not possible for arbitrary driving frequencies.

Part II of this thesis was entirely devoted to the effects of interactions in Floquet systems. Having started from a full quantum field theoretical approach, we first derived a semiclassical kinetic equation that models the dynamics and the scattering of quasiparticles in such systems. The essential approximation for the development of this Floquet-Boltzmann equation was a clear separation of time scales. Here, the rapid, oscillatory behaviour on time scales of $T_0 = 2\pi/\Omega$ was fully treated within the Floquet formalism giving rise to the notion of Floquet quasiparticles. We showed that the slow dynamics and scattering processes of the system is then captured by a familiar Boltzmann equation with adjusted properties: as the energy is only conserved modulo $\hbar\Omega$, the interacting Floquet system naturally heats up as time progresses. Therefore, generic Floquet systems are fundamentally

distinct from ordinary interacting quantum systems in the sense that true equilibration can only take place at infinite temperature. In order to study expected heating effects, we applied the Floquet-Boltzmann equation by describing a recent experimental realisation of the Haldane model by means of lattice shaking [23]. From analysing a corresponding homogeneous system we found that Floquet heating effects should be relevant on experimental time scales for typical parameter choices. Such effects are, however, suppressed by the experimental limitations of preparing initial low entropy states. Furthermore, we used the Floquet-Boltzmann equation to describe the dynamical evolution of a cold atom cloud in the presence of an additional shallow confining potential. In this case, spatially dependent heating characteristics lead to temperature gradients and subsequent particle and heat currents which we captured by an adequate hydrodynamic description of the problem. We found that particles do not just flow radially outwards using the provision of extra energy resulting from heating, but also that anomalous particle current can emerge. The latter aspect is a direct consequence of possible non-trivial Berry curvatures in the Haldane model. This Floquet version of the anomalous Nernst effect can be view as the result of an interplay of intrinsic Floquet heating, macroscopic diffusion and non-trivial topological properties.

In part III, we provided the theoretical background for a simulation of a one-dimensional topological edge state with cold atoms in a corresponding lattice geometry, as experimentally performed by the Weitz group [53]. Using an optical lattice with chirped amplitude one can effectively simulate a massive 1D Dirac equation with emerging chiral symmetry. Such a Dirac system can be shown to incorporate the same topological features as a system at the interface of two topologically distinct regions which are described by the SSH model. We gave an analytical discussion of the problem leading to quantitative predictions of experimentally observable quantities, such as the characteristic frequency. Most importantly, we showed that interactions of particles within the 3D cloud can be neglected for experimentally relevant parameter choices, hereby indeed allowing for an effective one-dimensional description of the system. Experimental results [53] in combination with a comparison to numerical simulations provided by us suggested the successful simulation of the targeted Dirac system. Furthermore, analysing the fluctuation spectrum yielded the emergence of dynamical instabilities in the interacting bosonic system. We could numerically show, however, that such effects are negligible on time scales of the conducted experiments.

For the future, it will be exciting to further pursue the ideas of quantum simulation and engineering. One possible perspective is the development of techniques to obtain enhanced control over the dynamics of a many-body quantum system. In the spirit of part I, for example, generalized forms of quantum ratchets could be used to provide a tool for steering transport in systems beyond 1D and cold atoms. Here, the explicit extension of such quantum machines to generally interacting system is an obvious challenge from a theoretical perspective. In cases where interactions are not too strong, one can even aim for explaining interaction effects within our developed Floquet-Boltzmann formalism.

Moreover, since Floquet engineering has proven to be exceptionally fruitful in creating and realising seemingly unreachable synthetic quantum systems, a deeper understanding of interaction effects also beyond the limits discussed in this thesis is desirable. One possible idea is certainly to simply extend the Floquet-Boltzmann formalism to regimes of larger interaction strengths by incorporating more sophisticated approximation schemes within the collision integral. Another interesting route to follow is the possible inclusion of additional and different interaction types. As ultimately macroscopic devices will most

probably need to rely on materials at room temperature, the extension of the Floquet-Boltzmann equation to more conventional systems will not just be intellectually exciting but also crucial for further practicable purposes. Here, the predicted physics might fundamentally change due to the typical coupling to a phononic bath. While a specific case of enhanced superconductivity due to driving has already been investigated recently within a Floquet kinetic equation approach [256], the extension to other model systems is still an open question. In this context, a potential paradigm change could take place: so far, most experimental Floquet realisation aimed at reducing interaction effects for successful quantum engineering, and the majority of theoretical studies focussed on interactions as being intrinsic, non-designed effects of Floquet systems. However, as, e.g., suggested by our discussion of realising the Floquet-Nernst effect in chapter 7, a possible exciting direction of research could be *interaction assisted Floquet engineering*. In these cases, one does not simply addresses questions about the consequence of interactions in already realised Floquet constructed systems, but instead deliberately uses interactions to engineer targeted effects and systems.

Another future aspect related to the last point, is the direct simulation of interacting topological quantum systems. No doubt, studying interaction effects in Floquet realised topologically non-trivial systems such as the Haldane model [23] or even in a dynamical version of it [111] appears appealing. Nevertheless, the general enterprise does not necessarily require a periodically driven systems but is relevant for the general realm of quantum simulation. For example, the bosonic 1D Dirac system discussed in chapter 8 holds prospects for the simulation of interacting topological quantum matter by studying the role of such interactions on the edge state. In order to support a possible experimental realisation by a thorough theoretical discussion, the analysis of dynamical instabilities in chapter. 9 needs to be tailored to experimental characteristics in future works.

Bibliography

[1] J. P. Dowling and G. J. Milburn, *Quantum technology: the second quantum revolution*, Philosophical Transactions of the Royal Society of London A: Mathematical, Physical and Engineering Sciences **361** (2003).

[2] D. P. DiVincenzo, *Quantum Computation*, Science **270** (1995).

[3] E. Dagotto, *Complexity in Strongly Correlated Electronic Systems*, Science **309**, 257 (2005).

[4] R. P. Feynman, *Simulating physics with computers*, International Journal of Theoretical Physics **21**, 467 (1982).

[5] I. Bloch, J. Dalibard, and W. Zwerger, *Many-body physics with ultracold gases*, Reviews of Modern Physics **80**, 885 (2008).

[6] I. Bloch, J. Dalibard, and S. Nascimbène, *Quantum simulations with ultracold quantum gases*, Nature Physics **8**, 267 (2012).

[7] W. S. Bakr, J. I. Gillen, A. Peng, S. Fölling, and M. Greiner, *A quantum gas microscope for detecting single atoms in a Hubbard-regime optical lattice*, Nature **462**, 74 (2009).

[8] J. F. Sherson et al., *Single-atom-resolved fluorescence imaging of an atomic Mott insulator*, Nature **467**, 68 (2010).

[9] E. Haller et al., *Single-atom imaging of fermions in a quantum-gas microscope*, Nature Physics **11**, 738 (2015).

[10] M. F. Parsons et al., *Site-Resolved Imaging of Fermionic 6Li in an Optical Lattice*, Physical Review Letters **114**, 213002 (2015).

[11] M. Greiner, O. Mandel, T. Esslinger, T. W. Hänsch, and I. Bloch, *Quantum phase transition from a superfluid to a Mott insulator in a gas of ultracold atoms*, Nature **415**, 39 (2002).

[12] U. Schneider et al., *Metallic and Insulating Phases of Repulsively Interacting Fermions in a 3D Optical Lattice*, Science **322** (2008).

[13] M. Cheneau et al., *Light-cone-like spreading of correlations in a quantum many-body system*, Nature **481**, 484 (2012).

[14] U. Schneider et al., *Fermionic transport and out-of-equilibrium dynamics in a homogeneous Hubbard model with ultracold atoms*, Nature Physics **8**, 213 (2012).

[15] S. Trotzky et al., *Probing the relaxation towards equilibrium in an isolated strongly correlated one-dimensional Bose gas*, Nature Physics **8**, 325 (2012).

[16] P. Bordia, H. Lüschen, U. Schneider, M. Knap, and I. Bloch, *Periodically driving a many-body localized quantum system*, Nature Physics , 4 (2017).

[17] A. Eckardt, *Colloquium: Atomic quantum gases in periodically driven optical lattices*, Reviews of Modern Physics **89**, 011004 (2017).

[18] M. Lohse, C. Schweizer, O. Zilberberg, M. Aidelsburger, and I. Bloch, *A Thouless quantum pump with ultracold bosonic atoms in an optical superlattice*, Nature Physics **12**, 350 (2015).

[19] S. Nakajima et al., *Topological Thouless pumping of ultracold fermions*, Nature Physics **12**, 296 (2016).

[20] J. Struck et al., *Engineering Ising-XY spin-models in a triangular lattice using tunable artificial gauge fields*, Nature Physics **9**, 738 (2013).

[21] N. H. Lindner, G. Refael, and V. Galitski, *Floquet topological insulator in semiconductor quantum wells*, Nature Physics **7**, 490 (2011).

[22] N. Goldman, J. C. Budich, and P. Zoller, *Topological quantum matter with ultracold gases in optical lattices*, Nature Physics **12**, 639 (2016).

[23] G. Jotzu et al., *Experimental realization of the topological Haldane model with ultracold fermions*, Nature **515**, 237 (2014).

[24] A. Polkovnikov, K. Sengupta, A. Silva, and M. Vengalattore, *Colloquium: Nonequilibrium dynamics of closed interacting quantum systems*, Reviews of Modern Physics **83**, 863 (2011).

[25] E. Altman, *Non equilibrium quantum dynamics in ultra-cold quantum gases*, arXiv:1512.00870 (2015).

[26] S. Hofferberth, I. Lesanovsky, B. Fischer, T. Schumm, and J. Schmiedmayer, *Non-equilibrium coherence dynamics in one-dimensional Bose gases*, Nature **449**, 324 (2007).

[27] M. Gring et al., *Relaxation and Prethermalization in an Isolated Quantum System*, Science **337**, 1318 (2012).

[28] T. Langen, R. Geiger, M. Kuhnert, B. Rauer, and J. Schmiedmayer, *Local emergence of thermal correlations in an isolated quantum many-body system*, Nature Physics **9**, 640 (2013).

[29] T. Kinoshita, T. Wenger, and D. S. Weiss, *A quantum Newton's cradle*, Nature **440**, 900 (2006).

[30] M. Schreiber et al., *Observation of many-body localization of interacting fermions in a quasirandom optical lattice*, Science **349** (2015).

[31] L. D'Alessio and M. Rigol, *Long-time behavior of isolated periodically driven interacting lattice systems*, Physical Review X **4**, 041048 (2014).

[32] A. Lazarides, A. Das, and R. Moessner, *Equilibrium states of generic quantum systems subject to periodic driving*, Physical Review E **90**, 012110 (2014).

[33] A. D. O'Connell et al., *Quantum ground state and single-phonon control of a mechanical resonator*, Nature **464**, 697 (2010).

[34] D. Deutsch, *Quantum Theory, the Church-Turing Principle and the Universal Quantum Computer*, Proceedings of the Royal Society of London A: Mathematical, Physical and Engineering Sciences **400** (1985).

[35] M. A. Nielsen and I. L. Chuang, *Quantum Computation and Quantum Information*, Cambridge University Press, Cambridge, 2010.

[36] S. Lloyd, *Universal Quantum Simulators*, Science **273** (1996).

[37] A. Kitaev, *Fault-tolerant quantum computation by anyons*, Annals of Physics **303**, 2 (2003).

[38] C. Nayak, S. H. Simon, A. Stern, M. Freedman, and S. Das Sarma, *Non-Abelian anyons and topological quantum computation*, Reviews of Modern Physics **80**, 1083 (2008).

[39] D. Castelvecchi, *Quantum computers ready to leap out of the lab in 2017*, Nature **541**, 9 (2017).

[40] M. Lewenstein, A. Sanpera, and V. Ahufinger, *Ultracold Atoms in Optical Lattices: Simulating quantum many-body systems*, Oxford University Press, 2012.

[41] K. Kim et al., *Quantum simulation of frustrated Ising spins with trapped ions.*, Nature **465**, 590 (2010).

[42] R. Blatt and C. F. Roos, *Quantum simulations with trapped ions*, Nature Physics **8**, 277 (2012).

[43] J. Clarke and F. K. Wilhelm, *Superconducting quantum bits*, Nature **453**, 1031 (2008).

[44] M. H. Devoret and R. J. Schoelkopf, *Superconducting Circuits for Quantum Information: An Outlook*, Science **339** (2013).

[45] B. P. Lanyon et al., *Towards quantum chemistry on a quantum computer*, Nature Chemistry **2**, 106 (2010).

[46] X. Peng, J. Zhang, J. Du, and D. Suter, *Quantum Simulation of a System with Competing Two- and Three-Body Interactions*, Physical Review Letters **103**, 140501 (2009).

[47] I. M. Georgescu, S. Ashhab, and F. Nori, *Quantum simulation*, Reviews of Modern Physics **86**, 153 (2014).

[48] M. W. Zwierlein, J. R. Abo-Shaeer, A. Schirotzek, C. H. Schunck, and W. Ketterle, *Vortices and superfluidity in a strongly interacting Fermi gas*, Nature **435**, 1047 (2005).

[49] J. Dalibard, F. Gerbier, G. Juzeliūnas, and P. Öhberg, *Colloquium: Artificial gauge potentials for neutral atoms*, Reviews of Modern Physics **83**, 1523 (2011).

[50] M. Aidelsburger et al., *Experimental Realization of Strong Effective Magnetic Fields in an Optical Lattice*, Physical Review Letters **107**, 255301 (2011).

[51] M. Inguscio, W. Ketterle, S. Stringari, and G. Roati, *Proceedings of the International School of Physics "Enrico Fermi", Course 191: Quantum Matter at Ultralow Temperatures*, IOS Press, proceeding edition, 2016.

[52] T. Salger, C. Grossert, S. Kling, and M. Weitz, *Klein Tunneling of a Quasirelativistic Bose-Einstein Condensate in an Optical Lattice*, Physical Review Letters **107**, 240401 (2011).

[53] M. Leder et al., *Real-space imaging of a topologically protected edge state with ultracold atoms in an amplitude-chirped optical lattice*, Nature Communications **7**, 13112 (2016).

[54] G. Floquet, *Sur les équations différentielles linéaires à coefficients périodiques*, Annales scientifiques de l'École Normale Supérieure **12** (1883).

[55] H. Lignier et al., *Dynamical Control of Matter-Wave Tunneling in Periodic Potentials*, Physical Review Letters **99**, 220403 (2007).

[56] J. Struck et al., *Quantum Simulation of Frustrated Classical Magnetism in Triangular Optical Lattices*, Science **333** (2011).

[57] R. A. Hart et al., *Observation of antiferromagnetic correlations in the Hubbard model with ultracold atoms*, Nature **519**, 211 (2015).

[58] K. B. Davis et al., *Bose-Einstein Condensation in a Gas of Sodium Atoms*, Physical Review Letters **75**, 3969 (1995).

[59] M. H. Anderson, J. R. Ensher, M. R. Matthews, C. E. Wieman, and E. A. Cornell, *Observation of Bose-Einstein Condensation in a Dilute Atomic Vapor*, Science **269** (1995).

[60] H. J. Metcalf and P. van der Straten, *Laser Cooling and Trapping*, Springer-Verlag, New York, 1999.

[61] R. Grimm, M. Weidemüller, and Y. B. Ovchinnikov, *Optical Dipole Traps for Neutral Atoms*, in *Advances in Atomic, Molecular and Optical Physics*, volume 42, pages 95–170, 2000.

[62] M. Inguscio, W. Ketterle, and C. Salomon, *Proceedings of the International School of Physics "Enrico Fermi", Course 164: Ultra-cold Fermi Gases*, IOS Press, 2007.

[63] K. Madison, K. Bongs, L. Carr, A. Rey, and H. Zhai, *Annual Review of Cold Atoms and Molecules: Volume 2*, World Scientific Publishing Company, 2014.

[64] T. Kovachy et al., *Matter Wave Lensing to Picokelvin Temperatures*, Physical Review Letters **114**, 143004 (2015).

[65] S. Giorgini, *Theory of ultracold atomic Fermi gases*, Reviews of Modern Physics **80**, 1215 (2008).

[66] T. Köhler, K. Góral, and P. S. Julienne, *Production of cold molecules via magnetically tunable Feshbach resonances*, Reviews of Modern Physics **78**, 1311 (2006).

[67] M. J. H. Ku, A. T. Sommer, L. W. Cheuk, and M. W. Zwierlein, *Revealing the Superfluid Lambda Transition in the Universal Thermodynamics of a Unitary Fermi Gas*, Science **335** (2012).

[68] L. Tarruell, D. Greif, T. Uehlinger, G. Jotzu, and T. Esslinger, *Creating, moving and merging Dirac points with a Fermi gas in a tunable honeycomb lattice*, Nature **483**, 302 (2012).

[69] G.-B. Jo et al., *Ultracold Atoms in a Tunable Optical Kagome Lattice*, Physical Review Letters **108**, 045305 (2012).

[70] N. Ashcroft and D. Mermin, *Solid State Physics*, Thomson Learning, 1st edition, 1976.

[71] B. Capogrosso-Sansone, N. V. Prokof'ev, and B. V. Svistunov, *Phase diagram and thermodynamics of the three-dimensional Bose-Hubbard model*, Physical Review B **75**, 134302 (2007).

[72] T. Esslinger, *Fermi-Hubbard Physics with Atoms in an Optical Lattice*, Annual Review of Condensed Matter Physics **1**, 129 (2010).

[73] M. F. Parsons et al., *Site-resolved measurement of the spin-correlation function in the Fermi-Hubbard model*, Science **353** (2016).

[74] J. Shirley, *Solution of the Schrödinger Equation with a Hamiltonian Periodic in Time*, Physical Review **138**, B979 (1965).

[75] H. Sambe, *Steady States and Quasienergies of a Quantum-Mechanical System in an Oscillating Field*, Physical Review A **7**, 2203 (1973).

[76] M. Grifoni and P. Hänggi, *Driven quantum tunneling*, Physics Reports **304**, 229 (1998).

[77] T. Dittrich et al., *Quantum Transport and Dissipation*, Wiley-VCH, Weinheim, 1998.

[78] N. Goldman and J. Dalibard, *Periodically Driven Quantum Systems: Effective Hamiltonians and Engineered Gauge Fields*, Physical Review X **4**, 031027 (2014).

[79] M. Bukov, L. D'Alessio, and A. Polkovnikov, *Universal High-Frequency Behavior of Periodically Driven Systems: from Dynamical Stabilization to Floquet Engineering*, Advances in Physics **64**, 139 (2015).

[80] A. Eckardt and E. Anisimovas, *High-frequency approximation for periodically driven quantum systems from a Floquet-space perspective*, 2015.

[81] I. Martin, G. Refael, and B. Halperin, *Topological frequency conversion in strongly driven quantum systems*, arXiv:1612.02143 (2016).

[82] F. Nathan, M. S. Rudner, N. H. Lindner, E. Berg, and G. Refael, *Quantized magnetization density in periodically driven systems*, arXiv:1610.03590 (2016).

[83] F. Casas, J. A. Oteo, and J. Ros, *Floquet theory: exponential perturbative treatment*, Journal of Physics A: Mathematical and General **34**, 3379 (2001).

[84] S. Blanes, F. Casas, J. A. Oteo, and J. Ros, *The Magnus expansion and some of its applications*, 2009.

[85] P. Pfeifer and R. D. Levine, *A stationary formulation of time-dependent problems in quantum mechanics*, The Journal of Chemical Physics **79**, 5512 (1983).

[86] H. Breuer and M. Holthaus, *Adiabatic processes in the ionization of highly excited hydrogen atoms*, Zeitschrift für Physik D: Atoms, Molecules and Clusters **11**, 1 (1989).

[87] U. Peskin and N. Moiseyev, *The solution of the time-dependent Schrödinger equation by the (t,t') method: Theory, computational algorithm and applications*, The Journal of Chemical Physics **99**, 4590 (1993).

[88] S. C. Althorpe, D. J. Kouri, D. K. Hoffman, and N. Moiseyev, *A time-independent wavepacket approach to the (t, t')-method for treating time-dependent Hamiltonian systems*, Chemical Physics **217**, 289 (1997).

[89] A. Eckardt and M. Holthaus, *Dressed matter waves*, Journal of Physics: Conference Series **99**, 012007 (2008).

[90] D. F. Martinez, *Floquet–Green function formalism for harmonically driven Hamiltonians*, Journal of Physics A: Mathematical and General **36**, 9827 (2003).

[91] D. F. Martinez, *High-order harmonic generation and dynamic localization in a driven two-level system, a non-perturbative solution using the Floquet–Green formalism*, Journal of Physics A: Mathematical and General **38**, 9979 (2005).

[92] N. H. Lindner, E. Berg, and M. S. Rudner, *Universal Chiral Quasisteady States in Periodically Driven Many-Body Systems*, Physical Review X **7**, 011018 (2017).

[93] H. Breuer and M. Holthaus, *Quantum phases and Landau-Zener transitions in oscillating fields*, Physics Letters A **140**, 507 (1989).

[94] H. Breuer, K. Dietz, and M. Holthaus, *Berry's phase in quantum optics*, Physical Review A **47**, 725 (1993).

[95] M. V. Berry, *Quantal Phase Factors Accompanying Adiabatic Changes*, Proceedings of the Royal Society of London A: Mathematical, Physical and Engineering Sciences **392**, 45 (1984).

[96] R. Bamler, *Phase-Space Berry Phases in Chiral Magnets: Skyrmion Charge, Hall Effect, and Dynamics of Magnetic Skyrmions*, PhD thesis, Universität zu Köln, 2016.

[97] D. W. Hone, R. Ketzmerick, and W. Kohn, *Time-dependent Floquet theory and absence of an adiabatic limit*, Physical Review A **56**, 4045 (1997).

[98] A. Zenesini, H. Lignier, D. Ciampini, O. Morsch, and E. Arimondo, *Coherent Control of Dressed Matter Waves*, Physical Review Letters **102**, 100403 (2009).

[99] J. Struck et al., *Tunable Gauge Potential for Neutral and Spinless Particles in Driven Optical Lattices*, Physical Review Letters **108**, 225304 (2012).

[100] T. Kitagawa et al., *Observation of topologically protected bound states in photonic quantum walks*, Nature Communications **3**, 882 (2012).

[101] M. Genske et al., *Electric Quantum Walks with Individual Atoms*, Physical Review Letters **110**, 190601 (2013).

[102] H. Miyake, G. A. Siviloglou, C. J. Kennedy, W. C. Burton, and W. Ketterle, *Realizing the Harper Hamiltonian with Laser-Assisted Tunneling in Optical Lattices*, Physical Review Letters **111**, 185302 (2013).

[103] M. Aidelsburger et al., *Realization of the Hofstadter Hamiltonian with Ultracold Atoms in Optical Lattices*, Physical Review Letters **111**, 185301 (2013).

[104] M. E. Tai et al., *Microscopy of the interacting Harper-Hofstadter model in the few-body limit*, arXiv:1612.05631 (2016).

[105] M. Aidelsburger et al., *Measuring the Chern number of Hofstadter bands with ultracold bosonic atoms*, Nature Physics **11**, 162 (2015).

[106] C. J. Kennedy, W. C. Burton, W. C. Chung, and W. Ketterle, *Observation of Bose–Einstein condensation in a strong synthetic magnetic field*, Nature Physics **11**, 859 (2015).

[107] B. M. Anderson, I. B. Spielman, and G. Juzeliūnas, *Magnetically Generated Spin-Orbit Coupling for Ultracold Atoms*, Physical Review Letters **111**, 125301 (2013).

[108] V. Galitski and I. B. Spielman, *Spin–orbit coupling in quantum gases*, Nature **494**, 49 (2013).

[109] M. Atala et al., *Observation of chiral currents with ultracold atoms in bosonic ladders*, Nature Physics **10**, 13 (2014).

[110] N. Fläschner et al., *Experimental reconstruction of the Berry curvature in a Floquet Bloch band*, Science **352**, 1091 (2016).

[111] N. Fläschner et al., *Observation of a dynamical topological phase transition*, arXiv:1608.05616 (2016).

[112] M. C. Rechtsman et al., *Photonic Floquet topological insulators*, Nature **496**, 196 (2013).

[113] Y. H. Wang, H. Steinberg, P. Jarillo-Herrero, and N. Gedik, *Observation of Floquet-Bloch States on the Surface of a Topological Insulator*, Science **342** (2013).

[114] T. Oka and H. Aoki, *Photovoltaic Hall effect in graphene*, Physical Review B **79**, 081406 (2009).

[115] T. Kitagawa, T. Oka, A. Brataas, L. Fu, and E. Demler, *Transport properties of nonequilibrium systems under the application of light: Photoinduced quantum Hall insulators without Landau levels*, Physical Review B **84**, 235108 (2011).

[116] T. Kitagawa, E. Berg, M. Rudner, and E. Demler, *Topological characterization of periodically driven quantum systems*, Physical Review B **82**, 235114 (2010).

[117] A. Gómez-León and G. Platero, *Floquet-Bloch Theory and Topology in Periodically Driven Lattices*, Physical Review Letters **110**, 200403 (2013).

[118] L. Foa Torres, P. Perez-Piskunow, C. Balseiro, and G. Usaj, *Multiterminal Conductance of a Floquet Topological Insulator*, Physical Review Letters **113**, 266801 (2014).

[119] V. Dal Lago, M. Atala, and L. E. F. Foa Torres, *Floquet topological transitions in a driven one-dimensional topological insulator*, Physical Review A **92**, 023624 (2015).

[120] H. Dehghani, T. Oka, and A. Mitra, *Dissipative Floquet topological systems*, Physical Review B **90**, 195429 (2014).

[121] M. S. Rudner, N. H. Lindner, E. Berg, and M. Levin, *Anomalous Edge States and the Bulk-Edge Correspondence for Periodically Driven Two-Dimensional Systems*, Physical Review X **3**, 031005 (2013).

[122] L. Jiang et al., *Majorana fermions in equilibrium and in driven cold-atom quantum wires*, Physical Review Letters **106**, 220402 (2011).

[123] P. Hauke et al., *Non-Abelian Gauge Fields and Topological Insulators in Shaken Optical Lattices*, Physical Review Letters **109**, 145301 (2012).

[124] A. G. Grushin, Á. Gómez-León, and T. Neupert, *Floquet Fractional Chern Insulators*, Physical Review Letters **112**, 156801 (2014).

[125] L. Wang, M. Troyer, and X. Dai, *Topological Charge Pumping in a One-Dimensional Optical Lattice*, Physical Review Letters **111**, 026802 (2013).

[126] P. Marra, R. Citro, and C. Ortix, *Fractional quantization of the topological charge pumping in a one-dimensional superlattice*, Physical Review B **91**, 125411 (2015).

[127] P. Titum, E. Berg, M. S. Rudner, G. Refael, and N. H. Lindner, *Anomalous Floquet-Anderson Insulator as a Nonadiabatic Quantized Charge Pump*, Physical Review X **6**, 021013 (2016).

[128] D. V. Else, B. Bauer, and C. Nayak, *Floquet Time Crystals*, Physical Review Letters **117**, 090402 (2016).

[129] L. Zhang, V. Khemani, and D. A. Huse, *A Floquet model for the many-body localization transition*, Physical Review B **94**, 224202 (2016).

[130] E. Bairey, G. Refael, and N. H. Lindner, *Driving-induced many-body localization*, arXiv:1702.06208 (2017).

[131] K. Jiménez-García et al., *Peierls Substitution in an Engineered Lattice Potential*, Physical Review Letters **108**, 225303 (2012).

[132] G. Jotzu et al., *Creating State-Dependent Lattices for Ultracold Fermions by Magnetic Gradient Modulation*, Physical Review Letters **115**, 073002 (2015).

[133] A. Eckardt et al., *Exploring dynamic localization with a Bose-Einstein condensate*, Physical Review A **79**, 013611 (2009).

[134] D. H. Dunlap and V. M. Kenkre, *Dynamic localization of a charged particle moving under the influence of an electric field*, Physical Review B **34**, 3625 (1986).

[135] A. Eckardt et al., *Frustrated quantum antiferromagnetism with ultracold bosons in a triangular lattice*, EPL (Europhysics Letters) **89**, 10010 (2010).

[136] S. Denisov, L. Morales-Molina, S. Flach, and P. Hänggi, *Periodically driven quantum ratchets: Symmetries and resonances*, Physical Review A **75**, 063424 (2007).

[137] T. Salger et al., *Directed Transport of Atoms in a Hamiltonian Quantum Ratchet*, Science **326**, 1241 (2009).

[138] F. D. M. Haldane, *Model for a Quantum Hall Effect without Landau Levels: Condensed-Matter Realization of the "Parity Anomaly"*, Physical Review Letters **61**, 2015 (1988).

[139] D. Jaksch and P. Zoller, *Creation of effective magnetic fields in optical lattices: the Hofstadter butterfly for cold neutral atoms*, New Journal of Physics **5**, 56 (2003).

[140] S. K. Baur, M. H. Schleier-Smith, and N. R. Cooper, *Dynamic optical superlattices with topological bands*, Physical Review A **89**, 051605 (2014).

[141] T. Dubček et al., *Weyl Points in Three-Dimensional Optical Lattices: Synthetic Magnetic Monopoles in Momentum Space*, Physical Review Letters **114**, 225301 (2015).

[142] N. Goldman et al., *Creating topological interfaces and detecting chiral edge modes in a two-dimensional optical lattice*, Physical Review A **94**, 043611 (2016).

[143] H. M. Price, T. Ozawa, and N. Goldman, *Synthetic dimensions for cold atoms from shaking a harmonic trap*, Physical Review A **95**, 023607 (2017).

[144] A. Quelle, C. Weitenberg, K. Sengstock, and C. M. Smith, *Driving protocol for a Floquet topological phase without static counterpart*, arXiv:1704.00306 (2017).

[145] R. Desbuquois et al., *Controlling the Floquet state population and observing micromotion in a periodically driven two-body quantum system*, arXiv:1703.07767 (2017).

[146] M. Genske and A. Rosch, *Directed motion of doublons and holes in periodically driven Mott insulators*, Physical Review A **90**, 043637 (2014).

[147] M. Smoluchowski, *Experimentell nachweisbare, der üblichen Thermodynamik widersprechende Molekularphänomene*, Physik. Zeitschr. **13** (1912).

[148] R. P. Feynman, R. B. Leighton, and M. Sands, *The Feynman Lectures on Physics, Vol. I*, Addison-Wesley, 1963.

[149] P. Reimann, *Brownian motors: noisy transport far from equilibrium*, Physics Reports **361**, 57 (2002).

[150] P. Hänggi, *Artificial Brownian motors: Controlling transport on the nanoscale*, Reviews of Modern Physics **81**, 387 (2009).

[151] F. Jülicher, A. Ajdari, and J. Prost, *Modeling molecular motors*, Reviews of Modern Physics **69**, 1269 (1997).

[152] R. D. Astumian, *Thermodynamics and Kinetics of a Brownian Motor*, Science **276**, 917 (1997).

[153] R. D. Astumian and P. Hänggi, *Brownian Motors*, Physics Today **55**, 33 (2002).

[154] V. Serreli, C.-F. Lee, E. R. Kay, and D. A. Leigh, *A molecular information ratchet.*, Nature **445**, 523 (2007).

[155] G. Mahmud et al., *Directing cell motions on micropatterned ratchets*, Nature Physics **5**, 606 (2009).

[156] H. Linke, *Experimental Tunneling Ratchets*, Science **286**, 2314 (1999).

[157] M. D. Blumenthal et al., *Gigahertz quantized charge pumping*, Nature Physics **3**, 343 (2007).

[158] M. V. Costache and S. O. Valenzuela, *Experimental spin ratchet.*, Science **330**, 1645 (2010).

[159] C. Drexler et al., *Magnetic quantum ratchet effect in graphene*, Nature Nanotechnology **8**, 104 (2013).

[160] M. Schiavoni, L. Sanchez-Palencia, F. Renzoni, and G. Grynberg, *Phase Control of Directed Diffusion in a Symmetric Optical Lattice*, Physical Review Letters **90**, 094101 (2003).

[161] R. Gommers, S. Bergamini, and F. Renzoni, *Dissipation-Induced Symmetry Breaking in a Driven Optical Lattice*, Physical Review Letters **95**, 073003 (2005).

[162] R. Gommers, S. Denisov, and F. Renzoni, *Quasiperiodically Driven Ratchets for Cold Atoms*, Physical Review Letters **96**, 240604 (2006).

[163] P. Reimann, M. Grifoni, and P. Hänggi, *Quantum Ratchets*, Physical Review Letters **79**, 10 (1997).

[164] H. Schanz, T. Dittrich, and R. Ketzmerick, *Directed chaotic transport in Hamiltonian ratchets*, Physical Review E **71**, 026228 (2005).

[165] J. Gong and P. Brumer, *Generic Quantum Ratchet Accelerator with Full Classical Chaos*, Physical Review Letters **97**, 240602 (2006).

[166] P. H. Jones, M. Goonasekera, D. R. Meacher, T. Jonckheere, and T. S. Monteiro, *Directed Motion for Delta-Kicked Atoms with Broken Symmetries: Comparison between Theory and Experiment*, Physical Review Letters **98**, 073002 (2007).

[167] A. V. Ponomarev, S. Denisov, and P. Hänggi, *ac-Driven Atomic Quantum Motor*, Physical Review Letters **102**, 230601 (2009).

[168] S. Denisov, S. Flach, and P. Hänggi, *Tunable transport with broken space–time symmetries*, Physics Reports **538**, 77 (2014).

[169] T. Salger et al., *Tuning the Mobility of a Driven Bose-Einstein Condensate via Diabatic Floquet Bands*, Physical Review Letters **110**, 135302 (2013).

[170] A. Browaeys et al., *Transport of atoms in a quantum conveyor belt*, Physical Review A **72**, 053605 (2005).

[171] Y. Miroshnychenko et al., *Quantum engineering: An atom-sorting machine*, Nature **442**, 151 (2006).

[172] D. J. Thouless, *Quantization of particle transport*, Physical Review B **27**, 6083 (1983).

[173] A. Rosch, D. Rasch, B. Binz, and M. Vojta, *Metastable Superfluidity of Repulsive Fermionic Atoms in Optical Lattices*, Physical Review Letters **101**, 265301 (2008).

[174] R. Sensarma et al., *Lifetime of double occupancies in the Fermi-Hubbard model*, Physical Review B **82**, 224302 (2010).

[175] R. Sensarma, D. Pekker, A. M. Rey, M. D. Lukin, and E. Demler, *Relaxation of Fermionic Excitations in a Strongly Attractive Fermi Gas in an Optical Lattice*, Physical Review Letters **107**, 145303 (2011).

[176] A. L. Chudnovskiy, D. M. Gangardt, and A. Kamenev, *Doublon Relaxation in the Bose-Hubbard Model*, Physical Review Letters **108**, 085302 (2012).

[177] N. Strohmaier et al., *Observation of Elastic Doublon Decay in the Fermi-Hubbard Model*, Physical Review Letters **104**, 080401 (2010).

[178] G. D. Mahan, *Many-particle physics*, Springer, 3rd edition, 2000.

[179] Y.-J. Lin, R. L. Compton, K. Jiménez-García, J. V. Porto, and I. B. Spielman, *Synthetic magnetic fields for ultracold neutral atoms*, Nature **462**, 628 (2009).

[180] Y. J. Lin et al., *A synthetic electric force acting on neutral atoms*, Nature Physics **7**, 531 (2011).

[181] M. C. Beeler et al., *The spin Hall effect in a quantum gas.*, Nature **498**, 201 (2013).

[182] A. Sørensen, E. Demler, and M. Lukin, *Fractional Quantum Hall States of Atoms in Optical Lattices*, Physical Review Letters **94**, 086803 (2005).

[183] A. Celi et al., *Synthetic Gauge Fields in Synthetic Dimensions*, Physical Review Letters **112**, 043001 (2014).

[184] S. Mandt, A. Rapp, and A. Rosch, *Interacting Fermionic Atoms in Optical Lattices Diffuse Symmetrically Upwards and Downwards in a Gravitational Potential*, Physical Review Letters **106**, 250602 (2011).

[185] E. H. Lieb and D. W. Robinson, *The finite group velocity of quantum spin systems*, Communications in Mathematical Physics **28**, 251 (1972).

[186] M. Genske, *Electric Quantum Walks with Individual Atoms*, MSc thesis (2012).

[187] K. v. Klitzing, G. Dorda, and M. Pepper, *New Method for High-Accuracy Determination of the Fine-Structure Constant Based on Quantized Hall Resistance*, Physical Review Letters **45**, 494 (1980).

[188] D. J. Thouless, M. Kohmoto, M. P. Nightingale, and M. den Nijs, *Quantized Hall Conductance in a Two-Dimensional Periodic Potential*, Physical Review Letters **49**, 405 (1982).

[189] M. Z. Hasan and C. L. Kane, *Colloquium: Topological insulators*, Reviews of Modern Physics **82**, 3045 (2010).

[190] X.-L. Qi and S.-C. Zhang, *Topological insulators and superconductors*, Reviews of Modern Physics **83**, 1057 (2011).

[191] B. Yan and C. Felser, *Topological Materials: Weyl Semimetals*, arXiv:1611.04182 (2016).

[192] S. Muhlbauer et al., *Skyrmion Lattice in a Chiral Magnet*, Science **323**, 915 (2009).

[193] N. Nagaosa and Y. Tokura, *Topological properties and dynamics of magnetic skyrmions.*, Nature Nanotechnology **8**, 899 (2013).

[194] N. Manton and P. Sutcliffe, *Topological Solitions*, Cambridge University Press, 2004.

[195] B. A. Bernevig and T. L. Hughes, *Topological Insulators and Topological Superconductors*, Princeton University Press, 2013.

[196] X.-L. Qi, T. L. Hughes, and S.-C. Zhang, *Topological field theory of time-reversal invariant insulators*, Physical Review B **78**, 195424 (2008).

[197] D. Tong, *Lectures on the Quantum Hall Effect*, arXiv:1606.06687 (2016).

[198] M. Nakahara, *Geometry, Topology and Physics*, Hilger, 1990.

[199] D. Xiao, M.-C. C. Chang, and Q. Niu, *Berry phase effects on electronic properties*, Reviews of Modern Physics **82**, 1959 (2010).

[200] Q. Niu and D. J. Thouless, *Quantised adiabatic charge transport in the presence of substrate disorder and many-body interaction*, Journal of Physics A: Mathematical and General **17**, 2453 (1984).

[201] M. Karski et al., *Quantum Walk in Position Space with Single Optically Trapped Atoms*, Science **325** (2009).

[202] A. Steffen et al., *Digital atom interferometer with single particle control on a discretized space-time geometry.*, Proceedings of the National Academy of Sciences of the United States of America **109**, 9770 (2012).

[203] C. Chamon, M. O. Goerbig, R. Moessner, and L. F. Cugliandolo, editors, *Topological Aspects of Condensed Matter Physics*, Oxford University Press, 2017.

[204] J. Ringot, P. Szriftgiser, J. C. Garreau, and D. Delande, *Experimental Evidence of Dynamical Localization and Delocalization in a Quasiperiodic Driven System*, Physical Review Letters **85**, 2741 (2000).

[205] M. Eckstein and P. Werner, *Damping of Bloch Oscillations in the Hubbard Model*, Physical Review Letters **107**, 186406 (2011).

[206] Altland Alexander and Ben Simons, *Condensed Matter Field Theory*, Cambridge University Press, 2 edition, 2010.

[207] A. Kamenev, *Field Theory of Non-Equilibrium Systems*, Cambridge University Press, 2011.

[208] T. Matsubara, *A New Approach to Quantum-Statistical Mechanics*, Progress of Theoretical Physics **14**, 351 (1955).

[209] J. Rammer, *Quantum transport theory*, Perseus Books, 1998.

[210] J. Schmiedmayer and J. Berges, *Cold Atom Cosmology*, Science **341** (2013).

[211] J. Berges, *Nonequilibrium Quantum Fields: From Cold Atoms to Cosmology*, arXiv:1503.02907 (2015).

[212] J. Schwinger, *Brownian Motion of a Quantum Oscillator*, Journal of Mathematical Physics **2**, 407 (1961).

[213] O. Konstantinov and V. Perel', *A Diagram Technique for Evaluating Transport Quantities*, JETP **12**, 142 (1961).

[214] L. P. Kadanoff and G. Baym, *Quantum statistical mechanics*, New York, W.A. Benjamin, 1962.

[215] L. V. Keldysh, *Diagram technique for nonequilibrium processes*, JETP **20**, 1080 (1964).

[216] L. Boltzmann, *Weitere Studien über das Wärmegleichgewicht unter Gasmolekülen*, Wiener Berichte **66**, 275 (1872).

[217] J. Ziman, *The Theory of Transport Phenomena in Solids*, Oxford University Press, 1960.

[218] J. Rammer, *Quantum Field Theory of Non-equilibrium States*, Cambridge University Press, 2007.

[219] J. Rammer and H. Smith, *Quantum field-theoretical methods in transport theory of metals*, Reviews of Modern Physics **58**, 323 (1986).

[220] A. Abrikosov, L. Gorkov, and I. Dzyaloshinskii, *Methods of quantum field theory in statistical physics*, Dover, 1963.

[221] A. Larkin and Y. Ovchinnikov, *Nonlinear conductivity of superconductors in the mixed state*, JETP **41**, 960 (1975).

[222] G. Baym and L. P. Kadanoff, *Conservation Laws and Correlation Functions*, Physical Review **124**, 287 (1961).

[223] G. Baym, *Self-consistent approximations in many-body systems*, Physical Review **127**, 1391 (1962).

[224] J. M. Luttinger and J. C. Ward, *Ground-State Energy of a Many-Fermion System. II*, Physical Review **118**, 1417 (1960).

[225] G. Stefanucci and R. van Leeuwen, *Nonequilibrium Many-Body Theory of Quantum Systems*, volume 54, Cambridge University Press, Cambridge, 2013.

[226] C. Wickles and W. Belzig, *Effective quantum theories for Bloch dynamics in inhomogeneous systems with nontrivial band structure*, Physical Review B **88**, 045308 (2013).

[227] B. Bezzerides and D. F. DuBois, *Many-Body Theory for Quantum Kinetic Equations*, Physical Review **168**, 233 (1968).

[228] X.-G. Wen, *Quantum Field Theory of Many-Body Systems*, Oxford University Press, 2007.

[229] A. Garg, D. Rasch, E. Shimshoni, and A. Rosch, *Large Violation of the Wiedemann-Franz Law in Luttinger Liquids*, Physical Review Letters **103**, 096402 (2009).

[230] S. Mandt, *Transport and Non-Equilibrium Dynamics in Optical Lattices. From Expanding Atomic Clouds to Negative Absolute Temperatures*, PhD thesis, Universität zu Köln, 2012.

[231] N. Schlünzen, J.-P. Joost, F. Heidrich-Meisner, and M. Bonitz, *Nonequilibrium dynamics in the one-dimensional Fermi-Hubbard model: Comparison of the nonequilibrium Green-functions approach and the density matrix renormalization group method*, Physical Review B **95**, 165139 (2017).

[232] N. Schlünzen and M. Bonitz, *Nonequilibrium Green Functions Approach to Strongly Correlated Fermions in Lattice Systems*, Contributions to Plasma Physics **56**, 5 (2016).

[233] N. Schlünzen, S. Hermanns, M. Bonitz, and C. Verdozzi, *Dynamics of strongly correlated fermions: Ab initio results for two and three dimensions*, Physical Review B **93**, 035107 (2016).

[234] K. Balzer, S. Bauch, and M. Bonitz, *Time-dependent second-order Born calculations for model atoms and molecules in strong laser fields*, Physical Review A **82**, 033427 (2010).

[235] A. Rios, B. Barker, M. Buchler, and P. Danielewicz, *Towards a nonequilibrium Green's function description of nuclear reactions: One-dimensional mean-field dynamics*, Annals of Physics **326**, 1274 (2011).

[236] M. Bonitz, T. Bornath, D. Kremp, M. Schlanges, and W. D. Kraeft, *Quantum Kinetic Theory for Laser Plasmas. Dynamical Screening in Strong Fields*, Contributions to Plasma Physics **39**, 329 (1999).

[237] P. Lipavský, V. Špička, and B. Velický, *Generalized Kadanoff-Baym ansatz for deriving quantum transport equations*, Physical Review B **34**, 6933 (1986).

[238] M. Genske and A. Rosch, *Floquet-Boltzmann equation for periodically driven Fermi systems*, Physical Review A **92**, 062108 (2015).

[239] A. Lazarides, A. Das, and R. Moessner, *Periodic Thermodynamics of Isolated Quantum Systems*, Physical Review Letters **112**, 150401 (2014).

[240] M. Bukov, M. Heyl, D. A. Huse, and A. Polkovnikov, *Heating and many-body resonances in a periodically driven two-band system*, Physical Review B **93**, 155132 (2016).

[241] M. Rigol, V. Dunjko, and M. Olshanii, *Thermalization and its mechanism for generic isolated quantum systems*, Nature **452**, 854 (2008).

[242] A. Russomanno, A. Silva, and G. E. Santoro, *Periodic Steady Regime and Interference in a Periodically Driven Quantum System*, Physical Review Letters **109**, 257201 (2012).

[243] D. Basko, I. Aleiner, and B. Altshuler, *Metal–insulator transition in a weakly interacting many-electron system with localized single-particle states*, Annals of Physics **321**, 1126 (2006).

[244] P. Ponte, A. Chandran, Z. Papić, and D. A. Abanin, *Periodically driven ergodic and many-body localized quantum systems*, Annals of Physics **353**, 196 (2015).

[245] A. Lazarides, A. Das, and R. Moessner, *Fate of Many-Body Localization Under Periodic Driving*, Physical Review Letters **115**, 030402 (2015).

[246] J. Rehn, A. Lazarides, F. Pollmann, and R. Moessner, *How periodic driving heats a disordered quantum spin chain*, Physical Review B - Condensed Matter and Materials Physics **94** (2016).

[247] D. A. Abanin, W. De Roeck, and F. Huveneers, *Theory of many-body localization in periodically driven systems*, Annals of Physics **372**, 1 (2016).

[248] S. Gopalakrishnan, M. Knap, and E. Demler, *Regimes of heating and dynamical response in driven many-body localized systems*, Physical Review B **94**, 094201 (2016).

[249] V. Gritsev and A. Polkovnikov, *Integrable Floquet dynamics*, arXiv:1701.05276 (2017).

[250] A. Russomanno, G. E. Santoro, and R. Fazio, *Entanglement entropy in a periodically driven Ising chain*, Journal of Statistical Mechanics: Theory and Experiment **2016**, 073101 (2016).

[251] T. J. G. Apollaro, G. M. Palma, and J. Marino, *Entanglement entropy in a periodically driven quantum Ising ring*, Physical Review B **94**, 134304 (2016).

[252] M. Rigol, V. Dunjko, V. Yurovsky, and M. Olshanii, *Relaxation in a Completely Integrable Many-Body Quantum System: An Ab Initio Study of the Dynamics of the Highly Excited States of 1D Lattice Hard-Core Bosons*, Physical Review Letters **98**, 050405 (2007).

[253] F. Lange, Z. Lenarčič, and A. Rosch, *Pumping approximately integrable systems*, arXiv:1608.03563 (2016).

[254] K. I. Seetharam, C.-E. Bardyn, N. H. Lindner, M. S. Rudner, and G. Refael, *Controlled Population of Floquet-Bloch States via Coupling to Bose and Fermi Baths*, Physical Review X **5**, 041050 (2015).

[255] T. Iadecola, T. Neupert, and C. Chamon, *Occupation of topological Floquet bands in open systems*, Physical Review B **91**, 235133 (2015).

[256] M. Babadi, M. Knap, I. Martin, G. Refael, and E. Demler, *The theory of parametrically amplified electron-phonon superconductivity*, arXiv:1702.02531 (2017).

[257] M. Bukov, S. Gopalakrishnan, M. Knap, and E. Demler, *Prethermal floquet steady states and instabilities in the periodically driven, weakly interacting bose-hubbard model*, Physical Review Letters **115**, 205301 (2015).

[258] D. Abanin, W. De Roeck, F. Huveneers, and W. W. Ho, *A rigorous theory of many-body prethermalization for periodically driven and closed quantum systems*, arXiv:1702.02942 (2015).

[259] E. Canovi, M. Kollar, and M. Eckstein, *Stroboscopic prethermalization in weakly interacting periodically driven systems*, Physical Review E **93**, 012130 (2016).

[260] A. Chandran and S. L. Sondhi, *Interaction-stabilized steady states in the driven O (N) model*, Physical Review B **93**, 174305 (2016).

[261] D. A. Abanin, W. De Roeck, W. W. Ho, and F. Huveneers, *Effective Hamiltonians, prethermalization, and slow energy absorption in periodically driven many-body systems*, Physical Review B **95**, 014112 (2017).

[262] S. A. Weidinger and M. Knap, *Floquet prethermalization and regimes of heating in a periodically driven, interacting quantum system*, Scientific Reports **7**, 45382 (2017).

[263] D. A. Abanin, W. De Roeck, and F. Huveneers, *Exponentially Slow Heating in Periodically Driven Many-Body Systems*, Physical Review Letters **115**, 256803 (2015).

[264] T. Kuwahara, T. Mori, and K. Saito, *Floquet–Magnus theory and generic transient dynamics in periodically driven many-body quantum systems*, Annals of Physics **367**, 96 (2016).

[265] T. Mori, T. Kuwahara, and K. Saito, *Rigorous Bound on Energy Absorption and Generic Relaxation in Periodically Driven Quantum Systems*, Physical Review Letters **116**, 120401 (2016).

[266] D. Poletti and C. Kollath, *Slow quench dynamics of periodically driven quantum gases*, Physical Review A **84**, 013615 (2011).

[267] C. Sträter, S. C. L. Srivastava, and A. Eckardt, *Floquet Realization and Signatures of One-Dimensional Anyons in an Optical Lattice*, Physical Review Letters **117**, 205303 (2016).

[268] N. Tsuji, T. Oka, P. Werner, and H. Aoki, *Dynamical Band Flipping in Fermionic Lattice Systems: An ac-Field-Driven Change of the Interaction from Repulsive to Attractive*, Physical Review Letters **106**, 236401 (2011).

[269] S. Choudhury and E. J. Mueller, *Stability of a Floquet Bose-Einstein condensate in a one-dimensional optical lattice*, Physical Review A **90**, 013621 (2014).

[270] S. Choudhury and E. J. Mueller, *Transverse collisional instabilities of a Bose-Einstein condensate in a driven one-dimensional lattice*, Physical Review A **91**, 023624 (2015).

[271] D. Martinez, R. Molina, and B. Hu, *Length-dependent oscillations in the dc conductance of laser-driven quantum wires*, Physical Review B **78**, 045428 (2008).

[272] S. Morina, O. V. Kibis, A. A. Pervishko, and I. A. Shelykh, *Transport properties of a two-dimensional electron gas dressed by light*, Physical Review B **91**, 155312 (2015).

[273] A. K. Eissing, V. Meden, and D. M. Kennes, *Renormalization in Periodically Driven Quantum Dots*, Physical Review Letters **116**, 026801 (2016).

[274] M. Eckstein and P. Werner, *Two-channel Kondo physics in a periodically driven single-impurity Anderson model*, arXiv:1704.02300 (2017).

[275] H. Dehghani, T. Oka, and A. Mitra, *Out-of-equilibrium electrons and the Hall conductance of a Floquet topological insulator*, Physical Review B **91**, 155422 (2015).

[276] H. Dehghani and A. Mitra, *Floquet topological systems in the vicinity of band crossings: Reservoir-induced coherence and steady-state entropy production*, Physical Review B **93**, 245416 (2016).

[277] L. Ruocco and Á. Gómez-León, *Transport signatures in topological systems coupled to ac fields*, Physical Review B **95**, 064302 (2017).

[278] N. Tsuji, T. Oka, and H. Aoki, *Nonequilibrium Steady State of Photoexcited Correlated Electrons in the Presence of Dissipation*, Physical Review Letters **103**, 047403 (2009).

[279] Y. Murakami, N. Tsuji, M. Eckstein, and P. Werner, *Nonequilibrium steady states and transient dynamics of superconductors under phonon driving*, arXiv:1702.02942 (2017).

[280] M. Knap, M. Babadi, G. Refael, I. Martin, and E. Demler, *Dynamical Cooper pairing in nonequilibrium electron-phonon systems*, Physical Review B **94**, 214504 (2016).

[281] N. Yao, A. Potter, I.-D. Potirniche, and A. Vishwanath, *Discrete Time Crystals: Rigidity, Criticality, and Realizations*, Physical Review Letters **118**, 030401 (2017).

[282] M. Weinberg et al., *Multiphoton interband excitations of quantum gases in driven optical lattices*, Physical Review A **92**, 043621 (2015).

[283] T. Bilitewski and N. R. Cooper, *Population dynamics in a Floquet realization of the Harper-Hofstadter Hamiltonian*, Physical Review A **91**, 063611 (2015).

[284] T. Bilitewski and N. R. Cooper, *Scattering theory for Floquet-Bloch states*, Physical Review A **91**, 033601 (2015).

[285] N. Tsuji, T. Oka, and H. Aoki, *Correlated electron systems periodically driven out of equilibrium: Floquet+DMFT formalism*, Physical Review B **78**, 235124 (2008).

[286] H. Aoki et al., *Nonequilibrium dynamical mean-field theory and its applications*, Reviews of Modern Physics **86**, 779 (2014).

[287] M. Bukov, M. Kolodrubetz, and A. Polkovnikov, *Schrieffer-Wolff Transformation for Periodically Driven Systems: Strongly Correlated Systems with Artificial Gauge Fields*, Physical Review Letters **116**, 125301 (2016).

[288] A. K. Eissing, V. Meden, and D. M. Kennes, *Functional renormalization group in Floquet space*, Physical Review B **94**, 245116 (2016).

[289] C. Zhang, F. Pollmann, S. L. Sondhi, and R. Moessner, *Density-matrix renormalization group study of many-body localization in floquet eigenstates*, Annalen der Physik , 1600294 (2017).

[290] F. Faisal, *Floquet Green's function method for radiative electron scattering and multiphoton ionization in a strong laser field*, Computer Physics Reports **9**, 57 (1989).

[291] T. Brandes, *Truncation method for Green's functions in time-dependent fields*, Physical Review B **56**, 1213 (1997).

[292] A. Robertson, V. M. Galitski, and G. Refael, *Dynamic Stimulation of Quantum Coherence in Systems of Lattice Bosons*, Physical Review Letters **106**, 165701 (2011).

[293] R. Frank, *Coherent control of Floquet-mode dressed plasmon polaritons*, Physical Review B **85**, 195463 (2012).

[294] W.-R. Lee and K. Park, *Dielectric breakdown via emergent nonequilibrium steady states of the electric-field-driven Mott insulator*, Physical Review B **89**, 205126 (2014).

[295] G. Sundaram and Q. Niu, *Wave-packet dynamics in slowly perturbed crystals: Gradient corrections and Berry-phase effects*, Physical Review B **59**, 14915 (1999).

[296] M. Pukrop, *Streuung in periodisch getriebenen Quantensystemen*, BSc thesis (2016).

[297] M. Mitrano et al., *Possible light-induced superconductivity in K3C60 at high temperature.*, Nature **530**, 461 (2016).

[298] S. Diehl et al., *Quantum states and phases in driven open quantum systems with cold atoms*, Nature Physics **4**, 878 (2008).

[299] L. M. Sieberer, M. Buchhold, and S. Diehl, *Keldysh field theory for driven open quantum systems*, Reports on Progress in Physics **79**, 096001 (2016).

[300] T. Uehlinger et al., *Artificial Graphene with Tunable Interactions*, Physical Review Letters **111**, 185307 (2013).

[301] A. H. Castro Neto, F. Guinea, N. M. R. Peres, K. S. Novoselov, and A. K. Geim, *The electronic properties of graphene*, Reviews of Modern Physics **81**, 109 (2009).

[302] C.-C. Chien, S. Peotta, and M. Di Ventra, *Quantum transport in ultracold atoms*, Nature Physics **11**, 998 (2015).

[303] A. Sommer, M. Ku, G. Roati, and M. W. Zwierlein, *Universal spin transport in a strongly interacting Fermi gas*, Nature **472**, 201 (2011).

[304] S. Krinner, D. Stadler, D. Husmann, J.-P. Brantut, and T. Esslinger, *Observation of quantized conductance in neutral matter*, Nature **517**, 64 (2014).

[305] D. Xiao, Y. Yao, Z. Fang, and Q. Niu, *Berry-Phase Effect in Anomalous Thermoelectric Transport*, Physical Review Letters **97**, 026603 (2006).

[306] R. Karplus and J. M. Luttinger, *Hall Effect in Ferromagnetics*, Physical Review **95**, 1154 (1954).

[307] N. Nagaosa, J. Sinova, S. Onoda, A. H. MacDonald, and N. P. Ong, *Anomalous Hall effect*, Reviews of Modern Physics **82**, 1539 (2010).

[308] J. Smit, *The spontaneous hall effect in ferromagnetics I*, Physica **21**, 877 (1955).

[309] J. Smit, *The spontaneous hall effect in ferromagnetics II*, Physica **24**, 39 (1958).

[310] N. A. Sinitsyn, A. H. MacDonald, T. Jungwirth, V. K. Dugaev, and J. Sinova, *Anomalous Hall effect in a two-dimensional Dirac band: The link between the Kubo-Streda formula and the semiclassical Boltzmann equation approach*, Physical Review B **75**, 045315 (2007).

[311] T. Liang et al., *Anomalous Nernst Effect in the Dirac Semimetal Cd 3 As 2*, Physical Review Letters **118**, 136601 (2017).

[312] N. R. Cooper, B. I. Halperin, and I. M. Ruzin, *Thermoelectric response of an interacting two-dimensional electron gas in a quantizing magnetic field*, Physical Review B **55**, 2344 (1997).

[313] D. Culcer et al., *Semiclassical spin transport in spin-orbit-coupled bands*, Physical Review Letters **93**, 046602 (2004).

[314] S. Onoda, N. Sugimoto, and N. Nagaosa, *Quantum transport theory of anomalous electric, thermoelectric, and thermal Hall effects in ferromagnets*, Physical Review B **77**, 165103 (2008).

[315] Z. Lenarčič, *private communication*, 2016.

[316] B. I. Halperin, *Quantized Hall conductance, current-carrying edge states, and the existence of extended states in a two-dimensional disordered potential*, Physical Review B **25**, 2185 (1982).

[317] B. A. Bernevig, T. L. Hughes, and S.-C. Zhang, *Quantum Spin Hall Effect and Topological Phase Transition in HgTe Quantum Wells*, Science **314** (2006).

[318] M. König et al., *Quantum Spin Hall Insulator State in HgTe Quantum Wells*, Science **318** (2007).

[319] M. Mancini et al., *Observation of chiral edge states with neutral fermions in synthetic Hall ribbons*, Science **349**, 1510 (2015).

[320] B. K. Stuhl, H.-I. Lu, L. M. Aycock, D. Genkina, and I. B. Spielman, *Visualizing edge states with an atomic Bose gas in the quantum Hall regime*, Science **349**, 1514 (2015).

[321] M. Leder, *Quantensimulation von relativistischen Effekten mit ultrakalten Atomen in variablen optischen Gitterpotentialen*, PhD thesis, 2016.

[322] W. P. Su, J. R. Schrieffer, and A. J. Heeger, *Solitons in Polyacetylene*, Physical Review Letters **42**, 1698 (1979).

[323] W. P. Su, J. R. Schrieffer, and A. J. Heeger, *Soliton excitations in polyacetylene*, Physical Review B **22**, 2099 (1980).

[324] M. Leder, *private communication*, 2016.

[325] E. P. Wigner, *On the Distribution of the Roots of Certain Symmetric Matrices*, The Annals of Mathematics **67**, 325 (1958).

[326] F. J. Dyson, *Statistical Theory of the Energy Levels of Complex Systems. I*, Journal of Mathematical Physics **3**, 140 (1962).

[327] M. R. Zirnbauer, *Riemannian symmetric superspaces and their origin in random-matrix theory*, Journal of Mathematical Physics **37**, 4986 (1996).

[328] A. Altland and M. R. Zirnbauer, *Nonstandard symmetry classes in mesoscopic normal-superconducting hybrid structures*, Physical Review B (Condensed Matter) **55**, 1142 (1997).

[329] A. P. Schnyder, S. Ryu, A. Furusaki, and A. W. W. Ludwig, *Classification of topological insulators and superconductors in three spatial dimensions*, Physical Review B **78**, 195125 (2008).

[330] S. Ryu and Y. Hatsugai, *Topological Origin of Zero-Energy Edge States in Particle-Hole Symmetric Systems*, Physical Review Letters **89**, 077002 (2002).

[331] M. Sitte, *Quantum Hall Effect and Surface Criticality in 3D Topological Insulators*, PhD thesis, Universität zu Köln, 2012.

[332] A. J. Heeger, S. Kivelson, J. R. Schrieffer, and W. P. Su, *Solitons in conducting polymers*, Reviews of Modern Physics **60**, 781 (1988).

[333] R. Jackiw and C. Rebbi, *Solitons with fermion number 1/2*, Physical Review D **13**, 3398 (1976).

[334] C. Kane, *Topological Insulators*, Contemporary Concepts of Condensed Matter Science **6**, 3 (2013).

[335] L. Lamata, J. León, T. Schätz, and E. Solano, *Dirac Equation and Quantum Relativistic Effects in a Single Trapped Ion*, Physical Review Letters **98**, 253005 (2007).

[336] R. Gerritsma et al., *Quantum simulation of the Dirac equation*, Nature **463**, 68 (2010).

[337] M. Leder, C. Grossert, M. Weitz, G. Cennini, and M. Weitz, *Veselago lensing with ultracold atoms in an optical lattice*, Nature Communications **5**, 063622 (2014).

[338] T. Salger, C. Geckeler, S. Kling, and M. Weitz, *Atomic Landau-Zener Tunneling in Fourier-Synthesized Optical Lattices*, Physical Review Letters **99**, 190405 (2007).

[339] C. Grossert, M. Leder, and M. Weitz, *Phase dependent loading of Bloch bands and quantum simulation of relativistic wave equation predictions with ultracold atoms in variably shaped optical lattice potentials*, Journal of Modern Optics **63**, 1805 (2016).

[340] L. P. Pitaevskii, *Vortex lines in an imperfect Bose gas*, JETP **13**, 646 (1961).

[341] E. P. Gross, *Structure of a quantized vortex in boson systems*, Il Nuovo Cimento **20**, 454 (1961).

[342] E. P. Gross, *Hydrodynamics of a Superfluid Condensate*, Journal of Mathematical Physics **4**, 195 (1963).

[343] C. E. Wieman, S. Stringari, M. Inguscio, and F. Società italiana di, *Bose-Einstein Condensation in Atomic Gases*, in *Bose-Einstein Condensation in Atomic Gases*, chapter Theory of, IOS Press, 1999.

[344] F. Dalfovo, S. Giorgini, L. P. Pitaevskii, and S. Stringari, *Theory of Bose-Einstein condensation in trapped gases*, Reviews of Modern Physics **71**, 463 (1999).

[345] A. J. Leggett, *Bose-Einstein condensation in the alkali gases: Some fundamental concepts*, Reviews of Modern Physics **73**, 307 (2001).

[346] L. Pitaevskii and S. Stringari, *Bose-Einstein condensation*, Oxford University Press, 2003.

[347] C. Pethick and H. Smith, *Bose-Einstein Condensation in Dilute Gases*, Cambridge University Press, 2 edition, 2008.

[348] X. Antoine and R. Duboscq, *GPELab, a Matlab toolbox to solve Gross–Pitaevskii equations I: Computation of stationary solutions*, Computer Physics Communications **185**, 2969 (2014).

[349] X. Antoine and R. Duboscq, *GPELab, a Matlab toolbox to solve Gross-Pitaevskii equations II: Dynamics and stochastic simulations*, Computer Physics Communications **193**, 95 (2015).

[350] X. Chen, Z.-C. Gu, and X.-G. Wen, *Local unitary transformation, long-range quantum entanglement, wave function renormalization, and topological order*, Physical Review B **82**, 155138 (2010).

[351] O. Vafek and A. Vishwanath, *Dirac Fermions in Solids: From High-T c Cuprates and Graphene to Topological Insulators and Weyl Semimetals*, Annual Review of Condensed Matter Physics **5**, 83 (2014).

[352] B. Wu and Q. Niu, *Landau and dynamical instabilities of the superflow of Bose-Einstein condensates in optical lattices*, Physical Review A **64**, 061603 (2001).

[353] Y. Nakamura, M. Mine, M. Okumura, and Y. Yamanaka, *Condition for emergence of complex eigenvalues in the Bogoliubov–de Gennes equations*, Physical Review A **77**, 043601 (2008).

[354] A. L. Fetter, *Nonuniform states of an imperfect bose gas*, Annals of Physics **70**, 67 (1972).

[355] B. Wu and Q. Niu, *Superfluidity of Bose–Einstein condensate in an optical lattice: Landau–Zener tunnelling and dynamical instability*, New Journal of Physics **5**, 104 (2003).

[356] K. Kobayashi, Y. Nakamura, M. Mine, and Y. Yamanaka, *Analytical study of the splitting process of a multiply-quantized vortex in a Bose–Einstein condensate and collaboration of the zero and complex modes*, Annals of Physics **324**, 2359 (2009).

[357] J. Takahashi, Y. Nakamura, and Y. Yamanaka, *Dynamical instability induced by the zero mode under symmetry breaking external perturbation*, Annals of Physics **347**, 250 (2014).

[358] N. Bogoliubov, *On the Theory of Superfluidity*, Journal of Physics (USSR) **11**, 23 (1947).

[359] P. G. De Gennes, *Superconductivity of Metals and Alloys*, Advanced Book Program, Perseus Books, 1999.

[360] M. Lewenstein and L. You, *Quantum Phase Diffusion of a Bose-Einstein Condensate*, Physical Review Letters **77**, 3489 (1996).

[361] M. Mine, M. Okumura, T. Sunaga, and Y. Yamanaka, *Quantum field theoretical description of unstable behavior of trapped Bose–Einstein condensates with complex eigenvalues of Bogoliubov–de Gennes equations*, Annals of Physics **322**, 2327 (2007).

[362] Y. Kawaguchi and T. Ohmi, *Splitting instability of a multiply charged vortex in a Bose-Einstein condensate*, Physical Review A **70**, 043610 (2004).

Danksagung

Zum Abschluss dieses lehreichen, spannenden und manchmal auch sehr fordernden Kapitels meines Lebens möchte ich mich bei allen Wegbegleitern ausdrücklich bedanken. Vor allem gilt mein Dank meinem Betreuer Prof. Achim Rosch. Ohne seine schier unendliche Begeisterung für die Physik und den damit verbundenen regen Austausch wäre diese Arbeit in dieser Form nicht zustande gekommen. Zudem geht mein großer Dank an Prof. Sebastian Diehl für die Übernahme der Zeitgutachterschaft sowie an Prof. Markus Grüninger für die unkomplizierte Übernahme des Prüfungsvorsitzes.

Ein spezieller Dank gilt auch Prof. Mark Rudner vom Niels Bohr Institut in Kopenhagen, welcher mich mit großer Gastfreundschaft empfangen und mit selbiger während meines Aufenthaltes in Dänemark betreut hat. Für den fachlichen Austausch und die spannende Zusammenarbeit der letzten Jahre möchte ich außerdem Prof. Martin Weitz und Dr. Martin Leder von der Universität Bonn danken. Ein großes Dankeschön geht zudem an Dr. Andreas Sindermann, der bei IT- aber auch sonstigen Problem stets zur Stelle war und seine Hilfe angeboten hat.

Während der letzten Jahre hatte ich die große Freude durch die "Bonn-Cologne Graduate School" sowie die "Deutsche Telekom Stiftung" gefördert zu werden. Mein ganz besonderer Dank gilt daher diesen beiden Organisationen, und hierbei vor allem Dr. Petra Neubauer-Guenther und Christiane Frense-Heck.

Für das gewissenhafte Korrekturlesen großer Teile meiner Arbeit bin ich Philipp Weiß, Henry Legg, Kevin O'Brien, Jan Gelhausen, Fabian Holling und Bernd Große Jüttermann zum Dank verpflichtet.

In den vergangenen Jahren habe ich das Büro mit Maria Hermanns, Christoph Schütte, Sarah Schröter, Laura Köhler und Jan Müller teilen dürfen. Vielen Dank für den Spaß im Büroalltag und die angenehme Atmosphäre. Von all den zahlreichen Gesichtern, die mir während meiner Arbeit begegnet sind, möchte ich mich vor allem bei Jonathan Lux, Stephan Buhrandt, Max Gerlach, Peter Bröcker, Carsten Bauer, Johannes Helmes, Finn Lasse Büßen und Zala Lenarčič für das tolle kollegiale Verhältnis bedanken. Ein ganz besonderer Dank geht an Benjamin Mille und Robert Bamler für die geteilte Momente auch außerhalb des Instituts und für die Freundschaft.

Zu guter Letzt möchte ich mich bei meinen engsten Freunden, meiner Familie, meinen Eltern und meinem Bruder Ferdinand bedanken, die es immer wieder schafften mich vor allem in schwierigen Zeiten neu aufzurichten und nie verzagten mir Kraft zu schenken. Mein größter Dank gilt Jana, die mir in allen komplizierten Momenten den Rücken freigehalten und mich jeder Zeit bedingungslos unterstützt hat.

Erklärung

Ich versichere, dass ich die von mir vorgelegte Dissertation selbständig angefertigt, die benutzten Quellen und Hilfsmittel vollständig angegeben und die Stellen der Arbeit – einschließlich Tabellen, Karten und Abbildungen –, die anderen Werken im Wortlaut oder dem Sinn nach entnommen sind, in jedem Einzelfall als Entlehnung kenntlich gemacht habe; dass diese Dissertation noch keiner anderen Fakultät oder Universität zur Prüfung vorgelegen hat; dass sie – abgesehen von unten angegebenen Teilpublikationen – noch nicht veröffentlicht worden ist sowie, dass ich eine solche Veröffentlichung vor Abschluss des Promotionsverfahrens nicht vornehmen werde. Die Bestimmungen der Promotionsordnung sind mir bekannt. Die von mir vorgelegte Dissertation ist von Prof. Dr. Achim Rosch betreut worden.

Köln, den 12. Oktober 2017

Maximilian Genske

Teilpublikationen

- M. Genske and A. Rosch,
  Directed motion of doublons and holes in periodically driven Mott insulators,
  Phys. Rev. A **90**, 043637 (2014)
- M. Genske and A. Rosch,
  Floquet-Boltzmann equation for periodically driven Fermi systems,
  Phys. Rev. A **92**, 062108 (2015)
- M. Leder, C. Grossert, L. Sitta, M. Genske, A. Rosch and M. Weitz,
  Real-space imaging of a topologically protected edge state with ultracold atoms in an amplitude-chirped optical lattice,
  Nat. Commun. **7**, 13112 (2016)